SEVENTH INTERNATIONAL CONFERENCE

ON

HIGH-PERFORMANCE MARINE VEHICLES

HIPER'10

Melbourne, Florida, USA, October 13-15, 2010

Dr. Ing. Prasanta K Sahoo, FRINA, MSNAME (Editor)

ISBN 978-1-4507-3231-4

ISBN 978-1-4507-3231-4

90000>

9 781450 732314

Printed & Published at

Florida Institute of Technology

150 W University Boulevard, Melbourne, FL 32901

USA

We acknowledge gratefully the support of our sponsors:

Florida Institute of Technology
High Tech with a Human Touch™

INTERNATIONAL SCIENTIFIC COMMITTEE

Dr. Prasanta K Sahoo, Florida Institute of Technology, USA
(Convenor) psahoo@fit.edu

Prof. Volker Bertram, Germanischer Llyod, Germany

Prof. Lawrence J Doctors, The University of New South Wales, Sydney, Australia

Prof. S K Bhattacharyya, IIT Madras, India

Prof. Geoffrey Swain, Florida Institute of Technology, USA

Dr. Magnus Lindgren, DNV, Australia & New Zealand, Australia

Prof V Anantha Subramanian, IIT, Madras, India

Prof. Carlo Bertorello, The University of Naples Federico II, Italy

Dr. Steven Jachec, Florida Institute of Technology, USA

Prof. Jeom K Paik, Pusan National University, South Korea

Prof. Jerzy Matusiak, Helsinki University of Technology, Finland

Dr. Stephen Wood, Florida Institute of Technology, USA

Dr. Stefano Brizzolara, University of Geno, Italy

Dr. R A Shenoi, University of Southampton, UK

Dr. Neil Bose, National Centre for Maritime Engg. and Hydrodynamics , Australia

Dr. Stefan Harries, Friendship Systems Gmbh, Germany

Dr. Ermina Begovic, University of Naples Federico II, Italy

Table of Contents **Page**

Seventh International Conference
On High-Performance Marine Vehicles
Melbourne, Florida, USA
13-15 October 2010

PREDICTING THE IMPACT OF DESIGN AND REQUIREMENT CHANGES ON HIGH PERFORMANCE AND CONVENTIONAL CRAFT

John Almeter, Naval Surface Warfare Center, Carderock Division, Norfolk, Virginia, USA,
John.almeter@navy.mil
David Eberhardt, Naval Surface Warfare Center, Carderock Division, Norfolk, Virginia, USA,
David.eberhardt@navy.mil

ABSTRACT

The paper presents a simple method for predicting the impact of design and requirement changes on high performance and conventional craft using a revised and expanded Normand's Number approach. The historical data and reports commonly used to calculate the Normand Number are not relevant to many types of high performance craft. The work presented overcomes these limitations. The estimated impacts on displacement, speed, required power and range for changes in payloads, hull materials, propulsion systems and margins can be predicted with the simple hand calculations and data contained in this paper. The revised and expanded Normand's Number approach is an easy and effective way of assessing and presenting the weight, speed and range sensitivities of a design. This can aid designers, operators and owners in making design and requirements decisions. The methods described in this paper can be applied to almost any type craft, including slow speed tankers, warships, planing craft, high speed multi-hulls and air cushion vehicles.

BACKGROUND

The Normand Number is the ratio of the total weight increase to the weight of a design change of a vessel while keeping the design performance unchanged (same speed, range and structural strength). As an example, adding a 1,000 kg piece of equipment to a ship could have a total weight impact of 3,000 kg to maintain the same speed, range, etc. The extra 2,000 kg accounts for increased horsepower, fuel, and structure. In this example, the Normand Number is three (3 = 3,000 kg / 1,000 kg). The weight of a design change (increase or decrease) could come from almost anything, including:

Extra or deleted equipment
Increased or decreased speed
Increased or decreased range
Heavier or lighter propulsion machinery
Heavier or lighter hull materials
More or less efficient propulsion machinery
Larger or smaller margins

Performance changes, such as increased speed, are treated as added weights. The total weight impact of the performance change is the Normand Number times the weight impact of the performance change.

Very simple and fast methods have been developed to predict the Normand Number for a wide variety of vessels. Harvald (1964) gives the Normand Number for barges, tankers, tugs, ferries, and numerous other displacement vessels. Hunbaker (1920) provides the calculation of the Normand Number for a dirigible. If a vessel's Normand Number is known, not only can the total weight impact of a change be calculated in minutes by hand, but also the change in fuel capacity and installed power.

The Normand Number has gone by different names and symbols and its history is discussed in Harvald (1964) and Toby (2009). The Normand Number approach is over a hundred years old.

NOMENCLATURE

Δ	Initial full load displacement
Δ_n	Full load displacement after changes
α	Displacement exponent for structural weight, $W_{100} \approx \Delta^{\alpha}$
β	Displacement exponent for propulsion weight, $W_{200} \approx \Delta^{\beta}$
μ	Displacement exponent for fuel weight, $W_{fp} \approx \Delta^{\mu}$
ρ	Mass density of water
A_n	Almeter Number, equation 14
B	Beam
B_c	Chine beam
$D\Delta$	Total change in displacement from DW_0
DW_0	Weight of a design change
g	Accelerations of gravity
F_{nL}	Froude Number based on length
$F_{n\nabla}$	Volumetric Froude Number
L	Length
LCG	Longitudinal center of gravity from the transom
N_n	Normand Number
P_n	New required power
P_o	Original power
R/W_n	New resistance to weight ratio
R/W_o	Original resistance to weight ratio
T	Draft
V	Speed
W_0	Portion of full load weight that is independent of displacement such as cargo
W_{100}	Structural weight (SWBS 100)
W_{200}	Propulsion system weight (SWBS 200)
W_{fp}	Propulsion fuel weight (not cargo fuel weight)

KEYWORDS

Normand Number, Preliminary Design, Concept Design, Feasibility Design, Weight Estimating, Synthesis, High Speed Craft, High Speed Vessel, High Performance Marine Vehicle

HISTORIC CALCULATION OF THE NORMAND NUMBER AND ITS DERIVATION

Detailed derivations for the approximations of the Normand Number are given in Hovgaard (1920), Harvald (1964), Manning (1945), Toby (2009), and Manning (1956). An alternate and simplified derivation of the approximation for the Normand Number is given below.

Displacement defined below in equation 1.

$$\Delta = W_0 + W_a + W_b + W_c + \ldots \tag{1}$$

Where

Δ	Full load displacement
W_0	Portion of full load weight that is independent of displacement such as cargo

W_a, W_b , W_c,, etc. are the portions of the full load weight that are proportional to full load displacement raised to a, b, c, etc., such as fuel and structure. Thus:

$$W_a = m\Delta^a \quad (2)$$
$$W_b = n\Delta^b$$
$$W_c = o\Delta^c$$
Etc.

Where m, n, o, etc. are constants for a given vessel.

If equation 2 is substituted into equation 1 and differentiated, the following results:

$$D\Delta = DW_0 + (am\Delta^{a-1} + bn\Delta^{b-1} + co\Delta^{c-1} + \ldots)\ D\Delta \quad (3)$$

This is a good estimate for $D\Delta$ as long as $D\Delta$ is a small percentage of Δ. DW_0 is the increase in cargo weight, the weight from additional equipment or anything else and $D\Delta$ is the overall weight increase resulting from DW_0. Equation 3 is manipulated to determine DW_0 as below.

$$DW_0 = D\Delta\ (1 - (am\Delta^{a-1} + bn\Delta^{b-1} + co\Delta^{c-1} + \ldots)) \quad (4)$$

As discussed earlier, the definition of the Normand Number is:

$$N_n = D\Delta / DW_0 \quad (5)$$

Substituting equation 4 into the definition of the Normand Number (equation 5) results in:

$$N_n = 1 / (1 - (am\Delta^{a-1} + bn\Delta^{b-1} + co\Delta^{c-1} + \ldots)) \quad (6)$$

If the numerator and denominator are both multiplied by Δ, the following happens:

$$N_n = \Delta / (\Delta - (am\Delta^a + bn\Delta^b + co\Delta^c + \ldots)) \quad (7)$$

If we substitute equation 2 into equation 7, the classic estimate below for the Normand Number is found.

$$N_n = \Delta / (\Delta - (aW_a + bW_b + cW_c + \ldots)) \quad (8)$$

The above equation is a good estimate for the Normand Number as long as the total change in displacement is a small percentage of the initial displacement, Δ.

The cited references of this paper provide calculated estimates for the Normand Number and values for the coefficients and constants required to predict the Normand Number for almost any type of vessel.

LIMITATIONS AND PROBLEMS WITH TRADITIONAL ESTIMATION OF THE NORMAND NUMBER

The Normand Number is a mathematically sound approach for predicting the total weight impact from design changes. Its derivation is well established. The key to the successful application of the Normand Number is using the proper coefficients and constants. Unfortunately, the historical references cited often use coefficients and constants that are often not legitimate for how engineers should be able to use the Normand Number. The critical assumption, going back to Normand (1901), is that after a weight is added, the non-dimensional loading stays the same – the vessel before and after the weight change is a geosim of each other. This means that the vessel has to grow in dimensions (length, beam, depth) as weight is added. The additional dimensional growth results in additional weight growth that in turn results in additional dimensional growth and still further weight growth. This assumed relationship can result in very large Normand Numbers, often over three, for many types of vessels. This is especially true for vessels with a low dead weight fraction.

The geosim assumption greatly limits the legitimate application of the Normand Number and can cause gross errors when the Normand Number approach is used where the geosim assumption is not met. In many cases, if not most, there are ***no*** legitimate naval architectural justifications to strictly meet the geosim requirement for modern high speed craft. Adding a weight, increasing speed, etc., may not result in a change in volume or the change in volume may be significantly less than that of the final weight change.

The only obvious argument for automatically assuming the geosim assumption was that it simplified the calculations for naval architects of a hundred years ago. Given our present knowledge and tools, this automatic simplification is not justified. However, if the geosim assumption is valid, then the Normand Number estimate historically used is generally correct.

The designer is cautioned to check that the added weight does not compromise stability, arrangements, or getting past hump speed. If the added weight causes issues in these areas, additional design changes may be required.
The Normand Number approach can also be used to expedite convergence of ship design synthesis programs that predict displacement using displacement as a variable.

PROPOSED NEW ESTIMATE FOR THE NORMAND NUMBER

The Normand Number estimate approach presented in this paper does not assume that the volume of the hull changes to meet the geosim requirements as in previous Normand Number prediction methods. The volume of the hull is assumed to be constant in the prediction of the Normand Number itself. However, the proposed method does allow volume to be added or deleted by treating it is an added or deleted weight. The proposed method for predicting the Normand Number assumes vessel proportions (length to beam and beam to depth) constant, but does allow the impact of changing proportions by treating it as an added or deleted weight. The modified Normand Number approach now presented allows vessel proportions to be changed and volume added or deleted as the user feels appropriate. The Normand Number as estimated from the approach proposed in this paper may be significantly different from that of previous prediction methods. The Normand Number predicted with this paper will typically be smaller, but can be larger in some cases. The proposed alternate approach for the Normand Number will greatly expand its applicability and accuracy for predicting the weight and performance impact of changes to a vessel's design.

The following equation is proposed to predict the Normand Number. It is applicable to many different types of vessels, including high performance craft.

$$N_n = \frac{\Delta}{\Delta - (\alpha W_{100} + \beta W_{200} + \mu W_{fp})} \tag{9}$$

Where

N_n	Normand Number
Δ	Full load displacement
W_{100}	Structural weight (SWBS 100)
W_{200}	Propulsion system weight (SWBS 200)
W_{fp}	Propulsion fuel weight (not cargo fuel weight)
α	Displacement exponent for structural weight, $W_{100} \approx \Delta^{\alpha}$
β	Displacement exponent for propulsion weight, $W_{200} \approx \Delta^{\beta}$
μ	Displacement exponent for fuel weight, $W_{fp} \approx \Delta^{\mu}$

The above equation is a good estimate for the Normand Number as long as the total weight change is not dramatic and the overall design change is not too extreme.

Standard United States Navy definitions of structural weight, W_{100}, and for propulsion weight, W_{200}, are used as given in SAWE (2001). The propulsion fuel weight, W_{fp}, corresponds to the fuel the vessel consumes to make range or meet endurance.

Outfit, electrical, auxiliary, weapons and electronics' weights are not included in the equation above because they generally do not change significantly when a vessel's weight is increased and the volume is fixed. If they are thought to change significantly, they can be added to the equation.

If there is a fundamental change to a specific weight group, such as saving weight by changing from steel to aluminum structure, then the weight impact for the weight group at the same displacement is calculated and subtracted from the weight group in equation 9 above. As an example, if the structural weight of a steel craft is 100 tons and if changing to aluminum saves 25 mtons (at same displacement) than the revised structural weight, W_{100}, is 75 mtons (100 mton – 25 mton). The 25 mton weight saving is now moved to the displacement independent weight group as a negative weight - which is not part of equation 9. The weight change also becomes part of DW_0. This is illustrated in the paper's examples.

If the structural weight, propulsion weight, or fuel weight are fixed, their corresponding exponent is set to zero. A weight could be fixed if the designer is willing to accept degradation in reliability, strength, speed, or endurance. If a weight becomes fixed it is moved into the W_o group.

If the predicted Normand Number is very large or negative, this means it is not practical to increase performance unless there is a fundamental change in the craft that improves performance, such as changing from steel to aluminum or changing to a significantly more efficient propulsion system.

INITIAL STRUCTURAL WEIGHT AND DISPLACEMENT EXPONENT FOR STRUCTURAL WEIGHT – α

The initial structural weight used in the Normand Number, equation 9, can be estimated using various methods if not known. References for high speed craft include: Cassedy (1977), Karayannis (1999), Vassiklos (1989), and Grubisic (2008).

If the structural weight varies proportionally with displacement, the displacement exponent for structural weight, α, is one, as assumed in some simple prediction methods. However, based on review of a range of prediction methods, weight data, and classification rules, this assumption is found not to be valid for a high speed vessel of constant volume. Much of the structure has little, if any, dependency on displacement for its weight. As can be expected, there is wide scatter in potential α. Overall, a value of 0.5 for α appears reasonable as a rough estimate where more rigorous structural analysis is not done. The exponent is only reasonable for modest changes in displacement.

INITIAL PROPULSION WEIGHT AND DISPLACEMENT EXPONENT FOR PROPULSION WEIGHT – β

The propulsion weight used in the Normand Number, equation 9, can be estimated using various methods if not already known. References for estimating the propulsion weight of high speed craft include: Cassedy (1977), Karayannis (1999), Vassiklos (1989), and Grubisic (2008).

The change in propulsion weight is assumed to vary linearly with the required power. If the propulsion efficiency is assumed constant, the new required power for the same speed can be estimated with the following equation.

$$P_n / P_o = \frac{R/W_n}{R/W_o} \frac{\Delta_n}{\Delta_o} \qquad (10)$$

Where

P_n	New required power
P_o	Original power
R/W_n	New resistance to weight ratio
R/W_o	Original resistance to weight ratio

At a given speed, where the geometry is fixed and the change in displacement is not excessive, the change in R/W can be estimated with the following equation.

$$\frac{R/W_n}{R/W_o} = \left(\frac{\Delta_n}{\Delta_o}\right)^{\delta} \qquad (11)$$

Substituting equation 11 into equation 10 results in:

$$P_n / P_o = \left(\frac{\Delta_n}{\Delta_o}\right)^{\delta+1} \tag{12}$$

Thus the displacement exponent for propulsion weight, β is:

$$\beta = \delta + 1 \tag{13}$$

If R/W does not vary with displacement and is constant, β equals one. If R/W increases with displacement, common at hump speeds, β is greater than one and if R/W decreases with displacement, common at very high speeds, β is less than one. The classical estimates for the Normand Number assumed that β equals two thirds based on the geosim assumption discussed earlier. β can be highly dependent on hull type, initial non-dimensional load and non-dimensional speed. As an example, β can be significantly greater than one at hump speeds and less than one half at post critical speeds for the same vessel.

β can be predicted using relevant prediction methods where displacement is varied and speed is kept constant. Generic estimates for β can be made using the figures that follow.

Figure 1 is a plot of β against the Volumetric Froude Number, $F_{n\nabla}$, for R/W predicted using the Soviet MBK planing series (Almeter (1989), Bun'kov (1974), Yegorov (1978)) for a chine length of 16 meters over the entire L/B range (2.50 to 3.75) and beam loading range of the series. As can be seen in the figure 1, there is a tremendous scatter when β is plotted against $F_{n\nabla}$. The same data is re-plotted in figure 2 using the Almeter Method as described in Almeter (1999). The Almeter Method is an approach for "collapsing" planing hull data. The data is plotted against the 10 base log of A_n as defined below.

$$A_n = \frac{\Delta}{\frac{1}{2}\rho\, LCG\, B_c\, V^2} \tag{14}$$

LCG Longitudinal center of gravity from the transom
B_c Chine beam
ρ Mass density of water

The Soviet BK planing series (Almeter (1989), Bun'kov (1969), Yegorov (1978)) is also plotted in figure 2 for a chine length of 32 meters over the BK's entire L/B range (3.75 to 7.0) and beam loading range of the series for Volumetric Froude Numbers from 2.5 to 4.2. The American Series 62 (Clement (1963) is also shown for the models with a L/B from 3.06 to 5.5 for a displacement of 45,000 kg at Volumetric Froude Number above 2.5. The scatter in figure 2 is significantly less than that of figure 1. This is a sensitive calculation and some scatter is unavoidable due to experimental and modeling errors. An additional cause of error is likely due to the BK and MBK's significant variation of deadrise from midship to the transom (hull warp) and Series 62's significant beam taper. The β trendlines for the three planing hull series are very similar despite their different hull shapes and different range of L/B and loadings. The equations for the trendlines are given below. Also given is the trendline equation for the combined BK and MBK series.

MBK Curve Fit $\beta = -5.0138 \log_{10}(A_n)^3 - 18.536 \log_{10}(A_n)^2 - 20.426 \log_{10}(A_n) - 5.5082$ (15)
BK Curve Fit $\beta = -1.8734 \log_{10}(A_n)^3 - 4.6172 \log_{10}(A_n)^2 - 0.75 \log_{10}(An) + 3.5007$ (16)
MBK & BK $\beta = 1.3123 \log_{10}(A_n)^2 + 5.3645 \log_{10}(An) + 5.5232$ (17)
Series 62 $\beta = 1.3241 \log_{10}(A_n) + 2.6756$ (18)

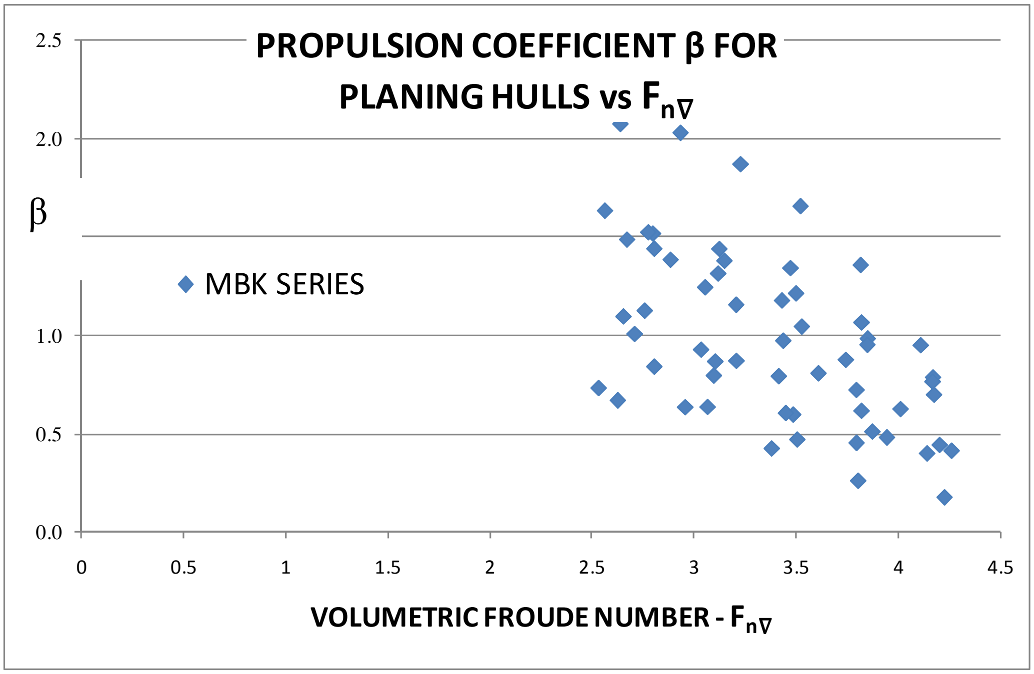

Figure 1: Propulsion Coefficient β for Planing Hulls vs $F_{n\nabla}$

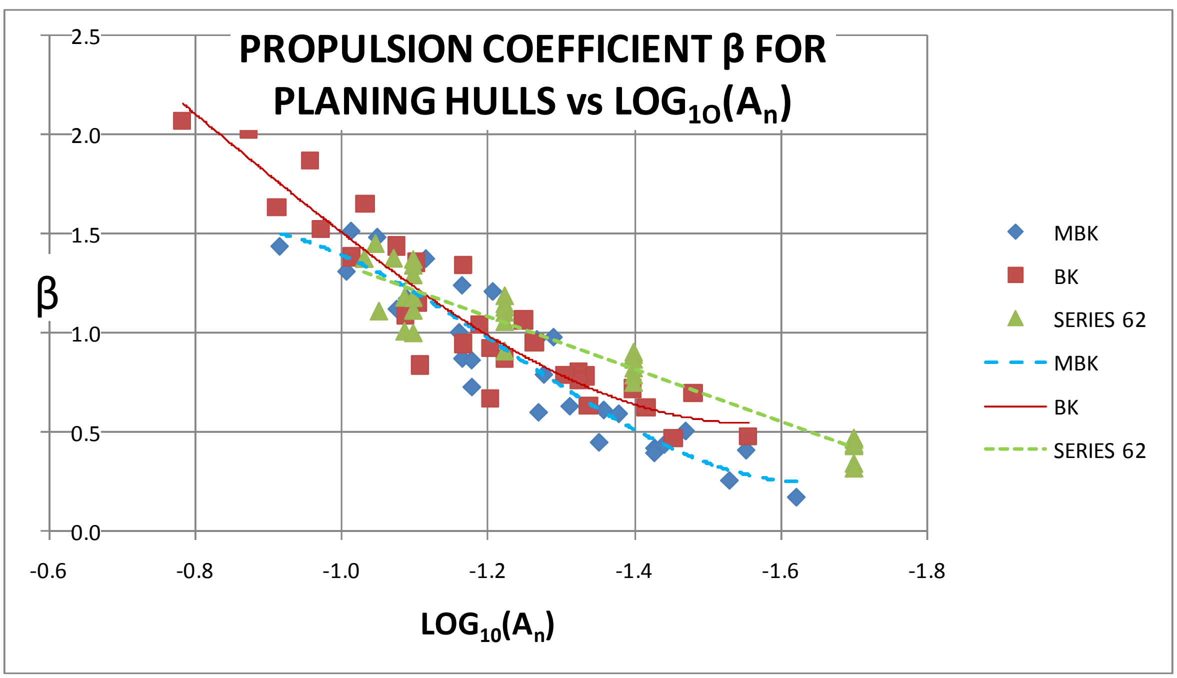

Figure 2: Propulsion Coefficient β for Planing Hulls vs $Log_{10}(A_n)$

Figure 2 shows that the powering exponent, β, is highly dependent on A_n. The left of figure 2 is at or just past hump speed and the right represents high speed planing. β is much larger at hump speed, which means that the increase (or decrease) in power is more sensitive to displacement changes at hump speed than at high speed planing. This is due to the hump drag being dominated by pressure drag, which is highly dependent on weight loading. Resistance during high speed planing is dominated by skin friction, which is highly dependent on wetted surface and wetted surface generally does not vary significantly if the longitudinal center of gravity is kept constant despite changes in loadings.

Figure 3 is a plot of β against Froude Number based on length, F_{nL}, for high speed displacement mono-hulls and catamarans. The prediction of β was made using the Thin Ship based program Ship Wave Prediction Evaluator (SWPE) (Tuck (2003), Almeter (2005)) for the demi-hull of the NPL catamaran series, Molland (1994). Analysis of the NPL data in Molland (1995) showed little difference in values of β for a NPL catamaran model and its demi-hull model alone over the speed range shown in figure 3. The prediction is based on fixed hull geometries. The waterline was raised or lowered on these fixed geometries to predict β. This obviously changed the beam to draft (B/T) ratio. The predictions are based on an initial static wetted length of 50 meters and a beam to draft ratio of two. At the lower hump speeds, β is greater than one, which indicates R/W increasing with displacement as anticipated. At the higher speeds, β is significantly less than one, which indicates R/W decreasing with displacement – also anticipated. β is highly dependent on Froude Number based on length and to a lesser degree on L/B (for constant initial B/T).

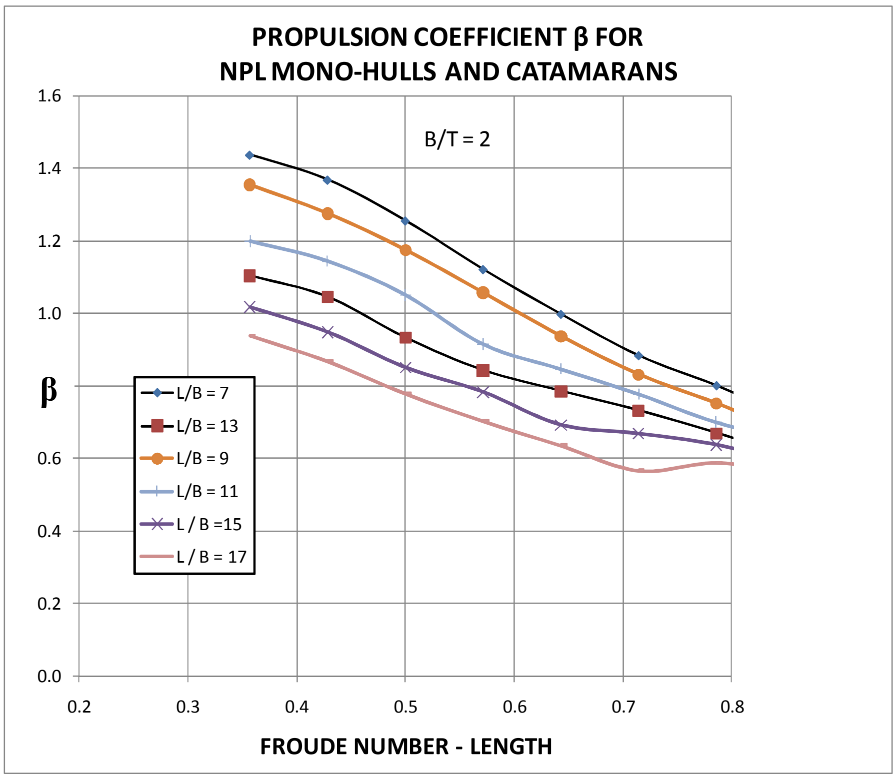

Figure 3: Propulsion Coefficient β for NPL Mono-Hulls and Catamarans – B/T =2

Predicted values of β for a B /T of 1.5 and 3.0 are given in figure 4. Like the B/T = 2 case in Figure 3, Froude Length is the dominant variable for β.

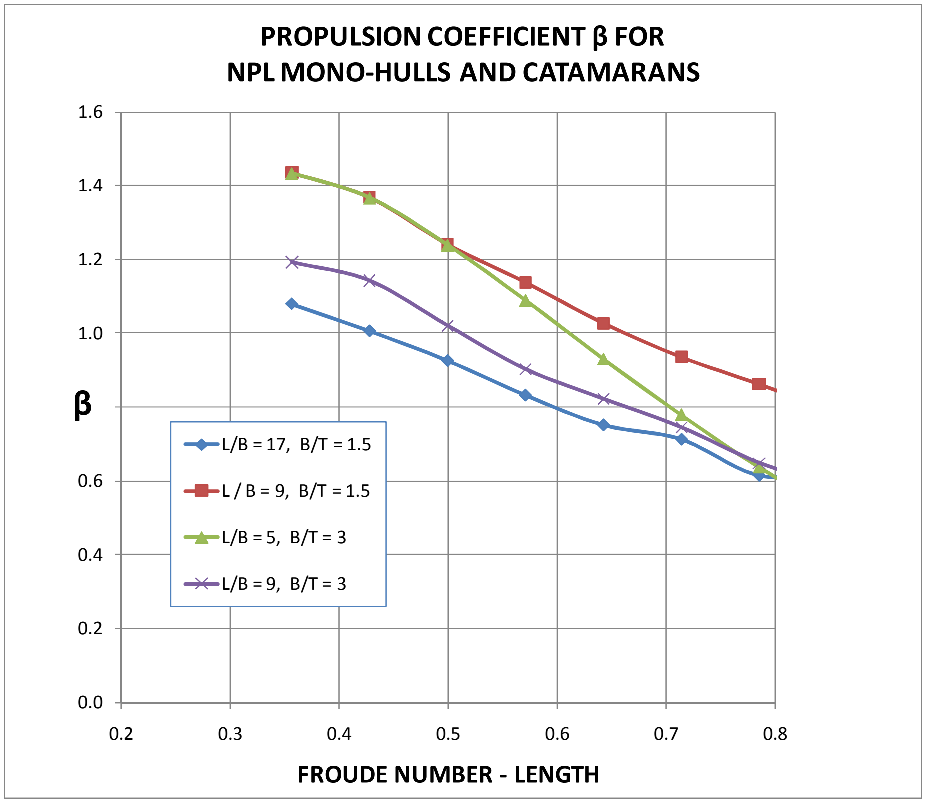

Figure 4: Propulsion Coefficient β for NPL Mono-Hulls and Catamarans – B/T = 1.5 and 3.0

Curve fits for the NPL series predicted values in figures 3 and 4 are give below.

L/B = 9, B/T = 1.5	$\beta = 0.722\ F_{nL}^2 - 2.2222\ F_{nL} + 2.1624$	(19)
L/B =17, B/T = 1.5	$\beta = 0.7771\ F_{nL}^2 - 1.919\ F_{nL} + 1.6759$	(20)
L/B = 7, B/T = 2	$\beta = 0.8072\ F_{nL}^2 - 2.52\ F_{nL} + 2.2803$	(21)
L/B = 17, B/T = 2	$\beta = 0.7041\ F_{nL}^2 - 1.6575\ F_{nL} + 1.434$	(22)
L/B =5, B/T = 3	$\beta = 0.8165\ F_{nL}^2 - 2.8988\ F_{nL} + 2.4352$	(23)
L/B =9, B/T = 3	$\beta = 0.\ 528\ F_{nL}^2 - 1.9167\ F_{nL} + 1.8364$	(24)

The ratio of the percent increase in power to the percent of the Weight of the Design change with respect to full load displacement is equal to $N_n\beta$ as given in the equation below.

$$\text{(Increase in Power/ Initial Installed power)} \ / \ (DW_0 / \Delta) \quad = \ N_n\beta \qquad (25)$$

Thus if N_n equals 2 and β equals 0.7, the ratio is equal to 1.4 (2 * 0.7).

The actual increase (or decrease) in power is:

$$\%\ \text{Increase in Power} = N_n\beta\ DW_0/D\Delta\ 100\ \% \qquad (26)$$

INITIAL PROPULSION WEIGHT AND DISPLACEMENT EXPONENT FOR PROPULSION WEIGHT – β WITH CHANGE IN SPEED OR POWER DENSITY

If the speed is changed, increased or decreased, the exponent β has to be based on the new speed. The propulsion weight, W_{200} has to be adjusted for the new speed. As an example, if the new speed requires ten percent less horsepower than the original speed for the same displacement, then the adjusted W_{200} would be ten percent less.

The difference between the original W_{200} and the adjusted W_{200} is treated as a "Weight of a Design Change", DW_0, in this case negative.

Similarly, if the propulsion weight to power ratio is changed, W_{200} weight has to be adjusted and the difference between the adjusted W_{200} weight and the original W_{200} weight is treated as part of "Weight of a Design Change", DW_0.

INITIAL PROPULSION WEIGHT AND DISPLACEMENT EXPONENT FOR PROPULSION WEIGHT – β WITH VARIABLE POWER AND NO CHANGE IN WEIGHT

Small changes in propulsion power often can be made without any changes in propulsion weight by simply increasing the rating of the engine. In such cases, β equals zero in the Normand Number prediction, equation 5.
The associated required increase in rating is predicted using equation 26 where β corresponds to the case where the propulsion weight does vary with installed power.

EXPONENT FOR PROPULSION FUEL WEIGHT – µ

The exponent for propulsion fuel weight is determined in the same way as the exponent β for power but at the speed used for range. If the speed used for range and for top speed are the same, µ equals β.

The ratio of the percent increase in propulsion fuel weight to the percent weight of the Weight of the Design change is equal to $N_n\mu$ as given in the equation below.

$$\text{(Increase in Propulsion Fuel / Initial Propulsion Fuel Weight) / (Weight of the Design Change }/\Delta) = N_n\mu \qquad (27)$$

Thus if N_n equals 2 and µ equals 0.7, the ratio is equal to 1.4 (2 * 0.7).

The actual increase (or decrease) in propulsion fuel is:

$$\%\ \text{Increase in propulsion fuel} = N_n\ \mu\ DW_0/D\Delta\ 100\ \% \qquad (28)$$

However, if the fuel weight is fixed, such that range is allowed to change with displacement, then µ equals zero and the percent change in range can be estimated as below.

$$\%\ \text{Change in Range} = \mu\ N_n\ DW_0\ /\ \Delta\ 100\% \qquad (29)$$

In the equation above, µ is the value used if fuel was not fixed.

EXPONENT FOR PROPULSION FUEL WEIGHT – µ - WITH CHANGE IN SPEED

If the speed for range is changed, increased or decreased, the exponent µ has to be based on the new speed. The propulsion fuel weight, $W_{fp,}$ has to be adjusted for the new speed. As an example, if the new speed requires ten percent less fuel than the original speed for the same displacement, the adjusted W_{fp} would be ten percent less. The difference between the original W_{fp} and the adjusted W_{fp} is treated as a "Weight of a Design Change".

WEIGHT OF DESIGN CHANGES

The "Weight of the Design Change" is the weight of a change without accounting for secondary weight impacts to account for the Weight of the Design Change such as increased fuel and installed power. As mentioned earlier the Weight of the Design Change can account for almost anything, including extra equipment and lighter propulsion equipment. The Weight of the Design Change could be positive or negative and there can be multiple Weight of the Design Changes that are combined.

Small changes in the following can be assumed to have a proportionally small weight impact within the areas they directly impact.

Specific Fuel Consumption – *Fuel Weight*
Structural Density – *Structural Weight*
Total Propulsion Weight to Horsepower Ratio – *Propulsion Weight*
Range – *Fuel Weight*
Propulsion Efficiency – *Fuel Weight, Propulsion Weight*
Resistance to Weight Ratio – *Fuel Weight, Propulsion Weight*

Typical lightship densities after subtracting out propulsion weights for various types of craft from Jacobson (2006) are given in figure 5 below. As can be shown, there can be a large variation in densities. Using figure 5, an additional 100 cubic meters of volume could add a nominal 5 to 20 mtons to DW_0, depending on the size and type of craft.

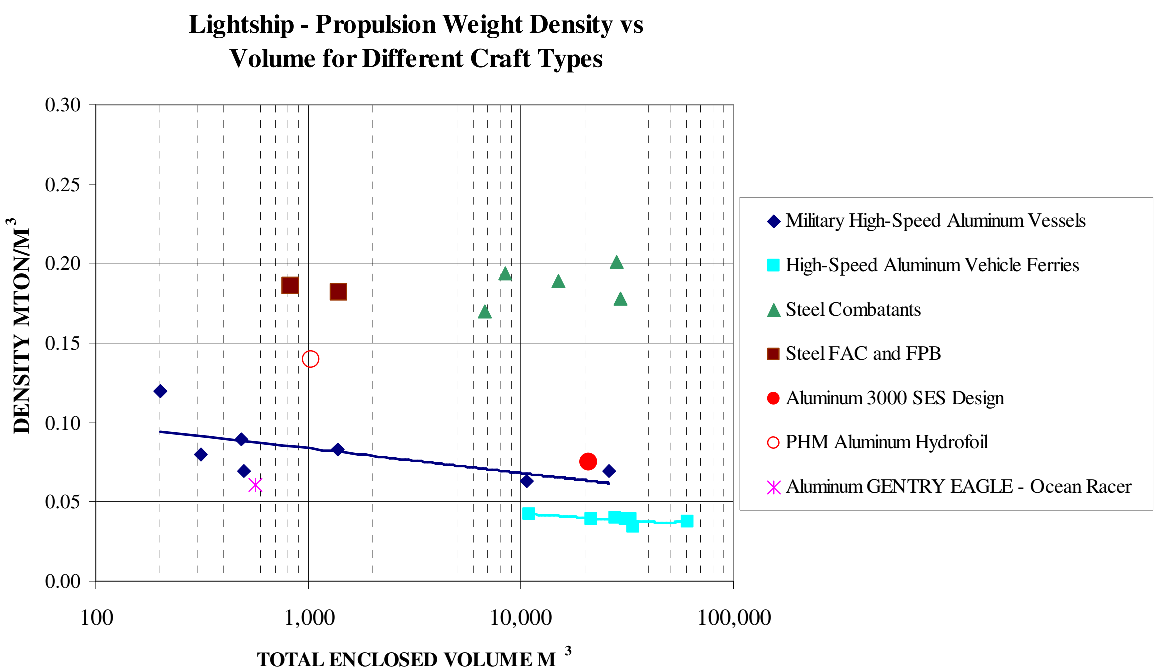

Figure 5: Lightship Excluding Propulsion Weight Density versus Volume for Different Craft Types

EXAMPLE OF NORMAND NUMBER AND TOTAL WEIGHT INCREASE CALCULATIONS

Assume the following initial conditions:

Displacement	130	mton	
Propulsion weight	20	mton	
Fuel weight	22	mton	
Structural weight	45	mton	
Speed for propulsion design	36	knot	(18.4 m /sec)
Speed for endurance	32	knot	(16.3 m / sec)
Hull type		Planing	
Chine length	32.5	meter	
Chine beam	6	meter	

43 mton is independent of the craft's weight and is equal to the Full Load displacement minus the structural, propulsion and fuel weights.

EXAMPLE A

The following changes are required:

Additional equipment	7	mton
Range	10	% increase
Fuel consumption from	0.24 to 0.22	kg / kw / hr

The speed is unchanged.

Exponents for weights (equation (9))

Structural, α	0.5	(typical)
Propulsion weight, β	1.40	
Fuel weight, μ	1.70	

The "Weight of Design Impacts" is 7.4 mton as shown below.

+ 7 mton (Additional weight)
+2.2 mton (From 10 % increase in range / fuel)
- 1.8 mton (From changing from 0.24 kg/kw/hr to 0.22 kg/kw/hr) = 22 mton – 0.22/0.24*22 mton
7.4 mton

β is calculated using figure 2 / equation (17) after calculating A_n with equation (14) for the speed for propulsion. The LCG is assumed to be 40 percent of the chine length (13 meter).

$$A_n = 0.094 \quad = \frac{130\ mton * 9800\ n/mton}{\frac{1}{2} * 1024 \frac{kg}{m^3} * 13\ m * 6m * (18.4 \frac{m}{\sec})^2}$$

$$\mathrm{Log}_{10}(0.094) \quad = -1.026$$

$$\beta = 1.40 \quad = 1.3123 * (-1.026)^2 + 5.3645 * (-1.026) + 5.5232$$

μ is calculated to be 1.70 as done for β, but with the speed for range.

The Normand Number is calculated as follows using equation (9):

$$N_n = 3.14 = \frac{130\ mton}{130\ mton - 0.5*45\ mton - 1.40*20 mton - 1.70*22.4 mton}$$

The fuel weight in the Normand Number equation above has been increased from 22 mton to 22.4 mton due to the fuel related design changes listed earlier. The total weight impact is calculated by multiplying the Normand Number by the Weight of Design Impacts.

Total Weight Impact = 23.2 mton = 3.14 * 7.4 mton

The final total weight = 153.2 mton = 130 mton + 23.2 mton.

From equation 26 and the data from the above example the percent increase in power is found to be 25 percent:

25 % = 3.14 * 1.7 * 7.4 mton / 130 mton * 100 %

The corresponding increase in propulsion weight is 5.0 mton (assumed constant power to weight ratio).

From equation 28 and the data from the above example the increase in fuel is found to be 7.2 mton:

7.2 mton = (3.14 * 1.70 * 7.4 mton /130 mton) * 22.4 mton + 0.4 mton

The last term in the equation above accounts for the initial change for the fuel (+2.2 mton – 1.8 mton).

EXAMPLE B

In Example A, the 7.4 mton initial weight increase has resulted in a predicted 23.2 mton total weight increase and a 25 % increase in power to maintain the same speed. These are huge increases and could easily force the design to become much larger and even unfeasible. As a result, let us assume that the top speed is reduced from 36 to 34 knots, causing a 10 % reduction in power and that the speed for range is reduced from 32 to 30 knots, causing a 5 % reduction in fuel all for the same initial displacement (130 mton).

The new "Weight of Design Impacts" is 4.3 mton as shown below.

+ 7.0	mton	Additional weight
+ 2.2	mton	From 10 % increase in range / fuel
- 1.8	mton	From changing from 0.24 kg/kw/hr to 0.22 kg/kw/hr
- 2.0	mton	From reducing power by 10% from speed reduction
- 1.1	mton	From reducing speed for range
4.3	mton	

The Normand Number is recalculated with the adjusted propulsion and propulsion fuel weights and recalculated exponents for the new speeds below.

$$N_n = 3.24 = \frac{130\ mton}{130\ mton - 0.5*45\ mton - 1.54*18 mton - 1.86*21.3 mton}$$

The propulsion and fuel weight terms and speed related exponents above have been adjusted to reflect the Weight of Design Impacts and speed changes just described. With a N_n of 3.24, the total weight increase is thus 13.9 mton. The new power is calculated to be 5 % percent greater than the original design using equation 26.

5 % = 3.24 * 1.54 * 4.3mton/130 mton * 100% * 0.9 – 10 %

The first term has 90 % to account for the 10 % reduction in power from the reduced speed as does the 10 % in the second term.

EXAMPLE C

The same initial condition is assumed and the only changes are the addition of the 7 mton of additional weight and the improvement of specific fuel coefficient from 0.24 kg / kw / hr to 0.22 kg / kw /hr. The total amount of fuel is kept constant and the reduction in range is accepted. The weight of structure is also kept the same and the associated degradation in strength is accepted. However, the speed is fixed and the installed power is allowed to increase.

Accordingly, the structural and fuel weight coefficients are now zero. The propulsion weight coefficient is the same as found in Example A. Thus the Normand Number is found to be 1.27 as calculated below. With the structural and fuel weights no longer dependent on displacement, the Norman Number is much smaller than in the previous examples.

$$N_n = 1.27 = \frac{130\ mton}{130\ mton - 0.0*45\ mton - 1.40*20 mton - 0.0*22\ mton}$$

DW_0 is 7 mton (weight of additional equipment) and the total weight impact, DΔ, is 8.9 mton (1.27 * 7). From equation 26, the increase in propulsion weight is 10 %. The loss in range using equation 29 is 12 %, but after correcting for the improvement in specific fuel coefficient, the loss is reduced to just 3 %.

EXAMPLE D

The same initial condition is assumed and the only changes are the addition of 7 mton of additional weight and a 20 percent decrease in structural density, such as from going from steel to aluminum. Since the speed has not changed, the power and fuel coefficients are the same as in Example A. The structural coefficient is also assumed unchanged. The structural weight is now 36 mton (0.8 * 45mton) and 9 mton lighter than the original 45 mton. The Normand Number is 2.79 as shown below.

$$N_n = 2.79 = \frac{130\ mton}{130\ mton - 0.5*36mton - 1.40*20mton - 1.70*22mton}$$

DW_0 is equal to -2 mton (7mton -9 mton). The total weight change, DΔ, is -5.6 mton and the new displacement is 124.4 mton. The change in propulsion weight and propulsion power is -6 percent from equation 26 for a weight savings of 1.2 mton. The change in fuel weight is -7 percent from equation 28 for a weight savings of 1.5 mton.

This matches the weight predicted from the weight equation based on displacement, equations 1 and 2.

$$\Delta_n = 124.4\ mton = 36mton\ (124.4/130)^{0.5} + 20\ mton\ (124.4/130)^{1.4} + 22\ mton\ (124.4/130)^{1.7} + 52\ mton$$

$$+ (-2\ mton)$$

The new displacement is the same as that predicted with the Normand Number. The 52 mton includes the initial weight that is independent of displacement and the 9 mton move from the structural weight. The -2 mton is DW_0.

These examples illustrate how quickly and easily the Normand Number approach as modified in this paper can be used to calculate the total weight, powering and fuel impacts of multiple design changes with minimal data on the original design with very simple equations. These examples also show that the Normand Number can be changed favorably reduced by changing the weight equation to make it less sensitive to the Weight of a Design Change. Significant performance increase is often dependent on this.

Conclusion

The Normand Number approach, as modified in this paper, presents a simple and quick way to predict the total weight, powering and fuel impacts of multiple design changes even when there is minimal data on an existing design. The Normand Number approach can be used for almost any type of vessel. The proposed modification to the Normand Number approach of not requiring similarity (geosim) greatly expands the legitimate use of the Normand Number approach. The Normand Number approach can also dramatically expedite convergence of synthesis models.

References

Almeter, J. (1989): “Resistance Prediction and Optimization of Low Dead Rise, Hard Chine, Stepless Planing Hulls”, SNAME, *STAR Symposium*, 1989

Almeter, J. (1999): “Resistance Prediction of Planing Craft From Similar Craft Using The Almeter Method”, *RINA Hydrodynamics of High-Speed Craft, London,* 1999

Almeter, J., Jacobson, D., et al (2005): “Review of Analytical Tools For The Us Army’s Theater Support Vessel”, *ASNE High Speed / High Performance and Craft Symposium*, July 2005

Bun’kov, M. (1969): “Calculating the Drag of Hard-Chine Boats”, *Katera I Iakhty*, No. 3 (19), 1969, in Russian (NAVSEA Translation No. 2150, 1987)

Bun’kov, M. (1974): “Study of the Resistance of Planing Hulls”, *Katera I Iakhty*, No. 2 (48), 1974, in Russian (NAVSEA Translation No. 2148, 1987)

Cassedy, W. (1977): "A Procedure to Evaluate the Feasibility of Naval Ship Designs", Master's Thesis, Massachusetts Institute of Technology

Clement, E., Blount, D. (1963): "Resistance Tests of a Systematic Series of Planing Hull Forms", SNAME Transactions, Vol. 71, 1963

Grubisic, I., (2008): "Reliability of Weight Predictions in the Small Craft Concept Design", *6th International Conference on High Performance Marine Vehicles*, Naples, Italy, 18-19 Sept, 2008

Harvald, S. A., (1964): "Normand's Number for Merchant Ships", *European Shipbuilding, Journal of the Ship Technical Society*, Vol. XIII, No. 1, pp. 14-23

Hovgaard, W. (1920): "General Design of Warships", E. & F. N. Spon, Ltd., London, pp. 30-46

Hunbaker, J. C. (1920): "Naval Architecture in Aeronautics", *Flight – The Aircraft Engineer & Airships*, Vol XII

Jacobson, D., Almeter, J. (2006): "Concept and Early Preliminary Design Methodologies for High-speed Vessels", *HIPER 06*, 2006

Karayannis T., Molland, A.F, Williams, Sarac Y. (1999): "Design Data for High-Speed Vessels", *FAST 99*, 1999

Manning, G. C. (1945): "The Basic Design of Ships", D. Vann Norstrand Company, Inc., New York, pp. 53-64

Manning, G. C. (1956): "The Theory and Technique of Ship Design", The Technical Press of the Massachusetts Institute of Technology, pp. 51-65

Molland, A., Lee, A. (1995): "Resistance Experiments on a Series of High Speed Displacement Catamaran Forms: Variation of Prismatic Coefficient", Ship Science Report 86, Feb 1995

Molland, A., Wellicome, J., and Couser, P. (1994): "Resistance Experiments on a Systematic Series of High Speed Displacement Catamaran Forms: Variation of Length-Displacement Ratio and Breadth-Draft Ratio", Ship Science Report No. 71, Mar 1994

Normand, J. A. (1901): "The Displacement and Dimensions of Ships – Approximate Rules for the Determination of the Displacement and Dimensions of a Ship in Accordance with a Given Programme of Requirements", *International Engineering Congress*, Glasgow (Reproduced in *Journal of the American Society of Naval Engineers*, Vol. XIV, No. 2, May 1902)

SAWE (2001): "Weight Estimating and Margin Manual for Marine Vehicles", Society of Allied Weight Engineers, Recommended Practice Number 14, 2001

Toby, A. S. (2009): "Normand's Number and Weight Equation", *Warship International*, Volume Number 46, Issue 4, pp 271-301

Tuck, E., Scullen, D. (2003): "Sea Wave Pattern Evaluation: SWPE 7.0 Simplified User's Guide", Scullen & Tuck Pty Ltd, 2003

Vassiklos, Markus (1989): "A Comparative Analysis of Small Advanced Naval Vehicles and Displacement Hull Naval Ship Design", PHD Thesis, Massachusetts Institute of Technology

Yegorov, I., Bun'kov, M., and Sadovnikov (1978): "Propulsive Performance and Seaworthiness of Planing Vessels", in Russian (Naval Sea Systems Command, Translation No. 1965, Oct 1981)

*Seventh International Conference
On High-Performance Marine Vehicles
Melbourne, Florida, USA
13-15 October 2010*

CFD SIMULATION OF PLANING HULLS

Stefano Brizzolara & Diego Villa
brizzolara@dinav.unige.it diego.villa@unige.it
Marine CFD Group, University of Genova, Italy

ABSTRACT

In the last century the CFD (Computational Fluid Dynamics) methods had an exponential growth of applications, due to the availability of user friendly codes and the increase of the computational performance, with the possibility to generalize the solution of the N.-S equation to more complex physical problems with multiple phases and free surfaces. Also the naval architecture community has started to intensively apply these methods for predicting steady and unsteady performance of ships and boats. Most of the effort, though, has been made for displacements hulls, while only few simple methods could be applied for planing hulls. That is probably due to the physical hydrodynamic complexity of the planing problem. The major problem is still open with regards to the determination of the actual possibilities of solutions and the level of confidence that can be expected from the numerical results

The paper summarizes the experience gained by the Marine CFD Group of University of Genova, presenting a selection of significant results that cover the research in the following areas: from the study of simple prismatic hull shapes, to the flow around d real hull shapes with steps and trim control appendages and propulsors. A large database and "know how" has been built to predict the dynamic attitude and the resistance for different types of full planing hulls with appendages.

INTRODUCTION

The solution of the hydrodynamic problem of a general planing hull advancing from stationary speed in calm water is still tackled with simplified approximated semi-empirical methods, mainly derived from the original Savitsky method, modified and (empirically) adjusted to allow for a dead-rise variation or to include the effect of spray rails.

Figure 1: Experimental flow pattern around a planing hull

In the recent past few more theories, mainly based on potential flow theories, were developed and tested, as in the method of Savander et al (2002). These methods, though, are based on rather crude approximations with regards to the shape of the hull form. They solve the problem of dealing with generally cambered (in longitudinal and transversal direction) planing hull forms, but still cannot allow for influences of appendages like spray rails and steps.

The flow around planing hulls, in fact, is rather complex from the hydrodynamic point of view, since this involves different physical phenomena having different length and time scales, such as thin spray flow, wave breaking, turbulent boundary layer (see Figure 1). The free surface waves are long and often affected by overturning and breaking phenomena. Under the bottom, in front of the stagnation line, a thin spray sheet is formed which normally sharply separates from the chines. The rest of the incoming fluid flow attached to the bottom forming a turbulent boundary layer with an oblique angle that depends on the local deadrise and trim angle of the hull and on the proximity of the streamline to the chine.

The other problem is the attitude assumed by the hull in planing conditions; this requires a routine that searches for the dynamic equilibrium of gravitational and hydrodynamic forces and moments acting on the hull. Virtually, all of the above problems are nowadays solvable with volume of fluid RANS solvers.

THE RESEARCH PATHWAY AND THE FIRST CASES

The problem of planing hulls was faced by the authors for the first time around year 2005, encouraged by the promising results published by Caponnetto (2001), followed by Azcueta (2003). The research program initiated with the study of very simple planing dihedral hull forms with 20 degree constant deadrise, as systematically tested by Kapryan & Weinstein (1952) and Chamblis & Boyd (1953), then continued with more realistic but still simple hull forms, taken from the Series 62 whose results will be summarized in the next section, for ending at the actual state of the art that feature general hull forms with appendages. Some of these applications will be illustrated in the last section.

In the case of constant deadrise hull forms, the CFD calculation were performed with Star-CD. The experimental attitude was used for RANS simulation and predicted lift, drag and trim moment were compared with the experimental results. An example of correlation of the numerical results obtained, entirely published in Brizzolara and Serra (2007), is presented in Figure 2 in the case of lift and drag.

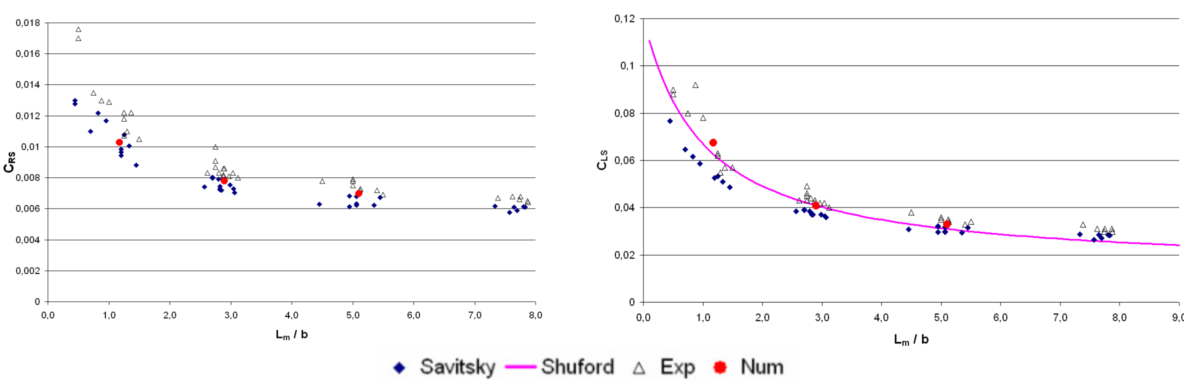

Figure 2: Dihedral planing hull with 6 deg trim. Comparison numerical Lift (C_L) and Drag (C_R) coefficients predicted with RANS with experimental results and other semi-empirical formulations

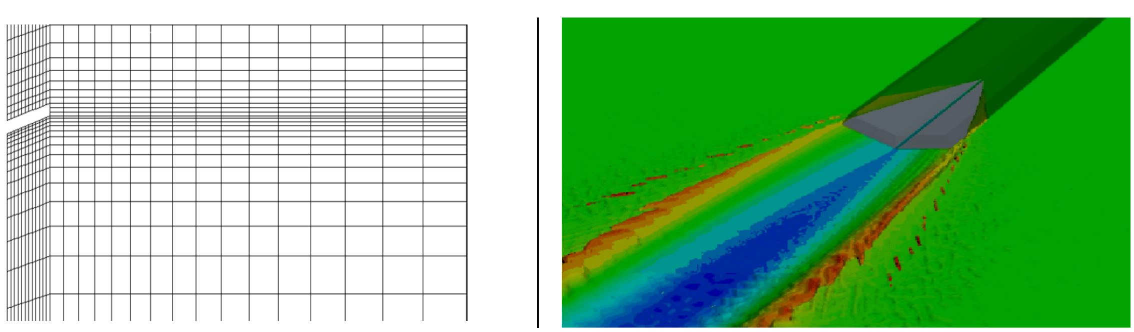

Figure 3: Mesh type (up) and Free surface (low) for a Dihedral planing hull case having 20 deg deadrise and 6 deg trim, at Fn_B=4.7. The spray area (dark yellow), the pressure area (gray) are correctly captures as well as the overturning divergent wave.

RANS calculations were run in model scale, using an initial structured body fitted mesh (as from Figure 3), then refined splitting the cells along their vertical dimension with two subsequent level, one close to the hull and the other in proximity of the free surface. A total number of 300000 prismatic elements, divided in 12 blocks, was sufficient to obtain convergence of the results. The domain was rather limited, due to the proper planing condition simulation speed range, only 1 length forward, 1 length aft, 0.8 length aside and 1 length below the hull were sufficient to verify the sensitivity analysis of boundary conditions. On the outlet a prescribed mean piezometric pressure was assigned. A high Reynolds k-ε turbulence model was used with a double layer law of the wall. The simulation was done in non-stationary condition to solve for the deformation of the free surface up to the stationary conditions, starting by flat initial free surface. Time step was adequately selected in order satisfy the Courant condition everywhere in the discrete domain.

The correlation of numerical results was made with the experimental results, as noticeable rather dispersed at lowest wetted lengths as shown in the example of Figure 2, and with semi-empirical formulations of Savitsky and Shufford (only for lift and centre of pressure).

The overall correlation of RANS results with the experiments was around 10% on drag and about 5% on lift and trim moment. In any case this appears to be fairly more accurate than that of semi-empirical methods. Already in these simulations unrealistic VOF distributions on the hull wetted surface were noted, namely values of 0.75/0.8 were predicted in areas where the hull should be lapped by pure water (i.e. VOF=1), but no means of correction were adopted. Similar problems have been noted in the next series of simulations with Series 62 and real hulls, but can be solved with a the new mesh typology and adequately corrected from the resistance point of view as explained in subsequent sections.

SERIES 62 WITH FIXED TRIM

The second step of validation has been made on the parent model of Series 62 (Clement & Blount, 1963) at different weight, speed and static trim conditions. The hull has a little more variation of the transverse sections at the bow, keeping a constant deadrise angle of 12.5 degrees at stern and smaller chine breadth at transom.

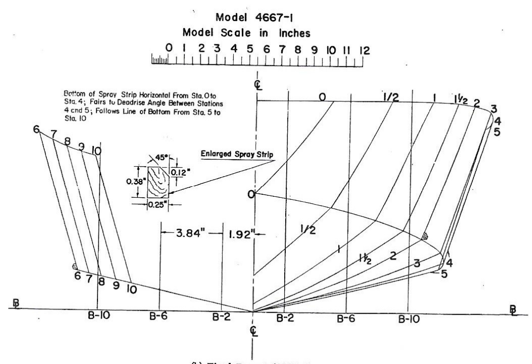

(b) Final Parent (4667-1)

Figure 4: Series 62 parent model

A first set of calculations, this time made with StarCCM+, have been performed on the model fixed in the experimental attitude in the complete planing speed range.

The mesh type was unstructured, mainly composed of Cartesian cells in the majority of the domain, by five extruded prism layers in the hull boundary layer and by trimmed cells in the region of transition. Mesh size and density was calibrated, by an extensive sensitivity study, resulting in a minimum number of about 700000 elements. The box like domain spans 1L forward, 1L aft, 2L below and 2L aside the hull (L = hull length). A higher mesh density in the far field would be requested at semi-displacement speeds. A special topology of the mesh was used, as presented in the transverse cut of Figure 7: a thin layer of cells placed in way of the chine was created in order to capture the thin spray sheet sharp detachment. This kind of mesh permitted to save thousands of cells while preserving good results in terms of hull flow characteristics. Still some diffusion of air below the bottom is visible especially at lowest speed, as shown in Figure 6: the lower VOF strips are originated at the stagnation line and are convected by the main flow at stern. This special mesh topology in way of the chines avoids the side to become unrealistically wetted. In fact, as from Figure 6 the VOF on the sides is rather well behaved: at the lowest speed the flared side above the chine is wetted at stern, while progressively it becomes dry as the speed is increased. Some spray curles are noted at the bow, blowed on the hull by the air flow.

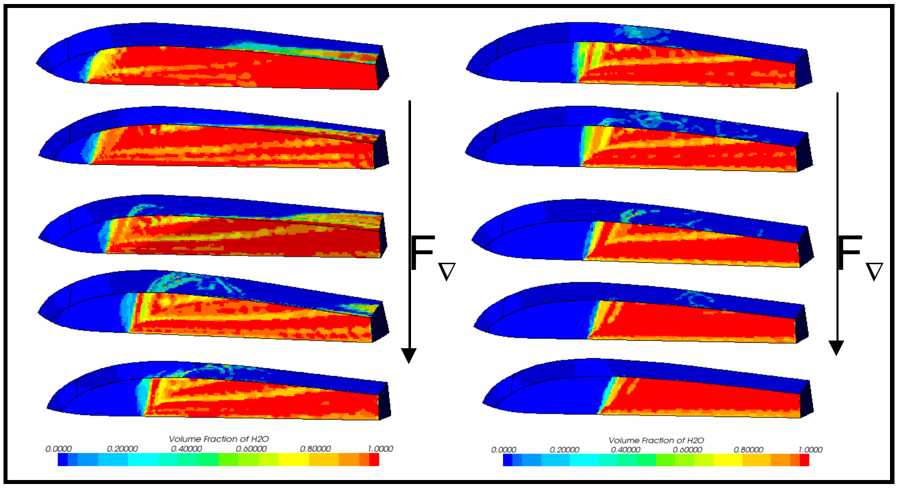

Figure 5: S-62, parent model: predicted wetted pressure and spray area on the wetted part of the hull as a function of Froude number

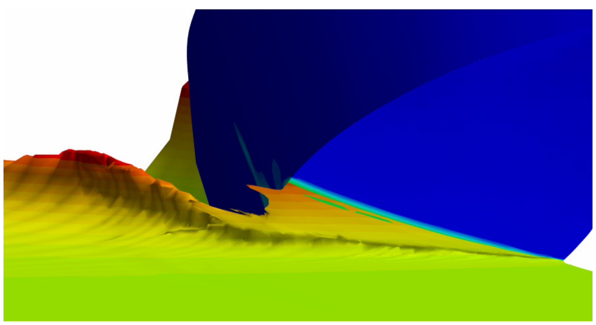

Figure 6: Spray and spilling wave at chine

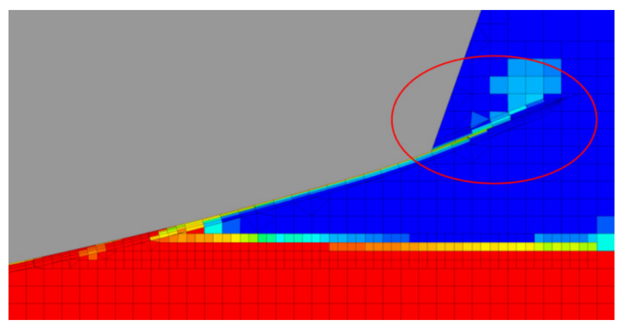

Figure 7: Special mesh type used in way of the chine

With this kind of mesh and settings, either the lift and longitudinal moment and the total drag result within an accuracy of 3% with respect to model tests.

SERIE 62 WITH FREE ATTITUDE: THE MARINE CFD GROUP METHOD

An external Java/C++ routine was developed by the Marine CFD Group (MCFDG) and linked to StarCCM+ solver (since from version 2) to change the position of the hull during the non stationary time step iterations in order to converge on the hull hydrodynamic equilibrium. Due to the symmetry of the problem, the equilibrium was reduced at the sole longitudinal plane, i.e. allowing for a variation of trim angle (τ) and draft (sinkage). The principle of the algorithm is illustrated by the flow diagram of Figure 8.

The unsteady simulation is launched with the hull in a first guessed dynamic attitude and a number of time steps are calculated with the hull in fixed position (static simulation), to avoid the initial unrealistic forces caused by the initial impulsive acceleration. Then the algorithm calculates the deviation of vertical force and longitudinal moment from the equilibrium condition. With the current attitude and these deviations by the Savitsky method (Savitsky equilibrium) applied on a dihedral equivalent hull, a correction of trim and sinkage is calculated. This attitude correction is applied smoothly to the rigid body over a number of time steps which depend on the given maximum rotational and translational speed. Then a sufficient number of time steps is run. The algorithm in the user routine linked to the solver automatically performs all these steps until convergence on the equilibrium. A final number of time steps (solution smoothness) is finally imposed to reach the undisturbed stationary equilibrium flow field.

In the newest version of StarCCM+ solver there is only recently the possibility to reach this equilibrium condition following the physics of the hull rigid body motions, launching a non stationary calculation (in any case needed for the free surface). But this method, which follows a not meaningful physics, is inherently affected by oscillation and can require considerable computational time to reach convergence. Special artefacts can be used also in this case, such as to decrease the inertia of mass or introduced an artificial damping coefficient.

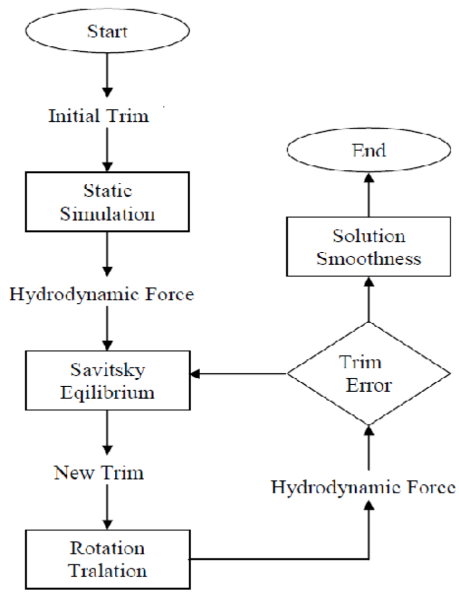

Figure 8: DINAV dynamic trim search algorithm

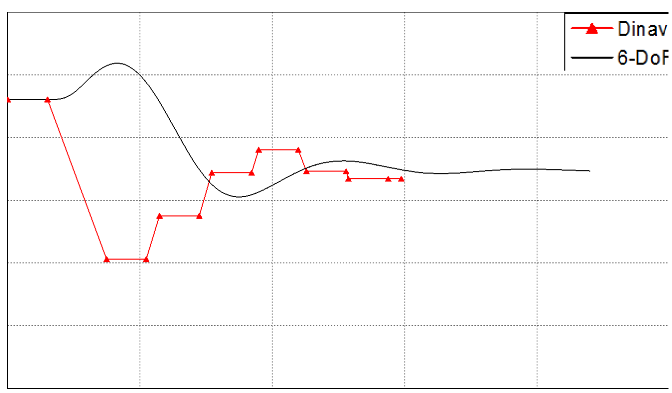

Figure 9: Convergence of dynamic trim angle: DINAV (red) vs 2DOF method

Figure 9 shows a comparison of the convergence of the MCFDG convergence algorithm against the 2DOF method. In the presented case, the two methods are almost equivalent in terms of efficiency, but it is possible to obtain better performance from the DINAV method by properly setting the number of time steps and the under-relaxation factor applied on the Savitsky's predicted trim and sinkage corrections. In both cases the final dynamic attitude is well predicted, as presented in the first two graphs of Figure 10. The accuracy of the predicted total resistance by the DINAV automatic procedure appears very satisfactory, as seen from the third graph of Figure 10, being within ±3% from the experimental results.

REAL HULL FORMS

Finally on the basis of the experience gained with the extensive systematic CFD simulation of different basic topologies of planing hull forms, the authors have applied the illustrated method to different real hulls, as built, i.e. with all the small geometrical details and appendages that can influence the dynamic attitude and the resistance.

An important role is normally played by the flared chines and the spray rails. An example of results obtained from the calculations is presented in Figure 11 and corelate with the test of Figure 1. The VOF distribution highlights some air ingestion in way of the spray rail which is only marginally present in the experiments. This convinced the authors to apply a correction to the predicted tangential force on each cell face at the hull wall inversely proportional to the volume of fluid calculated in the cell. For the rest the wave and spray formation and the dynamic attitude correlated very well against the experimental results. Also in this case, after the friction correction, the deviation of the numerically predicted total resistance at design speed was within the 5% against the measured value in towing tank experiments.

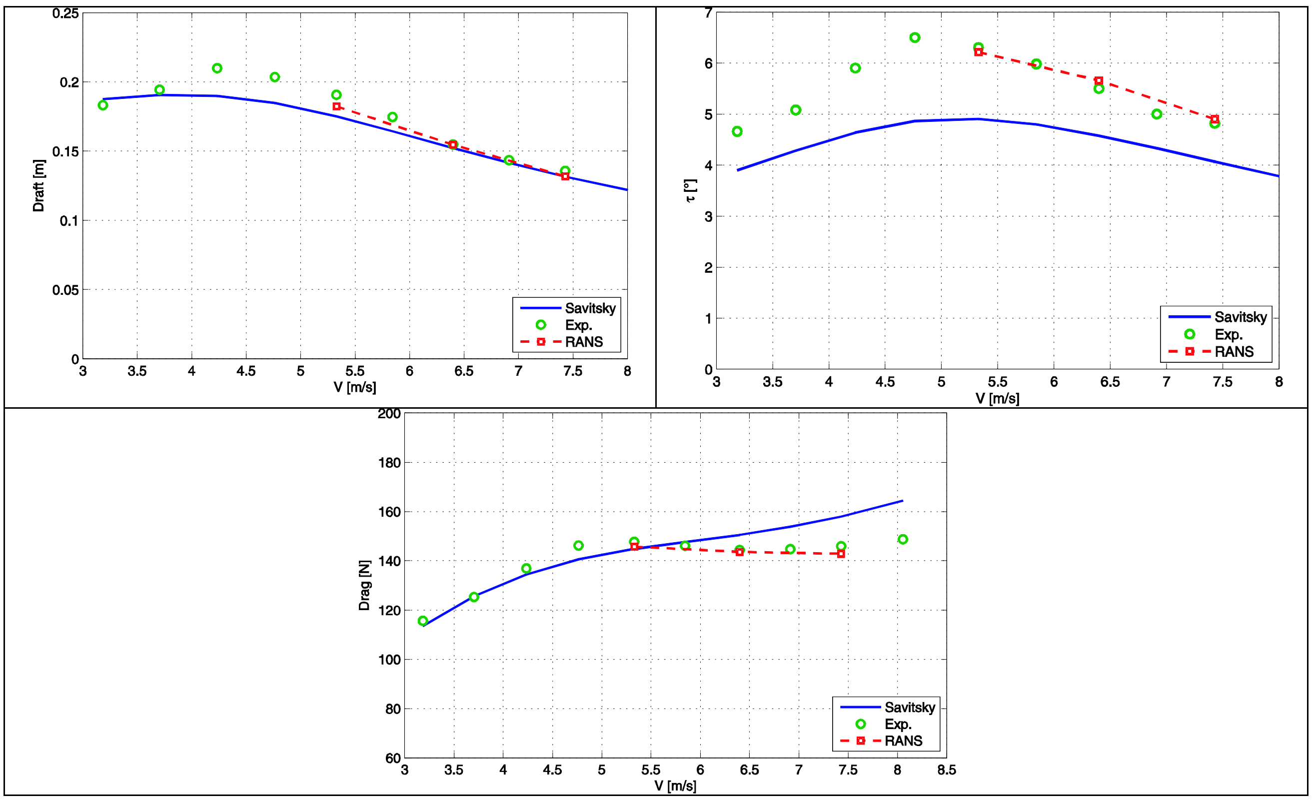

Figure 10: Dynamic Draft (up right), Trim (up left) and Total Drag (bottom): comparison of obtained CFD results on model 4667-1, with experiments and Savitsky method

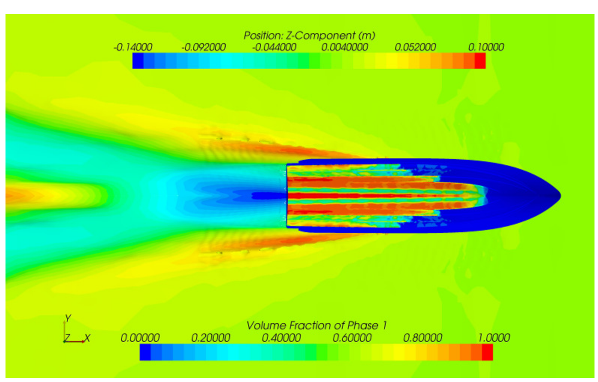

Figure 11: Fast 20m motoryacht, free surface elevation and VOF distribution under the hull (comp. Fig.1)

The effects of different configurations and shapes of spray rails has been investigated on a full scale high-speed inteceptor and a rubber boat hull. Figure 12 shows the pressure distribution calculated under the hull bottom. It can be noted that the upper part of the picture is without the spray rails, while the lower part is with the spray rails. The full scale validations have confirmed the capabilities of the RANS solver to adequately predict the influence of spray rails on the resistance and dynamic attitude of the hull. The general effect is to increase the hydrodynamic forces developed under the bottom if the ship attitude is fixed or it can reduced the running trim and sinkage if the hull is left free to move around its centre of gravity.

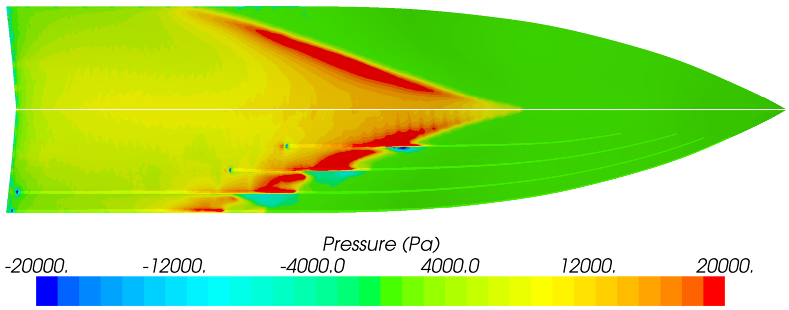

Figure 12: Appendages effect under the hull in terms of pressure coefficient.

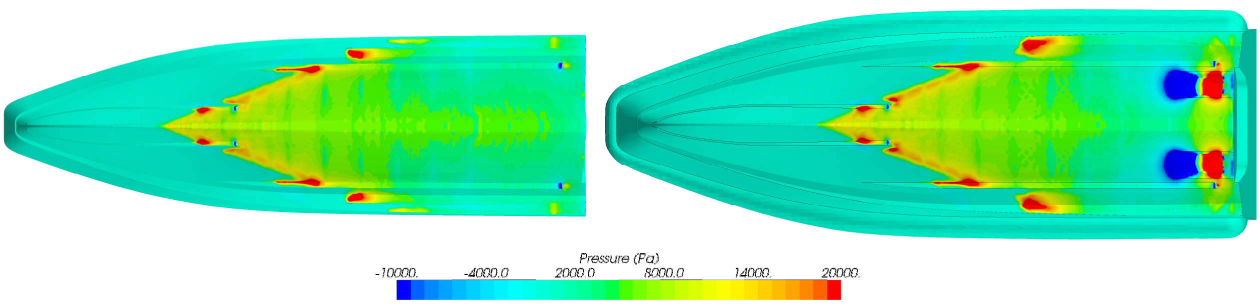

Figure 13: Fast 12m rigid keel rib with waterjet propulsion. Pressure distribution including WJ intake suction effect

An important feature to be included in CFD model is the action of the propulsors, either submerged screw propellers or waterjets. The action of the inclined thrust produced by waterjets or propellers can be included in the DINAV algorithm that searches for dynamic equilibrium. In addition to the inclined thrust effect, though, the propulsors can locally modify the flow field on the aft part of the hull, inducing additional hydrodynamic forces and moments which can affect trim and sinkage and hence the total resistance.

The case of Figure 13 features a fast planing hull with waterjet propulsion. The suction effect induced by the modelled waterjet intake under the hull is strong and is able to locally modify the pressure distribution and streamlines paths on the hull bottom. In the Figure 13 the difference in the pressure distribution between the same hull shape with and without the waterjets can be noted. The result of this effect is a variation of dynamic trim as large as one degree and a variation of total resistance of about 30% with respect to the bare hull, principally due to the dynamic attitude variation.

Finally for planing hulls, another important effect is induced by stern flaps or interceptors, a very frequent practice in the contemporary planing hulls of small to medium sized fast crafts. In this respect the authors have recently published, Brizzolara and Villa (2009), a comprehensive CFD study of the effects of these kind of appendages. In particular it has been shown some new relationships between the performance of the two types of appendage, and guidelines indicated selection of appropriate appendages for improved performance. The Figure 14 show the effect due to the two equivalent appendages in terms of local pressure coefficient and streamline path below a prismatic hull bottom.

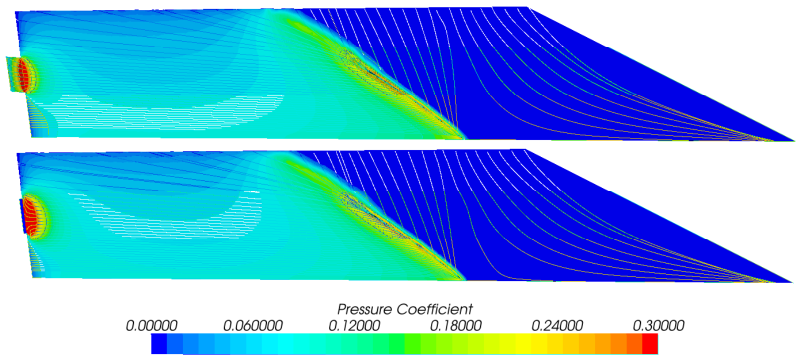

Figure 14: Appendages effect under the hull in terms of pressure coefficient.

CONCLUSIONS AND FURTHER PROSPECTS

The general conclusion, on the basis of an extensive series of simulations exemplified in this paper, is that RANS methods are mature to be used for accurate prediction of the resistance of planing hull in calm water including small appendages effects. The overall order of magnitude of the error noted after many validation studies is well within engineering purposes for planing hull forms and can be considered equivalent to that derived from a medium size towing tank facility.

Ad hoc meshes are often necessary to accurately resolve jet spray and wave breaking off the chines with a reasonable number of cells (less or in the order of one million). Special care should be given to the verification of the VOF distribution below the hull. This is very much related to the mesh quality and type and can affect the magnitude of the viscous resistance; while it does not influence significantly the pressure distribution. In certain cases correction on frictional resistance may be required.

The free surface waves, the pressure distribution and velocity flow field below the hull can be quite well predicted by the RANS solver with an adequate mesh and are almost unaffected by the VOF numerical diffusion under the hull.

The running attitude of the hull can be correctly predicted, as demonstrated, either with a dedicated iterative method based on Savitsky formulation or following the physics of the hull motion from an initial unbalanced guessed condition. The first method can offer better margin for efficiency in terms of computational time needed to reach the stationary condition, while the second can fall into large oscillating pitch and heave motions, physically consistent, but practically irrelevant.

Similar studies and simulations are planned to be repeated with OpenFoam. With this new solver, it will be interesting to compare the behaviour of the solution of the VOF and diffusion equations with respect to the commercial code applied in an industrial environment. The problem for this open source solver is shifted to the generation of the mesh which will require an ad hoc pre-processor, either commercial again or made for the purpose. In this respect the authors are working on a method to accurately and smoothly model 3D surfaces by a so called subdivision surface technique.

REFERENCES

Caponneto M., (2001) “Practical CFD Simulations for planing Hulls”, *HIPER 2001, High Performance Marine Vehicle*s, Hamburg

Azcueta R., (2003) “Steady and Unsteady RANSE Simulations for planing Crafts”, *International Conference on Fast Sea Transportation FAST 2003*, Ischia

Clement E. P. and Blount D. L., (1963), "Resistance Tests of a Systematic Series of Planing Hull Forms," *SNAME Transactions*, Volume 71, pp. 491-579

Brizzolara S., Serra F. (2007) "Accuracy of CFD Codes in the Prediction of Planing Surfaces Hydrodynamic Characteristics". *2nd International Conference on marine Research and Transportation, ICMRT"07*. ISCHIA. 28-30 Giugno, Vol. 1, pp. A-1-A-12, ISBN: 88-901174-3-5

Brizzolara S., Villa D. (2009), "A systematic CFD Analysis of Flaps / Interceptors Hydrodynamic Performance", *Fast 2009 Int. Conference on High Speed Fast Ship Design*, Athens

CD-ADAPCO (2009), "Star-CCM+ User and Theory Manual", version 4.04.011, 2009

Chambliss D.B., Boyd G.M. (1953), "The Planing Characteristics of two V-shaped Prismatic Surfaces having angles of Deadrise of 20° and 40°" , *Langley Aeronautical Laboratory, NACA Technical Note* 2876, Washington 1953.

Kapryan W.J. and Weinstein I. (1952), "The planing characteristics of a surface having a basic angle of dead rise of 20 degrees and horizontal chine flare", *Langley Aeronautical Laboratory, NACA Technical Note* 2804, 1952

Savander B.R., Scorpio S. M., Taylor R.K. (2002), "Steady hydrodynamic analysis of planing surfaces", *Journal of Ship Research,* vol. 46, no.4, pp. 248-279

Villa D., Vatteroni G., Brizzolara S. (2009) "CFD Calculations of Planing Hulls Hydrodynamics", *Star European Conference*, London, March 2009

Seventh International Conference
On High-Performance Marine Vehicles
Melbourne, Florida, USA
13-15 October 2010

ADVANCES IN THE USE OF ALUMINUM IN MARINE STRUCTURES

Robert A. Sielski
Naval Architect — Structures
Indio, California
RSielski@verizon.net

ABSTRACT

Recent research sponsored by U.S. Office of Naval Research program in ship structural reliability, The Aluminum Association and an ASTM marine task group, and the Ship Structure Committee has been reviewed. This paper represents an update to the SSC Aluminum Marine Structure Design and Fabrication Guide that guide was published in 2007 to serve as a reference to the shipbuilding industry to support their understanding of aluminum ship design and fabrication, and aid in the exploitation of aluminum as a building material.

The ASTM marine task group that developed ASTM specification is conducting marine environment testing of 5xxx-series specimens to determine susceptibility to stress corrosion testing. At-sea temperature measurements of aluminum structure on a ship operating in tropical environments were made to define a realistic time-temperature profile, which may indicate that the 5456-H116 alloy may not be suitable for weather deck applications. Other areas in which research is being conducted that are reviewed include fatigue and fracture of aluminum, ultimate strength of aluminum structures, and structural health monitoring of aluminum ships.

INTRODUCTION

Fabrication of craft with aluminum began in the early 1890s, and despite some early corrosion problems that occurred as the result of improper selection of alloy, aluminum saw increased marine use over the decades. In the 1940s, aluminum began to be adopted worldwide for fabrication of the superstructure of passenger ships and for military ships, a practice that continues today. Aluminum began to be used in the 1940s for pleasure craft and for workboats, the size of which has increase greatly over the years. The use of aluminum for the hulls of high-speed merchant vessels began in the 1990s with increased construction of high-speed ferries. These vessels have become so technologically advanced that they have surpassed the capabilities of many naval vessels; many navies today are adapting derivatives of these high speed vessels to combatant craft.

Recognizing the increased worldwide use of aluminum and the need for design and fabrication information, the Ship Structure Committee (SSC) in 2007 published the Aluminum Marine Structure Design and Fabrication Guide (Sielski, 2007). Since the publication of that report the interest in the use of aluminum in ship construction has resulted in advancements in knowledge, particularly as a result of the U.S. Office of Naval Research program in ship structural reliability and work of The Aluminum Association and an ASTM marine task group, and the SSC. This paper reviews some of the progress that is being made by these organizations, particularly by the U.S. Navy Office of Naval Research (ONR) program for ship structure reliability. The ONR is sponsoring research by a number of different investigators, including the U.S. Navy Naval Surface Warfare Center Carderock Division (NSWCCD), and holds regular team meetings of the investigators to ensure that all are aware of the work being conducted by others. Much of the results of research presented in this paper are extracted from presentations made at those meetings and associated workshops.

KEYWORDS

Aluminum, ship structure, material properties, ultimate strength, fatigue, fracture, structural health monitoring

ADVANCES IN MATERIALS

ASTM specification ASTM B 928, Standard Specification for High Magnesium Aluminum-Alloy Sheet and Plate for Marine Service and Similar Environments, was developed in 2003 by a Task Group on Marine Alloys of ASTM Committee B07 to address the problems of inter-granular corrosion seen in some 5xxx-series aluminum alloys. To help validate that specification, the ASTM marine task group conducted round-robin tests in ten laboratories to define better the ASTM G67 test procedure for intergranular corrosion susceptibility. As a result of the first round of testing, a revision to the ASTM G67 test method was made to include a section recommending the use of a verification sample in order to verify that a laboratory is operating within the desired limits. A second round robin test is planned to establish a verification standard for ASTM G67. The task group is also planning to conduct marine environment testing of 5xxx-series specimens to determine susceptibility to stress corrosion testing. In these tests, base metal and welded specimens of several 5xxx-series aluminum will be exposed to a marine environment, including ocean spray on a beach.

Stress corrosion cracking of a different nature has been seen in some ships, particularly where alloy 5456-H116 is used. The problem has been attributed to sensitization of the high-magnesium content alloy through higher service temperatures experienced over time. At-sea temperature measurements of aluminum structure on a ship operating in tropical environments were made to define a realistic time-temperature profile, which may indicate that the 5456-H116 alloy may not be suitable for weather deck applications. A recent task (Wong, 2009) has provided an estimate of the tendency of the environment to sensitize the aluminum structure, enabled the evaluation of 5xxx-series aluminum alloys for beta phase stability at naval service temperatures and durations before acceptance of the material for new construction or repair, measured the service environment temperature, and determined the thermal stability of naval aluminum alloys. The temperature of aluminum plates mounted on racks attached vertically and horizontally to on the X-craft *Sea Fighter* superstructure was measured between May 2007 and March 2008. During this period *Sea Fighter* transited to Florida from San Diego through the Panama Canal and performed some operations in Florida during this time. The thermal profile measured is shown in Figure 1.

In 1975 a similar effort was made to measure the temperature of exposed aluminum plate (Vassilaros and Czyryca, 1979). In that case, however, rather than measuring the temperature of a ship at sea, panels were exposed on the roof of a laboratory in Annapolis, Maryland between May and September, 1975. The results are also shown in Figure 1. The comparison in the figure shows that the new data by Wong reflects a slightly more benign environment than that of Vassilaros and Czyryca.

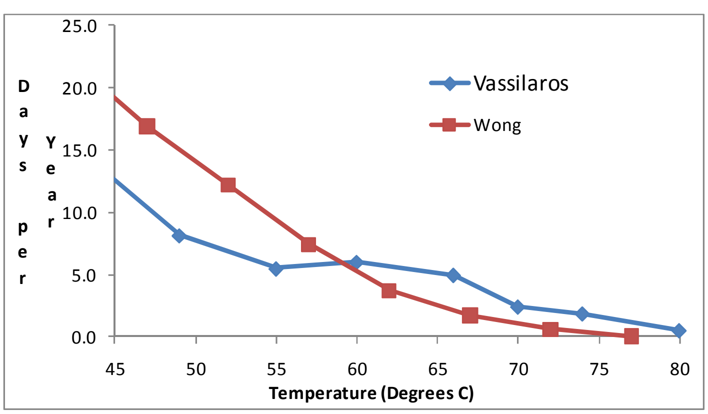

Figure 1: Comparison of thermal profiles from Vassilaros and Czyryca (1979) and Wong (2009).

The time and temperature behavior of aluminum heat-treated alloys 5456 and 5083 were determined to measure sensitization. It was noted that different alloys as well as different heats of plate of the same alloy sensitize at different rates. The equivalent time to sensitize at 100°C was calculated using the ratio of time to sensitize at the temperature in question divided into the time to sensitize at 100°C. This weighted number was then multiplied by the number of days per year from the Sea Fighter data at the temperature in question and the products were summed over the whole temperature range. These sums were then divided into the number of years to sensitize at 100°C to calculate the estimated time to sensitize. The result was that the estimated service life for recrystallized alloy 5083 is 2 to 7 years, recrystallized alloy 5456 is 5 years, and unrecrystallized alloy 5456 is 5 to 33 years. This conclusion of Wong for aluminum alloy 5456-H116 is similar to that reached by Vassilaros and Czyryca, who concluded that alloy 5456-H117 may approach the sensitized condition in less than five years.

ULTIMATE STRENGTH ANALYSIS OF ALUMINUM STRUCTURE

Ultimate strength analysis of aluminum structure is different from analysis of steel structure because of the difference in the shape of the material stress-strain curve, localized weak regions in aluminum welds, and the complex extrusions that are possible with aluminum have geometries that have not been addressed in prior studies of steel structure. Under the ONR program, advances have been made in ultimate strength analysis of simply supported aluminum plates, which showed good accuracy for peak plate strength and the load shortening curve (Collette, 2009). A formula for shear extension was developed based on the NACA/Stowell interaction approach.

The resulting buckling formula is given by the equation:

$$\sigma_{Buckle} = \eta\sigma_{Elastic} =$$

where:

σ_{Buckle} = buckling stress

$$\sigma_{Elastic} = k\frac{\pi^2 E}{12(1-\nu^2)}\left(\frac{t}{b}\right)^2$$

$$\eta = \frac{E_{SEC}}{E}\left[\frac{1}{2} + \frac{1}{2}\left(\frac{1}{4} + \frac{3}{4}\frac{E_{TAN}}{E_{SEC}}\right)^{\frac{1}{2}}\right]$$

The method was applied to the plate buckling strength determined experimentally by several previous investigators who measured the initial out-of-plane (IOOP) distortions, with the results for aluminum alloy 5083 shown in Figure 2. Collette made an additional correction for shear to the buckling strength equation but found that small amounts of shear did not affect the computed results.

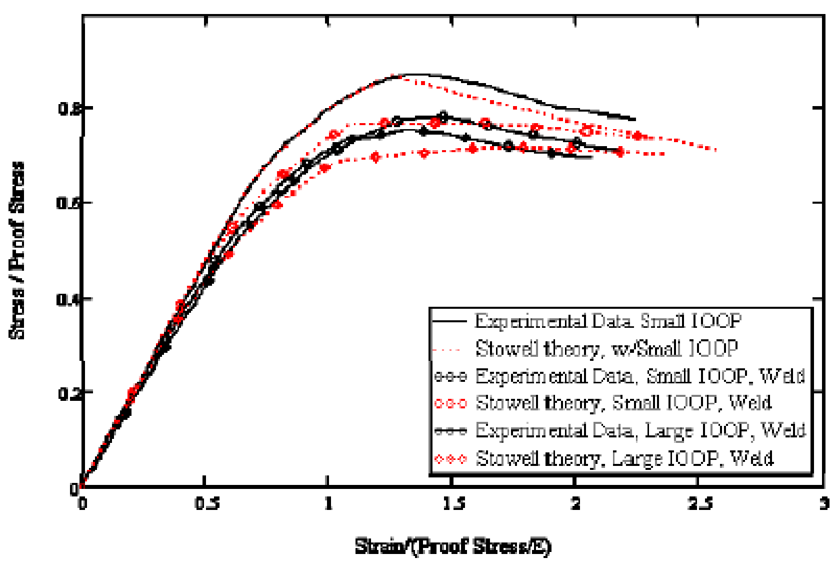

Figure 2: Comparison of plate strength calculated by modified Hopperstad/Stowell theory with experimental data (Collette, 2009).

The U.S. Navy's ship structure design tool, ULTSTR, is a semi-empirical code capable of predicting the ductile failure of steel grillage structures. Is was developed for steel structures, but recent upgrades have been made to address the properties of aluminum, including: 1) development of new strength and effectiveness curves based on the plate slenderness ratio β for 5xxx and 6xxx-series aluminum alloys, 2) definition of new failure strain for plate slenderness parameter definition, 3) definition of new parameters for the definition of the Heat Affected Zone (HAZ), 4) modification of the material definitions to improve and simplify the input of material parameters, 5) updating the stiffener local instability criteria to account for aluminum alloy behavior, 6) modification to include accommodation for the heat affected zone (HAZ) in built-up aluminum "T" stiffeners, and 7) expansion of the input for hard corner elements to allow for the explicit definition of residual stresses within the element. (Anderson, 2009).

Previous work by Jeom Paik sponsored by the Ship Structure Committee (Paik et al., 2008) on the collapse strength of fusion-welded aluminum panels has been extended by Paik to include friction stir welded panels, which were found to have greater strength because of reduced distortion and residual stress compared to the fusion-welded panels (Paik, 2009). Twelve panels were fabricated that were 1,200 mm long and 1,000 mm wide with four stiffeners along the length of the panel spaced 300 mm. The plate was either 5083-H116 or 5383- H116. The extruded tee stiffeners were of either 5083-H112 or 6082-T6. Two of the panels, which had 5383- H116 and 5083-H112 stiffeners, were fusion welded and the remainder were friction stir welded with the joint geometries as shown in Figure 3.

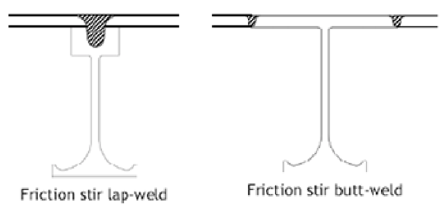

Figure 3: Friction stir weld geometries used for panel collapse tests (Paik, 2009).

After fabrication the panels were measured for residual stress and initial distortions. The friction stir welded panels had about one fourth as much distortion in the plate compared to the previous work by Paik on 76 fusion-welded panels. In the collapse testing of the friction stir welded panels delaminations occurred in the welds before the predicted ultimate strength was achieved. In spite of this, the collapse strength of the friction stir-welded aluminum panels was 10 to 20 percent greater that in equivalent fusion-welded aluminum structures. This implies that the friction stir welding procedure is certainly superior to the fusion welding procedure in terms of ultimate compressive strength performance, as long as the delamination in the friction stir welded region is prevented.

FATIGUE ANALYSIS OF ALUMINUM STRUCTURES

Fatigue crack propagation in aluminum ships can occur four times faster than in comparable steel ships, but those calculations can be conservative by a factor of eight if the effects of mean stress and residual stress are not properly accounted for. Tensile failure of aluminum structure has been analyzed in the past based on the use of the von Mises equivalent stress. However, testing and analysis have shown that the failure strain can be reduced by one-half or more if triaxial stress is present, showing the current practice to be extremely non-conservative. There is a clear need for testing of aluminum structures to confirm models of fatigue crack initiation and propagation. Towards that end, a test program has begun at NSWCCD to study these aspects of fatigue as well as ultimate strength of welded aluminum grillages (Devine, 2010). Planned test specimens are shown in Figure 4.

Stochastic description of structural fatigue initiation and propagation. has been developed by Collette et al. (2009) using a linked model of crack initiation and propagation. The model is very sensitive to the initial crack size that is assumed during the transition. Continuing efforts are researching extensions of this model to include through-life inspection updating results so that vessel safety can be assured in cases where the fatigue initiation life is less than the required service life, or fatigue cracks are fractural (critical). An example of the results of the method is shown in Figure 5.

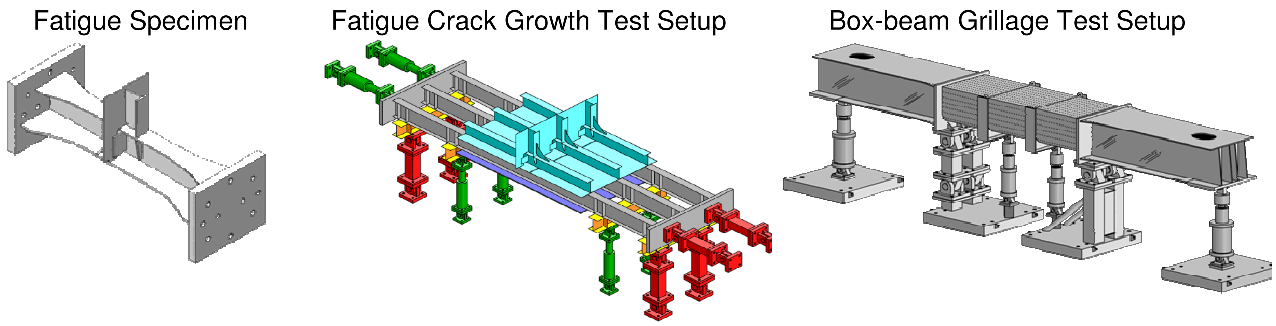

Figure 4: Proposed Specimens and test setups for NSWCCD fatigue and grillage collapse testing.

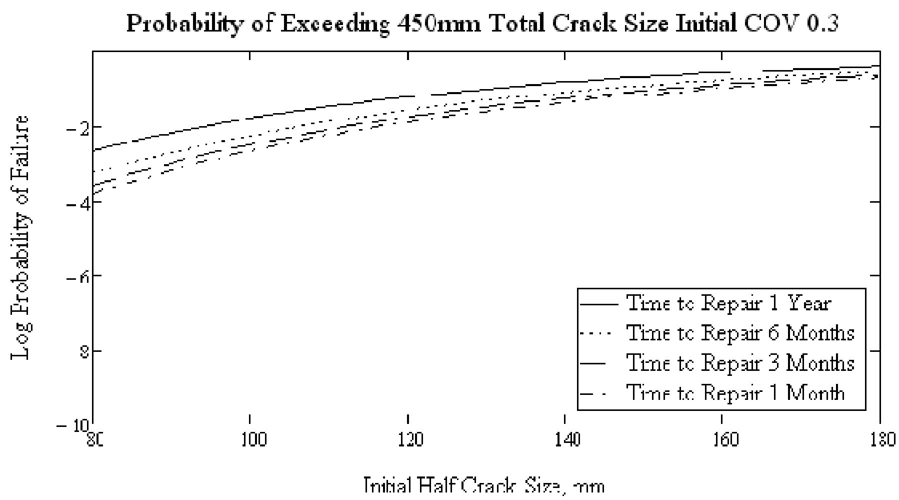

Figure 5: Stochastic prediction of fatigue crack growth failure (Collette et al., 2009).

FRACTURE OF ALUMINUM

To avoid testing of every structural configuration for crack propagation, the extended finite element method (XFEM) software is capable of modeling the advancing crack tip within elements (Lua et al., 2010). A demonstration was made using modified compact tension specimen geometries, with XFEM replicating the experimental crack propagation. The results for one specimen are shown in Figure 6.

During the 1980s a 95-foot aluminum structural evaluation model (ASEM) of an aluminum hull was extensively fatigue tested by NSWCCD (Johnson et al., 1984). A project is underway to use XFEM and a variety of other fatigue crack growth methodologies to predict the fatigue crack growth patterns that were observed during the ASEM testing. The rate of fatigue crack propagation in aluminum ship structure can be overestimated by a factor of as much as eight if the mechanisms that affect propagation such as mean stress and crack tip closure are not properly understood, and this reanalysis of older data will help promote that understanding.

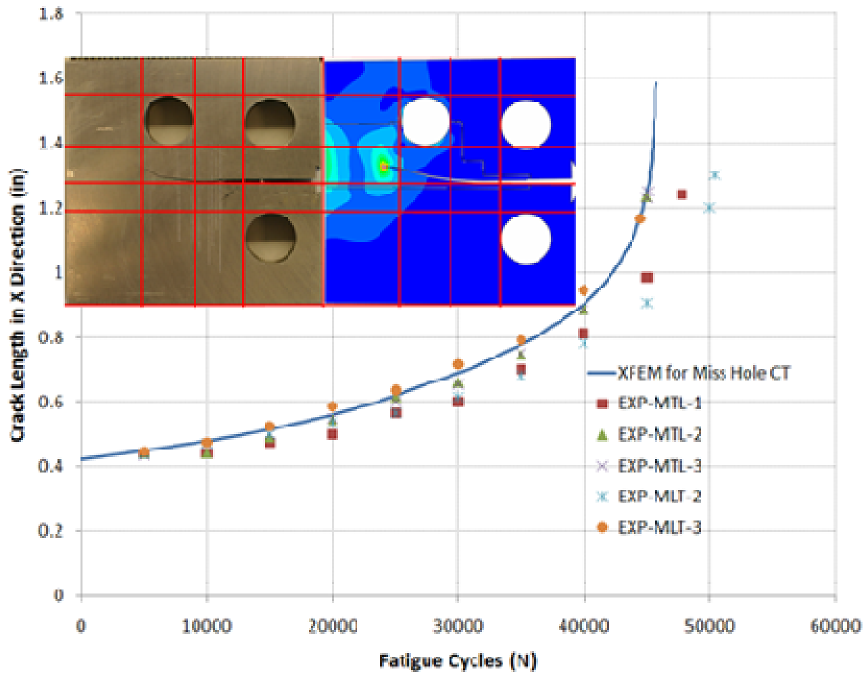

Figure 6: Comparison of XFEM prediction of fatigue crack growth and experiment (Lua et al., 2010)

Because of the particular vulnerability of aluminum to fatigue failure it is important that we understand the failure mechanisms that lead to crack initiation and propagation, rather than simply rely on the empirical basis on which most predictions are presently based. Important progress is being made in the understanding of crack propagation by Derek Warner and his associates at Cornell University, who are working to model fracture in aluminum at the level of individual atoms at the crack tip (Warner and Curtin, 2009). A quantum mechanics-based atomistic framework for fracture in aluminum has been built that helps to quantify the error that is present in empirical potentials that are commonly used to examine crack-tip energy, and a framework has been developed for examining void nucleation at particles through complex bonding. Modeling of the crack tip at the atomistic level is illustrated in Figure 7. Ductile fracture mechanisms at realistic loads and time scales have been ascertained through examination of nanovoid growth mechanisms and an upper bound on strength, providing a framework for more realistic atomistic simulations. Remaining work includes implementation of these results into a fracture model and making broader application. The properties of welds must be examined at an atomistic scale, including weld porosity and particle inclusions.

Traditionally, analysis of plasticity and ductile failure for most metals has been based on the use of the J_2 plasticity theory, which is comparable to using the von Mises equivalent stress, σ_{EQ}, because $\sigma_{EQ}, = \sqrt{(3 J_2)}$. Indeed, the von Mises stress has been extensively used for design, particularly when finite element analysis is used. For example, the American Bureau of Shipping guide for high speed craft (ABS, 2009) states that for all locations and members the allowable von Mises stress determined by finite element analysis should be equal to or less than 0.833 of the welded yield strength for aluminum and for steel.

An experimental and finite element analysis project was conducted (Gao et al., 2009) on 5083-H116 aluminum with three types of specimens tested; smooth and notched round tensile bars, grooved plane strain specimens, and Lindholm-type torsion specimens, which are round bars with a groove machined in the center. Each specimen type had a range of groove sizes used to produce differing degrees of triaxiality and Lode angle limit states. The geometry of each specimen was replicated in an ABAQUS finite element model in which the element size in the failure region was determined by the computational cell method based on the average spacing of the inclusions in the aluminum, which was determined by metallographic analysis, developing a porous plasticity model. The results of the testing and finite element analysis showed that the reduction in the critical failure strain with increasing triaxiality can be approximated by the empirical function EC = 0.55 e-1.365T. Therefore, the failure strain is reduced by about one-half if the triaxiality is 0.5, and reduced by factor of 15 if the triaxiality is equal to 2.

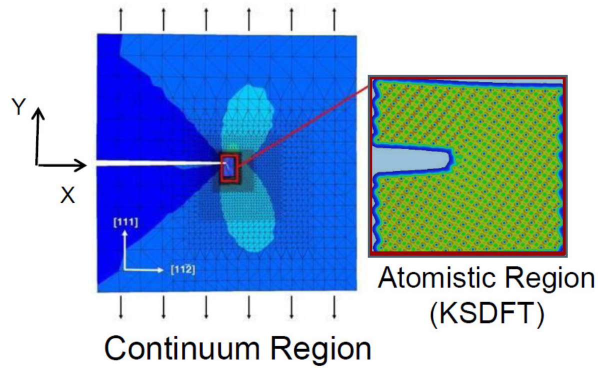

Figure 7: Atomistic modeling of the crack tip (Warner and Curtin, 2009).

STRUCTURAL HEALTH MONITORING

Structural health monitoring (SHM) is particularly important for aluminum ship structures because of the susceptibility to fatigue damage. Various methods for early crack detection are being developed, including thermal crack detection based on infrared camera technologies, vibration interferometry, imbedded wireless fatigue sensors that make an estimate of the fatigue damage, and pattern recognition approaches for identifying anomalous sensor readings that could be indicative of damage. A systematic model-based approach to structural health monitoring using dedicated forward modeling capability and inverse problem solutions has been developed. A structural health monitoring workshop was convened by ONR that included group discussions to discuss future ship structural health management and lifecycle cost visions and develop a road map to achieve these visions via SHM. A summary of presentations made at that workshop is given below.

A promising method of crack detection uses guided ultrasound waves that are sent with piezoelectric actuators/sensors in the pitch/catch configuration with one sensor receiving the signal from an actuator or in the pulse/echo configuration where the same device transmits and receives (Todd and di Scalea, 2009). Chaotically-modulated insonification waveforms use an ultrasonic carrier with bandwidth-controlled chaotic modulation to probe the structure and use predictive data-driven models rooted in pattern recognition to perform detection and classification of defects. Figure 8 show successful application of the method to detect damage in an aluminum plate. One difficulty with this method is that it is difficult to detect irregularities in complex geometries, such as ship structure.

Ultrasonic guided waves differ from conventional ultrasonic waves in that the receiver is placed at a distance from transmitter, permitting the ultrasound wave to travel through irregularities in the structure, such as a welded stiffener or laminations in a plate, being guided by the geometry of the structure. The waves can be used to inspect long lengths and an entire cross-section with increased sensitivity to defects due to the many features involved such as amplitude, frequency, mode shapes, and phase/group velocity. The method can target specific defects owing to mode structure choice (Todd and di Scalea, 2009). Flexible macro-fiber composite transducers can be used in the passive mode to detect guided acoustic signals

Current work by Nichols et al. (2009) focuses on providing estimates of the structure's condition and the degree of uncertainty in the estimate. The model-based approach to SHM uses data and models to estimate model parameters such as damage size, scope, etc. and then to assess the probability of damage occurrence and make a decision. With this method, there is no need for training data because damage parameters can be estimated directly. There is no need to correlate with previously observed patterns in the data, and the method is insensitive to sources of change other than damage. If the physics of the problem are uncertain, then multiple models can be posed. The method has been demonstrated through the modeling of a delaminated composite beam and then using noisy free-decay data to

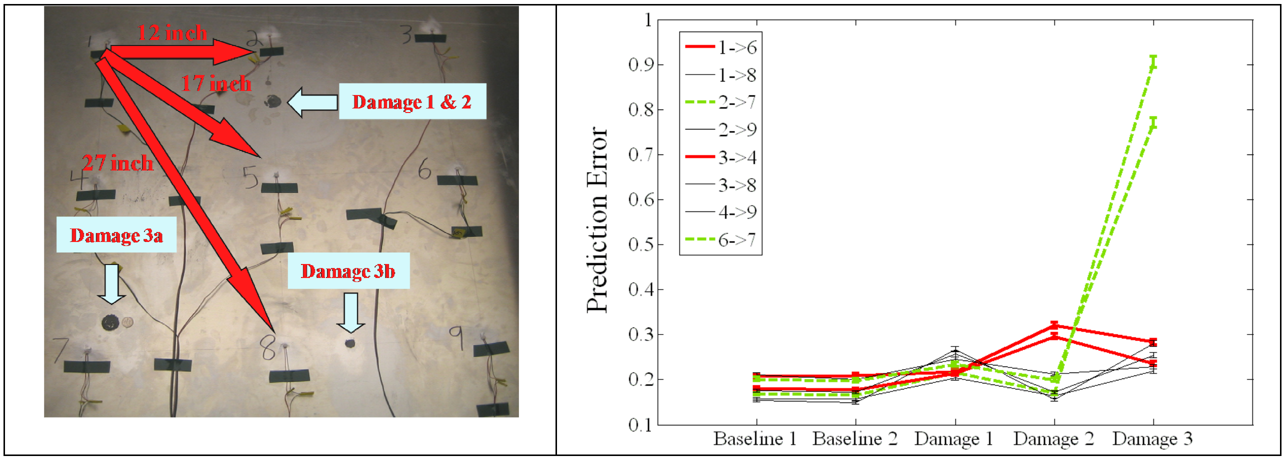

Figure 8: Detection of simulated corrosion using auto-regressive modeling of ultrasound waves from piezoelectric actuators/sensors (Todd and di Scalea 2009).

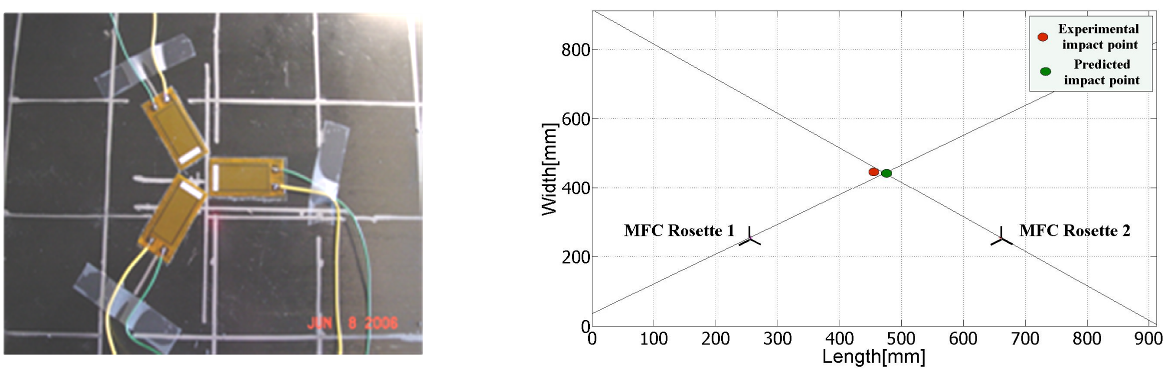

Figure 9: Prediction of impact point using ultrasonic guided waves from flexible macro-fiber composite transducers (Todd and di Scalea, 2009).

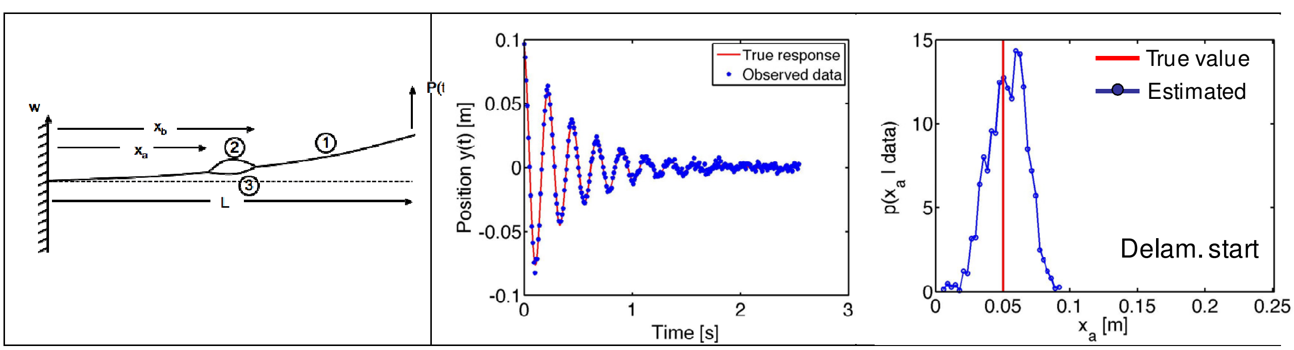

Figure 10: Detection of delamination in a composite beam using noisy free-decay data (Nichols et al., 2009).

can identify the damage start point, end point, and depth along with the associated confidence intervals (Figure 10). Using this approach delamination length and confidence intervals can be tracked over time, such as tracking a growing delamination using only noisy, free-decay response, such as wave slamming.

To arrive at a tenable framework for model-based SHM, a dedicated forward modeling capability has been developed using the finite element program CU-BEN and a suite of parallelized stochastic search tools, CU-PSST, to facilitate inverse problem solutions arising in model-based SHM system (Earls, 2010). A model-based approach can determine if something has changed in the hull structure, determine the location of the change, and identify what it is that has changed. This information then gives a basis for making a prognosis about the future performance of the hull structure. This prognosis is predicated on the existence of a robust and accurate forward model of the hull structure.

The SHM problem is posed in a system identification context through which, given some sparsely sensed response in an actual ship, various forwarding modeling hypotheses are tried out until the difference between the measured and modeled response is arbitrarily small. A projection from a continuous representation using Gaussian radial basis functions is adopted to significantly reduce the number of parameters over which the search is made. The process was demonstrated in a 10,000-element finite element model (Figure 11) of an idealized destroyer that has cracked frames simulated. The stochastic process found an “error” five times in each situation and then took the average to predict the damage. This demonstrates that a model-based SHM approach may be tenable within the current state of the art. Future directions in this on-going work include the use of Bayesian inferencing as a means for exploring the inverse solution.

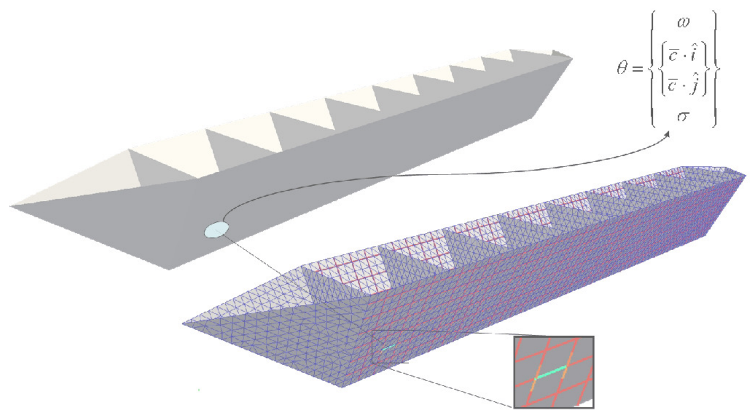

Figure 11: CU-Ben finite element model of destroyer with crack in hull (Earls, 2010).

Because it is impossible to instrument ship everywhere, sensor data is used to update global and local finite element models, reconciling measured data with a library of ship models. Updated models can provide fatigue assessment where there are no sensors, and the models can predict system behavior and hull vulnerabilities after damage is incurred. This updating was accomplished by Lynch and Law (2009) through Bayesian damage detection, an application of Bayes’ Theorem. This has been demonstrated in the detection of a crack in an aluminum plate using vibration measurements were model updating detected the crack location, depth, and severity (Figure 12).

Passive monitoring of the structural integrity of US Navy vessels from coherent processing of random vibrations recorded on a distributed sensor network during at-sea operation is being pursued. This is done by extracting estimates of the local structural impulse response between multiple sensor pairs by transforming each passive sensor into a virtual elastic source using the diffuse vibration interferometry technique (Sabra and Salvino, 2009). Estimates of the local structural impulse response between multiple sensor pairs are extracted by transforming each passive sensor into a virtual elastic source. Cross-correlation of all the vibration sensors in a distributed sensor network on a ship produces a coherent waveform to indicate the local structural response. The method was demonstrated on the HSV-2 *Norway* trials where the ship was instrumented with 35 strain gages creating 595 sensor pairs (Figure 13). Although temporal resolution was limited by a low sampling rate, little variations in the response of the hull were observed during the 6-day trial, as expected. The largest changes occurred along the keel, and these may have been due to fuel level changes or possible from temperature-induced stress. This demonstrates that diffuse vibration interferometry could provide low-cost and continuous on-board structural monitoring of Navy ships

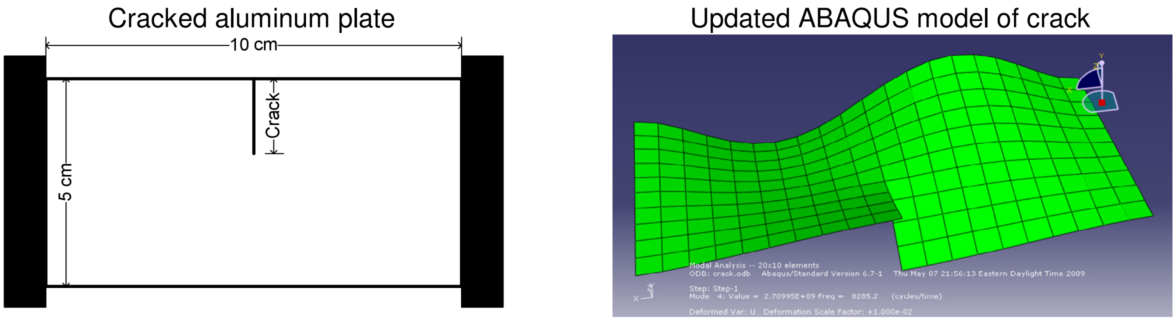

Figure 12: Crack in aluminum plate detected by updating finite element model based on measured mode shapes (Lynch and Law, 2009)

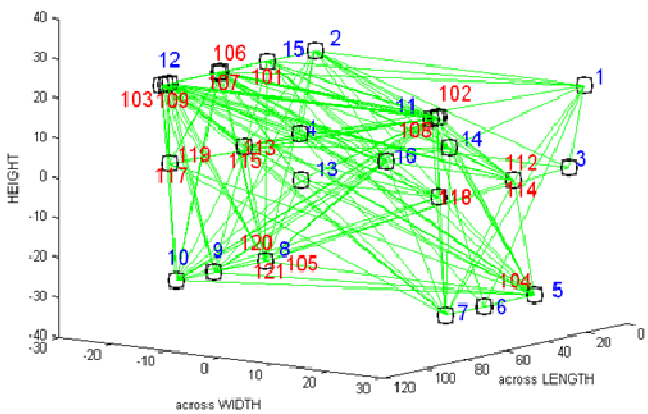

Figure 13: Strain gage network aboard high-speed ship (Sabra and Salvino, 2009).

INVESTIGATIONS BY NEWCASTLE UNIVERSITY

University of Newcastle have conducted initial scoping research to assess the strength characteristics of aluminium panels and plates with the eventual aim of developing valid methods to predict the ultimate strength of large aluminium high speed naval vessels (HSVs) (Benson et al., 2010) (Benson et al., 2009a). The strength characteristics of aluminium panel elements are required as an input in simplified progressive collapse analysis methods of the hull girder. The initial research has identified current uncertainties in the material characteristics and welding effects of marine aluminium alloys along with requirements for more extensive physical testing of typical HSV panels and grillages to validate numerical results. Finite element analyses have shown that the methods used to represent the stress-strain curve has a significant effect in determining aluminium plate ultimate strength characteristics

Analyses of the strength of stiffened panels in axial compression generally assume that the transverse frames are perfectly rigid and only permit rotation of the stiffeners at the supporting transverse frames. Reduced stiffness of the transverse frames can lead to additional deflection of a grillage as a whole and reduce the compressive strength, and can be a particular problem in aluminum structure because of the reduced elastic modulus. To analyze this situation, Benson et al. (2009b) performed finite element modeling of a series of aluminum and steel grillages. The grillages had ten longitudinals and six transverse frames. For all of the grillages, the stiffeners had a slenderness ratio, λ_s, of 0.4. The transverse frames were varied in size from tee shapes about 1.5 times as deep as the stiffeners to flat bars that were about the same depth as the stiffeners. The finite element models incorporated initial deflection in the plate and in the stiffeners. A heat affected zone (HAZ) was incorporated along the length of the stiffeners ad a tensile residual stress equal to the yield strength of the HAZ material was incorporated into the HAZ elements.

The aluminum grillages designated as Alu01, Alu02, and Alu03 were proportioned so that the plate slenderness ratio, β, was 3.0, 2.0, and 1.5 for the three series, respectively. The steel grillages had β equal to 1.5. Figure 14 shows the results of the finite element analyses, with the ratio of collapse strength, to yield strength, σ_{Max} / σ_0 plotted against the ratio of slenderness of the transverses to the slenderness of the stiffeners, λ_T / λ_s, with the rigid transverses having a ratio of 0.0. The results show a remarkably small dependence of the collapse strength on the stiffness of the transverse frames. For the series Alu03, which had the least plate slenderness, the ratio σ_{Max} / σ_0 reduced from 0.75 to 0.62, a reduction of about 20 percent, which is not insignificant, yet not a much of a reduction as one might expect from such flimsy flat bar transverse frames.

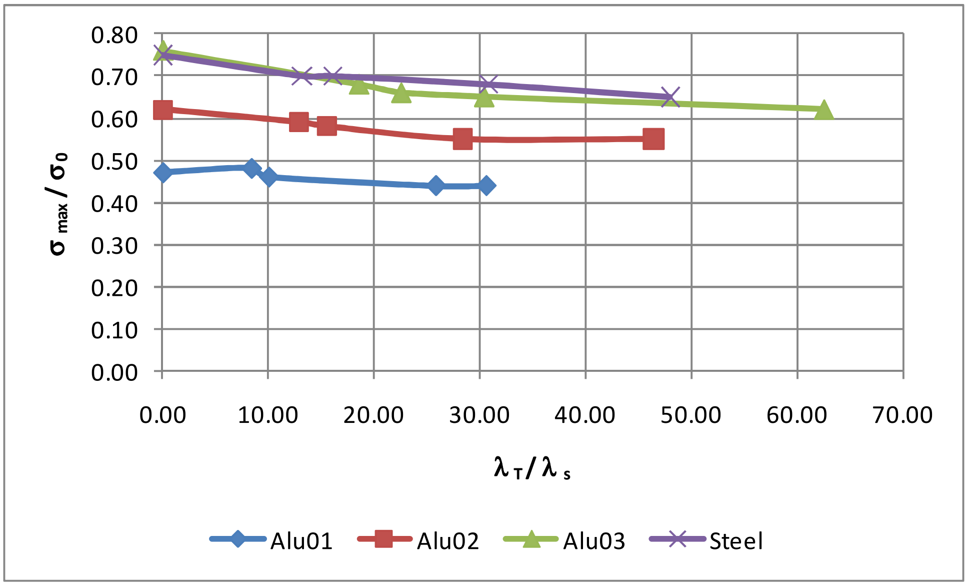

Figure 14: Effect of stiffness of transverse frames on collapse strength (Benson et al., 2010).

REPORTS OF THE SHIP STRUCTURE COMMITTEE

The collapse testing of friction stir welded panels by Paik reported as SSC report 456 was described above. There are several other recent reports of interest issued by the SSC on aluminum structure. Report SSC-454, Ultimate Strength and Optimization of Aluminum Extrusions (Collette et al., 2008) provides a means for the optimization of the design of aluminum panels that have extruded stiffeners either welded to plate or integrally extruded with the plate. With steel structural shapes, the designer is somewhat constrained by the number of available shapes because it is expensive for a steel mill to manufacture a new set of rollers to produce a special shape. With aluminum extrusions, the cost of a new die to produce a custom shape is relatively inexpensive, and thus the structural designer has the choice of designing a structural shape to fit a particular design, especially is a large mill order is involved. An example from the report is shown in Figure 15 where a series of optimized designs have been developed subject to constraints using either tee stiffeners, hat-shaped stiffeners, or sandwich panels based on the desired compressive strength of the structure. In this case, if a panel with integrally extruded tee sections was desired with a compressive strength of 108 MPa, a stiffener spacing of 153 mm on 2 mm-thick plate having 95.7 x 2.8 / 19.2 x 2.8 Tees would be selected.

The SSC is planning project SR-1465, Design and Detailing for High Speed Aluminum Vessels Design Guide and Training. This project will expand on the SSC aluminum guide, SSC- project would be to develop a design guidance note and prepare a marine industry training program for the design and detailing of high speed and conventional aluminum ship structures. Project SR-1467 , Incorporation of Residual Stress Effects in a Plasticity, Fracture, and Fatigue Crack Growth Model for Reliability Assessment of Aluminum Ship Structures will develop an experimentally calibrated and verified, computational tool which accurately predicts the plastic response and failure due to fatigue and ductile fracture under the influence of residual stresses of a structural aluminum alloy.

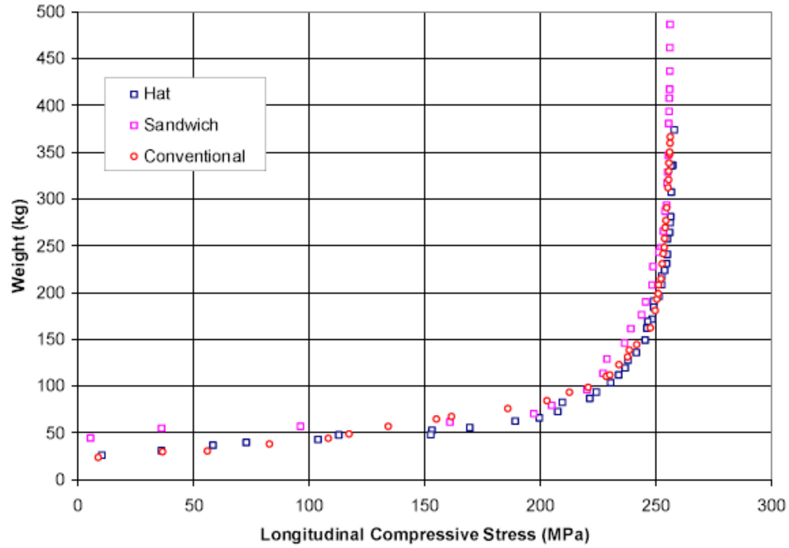

Figure 15: Optimum aluminum panel design (Collette et al., 2008)

CONCLUSIONS AND DISCUSSIONS

The work that has been reviewed is for the large part work in progress. However, this demonstrates that there is a significant amount of research being conducted on the use of aluminum in ship structures.

ACKNOWLEDGEMENT

Much of the information gathered for this report was the result of the U.S. Navy Office of Naval Research program in Ship Structural Reliability, sponsored by. Paul E. Hess. The support of Dr. Hess and ONR is greatly appreciated.

REFERENCES

ABS (2009), “Guide for Building and Classing High-Speed Naval Craft 2007”, American Bureau of Shipping, Corrigenda/Editorials – 15 December 2009.

Anderson, Karlin (2009). “Hull Structural Ultimate Strength Prediction for Navy Ships (ULTSTR)”, presentation made at the March 24–25 *ONR Ship Structural Reliability Program Team Meeting* held in Arlington, Virginia.

Benson, S., J. Downes, and R.S. Dow (2009a). “Requirements for Evaluating the Structural Strength of Aluminium Alloys for Use in Marine Platforms”, Document ID: ONR-UNEW-12-2 Structural Performance of Aluminium Naval Vessels, ONR Grant: N00014-07-1-0533, April 2009.

Benson, Simon, Jonathan Downes, and Robert Dow (2009b) “Collapse Modes and Ultimate Strength Characteristics of Aluminum Grillages in Large High Speed Craft”, presented at the *Tenth International Conference on Fast Sea Transportation (FAST 2009),* Athens, Greece, October, 2009.

Collette, Matthew, Nick Deodhar, and Daniel Liut (2009), “Stochastic Description of Structural Fatigue Initiation and Propagation”, presentation made at the *ONR Ship Structural Reliability Program Fracture Workshop* held in Carderock, Maryland, April 30, 2009.

Collette, Matthew (2009). “Improving Engineering Capability for Aluminum Structures of High-Speed Vessels”, presentation made at the *ONR Ship Structural Reliability Program Team Meeting* held in Arlington, Virginia, March 24–25, 2009.

Collette, Matthew, X. Wang, J. Li, J. Walters, and T. Yen (2008), “Ultimate Strength and Optimization of Aluminum Extrusions”, Ship Structure Committee report SSC-454, 2008.

Devine, Edward, David Kihl, Chandra Ullagaddi, Richard Chen, Benjamin Grisso, and Jeffrey Beach (2010), "Experimental Strength, Fatigue and Fracture Assessment", presentation made at the *ONR Ship Structural Reliability Program Team Meeting* held in Arlington, Virginia April 26–27, 2010.

Benson, S., J. Downes, and R.S. Dow (2010). "A Semi-analytical Method to Predict the Ultimate Strength and Collapse Behaviour of Orthogonally Stiffened Panels", *11th International Symposium on Practical Design of Ships and Offshore Structures*, September 20–24, 2010, Rio de Janeiro.

Earls, C.J. (2010). "Reduced Order Modeling to Enhance Thermal Imaging for Crack Detection", presentation made at the *Society for Industrial and Applied Mathematics Annual Meeting*, held in Pittsburgh, Pennsylvania July 6–16, 2010.

Gao, Xiaosheng, Guihua Zhang, and Charles Roe (2009). "A Study on the Effect of the Stress State on Ductile Fracture", International *Journal of Damage Mechanics OnlineFirst*, published on June 26, 2009 as doi:10.1177. 1056789509101917.

Johnson, Robert E., Jeffrey E. Beach, and Frederick S. Koehler (1984), "The Aluminum Ship Evaluation Model (ASEM) Cyclic Test Results", David W. Taylor Naval Ship Research and Development Center report DTNSRDS-84/094, December 1984.

Lua, Jim, Jay Shi, and N. Thammadi (2009). "XFEM Toolkit for Crack Path and Life Prediction of Aluminum Structures", AIAA-2009-2616. *50th AIAA/ ASME/ ASCE/ AHS/ASC Structures, Structural Dynamics, and Materials Conference*, May 4–7, 2009, Palm Springs, California.

Lynch, Jerome et al. (2009), "Multi-tiered Wireless Sensor Networks for Monitoring Operational Naval Vessels," *IMAC XXVII*, Orlando, Florida, February, 2009, Society for Experimental Mechanics.

Nichols, Jonathan M., M. Seaver, S. Trickey, K. Scandell, and L. W. Salvino (2009)." Real-time Strain Monitoring of a Navy Vessel During Open Water Transit," *Journal of Ship Research*, July, 2009.

Paik, Jeom Kee (2009), "Buckling Collapse Testing on Friction Stir Welded Aluminum Stiffened Plate Structures", Ship Structure Committee report SSC-456.

Paik, Jeom Kee, A.K. Thayamballi, J.Y. Ryu, J.H. Jang, J.K. Seo, S.W. Park, S.K. Soe, C. Renaud, and N.I. Kim (2008), "Mechanical Collapse Testing on Aluminum Stiffened Panels for Marine Applications", Ship Structure Committee report SSC-451.

Sabra, Karim G. and Liming W. Salvino (2009). Using DVI For Structural Health Monitoring of High-Speed Naval Ships, 7th International Workshop on Structural Health Monitoring, Stanford, September 2009.

Sielski, Robert A. (2007), "Aluminum Marine Structure Design and Fabrication Guide," Ship Structure Committee report SSC-452.

Todd, Michael and Francesco Lanza di Scalea (2009), "Proof-of-Concept Studies in Novel Guided Wave Methods for Metallic Structural Condition", Final Technical Report, Grant Number N00014-08-1-0973, University of California at San Diego, June 15, 2009..

Vassilaros, Michael G. and Ernest J. Czyryca (1979), "Natural Aging and Sensitization of 5000-Series Marine Aluminum Alloys", David W. Taylor Naval Ship Research and Development Center report DTNSRDC/SME-78/106, June 1979.

Warner, Derek H. and W.A. Curtin (2009). "Origins and Implications of Temperature Dependent Activation Energy Barriers for Dislocation Nucleation in FCC Metals," *ActaMaterialia* Vol. 57, No. 14, (2009), p. 4267-4277..

Wong, Catherine (2009), "Marine Aluminum Alloys Sensitization Failure Model", presentation made at the *ONR Ship Structural Reliability Program Team Meeting* held in Arlington, Virginia, March 24–25, 2009.

Seventh International Conference
On High-Performance Marine Vehicles
Melbourne, Florida, USA
13-15 October 2010

REDUCING FUEL CONSUMPTION IN MODERATELY FAST DISPLACEMENT SHIPS

Volker Bertram, Harry Vordokas
Germanischer Lloyd, Hamburg/Germany
volker.bertram@GL-group.com

ABSTRACT

The paper surveys engineering options to save fuel in moderately fast displacement and semi-displacement ships, typically ferries and RoPax vessels. The main focus lies on propulsion power, a secondary focus lies on auxiliary power. The main options for fuel savings are discussed, along with typical saving potential and tools to decrease power requirements and fuel consumption. New developments in simulation methods are described in more detail, such as formal optimisation of hull forms, free-surface CFD codes for fast ships, and design applications of CFD for superstructures. Case studies from the experience of GL Group illustrate the approaches to reduce fuel consumption.

KEYWORDS

CFD, Efficiency, Fuel Saving

INTRODUCTION

Mid-term and long-term fuel prices are expected to range from 500 to 1000 $/t including expected future surcharges for CO_2 (carbon-dioxide) emissions. The introduction of emission control areas, particularly in regions where most fast ferries operate, will lead to increased use of cleaner fuels. This will put significant pressure on the shipping industry to reduce fuel consumption. As a result, we should see a shift towards lower speeds and more fuel efficient designs in the high-performance marine vehicles industry. There are any many ways to reduce fuel consumption.

- reduce required power for propulsion
- reduce required power for equipment on board
- use fuel energy more efficiently for propulsion and on-board equipment
- substitute fuel power (partially) by renewable energies like wind and solar energy

Surveys on fuel saving options have been published before. Several HSVA (Hamburg Ship Model Basin) publications, Hollenbach et al. (2007), Mewis and Hollenbach (2007), Hollenbach and Friesch (2007), give rather comprehensive overviews of hydrodynamic options in design and operation of ships. Hochhaus (2007) discusses various approaches to recuperate energy losses from the main engine to use them for on-board equipment. However, these publications focus on partial aspects and do not consider the specific situation of fast ferries and ro-pax vessels. We will discuss more comprehensively the available options for these ships in the following.

REDUCE REQUIRED POWER FOR PROPULSION

We may use traditional hydrodynamic approaches to decompose the power requirements into resistance and propulsion aspects. While propulsor and ship hull should be regarded as systems, the structure may help to understand where savings may be (largely) cumulative and where different devices work on the same energy loss and are thus mutually excluding alternative.

Reduce resistance

There are many ways to reduce the resistance of a ship. On the most global level, there are two options:

- Reduce ship weight: The lightship weight may be reduced for example by lightweight materials and more sophisticated structural design involving possibly formal optimization. Also, fuel bunkers should be kept as low as possible.
- Reduce speed: Speed reduction is a very effective way to reduce fuel consumption and emission. HSVA reports fuel savings of 16-19% for containerships, for a speed reduction by 5%, Mewis and Hollenbach (2007). Isensee et al. (1997) pointed already out that transport efficiency increases drastically with decreasing speed. Figure 1 shows a modified Karman-Gabrielli diagram. The horizontal axis shows the speed of the vehicle and the vertical axis a specific transport energy demand (reverse transport efficiency), where the installed power is divided by the mass of the vehicle including cargo and its design speed. Some very fast ferries have transport efficiencies comparable to those of airplanes.

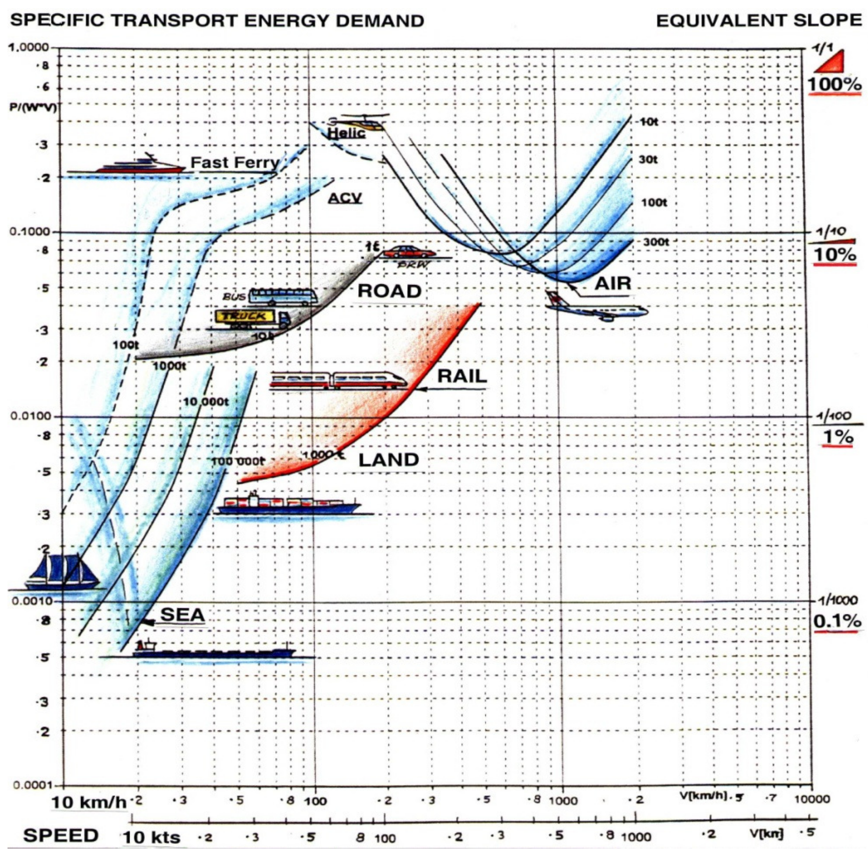

Figure 1: Transport efficiency vs speed for various vessels (modified Karman-Gabrielli diagram)

For given speed and displacement of a ship, the largest levers in ship design lie in the proper selection of general hull type, main dimensions and the ship lines. Ship model basins should be consulted to assess the impact of main dimensions, using their experience and data bases. On a more detailed level, for a given speed and ship weight, all components of the ship resistance, Bertram (2000), may offer fuel saving potential:

- <u>Frictional resistance of bare hull</u>: The frictional resistance (for given speed) depends mainly on the wetted surface (main dimensions and trim) and the surface roughness of the hull (average hull roughness of coating, added roughness due to fouling). Ships with severe fouling may require twice the power as with a smooth surface. Silicone-based coatings create non-stick surfaces similar to those known in Teflon coated pans. In addition to preventing marine fouling, these smooth surfaces may result in additional fuel savings. 1.5-2.5% averaged over 5-year intervals (time between docking) may be feasible, provided that the coatings are properly applied. Air lubrication has attracted much attention as a more sophisticated approach, but demonstrated savings are low and technical effort high. It is unlikely that commercial applications to ferries is seen for decades to come.

- Wave resistance of bare hull: For given main dimensions, wave resistance offers large design potential, particularly for monohulls. Moderate changes in lines can result in considerable changes of wave resistance. Bulbous bows should be designed based on CFD (computational fluid dynamics), but in most cases fast codes based on simplified potential flow models suffice, Bertram (2000). A formal optimization is recommended as this may offer 4-5% improvement for moderate to fast monohull ferries, Figure 2, Abt and Harries (2007), Oossanen et al. (2009). Optimization of the aftbody lines requires considerably higher computer resources due to the dominant effects of viscosity and turbulence. However, pilot applications show the feasibility of the approach and formal optimization of aftbody lines is expected to appear soon as a standard option in ship design. Hull optimization is also difficult for planing hulls, where we have no confidence in fast potential flow based codes and sophisticated CFD simulations are so far too expensive and sensitive for formal optimization.

- Residual resistance of bare hull (mainly due to flow separation): Flow separation occurs when the velocity gradients become too large in a flow. Large curvature in flow direction should then be avoided. Flow separation in the aftbody is delayed by the flow acceleration due to the propeller and different in model scale and full scale. CFD simulations may help in finding suitable compromises between hydrodynamic and other design aspects.

- Resistance of appendages: Appendages contribute disproportionately to the resistance of a ship. This is particularly important for fast ships where the appendages contribute significantly to the total resistance. CFD simulations can determine proper alignment of appendages, Figure 3.

- Rudder resistance: Rudders offer an often underestimated potential for fuel savings. Improving the profile or changing to a highly efficient flap rudder allows reducing rudder size, thus weight and resistance. High-efficiency rudders combine various approaches to save fuel, e.g. Beek (2004), Lehmann (2007). Savings of 2-8% are claimed by the manufacturers; we estimate that 1-3% is more realistic.

- Added resistance due to seaway: Added resistance in seaways changes considerably for different hull types. It is more important for fast ferries that for e.g. large containerships. Sea margins should then be chosen based on simulations rather than taking a global number like 15%, which does not reflect the actual need for additional power in seaways. Increasing ship length usually improves seakeeping and reduces added resistance in waves. Intelligent routing (i.e. optimization of a ship's course and speed) may reduce the average added resistance in seaways. For example, the Ship Routing Assistance system, Rathje and Beiersdorf (2005), was originally developed to avoid problems with slamming and parametric roll, but may also be used for fuel-optimal routing. However, GL experts estimate the saving potential to less than 1% for conventional displacement hull and most realistic scenarios. If applied, routing systems for fuel optimization should not only consider the added resistance to motions in waves, but also the higher rudder resistance due compensation of drift forces.

- Added resistance due to wind: Wind adds power requirements in two ways: (a) direct aerodynamic resistance on the ship and (b) indirect power demand due to drift in side winds. The effect can be evaluated in wind tunnel tests and CFD simulations, Figure 4, Schmode and Bertram (2002). Superstructures may be streamlined using CFD and even formal optimization, Harries and Vesting (2010).

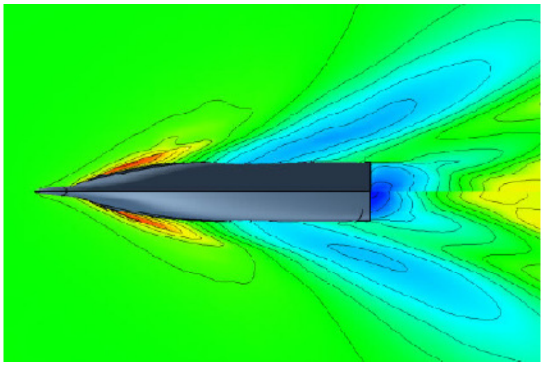

Figure 2: Hull line optimization of fast hull, Oossanen et al. (2009)

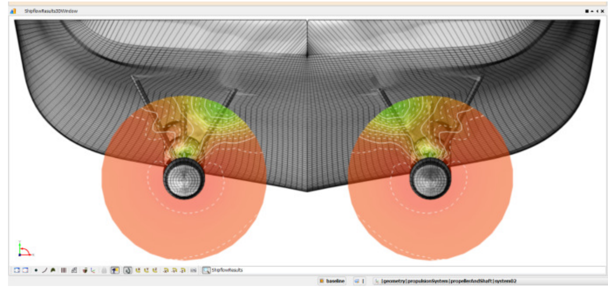

Figure 3: CFD for appendages of fast ferry, source: www.friendship-system.de

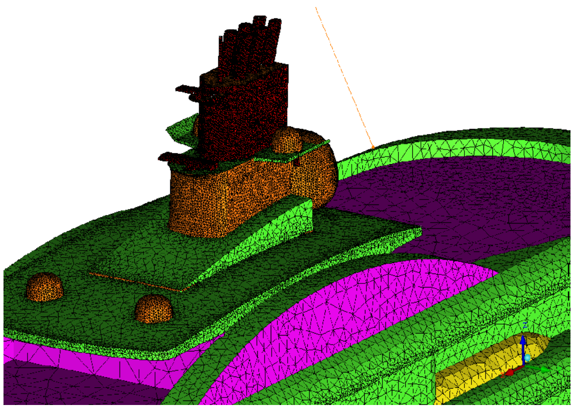

Figure 4: CFD analysis of ship superstructure

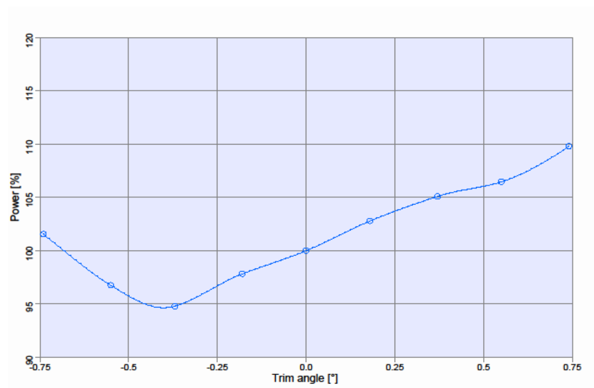

Figure 5: Simulation-based optimum trim (curve for one speed and one average draft)

For each draft and speed, there is a fuel-optimum trim. For ships with large transom sterns and bulbous bows, the power requirements for the best and worst trim may differ by more than 10%, Mewis and Hollenbach (2007). Systematic CFD simulations are recommended to assess the best trim and the effect of different trim conditions. Decision support systems for fuel-optimum trim based on such simulations have been proven to result in considerable fuel savings (typically 5% as compared to even keel) for relatively low investment, Figure 5, Hansen and Freund (2010). As the decision for the optimum trim is based on potential flow computations, this approach is applicable to displacement hulls. The benefit is generally expected to be larger for monohulls than for catamarans.

Improve propulsion

The propeller transforms the power delivered from the main engine via the shaft into a thrust power to propel the ship. Typically, only 2/3 of the delivered power is converted into thrust power. A special committee of the ITTC (1999) discussed extensively assorted unconventional options to improve propulsion of ships and the associated problems in model tests. In short, model tests for these devices suffer from scaling errors, making quantification of savings for the full-scale ship at least doubtful.

- Operate propeller in optimum efficiency point: The propeller efficiency depends among others on rpm and pitch. Fixed pitch propellers are cheaper and have for a given operating point a better efficiency than controllable pitch propellers (CPPs). They may be replaced if the operator decides to operate the ship long-term at lower speeds. CPPs can adapt its pitch and thus offer advantages for ships operating over wider ranges of operational points. Several refit projects have been reported, with savings up to 17% quoted due to new blades on CPPs, N.N. (2008). For high speeds, waterjets are more efficient than propellers. However, the general trend towards lower (moderate) speeds should favor propeller options for future ferries and ro-pax designs.

- Reduce rotational losses: For most ships, there is substantial rotation energy lost in the propeller slipstream. Many devices have been proposed to recover some of this energy. These can be categorized into pre-swirl (upstream of the propeller) and post-swirl (downstream of the propeller) devices. Typically 4% fuel savings are claimed for all these devices by manufacturers. But some of the claims appear questionable. CFD simulations should be use to evaluate effects of these devices at full scale. Contra-rotating propellers are a traditional device to recover the rotational energy losses, Schneekluth and Bertram (1998). More recently, podded drives and conventional propellers have been combined to hybrid CRP-POD propulsion, Ueda and Numaguchi (2006), claiming 13% fuel savings.
- Reduce frictional losses: Smaller blades with higher blade loading decrease frictional losses, albeit at the expense of increased cavitation problems. A suitable tradeoff should be found using experienced propeller designers and numerical analyses.
- Reduce tip vortex losses: The pressure difference between suction side and pressure side of the propeller blade induces a vortex at the tip of the propeller. This vortex (and the associated energy losses) can be suppressed (at least partially) by tip fins similar to those often seen on aircraft wings. The general idea has resulted in various implementations, differing in the actual geometric form of the tip fin, ITTC (1999), namely contracted and loaded tip (CLT) propellers (with blade tips bent sharply towards the rudder), Sparenberg-DeJong propellers (with two-sided shifted end plates), or Kappel propellers (with integrated fins in the tip region). However, for one ferry project in Scandinavia, savings for design speed were compensated with losses in off-design conditions for a Kappel propeller. In sum, the Kappel propeller did not result in net savings. The general lesson is that ships and propellers should be designed for real-life operational profiles rather than for just one design point.
- Reduce hub vortex losses: Devices added to the propeller hub have been promoted as cost effective fuel savings. Propeller boss cap fins (PBCF) were developed in Japan, ITTC (1999). Publications of the patent holders report 3-7% gains in propeller efficiency in model test and 4% for the power output of a full-scale vessel. Reported gains appear to be highly questionable, Junglewitz (1996).
- Operate propeller in better wake: The propeller operates in an inhomogeneous wake behind the ship. This induces vibrations, but also fluctuations around the optimum efficiency of the propeller blades. A more homogeneous wake translates then into better propeller efficiency. For slender hulls, the wake is already relatively good. Wake equalizing devices like Schneekluth nozzles (a.k.a. wake equalizing ducts (WED)), Grothues spoilers, vortex generators, Schneekluth and Bertram (1998), are therefore not attractive for fast ferry designs. They induce more resistance than they save in terms of propulsion. Instead, CFD should be used to optimize the lines considering hull, propeller and appendages together, Oossanen et al. (2009).

Resistance and propulsion and main engine interact. Partial improvements of individual components as possible as discussed so far, but the system analyses considering the interaction of the components offers additional saving potential.

Ships are frequently hydrodynamically tuned for one design speed, but later operated mostly at lower speeds. If designed for a more realistic mix of operational speeds, ships are estimated to exploit further fuel saving potential. Similarly, an even speed profile in operation saves fuel. This is largely a question of awareness. Fuel monitoring systems have proven to be effective in instigating more balanced ship operation with fuel savings of up to 2%.

REDUCE REQUIRED POWER FOR EQUIPMENT ON BOARD

There are various options to save power in the assorted energy consuming equipment onboard ferries. The saving potential depends on the ship type. Examples are in more efficient electronically controlled pumps, HVAC (heat, ventilation and air conditioning) ventilation systems, and energy saving lighting. Energy-saving lamps not only reduce the energy requirements for lighting, they also reduce the waste heat from the lamps and thus the energy needed by air conditioning systems to cool lighted rooms down again.

Avoid oversized main engines. Sea margins should be adapted to ship type, ship size and intended operational trade. This is especially true for fast ships. Sea margins should be selected based on simulations or experience for specific ship types, but not globally imposed. Margins for rare high-speed operation are expensive and may be better covered by falling back on the auxiliary engine power (power take-in (PTI) via shaft generator). Detailed engineering analyses can be used to assess feasibility and cost aspects of alternative configurations, Figure 6. For slow-steaming ships with controllable pitch propeller, it is better to reduce the brake mean effective pressure than the rpm. Intelligent monitoring and simulation software can combine engine supplier data and standard onboard monitoring data for a given operational profile to determine optimum combinations of propeller pitch and rpm.

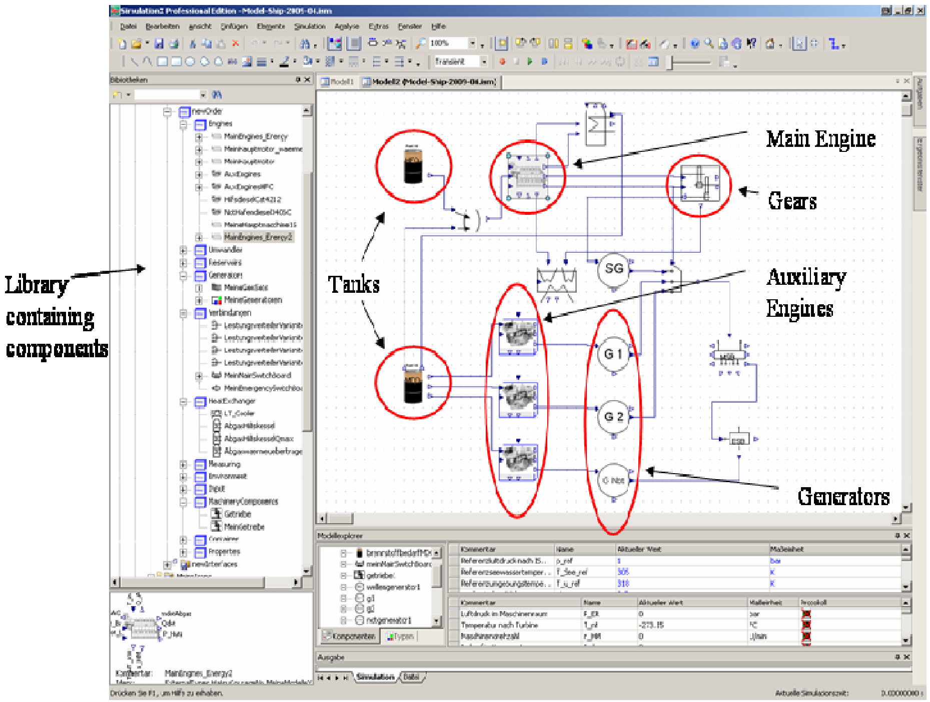

Figure 6: Machinery simulation tool, Freund et al. (2009)

Avoid oversized auxiliary engines. Better overall energy management systems may balance the energy demand of the consumers on board reducing peak demands allowing in turn a reduction of the generator capacity. This in turn reduces the weight of the ship. Simulations of the overall machinery system are able to predict fuel consumptions for provided energy consumer profile. These simulations allow assessment of alternatives and ultimately better balanced energy profiles.

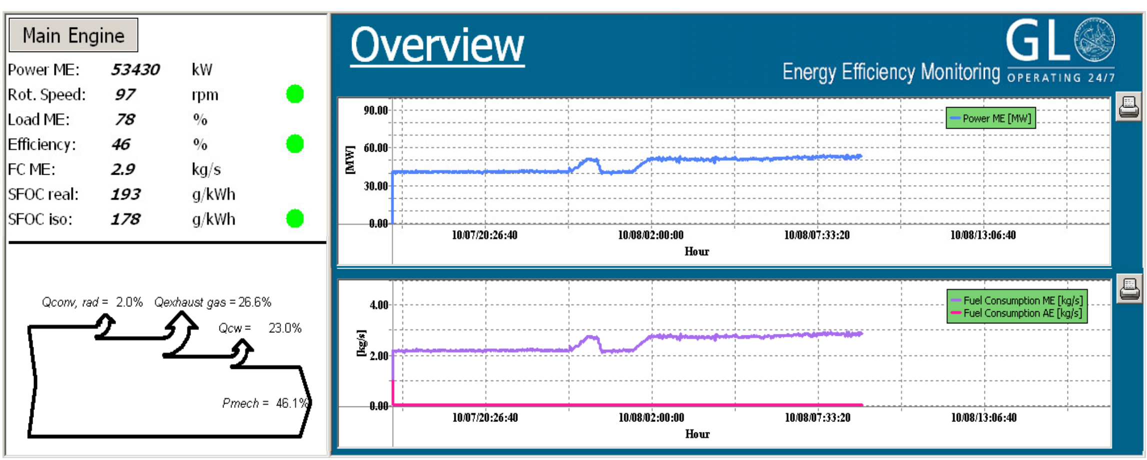

Figure 7: Energy Efficiency Monitoring for main engine

Our simulations are based on the software ITI SimulationX. The simulations can be adapted easily to different ships using a library of predefined machinery components. The simulations were validated for two ships, Freund et al.

(2009). The fuel consumption was calculated within 2% deviation of the reported noon data over periods of 4-8 weeks. Installed onboard, the current consumption of mechanical and electrical energy can be displayed in combination with the fuel consumption of the engines and their efficiency of power generation, Hansen and Freund (2010). In conjunction with the displayed time lines, the crew can evaluate their actions with regard to energy consumption, e.g. avoiding unnecessary peak loads requiring a higher number of running engines. An example is displayed in Figure 7, with the current values of the main engine displayed on the left with the related timelines on the right.

CONCLUSION

There are many technical levers to save fuel and thus emissions for ships. Unfortunately, there is large scatter in saving potential and quoted saving potential is unreliable. Manufacturers frequently quote best cases and sometimes extrapolate erroneously results from model tests to full scale ships. Despite these uncertainties, the compiled information may serve for a first assessment on a case by case basis and identification of most promising options. This requires interdisciplinary team work of clients and consulting experts. For a more quantitative assessment, dedicated analyses often based on simulations are required.

Despite these words of caution, there is wide consensus that significant potential for fuel saving exists and dedicated consultancy companies can support ship owners and operators in tapping into these potentials.

ACKNOWLEDGEMENTS

Many colleagues at FutureShip and Germanischer Lloyd have supported this paper with their special expertise, namely (in alphabetical order) Bettar El Moctar, Malte Freund, Heikki Hansen, Karsten Hochkirch, Volker Höppner, Andreas Junglewitz, Ralf Plump, Gerd-Michael Würsig.

REFERENCES

Abt, C., Harries, S. (2007), "A new approach to integration of CAD and CFD for naval architects", *6th Conf. Computer and IT Applications in the Maritime Industries (COMPIT)*, Cortona, pp.467-479. http://www.ssi.tu-harburg.de/doc/compit/compit2007_cortona.pdf

Beek, T. van (2004), "Technology Guidelines for Efficient Design and Operation of Ship Propulsors", Marine News, Wärtsilä.
http://www.wartsila.com/Wartsila/global/docs/en/ship_power/media_publications/marine_news/2004_1/technology.pdf

Bertram, V. (2000), Practical Ship Hyrodynamics, Butterworth and Heinemann, Oxford.

Freund, M., Würsig, G.M., Kabelac, S. (2009), "Simulation tool to evaluate fuel and energy consumption", *8th Conf. Computer and IT Applications in the Maritime Industries (COMPIT),* Budapest, pp.364-373
http://www.ssi.tu-harburg.de/doc/webseiten_dokumente/compit/dokumente/compit2009.pdf

Hansen, H., Freund, M. (2010), "Assistance tools for operational fuel efficiency*", 9th Conf. Computer and IT Applications in the Maritime Industries (COMPIT)*, Gubbio

Harries, S., Vesting, F. (2010), "Aerodynamic optimization of superstructures and components"*, 9th Int. Conf. Computer and IT Applications in the Maritime Ind. (COMPIT),* Gubbio

Harries, S., Hinrichsen, H., Hochkirch, K. (2007), "Development and application of a new form feature to enhance the transport efficiency of ships", Jahrbuch Schiffbautechnische Gesellschaft, Springer
http://futureship.net/downloads/2007_STGpaperInSAC_HaHiHo.pdf

Harries, S., Abt, C., Heimann, J., Hochkirch, K. (2006), "Advanced hydrodynamic design of container carriers for improved transport efficiency" *RINA Conf. Design & Operation of Container Ships*, London
http://futureship.net/downloads/RINAadvancedHydroDesTransEffFinalPaper.pdf

Hochhaus, K.H. (2007), „Umweltbetrachtungen zur Schiffahrt", *Hansa* 144/6, pp.70-76.

Hollenbach, U., Friesch, J. (2007), “Efficient hull forms – What can be gained”, *1st Int. Conf. on Ship Efficiency*, Hamburg, http://www.ship-efficiency.org/2007/PDF/HOLLENBACH_FRIESCH.pdf

Hollenbach, U., Klug, H., Mewis, F. (2007), *“Container vessels – Potential for improvements in hydrodynamic performance”*, *10th Int. Symp. Practical Design of Ships and Other Floating Structures (PRADS),* Houston.

Hutchison, B., Hochkirch, K. (2007), “CFD Hull Form Optimization of a 12,000 cu.yd. (9175 m3) Dredge”, *PRADS 2007*, Houston
http://futureship.net/downloads/2007_Hutchison_Hochkirch_Prads07_Dredge.pdf

Isensee, J.; Bertram, V.; Keil, H. (1997), “Energy efficiency and air pollution: A comparison of ships and other vehicles”, *FAST'97*, Sydney

ITTC (1999), “The specialist committee on unconventional propulsors”, *22nd Int. Towing Tank Conf.*, Seoul, http://ittc.sname.org/Unconventional%20Propulsion.pdf

Junglewitz, A. (1996), „Der Nabeneinfluß beim Schraubenpropeller“, PhD thesis, Univ. Rostock.

Mewis, F., Hollenbach, U. (2007), „Hydrodynamische Maßnahmen zur Verringerung des Energieverbrauches im Schiffsbetrieb“, *Hansa* 144/5, pp.49-58.

Lehmann, D. (2007), “Improved Propulsion with Tuned Rudder Systems*”, 1st Int. Conf. on Ship Efficiency*, Hamburg, http://www.ship-efficiency.org/2007/PDF/LEHMANN.pdf

N.N. (2008), “Reblading to enhance economy and comfort”, Marine Propulsion Feb/Mar, pp.54-55.

Oossanen, P.van, Heimann, J., Henrichs, J., Hochkirch, K. (2009), “Motor yacht hull form design for the displacement to semi-displacement speed range”, *10th Int. Conf. Fast Sea Transportation (FAST),* Athens
http://www.futureship.net/download/vanOossanen_etal_FAST2009_Paper143_090630.pdf

Schmode, D., Bertram, V. (2002), “Aerodynamic flow computations for a Superfast ferry”*, 3rd Int. Conf. High-Performance Marine Vehicles*, Bergen, pp.345-354

Schneekluth, H., Bertram, V. (1998), “Design for Efficiency and Economy”, Butterworth & Heinemann, Oxford.

Ueda, N., Numaguchi, H. (2006), “The first hybrid CRP-POD driven fast ROPAX ferry in the world”, *J. Japan Inst. Marine Eng.* 40/2, translated English version:

Van Oossanen, P., Heimann, J., Henrichs, J., Hochkirch, K. (2009), “Motor yacht hull form design for the displacement to semi-displacement speed range”, *10th Int. Conf. Fast Sea Transportation (FAST),* Athens
http://futureship.net/download/vanOossanen_etal_FAST2009_Paper143_090630.pdf

Seventh International Conference
On High-Performance Marine Vehicles
Melbourne, Florida, USA
13-15 October 2010

A SIMPLIFIED APPROACH AND INTERIM CRITERIA FOR COMPARING THE RIDE QUALITY OF HIGH SPEED CRAFT IN ROUGH WATER

Michael R. Riley, The Columbia Group, Norfolk, Virginia, USA
Dr. Tim Coats, Kelly Haupt, Donald Jacobson, Naval Surface Warfare Center Carderock Division Detachment Norfolk, Combatant Craft Division, Norfolk, Virginia, USA

ABSTRACT

This paper presents a generalized approach and interim criteria for computing the average of the 1/n^th^ highest accelerations when analyzing accelerometer data recorded during trials of manned and unmanned small boats and craft. The approach reduces subjectivity in the calculation and should help achieve repeatability when calculations are performed for different data sets and by different researchers. Engineering rational is presented for a quantitative Ride Quality Index as an indicator of the relative damage potential in wave slam events that can be used as a comparative tool for assessing the relative ride quality between different craft, at different speeds, in different sea conditions, or for different gauge locations. The general approach and the simple criteria may be used for initial comparative assessments of structural integrity, equipment susceptibility, or personnel comfort and safety. Example acceleration data and sample ride quality comparisons are presented.

NOMENCLATURE

A_i	Wave encounter peak acceleration (g)
A_j	Discrete acceleration data point within a data record
dB	Decibels
g	Acceleration due to gravity (32.2 ft/sec^2)
$H_{1/3}$	Significant wave height (feet)
Hz	Hertz
LCG	Longitudinal center of gravity
L_W	Average length of wave
m	Number of data points in a signal record
n	Number of highest values to average
N	Number of peak accelerations
RMS	Root mean square
RQI	Ride quality index
T	Wave encounter period (seconds)
T_w	Average wave period (seconds)
V_k	Craft average speed (knots)
x	Independent parameter
y	Dependent parameter

KEYWORDS

Craft, Wave Slam, Ride Quality, Shock Effects, Acceleration Data

INTRODUCTION

The Combatant Craft Division (CCD) of Naval Sea Systems Command (NAVSEA), Naval Surface Warfare Center Carderock Division conducts at-sea performance trials of planing craft (both manned and unmanned new technology prototypes and new acquisition) for numerous government agencies and private industry. During these trials accelerometers are typically installed to capture the dynamic motions of the craft in waves. These motions are of interest because they are applied in craft design and comparative craft evaluations to address multiple factors associated with seaworthiness, including hull design loads, stability, component ruggedness, and crew or passenger comfort and safety.

HISTORICAL PERSPECTIVE

In general terms the ride quality of any vehicle often includes a discussion of the effect of vehicle motions on passengers. This was especially true in the airline and automobile industries where noise, temperature, and vibrations in vertical and lateral directions are related to passenger comfort. The vibration amplitudes are typically characterized by root mean square (RMS) acceleration values [1]. It is no surprise that technical advances made in these fields greatly influenced marine vehicle researchers who applied statistical measures and used RMS acceleration criteria to compare the motions experienced on displacement hulls, surface effects ships, and hydrofoils with established criteria for motion sickness and fatigue [2].

In the mid-1970's it was reported that when marine vehicle motions include shocks or impulsive velocity change, then RMS acceleration values have no relation to crew comfort or the potential for injury for crest factors (peak acceleration to RMS ratio) greater than three [3]. It was also reported that there was a general dissatisfaction with the lack of valid hard data upon which meaningful comparisons of the ride quality could be based, and there was no fully satisfactory criterion for judging the ride quality of high speed craft in rough seas [4]. While many testimonials and subjective evaluations of ride quality could be provided by helmsman and passengers, there was no process for acquiring or processing recorded acceleration data for quantitative comparisons [5]. It was even reported that the valid comparison of the ride quality of different high speed craft could only be achieved by side-by-side trials using essentially duplicate instrumentation systems [4].

OBJECTIVE

The objective of this paper is to present a consistent approach to processing and analyzing acceleration data recorded during trials of manned and unmanned craft so that the results may be used to compare ride quality. The comparisons can include evaluating different craft, in different sea states, or for different gauge locations.

PEAK ACCELERATION DATA

Peak rigid body acceleration values recorded during tests of high speed craft on both model-scale and full-scale have served as key parameters for hull structure design and seakeeping comparisons[6,7].Typically, peak acceleration amplitudes recorded during a test sequence are tabulated, and averages are calculated using a peak-to-trough methodology adopted from ocean wave measurement techniques [8,9,10]. In addition to the RMS acceleration, three average values have been reported in numerous test and evaluation reports. These average values are referred to as the average of the one-third, one-tenth, and one- hundredth highest peak accelerations. They provide valuable information related to the amplitude of the largest peak accelerations recorded during a given period of time, and the larger number of lower-amplitude peak accelerations that occur during the same period of time. Peak accelerations are extracted from the acceleration time history by a peak-to-trough algorithm with a subjectively defined threshold, above which data are considered to be important for design or comparative study. The statistics are calculated by ordering extracted peak accelerations from highest to lowest, selecting the highest one-third (33%), one-tenth (10%), or one-hundredth (1%) peak values, and calculating the average. For example, the average of the one-tenth highest accelerations (typically used in craft design) is computed using equation (1).

$$A_{\frac{1}{10}} = \frac{1}{\frac{1}{10}N} \sum_{i=1}^{\frac{1}{10}N} A_i \quad (1)$$

A_i are the individual acceleration peaks (extracted from an acceleration time history) sorted in such a way that the largest amplitude acceleration has $i = 1$ and the lowest acceleration is $i = N/10$. The average of the one-third and one-hundredth highest acceleration values can be determined similarly. While the equation is simple and straight forward, its subjective implementation (due to the subjectivity of analyst choices in selecting A_i values) leads to different computational results by different analysts. The following sections present rationale and criteria for a generalized approach that obviates the subjectivity when selecting peak acceleration values from either full scale or model scale acceleration data.

The vertical acceleration record shown in Figure 1 is presented as a typical example time history. It was recorded at the longitudinal center of gravity (LCG) during trials of a 36-foot craft traveling at an average speed of 28 knots in seas with a significant wave height of 4.4 feet. The craft displacement is approximately 18,000 pounds, and its beam is 8 feet. A 240-second time period was selected to illustrate examples.

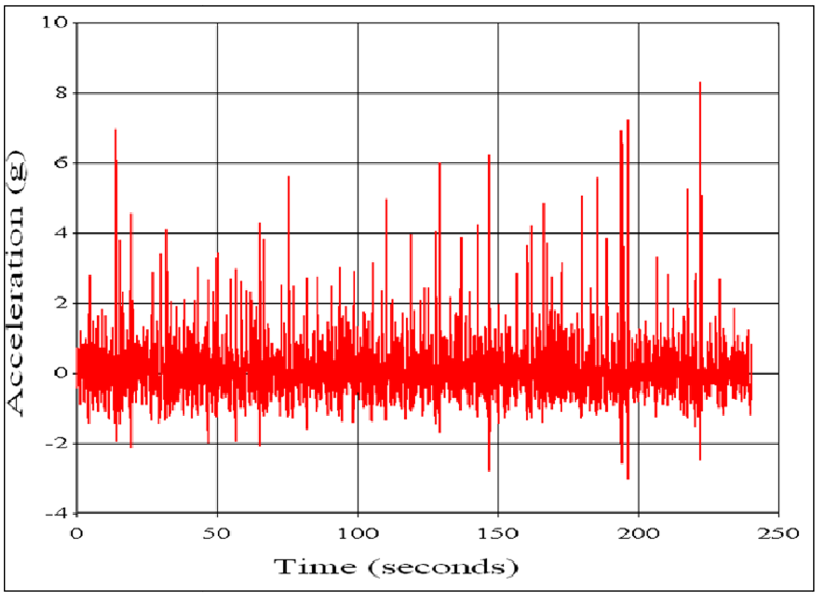

Figure 1: Vertical Acceleration at the Craft LCG

WAVE ENCOUNTER PERIOD

Figure 2 shows significant wave height ($H_{1/3}$) and average wave period (T_W) values from Pierson, Neuman, James data for fully risen sea state conditions[11]. Equation (2) is a fourth order polynomial fit of the significant wave height ($H_{1/3}$) and average wave period (T_W) data that predicts the trend within ± 2.5 percent and a 0.996 correlation coefficient for significant wave heights of 0.5 to 6.3 feet.

$$T_w = -\left(0.0133H_{1/3}\right)^4 + \left(0.1967H_{1/3}\right)^3 - \left(1.0553H_{1/3}\right)^2 + \left(2.8982H_{1/3}\right) + 0.4269 \quad (2)$$

If it is assumed that a craft is moving in head seas at a constant speed V_k in knots, it can be shown that the average wave encounter period (T) in seconds for water depths greater than 0.5 L_W is :

$$T = \frac{5.12T_w^2}{1.686V_k + 5.12T_w} \tag{3}$$

When equation (2) is substituted into equation (3) it can be shown that the average wave encounter period (T) is greater than 0.5 seconds for speeds up to 50 knots and significant wave heights greater than 1.6 feet. This corresponds to an average wave encounter frequency less than 2 waves per second. This is important because it means that the rigid body response of a craft moving at planing speeds in sea states greater than 1.6 feet will manifest itself as repeated acceleration pulses whose cyclic frequency is on the order of 2 Hertz or less. Any frequency content in the acceleration record greater than 2 Hertz is therefore coming from a source other than rigid body encounters with waves. It also means the average wave encounter period will be greater than 0.5 seconds. Any peak accelerations that occur within less than 0.5 seconds are most likely not due to rigid body motions. It is therefore recommended that peak-to-trough algorithms (used to implement equation (1)) use a 0.5 second time threshold buffer.

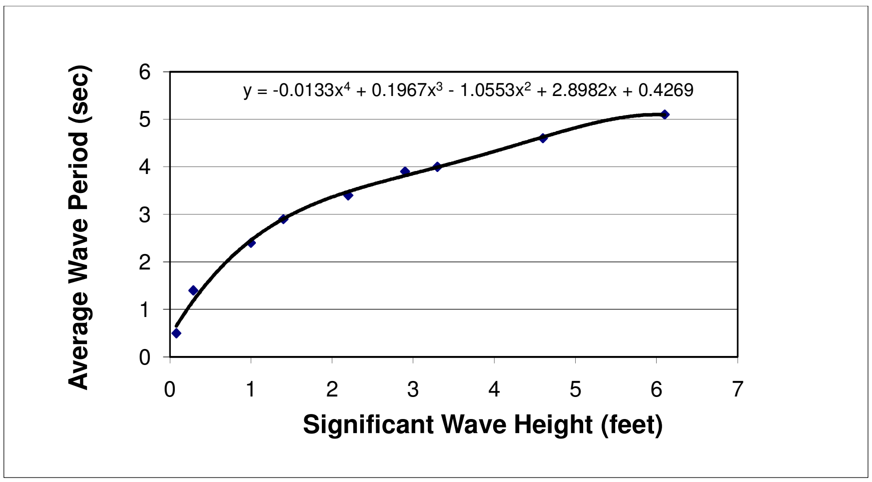

Figure 2: Average Wave Period versus Significant Wave Height

RIGID BODY MOTION

As shown in Figures 3 and 4 the prevalent source for frequency content other than rigid body motion in small boats and craft recorded at bow, LCG, and stern accelerometer locations is from local oscillations of contiguous structure in the vicinity of the gauge. Local flexure of deck plating or panels induced by wave slams or machinery vibrations, or even rotational motions of equipment installations are examples of likely high frequency responses observed riding on top of craft rigid body motions. For many applications of interest, including structural design, seakeeping comparisons, or impact events on crew or equipment, the rigid body acceleration is the parameter most often related to global loading conditions. It is therefore necessary to take extra steps to estimate the rigid body response by removing the local high frequency responses. Figure 4 presents the frequency spectrum of the Figure 1 acceleration record that highlights the presence of high frequency structural responses above the wave encounter frequency.

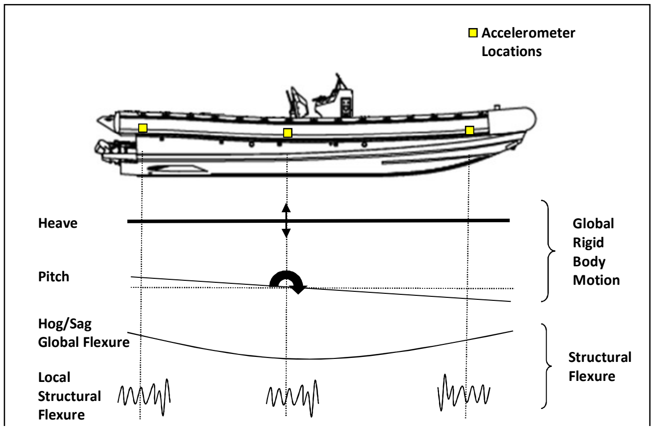

Figure 3: Local Flexure and Global Rigid Body Motions

Figure 5 shows a 4-second segment extracted from the typical acceleration record of Figure 1. The red curve is the original unfiltered record. It contains high frequency oscillations on the order of 24 to 26 Hz, most likely due to deck vibrations close to the gauge. These oscillations add significant amplitude to the acceleration response at the time of the wave slam peak acceleration response. Gauge placement should therefore focus on structural hard spots above bulkheads, frames, or girders to minimize local flexure.

The simple approach to removing high frequency responses is through the application of a low-pass signal filter. The black curve in Figure 5 illustrates an estimate of the rigid body acceleration by use of a 10-Hz low-pass filter. The peak acceleration for the filtered wave slam event is 3.50g. The same unfiltered wave slam has a peak of 5.29g.

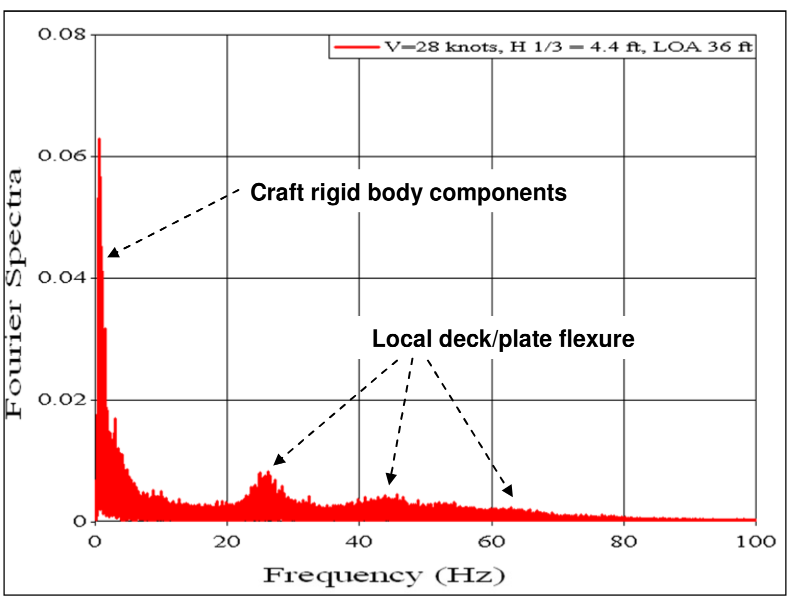

Figure 4: Frequency Spectrum of Typical Vertical Acceleration Record

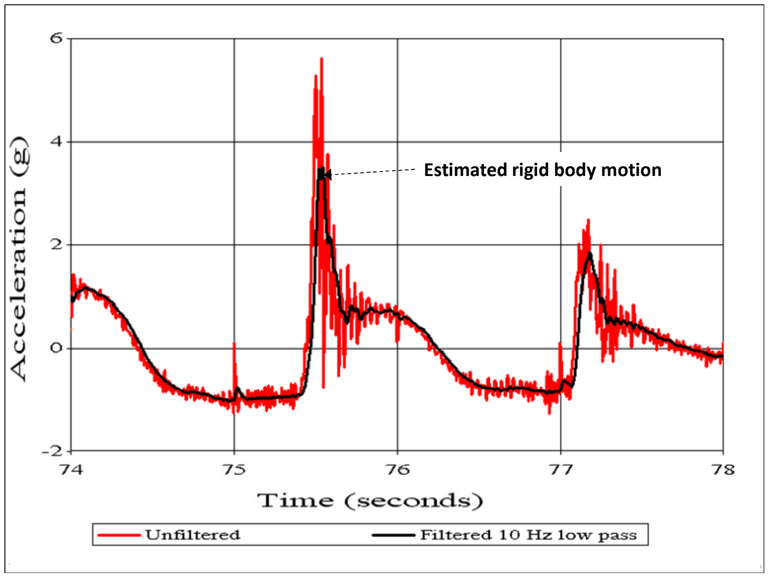

Figure 5: Unfiltered and Filtered Acceleration Responses

Low-pass signal filtering after inspection of frequency spectra has evolved as the process of choice, and inspection of many records for different small craft at different speeds has shown that a 10-Hz low-pass filter removes sufficient high frequency oscillation without excessive removal of peak rigid body response content. The data indicates the largest spectral amplitudes that correspond to rigid body motions are associated with frequencies below the 2-Hz threshold (0.5 second horizontal time buffer), and that significant flexural responses due to vibrations of structure in the vicinity of the accelerometer are typically greater than 18-20 Hz (well above the 10-Hz low-pass filter criteria). It is therefore recommended that a 10-Hz low pass data filter be initially considered for post-trial processing all craft data.

Care must be exercised during the frequency analysis for craft with larger length-to-beam ratios to ensure that flexure of the hull girder (hog/sag) is understood. The nominal 10-Hz filter value may have to be adjusted if global flexural responses are part of the data. The filter used for data presented in this paper was a Bessel two-pole filter with a characteristic 12 dB per octave attenuation (6 dB per octave per pole). The higher the filter order, the steeper the attenuation characteristic, and the more likely that unwanted frequencies will be attenuated. At the same time, as filter order increases, so does phase (or time) delay, although this delay has no effect on equation (1) computations. Different filter types have different characteristics for amplitude and phase response. While there are many kinds of filters (Butterworth, Bessel, and Kaiser Window, for example), those designed for amplitude accuracy provide results that are within a few percent of one another.

RMS ACCELERATION

The root mean square (RMS) is a measure of the average fluctuation about the mean for a time varying signal. For time varying signals with an average value of zero (craft acceleration data should be processed in such a way that the average value is zero), the RMS value is equivalent to the standard deviation, and is calculated using Equation (4).

$$RMS = \sqrt{\frac{\sum_{j=1}^{m} A_j^{2}}{m}} \qquad (4)$$

A_j are the discrete acceleration data points and m is the total number of discrete data points within the data record.

The RMS value of the acceleration time history shown in Figure 1 is 0.62g. Figure 6 shows a 5-second segment of the acceleration time history in Figure 1 with plus and minus RMS values indicated by dashed lines.

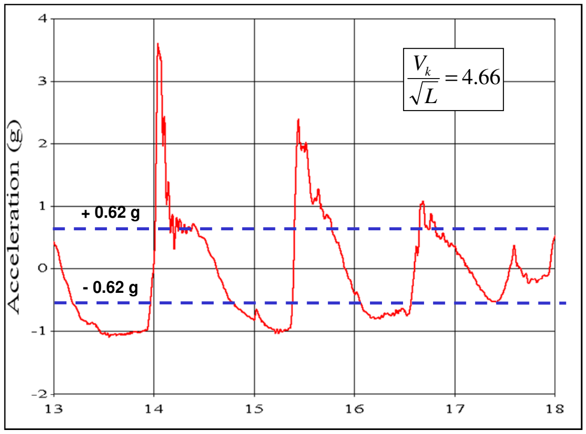

Figure 6: RMS Acceleration Correlation with Low-amplitude Responses

This figure illustrates that for high-speed craft operating in the planing regime, the RMS value correlates well with the lower amplitude values associated with buoyancy, hydrodynamic lift and drag, and gravity forces, and therefore serves as a rational baseline for counting higher peak accelerations caused by wave impacts. Wave slam events for planing craft typically dominate the loading regime of interest; therefore, determination of peak acceleration values for high-speed craft should focus on amplitudes greater than the RMS baseline value. It is therefore recommended that the vertical threshold in peak-to-trough algorithms be set equal to the RMS value of the acceleration record.

GENERALIZED $A_{1/N}$ COMPUTATIONAL APPROACH

The following four-step generalized approach is recommended for calculating the average of the 1/nth highest peak accelerations for a given acceleration time history recorded in any orientation axis [12,13]. The computational approach and the interim criteria are based on analysis practices that have evolved over a number of years at the Combatant Craft Division of Naval Surface Warfare Center, Carderock Division as a set of best-practices for achieving repeatability when computations are performed by different data analysts. Appendix A presents data acquisition system guidelines for measuring high speed craft rigid body motions.

1. FREQUENCY ANALYSIS

The first step in the data analysis process is the computation of a frequency spectrum in the 0.1 to 100 Hz range and plotting of the results as illustrated in Figure 4. If the largest spectral amplitudes are less than 2 Hz then the data can be low-pass filtered to estimate rigid body motions (remove higher frequency flexural components). If the largest spectral amplitudes exist in the 2 to 15 Hz range, other techniques such as multivariate data reduction (using three or more accelerometers) may be necessary to extract rigid body peak acceleration estimates.

2. 10-HZ LOW-PASS DATA FILTER

As a starting point for data analysis, application of a 10-Hz low-pass filter to the acceleration record to estimate rigid body acceleration motions is recommended. Experience has demonstrated that in some specific cases a filter frequency of 8 Hz or sometimes 12 to 15 Hz may be sufficient to extract rigid body estimates. The nominal 10-Hz value is recommended to establish a generalized value greater than the 2-Hz threshold, which still allows rigid body rotational components that may exist in the 2 to 4 Hz range.

3. RMS Calculation

The RMS value for the 10-Hz filtered acceleration record should then be calculated. Its value establishes a rational baseline for identifying higher acceleration peak amplitudes induced by wave impacts.

4. Calculation of the $A_{1/N}$ Values

A peak-to-trough algorithm with the following interim criteria to select peak amplitudes from the acceleration time history is recommended. The vertical threshold should be equal to the RMS acceleration for the time history, and the horizontal threshold should be equal to one-half the data sampling rate (i.e., 0.5 seconds).

The peak acceleration values are then tabulated from highest to lowest amplitudes and a cumulative percentage distribution curve can be derived. Finally, the average of the highest 1/nth peak values using equation (1) is calculated.

Example Calculations

After the typical acceleration record shown in Figure 1 was subjected to a 10-Hz low-pass filter, one-hundred fifty-one peak accelerations (this is a low sample size) were counted greater than the 0.62g RMS value. Figure 7 shows a 30-second segment illustrating the wave slam peaks selected (triangles) and the peaks ignored (circles) by the peak-to-trough computational procedure. The largest peak in the entire record was 5.31g. Figure 8 shows all one-hundred fifty-one peak acceleration values sorted and plotted from largest to smallest (left to right), and Figure 9 shows the cumulative distribution of all the peaks below discrete values. In each figure the average of the 1/3rd, 1/10th, and 1/100th highest acceleration values (2.41g, 3.48g, and 5.31g, respectively) are labeled.

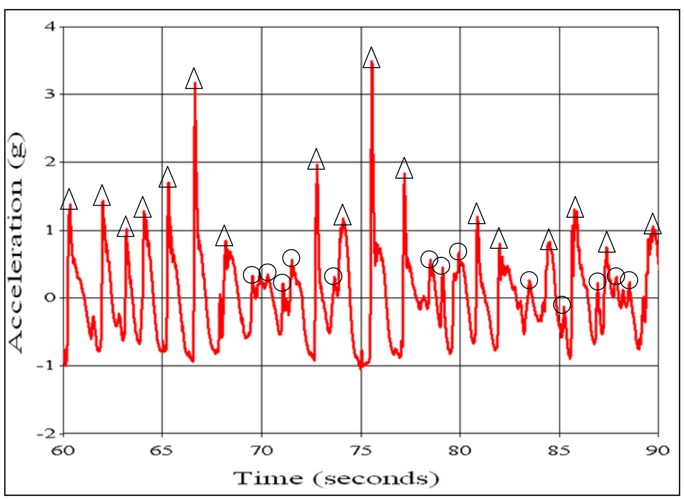

Figure 7: Peaks Selected Using Standard Criteria

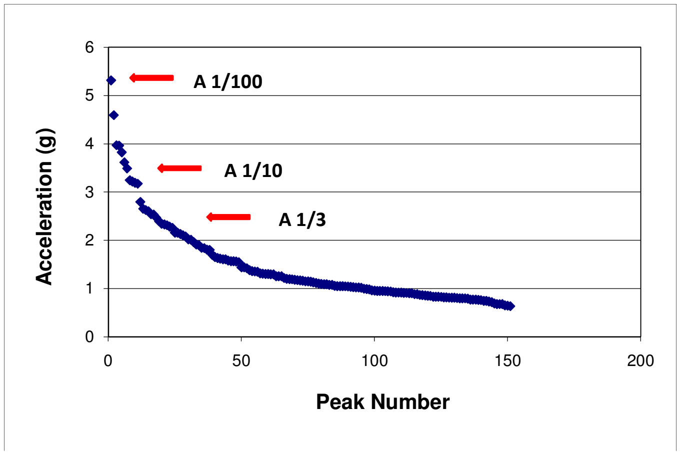

Figure 8: Sorted Peak Accelerations Greater than RMS

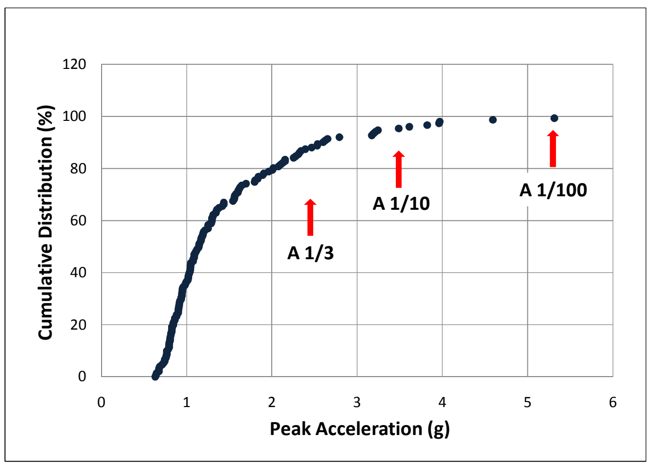

Figure 9: Peak Acceleration Cumulative Distribution

RIDE QUALITY INDEX

In the absence of a formal definition of what is often perceived as a set of very complex parameters (six degrees of freedom and numbers of wave slams could potentially be used to define ride quality), it is useful to use available vertical acceleration data in an attempt to quantify a first-order estimate of the change in the quality of a ride between test conditions I and II. These conditions may be different craft, different craft speeds, different sea states, or different gauge locations on a given craft. In simple terms a ride with lower amplitude accelerations associated with all wave slams and fewer wave slams at higher severities could be characterized as a better ride. The following paragraphs explain how a ratio of wave slam peak accelerations can be used as a relative indicator of ride quality.

As peak accelerations due to wave slam events increase in magnitude there is a proportional increase in the potential for structural damage, or equipment malfunction (or failure), or personnel discomfort, fatigue, or injury. Unfortunately there are few simple criteria other than estimates (corroborated by experience) for specifying levels at which damage occurs or comfort is exceeded and injury begins[7,9,14]. But the focus of this paper is on analytical process, therefore the remainder of the text will present ride quality comparisons in terms of the potential for damage to electronics equipment to illustrate the ride quality comparative approach and suggested data plotting formats.

Experience gained from impact tests of propulsion machinery and electrical (or electronics) equipment demonstrates that the potential for different types of damage (referred to as equipment failure modes) is a function of the change in rigid body velocity (at the base of the equipment) induced by the impulsive load [15,16,17,18]. In addition, it has been reported that for short duration accelerations the human body is sensitive to velocity change rather than the magnitude of the maximum acceleration[3]. These findings do not preclude the use of the peak acceleration parameter as a measure of damage potential due to a wave slam event, especially for impact events with duration times of the same order of magnitude. Reviews of many sets of high speed craft wave slam data (craft less than approximately 60 feet) indicate the impact periods are on the order of 100 to 300 milliseconds depending upon craft displacement, average speed, and wave height. Appendix B shows examples of the duration time of individual wave slam events. Within this relatively narrow range of impact durations an average acceleration value (average value during the impact event) would also be an appropriate parameter for first order quantification of the damage potential among many different wave slam events. A further simplifying assumption for the present comparative approach is that the peak acceleration varies proportionately with the average acceleration associated with the craft's response to an impulsive load. Therefore the peak vertical acceleration (of each wave slam event) is suitable for first order comparisons of damage potential and relative ride quality.

There are innumerable ways that components can fail during a wave slam (shock) event, and there is a very broad range of different types of equipment items produced by national and international manufacturers. It is therefore not practical to define specific shock amplitudes at which damage of any type will occur. To define such levels would be a very expensive undertaking that would require repeated testing of many expensive components. There is insufficient fragility data to quantify levels above which different types of failure modes begin to occur.

Failure mechanisms of equipment items may include failures of attachments, enclosures, and internal structures due to material overstresses or cyclic loads, or electrical failures due to disconnects of sub-components such as plugs, sockets, or circuit cards. Material overstresses or disconnects could occur due to a one-time severe wave slam event (maximum peak acceleration), or equipment malfunction or failure (due to disconnects) could be caused by repetitive impacts at lower amplitudes (lower peak accelerations) over a relatively long period of time. For example, in Figure 8 one of the large amplitude wave slam events could result in damage during a single slam event. The average of the highest $1/10^{th}$ (3.48g) and the $1/100^{th}$ (5.31g) peak accelerations are values that characterize the larger wave slam amplitudes.

Likewise in Figure 9 there are many more low amplitude wave slams (80 percent) with peak accelerations less than 2.0g. Even though this amplitude may not result in damage during a single slam event, the repetition over time of many impacts could cause disconnects of sub-components such as plugs, sockets, or circuit cards. Over very long periods of time the low amplitude wave slams could also cause problems related to material or personnel fatigue.

The use of a high amplitude peak acceleration value to characterize the damage potential of a single wave slam, and the use of a low amplitude peak acceleration value to characterize the damage potential of repetitive impacts is referred to as the high/low (hi/lo) damage criteria approach.

Based on the assumption that (1) the change in velocity during an impact event is directly proportional to the damage potential of the impact force, and (2) the duration time of different impacts are all of similar order of magnitude, and (3) the peak acceleration amplitude is proportional to the average acceleration during a wave slam event, then the ratio of peak vertical accelerations for test conditions I and II is a measure of the change in damage potential. The peak acceleration ratio can therefore be used as a ride quality parameter that is a relative indicator of the change in ride quality.

Figure 10 shows two sets of peak accelerations for hypothetical test conditions I and II. The amplitudes for condition I (values from Figure 8) are clearly all greater than condition II, so the conclusion would be that condition I is a more severe ride (or more punishing in terms of peak accelerations). Condition I may be more severe due to a higher average speed or a higher sea state. Figure 11 presents the same data points shown in Figure 10 in a different format. In this plot all peak accelerations (largest to smallest) recorded during condition I are compared with the corresponding (largest to smallest) peak acceleration recorded during condition II. In other words, the largest peak for each condition is plotted together, then each of the 2^{nd} largest peaks is plotted together, then each of the 3^{rd} largest peaks is plotted together, and so on until all pairs of peak accelerations are plotted. Data comparison points that fall on the dotted line (slope of one) have equal acceleration values and therefore have the same ride quality. Values below the dotted line indicate a better ride quality compared to condition I and points above the dotted line indicate a worse ride quality.

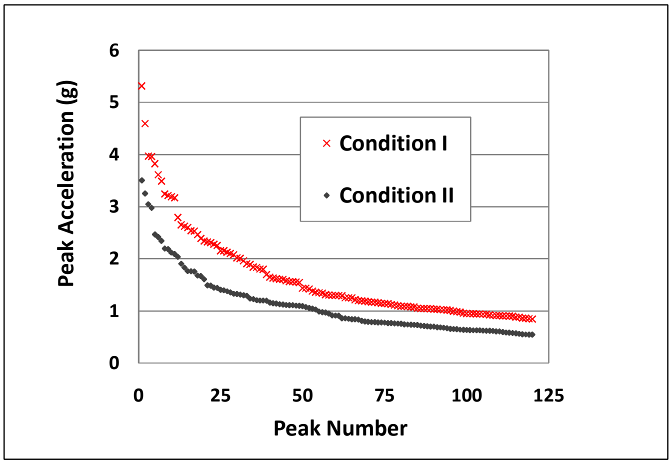

Figure 10: Example Condition I and II Peak Accelerations

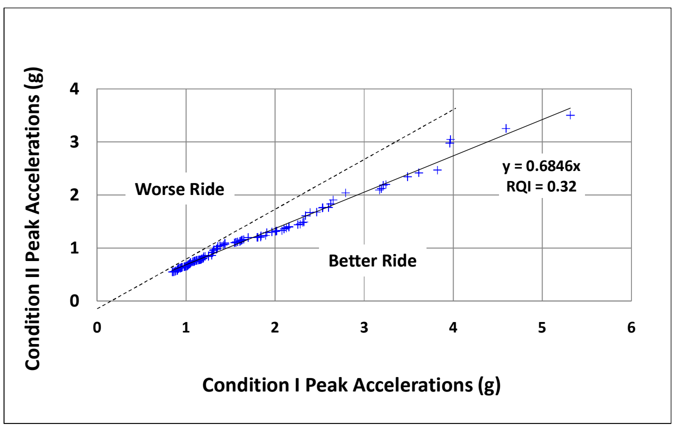

Figure 11: Ride Quality Index (RQI) Comparison Plot

The solid line with a slope of 0.68 is a linear least square fit of the data with the intercept set equal to zero. The slope is the approximate ratio of all acceleration values for condition II divided by all acceleration values for condition I, and can therefore be used as a relative indicator of the change in ride quality (i.e., damage potential). The Ride Quality Index (RQI) is defined as 1.0 minus the slope (or 1.0 minus the acceleration ratio). In Figure 11 the Ride Quality Index of condition II relative to condition I is 0.32. In percentage terms the condition II ride quality is 32 percent better (32 percent less severe) than condition I. Positive values of RQI indicate better ride quality. The larger the number the better the relative ride quality, and a lower relative potential for damage. Negative values of RQI indicate a worse ride quality. The larger the negative amplitude the worse the ride quality, and a higher relative potential for damage. The words “potential for damage” are used in a general sense and may apply to structural damage potential, equipment malfunction or failure potential, or personnel fatigue or injury potential.

Another approach to generating the relative Ride Quality Index is to plot the RMS, $A_{1/3}$, $A_{1/10}$, and $A_{1/100}$ values (listed in Table 1) as shown in Figure 12. The highest point in the figure is the $A_{1/100}$ values for conditions I and II (x-y pair), the next highest point is the $A_{1/10}$ values for conditions I and II, and so on. In this case the average Ride Quality Index (1.0-slope) is 0.29. Table 1 indicates that this value is a weighted average of the RQI values computed using the ratios of $A_{1/n}$ and RMS values. In this example the potential for damage due to the more severe slam event ($A_{1/100}$) is 0.34 (reduced on the order of 34 percent). The damage potential for the more frequent and repetitive lower amplitude slams ($A_{1/3}$ and $A_{1/10}$) have RQI values of 0.24 to 0.19, or a 19 to 24 percent better ride quality (or reduction in damage potential).

Table 1. Ride Quality Index for Different Shock Severities

Test	Condition I	Condition II	Ride Quality Index
A 1/100	5.31 g	3.50 g	0.34
A 1/10	3.48 g	2.82 g	0.19
A 1/3	2.41 g	1.87 g	0.24
RMS	0.62g	0.54g	0.13
1-Slope	na	na	0.29

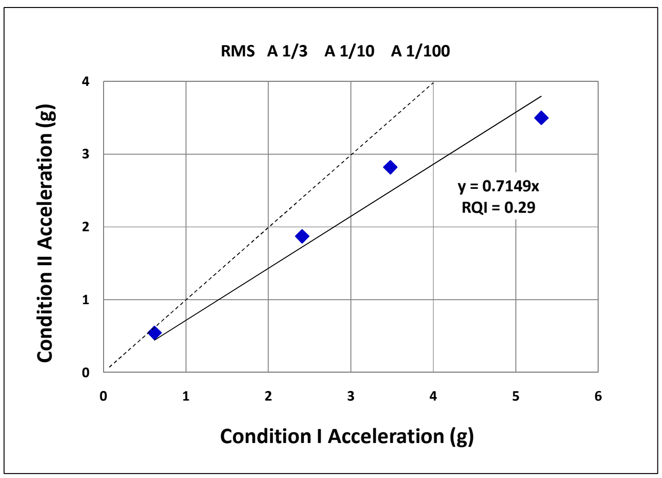

Figure 12. Average 1/nth Acceleration Ride Quality Index Comparison Plot

EXAMPLE COMPARISONS

The ride quality comparison approach can also be used to compare acceleration responses at different locations on a craft during a given trial period. For example, Figure 13 shows RMS, $A_{1/3}$, $A_{1/10}$, and $A_{1/100}$ values for vertical accelerations recorded at bow, helm, and stern locations compared to accelerations recorded at the longitudinal center of gravity (LCG). The comparison indicates the bow ride quality is approximately 122 percent worse (more severe) than the LCG, and the stern and helm location ride qualities are within -3% to +7% of the LCG location.

The ride quality comparison approach can also be used to compare acceleration responses for different headings of a craft in a seaway. Figure 14 shows RMS, $A_{1/3}$, $A_{1/10}$, and $A_{1/100}$ values for vertical accelerations recorded at the LCG for different headings compared to a head sea course. Average speeds varied slightly from one test run to the next. The ride quality for port bow seas is approximately 4 percent better than head seas, while stern and port quarter seas are 63 percent better.

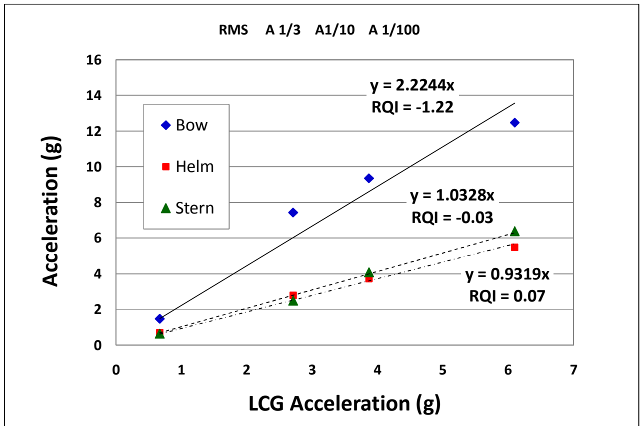

Figure 13: Location Ride Quality Comparison

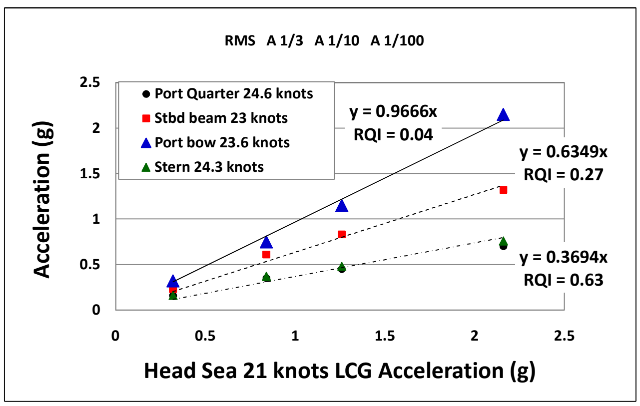

Figure 14: Craft Heading Ride Quality Comparison

SUMMARY

A four-step process has been presented as a generalized computational approach for computing the average of the $1/n^{th}$ highest acceleration when analyzing accelerometer data recorded during trials of manned or unmanned small boats and craft. Use of three interim criteria, including low-pass filtering at 10-Hz, a peak-to-trough vertical threshold equal to the acceleration record RMS value, and a peak-to-trough horizontal threshold equal to 0.5 seconds significantly reduces subjectivity in the calculation, and should help achieve repeatability when calculations are performed for different data sets and by different researchers.

Engineering rationale was presented for using the ratio of acceleration amplitudes (individual wave slam acceleration or average acceleration values) as a simple indicator of damage potential. The Ride Quality Index (1.0 – slope, or 1- acceleration ratio) provides a useful comparative ride quality number for assessments of relative damage potential due either to a single severe wave slam event, or due to cumulative damage caused by repetitive lower amplitude wave slams. The general approach and the simple criteria may be used for initial comparative assessments of structural integrity, equipment susceptibility, or personnel comfort and safety.

The combined use of the generalized peak-to-trough procedure for computing $A_{1/n}$ values with the comparative ride quality data plotting format and RQI values may foster future comparisons of the ride quality of different craft or for different test conditions of the same craft regardless of the source of the data.

REFERENCES

1. Symposium on Vehicle Ride Quality Held at Langley Research Center, Hampton, VA, 6-7 July 1972, NASA Technical Memorandum TM X-2620, October 1972.

2. Stark, D.R., "Ride Quality Characterization and Evaluation in the Low Frequency Regime with Applications to Marine Vehicles", Conference on Ergonomics and Transport, Swansee, UK, 1980.

3. Payne, Peter R., "On Quantizing Ride Comfort and Allowable Acceleration", Payne Incorporated, David Taylor Naval Ship Research and Development Center Working Paper 196-6, July 1976.

4. Ellsworth, W.M., "Hydrofoil Development – Issues and Answers", AIAA/SNAME Advanced Marine Vehicles Conference, San Diego, February 1974.

5. Jewell, D.A., "Hydrofoil Performance in Rough Water", AIAA/SNAME Advanced Marine Vehicle Conference, Paper 74-307, February 1974

6. Savitsky, Daniel and Brown, P.W., "Procedures for Hydrodynamic Evaluation of Planing Hulls in Smooth and Rough Water", *Marine Technology*, Volume 13, No. 4. October 1976.

7. Savitsky, Daniel, and Koelbel, Joseph, G., "Seakeeping of Hard Chine Planing Hulls", Technical and Research Panel SC-1 (Power Craft) paper, Society of Naval Architects and Marine Engineers, November 1992.

8. Zseleczky, John and McKee, Glen, "Analysis Methods for Evaluating Motions and Accelerations of Planing Boats in Waves", Hydrodynamics Laboratory, US Naval Academy, Davidson Laboratory, Stevens Institute of Technology, August 1989.

9. Coats, T., Haupt, K., Jacobson, A., Jacobson, D. and Pogorzelski, D. (September 2007). "MAST 2007 Working Towards Vertical Acceleration Data Standards", Naval Surface Warfare Center Carderock, Combatant Craft Division, MAST conference 2007 paper.

10. Munk, W. H. (December 1944). "Proposed Uniform Procedure for Observing Waves and Interpreting Instrument Records", Scripts Institute of Oceanography Wave Report 26.

11. Riley, M.R., Coats, T., Haupt, K.D., Jacobson, D.R., "The Characterization of Individual Wave Slam Acceleration Responses for High Speed Craft", Proceedings of the 29th American Towing Tank Conference, Annapolis, MD, August 2010

12. Riley, M.R., Haupt, K.D., Jacobson, D.R, "A Deterministic Approach for Characterizing Wave Impact Response Motions of a High Speed Planing Hull", American Society of Naval Engineers High performance marine Vehicle Symposium, November 2009.

13. Riley, M.R., Haupt, K.D., Jacobson, D.R., "A Generalized Approach and Interim Criteria for Computing $A_{1/n}$ Accelerations Using Full-Scale High Speed Craft Data", Naval Surface Warfare Center Report NWWCCD-23-TM-2010/13, April 2010.

14. Dobbins, Trevor, Schleicher, D., "Impact Count Index for High Speed Craft Motion Assessment", Multi-Agency Craft Conference, June 2009.

15. Harris, Cyril M., *Shock and Vibration Handbook Fourth Edition*, *Chapter 26, Part I,* McGraw-Hill, New York, 1995.

16. ANSI/ASA S2.62-2009 American National Standard Shock Test Requirements for Equipment in a Rugged Shock Environment.

17. Department of Defense Military Specification MIL-S-901D, "Requirements for Shock Tests, H.I. (High Impact) Shipboard Machinery, Equipment, and Systems, March 1989.

18. Department of Defense Military Standard, "Environmental Engineering Considerations and Laboratory Tests", MIL-STD-810G, 31 October 2008.

APPENDIX A: DATA ACQUISITION AND REPORTING GUIDELINES

Successful data acquisition begins with requirements definition. Key requirements must be defined, including the trials objectives, key parameters of the investigation, anticipated parametric variation, the required data resolution, and the post-trial data analysis methodologies to be applied. Historically, the acceleration response of the craft has been a key parameter for most design applications and seakeeping evaluations. Accelerometers are typically installed at three locations near the bow, the stern, and at the craft's longitudinal center of gravity (LCG) to measure rigid body motions. Primary installations are oriented in the vertical direction to capture heave and pitch responses, with additional accelerometers oriented longitudinally (fore-aft) and transversely (athwartship) depending upon the requirements of the investigation. For most applications the primary interest is for rigid body response data within the dc to 100 Hz frequency band. Standard practice is therefore to provide an analog pre-filter at 100 Hz with data sampled at 512 samples per second or higher. The following information should be included in documents that report computed average of the $1/n^{th}$ highest acceleration values: craft displacement, length, beam, draft, deadrise, and LCG; craft heading, average speed, and speed versus time if available; significant wave height, average wave period, and average wave length; instrumentation bandwidth, sampling rate, and anti-alias filter rate; typical 30-second time history with maximum peak acceleration, tabulated or plotted peak acceleration values (greater than the RMS value, presented largest to smallest), number of peaks, peak acceleration cumulative distribution plot, and tabulated acceleration values, including A_{PEAK}, $A_{1/100}$, $A_{1/10}$, $A_{1/3}$ and RMS. The presentation of Ride Quality Index comparison plots should include a discussion of all variables in the comparison (e.g., craft displacement, heading, speed, and significant wave height).

APPENDIX B: WAVE SLAM DURATION

Figure B1 presents eight example wave slams with expanded time scales to show just the impact period and the subsequent smooth portion of the curve associated primarily with hydrodynamic and buoyant forces. Each was normalized by dividing by its peak acceleration amplitude so that the maximum is 1g. The upper plot shows five impact events whose original peak values were from 3.1g to 3.8g. Three more slams whose original peaks were 1.9g, 4.5g, and 5.3g are compared in the lower plot. The fourth red curve on the lower plot is the average of the five curves in the upper plot. In general the impact pulse shapes rise from zero to a maximum in 50 to 80 ms, and have a total duration on the order of approximately 200 milliseconds. The good correlation illustrates the repeatability of the different wave slam events and suggests that, while the energies associated with each incident wave may be random, the response of the craft to individual slams is repeatable with amplitudes being a function of initial conditions just prior to each slam event[11,12]. The duration of wave slams for high speed planing craft (nominal 40 foot craft) are on the order of 100 to 300 milliseconds.

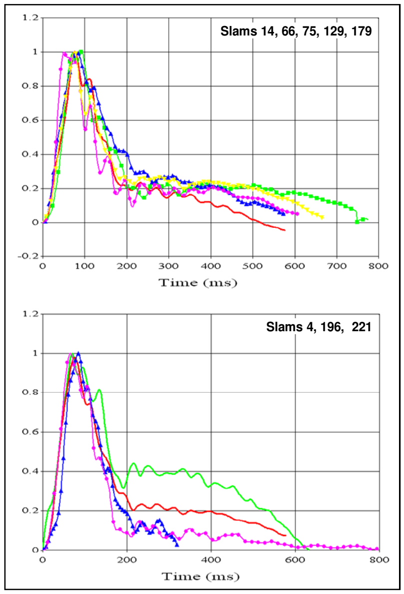

Figure B1: Normalized Pulse Shapes for Wave Slams

Seventh International Conference
On High-Performance Marine Vehicles
Melbourne, Florida, USA
13-15 October 2010

AN INNOVATIVE RESEARCH VESSEL REPLACEMENT FOR NEWCASTLE UNIVERSITY

M. Atlar, R. Sampson, J.R. Wightman-Smith, K-C Seo, E.J. Glover, D.B. Danisman and A. Mantouvalos
School of Marine Science and Technology
Newcastle University, UK
cavitation@ncl.ac.uk

ABSTRACT

As the existing research vessel of Newcastle University, the "R/V. Bernicia", reached the end of her viable service life in summer 2009, the need for a replacement vessel became apparent and led to the current replacement project. The R/V Bernicia was originally designed by the Department of Marine Technology and built locally on the River Tyne in Newcastle, UK. In keeping with this history of in-house design it was appropriate that the replacement vessel should be of a similar pedigree, but designed and operated in a more innovative way to meet the increasing demands of the University and the region. This paper reports on the conception and development of the replacement project in the School of Marine Science and Technology through the joint efforts of their students, academics and industry partners. The paper focuses on how the project has progressed to the building stage through the drafting of the vessel specifications, initial design activities, hydrodynamic hullform design and optimisation, model test verifications and concludes with a review of the current status.

INTRODUCTION

The R/V Bernicia was commissioned in 1973 having been designed by the Department of Marine Technology and built locally by Ryton Marine on the river Tyne. In keeping with this tradition of in-house design, it seemed only appropriate that the replacement vessel should be of a similar pedigree but designed and operated in a more innovative way to meet the increasing demands of the University and her main user, the School of Marine Science and Technology (MAST). Consequently, a number of final year and PhD projects have focussed on the issue, the results of which have been used to draft a vessel specification for an 18m aluminium catamaran that could be put to tender (Purchasing Services, 2009). The Invitation to Tender was issued in October 2009 and after careful consideration, the contract was awarded to Alnmaritec Ltd., an aluminium boat builder based in Blyth, Northumberland, UK. Subsequent activity has been based on design optimisation, model testing, the procurement of equipment and contractual finalisation, with building, which started in April 2010, scheduled to run until March 2011.

The main objective of this paper is to present how the replacement project started in the School of Marine Science and Technology by the joint efforts of the students and academics, and progressed to the point of construction in various stages starting from drafting of the vessel specifications, initial design activities, hydrodynamic hullform design and optimisation, model test verifications. It concludes with a review of the current status.

NOMENCLATURE

L/T	Length-draft ratio
L/B	Length-beam ratio (demi-hull)
LOA	Length Overall

Lwl	Waterline Length
P_B	Brake Power
P_E	Effective Power
P/D	Pitch-diameter ratio
$1+k$	Form factor
λ	Model scale factor

ABBREVIATIONS

ASB	Anti-slamming bulb
BAR	Blade area ratio
CFD	Computational fluid dynamics
CPP	Controllable pitch propeller
DVC	Deep-V catamaran
FPP	Fixed pitch propeller
IMO	International Maritime Organization
ITTC	International Towing Tank Conference
ITU	Istanbul Technical University
MAST	School of Marine Science and Technology, Newcastle University
MCA	Maritime and Coastguard Agency
PLA	Port of London Authority
RANS	Reynolds averaged Navier-Stokes
R/V	Research vessel
SWATH	Small waterplane area twin hull vessel
UNEW	Newcastle University

KEYWORDS

Research vessel, Deep-V catamaran, Newcastle University, Anti-slamming bulb, CFD, Model testing

VESSEL SPECIFICATIONS

The Research Vessel (R/V) Bernicia was a platform for international marine research and training with the addition of commercial charter studies. From her home port of Blyth, Northumberland, UK, the vessel was used daily for biological research, undergraduate teaching and commercial scientific charter in the North Sea and local estuaries. Routine work included e.g. conventional trawling (surface, mid-water and bottom), plankton sampling and bottom dredging, deep water sampling, sea floor coring and rock dredging at deep waters, soft sediment sampling, sea floor photography and the use of echo sounder and side-scan sonar systems.

During her service life, the R/V Bernicia mainly served the students and academic staff of the old Department of Marine Science to support Marine Biology teaching and research until 2003 when this department was merged with the Department of Marine Technology to form the current School of Marine Science and Technology (MAST), the largest marine school in Europe. As a result, the mission requirements of the vessel have been widened, not only addressing the demands of the marine scientists, but also addressing at the needs of Marine Technology students and academics. The 16m multi-purpose mono-hull vessel of stern trawler type was also available for charter and work at sea to a range of government and commercial organisations. Backup facilities and a wide range of marine biological and coastal management expertise as well as the recent addition of the marine technology expertise were available both on the main campus, supported by extensive marine science and technology facilities, and at the Dove Marine Laboratory situated along the North Sea coast. Two years prior to R/V Bernicia being sold, a group of Marine Technology MEng students drafted a specification for a modern replacement of Bernicia by consulting with the academic staff and eventually conducted an MEng group design project (Reid et al. 2007) for a 22m multi-purpose catamaran R/V which could achieve 25 knots top speed, almost tripling R/V Bernicia's top speed, which was approximately 8 knots. The choice of a catamaran hull for the new research vessel was an obvious one since such a hullform fulfils the requirements of shallow draft, large deck space, excellent stability and good speed potential with a low wash. The vessel was based on a novel "Deep-V" catamaran concept which originated in the School (Atlar, 1997), (Atlar et al. 1998) and further developed through numerous successive undergraduate projects e.g. (Duncan, 1997) and MSc projects e.g. (Haslam, 1995) and eventually by the recent PhD project (Mantouvalos, 2008) in which the world's first systematic Deep-V catamaran series (UNEW-DVC) was generated. Based on the series (Atlar et al, 2009), (Mantouvalos et al. 2009), the marine technology experts of the school designed a 14m new Port of London Authority (PLA) harbour patrol launch which is now a proven craft with low wash and high efficiency operating on the River Thames as shown in Figure 1. Such is the success of this 14m, 21 knots craft, that four sister vessels have been ordered and will be used as support vessels for the 2012 Olympic Games.

Figure 1: The first UNEW-DVC Series Application: 14m Patrol Launch "Lambeth" of Port of London Authority

The proven hullform of the PLA launch and previous student projects have formed the basis for drafting the specification (Purchasing Services, 2009) for the new 18m new research vessel with further novel features as discussed later on. The key issue in the mission specification was the multi-purpose and flexible role of the R/V enabling it to meet the marine science and technology needs as well as commercial requirements. For example, the vessel was to be able to provide a respectable bollard pull for bottom trawling activities and to keep station at a required position in strong wind, current and drift, as well as to achieve a top speed of 20 knots in calm weather for special missions, and 15 knots service speed up to SS4 with acceptable motion levels. More specifically it was expected that the new R/V would be a modern state-of-the-art platform to be operated by MAST and used by both the marine science and technology fields for teaching and research as well as chartering for consultancy. As a result, a wide range of oceanographic deck equipment and features were specified including a hydraulic A-frame system, 2 trawl winches, an auxiliary winch, a hydrographic winch, an anchor winch, a pot hauler, the deployment of ROV's through its moon pool, utilisation of modular laboratories, handling of a high speed RIB and the introduction of an observation tower for sea mammals and birds etc, all of which required a large useable deck area. In addition, the new R/V is expected to have good shallow water operation ability and drying out (beaching) capability on sands in a similar manner to the way in which the local Northumberland fishing boat 'coble' often does. Partly because of beaching and partly because of the evolved nature of their designs, these authentic boats have a distinctive droop bow and tunnel stern features, the latter to accommodate and protect their propellers, as shown in Figure 2. It is ironic that the proposed Deep-V hullform concept for the new R/V will have these features in an innovative way to further improve the efficiency of her hullform, arguably adapting the hullform of the cobles for the current needs of the University.

The requirement for relatively high speed for the new R/V is mainly for special consultancy needs and for marine technology teaching and research, apart from emergency cases for saving time. A sophisticated ship monitoring and performance analysis system developed through a recent PhD study (Hasselaar, 2010) will be an integral part of the onboard equipment, providing data on the ship speed, power, thrust, fuel consumption, vessel motions/accelerations and environment including wave spectra, in a scientific manner to evaluate the performance of e.g. new coating systems and the effect of marine growth on ship resistance and fuel consumption. Special observation windows at the stern will provide access to propellers to observe cavitation in conjunction with the measured propeller excited vibrations and noise. Further specifications of the vessel are given in Table 1.

Figure 2: Traditional Northumberland Coble showing the Anti-slamming Bow and Tunnel Stern Features

Table 1: R/V Further Specifications of new R/V

Length Overall	18.0m
Beam Overall.	7.0m
Design Draft	1.64m
Displacement (light)	28 tonnes
Payload	5 tonnes
Max Speed	20 knots
Cruising Speed	15 knots
Engines	2 x 610hp
Propulsion	5 bladed propellers
Classification	MCA Category 2

VESSEL DESIGN - BACKGROUND AND DETERMINATION OF MAIN PARTICULARS

The decision on the preliminary dimensions of the vessel was due to a combination of needs driven by her mission requirements, berthing restrictions and economical considerations. These main dimensions were applied to a catamaran with deep-V hull lines. As stated earlier, the selection of a catamaran for a research vessel was an obvious choice due to many reasons, but the selection of the Deep-V form was unusual and unique. In actual fact, the Deep-V catamaran concept has been initiated and been under continuous development at the School of Marine Science and Technology since mid-90s. This was based on the fact that displacement type Deep-V mono hullforms, which should not be confused with the planing type hard chine hullform that may also have V shape hull lines with lower dead rise angles, are being successfully exploited on fast ferry and other naval applications due their remarkable efficiency in seakeeping and hence speed in waves, e.g. (Serter, 1993), (Kehoe, 1987), (Coscia et al., 1998).

Catamarans inherently suffer from poor seakeeping performance unless they are designed as a SWATH, which has its own restrictions associated with speed and draft. Within this context, it would be only natural to combine the superior seakeeping performance of displacement type Deep-V hullforms with catamarans to improve their poor seakeeping behaviour and hence further complement their maintenance of speed in waves. This idea has been further developed through successive student based research studies and recently a PhD research project has been completed resulting in the first systematic Deep-V catamaran (UNEW-DVC) series (Mantouvalos, 2008). The main features of the series are such; the demi-hulls are symmetric with large deadrise angles that are constant after mid ship, and the bow section have Serter's trademark anti-slamming bow feature (Serter, 1989). The after body of the series hullforms finishes with a transom area that is equivalent to the mid-ship cross section area. Further details of UNEW-DVC series can be found in (Mantouvalos et al., 2009) including limited model tests supporting the series development.

The first building application of the UNEW-DVC series was a 14m harbour patrol launch "Lambeth" which was designed and model tested in the School for the Port of London Authority (PLA) with some modifications required by the owner (Sampson and Atlar, 2008). One of the modifications was at bow. The anti-slamming bow, as introduced by Serter in mono-hull Deep-V vessels, has an unusual bow profile, which starts with a slight droop below the keel around the mid-ship and increases gradually towards the bow (Serter, 1989). This provides the forebody with a continuous contact with the water and hence reduces the probability of emergence of the forefoot of the vessel, which in turn results in a reduced risk of slamming. This feature, which is used in the UNEW-DVC series, was modified in the PLA boat by avoiding the droop beyond the keel level. The other modification was at the after body with the introduction of a relatively steep angle of prammed after body with milder V shape cross-sections to accommodate her conventional propellers and stern gear with a 7 deg shaft inclination. The hull separation was relatively small and hence less than ideal due to bridge passage restrictions of the River Thames. The vessel had an 18 knot design speed and a 21.5 knot top speed achieved by 4 bladed trans-cavitating propellers which were designed and tested in the School's Emerson Cavitation Tunnel (Atlar et al., 2009). Lambeth was launched in July 2009 and has been reported to be an extremely fuel efficient and sea kindly vessel that can operate up to SS5 as well as being low wash, complying with the 0.5m max wave height criteria.

The success of Lambeth and the ageing R/V Bernicia prompted MAST to start a publicity and fund raising campaign with the objective of designing and building R/V Bernicia' s replacement in-house and locally, to provide a state-of-the-art and cost economical R/V for the University. In 2009, the UNEW Executive Board decided to approve 2/3 of the prospective replacement vessel cost while the remaining 1/3 would be left to MAST to raise through fund raising activities or its own resources. This was an ideal opportunity for MAST to make use of their world renowned expertise and networking to get the replacement project underway.

Within the above framework, a group of MEng students conducted their group design project (Reid et al, 2007) on the replacement of R/V Bernicia in 2008. Their 22m design was influenced by various innovative features that included a flexible operational speed range spanning 0 - 25 knots, with a service speed of 15 knots. This would be achieved by the use of twin water jets and a transom mounted retractable azimuthing thruster located between the demi-hulls at the wet deck level. The thruster would be used for slow speed operations as well as in emergency situations if required. The bow had Serter's anti-slamming bow and the entire features of the UNEW-DVC series were maintained. A general view of this concept vessel is shown in Figure 3.

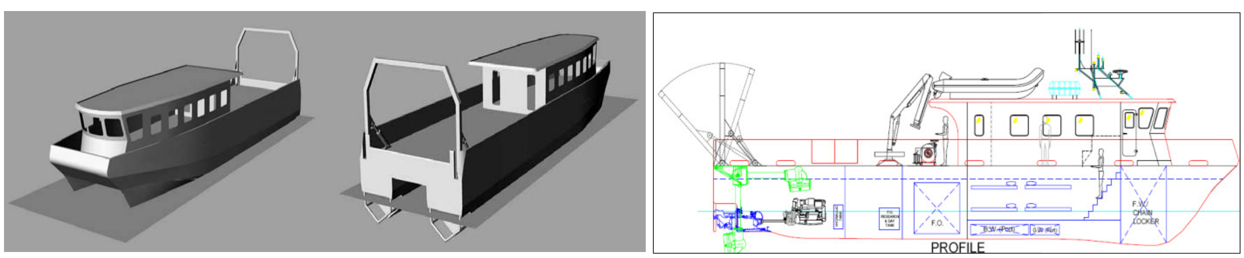

Figure 3: A General View of Concept R/V Proposed by 2007 UNEW MEng Students (Reid et al 2007)

Based on some useful findings from the above mentioned MEng group study and the design experience with the PLA boat, a parametric design study was conducted by (Sampson et al., 2009) in summer 2009 in order to determine the initial size and hullform of the new R/V to meet her mission requirements. By taking 18m LOA as the limit for the new vessel and bearing in mind the other limitations in terms of the maximum beam, water and air draught, preliminary weight and power estimations were conducted for four different candidate hullforms in the parametric study. Two of these hullforms were selected based on the true Deep-V from the UNEW-DVC series with anti-slamming bow whilst other two were based on the PLA boat without the modified anti-slamming bow feature. Each of the pairs had a waterjet and a propeller driven alternative as shown in Figure 4 in comparison.

The preliminary analysis using a potential based CFD code indicated that the propeller driven alternatives required less effective power for the same speed as well as displaying reduced wave making compared to the water jet driven alternatives. This was related to the reduced transom area due to pramming of the aft end for the propeller arrangements. The difference in effective power between the true deep-V and the PLA boat based alternatives was not clear cut depending on the speed range. However, the magnitudes were comparable. In this comparative analysis hull separation was fixed at 0.25L while the displacements of the hull forms varied between a minimum of 29 tonnes for the PLA based propeller driven hull, to a maximum of 33 tonnes for the UNEW-DVC based water jet driven hull.

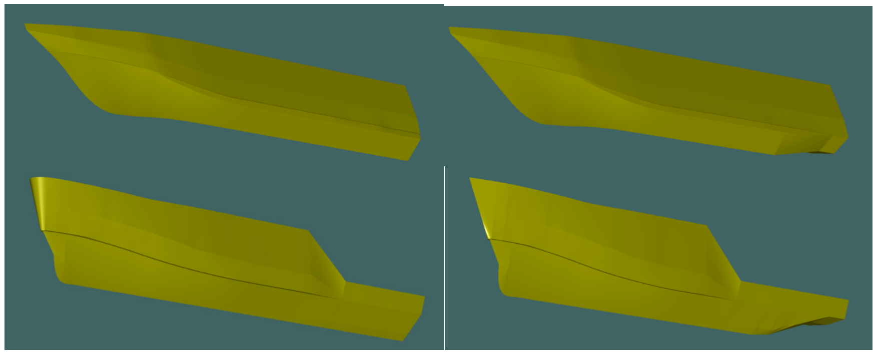

Figure 4: Alternative Hullforms Provided Basis for New R/V (Sampson et al., 2009)

The final decision between the four design candidates given above was for the propeller driven UNEW-DVC hullform, which was selected, not only on the basis of power saving, but also on other factors. For example, the relatively modest service speed of the prospective vessel (15 knots), a minimum 3 tons or more bollard pull requirement and the relatively heavier water jet propulsion options favoured the selection of conventional propeller drives for the new R/V as opposed to the water jet drive only or a combination of the two. A wide range of speed profile from a low speed trawling (2-3 knots), through 15knots service speed to 20 knots maximum speed did not rule out the consideration of a Controllable Pitch Propeller (CPP) system. However the choice of a fixed pitch (FP) based conventional propeller would be preferable in considering the lesser complexity of the FPP and lower efficiency of the CPP with its large hub and thicker sections for a relatively small diameter propeller which was to be a maximum of 800mm.

HULLFORM OPTIMISATION – FOREBODY

Having determined the preliminary dimensions and basic hull lines, the next step was to optimise the hull lines within a reasonable envelope of the preliminary dimensions. In this task the main focus was to improve the calm water performance of the hullform as well as the performance in waves. In this respect, it is known that the anti-slamming bow form of the hull would improve the slamming characteristics of the UNEW-DVC series as pioneered by Serter, however, it was decided to combine the anti-slamming bow with an optimised bulb form to further improve the resistance and vertical motion characteristics.

This novel bow configuration, which is called an "*Anti Slamming Bulb (ASB)"*, will not only improve the wave making in a conventional way by reducing bow waves and dynamic trim but it will also provide the hullform with increased damping in the vertical plane and hence to improve her vertical motions/accelerations in waves. This was particularly obvious in the PLA boat such that the reduced entry angles of this vessel, which reduced her shoulder waves and hence her wash characteristics, made the vessel relatively sensitive to the motions in vertical plane (Sarioz and Atlar, 2009). This was acceptable for the PLA boat which was operating in sheltered waters, but it would create concern for a research vessel considering her lifting operations as well as working in unsheltered waters. Based on this experience it was decided to introduce the unique *Anti slamming Bulb* (ASB) concept pioneered in MAST.

The optimisation of the forebody with the introduction of the ASB was conducted by the approach given in (Danisman and Atlar, 2003) where the objective function was chosen as the total resistance, which is assumed to be the sum of frictional drag and wave-making resistance. The frictional drag was formulated by ITTC-57 friction line while the wave making was obtained using the Michell integral, which is a linear formulation of the ship wave resistance expression based on the thin ship theory. In both formulations the ship's hull was represented by using "tent functions" for the sake of iterative computations and rapid surface representations and combined with the quadratic programming technique to search for the optimum. Once the optimal form was obtained, its performance analysis was conducted initially by a potential flow based panel code (SHIPFLOW) and later by a RANS based viscous solver (FLUENT) to validate it. . These codes take into account the hydrodynamic interference between the demi-hulls and therefore the hull separation optimisation was inherent in the overall optimisation as well as the forebody optimisation. As one would appreciate this was not a fully automatic optimisation process but one which required manual intervention and experience in hullform optimisation.

It has been planned that the ASB bow section of the hull would be built from a GRP or composite as a retrofit, although the main hull will be constructed from aluminium. Further thoughts have also been given to the manufacture of a conventional anti-slamming bow (without the bulb) and to conduct comparative full scale trials to demonstrate the effectiveness of the new concept ASB over conventional anti-slamming bow of Serter. Figure 5 shows the comparative profiles of the two bow forms i.e. ASB vs Serter's anti slamming bow and saving in the wave-making resistance.

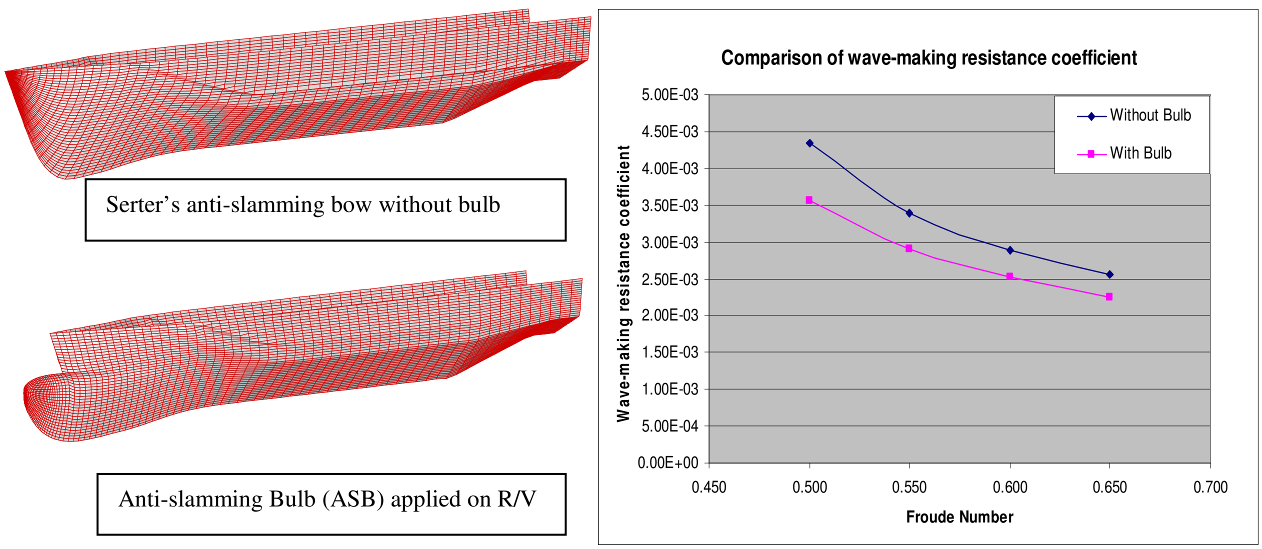

Figure 5: Effect of Anti Slamming Bulb (ASB) on the Wave-making Resistance of R/V

HULLFORM OPTIMISATION - AFTERBODY

Optimisation of the after body part of any vessel is not an easy task due to complex viscous flow activity interacting with the vessel's propulsor which operates in the wake of this flow. As stated earlier, the after body of the proposed true deep-V hull had to be prammed by a gentle cut-up angle of 14 deg to accommodate the propellers and stern gear to prevent their extension below the keel line. Furthermore it was decided to introduce a shallow tunnel (or propeller pocket) to enable the fitting of a relatively large diameter propeller with reduced tip losses and reduced shaft inclination. Such a shallow tunnel would also help to smooth the sharp wake peak at the bottom of the V shape hull in the propeller plane as well as provide more flexibility for relaxed tip clearances.

In selecting the most favourable after body configuration four different sterns, as shown in Figure 6, varying from 0% tunnel to 20% tunnel with different forms were analysed using potential and RANS based viscous solvers to compare their efficiencies in terms of resistance, wave making, form factors and wake flow characteristics. This analysis led to the selection of the after body section which provided least form drag (see Table 2), least stern wave height and least vertical motion at the tunnel exit as well as well ordered streamlines at the buttock of each demi-hull as shown in Figure 7.

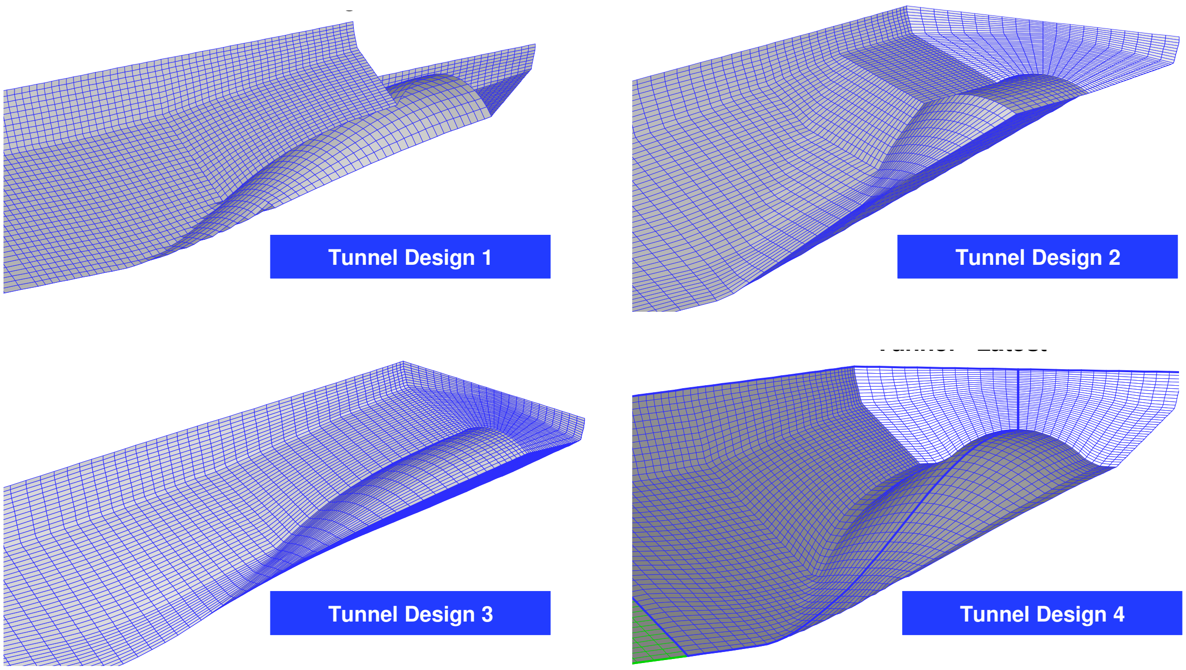

Figure 6: Different After Body Forms Explored with the After Body at the Bottom Left Selected

Table 2: Form Factor Prediction

Aft body type	Form factor (1+k)
Tunnel design 1	1.788
Tunnel design 2	1.507
Tunnel design 3	1.423
Tunnel design 4	1.650

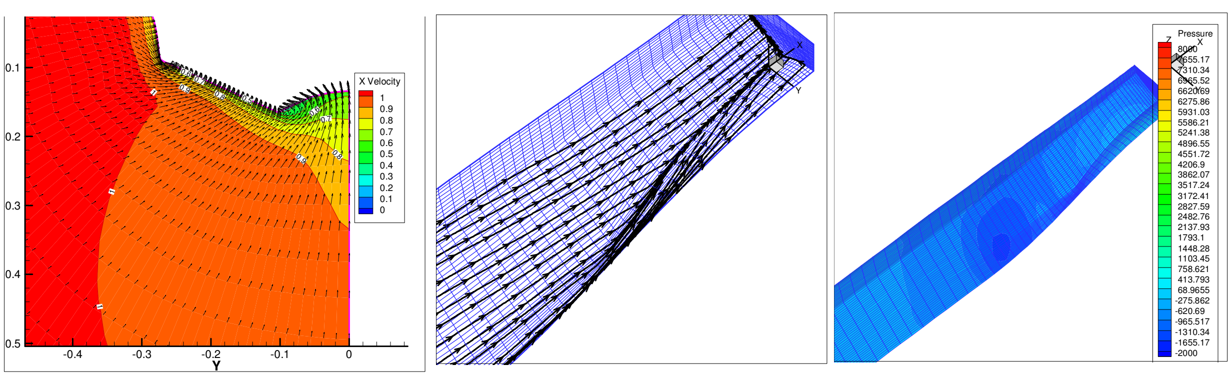

Figure 7: Selected After Body Flow Details (Wake, Streamlines and Pressure Distribution)

HULLFORM OPTIMISATION - APPENDAGES

The main appendages of the vessel were specified as conventional rudders, shafts, I-brackets, bow thruster openings and initially a partial central box keel in front of the hull rising at the aft to support the hull for beaching and dry docking purposes as successfully used in the PLA boat. However this latter appendage was converted to a skeg by extending it all the way from the rising point to the rudder stock to provide more protection to the propeller and stern gear from possible grounding and tangling with nets, fishing gears etc as requested by the skipper of the vessel, and shown in Figure 8. No specific optimisation process was applied on the appendages apart from designing such an unusual skeg that had to be structurally sound as well as generating minimal drag at high speeds.

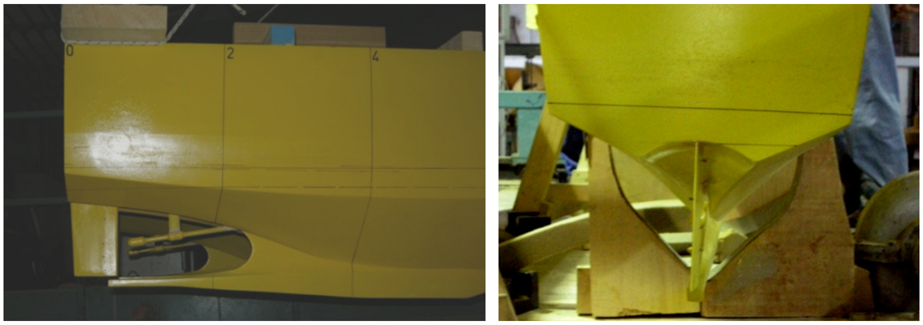

Figure 8: Appendage Details on Large Size Model

OPTIMISATION - ABOVE WATER HULLFORM

The above water hullform was dictated by the maximum air draft which imposed a height limit to the wheel house on the main deck. A reasonable wet deck clearance was allowed to avoid frequent wet deck slamming as no deadrise or jaw was introduced to the wet deck to lessen the impact of such slamming in order to keep the production cost low. She was given a reasonable bow flare with sufficient length to cover the foremost point of the bulb protrusion. Several different wheel house configurations were considered and final shape is under consideration as shown in the GA drawings following the wind tunnel tests analysis. A shelter area was introduced at the starboard side of the vessel to allow safe and dry work space on the main deck for the scientific staff and students. Figure 9 shows the general arrangement and an artist's impression of new R/V displaying the above mentioned fore and aft bodies as well as the appendage and above water hullform details.

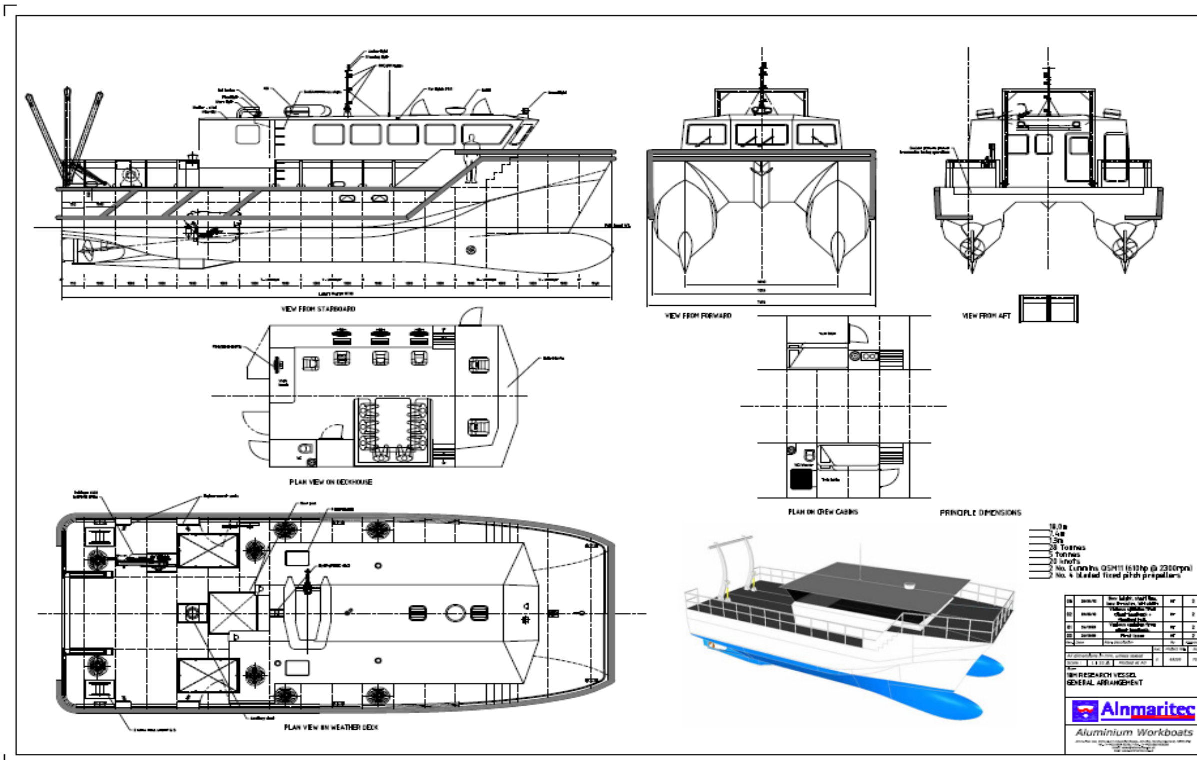

Figure 9: General Arrangement of New R/V

PROPULSION SYSTEM

Perhaps the most challenging aspect of the design was the selection of the propulsion system, a choice that was governed by the mission profile of the vessel, efficiency and production cost. The vessel has an unusually wide operating speed range (0-20knots), with 3 prominent sub-zones, which are 0-3knots zone for station keeping and trawling; around 15 knots zone when operating in service; and around 20 knots top speed zone in calm weather for special missions and emergency situations. Because of this operating profile and in spite of her relatively high speed mission, the water jet option was ruled out due to lower efficiencies at service speed and below, as well as the minimum of 3 ton-f bollard pull requirement. Although the use of CPPs could have been a good choice considering her distinctively wide ranging operational profile, this option was also ruled out since a conventional FPP can be compromised effectively to avoid the lower efficiencies of a CPP due to previously discussed reasons as well as its complexity and high cost. As a result an 0.8m diameter conventional FPP was designed for the 15 knots service speed, whilst still ensuring a minimum of 3 ton-f bollard pull at the engine's maximum torque, as well as providing a 20 knots plus top speed. In order to reduce the risk of one blade entering the shallow tunnel whilst another is simultaneously exiting (which could amplify the magnitude of the vertical blade rate forces (Blount, 1997)), a 5-bladed propeller was selected, whilst the optimum values of pitch ratio and blade area ratio were determined as P/D= 0.95 and BAR=0.75, respectively. These initial particulars were derived from the basic design of the propeller based on the Wageningen B-Series data. Tip clearance was selected to be 15% of the diameter at the top while a 10% clearance above the extension of the skeg plating was allowed. The clearance of the boss centre from the rudder stock was 0.5D whilst the shaft lines had a 7 degree inclination dictated by the engine location in the hull and the gearbox selection. The selected engines are Cummins diesel, type QSM11-610 (as preferred by the shipyard), with QuickShift gear boxes at a gear ratio of 1.75:1. Direct drive connection was selected considering its simplicity, weight, cost and reliability.

Further optimisation of the propeller using the state-of-the-art wake adaptation and design analysis was underway during the write-up of this paper and will be followed by the performance and cavitation tests that are to be conducted in the Emerson Cavitation Tunnel of UNEW.

SEAKEEPING AND MANOEUVRING ANALYSIS

Although the seakeeping and manoeuvring performance were not included directly in the optimisation process, by following a multi-criteria optimisation, these aspects as well as the basic naval architectural issues, such as stability, trim, etc, were cross checked to ensure that the optimised hullform met the required safety and other performance criteria.

As far as the seakeeping analysis was concerned, it is inherent with the DVC forms that the seakeeping behaviour is expected to be superior, at least when compared with other counterpart conventional catamarans (Atlar et al, 2009), while catamarans are inherently better in manoeuvring compared to mono-hulls due to their twin hull configuration. In addition the new R/V would be equipped with 2 bow thrusters which should improve the manoeuvring performance further.

Based on the preliminary weight estimation and distribution, the natural heave and pitch period of the vessel were found to be around 7s and 3s for heave and pitch, respectively, at zero speed. The results of strip theory based seakeeping analyses indicated that the vessel will be operable up to SS4, maintaining her service speed of 15 knots at acceptable level of motions and accelerations in the North Sea environment combined with an ITTC wave spectrum.

Although the application of the IMO manoeuvring criteria to a catamaran of this size does not have any legal implication, these criteria have been applied for turning and zig-zag (yaw checking) manoeuvres and it was noticed that the critical parameters of these manoeuvres comfortably comply with the criteria since catamarans are inherently turning unstable and directionally stable. The vessel's twin rudders, each with a minimum lifting area of 0.04LT were maintained to keep the vessel directionally stable with a projected area of 0.96 m^2 and aspect ratio of 1.2.

MODEL TESTS

Two sets of separate but complementary model tests were conducted to validate and verify the designed hullform in different towing tanks with different sizes of model, as shown in Figure 10. A 3.5m larger model (with a scale ratio, $\lambda = 5$) which formed basis for the main design activities, was tested in 160m long Ata Nutku Towing Tank of Istanbul Technical University (ITU) while a 1.5m smaller model ($\lambda = 12$) was tested in the 40m long Newcastle University (UNEW) towing tank to complement the larger model tests and provide further design support.

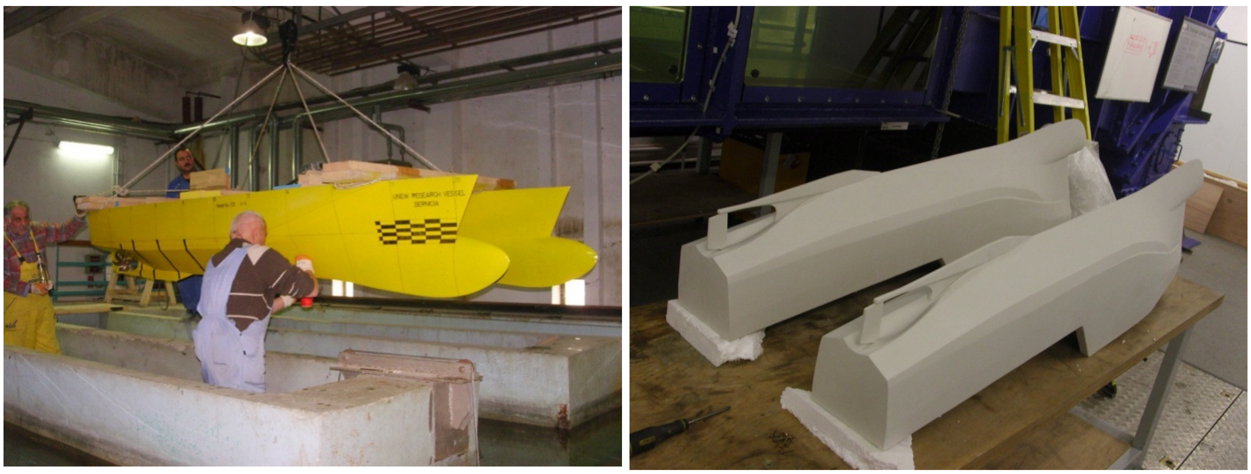

Figure 10: Two Different Size Models tested in ITU Tank (3.5m on the left) and UNEW Tank (1.5m on the right)

The model experiments in the ITU tank included calm water resistance tests and paint tests for the bare hull and appended hull in the fully loaded and ballast conditions, and also a wake survey and self-propulsion tests with a five bladed stock propellers. These experiments were supported with further flow observations around the bow and afterbody of the vessel using tufts in the ITU Circulation Channel facility. Limited seakeeping tests were also conducted in regular head sea conditions at the design speed.

Similarly, the tests in the UNEW Towing Tank, which also formed basis for the third year projects of a group of undergraduate students, involved bare hull calm water resistance tests and seakeeping tests for a wide range of wave frequencies in head and following seas at zero speed and service speed for the latter. Separate wind tunnel tests were also conducted with a specially made wooden above water model ($\lambda = 12$), which is shown in Figure 11, to predict the wind resistance characteristics of the above water hullform with two different wheelhouse structures in the UNEW combined wind, wave and current tank facility.

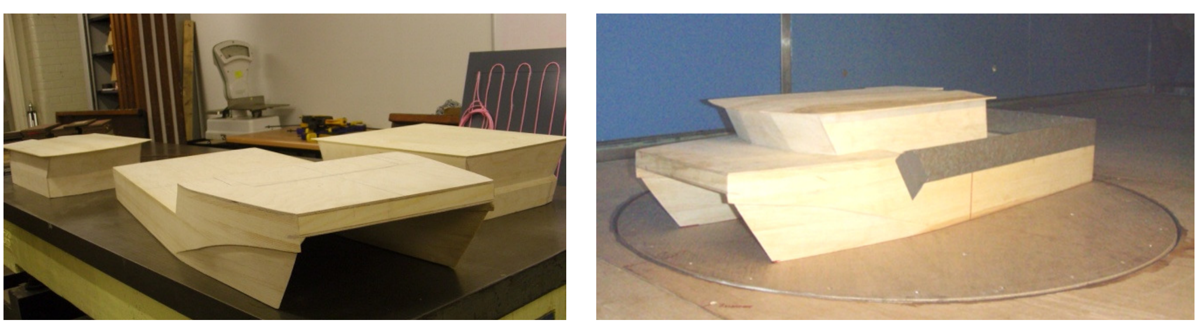

Figure 11: Model of Catamaran above water Hullform with Alternative Wheelhouses tested in UNEW Wind Tunnel

The large model tests, which took place earlier than the small size model tests, confirmed an efficient calm water performance of the designed hullform except for a slight spray observed from the upper foremost point of the bulbous bow at the corresponding full speed of 17 knots and above. This was eliminated effectively by transforming the bulb cross section from a nabla shape to an oval shape with a slight elongation of the bulb. The extrapolated effective power curve and engine brake power based on the towing and self-propulsion model tests respectively, are shown in Figure 12.

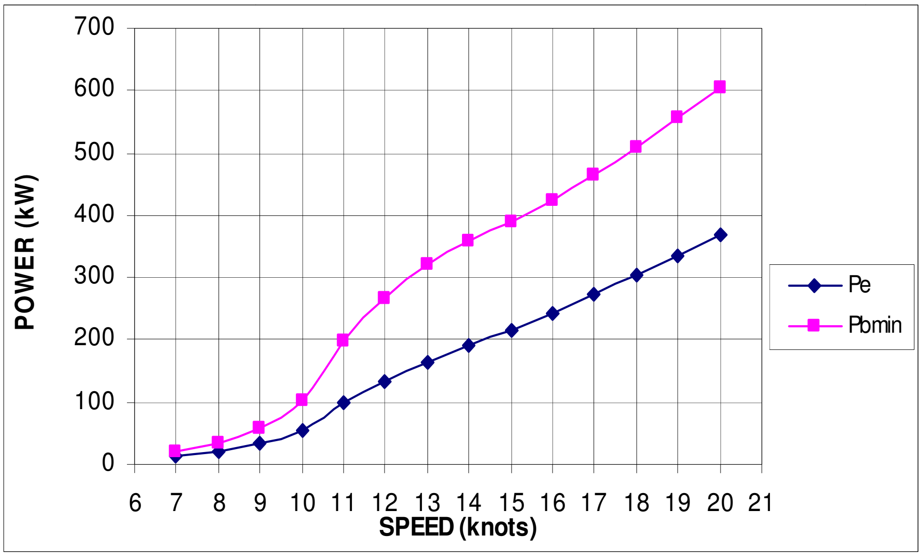

Figure 12: Effective Power (Pe) and Brake Power (Pbmin) Curves of R/V based on Model Tests in ITU Tank

The flow streamlines around the ASB and stern were favourable and without concern as shown in Figure 13. The model tests conducted in the UNEW Towing tank with the smaller scale model and the original bulb, presented comparable resistance curves to the ITU tank test results, while the form factor analysis with the smaller model indicated a value of $(1+k) = 1.5$. Comparison of the model test based resistance curves with the CFD predictions for three different separations, validated the CFD predictions and indicated that the lowest resistance occurred with the largest hull separation. The analysis of the small scale model tests were continuing during the write up of this paper.

Figure 13: Flow Patterns at the ASB and Tunnel Stern Regions Obtained from Paint Tests

CURRENT STATUS AND FUTURE WORK

Following the competitive tendering process, which took place in autumn 2009 based on the tender technical specification prepared by the MAST experts, the tender was awarded to the local aluminium boat builder Alnmaritec Ltd. of Northumberland and the official contract was signed in late March 2010. This initiated the detailed design work and building process in April 2010. The first stage of the process was to draw up a revised general arrangement to take into account the design refinements since the acceptance of the tender. The builder has since passed the design to their subcontractor BMT-Nigel Gee Ltd. for the structural optimisation and cutting pack development. The first plates were cut on 11 July 2010 and current delivery date of the new R/V is 28 February 2011. In the meantime, the fund raising activities to make up the remaining 1/3 rd of the total vessel cost have been continuing successfully with the local and international support from companies, government establishments, charity organisations and most importantly the Newcastle Marine Alumni all around the world.

CONCLUSIONS

Keeping with the tradition of in-house design and locally built research vessels, the School of Marine Science and Technology experts have designed an innovative 18m catamaran to replace the ageing research vessel of Newcastle University. The new vessel design is based on the 'home grown' world's first Deep-V catamaran series (UNEW-DVC) developed in the School through successive student projects to meet the challenging scientific and technological demands of the University and the North East region. The designed hullform with its multi-purpose role over a flexible speed range, has so far displayed efficient hydrodynamic performances based on the numerical and experimental analysis conducted, and forms a very sound basis for the full-scale vessel which is under construction locally and will be delivered in early 2011.

ACKNOWLEDGEMENTS

The authors gratefully acknowledge the funding and hence opportunity provided by the Newcastle University Executive Board in realising the replacement of the School of Marine Science and Technology's (MAST's) R/V, Bernicia. In addition numerous local, national and international companies, governmental organisations, individuals and Newcastle Alumni have been contributing to the replacement campaign in kind and/or otherwise. These contributions are gratefully acknowledged by the MAST and authors in realising their dream to come true, i.e. putting the UNEW-DVC research vessel in the waters of the North East.

REFERENCES

Atlar, M., (1997): "Recent Developments and the Emerging State of the Art in the High Speed Vessel World with a Personal View on Large Deep-V Hulls and their future Potential". *6th International Marine Design Conference, IMDC'97*, University of Newcastle upon Tyne, UK,

Atlar, M., Glover, E.J., Seo, K.-C., Sampson, R. and Paterson, I., (2009): "Wavelength 1200 Deep-Vee Catamaran, Propeller Design and Cavitation Tunnel Tests", MAST report no: MAST-2009-020, Newcastle University

Atlar, M., Haslam, B. And Mesbahı, E. (1998): "Deep-Vee hullforms and their Application to multı-hulls, 'Deep-VV' Catamaran". *1st European Symp. on Yacht and Small Craft Design,* University of Genova, La Spezia, October.

Atlar, M., Mantouvalos, A., Sarioz, E. and Sarioz, K., (2009): "A Fast Catamaran Ferry using a Displacement Type Catamaran", *13th Congress of Intl. Maritime Assoc. of Mediterranean IMAM 2009*, İstanbul, Turkey, 12-15 Oct.

Blount, D.L., (1997): "Design of Propeller Tunnels for High-Speed Craft", *Proceedings of 4th FAST Conference*, Sydney, July.

Coscia A., Elice I., Mangili L., Rossi L., Parodi M., (1998): "Application of Deep-V Hullforms to Fast Naval Crafts", *La Marina Italiana,* Italy, 2: 23-30.

Danisman, B and Atlar, M. (2002): "Further Optimisation of a Displacement Catamaran for Low Wash", MT report no: MT-2002-039, Newcastle University.

Duncan, K. L. F., (1997): "A Comparative Study of the Resistance Performance of the Wave Piercer and Deep-Vee Type Catamarans", *3rd Year M. Eng. Thesis*, Department of Marine Technology, University of Newcastle upon Tyne.

Haslam, B., (1996): "Deep-Vee Hullforms and their Suitability to High-Speed Catamarans", *3rd Year M. Eng. Thesis*. Department of Marine technology, University of Newcastle upon Tyne.

Hasselaar, T.W.F., (2010): "An Investigation into the Development of an Advance Ship Monitoring and Analysis System", *PhD Thesis*, School of Marine Science and Technology, Newcastle university.

Kehoe J. W., Brower K. S., Serter E. H., (1987): "The Deep-V Hullform – Improves Seakeeping and Combat System Performance", *Naval Engineers Journal,* 99(3): 39-54.

Mantouvalos, A. (2008): "The development of the 1st Deep-V Catamaran (DVC) Systematic Series", *PhD Thesis*, School of Marine Science and Technology, University of Newcastle.

Mantouvalos, A., Atlar, M. and Sampson, R. (2009): "Development of the first systematic Deep-V hullform series for displacement type high-speed catamarans (DVC Series)", *Proceedings of 10th FAST Conference*, Athens, October.

Purchasing Services, (2009): "Supply (Design, Build and Manufacture) of an 18m Aluminium Catamaran Research Vessel", *Invitation to Tender.* Purchasing Services, Newcastle University, UNT/608.

Reid, J., Andrews, D., Burdick, O., Christoforou, I. and McCaig, E. (2007): "R.V. Of Way, Design and Development of a Multi-Purpose Research Vessel", *MEng. Group Project, MAST*, Newcastle University, Vol. 1,

Sampson, R. and Atlar, M. (2008): "Wavelength 1200 Deep-Vee Catamaran Calm Water Resistance and Wash Test", MAST report no: MAST-2008-12, Newcastle University.

Sampson, R. and Atlar, M. (2009): "MAST Research Vessel Replacement Project Preliminary Vessel Selection", MAST report no: MAST-2009-021, Newcastle University.

Sarioz, K. and Atlar, M. (2008): "Seakeeping Performance Analysis of 12 m Final Deep V Harbour Patrol Launch", MAST report no: MAST-2008-13, Newcastle University.

Serter, E. H. (1993): "Hydrodynamics and Naval Architecture of Deep-Vee Hullforms", *Research-Developments-Design*, Published by the Author.

Serter, E.H. (1989): Hullforms. *United States Patent No 4*, 875,425, October.

Seventh International Conference
On High-Performance Marine Vehicles
Melbourne, Florida, USA
13-15 October 2010

TECHNOLOGICAL CHALLENGES FOR CONSTRUCTION AND CLASSIFICATION "TÛRANOR PLANETSOLAR"

Volker Bertram, Hasso Hoffmeister
Germanischer Lloyd, Hamburg/Germany
volker.bertram@GL-group.com

Steffen Müller
Knierim Yachtbau, Kiel/Germany

Andre Moltschaniwskyj
LOMOcean, Auckland/New Zealand

ABSTRACT

"Tûranor PlanetSolar" is the world's largest solar powered vessel. Its goal is to demonstrate the capabilities of current photovoltaic solar cell technology mounted on a low resistance platform. The state of the art wave-piercing catamaran hull design will be powered by efficient electric motors working on semi-submerged carbon-fiber propellers. The combination of these technologies allows the 85 t craft to run at a passage making speed of seven knots consuming on average just 20 kW of installed power, buffered from lithium ion batteries. The boat will operate in class. The structures were designed to GL Rules. The designer company has jointly developed load prediction mechanisms for boats which do not fit the standard rules. Mutually agreed "best engineering principles" were employed for structural analysis. This allowed optimization for strength and stiffness at reduced weight without sacrificing robustness and reliability.

KEYWORDS

Catamaran, Solar Power, Structure

INTRODUCTION

The goal is ambitious: Breaking the record for circumnavigating the globe in a vessel powered exclusively by solar panels by mid 2011. The solution: A carbon fiber wave-piercer catamaran exploiting a variety of high-tech features, the "Tûranor PlanetSolar", Table 1, Figure 1, www.planetsolar.org. This unique craft is intended to serve as the ultimate 'green' motor yacht. New Zealand's LOMOcean Design was responsible for the conceptual design and Knierim Yachtbau built the craft in Kiel/Germany. LOMOcean Design Ltd. is known for innovative boat designs that include wave-piercer motor-yachts such as high-speed paramilitary crafts and the "Earthracer", Ziegler et al. (2006), the record-breaking trimaran that circumnavigated on biodiesel fuel, rammed and sunk by a Japanese whale hunter in 2009.

DESIGN CONCEPT

The "Tûranor PlanetSolar" is not a stripped out race boat, optimized solely for the circumnavigation; after its record attempt, it will serve as a spacious motor yacht, with an interior arrangement offering six double cabins, each with en-suite bathroom, a large saloon and dining area plus a spacious aft deck and separate crew quarters. However, sunbathing space is at a premium, with over 500 m² of the deck surface covered in solar cells, with just a blister style wheelhouse breaking the expanse of blue-black paneling.

Table 1: Main data for "Tûranor Planetsolar"

Length overall	30.6 m	Solar panel area	537 m²
Beam	16.06 m	Max. engine power	2 x 60 kW
Beam (wings extended)	26.08 m	Cont. cruise-speed output	2 x 10 kW
Draft	1.30 m	Battery capacity	2910 kWh
Propeller diameter	2.00 m	Solar generator max ouput	93 kW

Figure 1: "Tûranor PlanetSolar" with detail of wheelhouse surrounded by solar panels

Solar panels still have a relatively low energy output compared to conventional fossil fuel concepts. As a consequence, the focus was on large deck area (increasing the available power) and low resistance (decreasing the power demand). This led to various basic design decisions:

- advanced composite materials for the platform structure
- lightweight solar panels and light-weight batteries for storage
- Lithium-ion battery packs (total weight 11 t)
- Slender hulls as a basic design choice and CFD (computational fluid dynamics) for local design changes contributed to the final low-resistance design.

The requirements of large deck space, low resistance and reasonable seakeeping led to the choice of a catamaran design. The two slender demi-hulls have only approximately 100 m2 wetted surface, making them hydrodynamically very attractive, but structurally very challenging.

The solar-powered concept meant automatically propulsion via e-motors. Batteries are needed for energy storage. The designers opted for "conventional" propulsion via shafts and propellers. The propeller concept was developed by Voith Turbo Marine Composite Technology, featuring half submerged, low revolution carbon propellers of large diameter, Figure 2. Both the propulsion and the electrical systems required individual assessment by the classification society, as they were not covered by standard rules. Germanischer Lloyd ensured expert reviews working closely with designers, building yard and suppliers.

The particular structural challenges of the vessel required state-of-the-art structural design, materials and production for the platform:

- Structural design & Materials

  For a preliminary study, a hull panel cut-out was used to compare the four common materials:

  a) 7.5 mm steel plate with 500 mm spaced steel stiffeners
  b) 9.5 mm aluminum plate with 500 mm spaced aluminum stiffeners

c) sandwich panels with 40 mm foam core and two 2.5 mm skins of E-glass laminate, with 1000 mm spaced stiffeners
d) sandwich panels with 30 mm foam core and two 2 mm skins of carbon laminate, with 1000 mm spaced stiffeners

For a fair comparison, the structural weights were based on hull structure loaded to a permissible degree, using pertinent safety philosophies for each material. Structural panel weights were calculated for a 1 m^2 panel. This size does not require stiffeners for sandwich panels. Table 2 indicates the relative weight differences. The most obvious choice for construction material was carbon sandwich technology, offering great stiffness and strength/weight ratio. However, further options to reduce weight, e.g. changing from foam sandwich to Nomex honeycomb, were waived for reasons of cost and production aspects. Finally, 20.6 t of carbon fiber fabrics, 11.5 t of foam core sheets and 23 t of epoxy resin and hardener went into the structures, contributing 2/3 of the vessel's total weight.

Figure 2: Stern view of "Tûranor PlanetSolar"

Table 2: Structural weight of stiffened hull panels

Steel panel	78 t/m^2
Aluminum panel	35 t/m^2
E-glass sandwich panel	16 t/m^2
Carbon sandwich panel	12 t/m^2

- Production

Knierim Yachtbau in Kiel/Germany was chosen as the building yard due to their reputation, having delivered numerous high-performance sailboats including Germany's Cup Challenger. However, never before had Knierim built a boat of that size. The actual construction had to be moved to a nearby shipyard's site (HDW) to have sufficient building space.

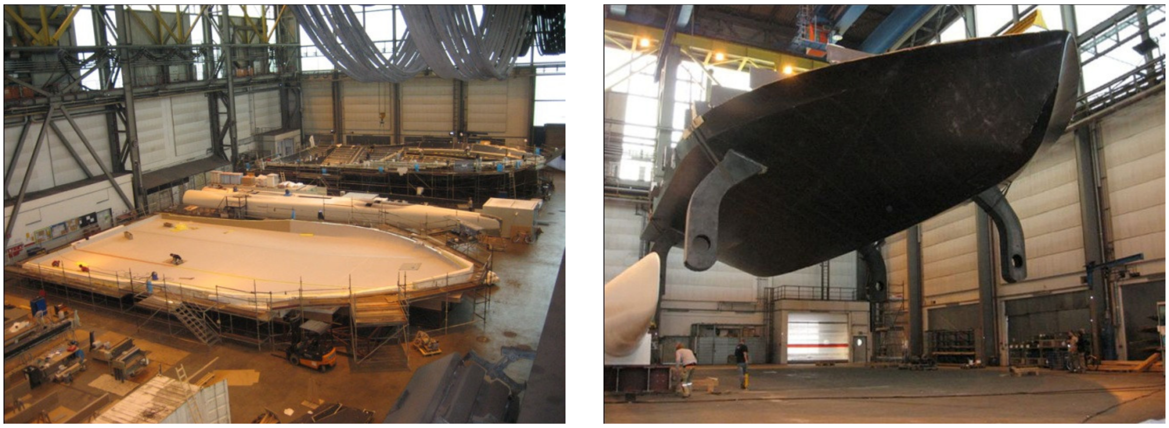

Figure 3: Modular production in the boat yard

In normal boatbuilding practice, the hull shell is be built over a male surface mould or in a female mould (if surface quality is highly important or for mass production). The impregnated fiber fabrics and the core are directly laid over or into the mould and cure. After releasing the sandwich hull shell from the mould, the open hull is equipped with internal structure, before finally the deck closes the structure. The challenge with "Tûranor PlanetSolar" was more-fold, because the demi-hulls had to be joined before attaching sponson arms and central hull to them, all built separately, Figure 3. All structure had to be incorporated before joining the modules. Openings were provided in the hulls to later incorporate batteries, propulsion system and other systems. This resulted in a fully integrated structure with almost no compromise to construction and installation sequence.

STRUCTURAL DESIGN ASPECTS

LOADS

The vessel is per definition not a high speed craft (HSC). Its average service speed is far below the minimum speed for an HSC, the maximum operational speed just within the limit. Nevertheless, the local design pressure methodology following GL HSC Rules was used to define local pressure maps. The basic design parameter for determining local pressures is the vertical design acceleration. The vessel was categorized as a passenger craft. The limit design vertical acceleration at the center of gravity is subsequently 1.0 g. Although the design methodology yielded a smaller value, the more conservative value of 1.0 g was chosen as base for structural assessment.

The side and bottom sea pressures were derived from the standard approach in the Rules. So were the impact (slamming) pressures on the demi-hull bottom. The "deck" of the demi-hulls was not categorized as a deck as per the Rules, but considered as part of the normal hull topsides. The sea pressures depend on the vertical offset of a load point. Since the demi-hull deck was considered to be submerged completely, a cross check versus possible hydrostatic submersion had to be made. A design pressure of 40 kPa (equivalent with 4 m water column) provided sufficient margin for the case where the hulls are submerged. Early model tests confirmed this assumption as being conservative enough.

The central hull does not touch the water surface in calm water. It is designed to divert water impacts, reducing slamming loads. It also serves as a buoyancy reserve for strong pitching motions. Thus, not only slamming but also regular sea loads had to be derived.

GLOBAL STRENGTH

The structural arrangement reflects the idea of smooth stress flow. The structural loads were predicted in a simplistic way, proven in a previous, similar project for the wave-piercing trimaran "Earthrace", Ziegler et al. (2006). At that time, extensive numeric seakeeping studies gave global design parameters (accelerations in 6 degrees of freedom) and local pressure histories on the hull surface. These pressure distributions were compared to values according to

GL Rules. Although the two vessels differ in speed, size and operation, the gained knowledge could be normalized. Especially for the partially submerged sections of the vessel, new simplified approaches were derived so that for future applications no extensive CFD (computational fluid dynamics) simulations would be necessary. This conversion from CFD results to commonly valid approaches requires engineering skills, understanding of the functionality as well as some conservative error margins.

The slender demi-hulls are particularly prone to global bending and shear loads. The hydrostatic and quasi-dynamic slamming pressures were combined in several load cases and integrated to form a basis for generating global loads. This way, global forces and moments were derived to compute the sectional integrity over the length of the hulls. At the same time, computations yielded internal intersection forces and moments at the link between demi-hull / girder, in the girder structure itself and at the girder attachment to the central hull.

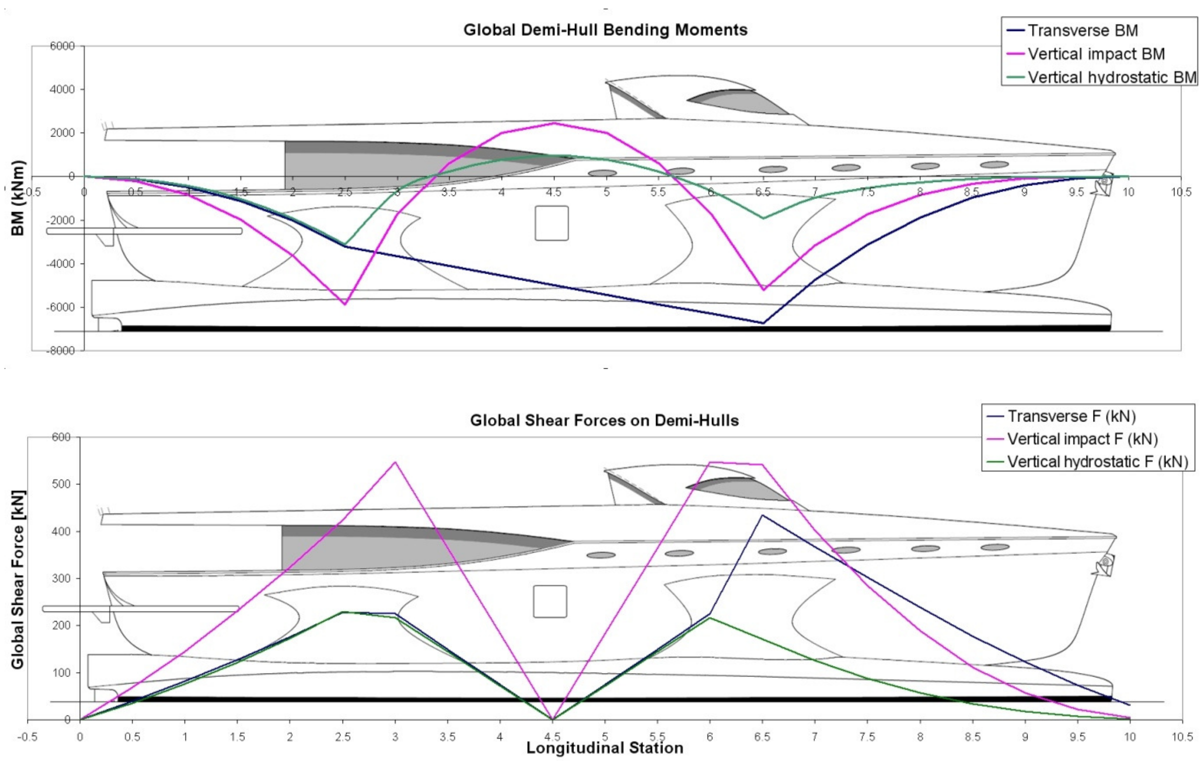

Figure 4: Bending (top) and shear (bottom) distributions

The following load cases were calculated as they should cover the worst scenarios:

1. Demi-hull vertical bending moment/vertical shear force

   The bottom shell is likely to encounter slamming as per GL Rules definition. Since slamming is an event of limited extent, slamming pressures were reduced to a certain extent and the pertinent surface pressures were integrated to obtain a global bending moment and shear force distribution, with the demi-hull held at the beam attachments. For more refined analyses, accelerated structural mass could be included, but this was considered as negligible for this vessel.

2. Demi-hull transverse bending moment and shear force

The one-sided sea pressures on the side shell of the demi-hulls were integrated to forces and moments. Based on experience from previous projects, sea pressures used for local analysis were reduced by 40% for global loads.

3. Demi-hull vertical bending moment and shear force from hydrostatics

In order to cover loads generated from partially or fully submerged structures, hydrostatic pressures were integrated over the full extent of the demi-hull.

EXAMPLE OF LOCAL STRUCTURAL EVALUATION: BOX GIRDERS AND THEIR ATTACHMENT

For the girders connecting the demi-hulls to the central hull, a more global perspective for loads was taken. The global loads used for evaluating the corresponding sections of the demi-hulls were also used to determine the girder design forces, except for the slamming loads. The integrated slamming pressures were considered too extreme to serve as girder design loads. Instead, the hydrostatic approach (listed under points 2. and 3. above) was taken. These integrated loads yield girder design forces in the region of half the vessel's displacement, both in vertical and horizontal direction. Thus, vertical design loads are roughly twice as high as the static steady state forces, roughly equal to the approach using a vertical design acceleration of 1g additional to gravity.

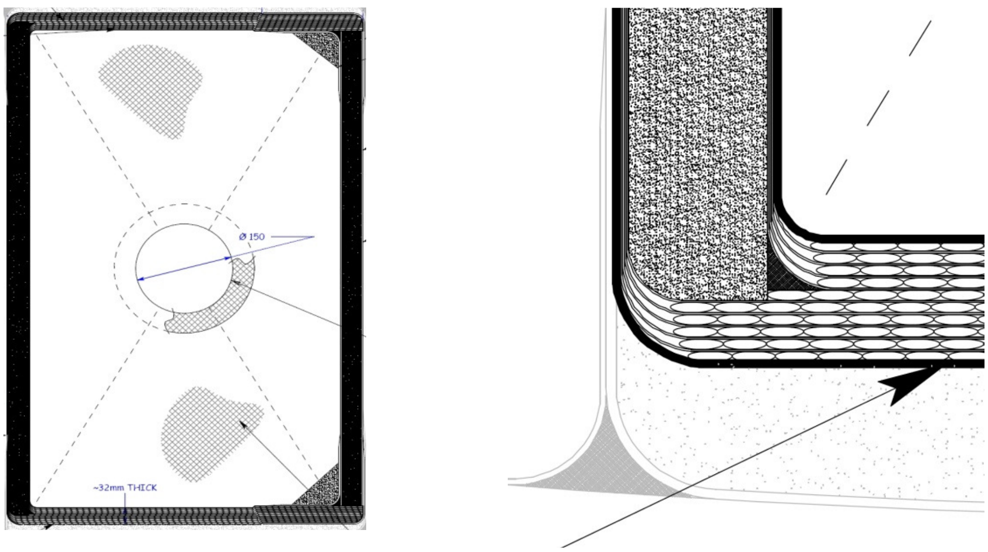

Figure 5: Section of cross beam (left) and detail of box girder corner (right)

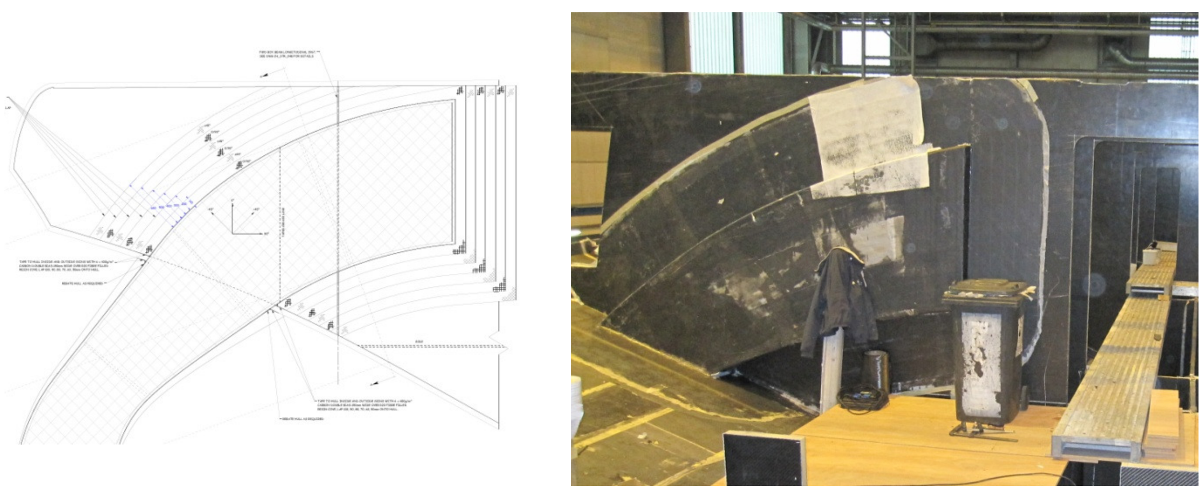

Figure 6: Attachment of box girder to the main bulkhead; schematic (left) and as built (right)

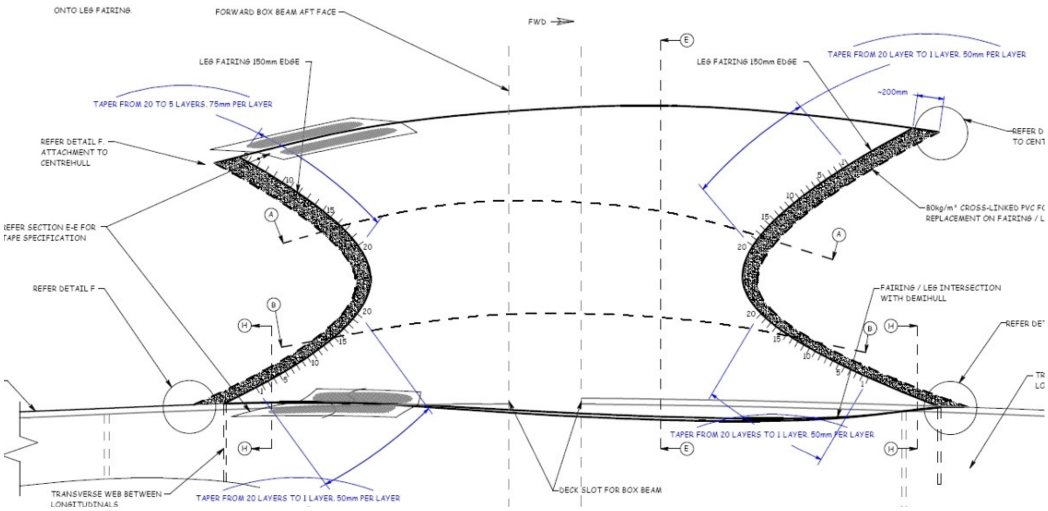

Figure 7: Beam fairing (lateral view)

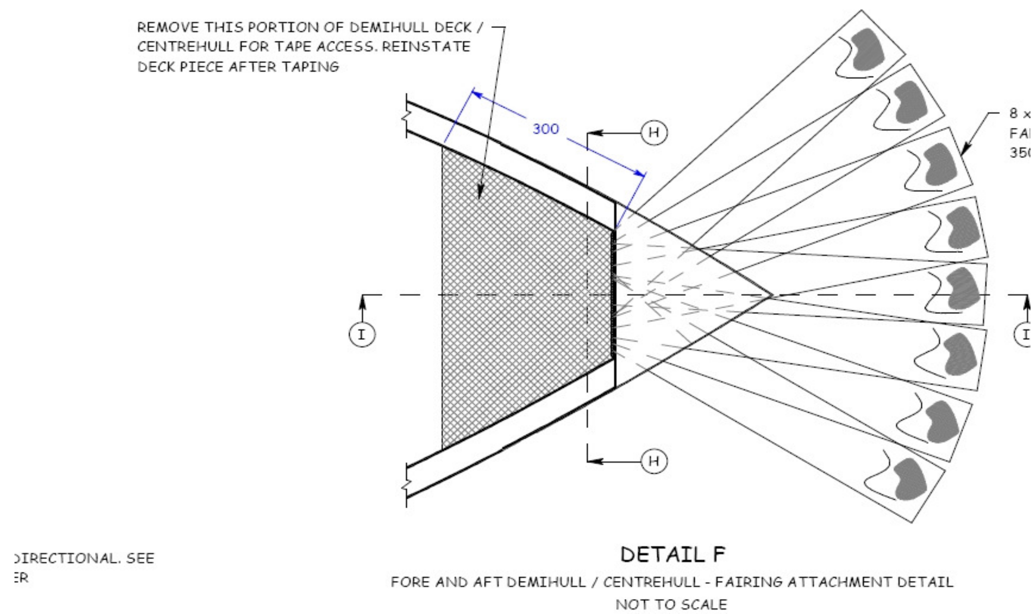

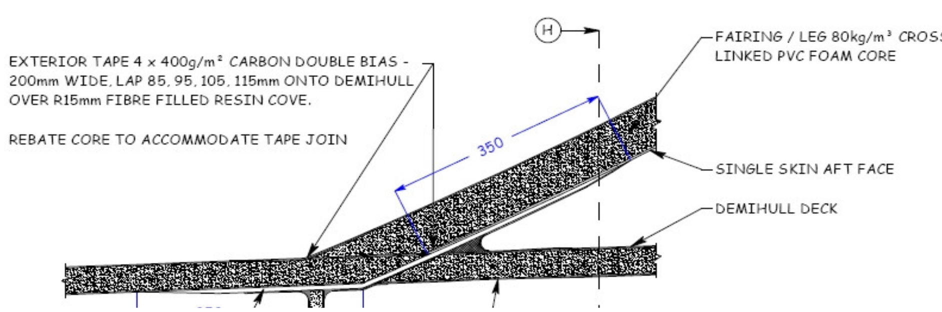

Figure 8: "Feathering of unidirectional tapes to underside of deck

The global design forces were then 450 to 650 kN. Reactions to these forces were calculated along the girder and at its support in the central hull. As the girder has a closed box format, Figure 5, laminates can be individually tailored to cope with shear forces in the box sides and tensile and compressive forces along its upper and lower flange. Usually, ±45° fabrics are used to cope with in-plane shear stresses and more 0° dominant laminates to carry tensile and compressive stresses and strains.

The box girder is connected to the central hull by placing the box girder in a slotted main bulkhead, Figure 6. The reaction forces at the inboard end of the girders is transmitted through tailored placement of bonding laminates in alternating directions due to the complexity of the loads. Due to the large cut-out in the center, the bulkhead was heavily reinforced by unidirectional tapes, in-line with major principal stresses occurring. Also, the box girder through-hull intersection is reinforced to carry loads in the hull's plane direction.

The cross beam box girders are designed to take the loads acting in the transverse plane of the vessel. Any forces acting in longitudinal direction (e.g. due to decelerations in seaways) are to be taken by the "beam fairings", Figure 2, which were designed for minimum aerodynamic and hydrodynamic drag as well as aesthetics. Due to their large span, they are designed to carry shear forces with relatively low investment of material. However, the structural attachment to the demi-hull and the central hull were a challenge for coping with the bending loads. This required not only integrating a shear connection/taping along the bond line but also effectively connecting the fairings at their aft and forward most location. In lateral view, the fairings show a large forward and aft edge curvature (3-dimensional), making it hard at first sight to effectively place unidirectional tapes which normally are very directional also in the practical placement. Apart from that, this curvature made it obvious to maintain the stress flow, extend the forward and aft tapes and "feather" them through a deck slot to the underside of the demi-hull decks. This very elegant solution is only possible with composite materials.

STRUCTURAL RESPONSE

For an efficient calculation of the structural response, the great variety of structural assemblies needs to be broken down, introducing simplifications and compiling categories to enable standardized procedures. The first step is a simplified modeling of the composite materials properties. This requires already interpretations of the expected structural function of the composite component. The composite layup is modeled following the Classical Laminate Theory (CLT). This theory reflects various material orthotropies (e.g. unbalanced solid laminates with dominant directions of fiber alignment or a simple sandwich laminate with different skins) and elasto-mechanical properties. The CLT model uses the so-called ABD matrix of a laminate, containing strain-stress relationships for all possible loads, like bending, in-plane axial tension/compression or shear. These may be coupled for very complex laminates. The ABD matrix can be relatively easily calculated for laminates subject to review. The actual engineering review combines the ABD matrix with engineering approaches yielding in the end strains and stresses. These need to be validated, e.g. by performing calculations with known results from plate and beam theory. This includes calculating effective widths of plates, regarding curvature of shells etc.

The resultant mechanical response of a structure was identified by assessing its strains (not stresses). Strains were assessed in two ways:

1. Strength related criteria:
   In-plane uni-axial strains occur in laminates under lateral pressure and global tension/compression and typically in flanges of reinforcement girders. In-plane shear strains typically occur in bulkheads and in webs of reinforcement girders.

   Instead of a complex failure mode analysis, a rather simple "maximum strain" criterion was applied to assess structural integrity. This criterion provides an appropriate limit for fiber reinforced composites provided the composite shows a fiber-dominant load transfer. The limits provided a sufficient margin over inter-laminar micro cracking and fiber failure in all in-plane directions. The criteria proposed the following limit values that should not be exceeded under structural loadings considered.

   - 0.25% in-plane uni-axial strain for carbon laminates
   - 0.45% in-plane shear strain for carbon laminates

- 0.35% in-plane uni-axial strain for E-glass laminates
- 0.70% in-plane shear strain for carbon laminates

For adhesive bonds and the structural evaluation of sandwich cores, safety factors serve to achieve sufficient integrity:

- Safety factor of 2.5 vs. core shear failure
- Safety factor of 2.5 vs. shear strength in an adhesive

In order to maintain the validity of beam and panel theory (bending without consideration of membrane effects), limitation of structural deflection under lateral pressure loads are:

- 1.5 % of effective panel span for single skin laminate panels
- 1.0 % of effective panel span for sandwich panels
- 0.5 % of unsupported span of a stiffener or girder
- 0.3 % of unsupported span of engine foundation

2. Stability related criteria:

The buckling of laminate panels needs to be considered for global in-plane compression and in-plane shear. The methodology used to attack this problem is based on simplified classical laminate theory, but includes assessment of solid plates and sandwich plates in global buckling. Especially for thin plated sandwich skins, local buckling (so-called skin-wrinkling) is addressed as well. A safety factor of 2.5 vs. panel buckling and skin wrinkling was imposed.

CONSTRUCTION AND DESIGN DETAILS

Unlike metals, fiber reinforced composites used for marine applications exhibit almost linear elastic behavior to failure. This is true as long as the structural response is fiber-dominated, which is preferred over a matrix-dominant behavior. Respecting this, composites show little or no yielding until failure. This aspect requires particular attention. Especially in structural details with stress concentrations, the static strength analysis requires special consideration. When stress concentrations are compensated appropriately, fatigue will not be critical.

This is valid for in-plane loads with fiber-dominated load absorption. However, through-thickness loading (especially shear and tension) cannot always be avoided and needs to be handled in an appropriately conservative way. "Intercracking" or delamination caused by overloading, impact or deficient structural design is considered to be the cause for subsequent failure of components and thus can be deemed as cause for fatigue in composites.

The following recommendations do not claim to be all-inclusive and are subject to amendments:

- In general, the basic laminate stacking sequence shall be homogeneous; preferably symmetrical and balanced, if no particular attention has to be paid to possible secondary affects.
- A laminate should consist of plies aligned in at least 4 distinct directions (e.g. 0°, ±45°, 90°), with not less than 10% plies in each direction. Ply angles should be aligned appropriately for major load direction(s). The following components are exemptions from this rule:
  - mainly in-plane shear loaded webs of girders, stiffeners, frames
  - local tape reinforcements
- Grouping of plies with the same fiber direction should be avoided, but total thickness of these plies may not exceed 1.5 mm (typically for carbon laminates).
- Not all parts are suitable for composites. Complex three-dimensional stress states may make suitable isotropic materials a preferred choice (e.g. local fittings).
- Inaccessibility of composite components needs to be considered in design with respect to inspection during production, in service and after damage.
- Generally we try to avoid forces that result in high interlaminar shear stresses due to the variability of the shear strength of laminate composites. We also try to avoid joints that result in significant peel stresses – once

again due to the difficulty in designing for this failure mode and the variability of joint strength on manufacturing quality, resin and modifier types, cove radius etc.

All structural details are subject to examination by Germanischer Lloyd. In general the following provisions shall be observed:

- The risk of peeling effects, e.g. induced by abrupt stiffness changes, must be minimized. Secondary bonding is always to be backfilled with suitably rounded filler bed.
- For mechanical fastenings, a domination of fiber orientation in one direction of more than 40 % is not advisable.
- Core chamfers of sandwich laminates should not be steeper than 1:3.
- Exposed fibers and sandwich cores shall be sealed with laminate.

SUMMARY AND OUTLOOK

Classical "cook-book" approaches hardly qualify to match requirements for light-weight designs. Especially for advanced composite designs, prescriptive rules are often too inflexible. Recent projects like:

- 37 m high-speed M/Y "Ermis^2" (58 kn)
- "Earthrace" ultra-slender power trimaran
- 21 m Vaka Polynesian sailing canoes
- 37 m high-performance sailing yacht "Bristolian"
- 31 m "Turanor Planetsolar"
- 65 kn high-speed interceptor patrol craft,

all constructed from composites show that characteristic tailored solutions for composite require particular attention and understanding. The variety of possibilities to design a particular component to suit its purpose is manifold and is often only bound to development budgets or creativity.

Germanischer Lloyd currently summarizes the experience of the last years in an isolated structural classification guide featuring approaches as presented exemplary in this paper. This guide will first be published within a new revision of HSC Rules, *GL (2011)*. It defines methods to predict relevant composite material characteristics. Along with the definition of the "First principles of Engineering" and the pertinent safety methodology, the package defines how to attack the proof for structural integrity to suit individual designs.

REFERENCES

Ziegler, W.; Fach, K.; Hoffmeister, H., El Moctar, O.M. (2006), "Advanced analyses for the EARTHRACE project", *5th Conf. High-Performance Marine Vehicles (HIPER),* Launceston, pp.101-108

GL (2002), "Rules for Classification and Construction", I Ship Technology, 3 Special Craft, 1 High Speed Craft, Edition 2002, Germanischer Lloyd, Hamburg

GL (2011), "Draft Rules for Classification and Construction", I Ship Technology, 3 Special Craft, 1 High Speed Craft, Edition 2011, Germanischer Lloyd, Hamburg

Seventh International Conference
On High-Performance Marine Vehicles
Melbourne, Florida, USA
13-15 October 2010

HIGH SPEED SMALL CRAFT AERODYNAMIC RESISTANCE

Carlo Bertorello,* Fabio Fossati, Sara Muggiasca****

***Department of Naval Architecture of Universita' di Napoli Federico II**
****Department of Mechanics of Politecnico di Milano**
bertorel@unina.it fabio.fossati@polimi.it sara.muggiasca@polimi.it

ABSTRACT

High cruising speed, at present commonly achieved by small size pleasure and working boats highlights the importance of aerodynamic drag and suggest to consider also aerodynamic lift.To this aim an experimental research program has been jointly carried on at Department of Naval Architecture of Universita' di Napoli Federico II and at Department of Mechanics of Politecnico di Milano.A 1:10 scale model of a planing pleasure boat, decked and GRP built, has been tested in towing tank to assess bare hull resistance, running trim and hull raise at Fn range 1.1-2.1.

In the wind tunnel the same model has been connected to a six DOF. dynamometric balance; a set of wedges has been used to set the scale model at trim angles and hull raises previously assessed in towing tank and a flat plane to simulate the water surface. Aerodynamic drag has been assessed at the same speed values used in the towing tank to evaluate the aerodynamic contribution to the total resistance. Then in order to check Reynolds number effect on the aerodynamic coefficients, further tests at higher wind speed values up to 16 m/s have been performed. The obtained results allow the assessment of scale models aerodynamic resistance and represent a contribution for a sound application of the experimental procedure used for planing craft resistance evaluation.

INTRODUCTION

The ship is a body interacting simultaneously with two fluids, water and air. Their relative importance on the ship behaviour and performances is different according to the considered type of vessel. In the motion resistance assessment of a cargo ship is usual and reasonable to neglect the aerodynamic component while when considering a racing powerboat the aerodynamic forces will result of the same order of magnitude of the hydrodynamic ones.
The effect of the air pressure on the ship motions and equilibrium has been known and considered from the earliest steps of marine technology as shown by the low freeboard of traditional craft used for fishing in windy areas. Generally air and wind forces are evaluated by means of empirical and numerical formulas, Koelbel (1971).The mentioned effect is negligible in relative terms for displacement ships with relative speed values in the Fn range 0.1 - 0.3, but it is significant for High Speed Craft and most important for small size planning vessels. In this case the total resistance is a function of the bare hull resistance, of the resistance due to appendages and of the aerodynamic drag force.

Although the first component is generally predominant, the contribute of air resistance is not negligible at higher relative speed. Furthermore, in the range of Fn 0.6-1.2 the improvement in hydrodynamic lift and the consequent reduction of wetted surface lead to a progressive reduction of the bare hull resistance when the speed increases, while the air component always grows up according to the squared velocity, increasing its the importance on the total. This behaviour was known from the beginning of the systematic study of hydrodynamic lift of V bottom small craft at Fn > 0.6 carried on in the early fifties of XX century and lead to the usual practice of adding the air component evaluated by means of empirical formulas to the ship hull resistance.In this work the aerodynamic effects in still air on motion resistance have been considered. The analysis is limited to still water conditions.

Within this frame, and regarding planing craft, the evaluation of aerodynamic resistance of scale models tested in towing tank becomes very important. In these tests the scale model motion resistance is measured and the full scale ship resistance is evaluated through the model ship correlation based on the Froude assumption. This considers the same “residual” resistance non-dimensional coefficient for both ship and model at a given Fn value. Viscous components, both hydro and aerodynamic cannot be scaled due to their dependence from the Rn and must be evaluated by empirical formulas for the scale model as well as for the ship.
Basically the Froude method can be summarized as

$$C_{TS}=C_R+C_{FS} \qquad (1)$$

$$C_R= C_{TM} - C_{FM} \qquad (2)$$

provided $V_S/V_M=\lambda^{1/2}$

In the expression of $C_{TM}= R_T /(1/2\ \rho\ V^2\ S)$ the Total Resistance R_T should be obtained subtracting the model aerodynamic resistance R_{AA} from the towing force. Unfortunately, very often the measured towing force is assumed as the bare hull total resistance, neglecting the aerodynamic component of the model resistance.

This can be acceptable for tests performed in displacement mode (Fn < 0.6) but leads to not adequate results when it is applied to High Speed Craft. The fact has been highlighted by ITTC (2008). If the high relative speed is achieved by hydrodynamic lift the effect of the aerodynamic component can be even more significant due to the peculiar trend of bare hull resistance with increasing speed values.

For this reason the assessment of the relative weight of the aerodynamic component on the model total resistance through the correlation of wind tunnel and tank tests seems necessary to get reliable results of planing craft experimental resistance assessment. The further extension of wind tunnel tests to higher speed values allows the evaluation of the aerodynamic coefficients relative to the used model. As this can be considered representative of planing craft hull form widely used, the identified drag coefficients values will lead to consider appropriately the model aerodynamic resistance in the general practice of planing craft towing tests. This work is focused on the scale model used in towing tests that are generally not fitted with superstructure; for this reason the emerged part of the hull is considered only.

NOMENCLATURE

B	Reference beam
C_D	Aerodynamic Drag coefficient
C_L	Aerodynamic Lift coefficient
CR	Residuary-resistance coefficient
C_T	Total-resistance coefficient
C_{TS}	Total-resistance coefficient of the ship
C_{TM}	Total-resistance coefficient of the scale model
C_{FS}	Viscous-resistance coefficient of the ship
C_{FM}	Viscous-resistance coefficient of the scale model
F_n	Froude number
g	Acceleration due to gravity
H	Hull raise (sinkage)
P_E	Effective Power
R_n	Reynolds number
R_T	Total resistance
R_{AA}	Aerodynamic resistance

S	Wetted-surface area
S_M	Scale Model Wetted-surface area
S_S	Ship Wetted-surface area
T_M	water temperature for the scale model
T_S	water temperature for the ship
V_S	Ship velocity
V_M	Scale model velocity
v	velocity
λ	scale factor
ν_M	water kinematic viscosity for the scale model
ν_S	water kinematic viscosity for the ship
ρ	Water density Air density
ρ_M	water density for the scale model
ρ_S	water density for the ship
τ	Longitudinal trim angle
Δ	Displacement weight

ABBREVIATIONS

DOF	Degree of Freedom
HSC	High Speed Craft
ITTC	International Towing Tank Conference

KEYWORDS

HSC Motion Resistance, Air Resistance, HSC tank testing

EXPERIMENTAL PROGRAM

The performed experimental program consisted in the tests of two identical models, one in the wind tunnel of Politecnico di Milano, the other in the towing tank of the University of Naples Federico II. The two series of tests were carried out for the same speed values ranging from 3.6 m/s to 6.4 m/s. In the tank the horizontal towing force, the longitudinal trim and the hull rise were measured. In the wind tunnel the hull was set at the same trim angle and sinkage resulting from tank testing. Aerodynamic components in the vertical and horizontal direction as well as pitching moment were measured. Furthermore, in the wind tunnel the testing has been continued to higher speed values, not achievable by the tank carriage, to assess the trends of aerodynamic coefficients. In this case the model was set with longitudinal trim and rise relative to the highest speed (6.4 m/s) achieved in the tank. Finally the onset flow profile has been identified through a set of pressure gauges at different heights from the surface level.

EXPERIMENTAL SETUP

POLITECNICO DI MILANO WIND TUNNEL

Figures 1 and 2 show an overview of the Politecnico di Milano facility: it is a closed circuit facility in a vertical arrangement having two test sections, a 4 x 4m high speed low turbulence and a 14 x 4m low speed boundary layer test section. A peculiarity of the facility is the presence of two test sections of very different characteristics, offering a very wide spectrum of flow conditions, from very low turbulence and high speed in the contracted 4 x 4m section (I_u<0.15%, V_{max}=55 m/s), to earth boundary layer simulation in the large wind engineering test section.

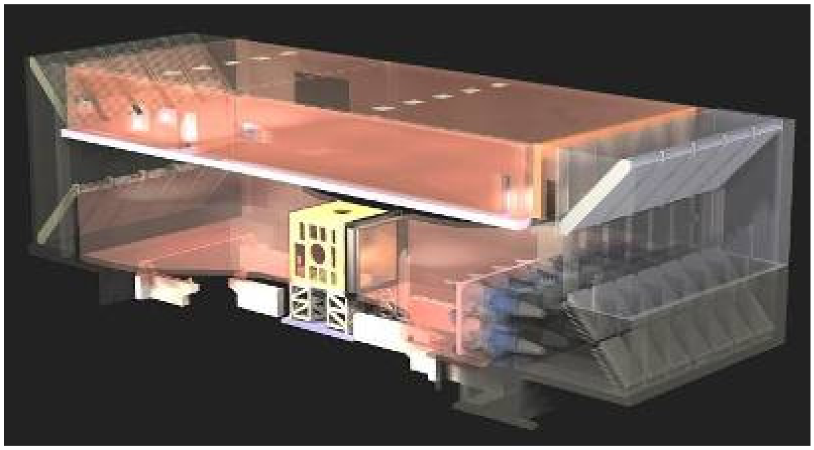

Figure 1: Politecnico di Milano Wind Tunnel

Focusing on the boundary layer test section, its overall size of 36m length, 14m width and 4m height allows for very large-scale wind engineering simulations, as well as for setting up scale models of very large structures including wide portions of the surrounding territory. The relevant height of the test section and its large total area (4m, 56m^2) allow for very low blockage effects even if large models are included. The flow quality in smooth flow shows 2% along-wind turbulence. A 13m diameter turntable lifted by air-film technology allows for fully automatic rotation of large and heavy models fitted over it (max load 100,000 N).

The long boundary layer test section is designed in order to develop a stable boundary layer and the flow conditions are very stable also in terms of temperature due to the presence of a heat exchanger linked in the general control loop of the facility. The Wind Tunnel is operated through an array of 14 axial fans organised in two rows of seven 2 x 2m independent cells. 14 independent inverters drive the fans allowing for continuous and independent control of the rotation speed of each fan. This fully computer controlled facility can help in easily obtaining, in conjunction with the traditional spires & roughness technique, a very large range of wind profiles simulating very different flow conditions and different geometrical scales. All the typical various sets of spires have been developed in order to simulate the different wind profiles and an original facility has been recently installed allowing for active turbulence control in the low frequency range.

Concerning the low-turbulence high-speed section, the large dimensions (4 x 4m) and the quite high wind speed (55m/s) enable quite high Reynolds numbers to be reached. In particular, with reference to yacht studies, the high-speed wind tunnel section allows development of specific appendage scale model tests typically on 1:2 scale model for IACC class keel and rudder models.

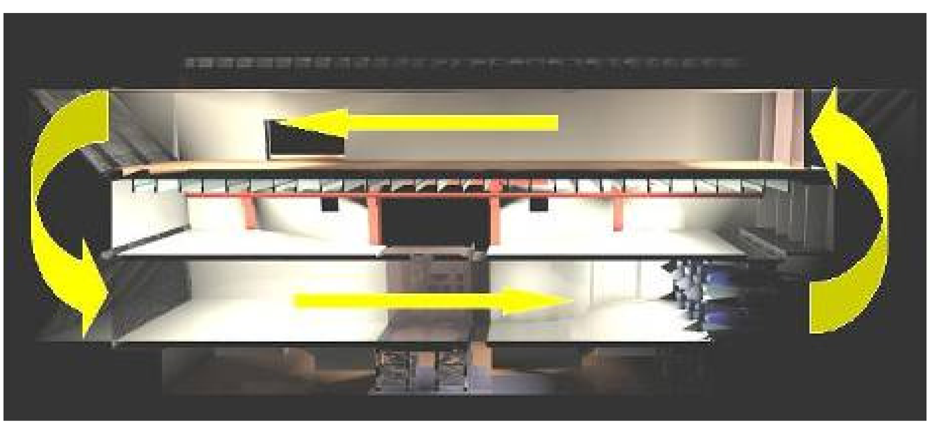

Figure 2: Wind tunnel vertical section

Figures 1 and 2 show an overview of the Politecnico di Milano facility: it's a closed circuit facility in a vertical arrangement having two test sections, a 4 x 4m high speed low turbulence and a 14 x 4m low speed boundary layer test section.

MEASUREMENT OF AERODYNAMIC FORCES

The 1/10 scale model of a planing pleasure boat, decked and GRP built, already tested in towing tank has been used to perform wind tunnel tests too. The model, consisting of the complete hull with deck, is mounted on a six component force balance, which is fitted on the turntable of the wind tunnel high speed test section (Figure 3). The turntable is automatically operated from the control room enabling a 360° range of headings.

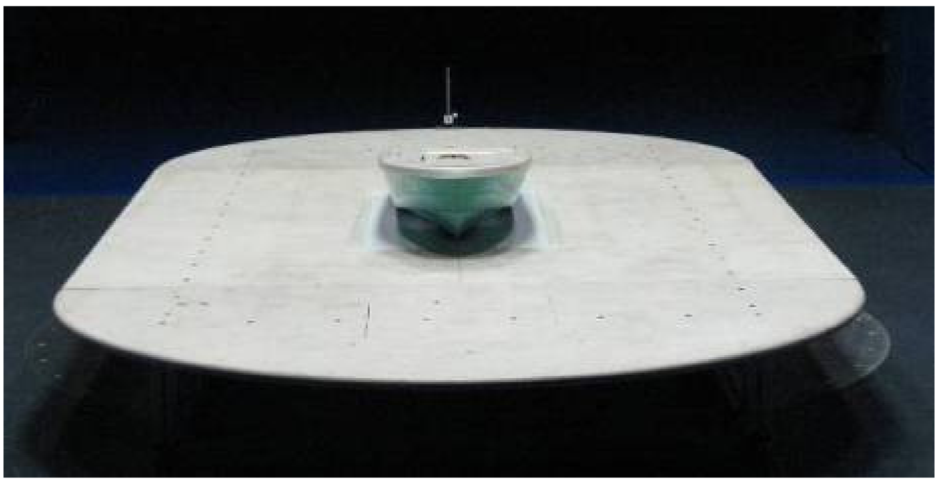

Figure 3: Scale model fitted on the turntable of the wind tunnel high speed test section

An high performance strain gauge dynamic conditioning system has been used for balance signal conditioning purposes (Figure 4).

Figure 4: The strain gauge dynamic conditioning system before model fitting

The balance is placed inside the yacht hull in such a way that X axis is always aligned with the yacht longitudinal axis and a set of wedges has been used to get the same trim angle and hull raise previously assessed in the towing tank tests.

A flat plane has been used to simulate the water surface (Figure 5) and air flow between the yacht waterline and the flat ground is prevented by means of a seal which reproduces the hull waterplane figure.

Figure 5: The scale model in the wind tunnel set with appropriate trim and sinkage

Data acquisition has been performed by means of National Instruments Data Acquisition Boards (16 bits, from 8 differential channels up to 64 single-ended) and suitably written programs according to Matlab standards. The data acquisition software calculates the forces and moments using the dynamometer calibration matrix.
The onset flow profile has been identified through four pressure gauges at different heights from the surface level (Figure 6).

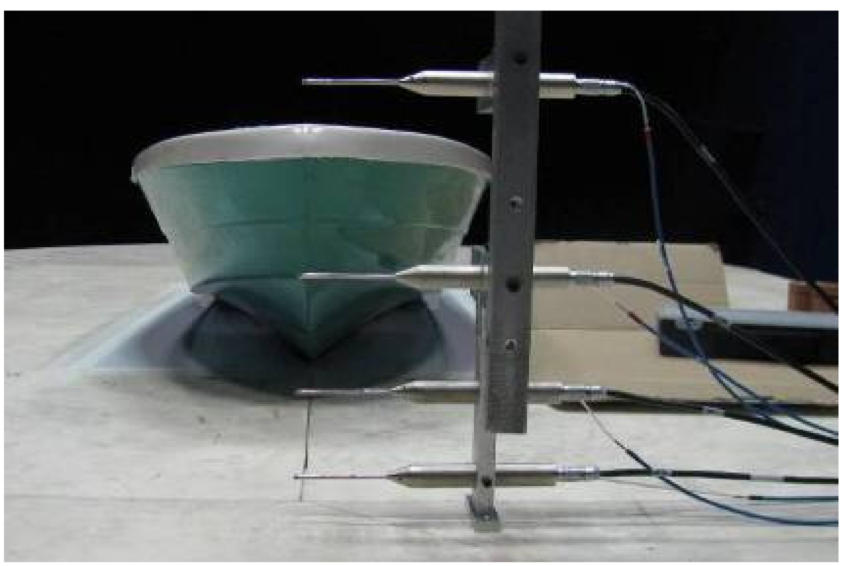

Figure 6: Pressure gauges for flow profile assessment

Figure 7 shows the onset wind vertical profiles measured at 4 different heights from the surface level for each test carried out at different wind tunnel speed. In the same picture horizontal line represent the yacht bow height corresponding to the mean hull raises previously assessed in the towing tank tests.

As can be seen the wind speed profiles are substantially uniform with height over the whole wind tunnel speed range investigated except in the boundary layer height which is less than 10% of the yacht bow height.

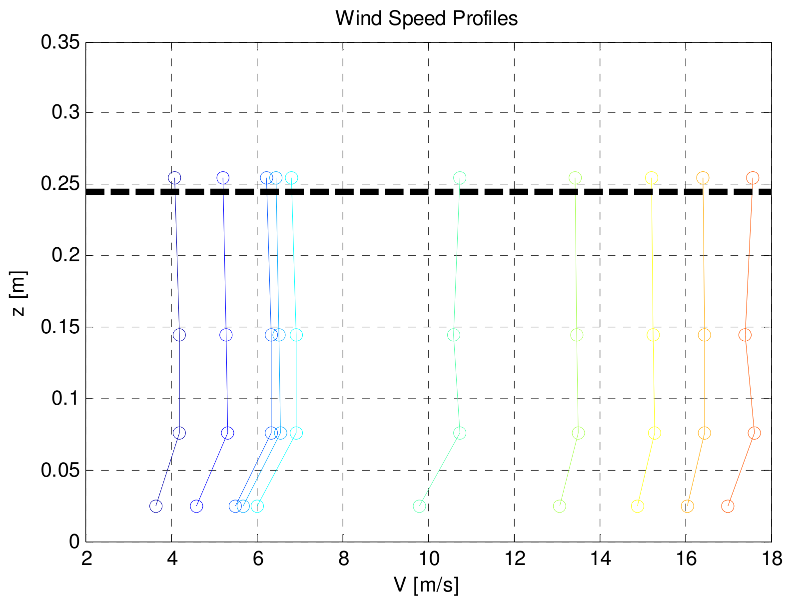

Figure 7: Wind speed profiles at investigated speed values

UNIVERSITA' DI NAPOLI FEDERICO II TOWING TANK

The resistance tests were performed at Towing Tank of Department of Naval Architecture (DIN) Of University of Naples which main dimensions are 135 m x 9 m x 4.5 m (depth). The towing carriage speed ranges from 0.1 to 7 m/s.

The scale model was towed by an horizontal force applied in correspondence of ship CG longitudinal position, 0.08 m above waterline. The model was free to pitch and to move on the vertical axis, but constrained as regard roll, yaw and drift. Scale model main characteristics are reported in Table 1. The towing set up can be seen in Figure 8, and is described in details in previous works, Bertorello (2009)

Table 1: Scale model main characteristics

L_{WL} (m)	1.09
B_{WL} (m)	0.360
T (m)	0.072
Δ (kg)	14.30
X_{CG} (m)	0.278
λ_{SHIP}	10.0

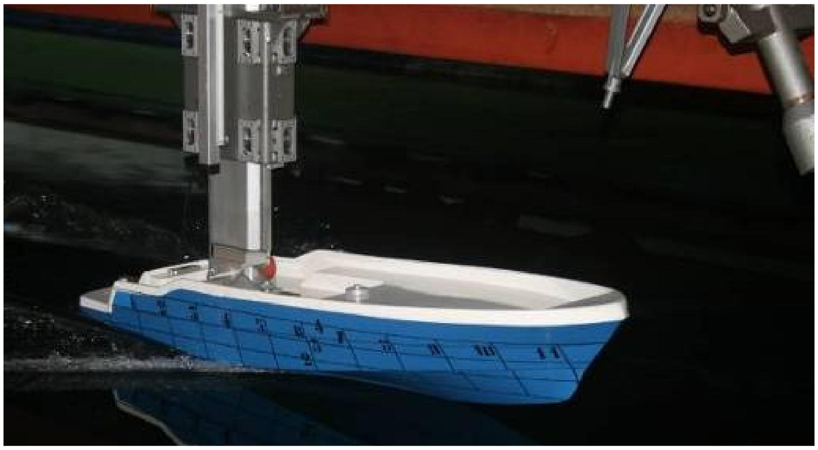

Figure 8: Scale model towing test at 6.06 m/s

RESULTS

In the following Table 2 the model total resistance R_T measured in the towing tank as well as model air resistance R_{AA} measured in the wind tunnel are reported for speed ranging from 3.7 to 6.4 m/s. The values of longitudinal trim angle and of hull rise resulting from towing tests and then used for the model set up in the wind tunnel are reported also. In the sixth column the percentage of the aerodynamic drag component with respect to the total resistance is shown.

Table 2: Scale model testing results

	τ	H	RAA	RTM	RAA%	Fn
(m/s)	(deg)	(mm)	(N)	(N)		
3.760	5.380	18.430	0.337	19.109	1.8	1.150
4.880	3.800	24.430	0.534	19.044	2.8	1.493
5.830	2.95	28.140	0.764	21.261	3.6	1.783
6.050	2.90	30.190	0.850	22.159	3.8	1.850
6.400	2.87	31.110	0.947	23.422	4.0	1.957

The trends of both R_T and R_{AA} are shown in figure 9.

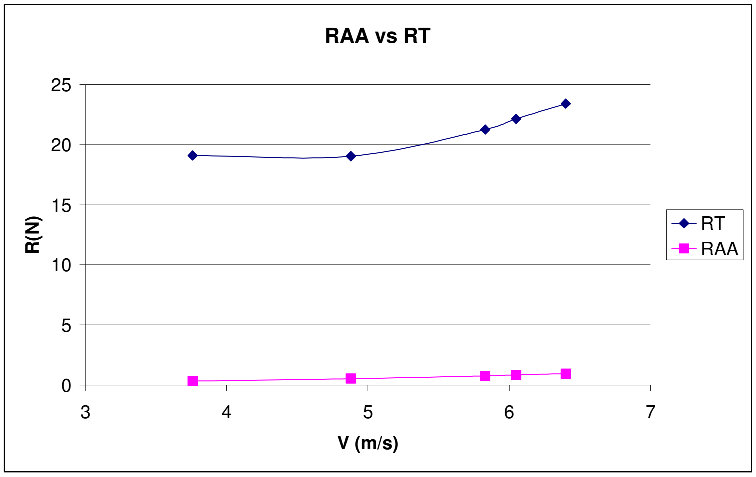

Figure 9: Trends of R_T and R_{AA}

As can be seen windage effects amount are within 1.8%-4% range of the total resistance measured in towing tank. As previously said wind tunnel the tests have been extended to higher speed values (up to the dynamometer max allowed load), not achievable by the tank carriage, to assess aerodynamics trend.
In Table 3 the measured values of the air component R_{AA} for higher speed values up to 16.61 m/s are reported

Table 3: R_{AA} values for speed range 10-16.6 m/s

V	RAA
(m/s)	(N)
10.00	2.275
12.75	3.674
14.39	4.680
15.49	5.413
16.61	6.207

Figure 10 summarizes the drag force measured at the different model trim values considered at the various speeds.

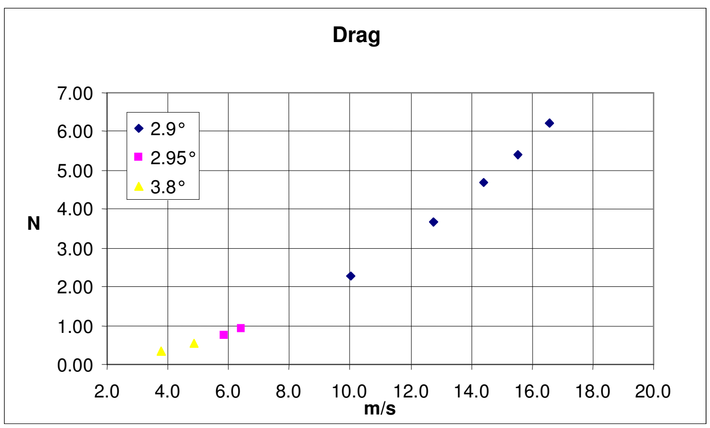

Figure 10: Drag Force vs model speed

Wind tunnel tests provide also aerodynamic lift force which is shown in figure 11. Positive values mean force directed upward.

Then aerodynamic drag and lift coefficients can be defined according to the following expressions:

$$C_D = \frac{Fx}{\frac{1}{2}\rho B^2 v^2}$$

$$C_L = \frac{Fz}{\frac{1}{2}\rho B^2 v^2} \tag{3}$$

where

- Fx is the aerodynamic drag force
- Fz is the aerodynamic lift force
- B is the hull maximum beam

- v is the ship speed
- ρ is air density

Finally the corresponding Drag and Lift coefficient for a general evaluation of the model R_{AA} are reported in figs. 12-13

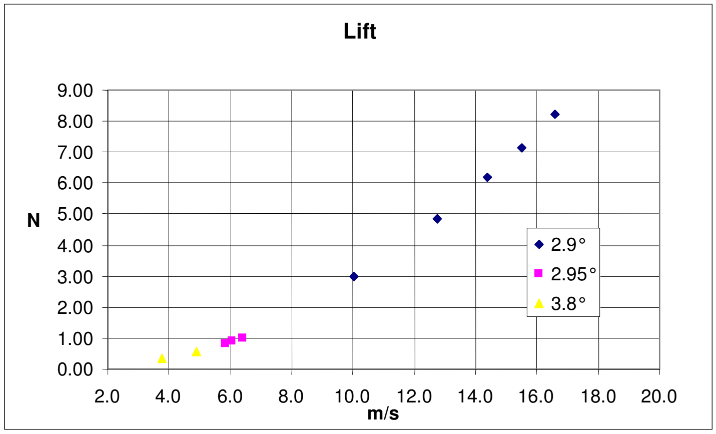

Figure 11: Lift Force vs model speed

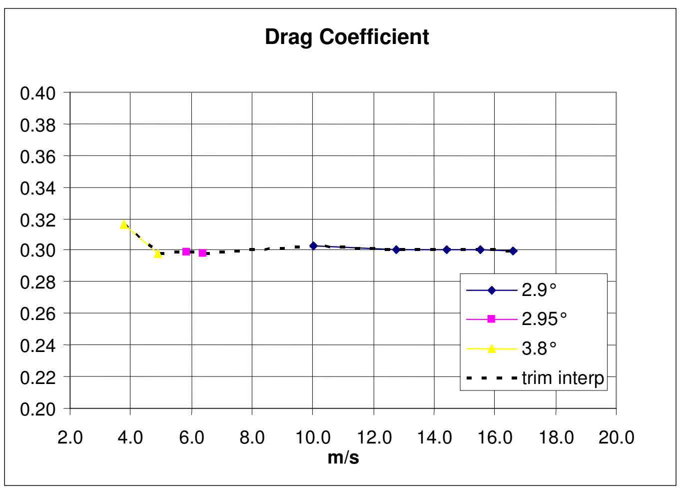

Figure 12: Drag coefficient vs model speed

From the obtained drag coefficient values it is possible to evaluate the relative weight of the aerodynamic resistance of the emerged part of the hull on the resistance of the ship in full scale. They are reported in the following Table 4. The table reports the ship resistance values obtained through the ITTC57 ship model correlation using the effective surface for Fn range 1.15-1.96 that corresponds to 23.1-39.3 kn ship speeds. The model aerodynamic resistance has been subtracted to the towing force. In the last column of the lower part the percentages of the aerodynamic resistance are reported.

As a reference and to compare the obtained result with values commonly used in the professional practice the RAA values have been calculated through the widely used formula by G.S. Baker reported in Koelbel 1971:

$$R_{AA} = 0.0012\ (3.3\ A_{TP} + A_{TS})\ v^2 \qquad (4)$$

where A_{TP} and A_{TS} are the projected areas of the emerged part of the hull and of the superstructure respectively. The projected area of the hull has been measured considering trim of 3.8 degrees for the first considered speed (23.1 kn) and trim of 2.9 degrees for all other speed values as well as the relative hull raise values. The results are reported in the following Table 5.

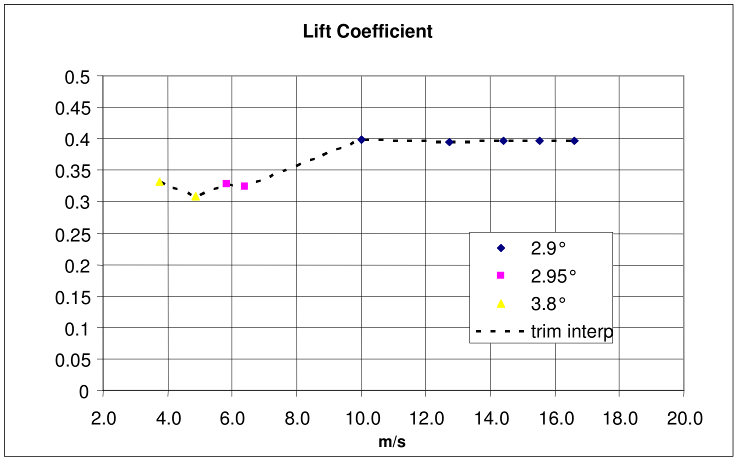

Figure 13: Lift Coefficient vs model speed

Table 4: Model-Ship correlation and R_{AA} values in full scale

LWL STAT (m)	1,090
T_M [°C] =	23,7
ν_M [m^2/s] =	9,22E-07
ρ_M [kp s^2/m^4] =	101,69

MODEL										
V_M	TOW	R_{AAM}	RT_M	R_{TM}	R_{Nm}	F_N	S_M	C_{TM}	C_{FM}	CR
(m/s)	*(N)*	*(N)*	*(kg)*	*(N)*			*(m2)*			
3,760	19,109	0,337	1,914	18,766	4,446E+06	1,150	0,344	7,738E-03	3,472E-03	2,057E-03
4,880	19,044	0,534	1,887	18,504	5,770E+06	1,493	0,313	4,978E-03	3,308E-03	1,670E-03
5,830	21,261	0,764	2,089	20,491	6,893E+06	1,783	0,298	4,057E-03	3,204E-03	8,533E-04
6,050	22,159	0,850	2,172	21,302	7,154E+06	1,850	0,296	3,943E-03	3,182E-03	7,605E-04
6,400	23,422	0,947	2,291	22,468	7,567E+06	1,957	0,293	3,754E-03	3,151E-03	6,036E-04

LWL STAT (m)	10,900
λ =	10
T_S [°C] =	15
ν_S [m^2/s] =	1,19E-06
ρ_S [kp s^2/m^4] =	104,60
g [m/s^2]	9,807

SHIP							
V_S	R_{NS}	C_{FS}	C_{TS}	R_{TS}	P_E	R_{AAS}	**%**
(kn)				*(kN)*	*(kW)*	*(kN)*	
23,1	1,091E+08	2,057E-03	4,115E-03	10,264	122,0	0,320	**3,11**
30,0	1,416E+08	1,982E-03	3,652E-03	13,963	215,5	0,538	**3,86**
35,8	1,692E+08	1,933E-03	2,787E-03	14,477	266,9	0,768	**5,31**
37,2	1,755E+08	1,923E-03	2,684E-03	14,915	285,3	0,827	**5,55**
39,3	1,857E+08	1,909E-03	2,512E-03	15,464	313,0	0,926	**5,99**

Table 5: R_{AA} values by Baker formula

v	A_{TP}	A_{TP}	R_{AA}	R_{AA}
(kn)	(m^2)	(ft^2)	(pd)	(kN)
23,1	6,3	67,819	143,490	0,639
30,0	6,05	65,128	232,114	1,034
35,8	6,05	65,128	331,282	1,475
37,2	6,05	65,128	356,756	1,589
39,3	6,05	65,128	399,228	1,778

It is possible to note that the values are higher in respect to those obtained using the coefficient assessed by the reported wind tunnel tests. This is could be due to different model hull form, test conditions, equipment etc. While it seems not fair to compare results obtained at so large time distance, the highlighted difference confirms the importance of the performed tests and suggests further and deeper investigations.

CONCLUSIONS AND DISCUSSIONS

In this paper an assessment of the relative weight of the aerodynamic component on the total resistance of a scale model of planing craft through the correlation of wind tunnel and tank tests is proposed. The identified aerodynamic drag coefficients values lead to consider appropriately the model aerodynamic resistance in the general practice of planing craft towing tests.
From the obtained results it is possible to conclude that windage effects amount are within 1.8%-4% range of the total resistance measured in towing tank for model speed up to 6.5 m/s.
In order to get reliable results of planing craft experimental resistance assessment, further extension of wind tunnel tests have been performed to higher speed values allowing the evaluation of the aerodynamic coefficients relative to the used model. Furthermore from the obtained drag coefficient values it is possible to evaluate (the relative weight of) the aerodynamic resistance of the emerged part of the hull (on the resistance) of the ship in full scale. With reference to the vessel hullform used in the present work, which can be considered representative of widely used planing craft hullform, the aerodynamic resistance due to the emerged part of the hull is within the range 3%-6% of the total resistance for the typical operational yacht craft speeds.
In the wind tunnel tests the vertical force and the pitching moment due to aerodynamic forces have been measured also. These data will be the first step for a future development of the research program. This will consider the effects of aerodynamic forces on vessel trim and resistance with the aim of a better refinement of the semi-empirical procedures widely used for planing craft resistance evaluation.

ACKNOWLEDGMENTS

This work has been financially supported by Universita' di Napoli Federico II within the framework of 2009-2010 research program. Politecnico di Milano Wind Tunnel staff is gratefully acknowledged for their help and continuous efforts in wind tunnel testing activities.

REFERENCES

Bertorello, C., Oliviero, L. (2009): "Hydrodynamic resistance assessment for not monohedral planino hull form" *Vol. 2 pp. 703-707, IMAM 2009 13th International Congress of International Marittime Association of Mediterranean 12-15 October 2009,* Instanbul Turkey

Clancy, L. J. (1975): "Aerodynamics",. *Pitman Publishing Limited*, London

Hoerner, S.F. (1965): "Fluid-dynamic drag", *Hoerner Fluid Dynamics, Brick Town, N. J.,* USA .

Hoerner, S.F, and Borst, H.V. (1985): "Fluid-Dynamic Lift", *Hoerner Fluid Dynamics, Brick Town, N. J.,* USA .

Isherwood, R.M. (1973) "Wind resistance of Merchant Ships", *Trans RINA Vol 115*, UK

ITTC – Recommended Procedures and Guidelines (2008): "Testing and Extrapolation Methods High Speed Marine Vehicles Resistance Test" *7.5-02 -05-01 Page 12*

Koelbel, J.G. (1971): "Guide to Powerboat Design" , *Naval Ship Sistems Command, Office of naval Research, Report n 120-2*
Thwaites, B. (1969): "Incompressible aerodynamics" *Dover Publications Inc., New York,* USA.

Walsh, D.E. (1983): "A Method for the Calculation of the Wind Resistance on High Speed Marine Craft" *Proc. Report 161 of the National Marine Institute Feltham,* U.K.

Walsh, D.E. (1983): "Measurement of Wind Forces and Moments on Models of Three representative High Speed Marine Craft" *Proc. Report 168 of the National Marine Institute Feltham,* U.K.

Seventh International Conference
On High-Performance Marine Vehicles
Melbourne, Florida, USA
13-15 October 2010

HYDRODYNAMIC PERFORMANCE EVALUATION OF HULL - WATERJET SYSTEM USING CFD AND EXPERIMENT

MD.Kareem Khan [1] and P.Krishnankutty [2]

[1] Scientist, Naval Science & Technological Laboratory, India
Email : *kareemkhan05@gmailcom*
[2] Professor, Indian Institute of Technology Madras, India
Email : *pkrishnankutty@iitm.ac.in*

ABSTRACT

Waterjet propulsion exhibits excellent propulsive performance and maneuverability within a specified speed range which are favorable for high speed applications and also for vessel maneuvers in restricted waters. The waterjet propulsor manufacturers provide only the performance data of waterjet system at a specified operational condition, without the vessel influence effects. But, the overall scenario of the waterjet system interaction effects on the performance of the vessel and that of the hull on the propulsors are neither known nor provided. Several experimental and numerical studies are being carried out worldwide to understand and evaluate the performance of hull - waterjet system as a whole. This paper tries to bring out the interaction between hull and waterjet system numerically using CFD methods based on the RANSE solvers and experimental investigations.

INTRODUCTION

Propellers have been in use in commercial and military vessels for more than a century. Advancement in computational facilities has enabled us to solve numerically the mathematical models representing more realistic flow around propulsor, which are further complemented by the improvements in ship model test facilities. The changing demands in mission profiles and the wide range of available engines and propulsors open the way to water jet propulsion systems which optimize the vessel's performance(at higher speeds). Studies have shown that waterjets are preferred over conventional propulsors in a range of high speed operation, Bulten (2006).

This paper presents a RANSE based simulation of the flow velocity over a hull - waterjet system, particularly at the inlet (intake), nozzle outlet areas and boundary layer profile at intake. It also aims at the use of a wind tunnel facility to measure the air-flow characteristics in a hull - waterjet system and then predict the hydrodynamic performance of the system based on the wind tunnel results. A waterjet propelled hull form and waterjet system geometry were chosen as the starting piece of work. A vessel condition (i.e. dynamic trim and immersion) operating with a Froude number of 0.6, for which the published literature (ITTC 2005) was available, has been selected for simulation of axial fluid flow over the hull - waterjet system in wind tunnel. Experimental test procedure in the wind tunnel involves similar concept of testing in towing tanks except the differences being the test facility and fluid medium.

Allison (1993) and Tervisga (1996) presented a theoretical model for understanding the physics of hull - waterjet system. Purnell et al (2002) discusses the issue of an efficient compact waterjet propulsion system for high speed application. Alder and Denny (1977) looked into the feasibility in design of waterjet propulsors with regard to conventional propeller design. MacPherson (1999) studied a parametric model for efficient waterjet performance in terms of speed-thrust-power curves along with engine power and rpm. Fujisawa (1995) throws light on the importance of the open water waterjet system tests in their performance evaluation. The committee on validation of waterjet test procedures setup by ITTC (1996, 2002, 2005) provides the guides lines for hydrodynamic testing and evaluation of hull-waterjet system in towing tanks. Murrin and Bose (2006) presented the basic methodology of testing waterjet system in wind tunnel.Bulten (2006) deals with the numerical (CFD) analysis of waterjet systems and present the flow phenomena occurring in the waterjet system.

NOMENCLATURE

B	Breadth of ship model
C_{p1}	Static pressure coefficient at intake
D	Depth of ship mode
E_j	Energy flux at station j
L	Length of model on waterline
Lbp	Length between perpendiculars of ship model
M_{xj}	Momentum flux at station j
P_{JSE}	Jet system effective power
Q_{bl}	Flow rate with in the actual boundary layer
Q	Volume flow rate through control volume
R_{BHm}	Bare hull resistance of model
R_n	Renolds number
T	Axial thrust
T_{net}	Net thrust
Vi	Velocity at capture area
V, Vs	Free stream velocity
Vx	Axial velocity
Z_n	Nozzle elevation
c_m	Momentum velocity correction coefficient
c_e	Energy velocity correction coefficient
d	Diameter of duct inlet
h	Height of intake at capture area
n	Integer (taken as 9)
t_j	Thrust deduction due to hull effects on waterjet system
t_r	Thrust deduction due to waterjet system effects on hull
t	Total thrust deduction fraction
$u(z)$	Velocity distribution in boundary layer
u_m	Momentum velocity
w_i	Width of intake at capture area
φ_m	Momentum flux
ρ	Specific mass of fluid
δ, δ_m	Boundary layer thickness
η	Efficiency

ABBREVIATIONS

CFD	Computational Fluid Dynamics
ITTC	International Towing Tank Conference
R/V	Research Vessel
AP	After Perpendicular
FP	Forward Perpendicular
IVR	Inlet Velocity Ratio
NVR	Nozzle Velocity Ratio

KEYWORDS
Waterjet system, Momentum flux, Boundary layer, Interaction efficiency, IVR, NVR, Wind tunnel, CFD.

HULL - WATERJET SYSTEM CONFIGUREURATION

The hull and waterjet conFigureuration selected for the present work are those of the US research vessel R/V Athena, the main particulars of which are given in Table 1. Model tests have been performed for this hull- waterjet system in various towing tanks for its performance prediction and it has been treated as a benchmark example. The same hull and duct forms of the R/V Athena are used in the present study, for both numerical and experimental work. As the geometric data of the impeller were not available, it was decided to perform the numerical simulation using an outlet boundary condition and a stock impeller for wind tunnel model tests.

Table 1: Main dimensions

S.No.	Parameter	
1	Length between perpendiculars	46.87 m
2	Beam	6.68 m
3	Displacement	260 long tons
4	Speed range	12 kn - 35 kn
5	Waterjet propulsion	Twin
6	Impeller diameter	0.6762m

PRESENTATION OF THEORETICAL MODEL

The basic presentation of the theoretical model is the earlier work of Tervisga (1996). The general principle underlying the thrust production of the jet propulsors is conservation of momentum. A consequence of this physical law is that a force is required to accelerate the fluid. This force is exerted on the fluid by an actuator (mechanical pump). In steady condition the action is counter balanced by a reaction exerted by the fluid on the actuator.

The reaction force can be identified as axial thrust T and is given as:

$$T = \phi_{mn} - \phi_{mi} \tag{1}$$

Subscripts 'n' and 'i' denote the nozzle and capture area, respectively. The momentum flux for a uniform flow can be written as:

$$\phi_m = \rho Q u_m \tag{2}$$

The flow rate, Q, is achieved by the integration of velocity distribution over a defined cross section area within the control volume and momentum flux is calculated with the obtained flow rate and velocity distribution.

For the operating conditions, the change in momentum flux is equal to the net thrust exerted by the jet on the hull (Tervisga, 1996).

$$\Delta M_x = T_{net} \tag{3}$$

The change in momentum in x-direction is determined over the system boundaries defined by the stations 2 and 7. In case of a parallel nozzle outflow, the assumption is justifiable that the vena contracta has the same diameter as the nozzle discharge, and hence the change in momentum flux can be determined from station 6:

$$\Delta M_x = M_{x6} - M_{x2} \tag{4}$$

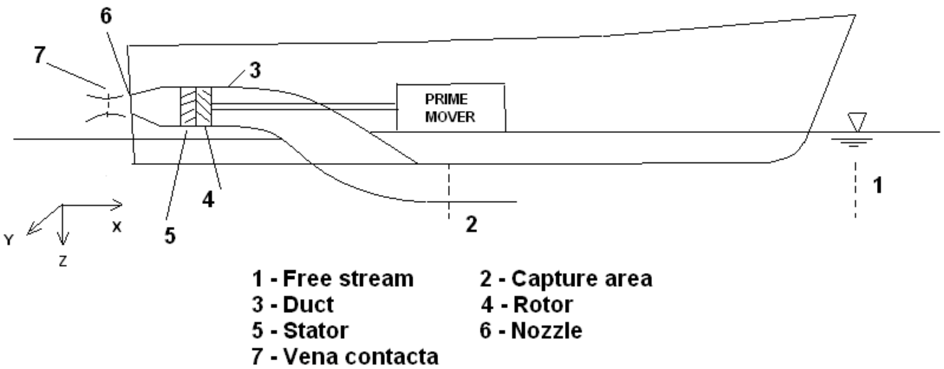

Figure 1: Control volume representation of hull – waterjet system

The energy flux which is used to calculate the power and the internal losses is obtained by integrating the local energy velocity V_j at station '*j*' as follows.

$$E_j = ½ \rho \int V_j^2 .d\, Q_j \qquad (5)$$

Effective jet system power is computed from the increase in energy between Station 2 and Station 6 and is given as:

$$P_{JSE} = E_6 - E_2 \qquad (6)$$

For free stream conditions jet efficiency reduces to ideal efficiency and is given as:

$$\eta_I = \frac{2}{1+NVR} \qquad (7)$$

Interaction effects on powering characteristics can be expressed as momentum and energy interaction efficiencies, considering the hull effect on waterjet performance and the waterjet effect on hull performance.

Momentum interaction efficiency is given as:

$$\frac{1}{\eta_{mI}} = 1 + \frac{1-c_m}{NVR-1} \qquad (8)$$

$$c_m = \frac{n+1}{n+2}\left(\frac{Q}{Q_{bl}}\right)^{\frac{1}{n+1}} \qquad for \quad h \geq \delta \qquad (9)$$

$$c_m = 1 - \frac{1}{n+2}\left(\frac{Q_{bl}}{Q}\right) \qquad for \quad h \geq \delta \qquad (10)$$

$$Q_{bl} = V_0 w_i (\delta_m - \delta_1) \qquad (11)$$

$$\delta_1 = \frac{1}{h+1}(\delta_m) \qquad (12)$$

Energy interaction efficiency is given as:

$$\frac{1}{\eta_{eI}} = 1 - \frac{g z_n}{\frac{1}{2} V_s^2 (NVR^2 - 1)} - \frac{(c_e^2 - 1)(1 - C_{p1})}{(NVR^2 - 1)} \tag{13}$$

$$c_e = \left(\frac{n+1}{n+3}\right)\left(\frac{Q}{Q_{bl}}\right)^{\frac{2}{n+1}} \qquad for \quad h \le \delta_m \tag{14}$$

$$c_e = 1 - \frac{2}{n+3}\left(\frac{Q_{bl}}{Q}\right) \qquad for \quad h \ge \delta_m \tag{15}$$

The total interaction efficiency is given as:

$$\eta_{Int} = (1-t)\frac{\eta_{eI}}{\eta_{mI}} \tag{16}$$

$$t = t_j + t_r \tag{17}$$

$$t_r = (T_{net} - R_{BH}) / T_{net} \tag{18}$$

$$t_j = (1- IVR)/(NVR-IVR) \tag{19}$$

EXTRAPOLATION SCHEME

The total resistance R_{BHm} of the vessel is measured from towing tank tests. The thrust T_{net} , flow rate Q , velocity measurements $u(z)$ are obtained from self propulsion condition tests in wind tunnel and these values are converted to the fluid–water condition. Boundary layer thickness values δ_m have been obtained from experimental and CFD analyses.

The velocity measurements at intake are taken at capture area (Figureure 1). The flow rate within the boundary layer is calculated as Q_{bl} . The boundary layer thickness, total bare hull resistance and velocities are extrapolated to the full size (Figureure 2) and then the propulsion characteristics of the prototype are obtained.

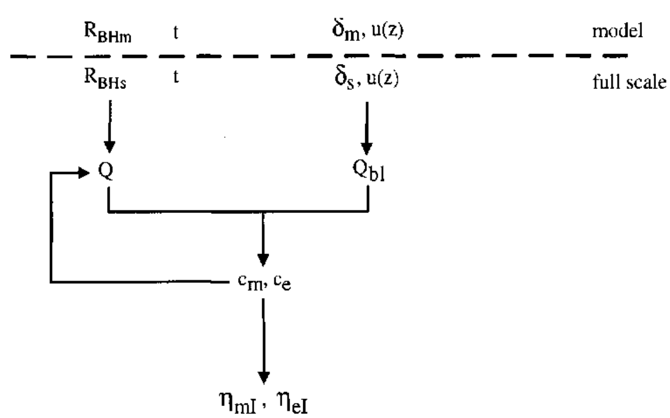

Figure 2: Extrapolation scheme

NUMERICAL (CFD) ANALYSIS

In the CFD analysis, the bare hull model was trimmed equal to dynamic trim (1.33 deg by aft) and immersion equal to dynamic heave (0.013m) condition and the viscous flow conditions at a free stream velocity of 4.401 m/s at model scale (as used in ITTC proceedings (2005)), was carried out. The velocity profiles at the capture area (located forward of ramp tangency point at a distance of 10% of the waterjet duct inlet diameter (Tervisga 1996)), so as to avoid the interaction with the duct, and the boundary layer thickness at this location for bare hull condition (i.e. without water jet operation) were obtained. The velocity profiles at capture area and boundary layer thickness with waterjet operation condition were also determined.

The references of global coordinates are located at point of intersection of AP, base line & center-plane. The inlet boundary is taken at a distance of $1L_{bp}$ forward of FP and the outlet boundary is taken at $4L_{bp}$ aft of AP. The transverse boundary walls are at a distance of 8B from the center-plane and the bottom boundary is taken 12D from the water level. As the hull is symmetrical about the longitudinal centre-plane, only one-half the region has been modeled for CFD analysis. Tetrahedral elements have been used for modeling the fluid domain, which results in the representation of the fluid boundaries with triangular elements. The CFD analyses have been carried out using the software Fluent®.

The scale ratio of the model used for the experiments is 1:8.556. The experiments were conducted for a free stream flow velocity of 4.401m/s in both the bare hull and self-propulsion conditions. In CFD analysis, a flow rate value obtained from model tests at the nozzle outlet was specified at the nozzle outlet boundary for self-propulsion operating condition. The position of capture area was taken as 10% of waterjet duct inlet length forward from ramp tangency point (i.e. x = 0.681m). The intake width was calculated as 1.3d (where d = 0.126m, waterjet duct inlet diameter). The intake height (h) was chosen same as that used in experiments (h= 6.62cm)

Hull analysis (Hull- without waterjet system):

The hydrodynamic behavior of the hull without water jet system, at model scale, was undertaken initially. The velocity profile at capture area and boundary layer thickness measurements were carried out. The details of the mesh size, operating conditions imposed and boundary conditions applied in the CFD analyses are presented in Table 2.

Table 2: Mesh size, boundary & operating conditions (Hull- without waterjet system)

1	Element type	Tetrahedral
2	Element size	4
3	Surface mesh size(domain)	0.4
4	Surface mesh size(hull)	0.1
5	Viscous model	SST k-ω , 2 equation model
6	Solver	Segregated implicit formulation
7	Solution control scheme	SIMPLE (first order upwind)
8	Convergence criteria	0.001

Boundary conditions		
1	inlet	velocity inlet 4.401 m/s
2	outlet	Pressure outlet
3	hull	wall
4	symmetry1 & 2	symmetry
5	far field	velocity inlet 4.401 m/s

Operating conditions		
1	Pressure	Atmospheric pressure
2	Density	998.2 kg/m^3
3	Kinematic viscosity	1.0037×10^{-6} m^2 / s
4	Temperature	20 deg centigrade

A grid independence study was carried out for the problem and an acceptable grid size from this study was used for further CFD analysis. The velocity distribution, boundary layer profile and thickness at different planes from the center-plane of hull at the capture area location were obtained from this analysis, Figures 3 & 4. Here axial flow velocity is negative as it is towards negative x-coordinate and “Z” value is the non-dimensional (i.e. Z = z/h).The flow parameters obtained from this analysis were used for evaluating the propulsion characteristics.

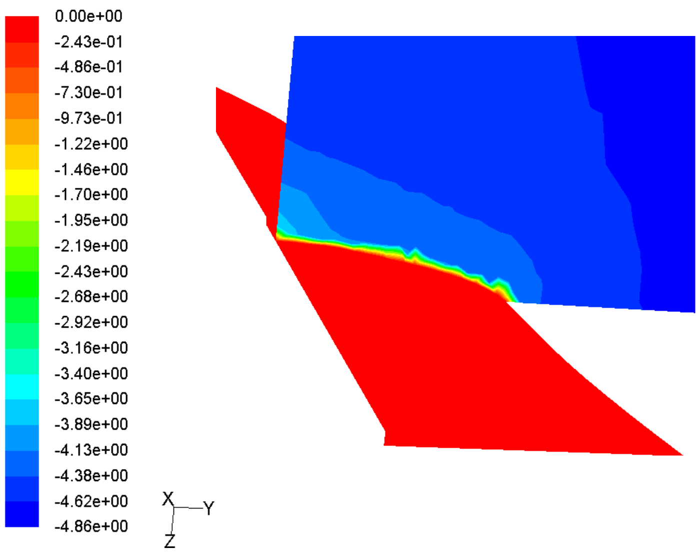

Figure 3: Velocity distribution at capture area location

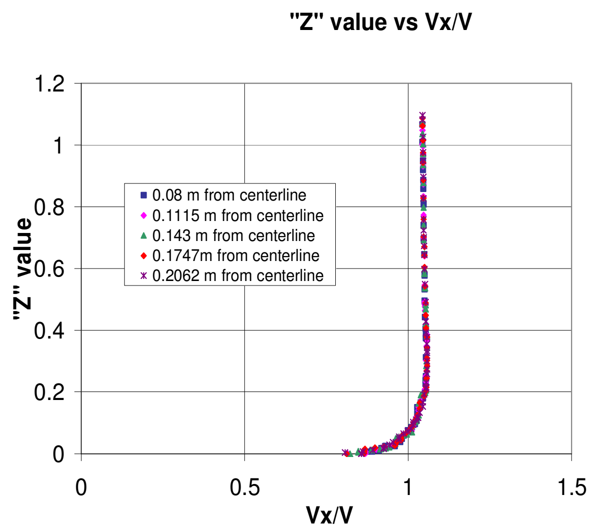

Figure 4: Boundary layer profile versus velocity ratios

Hull analysis (Hull-with waterjet system):

CFD analysis of hull with waterjet system was undertaken as a qualitative study to know the influence of waterjet system operation on velocity distribution at capture area. The flow rate at nozzle (ITTC 2005) was also given as input condition to simulate the effect of impeller/stator along with the inlet free stream velocity. The mesh (Figure 5) size and operating conditions used are same as in the previous case (i.e. hull-without waterjet system). The boundary conditions used for the case having hull - waterjet system are given in Table 3. The effect of waterjet system operation on the velocity distribution at capture area is shown in Figure 6.

Table 3: Boundary conditions (Hull -with waterjet system)

Boundary conditions		
1	inlet1	velocity inlet 4.401 m/s
2	inlet2(nozzle outlet)	mass flow rate 38.53 kg/m^3
3	outlet	pressure outlet
4	hull	wall
5	duct	wall
6	symmetry1	symmetry
7	symmetry2	symmetry
8	far field	velocity inlet 4.401 m/s

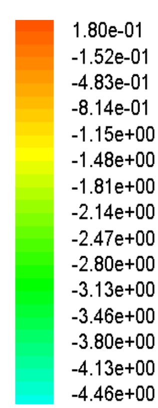

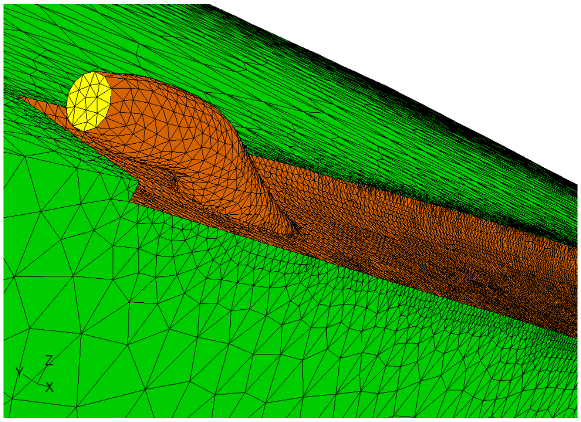

Figure 5: Hull - duct mesh

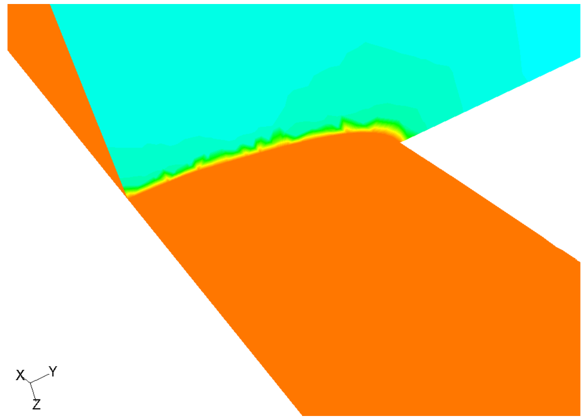

Figure 6: Velocity distribution at capture area location

The Hull duct analysis showed that there is considerable effect of the waterjet operation on the velocity profiles at capture area (Figure 6) which resulted in the decrease in the boundary layer thickness (Figure 7). CFD can be used as a tool to predict the hull - waterjet system interaction parameters if the hull - waterjet system geometries could be correctly modeled and simulated.

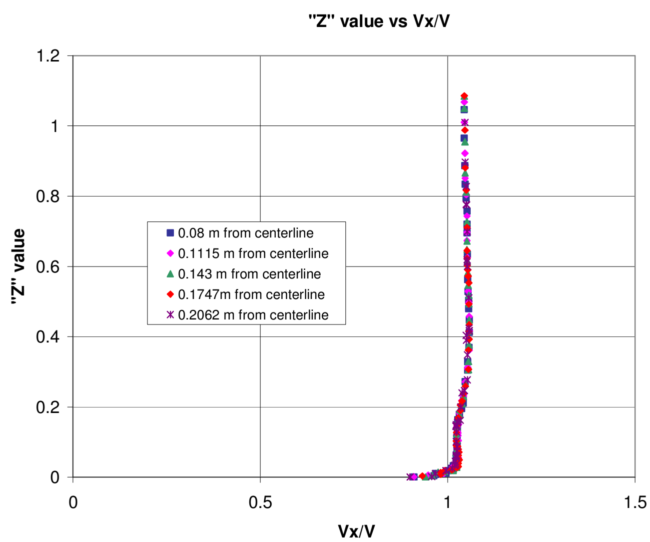

Figure 7: Boundary layer profile versus velocity ratios (Hull with waterjet system)

WIND TUNNEL EXPERIMENTS

Experiments were carried out to simulate the hull - waterjet system in wind tunnel. Basically, the performance of hull- waterjet system depends on the inflow and outflow characteristics of waterjet system and the hull-waterjet interaction. The experimental investigation consists of the following steps:

- Simulate the boundary layer profile over the hull (without waterjet system operation) at capture area for different wind speeds to obtain the wind speed at which the boundary layer profile in wind tunnel matches with that of the profile in fluid –water condition.
- Using applying appropriate scaling law, plot the scaled boundary layer profiles obtained from wind tunnel to fluid water condition for varying wind speeds against the ITTC (2005) boundary layer profile (in general

the boundary layer profile for fluid water condition can also be referred from CFD analysis/towing tank experiments).

- Select the wind speed at which a close match occurs between the scaled wind tunnel boundary layer profile and the above referred results.
- Perform self propulsion tests in wind tunnel at the above wind speed and measure the velocity profiles at nozzle outlet.

During the experimentation, care was taken to make the flow over the hull a turbulent one (as $R_n > 2 \times 10^5$) and the same was achieved by fixing sand paper strip, located on the model at 5% of model- length aft of fore-end.

Figure 8: Model of hull - waterjet duct system

A truncated hull model of 2.68 m long with waterjet duct and a stock impeller (Figure 9) constitutes the hull-waterjet assembly (Figure 8). Truncated model has a scale ratio 1:8.556 from aft portion to about four stations and then it has been faired to form forward portion. Model was truncated so as to accommodate it in the wind tunnel test section. Since the hull has the center-plane of symmetry, only one half of hull model was manufactured with the propulsion setup (Figure 10).

Figure 9: Stock impeller setup in duct

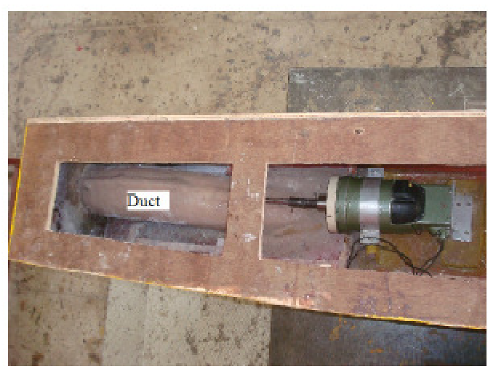

Figure 10: Propulsion setup (in side)

The tests were performed in the wind tunnel facility at Hydrodynamic Research Wing, Naval Science and Technological Laboratory, Visakhapatnam, India. The features of the wind tunnel facility are:

Test Section	: 1.5m x 1.5m x 4.0m
Plenum Chamber	: 4.3m x 4.3m x 4.0m
Contraction Section	: Varying from 4.3x4.3m square to1.5mx1.5m test section
Diffuser Section	: Varying from 1.5mx1.5m square to 3.048m dia. circular
DC motor	: 125kW, 750 rpm max.
Tunnel Fan	: 3.04m diameter, CFRP, 12 bladed
Max. Test Velocity	: 50 m/sec

Instrumentation setup includes pitot probe, DPT (differential pressure transducer). Measured quantities are velocity at capture area location, at nozzle outlet, boundary layer thickness, wind speed and rpm of the stock impeller. There is no influence of the pitot probe in measuring the velocity distribution on the flow as they are being measured just in front of the location required individually at capture area location and at nozzle outlet location. The operating condition in wind tunnel during tests is given in Table 4.

Table: 4 Operating conditions (wing tunnel tests)

1	Pressure	Atmospheric pressure
2	Density	1.15 kg/m^3
3	Kinematic viscosity	1.58x10^{-5} m^2 /s
4	Temperature	32 deg centigrade

Initially, the model equipped with propulsion setup, but in idle condition, was tested at different wind speeds. For simulating the boundary layer profile on the hull (ITTC 2005), the velocity measurements at capture area (Figure 11) are performed. Further, the experiments with the impeller working were done at this wind velocity. Next, the velocities at the capture area and at the nozzle outlet were measured by operating the impeller at different rpm to attain the model self propulsion point. The flow rates at nozzle outlet at corresponding impeller rpm were calculated and a graph for the net force i.e. the difference between the net thrust (extrapolated to fluid conditions) and total drag force (from ITTC model experiments (ITTC, 2005)) for different rpm value is drawn to attain the self propulsion rpm condition for the model. Again the tests are carried out at this rpm to obtain the velocity distribution at the nozzle outlet.

Assumptions involved in experimentation are:

- The boundary layer found in a truncated model is assumed to be same as the model without being truncated. (however it may be confirmed from CFD analysis)

- Reynolds number similarity (similarity between the model test condition in towing tank and in wind tunnel) is maintained during the experiments, as far as turbulence is concerned, by making use of stimulators ($R_n = 3.37\times10^6$ was maintained during wind tunnel tests corresponding to $R_n = 2.24\times10^7$ for the hull model in towing tanks, equivalent to a Froude number of 0.6 (ITTC, 2005).

- The following scaling law is assumed to hold good for extrapolation from fluid air in wind tunnel to fluid water condition. Subscripts *a* & *w* stands for fluid air and fluid water conditions, respectively.

$$\left(\frac{\delta}{L}\right)_a (R_n)_a^{\frac{1}{5}} = \left(\frac{\delta}{L}\right)_w (R_n)_w^{\frac{1}{5}}$$

The diameter of the waterjet duct outlet in model is 127.2mm. A non-uniform measurements grid was selected to measure velocity distribution and finally achieving the flow rate (Figure 11). The measurements are made in one quarter portion of the nozzle outlet (axi-symmetric flow is assumed). Boundary layer measurements, the boundary layer profile as well as the boundary layer thickness, without waterjet in operation enable us to decide about the free stream wind velocity required to be used in wind tunnel tests. The hull-waterjet system was tested in the trim /immersion condition corresponding to the dynamic trim/immersion condition of the model (ITTC, 2005). The experiments were carried out for wind speeds 26m/s, 19m/s and 20m/s. No turbulent stimulator was used in the hull model for wind speeds of 26 m/s and 19 m/s, but a turbulent stimulator was used in the experiments done for wind speed of 20 m/s. It has been noticed that the boundary layer velocity profile for the case of 20 m/s wind speed with turbulent simulator follows closer to that presented by ITTC (2005) when compared with other two experimental cases (Figure 12).

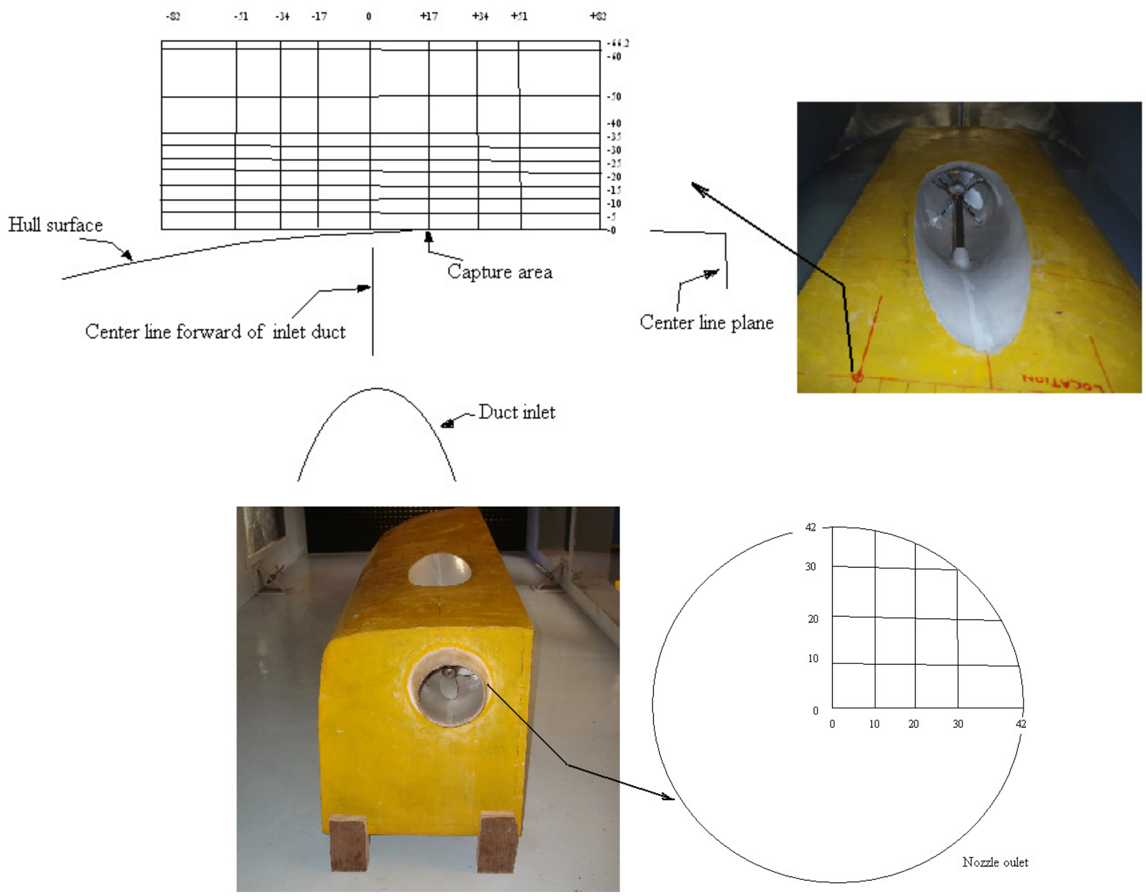

Figure 11: Schematic view of capture area and outlet nozzle measurement grids

Based on the above observations, the free stream wind velocity for further experiments was taken as 20m/s. For "hull without waterjet operation" condition the impeller rpm is maintained as zero and the velocity distribution at the capture area is acquired for a defined free stream condition. For "hull with waterjet operation" condition the impeller is rotated at self propulsion condition and the outlet nozzle velocity distribution is acquired. The test set up for both the conditions is shown in Figure 13-16.

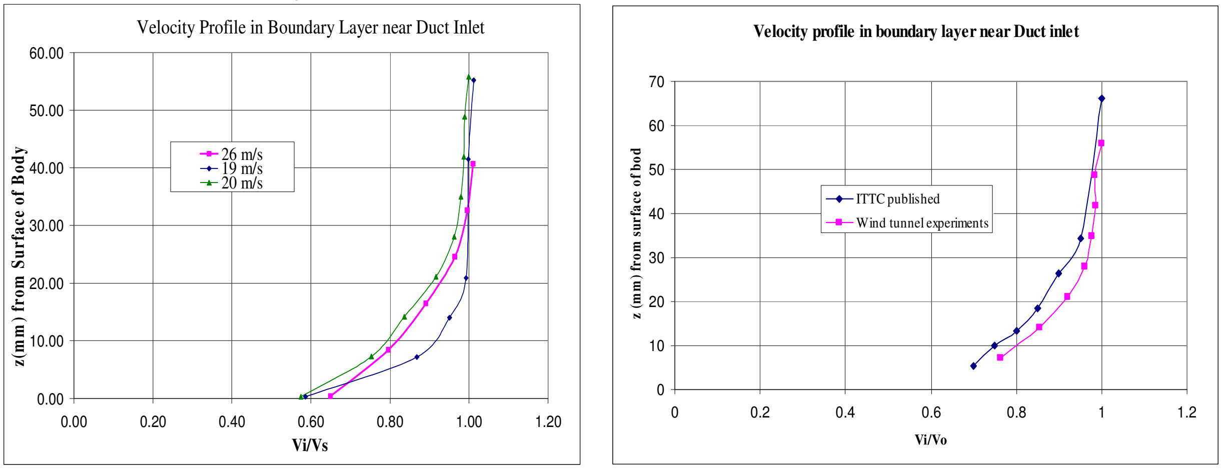

Figure 12: Velocity profile in boundary layer at capture area (hull - without waterjet operation)

The velocity distribution is calculated by making use of the measured dynamic pressure head which is obtained from the difference between the total pressure head (from the free stream) and the static pressure head at the capture area/nozzle outlet using pitot probe.

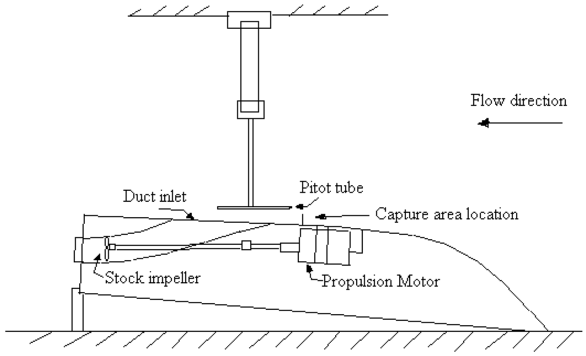

Figure 13: Setup for hull -without waterjet system

Figure 14: Velocity measurements at capture area

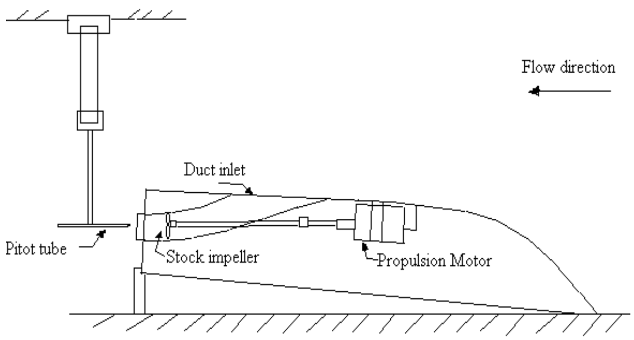

Figure 15: Setup for hull -with waterjet system

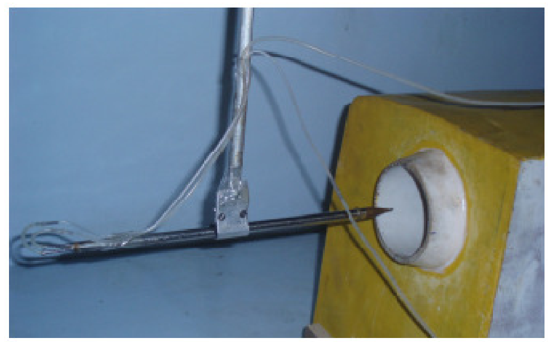

Figure 16: Velocity measurements at outlet nozzle

RESULTS AND DISCUSSION

The powering performance of a waterjet propelled vessel, R/V Athena, was carried out using numerical (CFD) and experimental (wind tunnel) techniques and both the results were extrapolated using ITTC 2005 guidelines to get the results of the prototype. ITTC (2005) waterjet performance prediction method was used to evaluate the powering characteristics of hull - waterjet system at full scale (for both CFD and experimental results).The basic concept of extrapolation is to use "flow rate identity" (i.e. similar IVR & NVR values for model and prototype).A comparison between published (ITTC 2005) and CFD extrapolated results are placed in Table 8.

Table 5: Hull analysis (6.26 lakh cells, hull-without waterjet system, model scale)

Parameter	CFD(present)	ITTC (2005)
Viscous Force (N)	103.29	99.49
Viscous coefficient	0.00275	0.00258
Capture height (cm)	6.62	6.62
Capture width (cm)	16.4	20.81
Inlet velocity (m/s)	4.08	4.05
IVR	0.93	0.92
Capture are flow rate (cum.m)	0.041	0.042
Boundary layer thickness (cm)	6.24	6.15

Table 6: Hull – duct analysis (6.26 lakh cells, hull-with waterjet system, model scale)

Parameter	CFD(present)	ITTC (2005)
Viscous Force (N)	106.34	-
Viscous coefficient	0.00284	-
Flow rate - outlet (cum.m)	6.58	0.0386
Nozzle velocity (m/s)	1.49	6.9
NVR	1.6	1.57
Boundary layer thickness (cm)	6.24	-
Inlet velocity (m/s)	0.99	-
IVR	6.24	-

Table 7: Model scale evaluated parameters from CFD analysis

Parameter	CFD (present)
Bare hull resistance (N)	239.19
Boundary layer thickness (cm)	6.24
Inlet velocity (m/s)	4.08
Free stream velocity (m/s)	4.401
Nozzle velocity (m/s)	6.58

Table 8: Comparison between CFD (present) and ITTC (2005) extrapolated results

Parameter		CFD(present)	ITTC(2005)
R_{BHm}	Bare hull resistance (N)	126.95	147.43
δ, δ_m	Boundary layer thickness (cm)	28.8	30.46
Vi	Inlet velocity (m/s)	11.96	11.85
V	Free stream velocity (m/s)	12.86	12.86
Vn	Nozzle velocity (m/s)	19.16	20.18
N	Rpm of impeller	-	8.63
M_{x2}	Momentum flux at station 2 (kN)	217.18	-
M_{x6}	Momentum flux at station 6 (kN)	309.56	-
T_{net}	Net Thrust (kN)	92.36	141.43
t_j	Thrust deduction fraction due to hull effects on waterjet system	0.125	0.123
t_r	Thrust deduction fraction due to waterjet system effects on hull	-0.37	-0.043
t	Thrust deduction fraction	-0.245	0.080
E_2	Energy flux at station 2 (kW)	1298.86	-
E_6	Energy flux at station 6 (kW)	2963.94	-
P_{JSE}	Jet system effective power (kW)	1665.08	2296.6
$T_{net} \cdot V$	Thrust power (kW)	1188.08	1818.66
η_{jet}	Jet efficiency	0.71	0.82
c_m	Momentum velocity correction coefficient	0.98	-
c_e	Energy velocity correction coefficient	0.96	-
η_o	Ideal efficiency	0.80	-
η_{mI}	Momentum interaction efficiency	0.96	-
η_{eI}	Energy interaction efficiency	0.88	-
η_{INT}	Interaction efficiency	1.14	-

The experimental results from wind tunnel have to be first extrapolated to fluid water condition using scaling law and then extrapolated to full scale. The analyzed measurements for capture area velocity distribution, outlet nozzle velocity distribution and boundary layer thickness in the wind tunnel extrapolated to fluid - water conditions & the ITTC (2005) model test results at a similar condition in towing tanks are presented in Tables 9 & 10.

Table 9: Wind tunnel model test results

Parameter	Wind tunnel (present)	ITTC (2005)
Capture height (cm)	6.62	6.62
Capture width (cm)	16.4	20.81
Inlet velocity (m/s)	3.87	4.05
IVR	0.88	0.92
Capture are flow rate (cum.m)	0.039	0.042
Boundary layer thickness (cm)	5.57	6.15
Nozzle velocity (m/s)	6.6	6.91
NVR	1.5	1.57

Table 10: Comparison of wind tunnel tests(present) and ITTC (2005) results

Parameter		Wind tunnel (present)	ITTC(2005)
R_{BHm}	Bare hull resistance (N)	119.87	147.43
δ, δ_m	Boundary layer thickness (cm)	25.71	30.46
Vi	Inlet velocity (m/s)	11.32	11.85
V	Free stream velocity (m/s)	12.86	12.86
Vn	Nozzle velocity (m/s)	19.29	20.18
N	Rpm of impeller	-	8.63
M_{x2}	Momentum flux at station 2 (kN)	194.97	-
M_{x6}	Momentum flux at station 6 (kN)	313.79	-
T_{net}	Net Thrust (kN)	119.22	141.43
t_j	Thrust deduction fraction due to hull effects on waterjet system	0.193	0.123
t_r	Thrust deduction fraction due to waterjet system effects on hull	-0.005	-0.043
t	Thrust deduction fraction	0.188	0.080
E_2	Energy flux at station 2 (kW)	1101.25	-
E_6	Energy flux at station 6 (kW)	3026.65	-
P_{JSE}	Jet system effective power (kW)	1925.19	2296.6
$T_{net} \cdot V$	Thrust power (kW)	1533.21	1818.66
η_{jet}	Jet efficiency	0.79	0.82
c_m	Momentum velocity correction coefficient	0.98	-
c_e	Energy velocity correction coefficient	0.96	-
η_o	Ideal efficiency	0.80	-
η_{mI}	Momentum interaction efficiency	0.93	-
η_{eI}	Energy interaction efficiency	0.98	-
η_{INT}	Interaction efficiency	0.86	-

SUMMARY AND CONCLUSION

Efforts have been made here to study and quantify the hydrodynamic interaction of a vessel hull and its waterjet propulsion system using numerical and experimental techniques. A wind tunnel facility has been used for the experimental study and the results obtained so have been extrapolated to the water condition using an evolved scaling law. The research vessel R/V Athena, which is being used by researchers as a benchmark example for the study of powering performance of a vessel fitted with waterjet propulsion (ITTC, 2005), was selected as the example problem in the present study. The numerical and experimental results have been compared with those presented with ITTC (2005) and are found to be encouraging.

The methodology of testing waterjet propelled craft in the wind tunnel has been shown to be a very promising one. The extrapolation for the velocity profiles from fluid-air to fluid-water using the scaling law worked fairly well, Wind tunnel results compare better with the ITTC (2005) experimental results than CFD ones in power prediction. A variation in the thrust deduction fraction between CFD analysis, wind tunnel experiments and ITTC experiments have been noticed, although the extrapolated efficiencies and required power do have a qualitatively good comparison. For a suitable water jet system, the experiments with stock impellers in wind tunnel can be carried out to simulate the flow rate and these results can be extrapolated to fluid-water condition. Wind tunnel experiments and CFD analysis are very much helpful for boundary layer thickness measurement, which has been the key factor used in the extrapolation methodology. Inspite of the above heartening results, the noticed differences in values for some of the hydrodynamic parameters when compared between CFD and wind tunnel experiment results with those given by ITTC (2005) invites attention for more indepth study into various aspects of the numerical (CFD) modeling and experimental (wind tunnel) setup, measurement and scaling law.

REFERENCES

Alder, R.S and Denny, S.B (1977): “Full scale evaluation of water jet impellers”, *Report NSRDC*.

Allison, J. (1993): “Marine waterjet propulsion”, *SNAME Transactions, Volume 101*.

Chesnakes, C.J (2003): “Velocity measurements inside the pump of gulf coast waterjet tow tank model 5600 “, *Hydromechanics directorate research and development report*, *NSWCCD- 50 TR- 2003/014*.

Fujisawa, N (1995): “Measurements of basic performances for waterjet propulsion systems in water tunnel “, *International Journal of Rotating Machinery , volume 2, No. 1, pp. 43-50*.

Lavis, D.R, Forstell, B.G and Purnell, J.G (2005): “Advanced compact waterjet propulsion for high-speed ships “, *The quarterly digest , volume 29.*

ITTC (1996), 21st International Towing Tank Conference, “Specialist committee on validation of water jet test procedures”.

ITTC (2002), 23rd International Towing Tank Conference, “Specialist committee on validation of water jet test procedures”, *Proceedings of 23rd ITTC , volume II*

ITTC (2005), 24th International Towing Tank Conference, “Specialist committee on validation of waterjet test procedures , *Proceedings of 24th ITTC , volume II.*

MacPherson, D.M (1999): “A universal parametric model for water jet performance ”, *HydroComp Inc. FAST '99.*

Murrin, D.C and Bose, N (2006): “ Waterjet propulsion system tested in a wind tunnel and compared with numerical simulation “, *International Journal of small craft technology , RINA* .

Terwisga, T. (1996): “ Waterjet hull interaction “ , *ISBN 90-75757-01-8.*

Bulten, H. (2006): “ Numerical analysis of a waterjet propulsion system “ *ISBN10: 90-386-2988-5 & ISBN-13: 978-90-386-2988-9*

Seventh International Conference
On High-Performance Marine Vehicles
Melbourne, Florida, USA
13-15 October 2010

COMPUTATION OF SLAMMING FORCE ON A PLANING HULL

Qingyong Yang and Wei Qiu
Ocean Engineering Research Centre
Memorial University of Newfoundland, St. John's, NL, Canada
qiuw@mun.ca

ABSTRACT

To simulate the motion of a planing hull in waves, it is important to accurately compute the slamming forces on the hull. Numerical studies have been carried out to compute slamming forces on planing hulls entering calm water with various pitch and roll angles, based on a Constrained Interpolation Profile (CIP) method. The multiphase problem governed by the Navier-Stokes equations was solved by the finite difference method on a fixed Cartesian grid. Density functions were employed to capture the solid body and the free surface interfaces. For the pressure computation, a Poisson-type equation was solved at each time step by the conjugate gradient iterative method. Computations were first carried out for the water entry of a 3D wedge, and numerical solutions were compared with experimental results. The computations were then extended to the water entry of a planing hull at various pitch and roll angles. The 3D results were compared with the solutions based on the strip theory and the 2D CIP method.

INTRODUCTION

The prediction of slamming forces is important in the simulation of planing hull motions. The slamming problem has been extensively studied by many researchers. Most work has been limited to 2D or simple wedge-type bodies. The theoretical analysis of the similarity flow induced by the wedge entry was first conducted by Wagner (1932). Armand and Cointe (1986) and Cointe (1991) extended Wagner's theory to analyze the wedge entry problem using matched asymptotic expansions for wedges with small deadrises. Furthermore, Dobrovol'skaya (1969) developed an analytical solution in terms of a nonlinear singular integral equation for the problem of the symmetrical entry of a wedge into calm water. Greenhow (1987) used Cauchy's formula to solve the wedge entry problems. In his work, both gravity and nonlinear free surface conditions were taken into account. Zhao and Faltinsen (1993) studied the water entry of a wedge using the boundary element method with constant elements. The jet tip at the intersection point of the body surface and the free surface was cut and two small constant elements were distributed. Chuang et al. (2006) developed a boundary element method based on desingularized Cauchy's formula. In their work, a numerical approach was also developed to remove the corner singularity at the intersection point of body surface and free surface. Kleefsman et al. (2005) solved the 2D slamming problem of symmetric bodies by the Volume of Fluid (VOF) method, and the finite volume discretization with a cut-cell method was applied on a fixed Cartesian grid. Kim et al. (2007) used the Smoothed Particle Hydrodynamics (SPH) method to simulate the water entry of 2D asymmetric bodies. Zhu et al. (2005) studied the water entry and the exit of a horizontal circular cylinder with the Constrained Interpolation Profile (CIP) algorithm (Yabe et al., 2001) in the 2D computational domain. Yang and Qiu (2007) solved the 2D water entry problems of symmetric and asymmetric wedges with various deadrise angles using the CIP method. The effect of the compressibility of air for small deadrise angles was also discussed in their work (Yang and Qiu, 2008).

The 3D effect can be significant in ship slamming problem. Relatively few attempts have been made to solve the impact problems of 3D bodies. Shiffman and Spencer (1951) studied the pressure distribution and slamming force on a cone. Troesch and Kang (1986) computed the slamming forces on a cusped body and a sphere based on the potential flow theory. Faltinsen and Chezhian (2005) modeled the hydrodynamic impact phenomenon for a water entry of 3D body with constant velocity using the boundary element method.

In this work, the 3D slamming problem has been solved using a CIP-based finite difference method on a fixed Cartesian grid. The free surface is captured with the CIP method to maintain a sharp interface, while allowing a large deforming free surface. A combined Lagrangian-Eulerian method is employed to model the 3D solid body surface. Density functions are used to identify the different phases in the multiphase problem. For the pressure calculation, a Poisson-type equation is solved at each time step by the conjugate gradient iterative method. Computations were first carried out for the water entry of a 3D wedge, and numerical solutions were compared with experimental results. The computations were then extended to the water entry of a planing hull at various pitch and roll angles. The 3D results were compared with the solutions based on the strip theory and the 2D CIP method.

NOMENCLATURE

δ_{ij}	Kronecker's delta function
ρ	Density of water (kg m^{-3})
σ_{ij}	Total stress (N m^{-2})
ϕ_m	Density function
Ω_m	Computation Domain
P	Pressure (N m^{-2})
c_s	Sound speed (m s^{-1})
$\hat{f}$	Interpolation function
t	Time (s)
u_i	Velocity (m s^{-1})
x_i	Spatial coordinates

ABBREVIATIONS

2D	Two-Dimensional
3D	Three-Dimensional
CIP	Constrained Interpolation Profile
SPH	Smoothed Particle Hydrodynamics
VOF	Volume of Fluid

KEYWORDS

Planing hull, Wedge, CIP, Slamming

MATHEMATICAL FORMULATION

The differential equations governing the compressible and viscous fluid are given as:

$$\frac{\partial \rho}{\partial t} + u_i \frac{\partial \rho}{\partial x_i} = -\rho \frac{\partial u_i}{\partial x_i} \tag{1}$$

$$\frac{\partial u_i}{\partial t} + u_j \frac{\partial u_i}{\partial x_j} = -\frac{1}{\rho}\frac{\partial \sigma_{ij}}{\partial x_j} + f_i \tag{2}$$

where t is the time; x_i (i=1, 2, 3) are the coordinates in Cartesian coordinate system; ρ is the mass density; u_i are the velocity components; and f_i are the body force.

As the temperature variation can be ignored, the equation of state is written as $p = f(\rho)$. Applying the equation of state to Eq. (1), the pressure equation can be obtained as

$$\frac{\partial p}{\partial t} + u_i \frac{\partial p}{\partial x_i} = -\rho c_s^2 \frac{\partial u_i}{\partial x_i} \tag{3}$$

where $c_s = \sqrt{\partial p / \partial \rho}$ is the sound speed, and p is the pressure.

For a Newtonian fluid, the total stress can be written as

$$\sigma_{ij} = -p\delta_{ij} + 2\mu S_{ij} - 2\mu\delta_{ij} S_{kk}/3$$
$$S_{ij} = \frac{1}{2}(\frac{\partial u_i}{\partial x_j} + \frac{\partial u_j}{\partial x_i})$$

where μ is the dynamic viscosity coefficient and δ_{ij} is the Kronecker's delta function.

Applying the fractional step approach, the numerical solutions of Eqs. (1) to (3), can be obtained in three steps as follows.

1. Advection phase

$$\frac{\partial \rho}{\partial t} + u_i \frac{\partial \rho}{\partial x_i} = 0 \tag{4}$$
$$\frac{\partial u_i}{\partial t} + u_j \frac{\partial u_i}{\partial x_j} = 0 \tag{5}$$
$$\frac{\partial p}{\partial t} + u_i \frac{\partial p}{\partial x_i} = 0 \tag{6}$$

2. Non-advection phase I

$$\frac{\partial u_i}{\partial t} = -\frac{2\mu}{\rho}\frac{\partial}{\partial x_j}(S_{ij} - \frac{1}{3}\delta_{ij} S_{kk}) + f_i \tag{7}$$

3. Non-advection phase II

$$\frac{\partial \rho}{\partial t} = -\rho \frac{\partial u_i}{\partial x_i} \tag{8}$$
$$\frac{\partial u_i}{\partial t} = -\frac{1}{\rho}\frac{\partial p}{\partial x_i} \tag{9}$$
$$\frac{\partial p}{\partial t} = -\rho c_s^2 \frac{\partial u_i}{\partial x_i} \tag{10}$$

The physical variables are updated at each fractional step by using the provisional results from the previous step. The advection phase is computed by the CIP method. The non-advection phase I, which includes a viscous term and a source term, is solved by the central finite difference method. For the non-advection phase II, a pressure-based algorithm is employed. A Poisson equation can be obtained based on Eqs. (9) and (10):

$$\frac{\partial}{\partial x_i}(\frac{1}{\rho^*}\frac{\partial p^{n+1}}{\partial x_i}) = \frac{p^{n+1} - p^*}{\rho^* c_s^2 \Delta t^2} + \frac{1}{\Delta t}\frac{\partial u_i^{**}}{\partial x_i} \tag{11}$$

where the superscript * and ** indicate the provisional values before and after the calculation of non-advection phase I. For a perfect incompressible fluid, it can be assumed that $c_s = \infty$, which leads to a simpler Poisson equation as follow:

$$\frac{\partial}{\partial x_i}(\frac{1}{\rho^*}\frac{\partial p^{n+1}}{\partial x_i}) = \frac{1}{\Delta t}\frac{\partial u_i^{**}}{\partial x_i} \tag{12}$$

A central difference method can be applied to discretize Eq. (12) to obtain the linear equations, which are then solved by a conjugate gradient method.

INTERFACE CAPTURING

In a multiphase computational domain, the density functions, ϕ_m (m=1, 2, 3), are introduced to identify the liquid, the solid body, or the air. These functions satisfy the following conditions:

$$\phi_m(x,y,z,t) = \begin{cases} 1 & (x,y,z) \in \Omega_m \\ 0 & otherwise \end{cases}$$

where Ω_m (m=1, 2, 3) denote the domains occupied by the liquid, solid and air phase, respectively.

The free surface can be captured by solving the following advection equation:

$$\frac{\partial \phi_1}{\partial t} + u_i \frac{\partial \phi_1}{\partial x_i} = 0 \qquad (13)$$

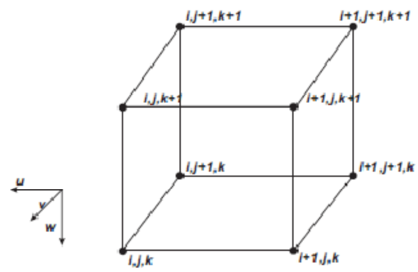

Figure 1: Upwind cubic cell

The CIP method uses a fixed Eulerian grid and employs a Lagrangian solution to determine the function value and its spatial derivatives at the new time step as follows:

$$f^{n+1}(x) = \hat{f}(x - u\Delta t)$$

where $\hat{f}$ is an interpolation function. For 3D problems, a cubic polynomial interpolation function is constructed as below in an upwind cell (see Figure 1).

$$\begin{aligned} \hat{f}_{i,j,k}(x,y,z) &= [(c_1\bar{x} + c_2\bar{y} + c_3\bar{z} + c_4)\bar{x} + c_5\bar{y} + \partial_x f_{i,j,k}]\bar{x} \\ &+ [(c_6\bar{y} + c_7\bar{z} + c_8\bar{x} + c_9)\bar{y} + c_{10}\bar{z} + \partial_y f_{i,j,k}]\bar{y} \\ &+ [(c_{11}\bar{z} + c_{12}\bar{x} + c_{13}\bar{y} + c_{14})\bar{z} + c_{15}\bar{x} + \partial_z f_{i,j,k}]\bar{z} \\ &+ c_{16}\overline{xyz} + f_{i,j,k} \end{aligned}$$

where $\bar{x} = -u\Delta t$, $\bar{y} = -v\Delta t$ and $\bar{z} = -w\Delta t$, and Δt is the time step. The 16 unknown coefficients are determined from the values of f, $\partial_x f$, $\partial_y f$ and $\partial_z f$ at grid points ($i+1, j, k$), ($i, j+1, k$) and ($i, j, k+1$) and those of f at points ($i+1, j+1, k$), ($i, j+1, k+1$), ($i+1,j,k+1$) and ($i+1, j+1, k+1$) depending on the signs of u, v and w.

The combined Euler-Lagrangian method is employed to capture the solid body surface. The body surface is represented by a set of panels with a concentration at the corners and locations with large curvatures. The contribution of each panel to the density function is denoted by a contribution factor as below:

$$\varepsilon = \int_{panel} F ds$$

where the function F is the distance from any point in the panel to the corresponding computational cell surface.

The density function for the solid surface is then calculated by

$$\phi_2 = \sum_{i=1}^{i=N} \varepsilon_i$$

where N is the total number of panels in the computational cell. The density function for air can be also obtained from $\phi_3 = 1 - \phi_1 - \phi_2$. After all the density functions for different phases (water, air and solid) are determined, the physical properties including viscosity and density can be calculated for each computational cell.

NUMERICAL RESULTS

The 3D slamming problems were solved by the numerical method described above. In the computations, the density and the viscosity of water and air are given as $\rho_1 = 1000 kgm^{-3}$, $\mu_1 = 10^{-3} kgs^{-1}m^{-1}$, and $\rho_2 = 1.0 kgm^{-3}$, $\mu_2 = 10^{-3} kgs^{-1}m^{-1}$, respectively. Computations were first carried out for the water entry of a 3D wedge with a deadrise angle of 30°. The hydrodynamic forces, pressure distributions and free surface elevations are presented. The numerical results were compared with the experimental results.

The geometry of the 3D wedge is given in Figure 2. Zhao et al. (1996) conducted the drop test for such a wedge at MARINTEK. The breadth, B, of the test section was 0.5*m*, the total length, L, was 1*m*, and the length of the measuring section was 0.2*m*. The maximum drop height was about 2*m*.

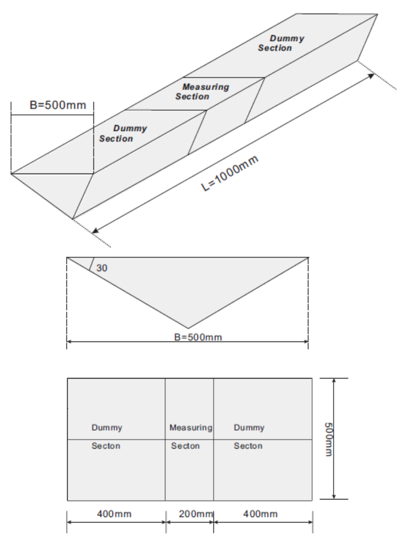

Figure 2: 3D wedge model

The time series of the computed hydrodynamic forces are compared with the experimental results (Zhao et al., 1996) in Figure 3. As shown in the figure, the numerical solutions by the 3D CIP method are a good agreement with experimental results. To investigate the effect of 3D flow, the hydrodynamic forces were computed by using various lengths of dummy sections. As shown in Figure 3, the computed maximum slamming force becomes smaller as the length of dummy section decreases, and the 3D flow effect tends to be significant. The 3D effect caused a reduction in the vertical slamming force. It can be shown the dummy sections used in the model tests were sufficiently long and the 3D flow effect was minimized. Figure 4 presents the comparison of numerical solutions for maximum pressures at four test points with the experimental results. They are in a reasonable agreement. In the figure, the pressure coefficient is defined by $C_p = \dfrac{P}{0.5\rho v^2}$. Figure 5(a) presents the pressure distribution on the mid wedge section and in the computational domain at the time instant when the spray roots of the jets reach the separation points. It can be shown that the maximum pressures occur near the separation points. Figure 5(b) shows the pressure distribution on the central plane.

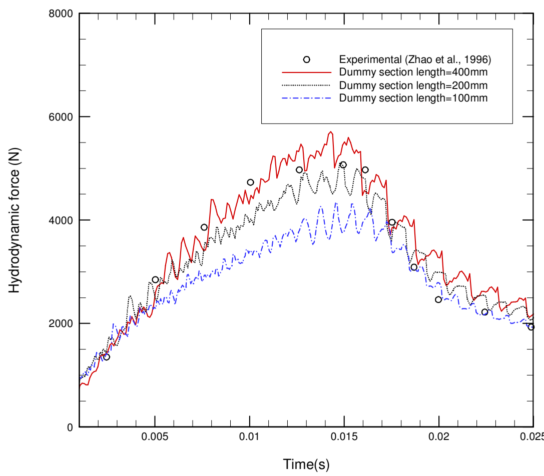

Figure 3: Hydrodynamic force on a wedge

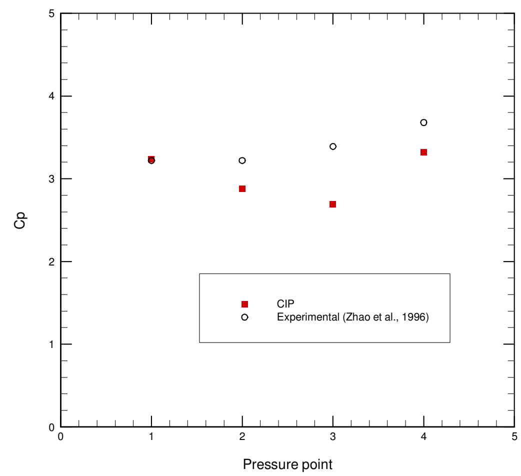

Figure 4: Measured and predicted pressures

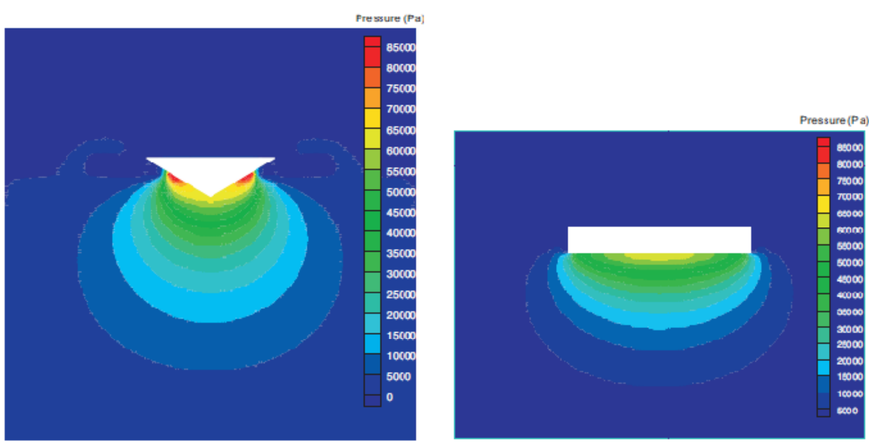

(a) (b)

Figure 5: Pressure distributions on sections of 3D wedge

The computations were extended to a prismatic planing hull entering the calm water at different pitch and roll angles. The prismatic hull geometry is shown in Figure 6. The surface of the planing hull was represented by 10,975 rectangular panels. The computational grid was 178×78×158 and the time step was chosen as 4.28×10^{-4} s. In the computation, the pitch and roll angles are set as 0, 5 and 10 degrees.

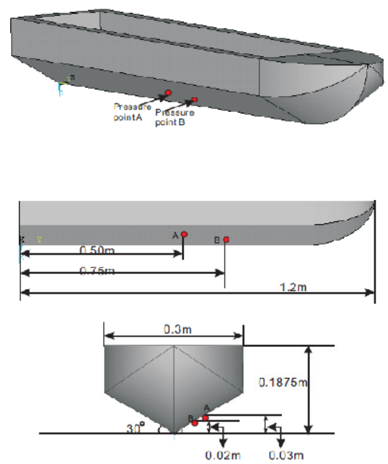

Figure 6: Geometry of planing hull

The slamming forces on the hull were computed by both the 3D and 2D methods. In the 2D method, the slamming forces were computed on 2D sections based on the 2D CIP method (Yang and Qiu, 2007) and the strip theory, as illustrated in Figure 7.

Figure 8 presents the maximum slamming force coefficients for different pitch and rolls angles. The force coefficient is given by $C_s = \frac{F}{0.5\rho v^2 L^2}$ where L is the length of hull and v is the vertical velocity. It can be observed that the computed forces by the 2D method are greater than those by the 3D method. It is mainly due to the 3D flow effect. As discussed previously, the 3D effect tends to cause a reduction of vertical slamming force on a wedge. The observation seems to be consistent. The difference between the 2D and 3D solutions become smaller with the pitch angle increased. The maximum slamming force coefficients predicted by the two methods increase slightly as the roll angle increased. As an example, Figure 9 shows the time history of vertical slamming forces on the planing hull computed by the 2D and 3D methods. Figure 10 presents the pressure distribution of the planing hull entering the water at 10-degree pitch angle and 0-degree roll angle at various time instants.

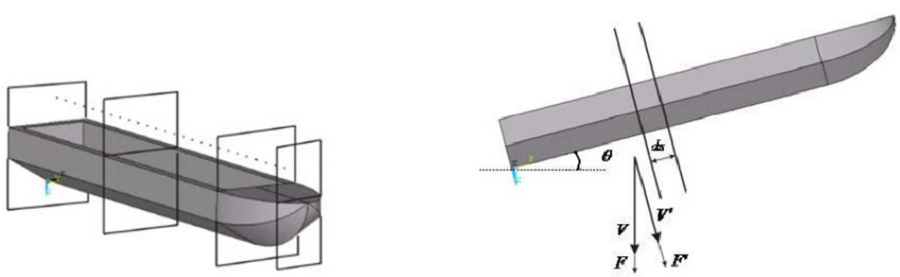

Figure 7: 2D strips and force/velocity components

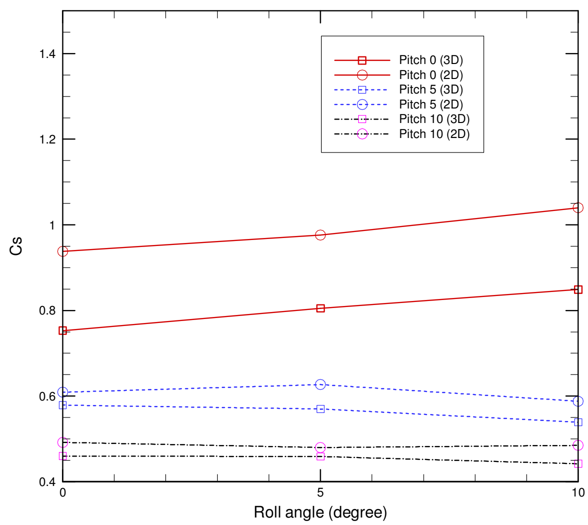

Figure 8: Maximum hydrodynamic force coefficients at different roll and pitch angles

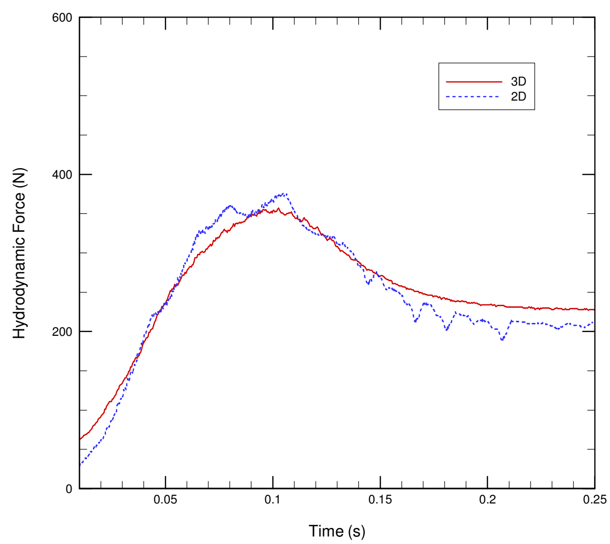

Figure 9: Time history of hydrodynamic force (pitch=5 degrees and roll=0)

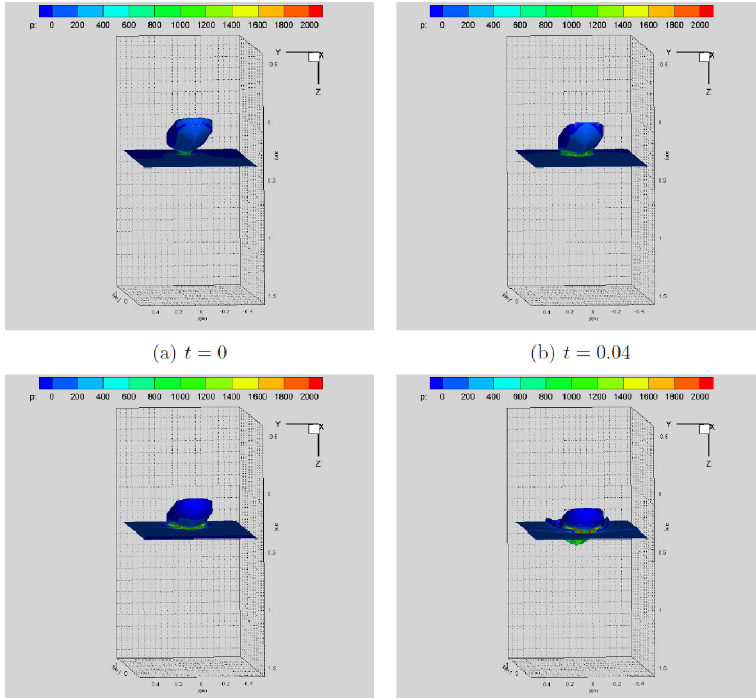

(a) $t = 0$ (b) $t = 0.04$

(c) $t = 0.08$ (d) $t = 0.1$

Figure 10: Pressure distribution on a planing hull at various time instants (pitch=10 degrees and roll=0)

CONCLUDING REMARKS

A CID method has been employed to compute the slamming forces on a planing hull entering the calm water at various pitch and roll angles. The multiphase problem governed by Navier-Stokes equations was solved based on the finite difference method. The nonlinear free surface was captured by the CIP method. Slamming forces, pressure distribution, and free surface deformation were predicted. Validation studies were first carried out for the water entry of a 3D wedge. The computations based on the 2D and 3D CIP methods were then extended to a planing hull. Preliminary results indicate that the predicted slamming forces by the 2D method are in general larger than those by the 3D method. Model tests of the planing hull entering water at a variety of pitch and roll angles are being conducted. The numerical results will be validated against the experimental data.

ACKNOWLEDGMENTS

This work was supported by the Natural Sciences and Engineering Research Council (NSERC) of Canada, Defence Research and Development Canada-Atlantic and Oceanic Consulting Corporation through a partnership program.

REFERENCES

Armand, J.L. and Cointe, R (1986): “Hydrodynamic Impact Analysis of a Cylinder”, *Proceedings of the Fifth International Offshore Mechanics and Arctic Engineering*, Tokyo, Japan, Vol. 1, pp. 609-634.

Chuang, J.M., Zhu, W. and Qiu, W. (2006): “Numerical Solutions of 2D Water Entry Problem”, *Proceedings of ISOPE2006*, San Francisco.

Cointe, R. (1991): “Free Surface Flows Close to a Surface-Piercing Body”, *Mathematical Approaches in Hydrodynamics (ed. T. Miloh)*, Soc. Ind. Appl. Maths, Philadelphia, pp. 319-334.

Dobrovol'skaya, Z.N. (1969): “On Some Problems of Similarity Flow of Fluid with a Free Surface”, *Journal of Fluid Mechanics*, Vol. 36, pp. 805-829.

Faltinsen, O.M. and Chezhian, M. (2005): “A Generalized Wagner Method for Three-Dimensional Slamming’, *Journal of Ship Research*, Vol. 49, No. 4, pp. 279-287.

Greenhow, M. (1987): “Wedge Entry into Initially Calm Water”, *Applied Ocean Research*, Vol. 9, pp. 214-223.

Kim, Y.W., Kim, Y., Liu, Y.M., and Yue, D. (2007): “On the Water-Entry Impact Problem of Asymmetric Bodies”, *Proceedings of 9th International Conference on Numerical Ship Hydrodynamics*, Ann Arbour, Michigan.

Kleefsman, K.M.T., Fekken, G., Veldman, A.E.P., Iwanowski, B. and Buchner, B. (2005): “A Volume-of-Fluid based Simulation Method for Wave Impact Problems”, *Journal of Computation Physical*, Vol. 206, pp. 363-393.

Shiffman, M. and Spencer, D.C. (1951): ‘The Force of Impact on a Cone Striking a Water Surface”, *Communications on Pure and Applied Mathematics*, Vol. 4, pp. 379-417.

Troesch, A.W. and Kang, C.G. (1986): “Hydrodynamic Impact Loads on 3-D Bodies”, Proceedings of *16th Symposium on Naval Hydrodynamics*, University of California, Berkeley.

Wagner, H. (1932): “Über Stoss und Gleitvorgänge an der Oberfläche von Flüssigkeiten”, *Z. f. Angew. Math. und Mech.*, Vol. 12, No. 4, pp. 193-235.

Yabe, T., Xiao, F. and Utsumi, T. (2001): “The Constrained Interpolation Profile Method for Multiphase Analysis”, *Journal of Computational Physics*, Vol. 169, pp. 556-593.

Yang, Q. and Qiu, W. (2007): “Numerical Solution of 2D Slamming Problem with a CIP Method”, The *Proceedings of VF-2007 International Conference on Violent Flows*, Research Institute for Applied Mechnamics, Kyushu University, Japan.

Yang, Q. and Qiu, W. (2008): “Computational of Slamming Forces on Wedges of Small Deadrise Angles Using a CIP Method”, *Proceedings of the 18th International Offshore and Polar Engineering Conference*, Vancouver, Canada.

Zhao, R. and Faltinsen, O. (1993): “Water Entry of Two-Dimensional Bodies”, *J. Fluid Mech.*, Vol. 246, pp. 593-612.

Zhao, R., Faltinsen, O. and Aarsnes, J. (1996): ‘Water Entry of Arbitrary Two-Dimensional Sections with and without Flow Separation’, *Proceedings of 21st Symposium on Naval Hydrodynamics*, Trondheim, Norway.

Zhu, X., Faltinsen, O. M. and Hu, C. (2005): “Water Entry and Exit of a Horizontal Circular Cylinder”, *24th International Conference on Offshore Mechanics and Arctic Engineering*, Halkidiki, Greece.

Seventh International Conference
On High-Performance Marine Vehicles
Melbourne, Florida, USA
13-15 October 2010

TIME-DOMAIN SIMULATION OF WET DECK SLAMMING – A HYBRID THEORETICAL AND EMPIRICAL APPROACH

Benjamin French
Australian Maritime College,
University of Tasmania.
b.french@amc.edu.au

Giles Thomas
Australian Maritime College,
University of Tasmania.
g.thomas@amc.edu.au

Michael Davis
School of Engineering,
University of Tasmania.
M.R.Davis@utas.edu.au

Damien Holloway
School of Engineering,
University of Tasmania.
Damien.Holloway@utas.edu.au

Luciano Mason
Australian Maritime College,
University of Tasmania.
L.Mason@amc.edu.au

ABSTRACT

Slamming is an important influence on the global strength and fatigue life of lightweight high-speed ocean-going catamarans. This paper presents a new method for estimating slam loading and occurrence rates for such vessels. The basis of this method is a time-domain boundary element seakeeping code using a Green function solution applicable at high Froude numbers.

Pressure, strain and seakeeping measurements have been conducted on a 2.5m hydroelastic segmented catamaran model in irregular waves. Strain measurements were used to determine slamming loads and locations on the wetdeck. This experimental data has been used to develop an empirical/stochastic model for calculating wetdeck slam loads on a high-speed catamaran.

When a slam is identified in the seakeeping simulation, the slam load is determined based on a regression analysis of the experimental data. The resulting load is then incorporated into the overall hydrodynamic load calculations within the time-domain simulation.

A case study is presented demonstrating the potential use of the method. The catamaran is simulated in four different operating conditions and the resulting slams are compared. With further development, it is intended that this module will provide an important tool for predicting slam occurrence rates and severity on catamarans operating in a variety of service conditions.

NOMENCLATURE

a_n	Slam load coefficients
B	Sectional beam (m)
C_s	Sectional friction coefficient
D	Vertical damping force (N)
$\overline{E}$	Average energy over one wavelength (J/m^2)
e	Predicted slam load residual
F_{slam}	Slam load factor $(1+\varepsilon)$
g	Acceleration due to gravity (m/s^2)

$H_{1/3}$	Significant wave height (m)
h_f	Two dimensional filling height (mm)
k	Wave number (m^{-1})
l	Vessel design length (m)
$L_{measured}$	Slam load measured during experimentation (N)
$L_{prdicted}$	Predicted slam load (N)
L_{slam}	Slam load (N)
$S(\omega)$	Energy spectral ordinate (m^2/(rad/s))
T_0	Modal period (s)
U	Vessel forward speed (m/s)
v	Section vertical velocity (m/s)
v_{rel}	Relative vertical velocity at the centre bow truncation (m/s)
x_{30}	Maximum heave motion (m)
x_{50}	Maximum pitch motion (rad)
γ	Wave heading (rad)
ε	Independent and identically distributed random variable
ζ_0	Wave amplitude (m)
ρ	Density (kg/m^3)
ω	Wave frequency (rad/s)
ω_e^*	Dimensionless encounter frequency $= \omega\sqrt{l/g}$

ABBREVIATIONS

CBT	Centre bow truncation
CFD	Computational fluid dynamics
RANSE	Reynolds-averaged Navier-Stokes equations
RAO	Response amplitude operator

KEYWORDS

Slamming, Seakeeping, Time-domain, Empirical, High-speed catamaran.

INTRODUCTION

Large lightweight high-speed catamarans are now being used in harsh ocean environments, particularly as military deployments. Structural design optimisation of these vessels is imperative and wave and slam loads need to be well understood in order to minimise structural weight and maximise transport capabilities and speed.

Slam loading occurs when a ship's structure impacts on the water surface; this commonly occurs in rough seas where there can be large differences in relative motions of the ship hull and water surface. Multi-hull vessels are particularly susceptible to impact loads on the wet-deck. Slamming loads are generally much larger than global wave loads and exceptional slams have been known to damage vessels and prolonged exposure to slamming is found to reduce the fatigue life of the vessel (Thomas et al., 2005).

The prediction of the occurrence rates and severity of slamming by a numerical simulation would be a useful structural design tool. By taking a statistical approach it would be possible to simulate the entire service life of the vessel. Long-term statistics of the vessel loading would then be investigated to gain insight into long-term wave loading, slam occurrence rates, slam loads and also the fatigue life of the vessel for a given environment (service route for example) and operating condition.

Many seakeeping codes have previously been developed by various authors to predict motions in regular and irregular seaways. Fewer codes incorporate slamming calculations, and those that do generally adopt an off-line approach - the motions and global wave loads are all pre-calculated before the addition of slam loads. Time-domain codes have an advantage over frequency-domain codes in that they can attempt to account for slam loadings as solutions are time stepped; therefore the position and velocities of the vessel are known in time. Three-dimensional codes are becoming popular for calculating dynamic loads and responses of vessels in waves, although currently fully 3D methods appear to offer little improvement over 2D or 2D+time methods (Zhao, 2003). Strip theories are still useful for engineering purposes since 2D and 2D+time theories are more robust and computationally economic than a complete 3D unsteady potential flow analysis (Applebee et al., 2008).

Some seakeeping codes attempt to incorporate slam calculations in both on and off-line models. The most common methods usually involve potential flow methods such as the Wagner and von Karman wedge entry method or computational fluid dynamics (CFD) to predict the pressure distribution over the surface of the slamming object. Those methods based on potential flow are generally two-dimensional approximations, which tend to overestimate the surface pressures on shapes impacting water. Due to the large computational requirements of CFD, it is generally employed as a post-processor when motion histories of the vessel motion and global loads are predetermined by a potential flow method.

An example of a time-domain program is LAMP (Large Amplitude Motions Program), which uses a time-stepping approach in which all forces and moments acting on the vessel are solved at each time step (Lin et al., 2007). Relative motions of the vessel and waves are determined for impact calculations in a slamming module postprocessor (Weems et al., 1998). Two models are available in this slamming module, a 2D empirical model used for global loads and a 2D nonlinear Wagner based method (Weems et al., 1998).

Two examples of successful codes utilising three-dimensional panel methods are PRECAL (Cappelletti et al., 2003) and WASIM (Lindemark et al., 2004). Due to computational requirements, full CFD solutions are not commonly available for global ship motion and loads simulations. Field equation solvers, such as FLUENT have been applied in seakeeping applications, but only for local problems, such as determining slamming loads (Applebee et al., 2008). One solution to this problem is to model ship motions with a panel method, and slamming with a RANSE (Reynolds-averaged Navier-Stokes equations) solver; this is the method used by El Moctar et al. (2005). They first used a linear frequency-domain Green function panel code GLPANEL to determine the appropriate design waves and ship motions and then a RANSE solver was used to calculate slamming loads. This method was found to be suitable for the design of a ship's structure that is susceptible to slamming.

The prediction of wet deck slamming on catamarans is further complicated by the catamaran demihulls and cross deck structure. Two-dimensional slam models, such as those based on Wagner's work, are generally limited to simple geometries and, as noted above, they can over predict slam pressures. Currently it is not feasible to perform seakeeping simulations with 3D CFD methods and so three-dimensional slam models are limited in their application. Due to the difficulties in predicting slamming loads accurately with numerical methods, an empirical/stochastic approach is adopted for the present model using scale model measurements as a basis for the slam module. However, it is important to note that new assumptions are made, the most obvious being that the scale model behaviour is representative of the full scale vessel behaviour.

The method presented here uses a time-domain seakeeping code based on a transient Green function solution to predict a time history of the motions of a 112m wave-piercing Incat catamaran. An empirical off-line slam model, based on scale model experimental seakeeping data, is used to calculate slam loads when slams are predicted to occur within the simulation.

MOTIONS PREDICTION

A two-dimensional time-domain strip-theory seakeeping program is used to predict the motions and global wave loads of a 112m Incat catamaran. It is based on the transient Green function solution for strips of water which are fixed in space and perpendicular to the direction of motion (Holloway and Davis, 2006). The solution for each strip starts when the bow enters the strip, and finishes when the stern leaves the strip. The Green function used satisfies the linearised free surface boundary condition; therefore if the water depth is considered to be deep, it is only necessary to place sources on the hull surface. This has the advantage of reducing the number of sources (and thus number of computations) required for a solution.

Large amplitude motions and irregular incident waves can be simulated realistically with this model because the hull is panelled at the instantaneous incident wave free surface at each time step. This requires the sources to be redistributed on the wetted hull surface at each time step. It is important to remember that the Green function linearises the free surface boundary condition; any non-linear effects resulting from large motions of the free surface are not modelled. The Green function solution determines the local pressures on each hull surface panel and the total force on the hull is found by integrating over the hull surface at each time step. The hull is then treated as a rigid body and instantaneous accelerations in heave, pitch, yaw and sway are determined. It is then possible to integrate the accelerations to determine the motion of the vessel through time.

This method includes implied added mass and damping in the transient Green function solution. The effect of implied added mass in particular means that there are mass and acceleration terms on both the right hand side (due to the hydrodynamic forces acting on the hull) and left hand side (the hull mass and acceleration being calculated for the next time step) of the motion equations, resulting in stiff equations. The problem of numerically integrating these equations is discussed by Davis and Holloway (2003a), (2003b), who introduced a method in which the change in hull position is calculated on the basis of a weighted combination of the acceleration computed for the current and previous time steps. The error from this method was shown to be much less than the error resulting from panelling the hull surface.

In order to account for the neglected frictional effects, a sectional friction coefficient, C_s, is introduced. The vertical damping force on each section is calculated as $D = \frac{1}{2} C_s \rho U v B$, where D is the force per unit length, B is the sectional beam, U is the forward speed of the ship and v is the vertical velocity of the section relative to local water surface. The main purpose of this damping force is to reduce maximum heave with smaller reductions in pitch; this simple approach is adequate to match test data to RAOs calculated from simulation results. The values for C_s vary, but are less than 0.15. In this application, a sectional friction coefficient of 0.1 was used to match motions from scale model testing.

An irregular wave version of this seakeeping code has subsequently been developed. Since the method is formulated in the time-domain and instantaneous wave heights are determined at all strips of water and at each time step, it is possible to use the principle of linear superposition of regular waves to create an irregular wave field. This assumes that nonlinear interactions of regular waves are negligible. An array of wave heights, frequencies, phases and headings are input into the program. Surface displacements, velocities and Froude-Krylov forces are calculated for each regular wave component at each water section and then summed to give the total surface displacement, velocity and Froude-Krylov forces.

An ideal wave spectrum can be represented by a series of regular waves of varying frequencies and amplitudes depending on the energy distribution of the wave spectrum. The average energy ($\overline{E}$) over a wavelength is given by Equation 1:

$$\overline{E} = \frac{\rho g \zeta_0^2}{2} \tag{1}$$

Figure 1 shows a wave energy spectrum that has been divided into a number of bands. The area under the wave energy spectrum is proportional to energy multiplied by density and gravitational acceleration. Therefore the nth regular wave component of the spectrum can be found by applying Equation 2, where the frequency of the representative regular wave component is the mid-point frequency of the band and $\overline{E}_n$ is the average energy over the nth frequency band. Random phases are assigned to each wave and a random deviation to wave heading (γ ± 0.17rad) is also given to each wave.

$$\zeta_n = \sqrt{\frac{2\overline{E}_n}{\rho g}} \tag{2}$$

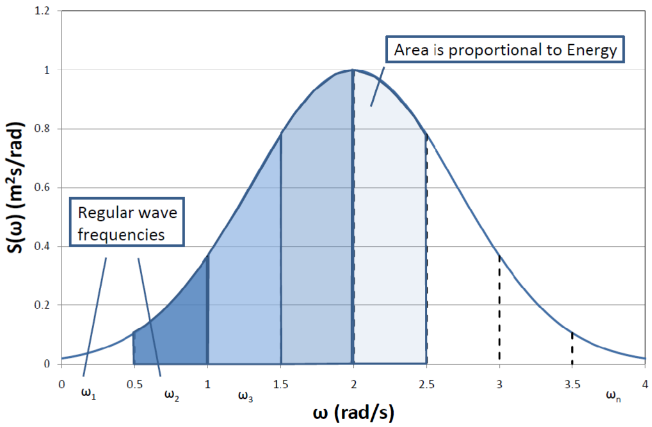

Figure 1: Example spectrum divided into bands. Each band can be represented by a single regular wave.

The new irregular sea version of the time-domain seakeeping code was verified by performing several program tests, ranging from simple tests such as examining ship motions in a regular wave created by the superposition of waves with identical frequencies and motions in a bi-chromatic wave to motions in idealised wave spectra. Response amplitude operators (RAOs) in idealised wave spectra were calculated and compared to those determined from regular wave methods. In the case of regular waves, a root-mean-squared method was used to determine peak motions. In the case of wave spectra, a Fourier transform method was used to determine frequency components of dominant energy and the ratio of ship response spectra to wave elevation spectra provided the RAO for that particular condition. Ensemble averaging of multiple Fourier transforms was used to reduce spectral leakage into other frequency bins.

Heave and pitch RAOs for a 112m Incat wave-piercing catamaran are shown in Figure 2. RAOs for three different wave heights were calculated for regular waves, these are compared to the RAO from a JONSWAP wave spectrum with a significant wave height of 2m and modal period of 10s. A non-linear response can be seen in the regular wave RAOs; in the heave plot, the peak response decreases and shifts to a lower modal frequency for larger wave heights and the pitch RAO rapidly decreases around $\omega_e^* = 5$. This non-linear response can be attributed to the influence of the centre bow of the Incat design entering the water in larger sea states. The irregular sea RAO can be seen to fall within the 'envelope' of the regular RAOs. This provided confidence in the validity of the seakeeping code to predict the vessel motions when compared to regular wave predictions. It should be noted that no ride controls were simulated in these computations, although the time-domain code does have the capability to simulate ride controls.

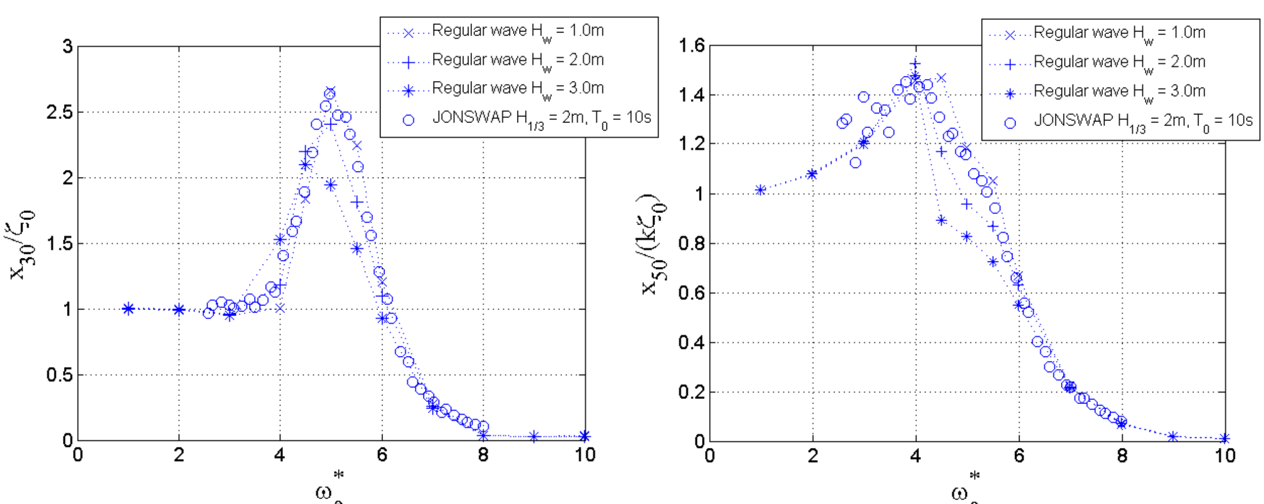

Figure 2: Heave and pitch RAOs for H_w = 1m, 2m and 3m, compared with the response from a JONSWAP spectrum with T_0 =*10s* and $H_{1/3}$ = *2m.*

SLAM MODEL

The aim of the model was to first identify slam events as they occur in the time-domain simulation and then calculate the resulting slam load. The slam identification criterion and slam load prediction method were based on results from model experiments.

Slam Identification: Slam events can be identified in the time-domain simulation by using a two-dimensional filling height criterion. The 2D filling height is an attempt to account for water displaced by the demihull and centre bow when the bow is immersed. This parameter was derived from scale model experimental results which showed that slams occurred prior to the relative immersion of the vessel reaching the maximum tunnel height. The 2D filling height is defined as the height of a rectangle with a breadth equal to the distance between the centre line of the ship and the centre of the demihull, with an area equal to the two-dimensional area underneath the centre bow arch at the centre bow truncation (CBT), (see Figure 3) (Lavroff, 2009).

The steady calm water wave pattern and dynamic trim are not modelled in the simulation. However they are accounted for by simulating the vessel in calm water conditions and using the resulting steady state sinkage and trim to adjust the heave and pitch results from the irregular sea simulations.

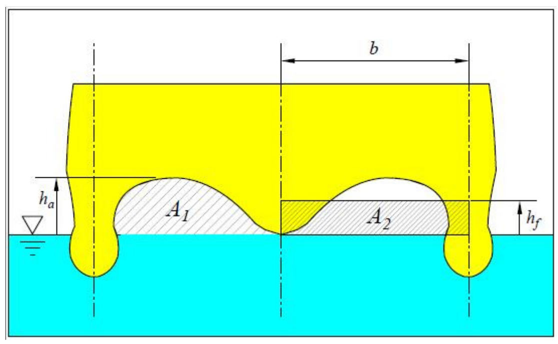

Figure 3: Cross-section of the 2.5m scale model catamaran at the CBT. $A_1 = A_2$. h_f is defined as the 2D filling height, from (Lavroff, 2009).

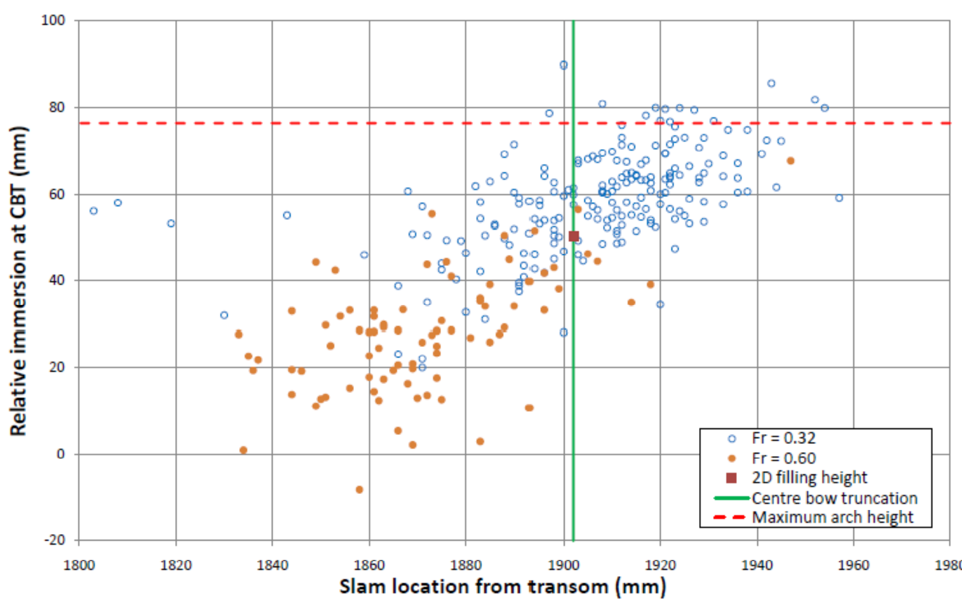

Figure 4: Association of the immersion at the centre bow truncation and slam location for two different Froude numbers.

The relationship between immersion of the CBT and slam location from scale model results can be seen in Figure 4. The 2D filling height appears to be an adequate initial slam identification mechanism; it is clear from Figure 4 that the majority of slams occur at immersions less than the maximum arch height. The maximum immersion at the CBT during a slam event tends to decrease for higher vessel speeds, many of the slam events recorded for Fr = 0.60 occurred at immersions less than the 2D filling height, this can be attributed to the slam occurring at a different location to where the relative immersion is measured. This observation is not accounted for in the current 2D filling height slam identification mechanism. Also of interest in this plot is the association between slam location and immersion. The slam location tends to move aft with less centre bow immersion as forward speed is increased. The decrease in relative immersion during slam events with an increase in Froude number suggests that the relative steady wave height generated by the vessel may have an influence on the filling height criterion. This is not currently included in the time-domain simulation.

In the presented slam module, a slam event is said to have occurred when the relative immersion at the CBT equals or exceeds the 2D filling height. Figure 5 demonstrates the application of the 2D filling height slam identification trigger. A 112m catamaran is simulated in the time-domain method, sailing at 38kts in a JONSWAP spectrum with significant wave height of 3m and modal period of 7s (headseas). The 2D filling height and maximum arch height at the CBT is included in the plot. The 2D filling height can be seen to be exceeded three times during this short section of simulation, therefore, according to the 2D filling height criterion, three slams have occurred over the 70s of simulated time. Circles on the relative velocity plot denote the relative vertical velocity subsequently used in the slam load calculations.

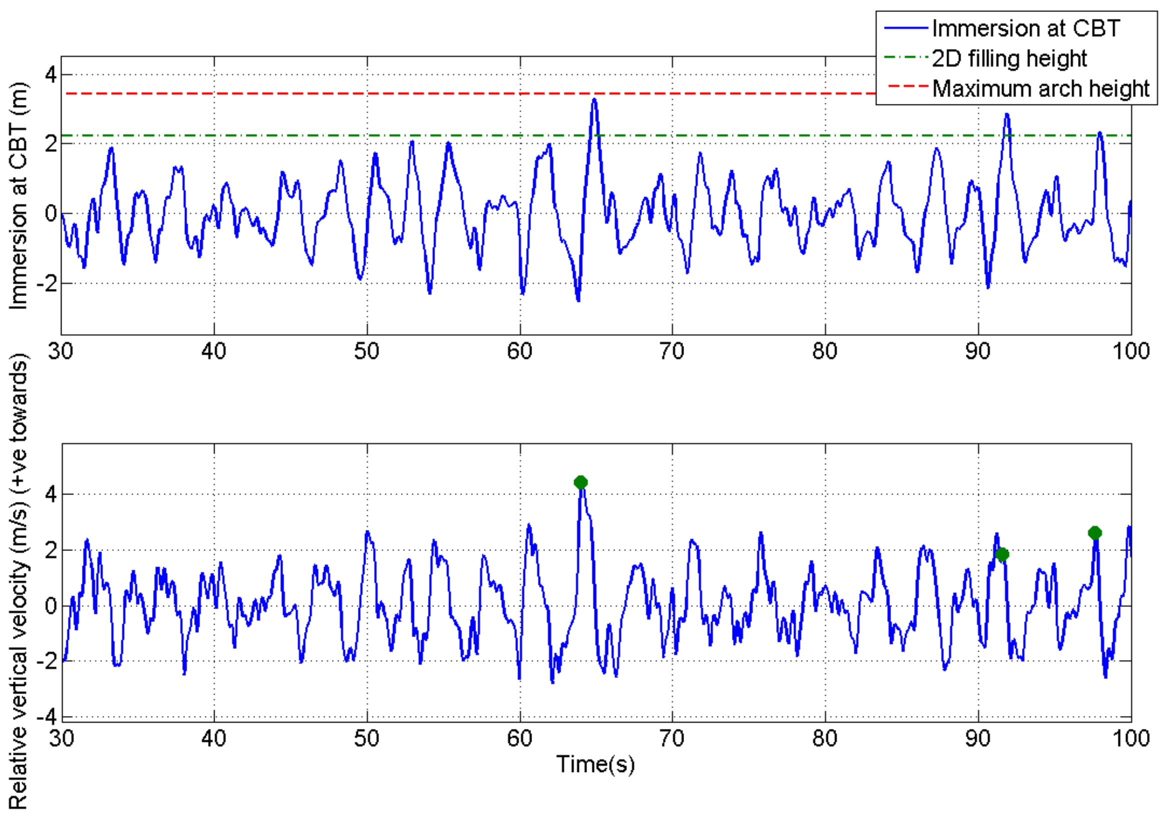

Figure 5: Relative immersion and heave velocity time traces of a 112m wave-piercing catamaran sailing at 38kts in head seas represented by a 3m, 7s JONSWAP wave spectrum. The circles on the velocity plot highlight identified slam events.

Slam Load Calculation: When a slam event is identified in the simulation the slam load calculation is based on a regression analysis of scale model testing in irregular sea. The scale model experimentation was conducted by Chamberlin and Matsubara (Chamberlin, 2008) and kinematic analysis carried out by Winkler (2009). A total of 284 slams were identified in an irregular sea representing a JONSWAP spectrum with a significant wave height of 3.75m and a model period of 8s, and vessel speeds of 20 and 38kts.

In the slam load model the only slam parameter considered is the maximum relative vertical velocity at the centre bow truncation *prior* to the slam. A quadratic least-squares fit is applied to the experimental data. The quadratic is forced through the origin (when relative vertical velocity is zero, the slam load is also zero). Therefore the predicted load basis equation can be written as:

$$L_{predicted} = a_1 v_{rel} + a_2 v_{rel}^2, \tag{3}$$

where the coefficients a_1 and a_2 are determined by a regression analysis of the irregular slamming data. Figure 6 shows the measured slam data with this line of best fit representing the predicted slam load ($L_{predicted}$). It is clear from this plot the data is weakly associated; for a given relative vertical velocity, a range of slam load magnitudes were measured. The slam load mechanism is not yet clear, therefore a random permutation is introduced to emulate the distribution of slam loads for a given relative vertical velocity.

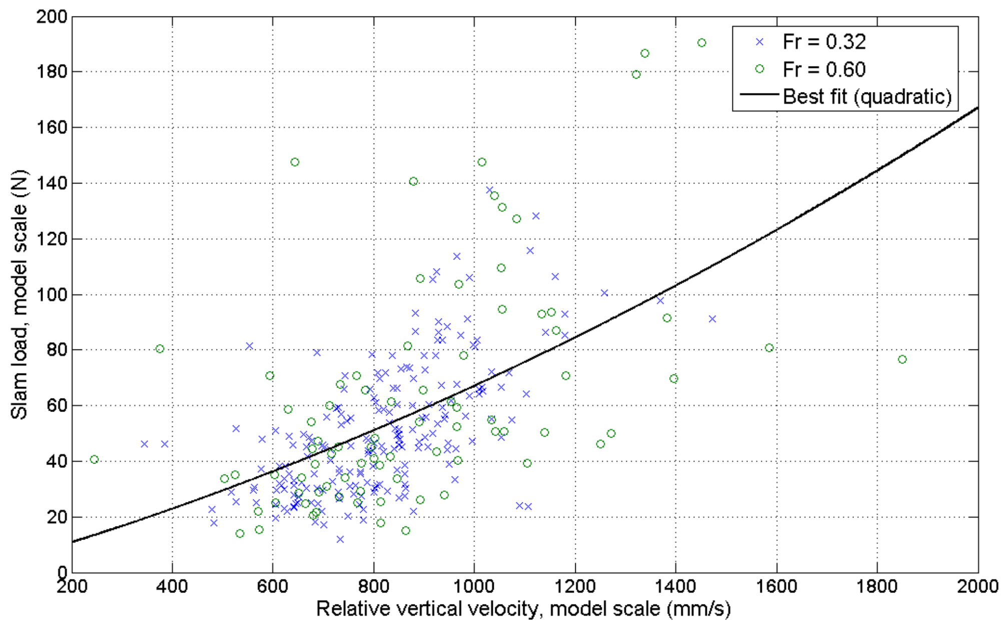

Figure 6: Line of best fit through the slamming data for two vessel speeds.

Analysis of the slam load residual suggested that the total slam load, L_{slam}, could be defined as:

$$L_{slam} = F_{slam} L_{predicted}. \tag{4}$$

Here F_{slam} is defined as:

$$F_{slam} = (1 + \varepsilon), \tag{5}$$

and ε is an identically and independent distributed random number based on the observed distribution of the residuals (e) of the experimental data. The experimental residual, e, is defined as:

$$e = \frac{\left(L_{measured} - L_{predicted}\right)}{L_{predicted}}. \tag{6}$$

Inspection of the distribution for slam factors computed from the load residuals, Figure 7, suggested that it can be approximated by a lognormal distribution. In this form, the slam factor distribution will have a mean of 1.0 and a standard deviation, calculated from the data, of 0.4763. To determine whether the slam factor distribution is lognormal, a chi-square goodness-of-fit test was performed. To test this hypothesis the measured slam load factors were divided into 9 bins with the first eight at 0.25MN load (full scale) increments and the last bin containing all loads greater than 2MN. For this arrangement, $\chi^2 = 6.29$, which falls well within the 95% confidence level, with the conclusion that the hypothesis cannot be rejected. Therefore, when a slam event occurs, the slam load is predicted from the basis equation (Equation 3) and then multiplied by a random factor derived from the appropriate lognormal distribution to give the actual slam load.

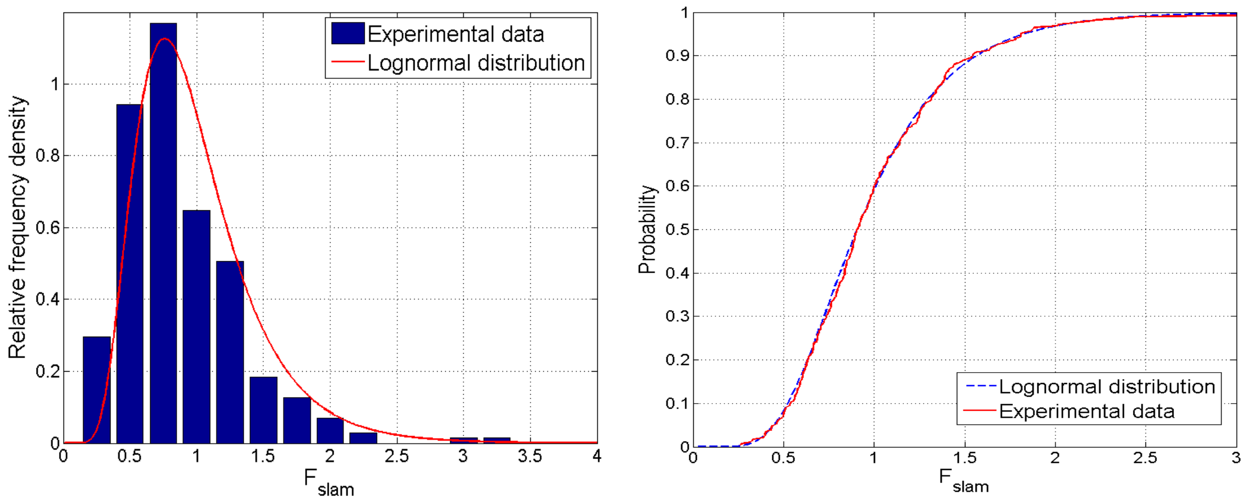

Figure 7: Relative frequency density distribution and cumulative distribution function of $F_{slam} = (1 + \varepsilon)$ compared with the lognormal distribution.

Slam Model Discussion: Wet deck slamming is a complicated process to predict accurately with numerical models. This approach acknowledges the fact that there is a non-deterministic aspect in the prediction of wet deck slam loads. An important parameter was identified and a regression analysis conducted. Ideally, all the dependant parameters would be selected and their relation to slam load would minimise the standard deviation of the residual, making the slam load as deterministic as possible. The initial model presented here consists of only one parameter, the relative vertical velocity at the CBT. However, if forward speed of the vessel is included in the basis equation:

$$L_{predicted} = a_1 v_{rel} + a_2 v_{rel}^2 + a_3 U \tag{7}$$

the standard deviation of the residual distribution decreases by 6.6%. This is just one simple variation of the basis equation that improves the fit to experimental data. Building on the work of Thomas et al. (2009), a complete parameter analysis will be conducted to determine the parameters which are most influential to the resulting slam load. Some parameters that can be considered are:

- Impact angle between ship hull and wave surface.
- Maximum immersion at CBT.
- Immersions at other locations on the ship.
- Velocity normal to the centre bow keel.
- Slam location on the ship.
- Deadrise angle of the centre bow at the slam location.

The model presented has been developed as an off-line module with the intention of implementing it into the time-domain seakeeping code described previously. Because of this off-line development, the motion history of the vessel is predetermined before the addition of slamming loads and thus slam loads are assumed not to influence the overall motion of the vessel. This is a standard assumption in many seakeeping codes; however it is not realistic. Upon implementation in the time-domain simulation, it is envisioned that slamming loads will have some modest impact on subsequent vessel motions.

The 2D filling height (and thus relative immersion at the CBT) is the only criterion used in identifying slam events. No attempt has yet been made to determine slam location. Slams tend to occur further aft on the vessel and at shallower immersions when the ship is sailing at high speed. This suggests that forward speed is an important parameter in both slam location and the centre bow immersion required for a slam event to take place. Experimental measurements have been performed on the 2.5m hydroelastic segmented model during April/May 2010, involving pressure measurements at six locations and capacitance wave probes at three locations along the wetdeck archways. This data will provide valuable insights into pressure trends and wave elevations within the wetdeck tunnel during slam events. Better understanding of the conditions that lead to slam events and their location along the vessel will then allow for the development of a more elaborate slam identification mechanism, slam location and even slam duration predictions.

CASE STUDY

A sample case study was undertaken to demonstrate a possible application of this method. Four idealised sea spectra, representative of real-world conditions, were selected and the 112m Incat catamaran sailed at 38kts in head seas, for 10 minutes (full size equivalent) in each condition. The number of slams, and the resulting slam loads were identified.

Table 1: Four conditions examined in the slamming simulation and the number of slams identified.

Condition Number	Vessel speed (kts)	Significant wave height (m)	Modal period (s)	Spectra	Duration of simulation	Number of slams identified
1	38	2	6	JONSWAP	10 minutes	0
2	38	3	7	JONSWAP	10 minutes	36
3	38	3.75	8	JONSWAP	10 minutes	105
4	38	4	8	JONSWAP	10 minutes	121

A sample time trace from Condition 2 can be seen in Figure 5. No slams were identified in Condition 1 ($H_{1/3} = 2m$, $T_0 = 6s$) whilst 36, 105 and 121 slams were identified in Conditions 2, 3 and 4 respectively. The slam occurrence rate appears to be excessive in the simulation, which suggests that the 2D filling height slam identification method is oversensitive and may require revision. Although the time-domain simulation does have provision for ride control computations, no ride controls were used in the simulation or during scale model tests; it is noted that ride controls can reduce vessel motions by up to 50%, which would result in lower slam occurrence rates.

Figure 8 displays the relative frequency distribution and the cumulative distribution for the scale model results and the three conditions where slamming was identified. Condition 3 represents the same sea state in which the scale model tests were conducted. It can be seen from the cumulative distribution function plot that Condition 4 gives the most severe slam loads; about 20% of all the slams calculated are in excess of 8MN, compared to less than 10% of the slams for Condition 3 and the scale model results. Condition 3 appears to be similar in severity to the scale model tests ($H_{1/3} = 3.75m$, $T_0 = 8s$), with a slightly higher probability of relatively less severe slams. Condition 3 contains a higher proportion of less severe slams (roughly one quarter of the slams identified are less than 2MN, compared to about 10% for the scale model tests) and also a larger amount of more severe slams.

This case study only used 10 minutes of simulated sea time for each condition. With a more refined slam model, it would be possible to simulate motions and loads on a vessel in many varying conditions for a sufficient amount of time required to perform a statistical analysis on the long term loading of the vessel. This will be a useful tool for designing a vessel with a particular service route in mind, or selecting a vessel for a given route.

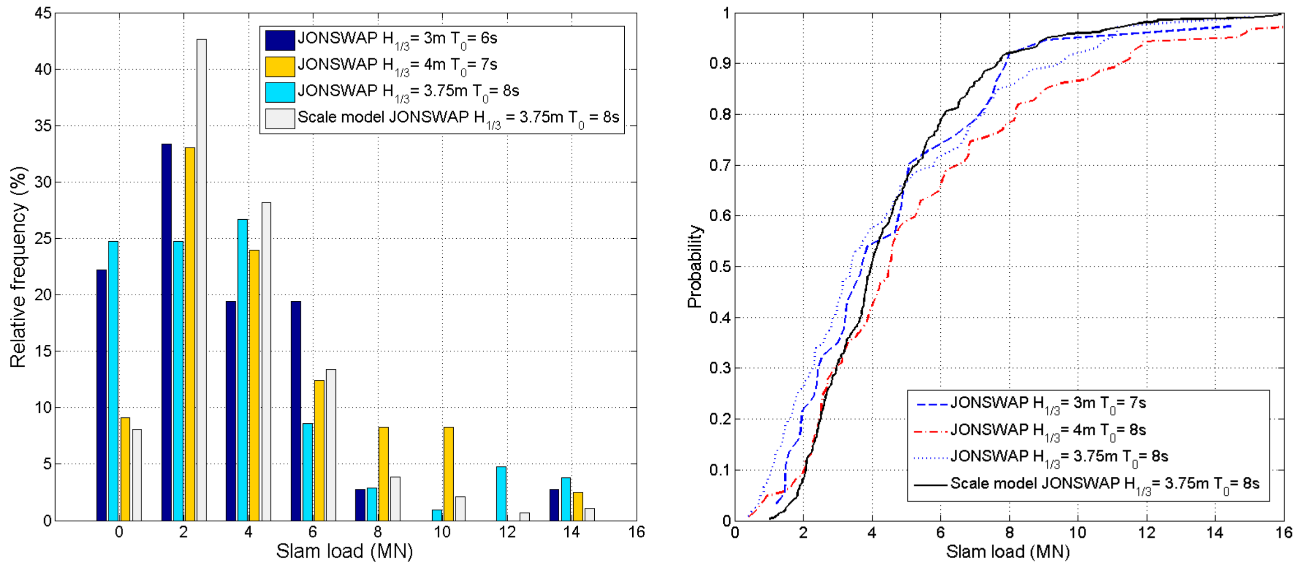

Figure 8: Slam load relative frequency distribution and cumulative distribution for slam loads determined in the slam module and scale model test results.

CONCLUSIONS

Slam loading is found to be not completely deterministic. A hybrid theoretical-empirical model has been developed to generate a slam load using previous experimental measurements as a basis. This model is able to produce a distribution of slams that follow the measured scale model experimental results if only relative vertical velocity between ship and the wave is considered. The relationship between relative vertical velocity and load is considered to be quadratic and the distribution of the residual approximates a lognormal distribution.

Online implementation in the time-domain program will involve storing wave and motion data for a number of time steps to allow recollection of velocity peaks occurring prior to the slam event. Application of the load in time and space will also need careful investigation. Currently this model only determines the magnitude of the slam load, but investigations into the distribution of the slam load in space and time will be conducted. Pressure measurements on the wet deck archway have been made in previous tests; these could give an indication into the distribution of the slam load. A plethora of experimental data has been gathered from the 2.5m hydroelastic segmented catamaran model since 2007. Analysis of this data will provide further insight into the nature of centre bow slamming and the basis of a more detailed empirical/statistical slam model.

As this data is analysed and trends identified, the slam model will be extended to identify slam events in the time-domain simulation, then predict slam locations, loads and load distributions and slam duration times all based on experimental results. This investigation will also provide a deeper understanding of the slamming process.

ACKNOWLEDGMENTS

This work has been supported by Incat, Revolution Design Pty Ltd and the Australian Research Council. Mr Kim Chamberlin and Mr Shinsuke Matsubara conducted the scale model experimentation and Mr Stefan Winkler carried out analysis of the data gathered. Without their contributions, this paper would not have been possible.

REFERENCES

Applebee, T., Crossland, P., Grigoropoulos, G., Hermanski, G., Kim, Y., Kishev, R., Matsumoto, K., Hua,. J. and Fathi, D. (2008): “The Seakeeping Committee – Final Report and Recommendations to the 25th ITTC”, *Proceedings from the 25th International Towing Tank Conference*, pp 209-262.

Cappelletti, A., Pino, E., Sebastiani, L., Boccalatte, C., Viviani, M., Bruzzone, D., and Brizzolara, S. (2003): "Experience on the Application and Validation of the Theoretical Methods for the Seakeeping", *Proc. Seventh International Conference on Fast Sea Transportation* (*FAST '03*), Ischia (Gulf of Naples), Italy, Vol. 2, pp 37-42.

Chamberlin, K. (2008): "Characterisation of High-Speed Catamaran Slam Events in Irregular Waves", B.Eng. Thesis, Australian Maritime College.

Davis, M. and Holloway, D. (2003a): "Seakeeping Computations of Semi-SWATHs at High Froude Number", *International Journal of Maritime Engineering,* Vol. 145, No. A2, pp 1-14.

Davis, M. and Holloway, D. (2003b): "The Influence of Hull Form on the Motions of High Speed Vessels in Head Seas", *Ocean Engineering,* Vol. 30, No. 16, pp 2091-2115.

El Moctar, O., Brunswig, J., Brehm, A. and Schellin, T. (2005): "Computation of Ship Motions in Waves and Slamming Loads for fast Ships Using RANSE", *Proc. Eighth International Conference on Fast Sea Transportation (FAST '05),* St. Petersburg, Russia.

Holloway, D. and Davis M. (2006): "Ship Motion Computations Using a High Froude Number Time Domain Strip Theory", *Journal of Ship Research,* Vol. 50, No. 1, pp 15-30.

Lavroff, J. (2009): "The Slamming and Whipping Vibratory Response of a Hydroelastic Segmented Catamaran Model", PhD Thesis, University of Tasmania.

Lin, W., Collette, M., Lavis, D., Jessup, S., and Kuhn, J. (2007): "Recent Hydrodynamic Tool Development and Validation for Motions and Slam Loads on Ocean-Going High-Speed vessels*", Proc. 10th International Symposium on Practical Design of Ships and Other Floating Structures,* Houston, Texas.

Lindemark, T., Kamsvag, F. and Valsgard, S. (2004): "Fatigue Analysis of Gas Carriers", *Proc. Design and Operation of Gas Carriers,* Royal Institution of Naval Architects, London.

Thomas, G., Davis, M., Holloway, D. and Roberts, T. (2005): "The Influence of Slamming and Whipping of the fatigue Life of a High-Speed Catamaran"*, Proc. Eighth International Conference on Fast Sea Transportation (FAST '05),* St. Petersburg, Russia.

Thomas, G., Davis, M., Holloway, D., Roberts, T., Matsubara, S., Lavroff, J., Amin, W., Chamberlin, K., and Dove, T. (2009): "Characterisation of Slam Events of a High-Speed Catamaran in Irregular Waves", *Proc. Tenth International Conference on Fast Sea Transportation (FAST '09),* Athens, Greece, pp 177-188.

Weems, K., Zhang, S., Lin, W., Bennett, J. and Yung-Sup, S. (1998): "Structural Dynamic Loadings Due to Impact and Whipping", *7th International Symposium on Practical Design of Ships and Mobile Units,* The Hague, Netherlands, Vol. 11, pp 79-85.

Winkler, S. (2009): "Classification of High-Speed Catamaran Slam Events in Irregular Waves", Research Report, Australian Maritime College, University of Tasmania.

Zhao, R. (2003): "A Nonlinear Time Domain Simulation for Predicting Wet-Deck Slamming of Catamaran", *Proc. Seventh International Conference on Fast Sea Transportation* (*FAST '03*), Ischia (Gulf of Naples), Italy, Vol. 2, pp 95-102.

Seventh International Conference
On High-Performance Marine Vehicles
Melbourne, Florida, USA
13-15 October 2010

NUMERICAL SIMULATION OF SURFACE EFFECT SHIP AIR CUSHION AND FREE SURFACE INTERACTION

David J. Donnelly and Wayne L. Neu
Aerospace and Ocean Engineering
215 Randolph Hall
Virginia Tech
Blacksburg, VA 24061
ddonnell@vt.edu and neu@vt.edu

ABSTRACT

Numerical simulation of a surface effect ship and the interactions between the ship's air cushion and the water surface is a complex task that has yet to be demonstrated. This paper presents the results from the computational fluid dynamics simulations of surface effect ship model tests. The model tests being simulated are of a generic T-Craft model running in calm seas through a range of Froude numbers and in two head seas cases with regular waves. Simulations were created using CD-adapco's STAR-CCM+ and feature incompressible water, compressible air, pitch and heave degrees of freedom, no viscosity, and the volume of fluid interface-capturing scheme. The seals are represented with rigid approximations and the air cushion fans are modeled using constant momentum sources. Drag data, cushion pressure data, and free surface elevation contours are presented for the calm seas cases while drag, pressure, heave, and roll data are presented for the head seas cases. While the simulations presented show promise in current commercial CFD SES modelling capabilities, much more must be done to make the simulations as accurate as possible, including the simulation of dynamic flexible seals and turbulent viscous flow.

INTRODUCTION

As the capabilities of computational fluid dynamics (CFD) and the availability of computing power grow, CFD is being utilized in an ever increasing number of applications. While CFD has played a role in naval architecture and ship design for some time, a full simulation of both the air cushion and water response under and around a surface effect ship (SES) has not been previously demonstrated. This paper presents the results of numerical simulations of recent tests of a SES model done at the Naval Surface Warfare Center Carderock Division (NSWCCD). The computations use the commercial CFD code STAR-CCM+ by CD-adapco.

The main goal of the work presented in this paper is to explore the possibilities and methods behind simulating a SES using commercial CFD software. The simulations are used to explore the complex free surface geometry that develops around and underneath the air cushion and side hulls at various speeds. While the motions and forces on a SES model can be easily determined during model testing, the free surface geometry is difficult to visualize and monitor. Through CFD simulation, this free surface geometry can be measured and easily visualized in many ways. The free surface geometry from the simulated model tests and a comparison of some of the forces and motions of the simulations and model tests are presented in this paper.

NOMENCLATURE

R_W	Wavemaking drag due to air cushion
p_c	Air cushion pressure
B_c	Air cushion beam
l_c	Air cushion length
g	Gravitational acceleration
ρ_w	Water density
C_W	Coefficient of wavemaking drag due to air cushion
U	Characteristic velocity
Δx	Local grid size
Δt	Timestep

ABBREVIATIONS

CFD	Computational fluid dynamics
SES	Surface effect ship
NSWCCD	Naval Surface Warfare Center Carderock Division
LMSR	Large medium speed roll-on roll-off ship
VOF	Volume of fluid
DOF	Degree of freedom
CFL	Courant-Friedrichs-Lewy number

KEYWORDS

T-Craft, Surface Effect Ship, Air Cushion, Free Surface, CFD, Volume of Fluid

AIR CUSHION THEORY

The concept of the SES and the air cushion vehicle arose from the need for high speed, high payload ships that are not subject to the slamming in seaways of planing craft or the hydrodynamic resistance limitations of displacement ships. The key design feature behind these concepts is a pressurized air 'cushion' that is trapped between the water and the hull of the lifted body. This decreases contact with the water surface, reducing the slamming forces, wavemaking drag, and frictional resistance. A fan replaces the air that escapes the cushion through leakage, keeping the air cushion at a relatively constant pressure. The SES uses rigid side hulls, similar to a catamaran's, and flexible bow and stern seals to trap the air cushion. Only simulations of an SES type design are analyzed in this paper.

The steady drag of a SES can be broken into the following components: wavemaking drag due to the air cushion and sidehulls, aerodynamic profile drag, seal drag, friction drag due to the sidehulls, appendage drag, hydrodynamic momentum drag due to the cooling water for the engines, aerodynamic momentum drag, and drag due to the differential air momentum leakage from the bow and stern seals (Yun and Bliault, 2000). The wave making drag due to the air cushion can be calculated using Equation 1 (Yun and Bliault, 2000), below.

$$R_w = C_w \left[\frac{p_c^2 B_c}{\rho_w g} \right] \tag{1}$$

In this equation R_w is the wavemaking drag, p_c is the cushion pressure, B_c is the beam of the cushion, l_c is the length of the cushion, ρ_w is the water density, g is the gravitational acceleration, and C_w is the wave making drag coefficient which is a function of Froude number and the cushion's length to beam ratio. This equation is valid for a rectangular air cushion with uniform pressure operating in a channel of infinite depth and a width greater than ten times the cushion length. The wavemaking drag due to the air cushion has a considerable "hump" that is due to the wavelengths of waves generated by the pressure cushion and their interaction with the craft. As speed is increased from "pre-hump" speeds to hump speed and higher, the wavelengths grow to significantly longer than the craft, and the wave making drag will decrease. For an air cushion with a length to beam ratio of four, similar to the SES design discussed in this paper, the primary drag hump occurs at a Froude number of about 0.8 (Yun and Bliault, 2000). Other factors affecting the air cushion wavemaking drag include the water depth, the acceleration, and the yaw of the air cushion.

T-CRAFT AND MODEL TESTING PARAMETERS

The Transformable Craft, or T-Craft, is a landing craft prototype being designed to exceed current limitations in speed, range, and load capacity. The U.S. Office of Naval Research is funding the design of this concept ship that is capable of transforming into three unique types of ships; a catamaran, a SES, and an air cushion vehicle. Some of the main objectives of the T-Craft are the capability to transport ten M1A1 tanks, have an un-refueled range of 600 nautical miles while loaded, a crew size of only two, and the capability to climb a 2% sloping beach (Cooper, 2009). The T-Craft is designed to transit to and from a sea base and is intended to operate in close proximity to a large medium speed roll-on roll-off ship (LMSR) for cargo loading from an external ramp.

The NSWCCD completed model testing of a generic T-Craft design operating as a SES both alone and connected to or near an LMSR model in 2008. The generic T-Craft design includes design features from each of three contract hull designs from Alion, Umoe Mandal, and Textron Marine. Figure 1 shows the model with a pressurized air cushion in the water. The model features rigid side hulls with three seals that separate the air cushion into fore and aft sections. The bow and transverse seals are finger type seals while the aft seal is a double lobe type seal. Figure 2 shows the underside of the T-Craft model, revealing the seal configuration. Two flangemount blower fans blow air into channels through the foam board in the hull to pressurize the air cushions. Characteristics of the model can be seen in Table 1 below.

During August through October in 2008, ONR sponsored multiple-body seakeeping model tests involving the T-Craft model operating as a SES alone and connected to or near a model of an LMSR. The model testing was conducted in NSWCCD's Maneuvering and Seakeeping facility allowing testing in calm seas as well as numerous wave conditions. While the test matrix consisted of the T-Craft model and LMSR model in side-by-side, tandem, and Med-Moor conditions, only the tests that involved just the T-Craft are considered for numerical analysis. Several instruments were attached to the model to measure and record the relative motions, forces, and free surface interactions experienced by the model. Model runs that were simulated include calm seas at Froude numbers of 0.08, 0.2, 0.4, and 0.6, corresponding to a full scale speed of 4, 10, 20, and 30 knots, and two regular waves head seas conditions at a Froude number of 0.6.

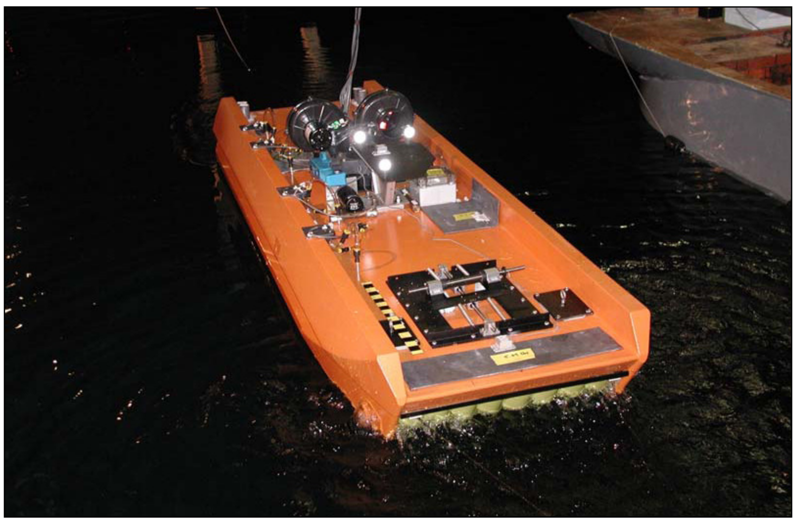

Figure 1: NSWCCD Model Number 5887, generic T-Craft model (Bishop et al, 2009)

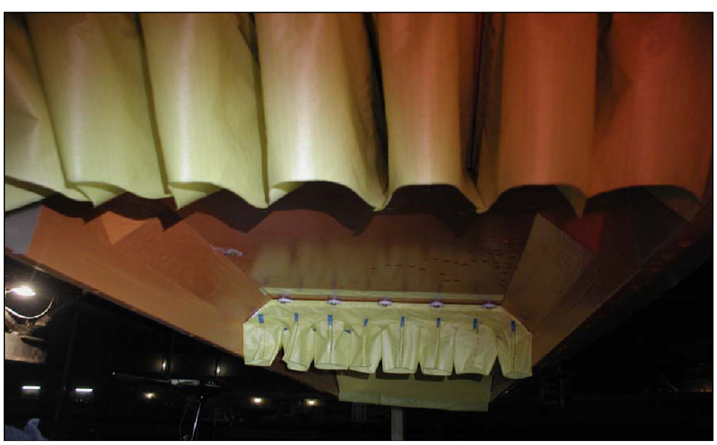

Figure 2: Underside of T-Craft model with seals (Bishop et al, 2009)

Table 1: T-Craft Model Characteristics

Linear Scale	1: 30.209
Length Overall	2.5273 m
Length Waterline (off cushion)	2.4892 m
Length Waterline (on cushion)	2.352 m
Beam Max	0.7366 m
Cushion Width	0.5461 m
Cushion length	2.2225 m
Displacement	54 kg
LCG, forward of wet deck transom	1.231646 m
VCG, below deck	0.0023 m
Moment of Inertia in Pitch	27.9 kg-m^2

NUMERICAL SIMULATION

The commercial CFD code STAR-CCM+ by CD-adapco was used to create numerical simulations of the model tests. STAR-CCM+ features automated meshing, integrated post-processing, an ever increasing library of solvers and capabilities, and an easy-to-use tree-based user interface. Several of STAR-CCM+'s standard mathematical physics model solvers proved to be valuable to these simulations, which is one of the main reasons the program was used.

Since the simulations discussed were solved as inviscid and isothermal, the governing equations in the calculation are the Euler equations. These equations are derived by removing the viscosity terms from the Reynolds-averaged Navier-Stokes equations and include a continuity equation and a momentum equation for each of the dimensions. Solving these equations will generate the local pressure and velocity components of the fluid. STAR-CCM+'s multiphase segregated flow model is used to separate the governing equations for both the water and air. The water is modeled as an incompressible fluid while the air is modeled separately as a compressible ideal gas. In preliminary simulations using incompressible air, it was found that the craft's motions created large pressure fluctuations causing unrealistic free surface responses. These were mitigated by the assumption of compressible air. This model requires an extra equation, the equation of state, to solve for the compressible air's density.

The Volume of Fluid (VOF) method model in STAR-CCM+ is used to govern the air and water free surface interactions. The volume of fluid method is an interface-capturing type scheme used to capture the free surface between two fluids. Cells are assigned a volume fraction of fluid for each fluid, which sum to one. In this method, the two fluids mix at their interface and the physical properties are taken as averages, weighted by the volume fraction of each of the fluids in these cells. The free surface is considered to be the region between cells comprised entirely of each of the two fluids, or where the volume fraction of either fluid is one half. The convection of the volume fraction requires the solution of an additional transport equation as well as schemes to ensure the region immediately surrounding the free surface remains well resolved (Muzaferija 1998).

The six degree of freedom solver (6-DOF) in STAR-CCM+ allows the computational domain to move in any of the translational or rotational degrees of freedom. When using this model, a solid body is selected that will react to both the natural forces such as buoyancy, drag, and gravity or to user defined forces. Though the reaction to the forces on the body only is computed, the whole computational domain is moved to preserve the mesh. With this model, the domain moves with a body centered local coordinate system while the flow remains moving relative to a global coordinate system. The 6-DOF solver updates the flow field relative to the global coordinates as the domain moves through them. The simulations discussed here have only two degrees of freedom enabled, translational heave and rotational pitch.

A VOF waves model is used with the 6-DOF solver to help set up the multiphase domain. The domain is initialized into water and air sections with the free surface level set close to the natural waterline for the stationary T-Craft model, on cushion. The forward velocity is set in this model as the current and wind since the longitudinal degree of freedom is turned off. The free surface can be set up as flat or with either first order or fifth order waves. This model automatically sets up functions to be used for the boundary conditions that will update with the progression of waves.

An additional user-defined field function is used to initialize pressure in the air cushion. Initializing the solution with the free surface close to the natural waterline and with the correct cushion pressure will allow the solution to approach a semi-steady state as quickly as possible, reducing the overall computation time.

The temporal discretization solver is first order implicit unsteady. With this model, solutions are found at time steps and marched through time. For these simulations, twenty inner iterations between time steps are used to ensure low residuals for higher accuracy. The time step used for each of the simulations is governed by the Courant-Friedrichs-Lewy (CFL) number. The CFL number is the relationship between local grid sizing, Δx, characteristic velocity, U, and the timestep, Δt, and is seen in Equation 2. By limiting the timestep size to give a CFL number of one or less, no more fluid enters a cell than is available in the upwind cell for each timestep. Though simulations using a CFL number greater than one can give solutions, they are not time accurate.

$$\mathrm{CFL} = \frac{U\Delta t}{\Delta x} \tag{2}$$

The simulations discussed use three-dimensional half-models with a symmetry plane down the centerline of the T-Craft model. The computational domain is a rectangular prism that extends three meters in front of, behind, and below the T-Craft; two meters above, and a little more than three meters out from the side of the model geometry. The numerical domain was kept small to reduce the number of cells in the mesh and the total simulation computation time. This may affect the accuracy of the simulation, especially in the far field and near the sides of the domain, however the free surface effects under the air cushion and around the hull are the main focus of these simulations. The forward, bottom, and side (opposite the symmetry plane on centerline) faces are velocity inlets. The aft face is a pressure outlet to allow the disturbed free surface wake to flow through with no reflection of wave energy. The top face is also a pressure outlet to allow air in from the top to be used by the fans, if necessary. The volume fraction, velocity, and pressure settings for these faces are set as pre-determined field functions from the VOF Waves model, discussed more above.

The T-Craft model's seals were simplified for the simulations discussed. The bow and transverse finger seals and aft lobed seal are replaced with flat surfaces. This allows larger and more regular surface cells which leads to fewer total cells. Referring to Equation 2, an increased cell size will decrease the CFL number and allow for a larger time step, resulting in a much less computationally expensive simulation. To prevent the plowing effect caused by rigid seals, the seals are shortened to close to the natural waterline. This leaves a gap between the seal and the water surface, allowing some air to escape the cushion and water to pass freely or with minimal resistance beneath the seal. For the simulations of the T-Craft model at Froude numbers of 0.2, 0.4, and 0.6, two seal length configurations were used in an attempt to minimize the gap between the free surface and the seals and thus minimize the air leakage. The seal lengths for each configuration were determined through a crude and quick estimation and correction and are cut horizontally. For the Froude number 0.2 simulations, seal configuration "Seals 1" features slightly longer bow and transverse seals than "Seals 2". For the Froude number 0.4 simulations, "Seals 1" has shorter fore and aft seals than "Seals 2" and both seal configurations feature an elongated transverse seal. For the Froude number 0.6 simulations, "Seals 2" features slightly longer bow and transverse seals than the "Seals 1" configuration.

The fans are represented by volumes known as "momentum sources". These momentum sources add a constant value of momentum through the volume in the desired direction. The momentum added is equal to the pressure on the bottom outlet face divided by the height of the volume or, the force on the bottom face divided by the volume. To reach a desired cushion pressure, the momentum source's momentum value can be changed according to the derivation described above. The momentum source works to keep the cushion pressure fixed by pushing an unlimited amount of air into or out of the cushion as the cushion pressure decreases or increases from the desired value. Using this method to represent the air cushion fans allows outflow through the momentum sources when the cushion pressure exceeds the desired value. A fan curve may be entered into the momentum source to control the amount of airflow through them. Using a fan curve would ensure the correct modeling of the inflow, however it would not ensure accurate cushion pressures since the amount of air leakage out of the cushion is not properly simulated. Because of the uncertainty of the seal modeling, it was found more important to match the cushion pressure rather than the airflow into and out of the cushion. The forward and central momentum sources are located in the same location as the air cushion inlets on the T-Craft model. The aft momentum source is moved slightly forward of the aft lobe seal, since the seal lobes' internal pressures are not simulated.

The automated meshing and surface mesh editing features in STAR-CCM+ were used to mesh the numerical domain. The mesh model is called a "Trimmer" mesh, which features hexagonal cells. The cell characteristic length on the surface of the craft and in the vicinity of the free surface is two centimeters. Figure 3 shows the surface mesh on the T-Craft model with full seals that have not been shortened. Cell size increases as the distance from the free surface increases with the characteristic length doubling each time the size is increased. This can be seen in Figure 4 which shows the mesh on the symmetry plane. The total number of cells is about 2.5 million.

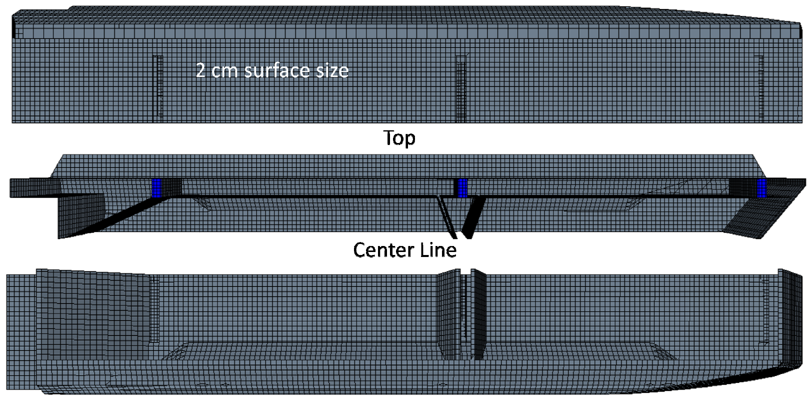

Figure 3: Surface mesh on T-Craft model

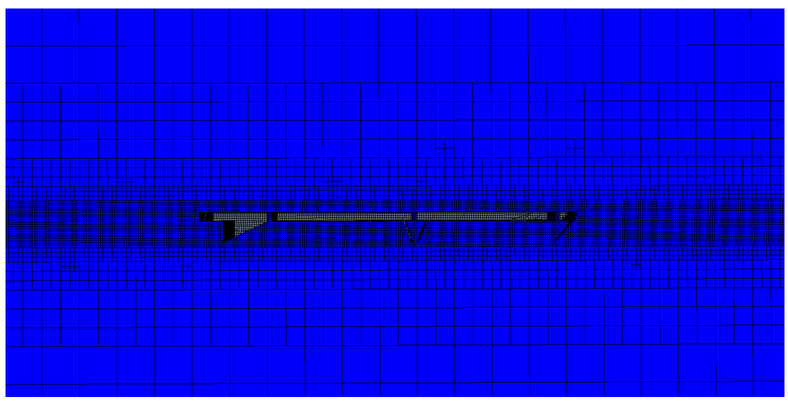

Figure 4: Mesh on symmetry plane

RESULTS

Though several characteristics of the model testing were monitored, only a few of these characteristics are worth comparing to the numerical simulations. Roll and yaw motions are not used for comparison because they are neglected in the simulations. These motions cannot be simulated using a half model with longitudinal symmetry. Though pitch angle is monitored in both the simulation and the model testing, the zero pitch angle of the model testing is unknown, preventing comparison. The heave and draft of the simulation is assumed to be correct through matching the cushion pressures, which should result in the correct buoyancy and air cushion forces. Below, results are presented for cushion pressure, drag, and surface elevation contours for the calm seas model testing at Froude numbers of 0.08, 0.2, 0.4, and 0.6.

Simulating the air cushion pressure correctly is vital to the solution accuracy. The air cushion supports much of the weight of the T-Craft while the rest of the weight is supported by the buoyancy force from the side hulls. The cushion pressure dictates the sinkage of the craft and the amount of the craft supported by the side hull buoyancy. At low Froude numbers, the wavemaking drag due to the air cushion makes up a large part of the total drag. For an air cushion with a length to beam ratio close to four, like the T-Craft model, this is true until a drag hump is reached at a Froude number of about 0.8, after which the wavemaking drag due to the air cushion is reduced. As seen in Equation 1, the total wavemaking drag due to the air cushion is sensitive to changes in pressure as the pressure term in the equation is squared. For these simulations, air cushion pressure is monitored at the same locations as the model testing except in the stern lobe seal, since the lobe pressure was not modeled. These locations are in the forward cushion, the transverse seal, and the aft cushion. Figure 5 shows a plot of the simulation's air cushion pressure monitors compared to those from the model test for a Froude number of 0.6.

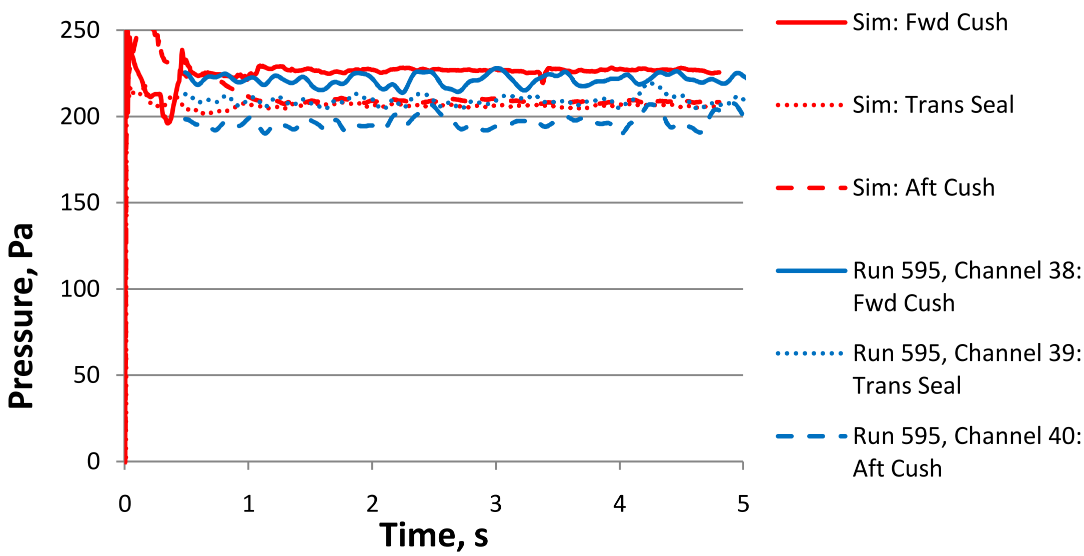

Figure 5: Air cushion pressure monitors, Fn=0.6

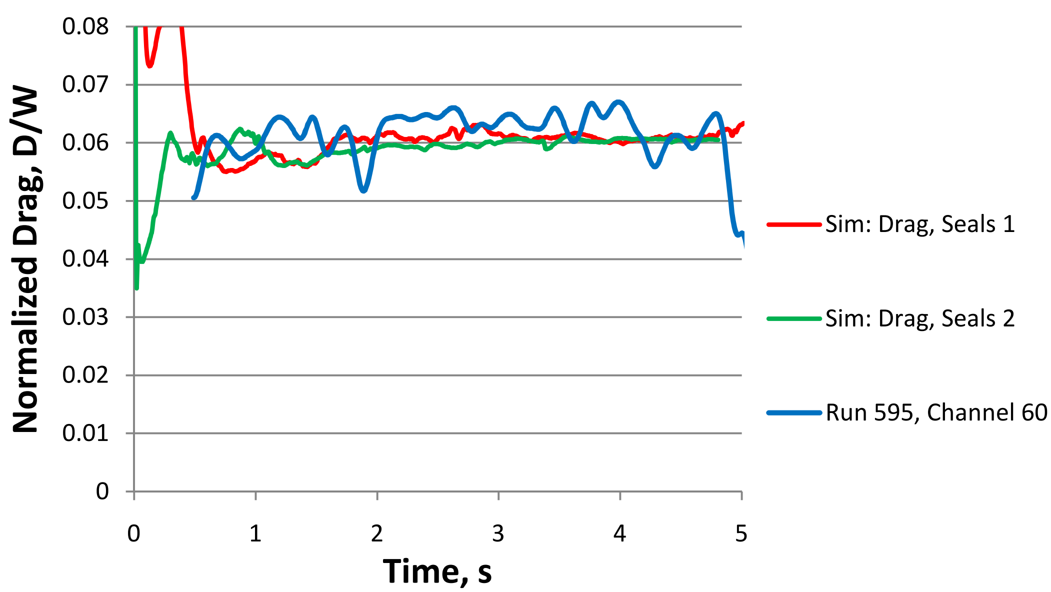

Figure 6: Normalized drag for simulations and model test, Fn=0.6

It can be seen that the air cushion pressures are very close when comparing the simulation to the model test. The pressure isn't constant but fluctuates around a mean value. The simulation's cushion pressure does not fluctuate as much as the model test's due to the constant momentum fan approximation and rigid seals . Large differences in forward and aft cushion pressures proved difficult to simulate due to the shortened, rigid, transverse seal that depending on the gap distance from the free surface, may not completely separate the air cushion into forward and aft sections.

As discussed earlier, SES total drag is the sum of several factors. Some components of the drag are not correctly simulated or calculated at all in the simulations being discussed. Skin friction on the hull and seals is not modeled at all since the air and water are treated as inviscid. Simulating the seals as rigid may be another source of error. In the model tests, the dynamic seals would inflate with air pressure and fold from water pressure while the rigid seals do not change in the simulation leading to urealistic free surface disturbance and added drag. The seals can be retracted from the water surface completely, thus eliminating all seal drag, but this may alter the pressure distribution on the surface and the craft's response. This condition sets a lower bound on the possible drag value. Once the seals are lengthed to the point where they contact the water surface, the calculated drag will rise quickly with increasing seal length. The goal was to adjust the seal lengths such that a simulation is produced which accurately represents the attitude of the craft and the enclosed pressure distribution without adding the unrealistic effects of dragging rigid seals through the water. The resulting rigid seal length is such that there is only small and intermittent contact with the water surface. The fact that the resulting total drag calculated is close to the measured drag is one indication of the accuracy of the drag from the air cushion and side hull effects. While seal length could be adjusted to match the measured drag, this is artificial manipulation of the simulation and was not attempted. Drag data for a Froude number of 0.6 is compared in Figure 6 below. In this figure, drag from simulations of two different seal length configurations are pressented.

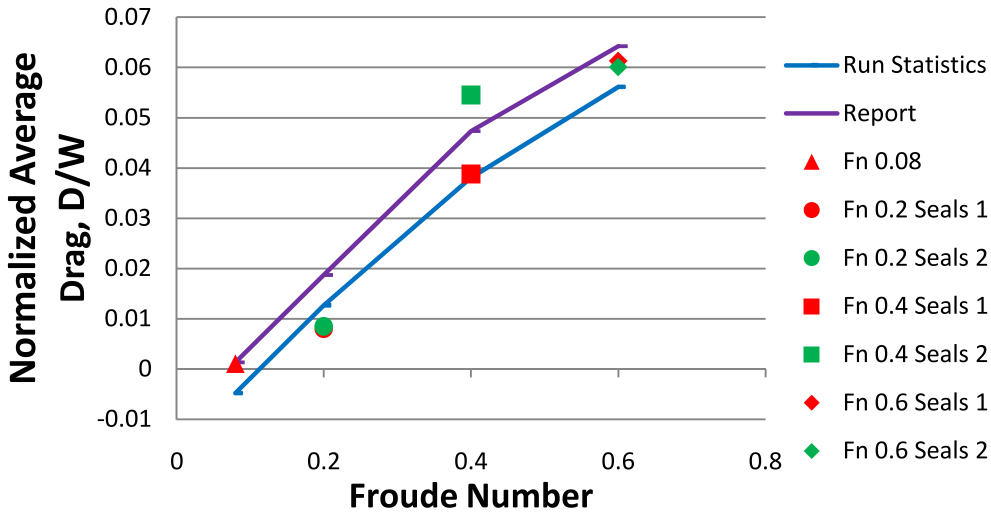

Figure 7: Normalized average drag for simulations and model tests

The simulations' and the model test's drag values are very close. It can be seen that during model testing, the drag fluctuates more than in the simulations. Drag values from the simulations before one second diverge due to the initialization of the flow field. It takes a second or two of simulation time for the flow field to react to the boundary conditions and become steady. Figure 7 shows average drag data from each of the simulations and model tests. The two data series labeled "Run Statistics" and "Report" are both from model testing, however the data labeled "Report" has a correction factor added to it (Silver, 2010). For each of the simulations, drag data is averaged starting after two seconds of run time to allow the flow to develop from initial conditions and become steady. It can be seen that the average drag values between simulations and model testing are comparable. For a Froude number of 0.2 and 0.6 changing the seal length slightly did not have much effect on the drag, however at a Froude number of 0.4 it did. For the simulations with a Froude number of 0.4, the fore and aft seals were lengthened slightly for the second seal configuration. This caused the rigid seals to penetrate the free surface which causes an increase in drag as the rigid seals plow through the water.

Examining the free surface around and especially beneath the hull and air cushion can prove to be very valuable in design. Flow features can be observed that may lead to changes in the design of the cushion seals or hull form. Figure 8 shows the simulated free surface elevation contours from each Froude number tested, presented on the same scale for comparison. In the figure, the hull is made transparent and the white areas show where the side hulls pierce the free surface. Though throughout the simulations these contours had small variations over time, the main flow features are present for the simulations' entirety. Changing the seal length did not prove to have a considerable effect on the free surface patterns.

After examining the free surface elevation contours it is clear why the air cushion is the cause for a lot of the wave making drag at low Froude numbers. Internal waves under the cushion and between the hulls can be seen at each of the Froude numbers. At the lowest velocity, Froude number of 0.08, there are many waves between the hulls that have a short wavelength. As the craft accelerates to a Froude number of 0.2, the wavelengths grow to about a quarter of the T-Craft's length with four full wavelengths visible between the hulls. At a Froude number of 0.4 the wavelength grows to almost the entire length of the T-Craft. Notice how the second wave hump is located towards the stern of the craft and clearly interacts with the aft seal. The wavelength grows to longer than the ship at a Froude number of 0.6 and the wave trough is close to the stern of the T-Craft. It can be seen that though the wave patterns at lower

Froude numbers are much more complex, the amplitude of the waves is much smaller. It is important to note that these internal waves are not two dimensional but rather vary across the beam of the ship as well. This three-dimensionality may be due to the wavemaking of the side hulls and the waves' interactions between them. Note the angle of the crest relative to the hull in the surface elevation contours from the Froude number 0.4 simulation.

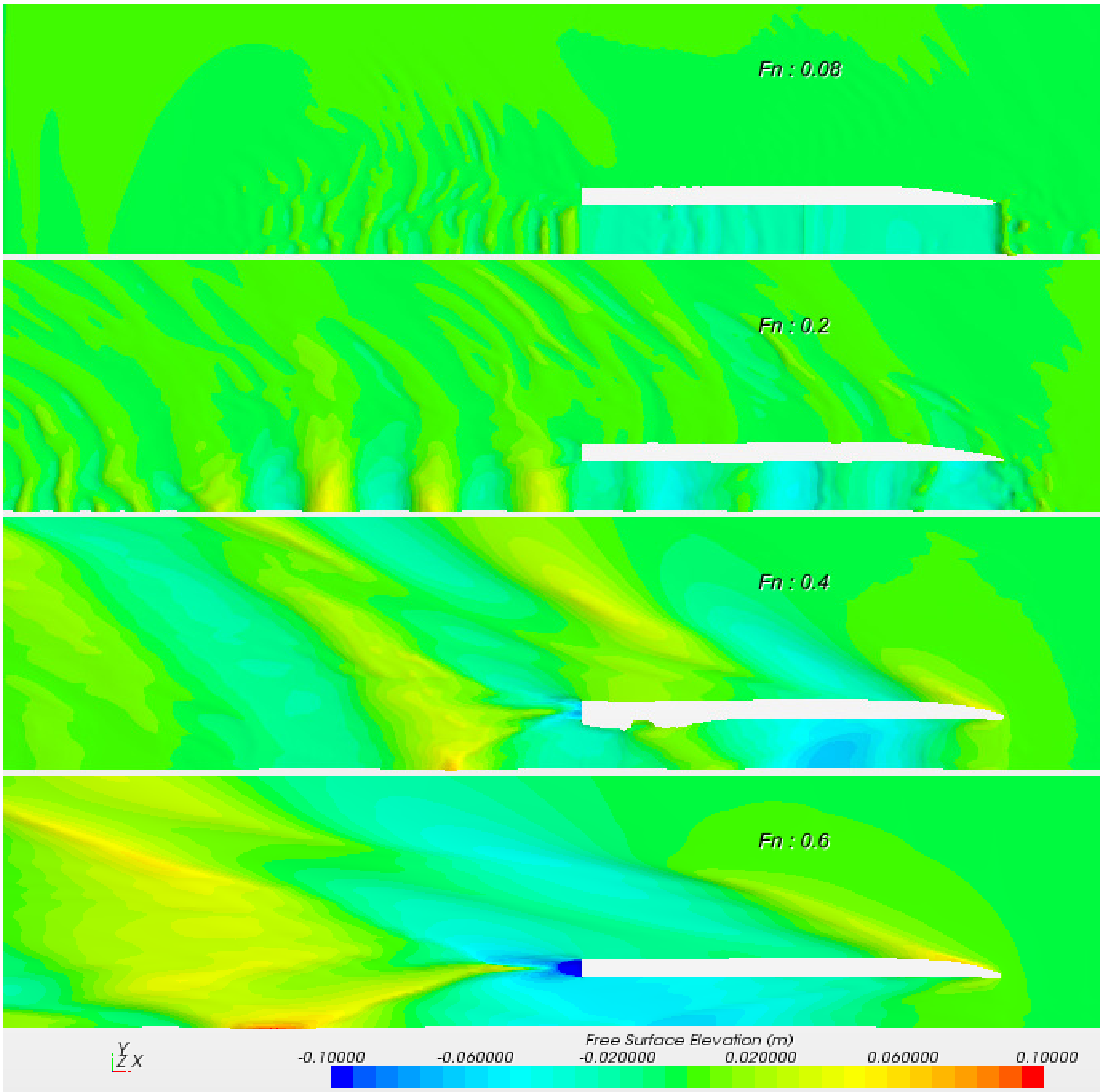

Figure 8: Free surface elevation contours plotted with same scale

Simulations of the two regular wave cases at a Froude number of 0.6 were also conducted; data from one of these cases is presented. It is important to note that while the wave height and frequency of the waves are accurate in the simulation, the phase in time is not. For the plots presented, the time values have been shifted to match the wave phase using the heave data as a phase reference. Since the incident wave frequency is matched between the model test and the simulation, the predominant frequencies of the responses agree. The average values of the heave and pitch data for the simulation and model test are set to zero, to make comparing oscillation amplitudes easier. Figure 9 shows the pressure in the forward cushion for the regular waves simulation and model test at the same location as in Figure 5. Like the calm seas runs, the air cushion pressure between the model and simulation are very similar, however, the simulation does not show the same amplitude pressure drop than in the model run. This may be attributed to the estimation of the fans as a momentum sources that will pressurize the air cushion much quicker than blower fans. Figure 10 shows the heave for the simulation and model test. The heave data from the simulation has larger amplitude and much more regular fluctuations than the model test. Figure 11 is a plot of the pitch angle for the simulation and model test, negative pitch is bow up. The simulation accurately estimates the pitch of the craft, though the amplitude of the fluctuation varies slightly more in the simulation.

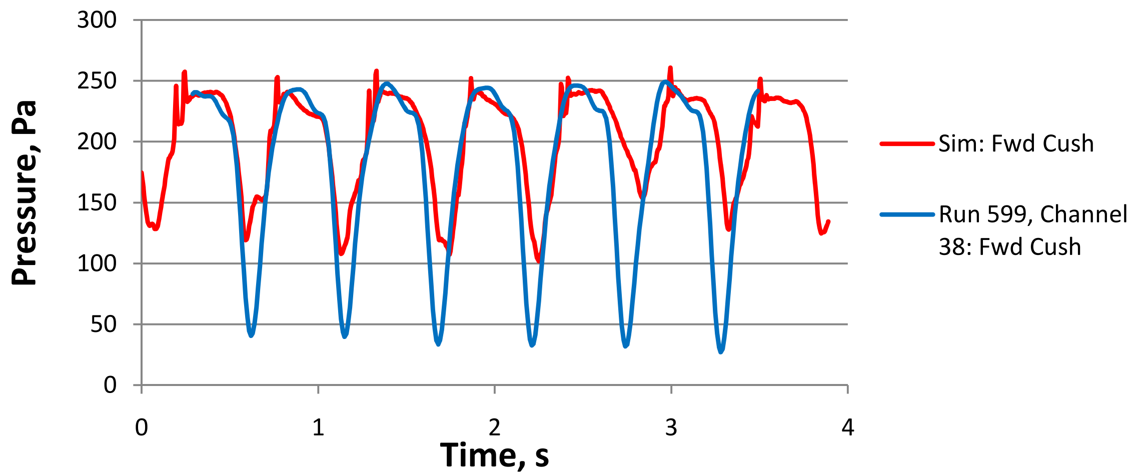

Figure 9: Forward air cushion pressure, regular waves Fn=0.6

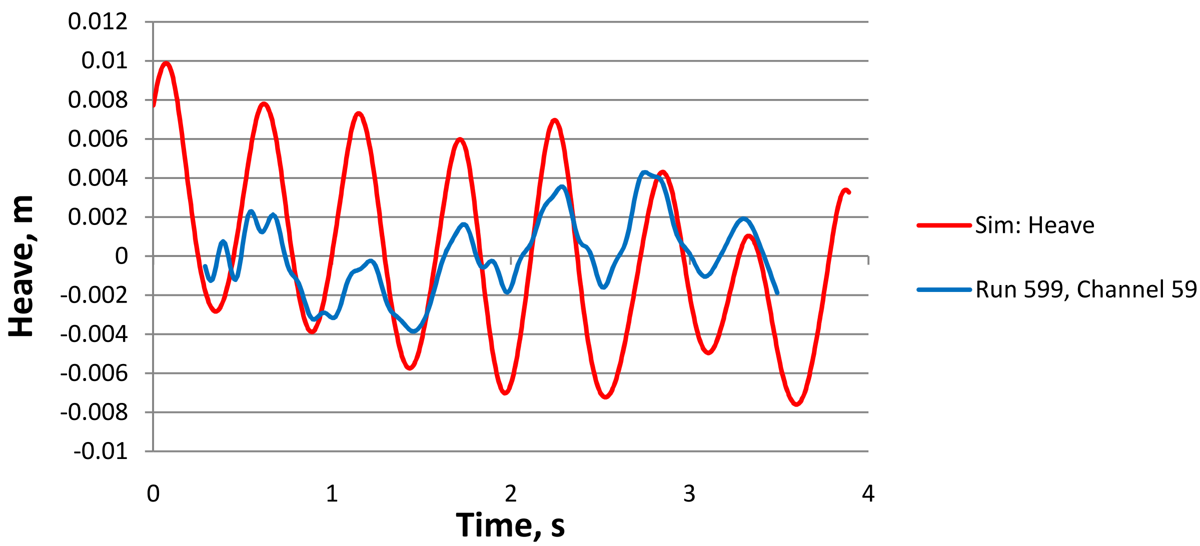

Figure 10: Heave motion amplitude, regular waves Fn=0.6

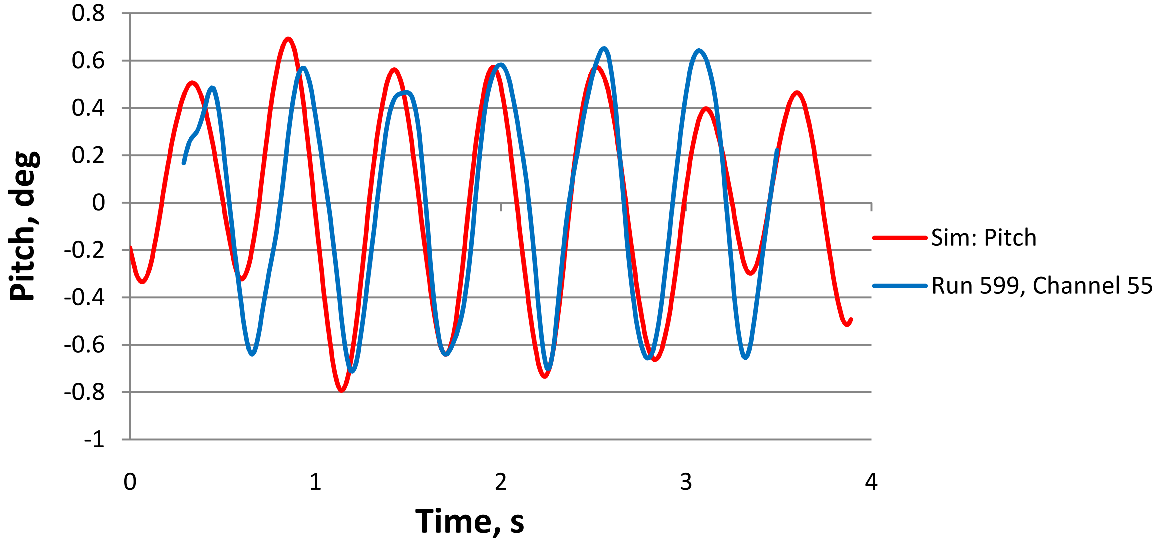

Figure 11: Pitch angle amplitude, regular waves Fn=0.6

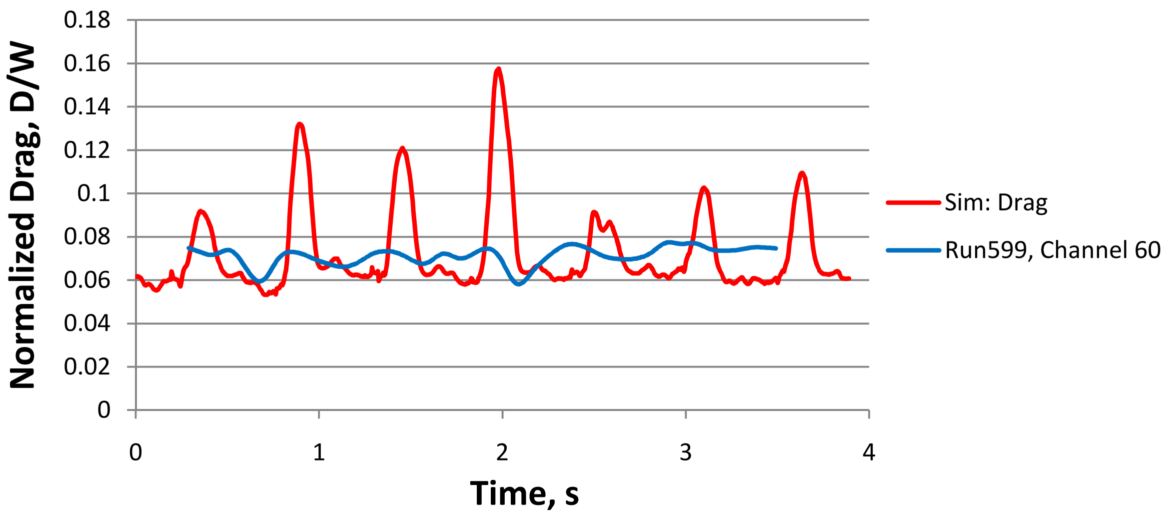

Figure 12: Drag comparison, regular waves Fn=0.6

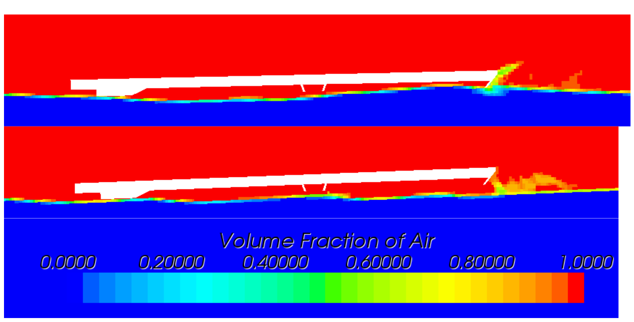

Figure 13: Volume fraction of water on symmetry plane, pitch orientations in waves

Figure 12 is a plot of the drag for both the simulation and the model test. The amplitude of the drag fluctuations for the simulation are much larger than those for the model test. The minimum drag values of the simulation match up well with the drag from the model testing, while the maximum values are much larger. Notice that the phases of the fluctuations do not agree.

After examining the free surface it is clear what causes the high amplitude peaks in drag in the simulation with waves. As a wave approaches the bow of the craft it crashes into the rigid bow seal. This causes an intense slamming force as the water pushes against the seal. This force pushes the bow of the T-Craft up and lifts it out of the water. Figure 13 shows the volume fraction of air on the symmetry plane during these two described orientations. The top of the figure shows the bow down orientation with water slamming against the bow seal. The bottom shows an event where the bow has been pushed out of the water completely, reducing the drag and allowing cushion pressure to escape. As the craft's bow slams back down to the water surface, the air cushion pressure is increased and the drag spikes. The dominant fluctuations in drag observed in the simulation are likely due to an effect not present in the physical model – that of the water impact on the rigid seals.

Figures 14 and 15 plot the fluctuation of the drag, heave, and pitch from their respective average values for the simulation and model test, respectively. The normalized drag is multiplied by a factor of 20 and the heave is now plotted in centimeters rather than meters. When comparing the the two figures it can be seen that in both, the pitch peaks and troughs occur about a half of a wavelength after the heave fluctuation peaks and troughs. The major difference between the simulation and the model test is the drag's fluctuation phase when compared to the heave and pitch. As seen in Figure 14, the drag peaks in the simulation occur right after the pitch fluctuation peak, when the craft is oriented the most bow down. In Figure 15, it can be seen that the drag peaks for the model test occur between the peaks of the pitch and heave fluctuation peaks. The reason for this is not fully understood but is likely related to the amplified motions and large forces that are cuased by the rigid seals.

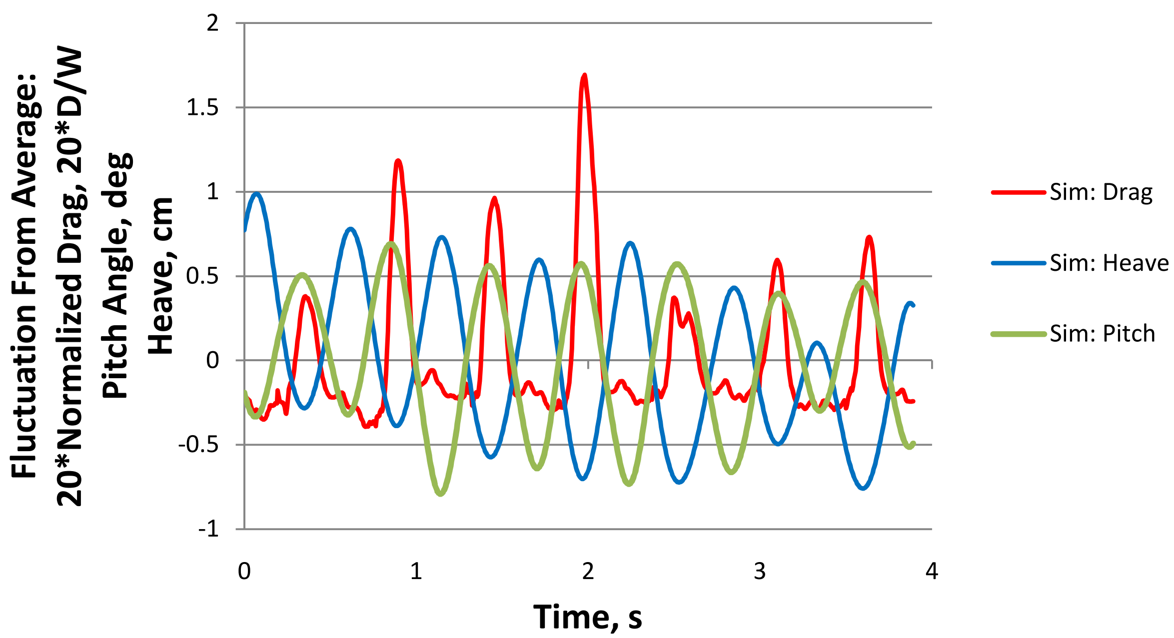

Figure 14: Drag, heave, and pitch fluctuations from average, simulation in waves

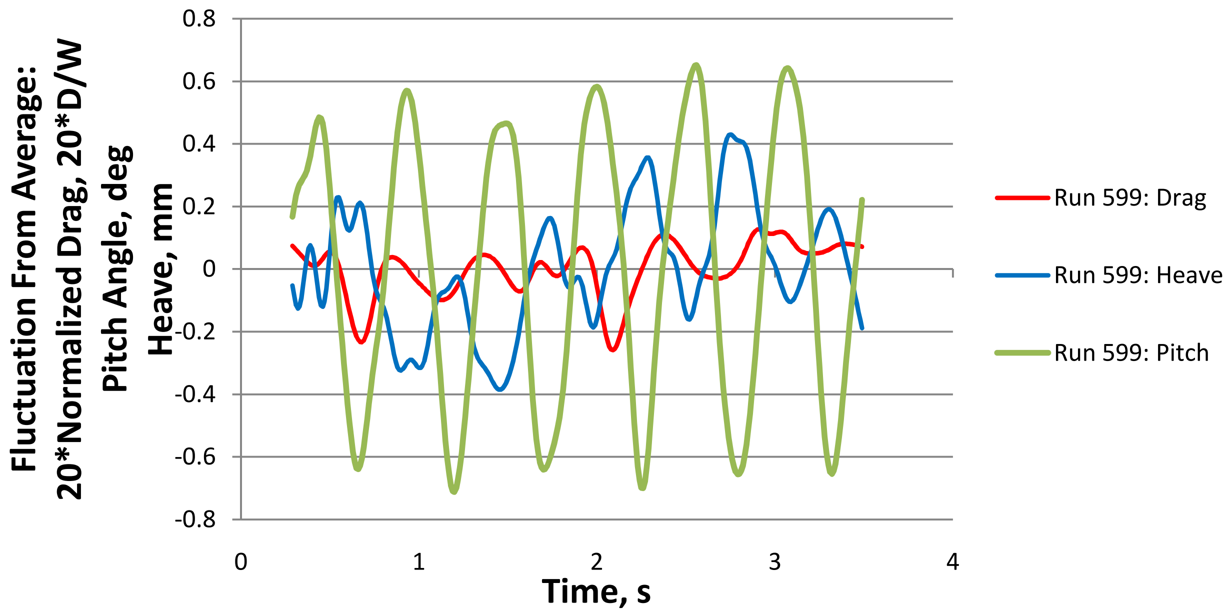

Figure 15: Drag, heave, and pitch fluctuations from average, model test in waves

CONCLUSIONS AND DISCUSSIONS

It is clear that accurately simulating the motions, forces, and free surface interactions of a surface effect ship with a pressurized air cushion using CFD is a daunting task that involves several components. While the simulations presented show the promise of current commercial CFD modelling capabilities, much more must be done to improve the accuracy of the simulations. It is believed that the largest source of error is due to the rigid seal approximations. To accurately model the forces on an SES with flexible seals, the simulation's seals must also be dynamic. Shortening the rigid seals to above the natural waterline prevents them from plowing through the water, however it may under estimate the seal drag and it leaves a large gap for air leakage. Lengthening the seals to below the waterline does not allow any air leakage and causes a gross over estimation of the seal drag. As the long, rigid seals plow through the water they cause an exaggeration of the heave movement and drag force on the craft, especially in waves. Another source of error is due to the lack of viscous effects in the simulations. Using a turbulent solver and a boundary layer mesh would reveal any turbulent structures and allow the calculation of shear drag on the hull.

After reviewing the free surface elevation contours, the complexity of the waves internal to the hull and air cushion at lower Froude is apparent. Both the amplitude and wavelength of these waves increase with speed. These waves are three dimensional and have unique interactions with the side hulls and seals at different Froude numbers. This work has proven that commercial CFD can be a useful tool in the calculation and visualization of these waves.

ACKNOWLEDGMENTS

The authors would like to acknowledge and express gratitude to the U.S. Office of Naval Research for their encouragement and financial support throughout the course of this research work.

REFERENCES

Bishop, R. C., Silver, A. L., Tahmasian, D., Lee, S. S., .Park, J. T, Snyder, L. A., and Kim, J. 2009. "T-Craft seabase Seakeeping Model Test Data Report," NSWCCD-50-TR–2009/055, Hydro-mechanics Department Report.

Star-CCM+ ver. 5.04.006 User Guide, 2010 CD-adapco.

Cooper, K. “Sea Base Enabler Innovative Naval Prototype Transformable Craft (T-Craft), SD-5 Panel Brief” 2009 Office of Naval Research.

Muzaferija,S. and Perić, M. “Computation of free-surface flows using interface-tracking and interface-capturing methods”, Chap. 2 in O. Mahrenholtz and M. Markiewicz (eds.), *Nonlinear Water Wave Interaction,* Computational Mechanics Publications, Southampton, 1998.

Silver, A. Personal communication. 2010, Ft. Lauderdale.

Yun, L. and Bliault, A.. *Theory and Design of Air Cushion Craft*, 2000, L. Yun and A. Bliault, Bath Press, Great Britain.

Seventh International Conference
On High-Performance Marine Vehicles
Melbourne, Florida, USA
13-15 October 2010

SEAKEEPING SIMULATIONS FOR HIGH-SPEED VESSELS WITH ACTIVE RIDE CONTROL SYSTEMS

Michael J. Hughes
Naval Surface Warfare Center, Carderock Division
9500 MacArthur Blvd., West Bethesda, MD 20817
Michael.J.Hughes@navy.mil

ABSTRACT

The paper examines the ability of the seakeeping simulation code VERES to assess the performance of an active ride control system for a high-speed catamaran. The paper compares two methods used to specify settings for the generic ride control algorithm in VERES, when the details of the actual controller on a vessel are unknown. The VERES predictions are compared to data from full-scale trials performed on a high-speed wave piercing catamaran. Trials were performed with both a T-foil and trim tabs actively controlled as well as with the T-foil retracted and only the trim tabs actively controlled. In addition to comparing the predicted motions with the motions measured during the trials, the ability of the simulation tool to predict the difference in motions with and without the T-foil is also assessed. When using data from full-scale trials for validation, the uncertainties relating to the direction and variability of the wave field must be accounted for. The details of the ride control algorithm and gain settings used for the catamaran were unknown, but the time history of the trim tab and T-foil deflection angles were recorded during the trials. The generic ride control algorithm inherent to VERES was used with the controller gains adjusted to match the RMS foil and tab deflection angles measured during the trials. The procedure developed to set up the generic controller algorithm for different speeds and sea states can also be applied to evaluate the effectiveness of different ride control systems during preliminary design, when details of the ride control algorithm are not yet defined.

INTRODUCTION

High-speed multihull vessels, with very few exceptions, utilize active ride control systems (RCS) to reduce motions in higher sea states. These types of vessels are commonly used as high-speed ferries where the RCS is used to improve passenger comfort. In recent years, the US Navy has also developed an interest in high-speed multihull vessels for use as intertheater transport vessels or littoral combat ships. Computational seakeeping simulation tools can be used to aid the design of these vessels and develop operator guidance for these vessels for naval applications. The RCS can have a significant influence on the vessel motions, so it is important that the computational tools accurately model the RCS. In most cases the ride control algorithms used to control deflections of the lift devices are proprietary, so while information is usually available describing the geometry of the lift devices, typically no information is available regarding the algorithm or gain settings used by an RCS. Using computational tools to predict the motions of these vessels without knowing the control algorithm or gain settings used by the RCS requires that some assumptions be made. This paper describes two methods for setting the input for a generic RCS control algorithm in the simulation tool VERES. The assumption is that if the generic RCS model produces the same RMS deflections of the lift devises as the actual RCS, reasonable predictions of the benefits of the RCS will be attained.

The methods described to estimate the control algorithm can also be used to evaluate the effect of RCS devices during preliminary design, before the details of the actual RCS are determined.

The Navy has several tools available to predict the seakeeping performance of high-speed multihull vessels, ranging from a strip theory tool (VERES) to 3-D boundary element methods (LAMP and AEGIR), and Unsteady RANS methods such as CFDShip-Iowa. These tools have been compared with model test data for high-speed catamarans and trimarans without ride control systems, and in general good correlation has been shown. Comparisons of VERES predictions to model tests for several high-speed multihull vessels can be found in O'Dea (2005). Stern et. al. (2006) show comparisons of predictions from VERES, AEGIR and CFDShip-Iowa to model test data for a high-speed catamaran. Zhang et. al. (2003) shows the correlation of LAMP predictions with model test data for the same case. There has been little work done to correlate the predictions from the tools with data for a vessel with an active RCS. The data available for the validation of the seakeeping performance of high-speed vessels with active ride control systems are very limited. Seakeeping model tests are usually performed without active ride control systems. The small size of the model-scale fins, trim tabs and/or interceptors would result in significant scaling effects, which would limit the value of including active ride control systems in model tests. Also the ride control algorithms are typically unknown. In this paper the data from the full-scale trials of a wave piercing catamaran are used to compare with the predictions from VERES.

ABBREVIATIONS

CFD	Computational Fluid Dynamics
LAMP	Large Amplitude Motion Program
MDI	Maritime Dynamics, Inc. (now part of Naiad Dynamics, Inc.)
NSWCCD	Naval Surface Warfare Center, Carderock Division
RANS	Reynolds Averaged Navier-Stokes
RAO	Response Amplitude Operator
RCS	Ride Control System
RMS	Root Mean Square

KEYWORDS

Seakeeping, Catamaran, Ride Control, CFD

MODELING RIDE CONTROL SYSTEMS IN VERES

Ride Control System Basics

The ride control system on a typical high-speed catamaran is shown schematically in Figure 1. At the stern there are a set of lift devices and another lifting device is located forward, typically about 20-30% of the length from the bow. The aft lift effectors can be either trim tabs or interceptors mounted to the transom of each hull. The forward lift effectors can be a set of fins mounted flush with each hull or T-foils mounted below each hull or a single larger T-foil mounted on a strut attached to the wetdeck on the centerline of the vessel. The foils may be either all movable or have movable flaps. A set of motion sensors consisting of accelerometers, inclinometers and rate gyros are installed to measure the motions of the ship to provide feedback to a control algorithm. The control algorithm computes the desired deflections of the lifting devices to reduce the unsteady motions of the vessel. Hydraulic or electric actuators are then used to deflect the fins, foils, trim tabs and/or interceptors. The question mark in the box representing the controller in Figure 1 indicates that the details of the control algorithm are often proprietary and therefore not available to an engineer performing a seakeeping analysis.

The VERES Program

VERES is a strip theory ship motion prediction code, developed by MARINTEK (Fathi and Hoff, 2004) and (Fathi, 2004). It implements both ordinary strip theory (Salvesen et al., 1970) as well as the high-speed theory of Faltinsen and Zhao (1991). It has the capability of handling both monohull and multihull vessel geometries. The strip theory solves frequency domain equations of motion, to obtain the transfer functions defining the response of the vessel to regular waves at a specified set of frequencies. A postprocessor is used to derive useful statistical information in irregular seas. More details on the theory and use of VERES can be found in (Fathi and Hoff, 2004) and (Fathi, 2004). A correlation study was performed (O'Dea 2005), which compared VERES predictions to available model test data for several high-speed catamarans and trimarans. The study compared mainly heave and pitch Response Amplitude Operators (RAOs) in regular head seas along with heave, pitch and roll RAOs for a limited number of oblique wave cases. The study concluded that VERES showed a "generally reasonable correlation" for these hulls. Typically the predicted RAOs were within 20% of the model test values, with VERES tending to over-predict the peak (resonant) response, particularly pitch response for the catamarans. VERES is primarily a frequency domain tool, although it includes an option to perform time domain simulations using the hydrodynamic coefficients computed in the frequency domain and including some non-linear effects. In this paper only the frequency domain capabilities of VERES are examined.

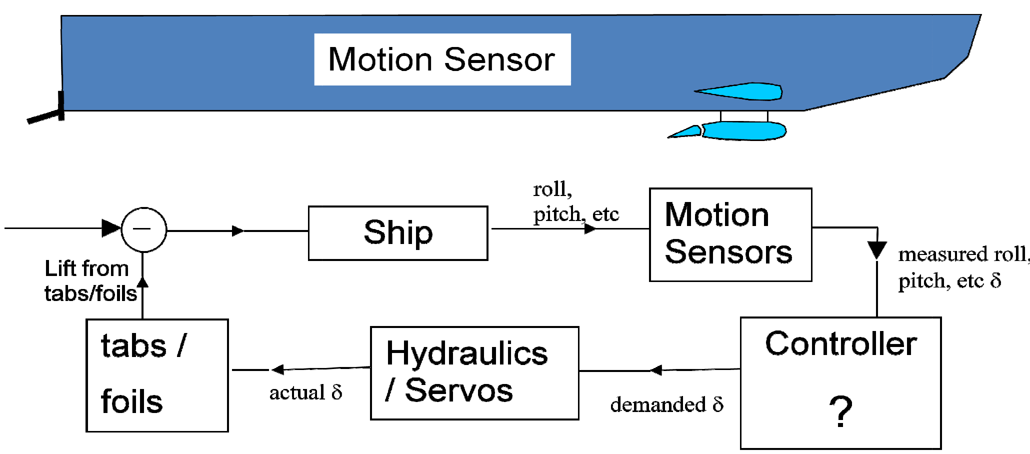

Figure 1: Schematic of typical ride control system on a high-speed catamaran

Modelling RCS lift forces in VERES.

VERES models control surfaces such as anti-roll fins, T-foils and trim tabs, by including the lift generated by these devices as point forces. The details of the flow around the control surfaces are not computed. The added mass of each device is also included based on the planform area and the formula for the added mass from a flat plate. Devices such as interceptors (vertical plates mounted at the transom), which move vertically instead of rotationally, can be approximated as equivalent hydrofoils in VERES. The lift generated by each device is assumed to vary linearly with angle of attack based on an empirical lift slope coefficient, $C_{L\alpha}$. Using this approximation the oscillating lift on each device is computed and incorporated into the predicted Response Amplitude Operators (RAOs).

$$Lift = C_{L\alpha} \tfrac{1}{2} \rho S V^2 \alpha \qquad (1)$$

$C_{L\alpha}$ can either be specified by the user or computed by VERES based on the planform area and aspect ratio of the foil. If computed by VERES, the formula derived from Prandtl's low aspect ratio airfoil theory is used:

$$C_{L\alpha} = \frac{2\pi}{1 + 2/A_s} \qquad (2)$$

where A_s is the aspect ratio of the foil (including the flaps). There is a wealth of empirical data available for estimating the lift on conventional fins and foils such as the classic work of Hoerner (1965) and the extensive study by Whicker, L.F and Fehlner L.F (1958), who developed the formula shown below which is used to estimate the values for $C_{L\alpha}$ in the current work.

$$C_{L\alpha} = \frac{(0.9)\,2\pi\, A_S}{\left(\cos\Lambda\sqrt{\frac{A_S}{\cos^4\Lambda}+4}\right)+1.8} \tag{3}$$

where Λ is the sweep angle of the quarter chord line of the foil. For foils that are not fully movable, but have movable flaps covering part of the chord, a "flap effectiveness factor", κ, is used to compute an effective deflection angle for the foil following the process described by Abbott and von Doenhoff (1959). For a typical T-foil with a movable flap covering about 35% of the total chord, a value of κ=0.65 is used. The effective angle of attack for computing the lift from Equation 1 is defined as:

$$\alpha_{eff} = \alpha + \kappa\delta_{flap} \tag{4}$$

where the angle of attack, α, is derived from the motion of the ship and the undisturbed wave orbital velocity.

Less empirical data is available for the lift generated by trim tabs and interceptors. Some studies have examined the steady force produced by a trim tab or interceptor in calm water to control trim. Savitsky and Brown (1975) derived a formulation to estimate the force on a trim tab hinged under the bottom of a planing hull. More recently Dawson and Blount (2002) developed a procedure to estimate the force on an interceptor by using the Savitsky and Brown (1975) equation for the force on a trim tab and developing a relation between the equivalent vertical movement of the interceptor plate and the deflection angle of the trim tab flap. Villa, D. and Brizzolara, S. (2009) used CFD to develop similar expressions for the forces on both trim tabs and interceptors. A background presentation prepared for NSWCCD by Maritime Dynamics, Inc, (MDI 2003b, now part of Naiad Dynamics, Inc.) on RCS simulations provided the following formula for use as a simple estimate of the lift on a trim tab:

$$C_{L\alpha} = \frac{1}{10*\left(1+\frac{1}{A_S}\right)^2}, \text{ for trim tabs per degree.} \tag{5}$$

The MDI presentation suggested using Equation 5 when more detailed CFD analysis or empirical data is not available for the trim tab, and suggested approximating the lift on an interceptor as 60% of the lift on a trim tab with an equivalent span and an aspect ratio of 2.0. In the current work, Equation 5 is used to estimate $C_{L\alpha}$ on trim tabs.

Generic Ride Control Algorithm

VERES includes the control algorithm described by Lloyd (1989) and shown in Equation 6 for a RCS device used to reduce the amplitude of the heave, roll and pitch motions. Equation 6 is used in VERES to determine the amplitude of the flap deflection angles of the ride control devices.

$$\begin{aligned}\delta = &-K_{Gz}\frac{K_{1Z}+K_{2Z}s+K_{3Z}s^2}{b_{1Z}+b_{2Z}s+b_{3Z}s^2}(\eta_3+y_Z\eta_4-x_Z\eta_5)\\ &-K_{G\phi}\frac{K_{1\phi}+K_{2\phi}s+K_{3\phi}s^2}{b_{1\phi}+b_{2\phi}s+b_{3\phi}s^2}\eta_4\\ &-K_{G\theta}\frac{K_{1\theta}+K_{2\theta}s+K_{3\theta}s^2}{b_{1\theta}+b_{2\theta}s+b_{3\theta}s^2}\eta_5\end{aligned} \tag{6}$$

where: η_3, η_4 and η_5 are the heave, roll and pitch motion respectively of the ship at the CG, y_Z and x_Z specify the distance from the CG to the vertical motion sensor, and s is the Laplace transform operator (d/dt). The remaining terms in Equation 6 are coefficients that the user must supply as input to VERES. The user must also specify which ship motions are to be controlled by each device. The options listed within VERES are vertical and relative vertical motions, and roll, pitch and yaw motions. Then, for each set of foils, the following parameters must be specified for each controlled degree of freedom (i.e. if there are two sets of foils, fwd. and aft, and they are both used to control heave, pitch and roll motions, six sets of parameters must be specified):

- Motion sensitivity, K_1
- Velocity sensitivity, K_2
- Acceleration sensitivity, K_3
- Overall Gain, K_G
- Fixed controller coefficients, b_1, b_2 and b_3

If either vertical motions or relative vertical motions are selected, the user must also input the transverse and longitudinal location of the motion sensor that measures the vertical or relative vertical motion. In the calculations presented in this paper, it was assumed that the RCS was used only to reduce pitch and roll motions, in which case the overall heave gain coefficient, K_{Gz} is set to zero. In the current work, the sensitivity coefficients (K_1, K_2, and K_3) were all set to 1.0, so the controller algorithm would be equally responsive to velocities, accelerations and displacements, and only the overall gain coefficients, $K_{G\phi}$ and $K_{G\theta}$,, were changed. The fixed controller coefficients were left as their default values, b_1=1.0, b_2=0.5 and b_3=0.05. The overall gain coefficients for controlling the pitch and roll motion, $K_{G\phi}$ and $K_{G\theta}$, are specified to achieve the desired RMS values for the deflection of each device in the specified sea state and at a specified speed and heading.

The data from the full-scale trials discussed later in this paper included the time history of the trim tab and T-foil flap deflections for each run. For the VERES calculations performed to correlate with that data, the overall gain coefficients for each device could be adjusted to match the RMS deflections recorded during the trials. For design studies, appropriate target RMS deflection values can be estimated from analysis of the foil geometry. Guidance from a study performed by Naiad Dynamics, Inc. for NSWCCD (MDI 2003a, 2003b) and more recent consultations with Naiad Dynamics (Schaub)[1] suggested the following constraints be considered when estimating the RMS deflection angles for various ride control devices:

- Trim tabs should have RMS deflection angles of 4 to 5 degrees for the typical installation. Hydraulic power constraints could limit motions at high speeds.
- Fins and foil RMS motion limits are based on estimates of cavitation inception. The CFD based cavitation inception C_L for each speed can be used as a measure of the maximum RMS value thus implying a little cavitation near the maximum angles of the simulation. A typical T-foil might be limited to about 6 degrees RMS at 35 knots and 4.8 degrees RMS at 42 knots.
- The maximum deflection angle limits based on mechanical constraints are approximately 10° for the trim tabs, 20° for the T-foils.

VERES solves the linear frequency domain equations of motion for the response of the vessel in unit amplitude regular waves at set of wave frequencies. These equations include added mass, damping and restoring force terms on the left hand side and wave exciting force terms on the right hand side. For a case without any foils or trim tabs, all the terms are computed from the hull geometry by the strip theory in VERES. The forces from the RCS devices are incorporated directly into these equations as additional added mass, damping and restoring and wave exciting force terms. The lift on a foil is assumed to be directly proportional the angle of attack, which is computed from the foil deflection, wave orbital velocities, and the velocity and orientation of the vessel. The angle of attack on the foil resulting from the vessel motion and orientation results in additional damping and restoring force terms in the equations of motion and the angle of attack on the foil resulting from wave orbital velocities results in additional wave exciting force terms. The sensitivity coefficients in the controller algorithm shown in Equation 6 determine whether the actively controlled deflection angle of the foil results in additional added mass, damping or restoring force terms. Since the foil deflection is computed using an algorithm where the deflection is linearly proportional to the vessel motion, and the vessel motion computed by VERES is linearly proportional to wave amplitude, the foil deflections and lift will be linearly proportional to the wave amplitude at each wave frequency for a given set of ride control settings. A complex transfer function can be computed to describe the deflection angle and lift force from a foil at each wave frequency as shown in Equation 7.

[1] Benton Schaub, Naiad Dynamics, Inc. (Formerly Maritime Dynamics Inc.), Private Communications.

$$\delta = \sum_{n=1}^{N} TF(\omega_n) a_n e^{i\omega_n t} \qquad Lift = \sum_{n=1}^{N} TF(\omega_n) a_n e^{i\omega_n t} \qquad (7)$$

The influence of the ride control algorithm and its associated gain settings are incorporated directly into the linear response amplitude operators (RAOs), so for a given set of gain settings, both the flap deflection angle and lift produced by a foil vary linearly with wave amplitude for a regular wave at each wave frequency. For a vessel travelling in irregular waves, this means that a RMS deflection of a foil will increase with increasing significant height, but will also vary depending on the modal period and spectral shape. If it is desired to use the control algorithm in VERES to achieve a desired RMS value for the deflection of trim tab or foil at a given speed, the gain settings would need to be adjusted for each wave spectrum encountered.

SETTING CONTROLLER GAIN COEFFICIENTS

Two methods were examined to set the input for the VERES ride control algorithm. The methods are referred to as "method 1" and "method 2" on the figures appearing later in this paper. Method 1 uses an iterative approach to manually adjust the controller gain settings, while method 2 uses the equivalent linearization option in VERES.

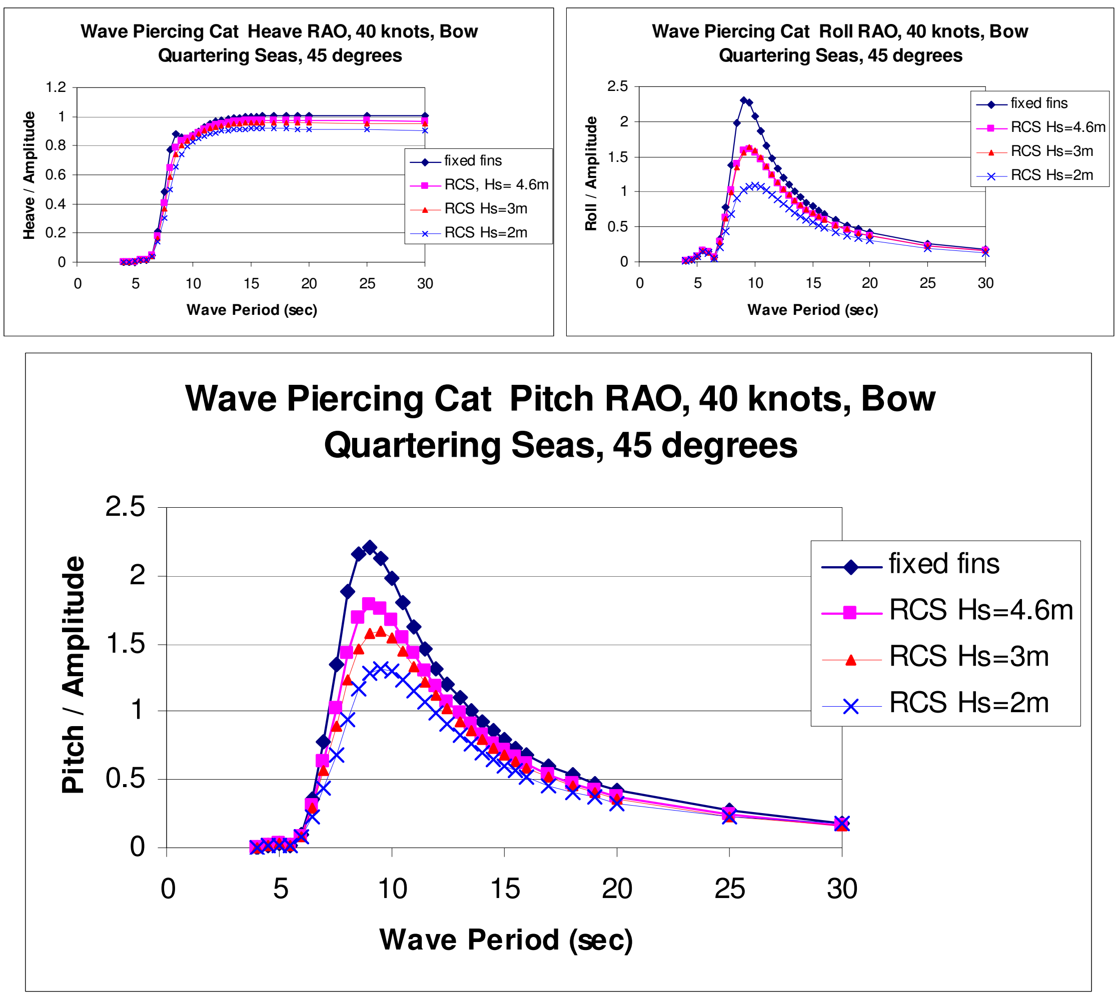

Figure 2: Comparison of heave, roll and pitch RAOs for a conceptual wave-piercing catamaran at 40 knots with gains adjusted to allow the foils to reach their RMS limits based on a Pierson-Moskowitz spectrum with Hs=4.6, Hs=3.0m and Hs=2.0m.

Method 1: the iterative approach

In this approach some initial overall pitch and roll gains are assumed and VERES is used to predict the vessel response with these initial gain settings. The VERES program does not output any statistics for the deflection angles of the foils. The RAOs computed by VERES are written to a text file as complex numbers, which preserves the phase information in the vessel response. In order to compute the RMS deflection angle of each foil, a separate program was developed. This program reads the complex transfer function for the pitch and roll motion from the VERES output and applies them to Equation 6. The output from this program provides a response function for the foil deflection. This foil deflection response function is the foil deflection angle resulting from unit wave amplitude as a function of wave frequency. The square of this function multiplied with the wave spectrum is then integrated to obtain the RMS value of the foil deflection. Using this procedure, the RMS deflection angles in head seas, bow quartering and beam seas in the wave spectrum measured during the trials were computed and the gain settings were either increased or decreased accordingly to match the RMS flap deflection angles recorded during the trials. The overall pitch gain, $K_{G\theta}$, is adjusted to match the measured RMS flap deflections in head and bow seas, the overall roll gain, $K_{G\phi}$, is adjusted to match the RMS flap deflections in beam and bow seas.
This process is repeated in an iterative manner to determine the gain settings that result in predicted RMS flap deflections that are very close to the flap deflections measured during the trials. The entire iterative process must be redone for every combination of wave spectrum and speed. Since with the linear control algorithm in VERES, the trim tab and foil flap deflection vary linearly with wave amplitude, the wave spectrum has a large influence on the gain settings, which in turn has a large influence on the predicted vessel response. This is demonstrated in Figure 2, which shows the VERES predicted heave, roll and pitch response for a conceptual wave piercing catamaran with trim tabs and T-foils at 40 knots in bow quartering seas. The gains are adjusted using "method 1" as described above to achieve the same RMS flap deflections in Pierson-Moskowitz wave spectra with significant wave heights of 2m, 3m and 4.6m. Significant variation in the predicted pitch and roll RAOs are observed depending on the wave spectrum used to determine the gain coefficients. Figure 2 indicates that the improvement in performance provided by the RCS may be significantly higher in lower and moderate sea states compared to high sea states.

Method 2: equivalent linearization

VERES performs an equivalent linearization to incorporate the effect of the maximum working angle when computing the RAOs. In "method 1" the equivalent linearization option was not used. In "method 2" the equivalent linearization moderates the trim tab and foil flap deflections to obtain the desired values in a specified wave spectrum. The equivalent linearization requires the user to input a maximum flap deflection angle and a wave amplitude, so it may be “tuned” to a specific sea state. The process is applied during the calculation of the vessel response in regular waves, and essentially adjusts the gains automatically to limit the amplitude of the sinusoidal flap deflection to the specified maximum value for a regular wave with the specified wave amplitude. This adjustment is done separately at each wave frequency. For "method 1" the gain settings are constant for all wave frequencies, and adjusted to obtain the desired RMS deflection for the specified distribution of wave energy over all frequencies (the wave spectrum), while for method 2, the gains are essentially adjusted independently at each wave frequency, to obtain the desired RMS deflection for a regular wave with the specified wave amplitude at each wave frequency. It is not obvious what wave amplitude should be specified to obtain the correct tab and foil flap deflections for a given wave spectrum. In the current study, the significant wave amplitude was specified as the input for the wave amplitude used for the equivalent linearization. The wave amplitude has a significant influence on the RAOs as demonstrated in Figure 3, which shows VERES predictions for the pitch RAO for a wave piercing catamaran in head seas at 20 knots, with the ride control input specified according to "method 2", with same specified maximum deflection angle, but different wave amplitudes. The user specifies a maximum deflection angle, which assuming sinusoidal motion for the flap, can be related to the RMS deflection by:

$$\delta_{\max} = \sqrt{2}\,\delta_{\mathrm{RMS}} \tag{8}$$

From a user's perspective method 2 is much quicker and easier than method 1, as an iterative process with manual adjustments of the gains is not required for each speed and sea state. Method 1 should result in a more accurate representation of the flap deflections corresponding to a specific wave spectrum. Figure 4 compares the predicted pitch and roll RAOs for a wave piercing catamaran with active trim tabs obtained using method 1 and method 2 for the same input wave spectrum (the spectrum shown in Figure 6a). These are also compared with the RAO predicted for the same vessel without trim tabs. Both methods achieve roughly the same reduction in the peak pitch response and method 1 shows a slightly larger reduction in the peak roll response. For large wave periods method 2 shows a much larger reduction in both the pitch and roll response, which is probably not realistic as the vessel will likely contour the waves when travelling in very long waves. If most of the wave energy is concentrated at wave periods below 10 seconds, one would anticipate the two methods to predict similar motions, while if there is significant energy at longer wave periods, some differences are expected.

CORRELATION WITH FULL-SCALE TRIALS

Comparisons are made between the VERES predictions and data from the full-scale trials for a wave piercing catamaran. The ride control system on the vessel consisted of a pair of trim tabs mounted to the transom of each side hull, and a large T-foil mounted to the wetdeck of the catamaran on the vessel centerline. The T-foil was retractable, so it could be pulled out of the water and stowed beneath the wetdeck. The T-foil had controllable flaps covering about 35% of the chord, and the T-foil strut could also be pivoted to adjust the angle of incidence. In the current analysis, only the flap motion of the T-foil is modeled. Restrictions on the distribution of the full-scale trials data prevent the details of the hull geometry of the wave piercing catamaran from being published here, and the scales on the y-axis of the plots have been removed; however, these restrictions still allow for comparisons between the trials and calculations. The heading convention is such that 0˚ corresponds to head seas, 90˚ to beam seas and 180˚ to following seas.

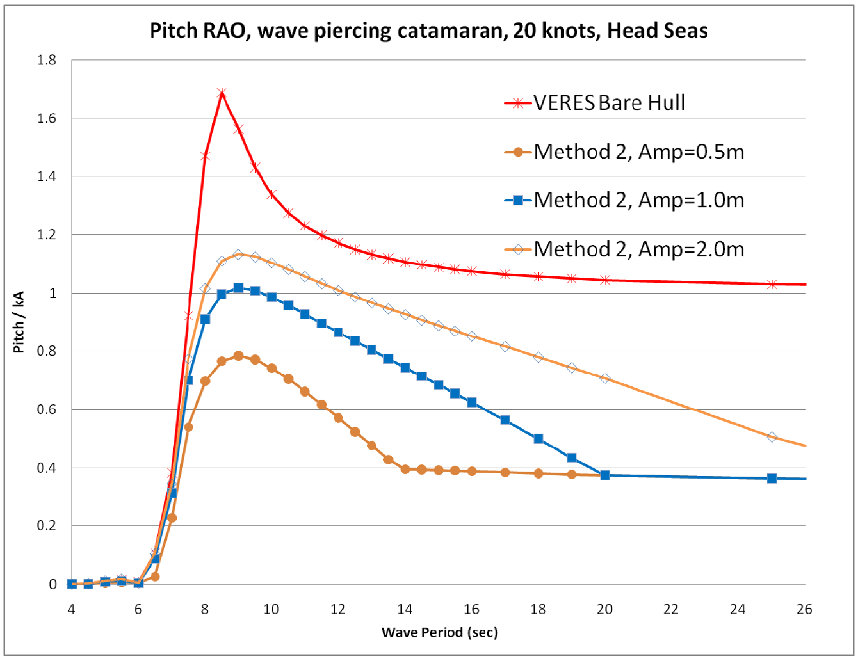

Figure 3: Influence Roll RAO in bow quartering seas for a wave piercing catamaran at 20 knots, examining two methods for specifying controller gain coefficients.

Correlation with data from full-scale trials is challenging because the description of the incident wave field encountered during the trials is not sufficient to define the incident waves for input in the computer simulation. In the current set of trials a measurement of the wave spectrum before and after each octagon was performed using a TSK wave height system installed at the bow of the ship. The TSK wave probe provides a point spectrum showing the distribution of wave energy across wave frequencies, but does not indicate the direction of the waves or amount of wave spreading or if the seas are bi-directional. The primary wave direction is observed by the operators and an octagon maneuver is performed as shown in Figure 5 to obtain data at various headings. In choosing runs to use for the correlation, the pitch and roll response as a function of heading was examined to rule out octagons where there was clearly a strong swell component to the seas in a direction other than the primary wave direction. For providing input into VERES a spectrum is formed by averaging the measured spectrum recorded at the beginning and end of the octagon maneuver. A 2-peak JONSWAP spectrum was then fitted to the spectrum, as VERES requires a theoretically defined spectrum. The resulting spectra obtained for two of the octagons from the trials are shown in Figure 6. The runs referred to as "Octagon A" corresponded to a case where the ship travelled at 20 knots in a high Sea State 4 (H_S=2.3m). The runs referred to as "Octagon B" corresponded to a case where the ship travelled at 35 knots in low Sea State 5 (H_S=2.7m). For both Octagon A and Octagon B, the T-foil was retracted out of the water and only the trim tabs were used to reduce the vessel motions. The modal period was longer during the Octagon B runs. Both spectra show a secondary peak at a shorter wave period than the modal period. As no information is available for the amount of wave spreading in the waves during the trials, a $\cos^2$ spreading function was applied assuming a 90° spreading angle in the VERES calculations. In order to investigate the influence of wave spreading, a set of simulations were performed both with purely long crested waves and with the spreading function applied. Figure 7 shows the comparison of VERES predictions, with method 1 used to set the input for the control algorithm for both the long and short crested calculations in Octagon A. The biggest influence of short crested waves is seen for the roll response in head seas and the pitch response in beam seas, but the wave spreading clearly influences both the pitch and roll at all headings.

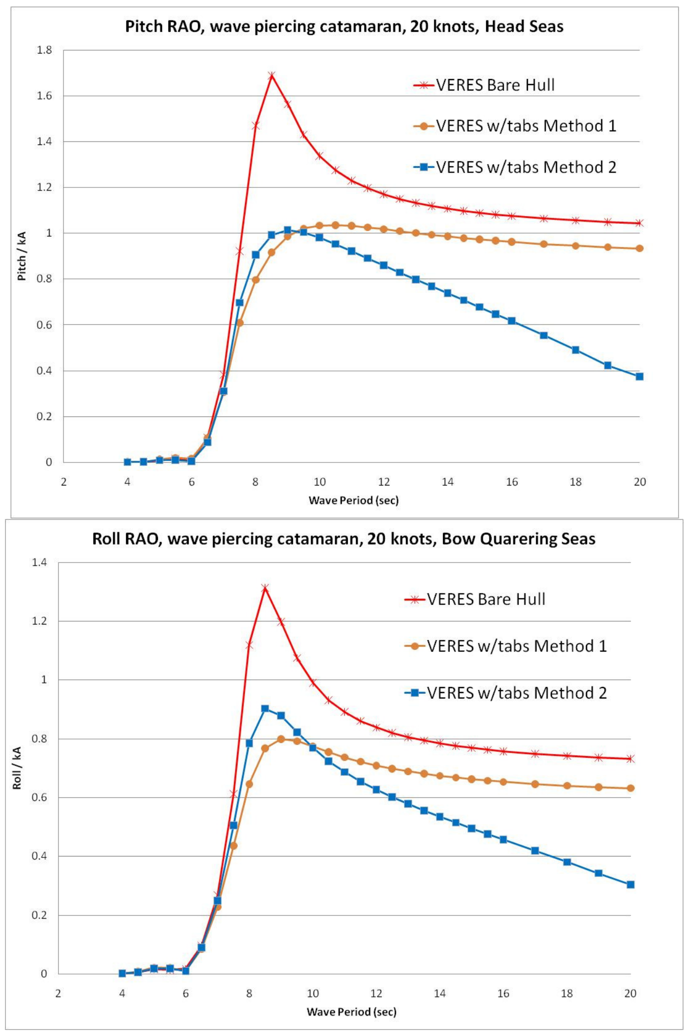

Figure 4: Pitch RAO in head seas and roll RAO in bow quartering seas for a wave piercing catamaran at 20 knots, examining two methods for specifying controller gain coefficients.

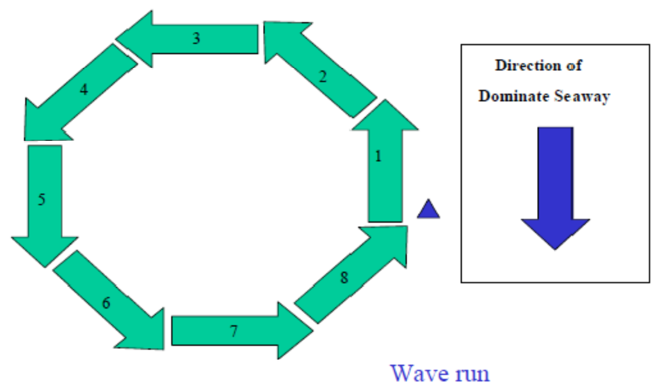

Figure 5: Octagon maneuver pattern

The comparison of the predicted motions with the trials data for Octagon A is shown in Figure 8. Results are shown for the RMS roll and pitch angle and the RMS vertical acceleration measured by an accelerometer placed near the bow of the vessel. Predictions were made for the vessel with no trim tabs (labeled "bare hull" on the plots) as well as with actively controlled trim tabs predicted using the iterative method (method 1) and the equivalent linearization method (method 2). The trials were performed with the trim tabs actively controlled. There is no trials data available for this vessel with the trim tabs locked at a fixed angle for any condition. For this case the vessel is traveling at 20 knots and the modal wave period was about 9 seconds. For the predicted response with the trim tabs active, there are only minor differences in the predicted roll, pitch, and bow acceleration using methods 1 and 2 for all the headings examined. Both methods predict reduced pitch and roll motion and larger bow accelerations with the trim tabs active compared with the bare hull response. The trials data falls between the predicted results for the bare hull and vessel with actively controlled trim tabs, with the trials data closer to predictions with the trim tabs included for most of the values, particularly for the pitch response. The same comparisons for Octagon B are shown in Figure 9. For this case the vessel is travelling at a higher speed, 35 knots, in a wave spectrum with a longer modal period of about 12 seconds. For Octagon B, there are larger differences in the predicted response obtained using method 1 and method 2 to specify the controller input relative to Octagon A. This is likely a result of the longer modal period with more wave energy at longer wave periods, as Figure 4 indicated larger differences in the RAOs predicted using methods 1 and 2 at longer wave periods. Method 1 predicts a larger reduction in the pitch and roll response and a smaller increase in bow acceleration at all headings. The trials data again falls between the bare hull predictions and the predictions with the tabs active for the pitch and roll response at most cases, with the trials data closer to the predictions obtained with the tabs using method 2.

Some additional cases were examined with the T-foil deployed and the T-foil flaps actively controlled. The goal was to examine nearly identical octagon runs with both the trim tabs and T-foil deployed and with only the trim tabs active and the T-foil retracted out of the water. This would allow for a direct comparison of the ability of VERES to predict the influence of the T-foil. There were only a few cases during the trials for which the vessel was operated at the same speed in a similar wave spectrum with the T-foil deployed and retracted. As the sea conditions vary during the trials, no two octagons will see exactly the same wave spectrum. Two octagons were examined that were performed in succession at the same speed (35 knots) first with the T-foil deployed and then with the T-foil retracted. The wave spectra corresponding to these two octagons are shown in Figure 10.

Octagon C shows the spectrum measured while the T-foil was deployed and Octagon D shows the spectrum measured while the T-foil was retracted. While the spectra are nearly the same near the peak period of around 11 seconds, there is some loss of wave energy at the secondary peak around 7 seconds. The same two-peak JONSWAP spectrum is used in the VERES calculations for the runs with and without the T-foil. The comparison between trials results and the VERES predictions are shown in Figure 11 for the pitch motion and bow acceleration. The VERES predictions used method 2 to specify the ride control settings for trim tabs and T-foils. Since the T-foil is mounted on the centerline of the vessel, the controller input for VERES is set to reduce only the pitch motions, while the trim tabs were set to reduce both pitch and roll motions. The trials data from Octagon C shows the peculiar result that the measured RMS pitch angle was higher in bow and beam seas than in head seas. This indicates perhaps that the seas were bi-directional or an error in the observed primary wave direction during the trials. The VERES predictions show the expected result that both the bow accelerations and pitch motion increase as the heading approaches head seas. The VERES predictions show the greatest benefit from the T-foil in head and bow seas. The trials indicate the T-foil has the most influence in bow and beam seas. VERES predicts a similar magnitude for the reduction in pitch motion and bow acceleration due to the T-foil being deployed.

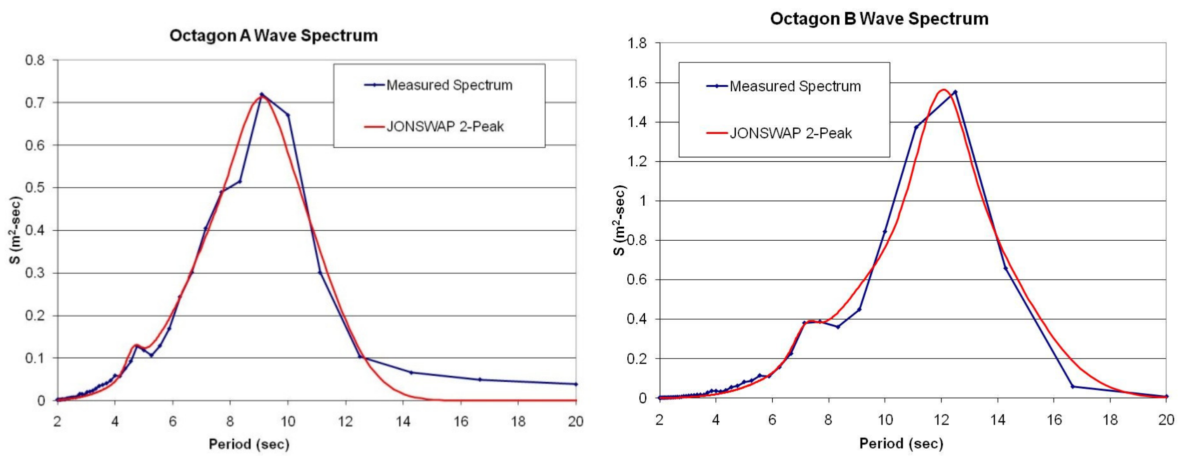

Figure 6: Measured and approximated wave spectra for two octagons examined during trials

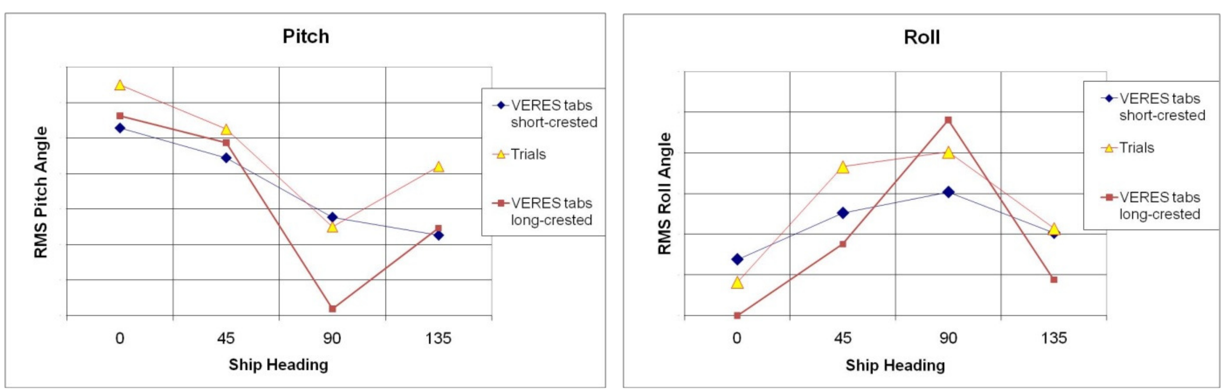

Figure 7: Comparison of predictions assuming short-crested and long-crested seas at 20 knots in Octagon A wave spectrum

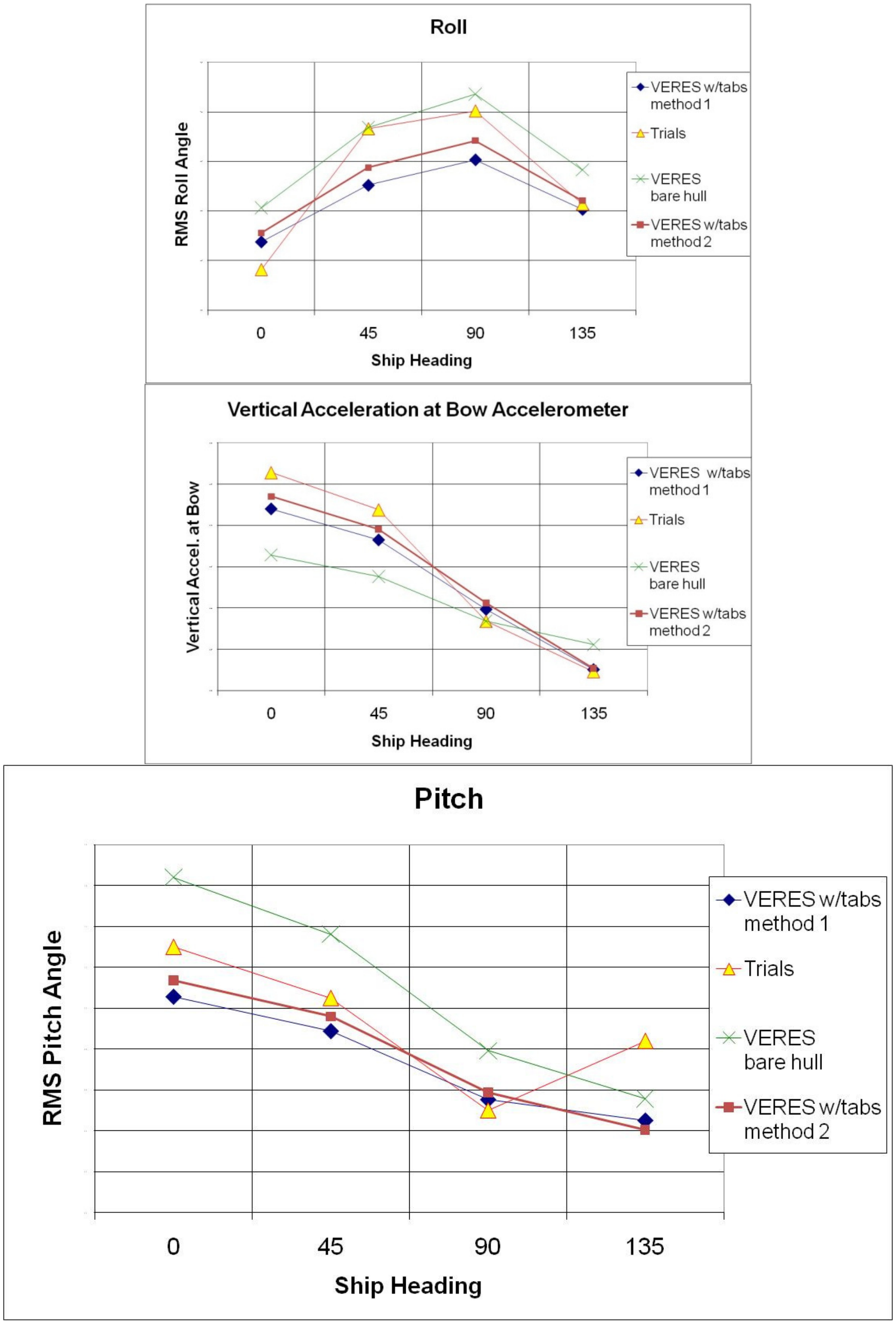

Figure 8: Comparison of predictions and trials for wave piercing catamaran with trim tabs active travelling at 20 knots in Octagon A wave spectrum with two methods for specifying controller gains.

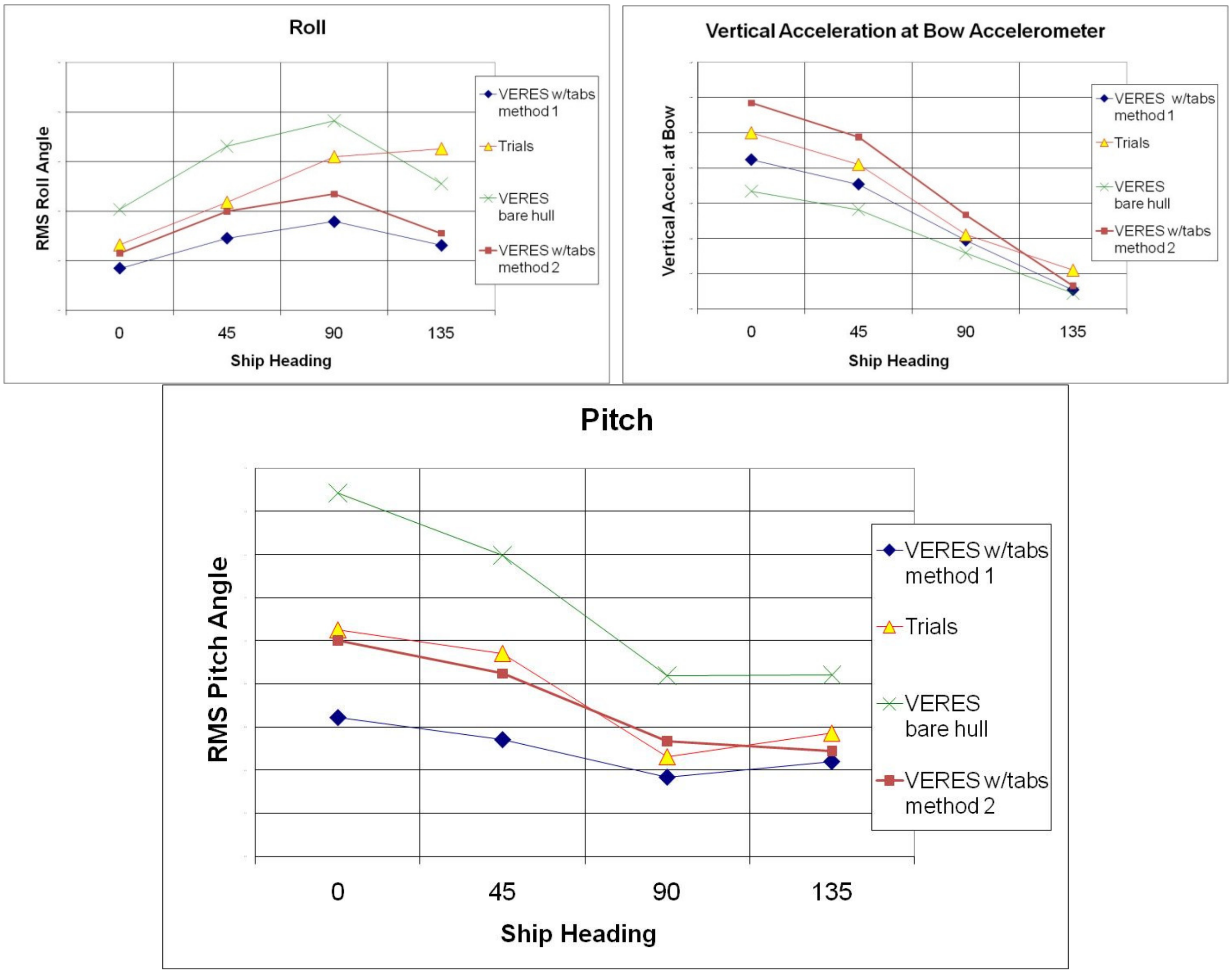

Figure 9: Comparison of predictions and trials for wave piercing catamaran with trim tabs active travelling at 35 knots in Octagon B wave spectrum with two methods for specifying controller gains.

CONCLUSIONS AND DISCUSSION

Two methods have been demonstrated for modelling the RCS for a high-speed catamaran in VERES. The two methods predict similar motions for a wave piercing catamaran in seas with a short modal period, while some differences in the predicted motions are observed in seas with a longer modal period. The VERES predictions using both methods have been compared to data from the full-scale trials for a wave piercing catamaran. While it is not possible to make any quantitative statement regarding how accurately VERES models the RCS due to limited information describing the encountered seas during the trials and a lack of trials data with the trim tabs locked in a fixed position, some qualitative conclusions can be made. Generally the VERES predictions show a significant benefit from actively controlled trim tabs and T-foils for reducing both pitch and roll motions. For the cases examined with only the trim tabs active, VERES shows reasonable correlation with the trials data for the predicted pitch response, but may over-predict the benefit of the trim tabs to control roll motion. VERES predicts roughly the correct magnitude for the reduction in pitch motion and bow acceleration from the T-foil. There are a variety of sources for discrepancies between the VERES predictions and the trials data.

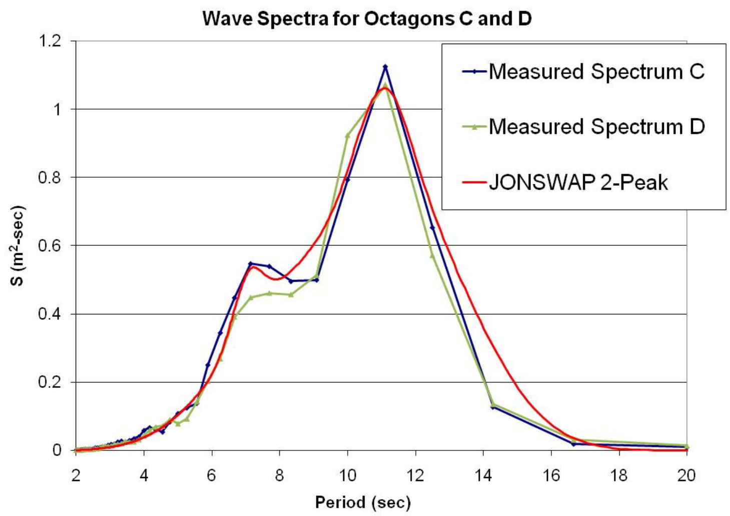

Figure 10: Comparison of wave spectra from trials for wave piercing catamaran with only trim tabs (Spectrum C) and with both trim tabs and T-foil deployed (Spectrum D).

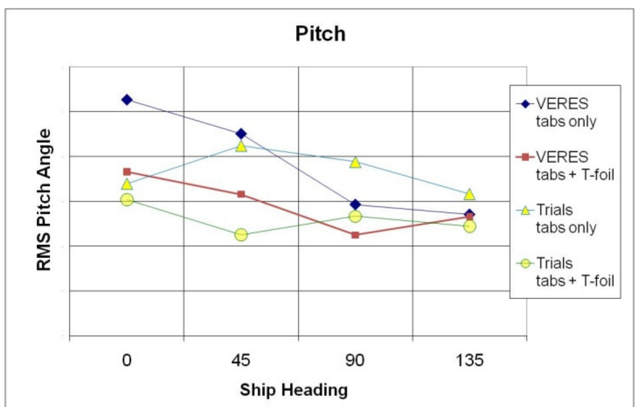

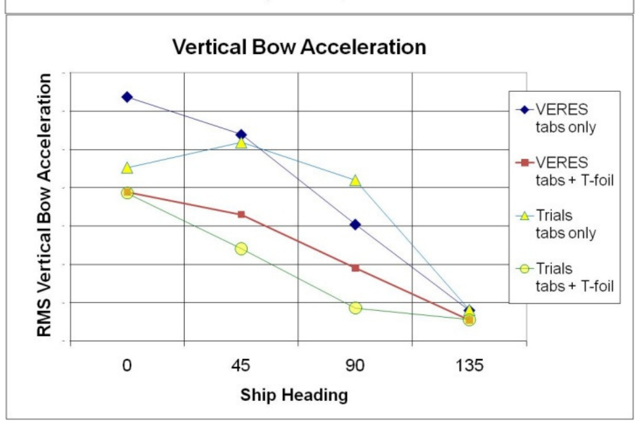

Figure 11: Comparison of predictions and trials for wave piercing catamaran with only trim tabs and with trim tabs and T-foil deployed.

Among these are:

- Differences in the incident wave field between the trials and VERES predictions.

- Assumptions made concerning the control algorithm in the VERES calculations. Perhaps the control algorithm on the actual vessel was designed to limit accelerations at specific locations instead of only reducing roll and pitch motions.
- Error in computing the lift force on the trim tabs and T-foils. VERES treats both the trim tabs and T-foil as submerged foils, assuming a lift force that is linear with the angle of attack on the foil. The angle of attack is derived from the hull motion and wave orbital velocities. Including the wave orbital velocity in angle of attack is appropriate for a submerged T-foil, but less appropriate for a trim tab flap, where the flow leading into the trim tab must be tangential to the hull.
- Errors in the VERES predictions for the bare hull vessel response. Since there is no trials data available for the bare hull, it is not possible to determine what part of the difference between trials data and VERES predictions should be attributed to errors in modelling the ride control system, and what should be attributed to errors in predicting the response of the bare hull. The wave piercing catamaran has a large wedge shaped center-bow structure under the forward wetdeck, which although above the calm water surface will enter and exit the water in waves and have an influence on the motions. A linear seakeeping tool such as VERES uses only the hull geometry below the calm water surface does not account for this feature of the hull geometry.

There are potential advantages to using a time-domain method to model vessels with RCS, such as the boundary element methods LAMP and AEGIR or the time-domain option in VERES. These advantages include the ability to incorporate non-linear control algorithms and non-linear formulae for the lift force generated by trim tabs and interceptors. In addition some of the non-linear influence of the hull geometry on the hydrostatic and wave exciting forces can also be modelled in the time-domain. A model test data set for a vessel with an active RCS would be beneficial for validating simulation tools. The model test data should include runs for both the bare hull and with the RCS installed in the same wave conditions, so that the ability of the simulation tools to predict the reduction in motions due to the RCS could be directly validated.

ACKNOWLEDGMENTS

The author would like to thank Dr. John Barkyoumb and the Naval Innovative Science and Engineering Program at NSWCCD for support of this work. The author would also like to thank Ben Schaub from Naiad Dynamics, Inc. for his guidance and advice on modeling ride control systems and Robert Bachman and Matthew Powell from the Seakeeping Division at NSWCCD for their assistance providing and understanding the full-scale trials data.

REFERENCES

Abbott, I.H. and von Doenhoff, A.E. (1959): *Theory of Wing Sections*. Dover Publications, Inc., New York.

Dawson D. and Blount D. (2002): "Trim Control", Professional Boatbuilder, No 75.

Faltinsen, O. M. and R. Zhao (1991): "Numerical Predictions of Ship Motions at High Forward Speed", *Phil. Trans. Royal Soc. London*, Vol. 334 pp. 241–252.

Fathi, Dariusz and Hoff, Jan Roger (2004): *ShipX Vessel Responses (VERES) Theory Manual*, February 2004.

Fathi, Dariusz (2004): *ShipX Vessel Responses (VERES) Ship Motions and Global Loads, User's Manual*, December 2004.

Hoerner, S.F. (1965): *Fluid Dynamic Lift: Theoretical, Experimental and Statistical Information*, Hoerner Fluid Dynamics

Lloyd, A.R.J.M. (1989): *Seakeeping: Ship Behaviour in Rough Weather*, Ellis Horwood Limited.

MDI (2003a): Maritime Dynamics, Inc., Technical Memorandum MD-R-2836-02, Rev A. "*Seakeeping Predictions for Center for Innovation in Ship Design 86M Catamaran.*"

MDI (2003b): Maritime Dynamics, Inc. Technical Memorandum MD-R-2836-01, "*Catamaran Seakeeping Simulation Program Background Introduction and Briefing*"

O'Dea, John (2005): "*Correlation of VERES Predictions for Multihull Ship Motions*" NSWCCD-50-TR-2005/021 Sept 2005.

Salvesen, N., E. O. Tuck and O. Faltinsen (1970): "Ship Motions and Sea Loads", *Transactions SNAME*, Vol. 78, pp. 250–287.

Stern, F., Carrica, P., Kandasamy, M., Gorski, J., O'Dea, J., Hughes, M., Miller, R., Kring, D., Milewski, W., Hoffman, R., & Cary, C. (2006): 'Computational Hydrodynamic Tools for High-Speed Sealift'. *Transactions SNAME*, Vol. 114.

Villa, D. and Brizzolara, S. (2009): "A Systematic CFD Analysis of Flaps / Interceptors Hydrodynamic Performance", *Proc. Tenth International Conference on Fast Sea Transportation (FAST 2009)*, Athens, Greece, pp. 1023-1038

Whicker, L.F and Fehlner L.F (1958): *Free Stream Characteristics of a Family of Low Aspect Ratio Control Surfaces for Application to Ship Design*. DTRC Report No. 933.

Zhang, S., Weems, K.M. and Lin, W.M., "A Validation Study of the Large Amplitude Motion Program (LAMP) for a High-Speed Catamaran -- Delft Catamaran 372,", SAIC Report 03-1042, December 2003

Seventh International Conference
On High-Performance Marine Vehicles
Melbourne, Florida, USA
13-15 October 2010

SUPPORT STUDIES FOR NEWCASTLE UNIVERSITY'S RESEARCH VESSEL REPLACEMENT PROJECT

Douglas Conway, David Stephens, Denis Vasiljev, Shane Neill
Newcastle University
UK
cavitation@ncl.ac.uk

ABSTRACT

Newcastle University is currently investing in a state-of-the-art 18m research vessel, which has been designed and developed by a team within the School of Marine Science and Technology. The design is based on a totally new 18m Deep-V hullform, pioneered by the School. This paper covers some of the fundamental design topics addressed by the team in the development and optimisation of the new research vessel (R/V). Undergraduate students have worked alongside the live project performing research, model testing and computational analysis. From this research some interesting results and conclusions can be drawn. The topics covered in this paper are: the comparison of calm water resistance characteristics of the new Deep-V hullform at different hull separations; seakeeping tests with comparison between computation and model tests; optimum fixed pitch propeller selection and comparison of two different wheelhouses in wind tunnel tests looking at the non- dimensional wind coefficients for drag and cross forces.

INTRODUCTION

The work presented in this paper is that of four undergraduate Marine Technology Students at Newcastle University, who worked alongside the live design project, running model test verifications in the University's own research facilities to help provide more information to the project overall. This paper is presented in four parts; calm water resistance analysis, propulsion analysis, seakeeping analysis and wind resistance analysis. Within each part the authors have presented the major findings from their undergraduate projects (Vasiljev (2010), Neill (2010), Stephens (2010) and Conway (2010)) in support of the main design study of the new research vessel, which is described in a separate paper of this conference (Atlar et al, 2010).

NOMENCLATURE

A_F	Frontal Area
A_L	Lateral Area
B/T	Beam-draft ratio
C_B	Block coefficient
C_C	Non-Dimensional Cross Force Coefficient
C_D	Non-Dimensional Drag Force Coefficient
C_{FITTC}	ITTC 1957 ship-model correlation line
C_P	Prismatic coefficient
C_a	Non-Dimensional resistance allowance
C_R	Residuary-resistance coefficient
C_T	Total-resistance coefficient
C_W	Wave-resistance coefficient
C_X	Non-Dimensional Coefficient in X direction
C_Y	Non-Dimensional Coefficient in Y direction

F_n	Froude number
Hz	Hertz
J	Advance Coefficient
K_Q	Torque Coefficient
K_T	Thrust Coefficient
Kn	Knots
L/B	Length-beam ratio (demihull)
LOA	Length Overall
Lwl	Waterline Length
s	Demihull Separation
P_B	Brake Power
$P_{B(In)}$	Installed Brake Power
P_D	Delivered Power
P_E	Effective Power
Q	Torque
RAO	Response Amplitude Operator
R_n	Reynolds number
R_T	Total resistance
S	Wetted-surface area
T	Thrust
V	Velocity
X	Force in X Direction
X_3	Heave
X_5	Pitch Angle
Y	Force in Y Direction
ε	Heading Angle
g	Acceleration due to gravity
s/L	Demihull separation-length ratio
$1+k$	Form factor
kW	Kilowatt
m	Metres
t	Tonnes
η_D	Propulsive Efficiency
η_H	Hull Efficiency
η_O	Propulsor Efficiency
η_R	Relative Rotary Efficiency
η_S	Shaft Efficiency
ρ	Air Density
ρ	Water density
Δ	Displacement weight
u	Air Velocity
ζ	Wave Amplitude

ABBREVIATIONS

BAR	Blade Area Ratio
CFD	Computational Fluid Dynamics
DVC	Deep-V Catamaran
ITTC	International Towing Tank Conference
ITU	Istanbul Technical University
NPL	National Physics Laboratory
RPM	Revolutions Per Minute
rps	Revolutions Per Second
UNEW	Newcastle University
VWS	Berlin Model Basin

KEYWORDS

Catamaran, Resistance, Wave Resistance, CFD, Air Resistance, Research Vessel, Seakeeping, Propeller Selection, Deep-V.

CALM WATER RESISTANCE – NUMERICAL ANALYSIS

Based on previous intensive research conducted by Newcastle University, a Deep-V hullform was proposed for the new research vessel. The addition of a tunnel stern and a unique anti-slamming bulbous bow further enhanced this hullform by lowering the shaft angle and reducing the risk of damaging the propeller, as well as enhancing flow over the propeller to improve propulsive efficiency. To validate the choice of hullform, comparisons were made with four suitable and appropriate alternatives.

Initially, for purposes of the comparison, the four different hullforms were modelled in *FormSys MaxSurf 14* software. These models were then assessed in *Flowtech Shipflow 2.4* CFD code. The software is potential flow based and was used only for the comparison of the hullforms, however, it showed relatively good results when compared to the model test results obtained at a later stage.

The four proposed hullforms for comparison are presented in Figure 1 and their general particulars are given in Table 1. The individual hullforms may be described as follows:

- **DVC BB** – Deep-V Catamaran with Anti-Slamming Bulbous Bow - This was the design hullform and was mainly a modified Deep-V form.
- **DVC** – Deep-V Catamaran. This hullform was produced by removing the bulbous bow from the design hullform whilst other parameters were not changed.
- **NPL** – Pure NPL series round bilge hullform given by Bailey (1976).
- **NPL BB** – NPL with bulbous bow hullform. The hullform is a modified NPL series hull based on the results published by Danisman et al (2001).

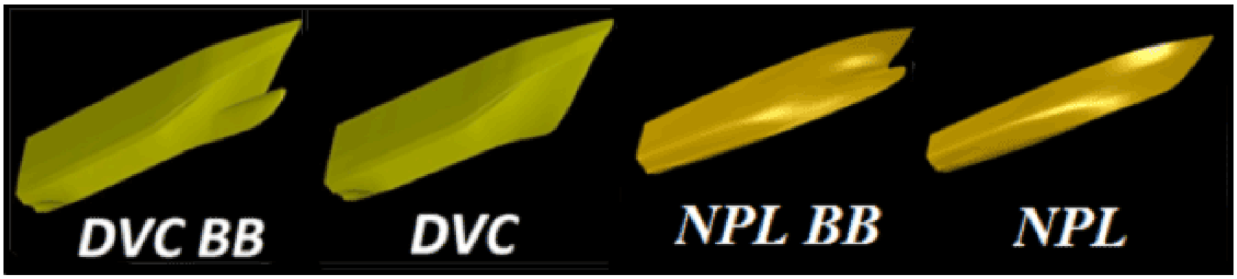

Figure 1: Modelled Hullforms used in Design Study

Table 1: General Particulars of Produced Models

Hullform Comparison [demihulls]				
	DVC BB	**DVC**	**NPL BB**	**NPL**
Δ [t]	18.007	17.016	18.188	18.022
∇ [m^3]	17.568	16.601	17.744	17.582
T [m] (Extreme)	1.63	1.66	1.255	1.23
WSA [m^2]	52.537	48.035	48.718	45.959
%WSA	100%	91.4%	92.7%	87.5%
LWL [m]	16.469	16.47	16.721	16.782
BWL [m]	1.964	1.965	2.025	1.923
L/B	8.39	8.38	8.26	8.73
C_B	0.333	0.310	0.421	0.443
LCB from transom % Lwl	49.008	46.067	47.387	41.624
LCF from transom % Lwl	42.660	42.649	43.066	41.839

Models were made to be approximately the same displacement except the DVC, which was made to mainly show the resistive effect of the anti-slamming bulbous bow and hence a similar draft to the DVC BB was retained. The linear solver in the CFD code was used to predict the wave making resistance in the free trim and sinkage condition. This provided faster and more stable convergence, and a larger speed range available for assessment than with the non-linear solver. The interaction effect between the demihulls was also considered.

It is notable how disadvantageous the conventional round bilge hullform (NPL) is when compared to the modified NPL BB and Deep-V hulls at pre-planing speeds as shown in Figure 2. The designed hullform shows a well-expressed lower Cw at the middle of the displacement speed (Fn = 0.4– 0.55). As can be seen in Table 2, a reduction of 25.7% can be seen for the design speed (Fn = 0.6) compared to NPL. Compared to the NPL BB and DVC hullforms, a drop of 4.5% is observed. At the maximum speed (Fn = 0.8) the designed hullform becomes disadvantageous in wave-making compared to the DVC and NPL BB hullforms.

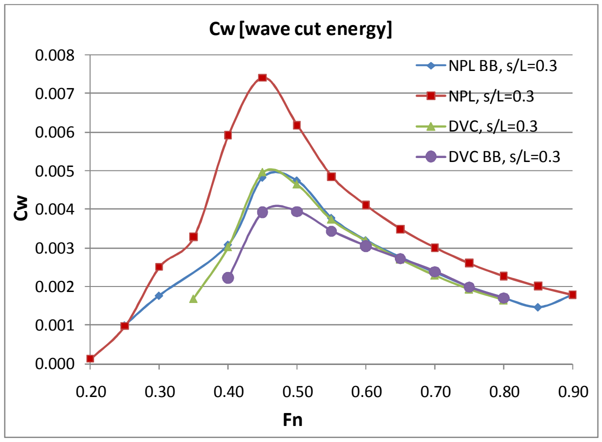

Figure 2: Wave Cut Energy Coefficient

Table 2: Relative Cw Comparison

Relative drop in Cw for DVC BB hullform comparing to other three hullforms						
	Fn	**0.45**	**0.50**	**0.60**	**0.70**	**0.80**
Cw (wave cut energy)	**DVC**	20.7%	14.9%	4.4%	-4.4%	-3.1%
	NPL	46.9%	36.0%	25.7%	20.6%	25.2%
	NPL BB	18.5%	16.7%	4.5%	-1.4%	-0.4%

The designed hullform is eminently suited to the research vessel market due to the lower wave-making characteristics at medium speed. For the designed vessel (Lwl = 16.47 m) Froude number 0.6 corresponds to 15 knots, while for a vessel of 30m long, it results in a speed of 20 knots.

MODEL TESTING AND EXTRAPOLATION TO FULL-SCALE

The model (Figure 3) was fabricated at 1:12 scale, resulting in a LOA = 1.5m. It was tested in Newcastle University's towing tank covering the full range of operational speeds. Numerous runs were made to investigate the hydrodynamic characteristics of the designed hullform at different speeds and hull separations.

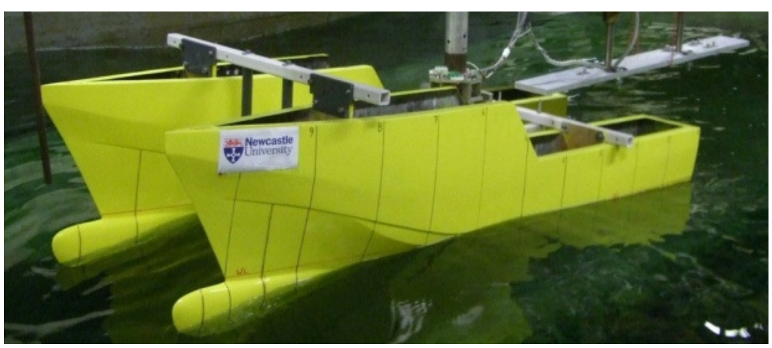

Figure 3: Newcastle DVC BB Model

The model was tested at 3 demihull separations: s/L = 0.24, 0.3 & 0.36. These values were chosen as this represented a one metre shift at full scale. As shown in Table 3, separation has the greatest effect at a medium speed. Comparing experimental results it was seen that resistance was affected by around 6.8% either way at the design speed and 4-4.8% at the maximum speed. The total resistance decreased with increased separation in all cases, reaching saturation at a higher speed. The design separation s/L = 0.3 (4.941 m) was chosen as it was the largest possible for the optimal operational condition considering cost and structural implications.

Table 3: Relative Resistance Comparison for Different Separations

Relative resistance comparison between Design separation (s/L=0.3) and alternatives			
Speed, Fn		**0.60**	**0.80**
s/L	**0.36**	-6.7%	-4.8%
	0.24	6.8%	3.8%

Initially the form factor was derived by using a *Fluent* code that employs a RANS solver. The result was: 1+k=1.51. This was proved to be correct by experiments with a result of 1.5.

Using C_R values derived from model tests (Figure 4) and based on ITTC procedures (Equation 1), extrapolated full-scale results were produced.

$$C_T = C_R + C_{f\_ITTC}(1+k) + C_a + C_{app} \tag{1}$$

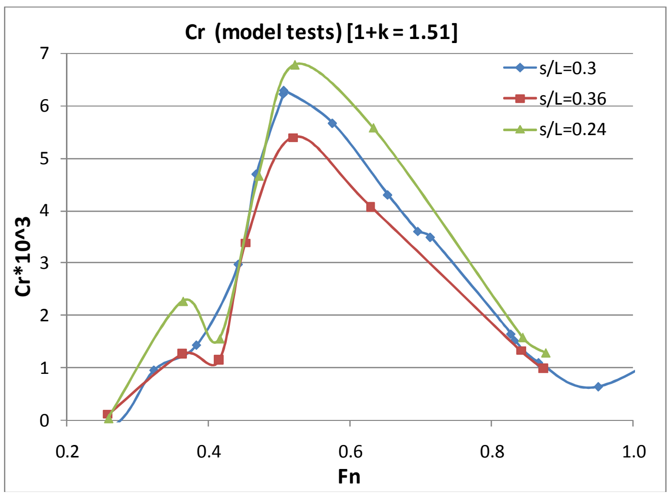

Figure 4: Residual Coefficients (derived from model testing)

The Extrapolated total resistance coefficient and a predicted effective power curve for the three separations can be seen in Figures 5 & 6.

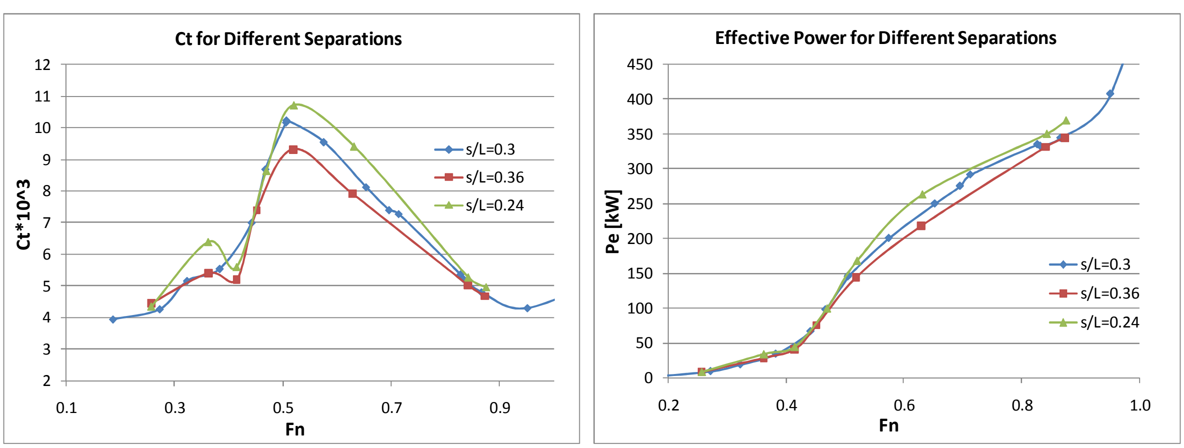

Figures 5&6: Predicted Total Resistance Coefficient and Predicted Effective Power for Different Separations

Results were corrected for a shallow water effect using Schlichting's chart (Lewis 1988), which mainly had an effect at higher speed (Fn > 0.75). Appendage resistance was included using Holtrop & Mennen's empirical method (Holtrop and Mennen 1982). This has taken into account the shaft, shaft brackets, propeller, skeg and rudder. Finally a model-ship correlation allowance coefficient ($C_a = 0.4x10^{-3}$) was introduced to take other resistance factors into account.

In summary, the analysis resulted in a predicted effective power of 220 kW at the design speed of 15 knots (Fn = 0.6) and 340 kW for a maximum speed of 20 knots (Fn = 0.8).

PROPULSION ANALYSIS

As stated in the main design study (Atlar et al. 2010), the mission profile of the new research vessel requires it to achieve a maximum speed above 20 knots and a cruising speed of 15 knots, yet to provide a reasonable pulling power at speeds less than 5 knots. A preliminary decision on the main engines indicated two 610 HP (455 kW) Cummins diesel engines with 800mm maximum diameter fixed pitch propellers. In this analysis the effective power curve was selected based on model tests conducted at the ITU towing tank with a large (3.5m) model, as well as the wake fraction and thrust deduction fraction as reported in ITU (2010). In order to meet the basic requirements, a suitable fixed pitch propeller analysis was conducted through the use of the Wageningen B Series in conjunction with BP~δ diagrams and associated calculations to calculate optimum propeller efficiency, optimum RPM and optimum pitch/diameter ratio for the chosen design speed of 15 knots. To complete the procedure, the extent of cavitation was checked using the relevant Burrill diagram. A total of nine different propellers were selected and analysed. The candidate propellers ranged from 3 to 5 blades all with varying Blade Area Ratios (BAR). The propeller diameter was fixed due to the geometry of the hull at 800mm in this preliminary analysis though this would need to be further checked for the possibility of excessive hull vibrations.

Further to the mission requirements, the performance of each propeller was analysed at different speeds to establish the overall performance in each case. Inevitably there was a large variation between the optimum conditions for each speed and each propeller, requiring a carefully judged compromise offering the best overall performance to be made. Although no particular attention was given in this analysis, the requirement of a minimum 3t bollard pull further compromised the propeller design as discussed in the main design study, Atlar et al (2010). Ultimately, as the vessel is to have a design speed of 15 knots, the optimum fixed pitch propeller was principally designed to reflect this. An additional check was made to ensure that the vessel would have sufficient reserve power for the other machinery and scientific equipment onboard. The preliminary analysis indicated that the most efficient propeller design was the B5.75. That is to say a 5 bladed propeller from the Wageningen B series with a BAR of 0.75. Table 4 shows the propeller advance, thrust and torque coefficients, propulsive efficiency and delivered power for the B5.75 at a fixed pitch/diameter ratio of 1.05 and corresponding speeds.

Table 4: B5.75 Performance Characteristics

V (knots)	P/D	η_O	J	K_T	$10K_Q$	η_D	P_D (kW)	n (rps)	N (RPM)
5	1.05	0.671	0.796	0.182	0.3318	0.649	3.42	3.7	219.3
10	1.05	0.637	0.707	0.213	0.3770	0.588	46.84	8.4	502.9
15	1.05	0.628	0.692	0.221	0.3876	0.602	176.83	12.9	775.8
20	1.05	0.665	0.758	0.188	0.3404	0.648	279.45	15.7	943.6

For a final analysis of this propeller, the pitch/diameter ratio was varied from 1 – 1.15 for the entire speed range from 5 – 20 knots. Table 5 below shows the data related to this.

The results for the theoretical optimum propeller design characteristics are presented in Table 5 which includes the efficiency coefficients, torque and thrust values, effective power, installed power and RPM for each speed. A preliminary blade area check based on the Burrill's criteria indicated that the selected blade area ratio would present a risk of cavitation beyond the cruising speed of 15knots, thus requiring further analysis. This was not conducted due to the preliminary nature of this study, although rigorous cavitation analysis was conducted using a suitable lifting surface code in the main design study mentioned earlier.

Table 5: Variation of Pitch/Diameter Ratio

V (knots)	P/D	η_H	η_R	η_O	η_D	T (kN)	Q (N-m)	P_D (kW)	$P_{B(in)}$ (kW)	N (RPM)	Calc BAR
5	1.15	0.983	0.983	0.674	0.652	1.1	169.9	3.8	4.3	212.1	
6	1.15	0.973	0.983	0.681	0.651	1.5	229.6	6.0	6.8	250.8	
7	1.15	0.962	0.983	0.680	0.643	2.0	321.4	9.9	11.3	295.6	
8	1.15	0.951	0.983	0.673	0.629	2.9	453.3	16.4	18.6	345.8	0.326
9	1.1	0.945	0.983	0.661	0.614	4.1	610.7	26.4	29.9	412.5	0.383
10	1.1	0.939	0.983	0.637	0.588	6.3	920.3	46.9	53.1	486.4	0.517
11	1	0.925	0.983	0.606	0.551	10.1	1351.6	88.4	100.3	624.8	0.654
12	1	0.920	0.983	0.604	0.546	12.4	1654.2	119.4	135.4	689.5	0.735
13	1.05	0.926	0.983	0.610	0.555	14.0	1941.3	145.3	164.7	714.7	0.814
14	1.05	0.950	0.983	0.618	0.577	14.9	2078.3	162.8	184.6	748.0	0.837
15	1.05	0.974	0.983	0.628	0.602	15.5	2176.6	176.8	200.5	775.8	0.856
16	1.05	0.989	0.983	0.637	0.619	16.2	2290.0	193.3	219.2	806.1	0.861
17	1.05	0.993	0.983	0.645	0.630	17.0	2414.6	212.1	240.5	839.0	0.864
18	1.1	0.997	0.983	0.652	0.639	17.9	2640.2	233.3	264.6	844.0	0.929
19	1.1	0.997	0.983	0.659	0.646	18.7	2782.2	255.2	289.4	876.0	0.936
20	1.1	0.991	0.983	0.667	0.650	19.5	2924.6	279.4	316.8	912.3	0.948

In conclusion of these findings, the maximum delivered power for 20 knots (top design speed) is 279.45 kW per shaft. The required installed power for this condition is 316.84 kW and as the proposed engines have a maximum output of 449 kW each, there is clearly sufficient surplus power available with the possibility of increasing the maximum speed beyond 20 knots, subject to further propeller analysis.

SEAKEEPING NUMERICAL ANALYSIS

In this section a comparison is made using the heave and pitch data for the design hullform from both TRIDENT FD-Waveload, a panel based software, and the model testing completed in Newcastle University towing tank on a 1:12 scale model. Data for a round bilge (NPL hull, Figure 1) was also modelled using numerical methods enabling the relative performances of the hulls to be compared and the software to be evaluated.

TRIDENT-FD Waveload was chosen as the software is capable of predicting hull motion, hull pressure distribution and sea loads on ships, both with single and multi hulls. It uses a potential flow, three-dimensional panel-method based on a zero speed Green function with forward speed corrections in the frequency domain (Martec 2009). Of interest to this study is the software's ability to produce regular waves and then predict the hull motions in 6 degrees of freedom; other functions may be used in further tests. Once a series of offsets had been produced for the hull, a sensitivity study was conducted to investigate the effect of changing the panel size on both RAO results and calculation times. The number of panels was varied between 70-4198 per hull giving a range of results, from which 240 panels per hull was chosen as being optimal, as increasing the number of panels had little effect other than to increase calculation time.

Numerical analyses were conducted on both hull shapes in regular sinusoidal waves, varying heading, ship speed and wave frequency following the parameters in Table 6. The heave and pitch results were then plotted as m/m and deg/m respectively against increasing wave frequencies, as shown in Figs 7 to 14, including the comparisons with the model tests.

Table 6 : Seakeeping Test Parameters

Ship Speed	Wave Frequency	Wave Heading	Wave Amplitude
0-20 Kn	0.5-4.0 rad/s	0 and 180 Deg	1 Meter
5 Increments	20 increments	2 Increments	1 Increment

SEAKEEPING MODEL TESTS AND COMPARATIVE RESULTS

The 1:12 scale model was tested in the Newcastle University towing tank in a series of experiments simulating speeds from 0-15 knots and a range of wave frequencies as shown in Table 7. The waves were created using paddle wave makers placed at one end of the tank. The model was towed into or away from the waves and a dynamometer was used to measure the heave and pitch of the vessel.

Table 7: Seakeeping Wave Frequencies

Full Scale Speed (knots)	Froude Number	Model Speed (m/s)	Full Scale equivalent wave frequencies (Rad/S)	Model wave frequencies (Hz)
0	0.00	0.00	0.7-3.2	0.4-1.8
0	0.00	0.00	0.9-3.6	0.5-2.0
15	0.61	7.72	0.7-2.5	0.4-1.4
5	0.20	2.57	0.7-2.2	0.4-1.2

CFD modelling produced a series of results comparing the NPL round bilge hull and the Deep-V hull as shown in Figures 7 to 10.

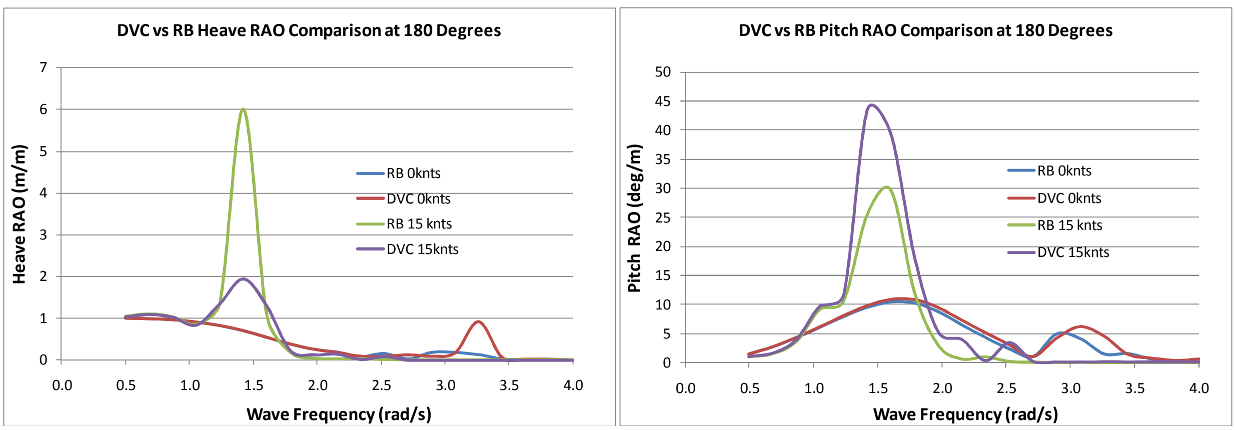

Figures 7 & 8: Heave and Pitch Comparison of Deep-V and Round Bilge at 180 Degrees (Head Waves)

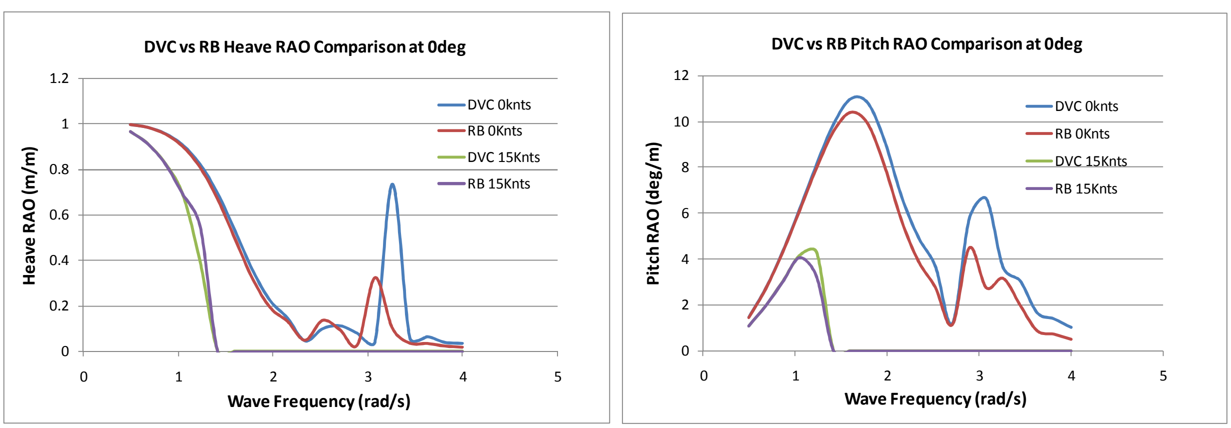

Figures 9 & 10: Heave and Pitch Comparison of Deep-V and Round Bilge at 0 Degrees (Following Waves)

Comparing the results of the model testing to the computed predictions, the validity of the predictions can be noted in Figures 11 to 14.

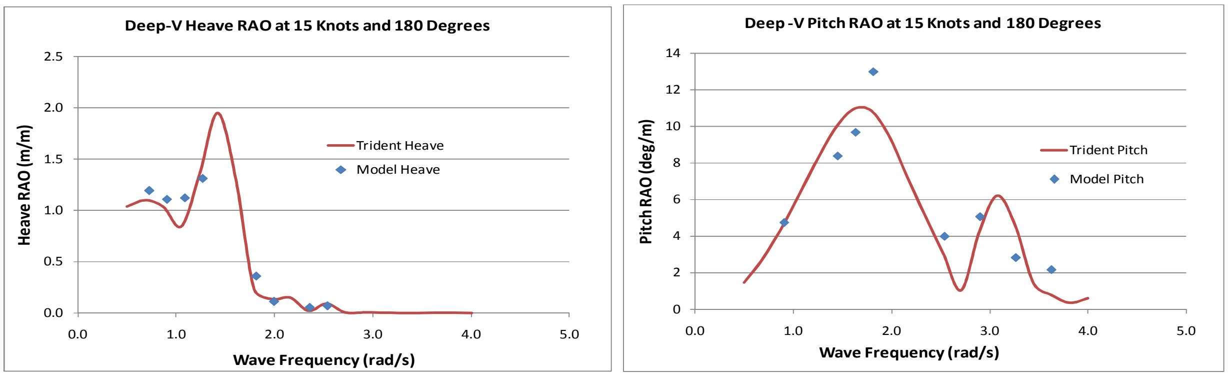

Figures 11 & 12: Deep-V Heave and Pitch RAOs at 15 Knots and 180 Degrees (Head Waves)

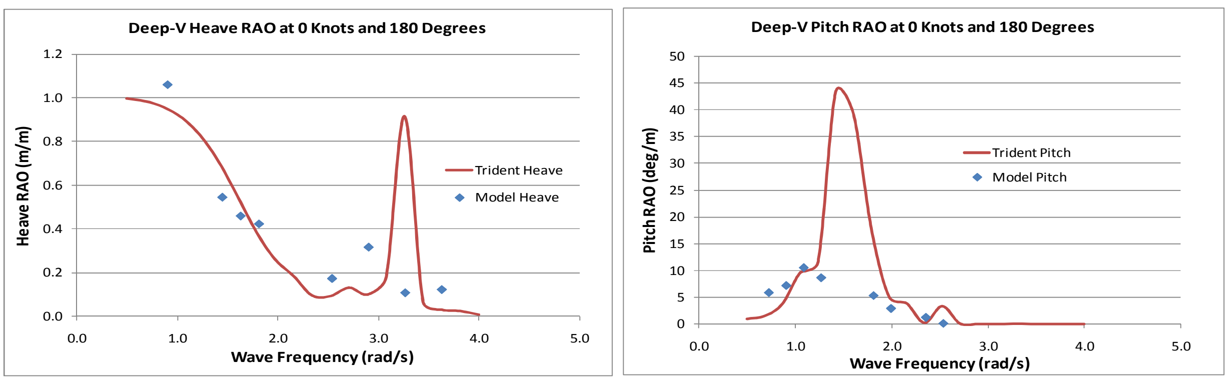

Figures 13 & 14: Deep-V Heave and Pitch RAOs at 0 Knots and 180 Degrees (Head Waves)

When comparing the results from the numerical analysis of the two hullforms, overall the Round Bilge hull appeared to be marginally kinder, having very slightly lower motions in following waves and a better pitch response in head waves, but a worse heave response. It must be remembered though, that the Round Bilge has a fuller block coefficient as well as a beneficial B/T ratio in order to equal the displacement of the Deep-V hull. These advantages provide the hull with better damping characteristics for the size and displacement of the hull, but may have detrimental effects on other aspects of the hulls performance such as the resistance and propulsive efficiency. Taking this into account the Deep-V hull was considered to have the better seakeeping responses, because although the motions may appear greater, the vessel’s finer entrance to the water and anti-slamming bow mean that it would create lower pressures on the hull and less slamming, making for a more comfortable ride.

Model testing generally showed a strong correlation with the predicted results, showing similar shaped curves and magnitudes (discounting the ‘rogue’ peak frequencies). The position of these predicted large peaks correlated closely to smaller peaks found when model testing which signified good accuracy in predicting the location of the response if not the magnitude. This is likely to be because not all the damping is accounted for by *TRIDENT*, especially viscous damping, which was not input. The peak values occurred at a similar encounter frequency to the natural frequency of the motion, which is an additional indication that the results are reasonable.

The anti-slamming bulbous bow was found to improve the seakeeping characteristics of the vessel. This design feature appeared to discourage the hull from leaving the water as readily in heave and pitch, hence slamming was avoided. When the hull did leave the water, a combination of the drooped bow and the very fine entry meant that there was very little slamming when re-immerging. Some occurrences of stern slamming were noted in following waves when at the peak frequencies for heave and pitch. This was perhaps to be expected as the tunnelled stern does not re-enter the water as smoothly as the bow does, however, it can be mitigated by the vessel’s flexible speed range allowing such frequencies to be avoided.

WIND RESISTANCE ANALYSIS

Two wheelhouse designs were tested in the Combined Wind, Wave and Current Tank at Newcastle University. The first wheelhouse design was based on the proposed design by Alnmaritec, the builder of the new vessel. This wheelhouse model was named DVC-WH1. This design was taken from the Port of London Authority vessel *'Lambeth'*, an existing vessel that Newcastle University provided design expertise for. The *Lambeth* was the first vessel to be built from the UNEW Deep-V catamaran series. The second wheelhouse design was based upon ideas from Mantouvalos (2010) and was denoted DVC-WH2 This design was considered to be a more aesthetically pleasing wheelhouse using tapering and angled walls to make the wheelhouse more 'eye-catching'. Both models are shown in Figure 15.

TANK TESTING

Before any models could be made or tank testing could commence, both designs were modelled in Maxsurf to give a 3D impression of what they would look like. This also allowed the surface areas to be calculated, which was useful as they were later used to determine the non-dimensional coefficients. It also allowed the designs to be optimised so that the surface areas were of similar size to allow for a fairer test. The University's combined wind/wave/current tank was converted into a wind tunnel with the introduction of a false floor above the waterline. The two wheelhouses shown in Figure 15 were constructed from wood, as well as above water profile of the vessel. The model was constructed at 1:18 scale, to ensure it would fit across the combined tank avoiding significant blockage factors. Table 8 shows the general particulars of the model.

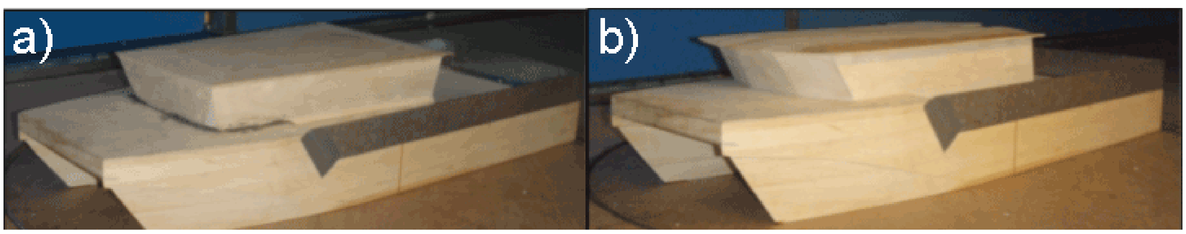

Figure 15: Wind Tunnel Models for (a) DVC-WH1 and (b) DVC-WH2

Table 8: Wind Model General Particulars

	Full Scale	**Model**
Scale Factor	1	18
Length	18m	1m
Breadth	7m	0.386m
Distance between demihulls	4.941m	0.274m
Demi-Hull Width	2m	0.111m
Weather Deck Height (from Waterline)	1.549m	0.086m
Fore Deck Height (from Waterline)	2.549m	0.142m
DVC-WH1 Wheelhouse Frontal Area	22.03m^2	0.068m^2
DVC-WH1 Wheelhouse Lateral Area	56.13m^2	0.173m^2
DVC-WH2 Wheelhouse Frontal Area	22.79m^2	0.070m^2
DVC-WH2 Wheelhouse Lateral Area	54.78m^2	0.169m^2

The wheelhouse proposed by the prospective boat yard incorporated a shelter on its aft starboard corner to create an exterior working area with protection from the weather. This made the vessel asymmetric which provided an interesting insight in the results when compared to the symmetrical wheelhouse results.

Testing was carried out at different angles of attack, at 30° increments, so as to generate enough information about the vessel when sailing at any angle. The models were also tested at 4 different wind speeds of 5, 10, 15 & 20m/s. As the DVC-WH1 (Alnmaritec) design was asymmetric it was tested from 0°- 360° where as DVC-WH2 (Mantouvalos) design was only tested from 0°-180° due to its symmetry.

The tests carried out were repeated 3 times for each wind speed and heading angle and then the average was taken to give the most accurate result. The non-dimensional coefficients were found following the system employed by Blendermann (Blendermann, 1996) and thus C_X and C_Y were calculated using the following formulae:

$$C_X = \frac{X}{\frac{1}{2}\rho u^2 A_F} \qquad\qquad C_Y = \frac{Y}{\frac{1}{2}\rho u^2 A_L} \qquad\qquad (2\ \&\ 3)$$

When C_X was plotted for all angles and wind speeds, the graph showed a variation in non-dimensional coefficients. This would suggest the result were Reynolds' dependent, however literature, (Blendermann, 1996) (Molland & Barbeau, 2003) suggests not and that the problem was actually due to boundary layer separation and non-uniform flow.

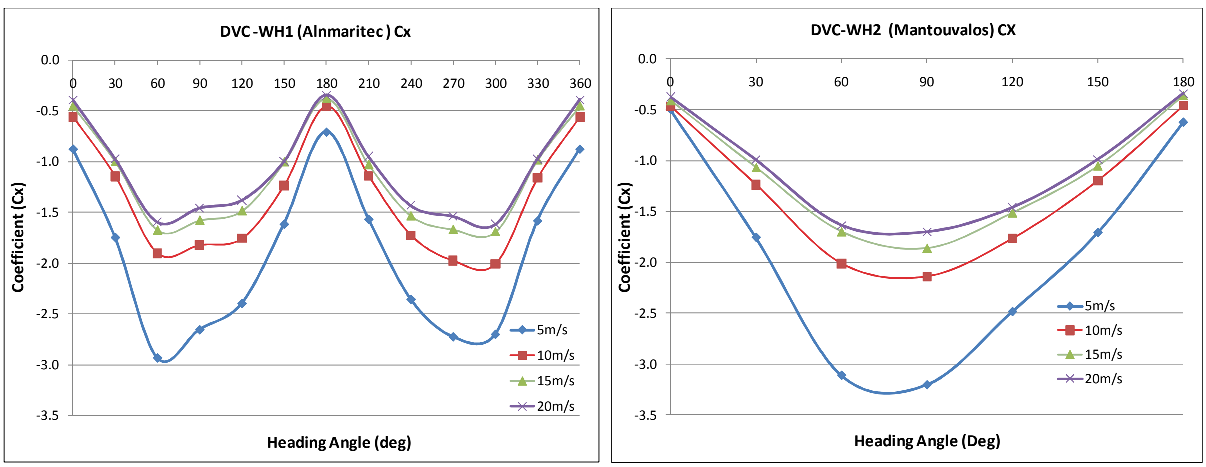

Figures 16 & 17: Cx versus Heading angles for DVC-WH1 and DVC-WH2

Consideration of Figures 16 and 17 suggests that convergence is starting to occur between 15m/s and 20m/s and so the results from 20m/s were used to calculate the coefficients. The facilities did not permit testing at higher speeds within the given time period. In future work, it is recommended to test at speeds of 25m/s and 30m/s to verify whether further convergence occurs. A comparison of C_X in Figure 18 reveals that the DVC-WH1 design is marginally more efficient, however more interestingly it shows the effect of asymmetry. The symmetrical wheelhouse experiences the greatest force at 90° where as the asymmetrical design experiences a greater force at 60° not 90°. It should be noted that for the majority of the angles, the force experienced by both designs was very similar.

Following the work of Blendermann, Drag and Cross Coefficients were found using the following formulae (Equations 4 & 5):

$$C_D = C_Y \sin\varepsilon - C_X \cos\varepsilon \qquad (4)$$

$$C_C = C_X \sin\varepsilon + C_Y \cos\varepsilon \qquad (5)$$

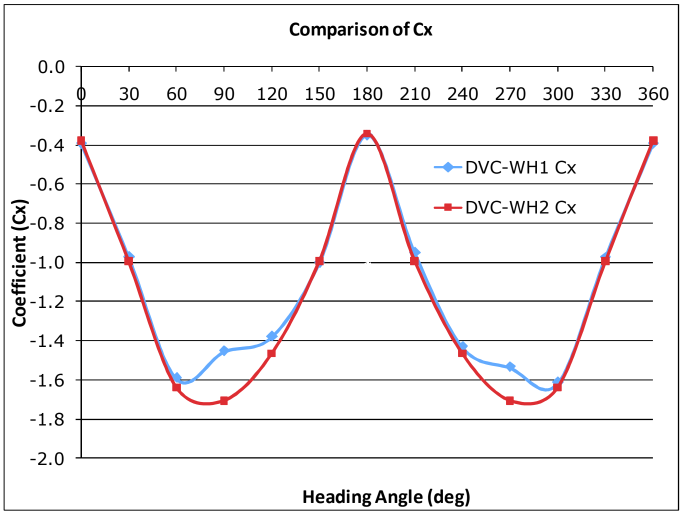

Figure 18: Comparison of Cx for DVC-WH1 (Almaritec) and DVC-WH2 (Mantouvalos)

Once again, the plots show great similarity in results between the two designs in Figures 19 & 20. Although roll and yaw moments were recorded and calculated, the results were not that which were expected or shown in literature (Blendermann, 1996), and so they were discarded with an assumption of experimental error.

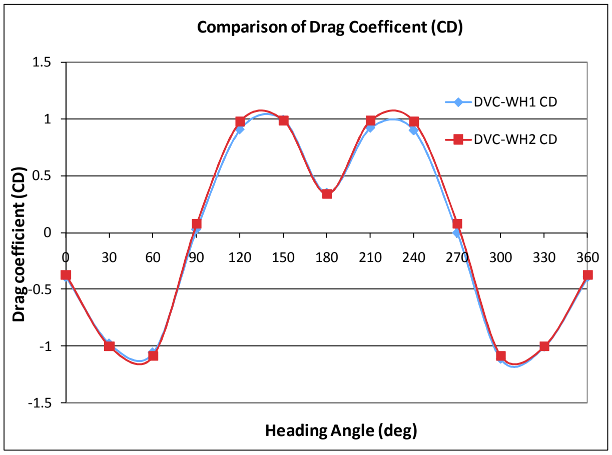

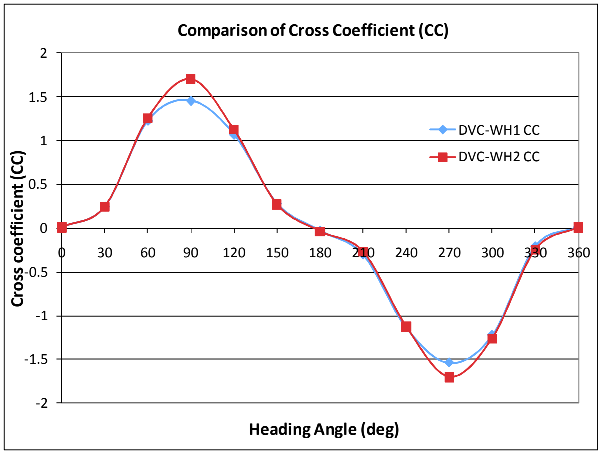

Figures 19 & 20: Comparison of Drag and Cross coefficients for the two Wheelhouse Designs

Whilst there is little difference between the wheelhouses from a resistance point of view, this is often of secondary importance in selecting a wheelhouse design, as cost, practicality, ergonomics and ultimately aesthetics also have to be considered. The results have however given a useful insight into the general wind resistance behaviour and magnitude. The airflow around the wheelhouse and between the tapered hulls of a high speed catamaran is clearly a highly complex system. With more time smoke testing would have been carried out to look at how the air interacted with the vessel. It would also be informative to repeat the testing using hot wire anemometers positioned around the vessel and fore and aft of the test area, to measure the wind velocity distribution to help obtain more meaningful results.

CONCLUSIONS

The objective of this paper is to report on the studies carried out by four undergraduate students in support of Newcastle University's research vessel replacement project. Analysis was conducted in the following areas; calm water resistance, propulsion, seakeeping and wind resistance. The procedures have been described and the salient results presented. The following conclusions can be drawn:

- CFD analysis showed the Deep-V catamaran hullform pioneered by Newcastle University to be advantageous in terms of wave making resistance when compared to a round bilge hullform (NPL series) of similar dimensions.
- The addition of a slim bulbous bow further improved the resistance characteristics.
- Scale model tests established the benefits of optimising the hull separation and confirmed the preliminary effective power estimates.
- The propulsion analysis indicated that the most efficient propeller design for the demanding mission profile would be an 800mm dia. B5.75 with a pitch/diameter ratio of 1.05 from the Wageningen B series, and that further analysis would be required due to a risk of cavitation beyond the cruising speed of 15 knots and to meet certain bollard pull demands.
- The proposed engine/hull combination was shown meet the design speed parameters comfortably.
- The seakeeping software analysis suggested that the deep-V hull is slightly more sensitive than the round bilge in certain situations although model tests revealed that the software, whilst generally representative of the behaviour, was over estimating the magnitude of the peaks in the motions. Overall it was felt that Deep-V hullform was more sea-kindly due to its anti-slamming design.
- The wind resistance analysis compared two wheelhouse designs and measured the forces at different wind speeds and angles. Whilst in terms of resistance there was little to choose between the two designs, a valuable insight into the magnitude and general behaviour of these forces was established.

ACKNOWLEDGMENTS

The authors would like to express their sincere gratitude to Professor Mehmet Atlar, Dr James Wightman-Smith and Dr K-C Seo for their help and guidance in producing this paper, as well as their knowledge and support during the testing period. Kind efforts from Dr Rod Sampson of STC Inc at the initial stage of this study are highly appreciated. We would also like to thank the facilities staff of Newcastle University's hydrodynamic laboratories for ensuring all testing was completed on time and to a high standard. Finally we would like to thank Newcastle University's School of Marine Science and Technology for the resources, facilities and funding provided which allowed these tests to be conducted.

REFERENCES

Atlar, M., Sampson, R., Wightman-Smith, J.R., Seo, K.C., Glover, E.J., Danisman, B.D. and Mantouvalos A. (2010): "An Innovative Research Vessel Replacement for Newcastle University", *Proc. 7th International Conference of High-Performance Marine Vehicles (HIPER '10),* Melbourne, USA

Bailey, D. (1976): "The NPL High Speed Round Bilge Displacement Hull Series", *RINA Publications*

Blendermann, W. (1996): "Wind Loading of Ships - Collected Data from Wind Tunnel Tests in Uniform Flow", Institut fur Schiffbau der Universistat Hamburg

Conway, D. (2010): "Wind Resistance Testing and General Arrangement of 18m Research Deep-V Catamaran" *3rd Year M. Eng. Thesis*, Department of Marine Technology, Newcastle University

Danisman, D.B. Goren, O., Insel, M., Atlar, M. (2001): "An Optimization Study for the Bow Form of High-speed Displacement Catamarans" *Marine Technology*, pp 38, 116-121

Holtrop, J., Mennen, G.G.J. (1982): "An Approximate Power Prediction Method" *ISP*, 29 July 1982

ITTC (2002): "*ITTC - Recommended Procedures and Guidelines*", Rev. 01

ITU (2010): “School of Marine Science and Technology of Newcastle University 18m Research Vessel Model Tests”, Istanbul Technical University, Faculty of Naval Architecture and Ocean Engineering Report, Project No: 2010-UNEW-P01, April 2010.

Lewis, E.V. (1988): “*Principles of Naval Architecture Vol. 2: Resistance, Propulsion and Vibration”*, Jersey City, N.J, Society of Naval Architects and Marine Engineers

Mantouvalos, A. (2008): “The Development of the First Deep-Vee Catamaran (DVC) Systematic Series”. *PhD Thesis*. Newcastle University

Mantouvalos, A. (2010): Design and styling consultancy study carried out on behalf of Newcastle University

Martec (2009): "*FD-WaveLoad 2007 User Guide.*"

Molland, A. F. and Barbeau, T.E. (2003): "An Investigation into the Aerodynamic Drag on the Superstructure of Fast Catamarans", *Transactions of The Royal Institution of Naval Architects,* Volume 145

Neill, S. (2010): “Propulsion Selection for the New Research Vessel at Newcastle University” *3rd Year M. Eng. Thesis*, Department of Marine Technology, Newcastle University

Stephens, D. (2010): “Seakeeping Study of a New Deep-V Catamaran Research Vessel” *3rd Year M. Eng. Thesis*, Department of Marine Technology, Newcastle University

Vasiljev, D. (2010): “Deep-V Catamaran with Anti-Slamming Bulbous Bow Resistance Evaluation and Comparison to the Alternative Hullforms to find the Optimum Design Solution” *3rd Year M. Eng. Thesis*, Department of Marine Technology, Newcastle University

Seventh International Conference
On High-Performance Marine Vehicles
Melbourne, Florida, USA
13-15 October 2010

INVESTIGATING MULTI-DIMENSIONAL DESIGN SPACES USING FIRST PRINCIPLE METHODS

Stefan Harries
Benzstr. 2, D-14482 Potsdam, Germany
harries@FRIENDSHIP-SYSTEMS.com

ABSTRACT

Design often means finding good compromises while the knowledge about the final product is still limited. In particular, when new ideas are developed the fast accumulation of relevant data is of high importance. In the initial design phase naval architects often rely on suitable baselines, do literature studies or utilize systematic series. In this paper a further approach shall be elaborated: systematically investigating multi-dimensional design spaces using first principle methods. An example is presented for a fast mega-yacht around 80m in length with speeds up to 20kn. Hull form development and energy consumption being of paramount importance for an entire project, the mega-yacht's hydrodynamics was studied using a combination of non-linear free surface potential flow and boundary layer simulations. Utilizing a parametric hull model, a formal exploration was undertaken to come to know the design space. The work was realized within the FRIENDSHIP-Framework for Computer Aided Engineering coupled to SHIPFLOW as the engine for Computational Fluid Dynamics. Visualizations are done via standard relationship diagrams, including regressions, but also by means of a response surface methodology, allowing a transfinite view. This enables the design team not only to identify promising candidates for subsequent analyses but also supports their decision making when changes are requested.

INTRODUCTION

Design is making decisions on the basis of insight and options, often by finding a suitable compromise between conflicting targets. Numerical flow simulation, parametric design and increasing computer power have made formal optimization techniques popular in product development. In particular, deterministic and stochastic strategies are employed to improve designs for one or several objectives. This leads to simulation-driven design in which products or parts of them, for instance their functional surfaces, are derived from key performance measures such as resistance (e.g. Harries (2008), Peri et al (2007)), wake quality (Brenner et al (2009)), pressure rise (Palluch et al (2009)), exhaust gas concentration (Harries and Vesting (2010)), propulsive efficiency (Druckenbrod et al (2010)) or cost (Rigo et al (2008)).

Typically, the engineers set meaningful objectives and important constraints and then launch a thorough optimization that then often requires a few days of number crunching, producing several hundred (and sometimes thousands) of variants. However, an idea of the design space needs to be present beforehand so as to pose the right questions. Here, formal optimization techniques can be applied, too. However, this appears to have gotten little attention so far. Two situations come to mind directly which relate to initial design:

- Building up relevant design data early into a newbuilding project and
- Decision support for anticipated design changes.

The first situation is particularly relevant in cases where a new design deviates considerably from any available parent. This might be because the design department has not yet been engaged in developing a certain type of vessel or, even more challenging, no reliable references can be found due to a product's novel character. Here, first principle methods – i.e., simulations that build directly on the established laws of physics – assist greatly in deriving dependencies and showing trends.

The second situation, meanwhile, is not atypical of the dynamics that naval architects encounter with owners that change their minds rather quickly ("I would like to have…") or with decision makers that are difficult to bring together. If new ideas come up that need to be assessed while everyone is still around the table ("what would happen if…") then a project can be pushed efficiently if some of these changes and wishes have been anticipated, at least on the basis of an educated guess. Formal techniques of systematic design space investigation may then be utilized to work out comprehensive sets of variants beforehand. While the exact nature of the changes is naturally unknown, indicators and trends can be developed to support the decision process, possibly improving ad-hoc decisions under uncertainty.

The paper's focus being design methodology, an example application in design space analysis and decision support is presented for a mega-yacht of L_{OA} about 80m and L_{PP} around 70m with speeds of 14kn (travel), 16kn (cruise) and 20kn (maximum), corresponding to Froude numbers of 0.275, 0.314 and 0.393, respectively. A fully parametric model of the mega-yacht was developed to allow for meaningful hull variations. The yacht's calm water hydrodynamics was determined with the well-known *SHIPFLOW* code, using non-linear potential flow theory for the free surface wave making problem and thin boundary layer theory for an approximation of frictional resistance. A design-of-experiments (DoE) with 200 variants was conducted to establish a data base that yields the necessary insight for a deeper understanding of the impact of changes. The *FRIENDSHIP-Framework* was used to (i) set up the parametric model, (ii) control the execution of the external flow solvers for a first principle ranking and (iii) provide the necessary variant management. Finally, a multi-dimensional response surface for total resistance, i.e., a meta-model, was generated applying a Kriging approach.

NOMENCLATURE

B	Maximum beam
C_B	Block coefficient
C_F	Frictional resistance coefficient
C_M	Sectional area coefficient at midships
C_{Pfor}	Prismatic coefficient of the forebody
C_T	Total resistance coefficient
C_W	Wave resistance coefficient from pressure integration
$C_{WwaveCut}$	Wave resistance coefficient from wave cut analysis
$DWL_{fullness}$	Coefficient of the curved part of the design waterline in the forebody
$\mathrm{F_n}$	Froude number
FP	Forward perpendicular
KM	Transverse metacentre above keel
L_{OA}	Length over all
L_{PP}	Length between perpendiculars
$\mathrm{R_n}$	Reynolds number
R_T	Total resistance
$R_{WwaveCut}$	Wave resistance from wave cut analysis
S	Wetted surface area
T	Design draft
X_{CB}	Longitudinal center of buoyancy
∇	Displacement volume
$\Re^2$	Two-dimensional (parameter) space
$\Re^3$	Three-dimensional (Cartesian) space
$\Re^n$	n-dimensional (design) space

ABBREVIATIONS

CAD	Computer Aided Design
CAE	Computer Aided Engineering
CFD	Computational Fluid Dynamics
DoE	Design-of-Experiments
DWL	Design waterline
FOB	Flat of bottom
FOS	Flat of side
RSM	Response Surface Methodology / Response Surface Model
SAC	Sectional area curve
2d	Two-dimensional
3d	Three-dimensional

KEYWORDS

Mega-yacht, CAD, CAE, CFD, Simulation-driven Design, Response Surface Methodology, Resistance

PARAMETRIC MODEL

A fully parametric model was developed within the *FRIENDSHIP-Framework* for a round bilge mega-yacht. Assuming a classical twin-screw design with bulbous bow and skeg, the bare hull was subdivided into a forebody and an aftbody region, joined at the maximum section, see Figure 1. For simplicity the skeg, shafts, brakets, propellers, rudders, thrusters and other appendages were neglected. The bulb was fitted to the bare hull within a region of transition aft of the forward perpendicular.

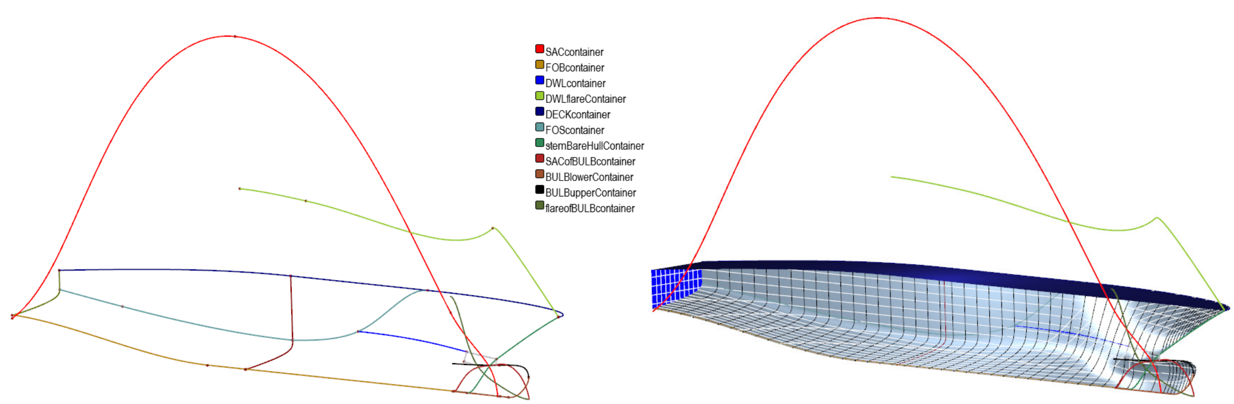

Figure 1: Parametric model of round bilge mega-yacht

A fully parametric model does not assume a given parent hull (as opposed to partially parametric modeling). It can be adjusted to match a baseline, too, but is more frequently used to build up the entire geometry from scratch. Functional surfaces often display a common building code into a certain direction. The planar sections of a ship hull usually change very little when going incrementally in longitudinal direction, save for deliberate discontinuities. (Similarly, the profiles of a propeller do not change that much when going in radial direction.)

As depicted in Figure 1 the topology of the presented model consists of the following curves in longitudinal direction:

- Positional curves, namely flat of bottom (FOB), design waterline (DWL), flat of side (FOS) and deck (DECK) when starting with the keel and going upward,
- Integral curves, namely the sectional area curves for the bare hull (SAC) and the bulb (SACofBULB),
- Differential curves, namely the sectional flare at the design waterline (DWLflare) and top flare of the bulb (flareOfBULB).

These longitudinal curves provide the necessary input for the modeling of sections and, hence, the building of surfaces. Within the *FRIENDSHIP-Framework* two special entities were applied: *FSplines* and *MetaSurfaces*. *FSplines* allow the generation of fair curves with flexible (and possibly small) sets of parameters such as start and end points, tangents and area values. Essentially they are planar B-spline curves optimized for fairness with the input parameters treated as equality constraints, see Harries (1998). Meanwhile, *MetaSurfaces* are novel surface entities developed for collecting information available in two distinct directions. They yield the Cartesian coordinates of any point on the surface for any pair of surface coordinates u and v, basically giving an unambiguous mapping from $\Re^2$ to $\Re^3$ as would, say, Bézier or B-spline surfaces, too. However, they are more flexible as they do not assume any particular representation with regard to the curves they capture, see Palluch et al (2009) and FRIENDSHIP SYSTEMS (2009) for details. In this way, the entire hull form is defined by a set of around 50 parameters such as L_{PP}, B, T, C_M, C_{Pfor}, $DWL_{fullness}$, L_{Bulb} and so forth.

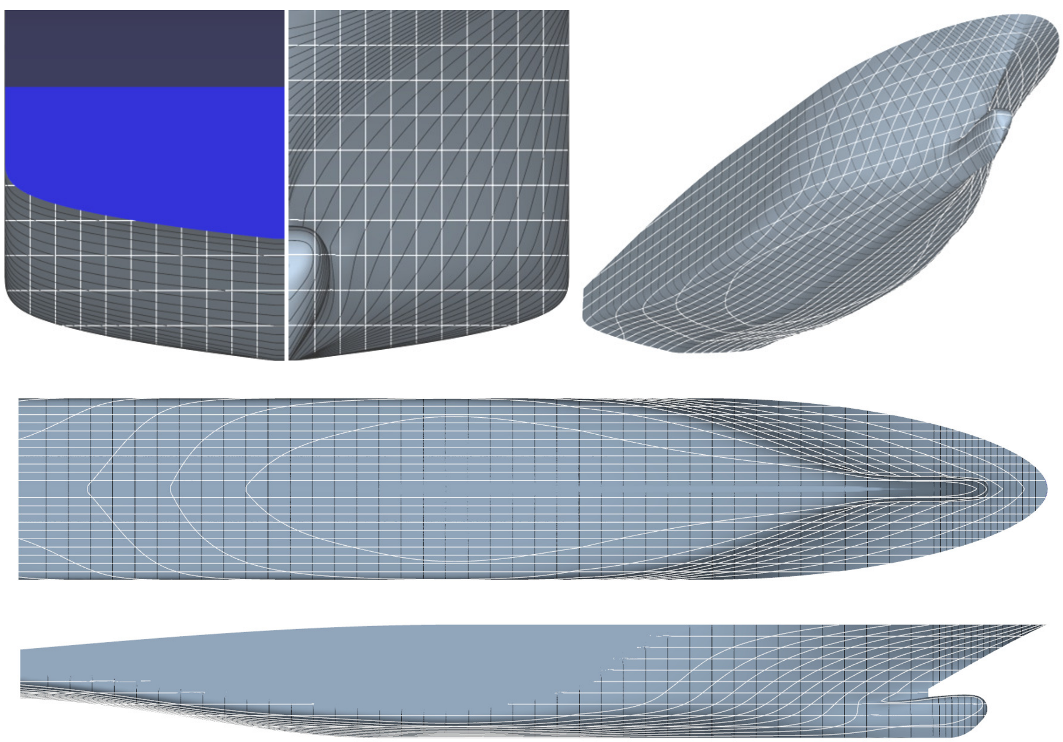

Figure 2: Bare hull with bulbous bow generated by means of fully parametric modeling

Figure 2 shows the body plan, waterlines, a side and a perspective view of a representative instance of the parametric model. Changing geometry is a matter of selecting one or several of the parameters that define the geometry and letting the *FRIENDSHIP-Framework* determine the new hull form. On a standard notebook this takes no more than a few seconds since a mechanism is utilized known as lazy fetching: All elements know their current status of being either *up-to-date* or *out-of-date* and are aware of their clients and, hence, act as suppliers that provide information to other elements in the model's hierarchy. Every single change of any (design) element is spread throughout the entire dependency tree. If an element is asked to deliver one of its properties, for example a double value, it may readily do so if *up-to-date*. If the element is *out-of-date*, however, it asks all its direct suppliers for their input. Should one, several or all of its suppliers happen to be *out-of-date*, too, the call for updates is propagated downwards. (Recursions are avoided by a one-way dependency check at the time of creation of each element.) A selection of the *Dependencies* is presented in Figure 3 (right part) as a zoomed in portion of an entire screen shot (left part) that displays the *ObjectTree* on the left, the *Dependencies* view in the upper part of the central window and, in addition, the offsets used for hydrostatics calculations. The free variable $DWL_{fullness}$, i.e., the fullness of the curved part of the design waterline starting at the forward point of intersection with the flat of side and leading all the way to the forward perpendicular, is selected (see zoomed in portion). An *FSpline* called DWL_{fwd} is identified as a client of $DWL_{fullness}$ (as would be expected). One level further on in the hierarchy, there is an entity called $DWL_{container}$ that apparently is a client of DWL_{fwd} and, consequently, of $DWL_{fullness}$, too. (Note that free variables, by definition, do not have any suppliers but clients only.)

Going deeper down into the hierarchy (not shown here), the surfaces of the forebody also depend on $DWL_{fullness}$ (via $DWL_{container}$ and DWL_{fwd}). Figure 4 illustrates the effect of changing $DWL_{fullness}$ in a single parameter variation. Here the design waterline becomes more slender from left to right while all other input is maintained. This means that also the sectional area curve is kept. Hence, new sections follow the modified waterline but feature the same area. Differences can best be observed by looking at the section for which the curvature distribution is displayed as porcupines. Looking from left to right in Figure 4, the transition between curved and flat regions at the flat of side grows more pronounced while the buttocks become more curved towards the bow. (The pictures are taken for the same region of the hull in exactly the same perspective. The arrows emphasize the areas of interest.)

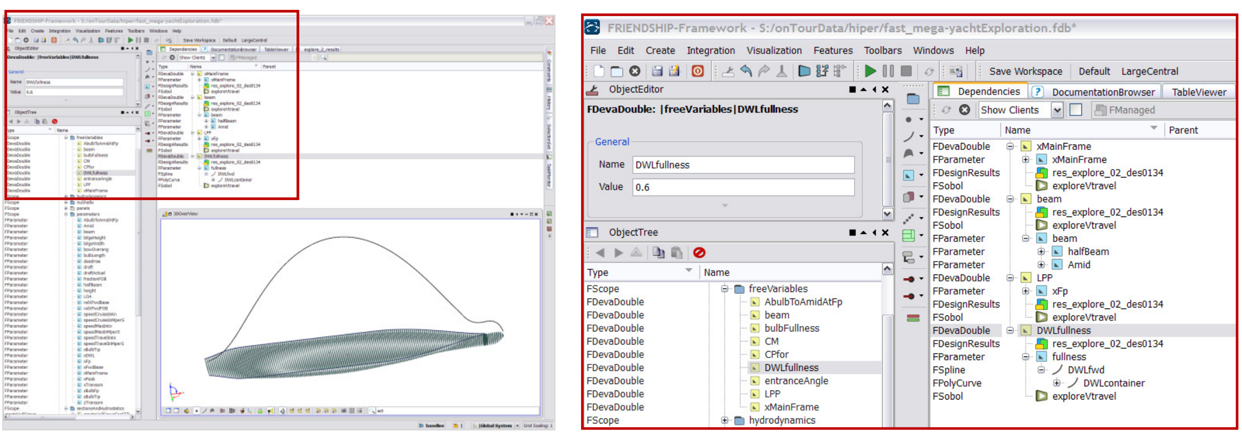

Figure 3: Selected dependencies within the parametric model and zoomed in portion

FLOW SIMULATIONS

Flow simulations need to be chosen in a trade-off between accuracy and effort. Currently, in order to understand the impact of changing main dimensions in the initial design of a fast vessel it should suffice to employ potential flow theory to compute the non-linear wave resistance problem with free sinkage and trim. Since the boundary layer of a fast round bilge monohull should not be substantial this can be combined with a calculation of the frictional resistance via thin boundary layer theory. At a later stage, for instance when fine-tuning brakets, a RANSE calculation should be undertaken to capture the viscous phenomena well enough, see e.g. Brenner (2008).

For the flow simulations of the mega-yacht *SHIPFLOW XPAN* and *XBOUND* by FLOWTECH (2004, 2009) were utilized. *SHIPFLOW* follows a zonal approach and allows an increase of complexity for the flow analysis depending on the design phase. Besides, it is tightly integrated within the *FRIENDSHIP-Framework*, see e.g. Abt and Harries (2007) for details, making it ready-to-go for the systematic investigation.

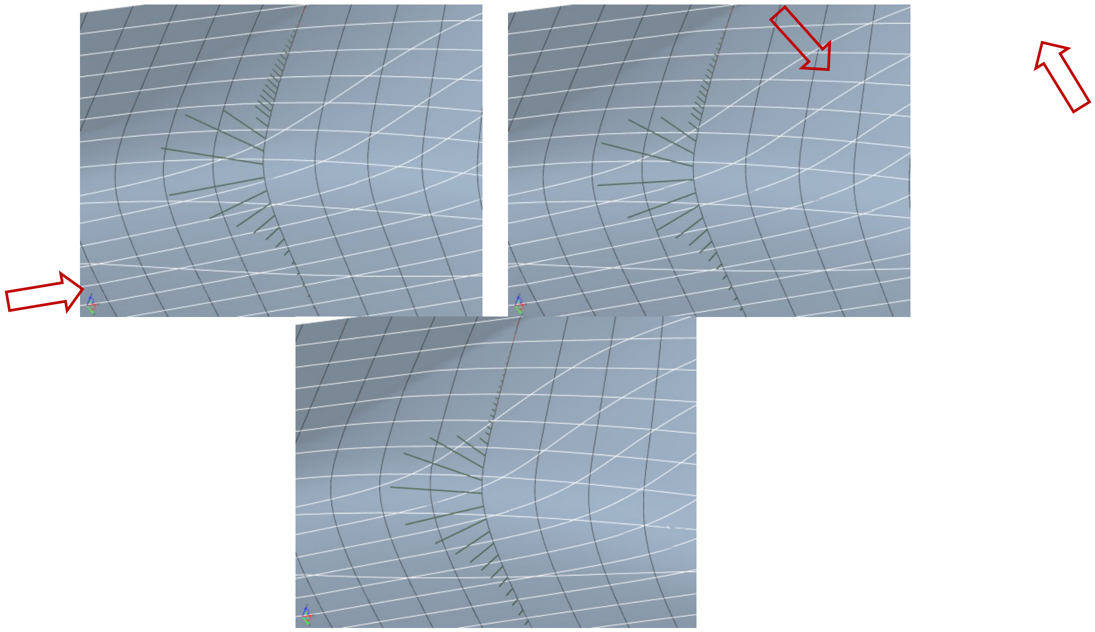

Figure 4: Zoomed in region in the forebody close to the FOS for $DWL_{fullness}$ = 0.58, 0.60 and 0.62

Figure 5 shows the panelization of both the free surface and the hull (upper part) along with resulting waves and streamlines (lower part) at 20kn, corresponding to Froude number $F_n = 0.393$ for $L_{PP} = 70$m. For both *SHIPFLOW XPAN* and *XBOUND* the default settings were taken (apart from an increased number of streamlines and associated tracing points). Wave resistance was calculated from both pressure integration over the hull and transverse wave cut analysis (for cross-validation). The total resistance R_T was computed by summing up the wave resistance from wave cuts and the frictional resistance R_F from boundary layer analysis at full scale with Reynolds number $R_n = 7.2\ 10^8$. All other resistance components were simply neglected since the focus was put on comparing and judging variants. The underlying assumption therefore is that variants perform similarly with regard to appendage resistance, air resistance etc. – which should be reasonably accurate at this stage.

The flow simulations were done on a standard dual core notebook and took about four to five minutes per variant and speed, convergence of the free surface problem typically being achieved within 10 to 12 iterations. With a CFD license for both cores around 200 designs could be computed in one overnight job.

DESIGN SPACE INVESTIGATION

A systematic design space investigation was performed via a Sobol algorithm, Press et al (2007). Nine free variables were considered such as length, maximum beam, sectional area coefficient at midships etc., see Table 1 (red box) for details, establishing a nine-dimensional space $\Re^9$. All variables are potential candidates for change at the point when main dimensions are somewhat established but not yet completely fixed. The vessel's design draft, however, was kept constant at 3.9m.

200 variants were studied – each for three speeds, resulting in a total of 600 CFD runs. The speeds of interest were travel speed of 14kn for large ranges, cruising speed of 16kn and, very importantly, maximum speed of 20kn for high performance. For hydrostatics and -dynamics an actual draft of 3.6m was prescribed so as to be able to reach the maximum speed with a total of 7000kW of installed power (corresponding to two MTU 16V595 TE 70 at 4680 HP each).

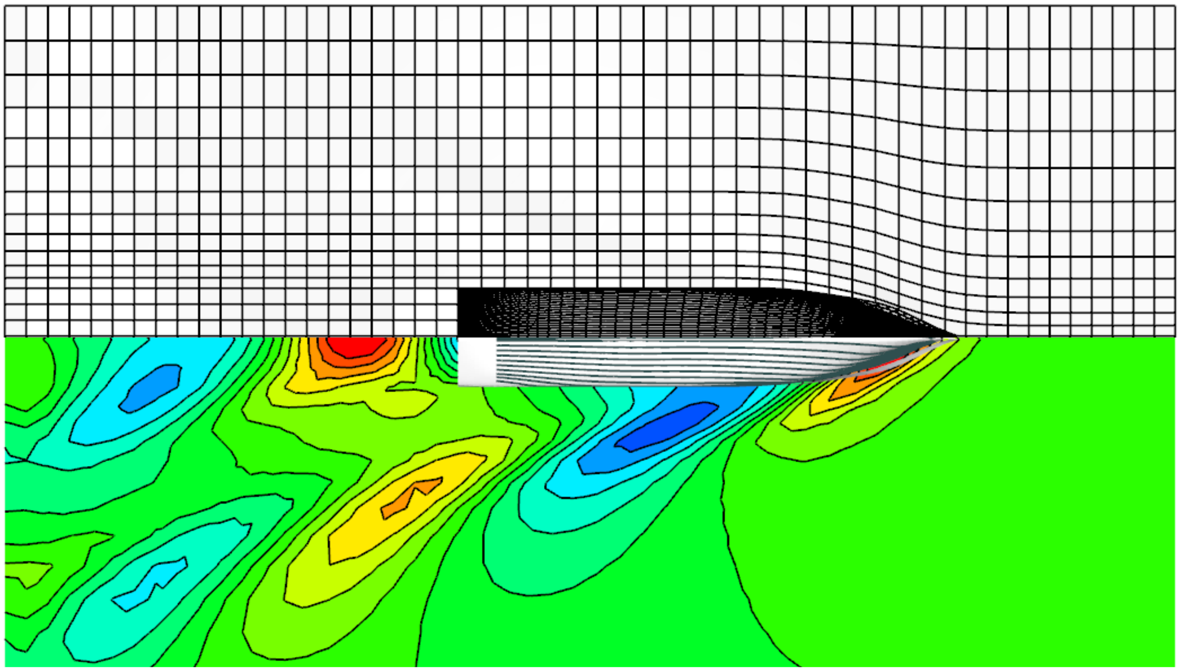

Figure 5: Panelization of free surface and hull along with waves and streamlines at F_n = 0.393

Table 1: Free variables along with bounds and an excerpt of variants and results

		beam	LPP	CPfor	CM	AbulbToAmidAtFp	bulbFullness	DWLfullness	entranceAngle	xMainFrame	CW	CWwaveCut
	Attribute	Active	Active	Active	Active	Active	Active	Active	Active	Active		
	Name	**beam**	**LPP**	**CPfor**	**CM**	**AbulbToAmidAtFp**	**bulbFullness**	**DWLfullness**	**entranceAngle**	**xMainFrame**	**CW**	**CWwaveCut**
	Scope	|freeVariables	|freeVariables	|freeVariables	|freeVariables	|freeVariables	|freeVariables	|freeVariables	|freeVariables	|freeVariables	hydrodynamics	|hydrodynamics
	Lower Bound	14	68	0,6	0,82	0,092	0,75	0,58	14	0,44	-82,6862	0,00201555
	Upper Bound	14,25	72	0,63	0,89	0,098	0,85	0,62	18	0,48	,23865	8,31097
	Feasible Designs: 68 %											
	Mean Utilization Index											
	Mean	14,124	70,0007	0,615043	0,854918	0,0950058	0,799982	0,600105	15,9761	0,460143	-0,503401	0,0809973
	Sample Standard Deviation	0,0722906	1,16049	0,00876428	0,020189	0,00173614	0,0288097	0,0116152	1,15471	0,0115427	6,91497	0,734026
☐	✓ explore_02_des0000	14,082	71,9375	0,600469	0,836406	0,0964062	0,773438	0,601875	16,8125	0,464375	0,00249294	0,00201555
☐	✓ explore_02_des0001	14,1133	69,4375	0,626719	0,880156	0,0926562	0,760938	0,616875	17,3125	0,459375	0,00357527	0,00274247
☐	✗ explore_02_des0002	14,2383	71,4375	0,611719	0,845156	0,0956562	0,810937	0,596875	15,3125	0,479375	0,00288108	0,0022604
☐	✗ explore_02_des0003	14,1758	68,4375	0,604219	0,862656	0,0971562	0,785937	0,586875	16,3125	0,449375	0,00350442	0,00278513
☐	✓ explore_02_des0004	14,0508	70,4375	0,619219	0,827656	0,0941562	0,835938	0,606875	14,3125	0,469375	0,00296891	0,00231685
☐	✓ explore_02_des0005	14,0352	69,6875	0,602344	0,840781	0,0945312	0,829688	0,614375	16,0625	0,456875	0,00296934	0,002373
☐	✗ explore_02_des0006	14,1602	71,6875	0,617344	0,875781	0,0975312	0,779687	0,594375	14,0625	0,476875	0,00304201	0,0023902
☐	✓ explore_02_des0007	14,2227	68,6875	0,624844	0,823281	0,0960312	0,804688	0,584375	17,0625	0,446875	0,00328841	0,00258169
☐	✓ explore_02_des0008	14,0977	70,6875	0,609844	0,858281	0,0930312	0,754687	0,604375	15,0625	0,466875	0,00304567	0,00238643
☐	✗ explore_02_des0009	14,0664	68,1875	0,621094	0,849531	0,0952812	0,767188	0,619375	14,5625	0,451875	0,00365702	0,00283073

Tabel 1 presents the free variables' lower and upper bounds set for the Design-of-Experiments (DoE). In addition, the first 10 variants are given with the values they assume during the exploration (the remaining 190 look similar). Two of the many items of interest, the wave resistance coefficients C_W and $C_{WwaveCut}$, are shown, too. One may notice that some of the designs are marked as feasible (green icons with tick marks) while others are identified as infeasible (red icons with crosses). The latter designs are those that do not pass all inequality constraints. Tabel 2 states the eight inequality constraints formulated for stability, minimum displacement volume, the feasible range of the longitudinal center of buoyancy and so forth.

Table 2: Inequality constraint along with an excerpt of results

XCB	XCF	LOA	RTtoDisp	ZCB	GMmin	GMmax	volumeMin	XCBmin	XCBmax	trimConstraint	PBmax	RWtoRWwave
XCB	XCF	LOA	RTtoDisp	ZCB	GMmin	GMmax	volumeMin	XCBmin	XCBmax	trimConstraint	PBmax	RWtoRWwave...
|hydrodynamics	|hydrodynamics	|parameters	|hydrodynamics	|hydrodynamics								
32,7035	28,1133	79,1635	115,964	-1,42617	>= 1.8	<= 2.5	>= 1800	>= 33	<= 35	>= -0.12	<= 7000	<= 0.333333
35,3237	33,3386	83,2415	142,246	-1,29283								
					98 %	88 %	92.6667 %	92.6667 %	95.3333 %	96.6667 %	95.3333 %	95.3333 %
					4.56686 %	16.5464 %	9.01434 %	9.43782 %	6.45664 %	91.6864 %	1.11604 %	105.431 %
33,9383	29,3694	81,2113	127,846	-1,35312	2,22671	2,22671	1897,04	33,9383	33,9383	14,8643	6008,33	0,460097
0,624449	0,627308	1,19714	7,03455	0,0309883	0,227192	0,227192	63,5648	0,624449	0,624449	176,799	305,666	2,29282
34,7092	30,2811	83,2092	115,964	-1,31204	2,4719	2,4719	1869,96	34,7092	34,7092	0,067344	5380,96	0,236853
33,7876	29,2679	80,6303	131,584	-1,3901	2,00321	2,00321	1960,69	33,7876	33,7876	0,0998815	6402	0,303668
34,9833	30,1913	82,6934	121,567	-1,32898	2,53314	2,53314	1920,37	34,9833	34,9833	0,00442787	5792,99	0,274586
32,8185	28,3703	79,5987	136,239	-1,36448	2,14312	2,14312	1863,62	32,8185	32,8185	0,210127	6300,32	0,258263
34,417	29,7849	81,6618	125,462	-1,31149	2,47183	2,47183	1837,1	34,417	34,417	0,039371	5719,39	0,281445
33,5053	29,3747	80,8882	127,446	-1,3159	2,41452	2,41452	1818,7	33,5053	33,5053	0,145198	5751,61	0,251303
35,1357	30,1682	82,9513	121,675	-1,3784	2,1382	2,1382	2005,1	35,1357	35,1357	-0,0117029	6053,99	0,272704
33,2527	28,4889	79,8566	132,633	-1,33596	2,34841	2,34841	1816,67	33,2527	33,2527	0,151507	5979,02	0,273744
34,2801	29,768	81,9197	124,567	-1,34619	2,2788	2,2788	1908,81	34,2801	34,2801	0,0689867	5900,21	0,276245
32,9716	28,7178	79,3408	138,933	-1,34295	2,25681	2,25681	1835,72	32,9716	32,9716	0,175816	6328,73	0,291898

Table 3: Best variants and their performance

	beam	LPP	CPfor	CM	AbulbToA	bulbFullne	DWLfullne	entrance	xMainFrar	RT	volume	GM	KM
Attribute	Active	Active	Active	Active	Active	Active	Active	Active	Active				
Name	**beam**	**LPP**	**CPfor**	**CM**	**AbulbToA...**	**bulbFullness**	**DWLfullness**	**entrance...**	**xMainFrame**	**RT**	**volume**	**GM**	**KM**
Scope	|freeVariables	|freeVariables	|freeVariables	|freeVariables	|freeVariables	|freeVariables	|freeVariables	|freeVariables	|freeVariables	|hydrodynamics	|hydrodynamics	|hydrodynamics	|hydrodynamic
Lower Bound	14	68	0,6	0,82	0,092	0,75	0,58	14	0,44	220250	1771,85	1,70881	8,00881
Upper Bound	14,25	72	0,63	0,89	0,098	0,85	0,62	18	0,48	279800	2053,87	2,79648	9,09648
Feasible Designs: 68 %													
Mean Utilization Index													
Mean	14,124	70,0007	0,615043	0,854918	0,0950058	0,799982	0,600105	15,9761	0,460143	248184	1897,04	2,22671	8,52671
Sample Standard Deviation	0,0722906	1,16049	0,00876428	0,020189	0,00173614	0,0288097	0,0116152	1,15471	0,0115427	12626	63,5648	0,227192	0,227192
explore_02_des0084	14,0342	71,8281	0,604805	0,824648	0,0970391	0,779297	0,583594	14,4531	0,454219	220250	1841,25	2,36412	8,6641
explore_02_des0000	14,082	71,9375	0,600469	0,836406	0,0964062	0,773438	0,601875	16,8125	0,464375	222270	1869,96	2,4719	8,7719
explore_02_des0060	14,0254	71,2812	0,611016	0,822734	0,0961719	0,791406	0,592812	16,2188	0,459062	223512	1831,07	2,39424	8,6942
explore_02_des0034	14,248	71,9688	0,616172	0,821641	0,0927031	0,839844	0,592187	15,1562	0,453437	224207	1884,41	2,54689	8,8468
explore_02_des0072	14,0957	71,1562	0,604453	0,838047	0,0926094	0,832031	0,619062	17,8438	0,462813	226857	1860,66	2,52334	8,8233
explore_02_des0054	14,1816	71,7812	0,607266	0,848984	0,0954219	0,828906	0,607812	15,7188	0,444063	229234	1923,55	2,33034	8,6303
explore_02_des0036	14,0605	70,9688	0,608672	0,839141	0,0972031	0,814844	0,602187	14,1562	0,443437	229381	1864,57	2,27605	8,5760
explore_02_des0096	14,0889	71,7031	0,609492	0,844336	0,0949766	0,844922	0,609844	15,5781	0,467969	229930	1900,59	2,41726	8,7172
explore_02_des0020	14,0371	71,0938	0,617109	0,832578	0,0955156	0,849219	0,580937	17,2812	0,474687	230172	1864,57	2,29413	8,5941
explore_02_des0030	14,1543	70,4688	0,604922	0,830391	0,0979531	0,752344	0,597187	17,6562	0,458437	230317	1834,92	2,49776	8,7977

Figure 6 depicts the Sobol distribution for four of the nine free variables within a subset of 150 variants in which infeasible designs were filtered out. It can be seen that the design space is covered evenly (as is the Sobol's intention). Figure 7 presents the correlations between the wave resistance coefficients $C_{WwaveCut}$ as one important objective and four of the free variables. The diagrams stem from a standard report generated by the *FRIENDSHIP-Framework* for an overview. The length between perpendiculars proves to have a strong impact (upper left diagram). Longer vessels are, not surprisingly, beneficial from a hydrodynamics point of view. Moreover, a wider beam tends to produce higher resistance which, again, is reasonable. The midship area also influences the wave resistance coefficient quite a bit. Meanwhile, the fullness of the curved part of the design waterline does not show any particular trend.

One should note that these diagrams (Figure 7) do not feature single parameter variations but contain the effects of changing all free variables at a time according to the quasi-random DoE (Figure 6). Let us consider $C_{WwaveCut}$ vs. L_{PP} in further detail: Both the linear (blue) and quadratic (red) trend lines fall from around 2.85 10^{-3} at 68m toward 2.15 10^{-3} at 72m, the mean being 2.5 10^{-3}. Hence, the average wave resistance coefficient for the longest ship is approximately 75% of the shortest. The band width is roughly 0.4 10^{-3}, giving an appreciation that for any particular length there are designs which perform 8 to 10% better or worse than the average depending on the values of all other free variables.

Within the *FRIENDSHIP-Framework* any combination of objectives, constraints, free and dependent variables can be visualized in 2d, 3d, 4d (Cartesian coordinates plus marker size) and 5d plots (4d plus marker color). Figure 8 gives a 3d example, featuring the total resistance R_T vs. displacement volume ∇ at the actual draft and the initial stability criterion *KM*. While resistance and displacement are often objectives initial stability is typically assessed according to safety and comfort.

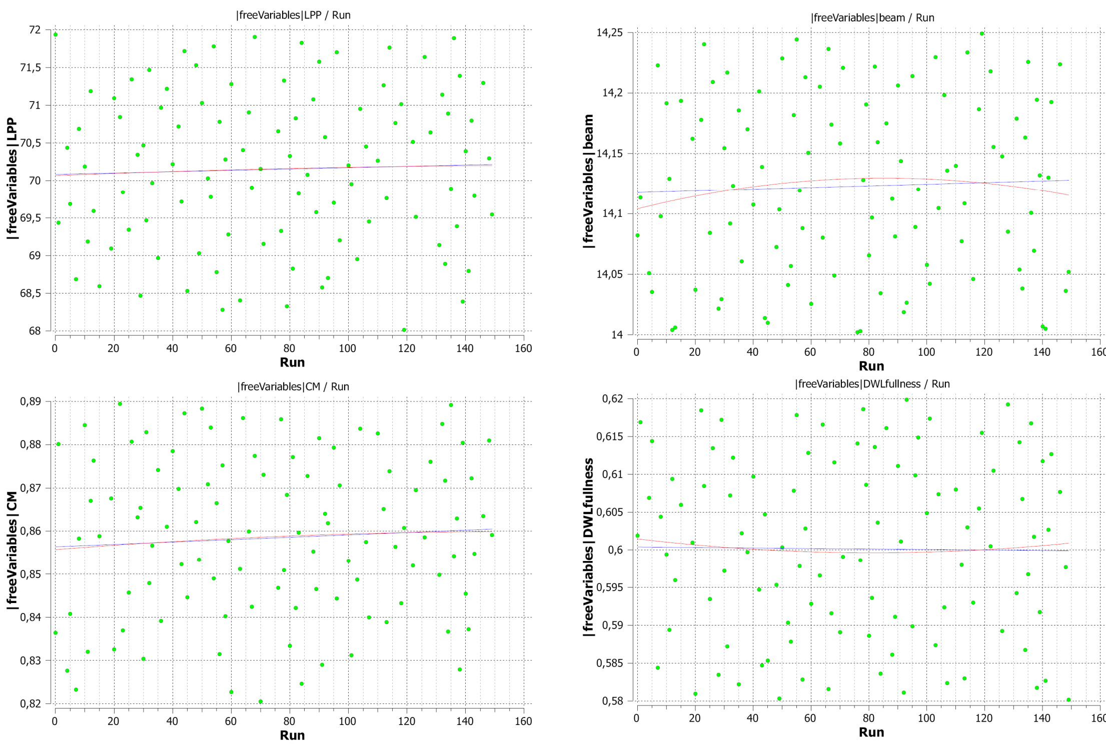

Figure 6: Sobol distribution of selected free variables

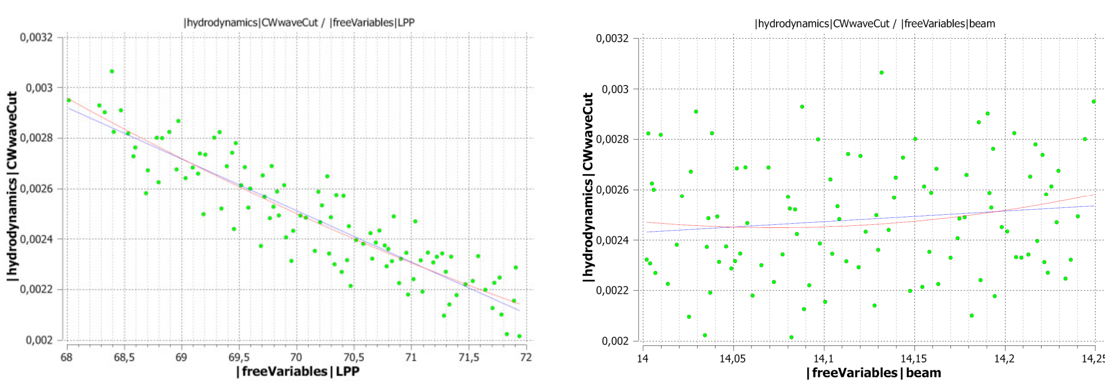

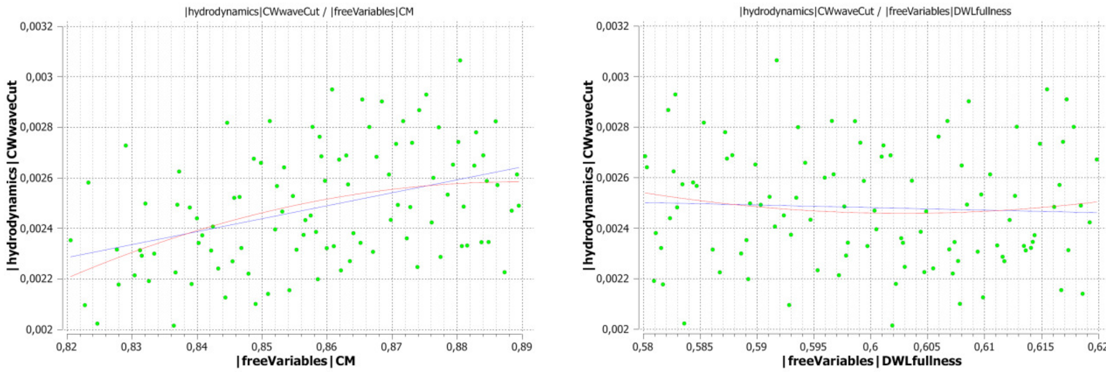

Figure 7: Correlations between an important objective and selected free variables

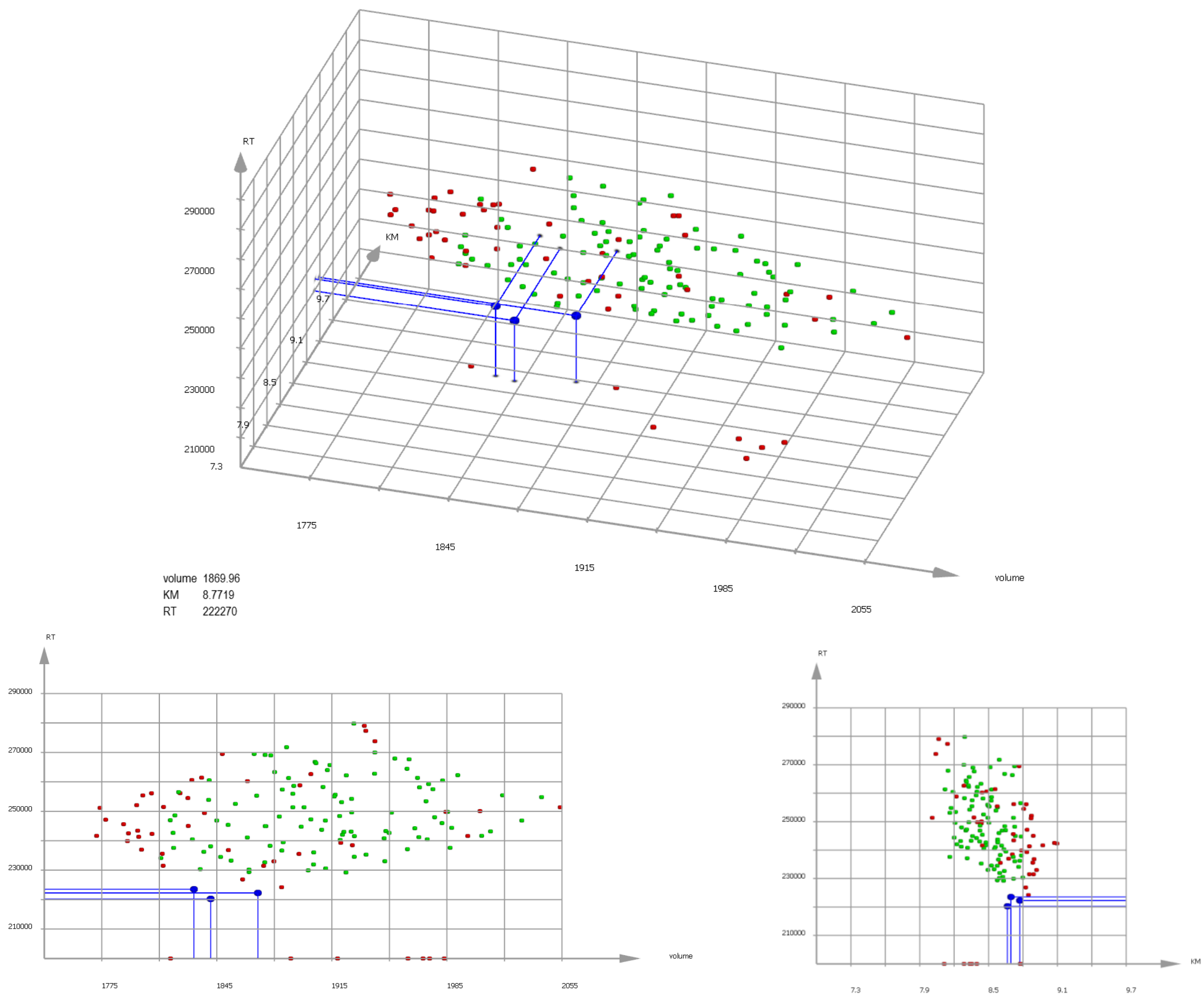

Figure 8: Total resistance vs. volume and stability

Feasible designs are marked as green points, infeasible designs as red points. While the 3d plot helps to get a general idea, the 2d projections R_T vs. ∇ (left lower part in Figure 8) and R_T vs. KM (right part) make it easy to judge in which direction to look for possibly design improvements or, in case changes are requested, to develop an appreciation at which cost or benefit they can be realized: More displacement will probably have to be paid by larger resistance while larger initial stability actually yields a trend towards lower resistance values. The spread of the data gives further indication of how much favorable and unfavorable designs lie apart. Since all designs are quasi-random creations within the design space it may be assumed that very good and rather bad designs are present. Hence, the designer may guess how much general room for improvement there is and how any particular candidate performs in comparison to the pack. For instance, if the current design is rather close to the best variants already the leeway for further improvement is probably small and vice versa.

Naturally, one should not forget that these findings are only meaningful in the context of the chosen parametric model, hence, the design space established, and that they rely on the validity of the simulations. Even though these simulations are built on first principles there are notable simplifications, for instance the wave resistance analyses leave out viscosity.

Figure 8 highlights three designs of distinguished performance. They are the designs that turned out to be best, not only with regard to total resistance at maximum speed but also at lower speeds. Table 3 summarizes the results. Design des_0134 (named explore_02_des0084 in Table 3) yields the lowest resistance at maximum and at cruise speed while des_0050 (named explore_02_des0000 in Table 3) gives second best total resistance at maximum speed, best wave resistance at cruise speed and lowest wave resistance at travel speed. Third-placed design des_0110 (named explore_02_des0060 in Table 3) furnishes the lowest total resistance at travel speed. This means that, interestingly, these designs are rather robust when it comes to speed changes. Figure 9 presents des_0134 in perspective view. As can be read from Table 3 this vessel belongs to the longer and finer instances in the design space.

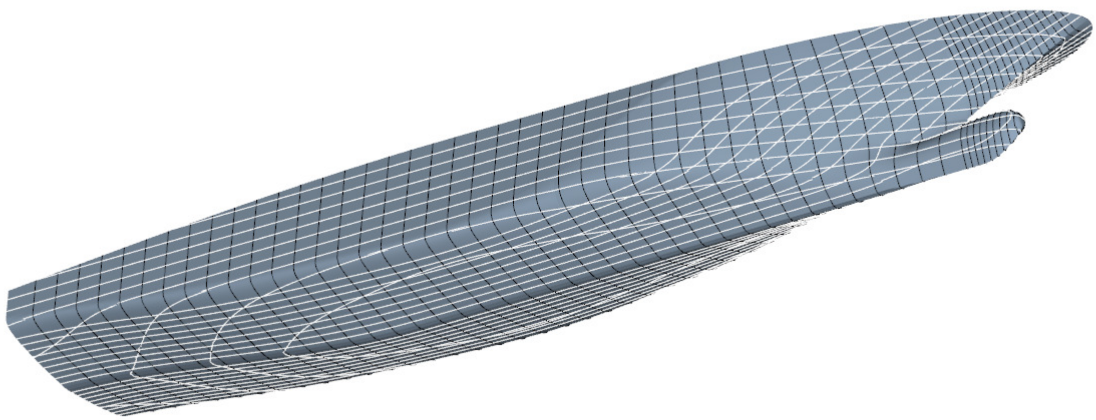

Figure 9: Best performing candidate from DoE

RESPONSE SURFACE METHODOLOGY

The diagrams and tables presented so far offer a finite (or discrete) view of the design situation. A transfinite view can be gained when utilizing response surface methodology. Response surfaces interpolate or approximate multi-dimensional data sets generated from complex models that, typically, would need substantial resources to solve – as is the case with CFD simulations (and even more so for experiments). In this sense they are meta-models, going one level of abstraction beyond the physical, mathematical and numerical models used to simulate system behavior. Various techniques are available, see Myers and Montgomery (2009) and Peri (2009).

Even though determining the hydrodynamic performance for three speeds of a mega-yacht's variant is comparably quick, say 15 minutes of total CPU time, it is still longer than one is prepared to wait in an interactive work flow. A Kriging approach on the basis of anisotropic variograms was therefore taken to determine a meta-model for total resistance and stability, see Tillig (2010) for an elaboration. A simple check for several vessels that were not used in establishing the meta-model gave deviations between the CFD and RSM values around 1% for stability and around 1.5% for total resistance. For a ranking of variants this seems to be promising enough even though the absolute values would probably not fully match experimental results (but model basins frequently report measurement accuracy in the range of one to two percent).

Figure 10 illustrates the dependency of total resistance R_T from (i) length and beam (left column) and (ii) the fullness of the design waterline and its entrance angle at FP (right column). For the Kriging the free variables were normalized to the interval [0, 1] using the corresponding bounds set in the DoE (see Table 1), i.e., zero equals the lower bound and one yields the upper bound. Figure 10 depicts iso-parameter surfaces of the nine-dimensional meta-model: while two free variables change the remaining seven free variables stay constant. For the illustration the constant free variables were chosen at 0.25 (lower part of Figure 10), 0.5 (middle part) and 0.75 (upper part). In general the resistance appears to be rather well-behaved (not many local minima). In the left column it can be nicely observed that for almost any beam the longer the vessel the better. However, for the longest vessels there are resistance minima for beam values larger than the lower bound. In the right column there are minima that lie in the middle of the intervals, meaning that it is not necessarily the extreme values that will eventually produce an optimum hull.

Finally, with a response surface that produces results more or less instantaneously any subsequent investigation can of course be sped up tremendously. Larger scale optimizations can now be undertaken for the entire set of free variables or any subset, depending on the designers' choice. Figure 11 illustrates such an optimization in which all free variables were allowed to change by means of a TSearch algorithm, see FRIENDSHIP SYSTEMS (2009). Some 224 designs were evaluated via the RSM within 11 minutes (instead of around 8 hours that would have been needed for a similar process on the basis of CFD simulations).

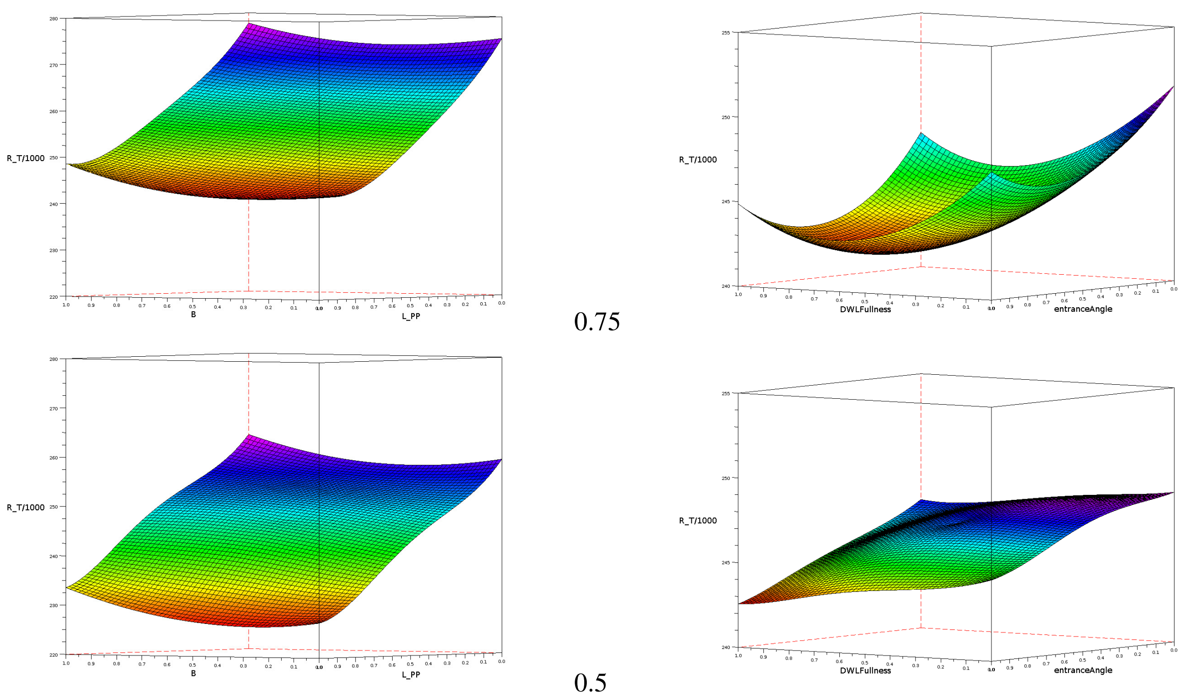

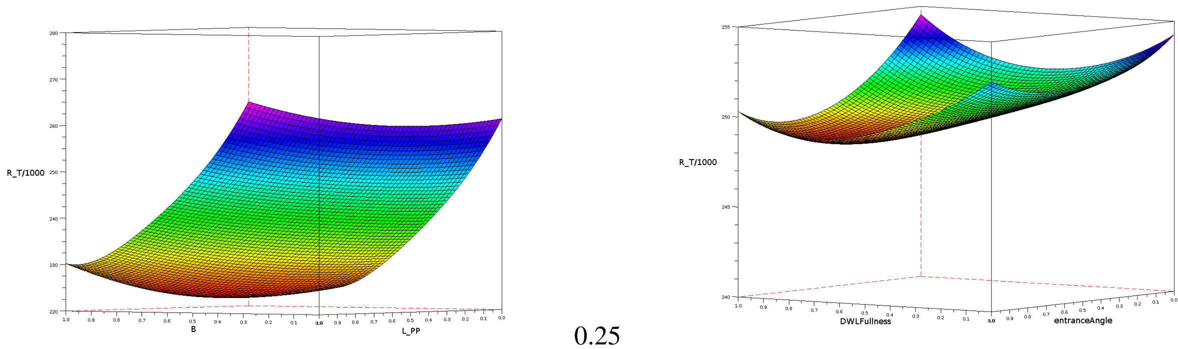

Figure 10: Response surface visualization for total resistance as a function of normalized length and beam (left column) and normalized fullness of DWL and entrance angle (right column)

The best hull from the TSearch exploitation was analyzed by CFD, too. The RSM gave a slight underestimation of total resistance by -1.8%. When comparing the hull to the exploration results it turns out that it performed practically the same as the best vessel from the DoE, namely des_0134 (Table 3). Total resistance is 0.2% higher but displacement volume increased by 1% for almost identical length (71.83m vs. 71.91m). Beam is slightly larger with 14.11m instead of 14.03m, leading to an augmentation of *KM* by 1.1%. One may cautiously conclude that des_0134 already performed really well but that alternatives can be found which are equally good in terms of hydrodynamics and somewhat different in hydrostatics, opening the naval architects additional options for their decisions.

As a final example, let us assume that L_{PP} and B need to be fixed to 70m and 14.2m, respectively. Then a new RSM optimization can be undertaken with the seven remaining free variables in the confined design space. Again this takes just a few minutes and one gets a number of promising candidates. The results give a good indication how much the newly imposed restrictions will cost in terms of resistance at maximum speed, namely 6.4% more than des_0134 that is longer and hence not feasible anymore, yet 5.8% less than the best from the original DoE for which length and beam are filtered to comply with the chosen main dimensions.

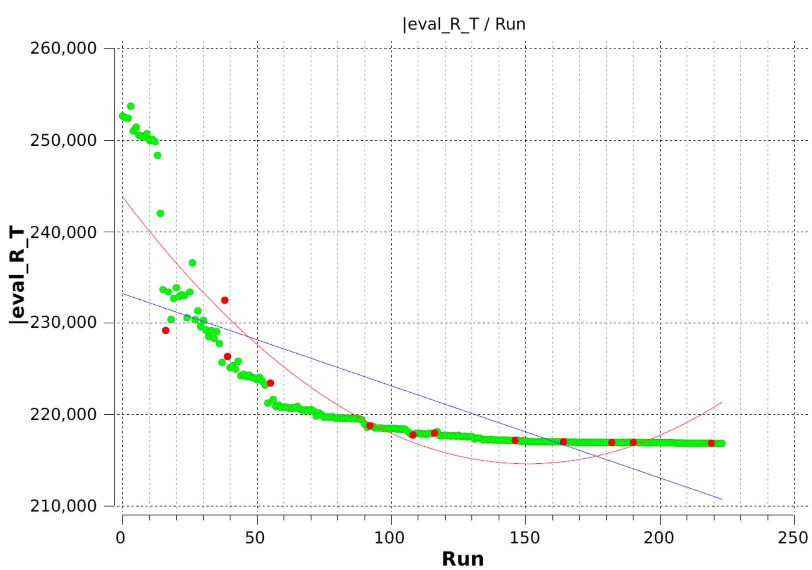

Figure 11: TSearch history for an RSM based optimization

CONCLUSION

In ship design the non-linear relationships between competing objectives, constraints, free and dependent variables is very challenging to grasp. A design spiral is the natural answer to cope with the complexity of the system. An additional design approach is proposed to utilize first principle methods for investigating and understanding multi-dimensional design spaces, bringing together more pieces of information in shorter time. The approach is illustrated for a fast mega-yacht. It builds on a suitable parametric model, here for shape generation and variation. The parameters chosen to be free (and independent) span the design space. They are regarded as the free variables of an optimization problem. Important objectives and constraints such as hydrostatics and hydrodynamic performance are determined by means of simulation. The design space is systematically and automatically explored utilizing formal methods. Tables and diagrams generated from comprehensive design sets assist in finding correlations, identifying (in)feasible regions and seeing (un)favorable combinations. A synopsis is given in Figure 12. Response surface methodology further supports the work flow. Not only is it useful in visualizing the design situation but it also speeds up subsequent optimization jobs. All this is believed to bear the potential of bringing naval architects into the more comfortable situation of better comprehending their design tasks at hand – either in becoming familiar with a novel design idea more quickly early into a project or in faster matching their product to a client's evolving needs.

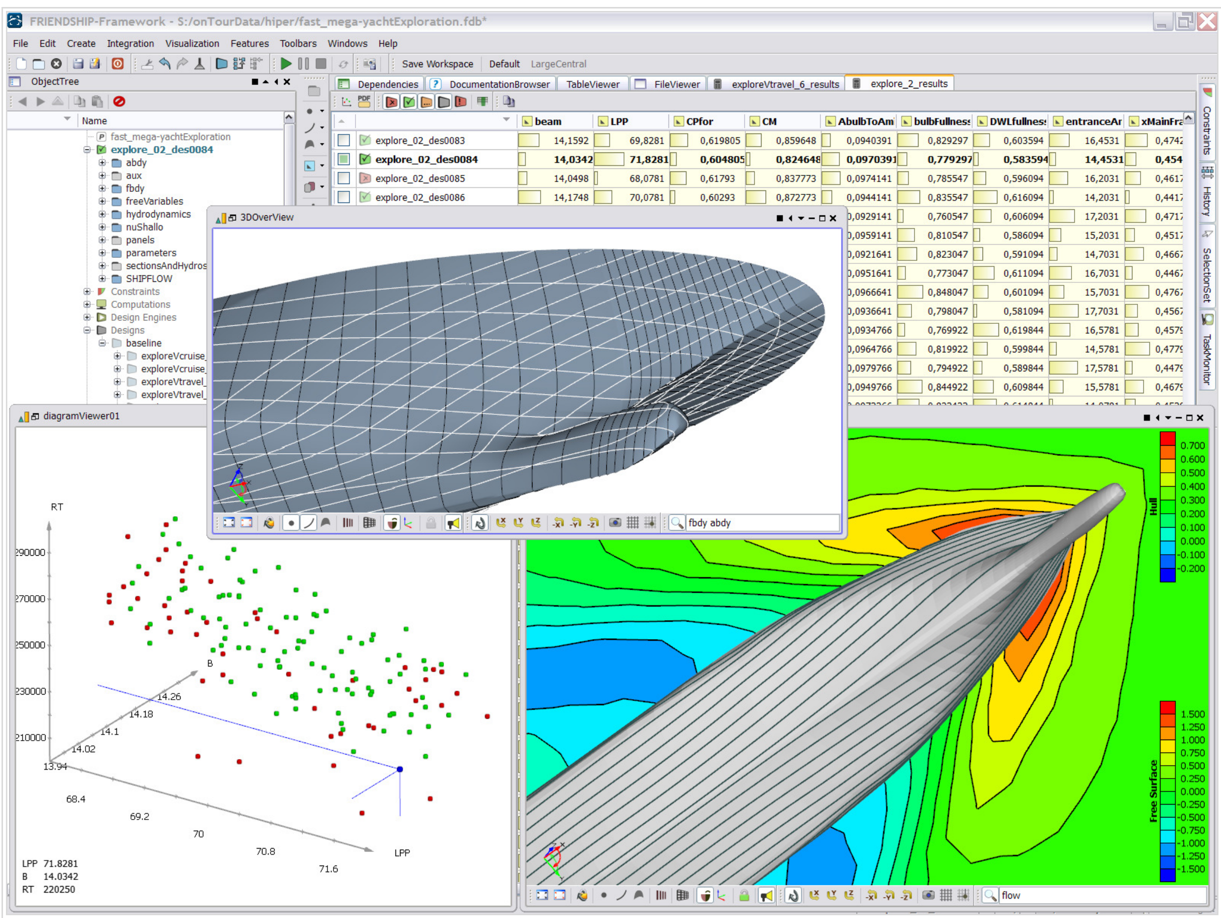

Figure 12: All data combined and presented within the *FRIENDSHIP-Framework*

ACKNOWLEDGMENTS

The author would like to thank Fritz Bohl and Fabian Tillig for their support in realizing this paper. While Fritz Bohl laid important foundations in his diploma thesis on mega-yacht design in cooperation with a relevant industry partner, Fabian Tillig developed the response surfaces methodology applied here and produced the corresponding figures.

REFERENCES

Abt, C. and Harries, S. (2007): "A New Approach to Integration of CAD and CFD for Naval Architects", *6th Int. Conference on Computer Applications and Information Technology in the Maritime Industries (COMPIT)*, Cortona, Italy

Abt, C., Harries, S., Wunderlich, S. and Zeitz, B. (2009): "Flexible Tool Integration for Simulation-driven Design using XML, Generic and COM Interfaces", *8th Int. Conf. on Computer Applications and Information Technology in the Maritime Industries (COMPIT)*, Budapest, Hungary

Bohl, F. (2009): "Entwicklung eines CFD basierten Modells für ein Virtual-Prototyping von Megayachten", Diploma thesis (in German), Technical University Berlin, Germany

Brenner, M. (2008): "Integration of CAD and CFD for the Hydrodynamic Design of Appendages in Viscous Flow", Diploma thesis, Technical University Berlin, Germany

Brenner, M., Abt, C. and Harries, S. (2009): "Feature Modelling and Simulation-driven Design for Faster Processes and Greener Products", *14th Int. Conference on Computer Applications in Shipbuilding (ICCAS)*, Shanghai, China

Druckenbrod, M., Hundemer, J., Abdel-Maksoud, M. and Steden, M. (2010): "Optimisation of Single- and Multi-Component Propulsors", *9th Int. Conf. on Computer Applications and Information Technology in the Maritime Industries (COMPIT)*, Gubbio, Italy

FLOWTECH International AB (2004): "XPAN / XBOUND Theory", Gothenburg, Sweden

FLOWTECH International AB (2009): "SHIPFLOW 4.3 Users Manual", Gothenburg, Sweden

FRIENDSHIP SYSTEMS (2009): "User Guide *FRIENDSHIP-Framework*", Potsdam, Germany

Harries, S. (1998): "Parametric design and hydrodynamic optimization of ship hull forms," Mensch & Buch Verlag, Germany, ISBN 3-933346-24-X

Harries, S. (2008): "Serious Play in Ship Design", *Tradition and Future of Ship Design in Berlin*, Colloquium, Technical University Berlin, Germany

Harries, S. and Vesting, F. (2010): "Aerodynamic Optimization of Superstructures and Components", *9th Int. Conf. on Computer Applications and Information Technology in the Maritime Industries (COMPIT)*, Gubbio, Italy

Myers, R. H. and Montgomery, D. C. (2009): "Response Surface Methodology: Process and Product Optimization Using Designed Experiments", John Wiley and Sons, Inc., Hoboken

Palluch, J., Starke, A. and Harries, S. (2009): "Parametric Modeling for Optimal Components in Turbomachinery", *Worldwide Turbocharger Conference*, Hamburg, Germany

Peri, D. (2009): "Self-Learning Metamodels for Optimization", Schiffstechnik Bd. 56 / Ship Technology Research Vol. 56

Peri, D., Pinto, A., Zotti, I. and Campana, E.F. (2007): "Simulation-Based Design of a Bulb-Cat Configuration", *6th Int. Conference on Computer Applications and Information Technology in the Maritime Industries (COMPIT)*, Cortona, Italy

Press, W., Teukolsky, S., Vetterling, W. and Flannery B. (2007): "Numerical Recipes – The Art of Scientific Computing", Cambridge University Press, New York, USA

Tillig, F. (2010): "Parametric Modeling and Hydrodynamic Analysis of Twin-Skeg Vessels", Diploma thesis, Technical University Berlin, Germany

Toderan, C., Guillaume-Combecave, J.-L., Boukaert, M., Hage, A., Cartier, O., Caprace, J.-D., Amirouche, A.; Constantinescu, A., Pircalabu, E. and Rigo, P. (2008): "Structural Optimization of a 220 000 m^3 LNG Carrier", 7th *Int. Conference on Computer Applications and Information Technology in the Maritime Industries (COMPIT)*, Liège, Belgium

Seventh International Conference
On High-Performance Marine Vehicles
Melbourne, Florida, USA
13-15 October 2010

EXPERIMENTAL AND NUMERICAL INVESTIGATION ON INTERCEPTORS' EFFECTIVENESS

Fabio De Luca	Claudio Pensa	Alessandro Pranzitelli
Università degli Studi di Napoli "Federico II"	Università degli Studi di Napoli "Federico II"	University of Leeds
fabio.deluca@unina.it	claudio.pensa@unina.it	A.Pranzitelli@Leeds.ac.uk

ABSTRACT

The use of controlling dynamic trim with interceptors is spread in a wide range of ships and boats. They typically work at best on planing or semi-planing hulls. Nevertheless over the last years they have been tested at displacement speeds, producing remarkable results. This is not strictly consistent with the usual theory that directly correlates lift and drag as a function of dynamic trim.

In order to achieve a good understanding of how the interceptor works, a research project has been started at the Dipartimento di Ingegneria Navale of the Università degli Studi di Napoli "Federico II" using a CFD RANS-multiphase code and Towing Tank experimental tests.

In particular a 2D flow on flat surface model has been analysed by CFD code to evaluate velocity and pressure distribution for $Rn = 10^7$*.Tests are performed with fixed trim. Data are obtained for different trim to evaluate variation of* C_L, C_D, C_M *coefficients. The data thus obtained help clarify the influence of* C_L *and* C_M *coefficients on flat surface resistance. At the same time, an experimental study on efficiency of interceptor and effectiveness installed on a V shaped bottom hulls has been performed.*

Data are now available on two hull geometry: warped and prismatic. Models have been tested on a wide range of displacements and dimensions of interceptors. Finally, influence of combined effect of centre of gravity position and interceptor's configuration will be shown.

INTRODUCTION

According to the common view, the effectiveness of interceptors is strictly correlated with the trim reduction and the consequent decrease of the resistance induced by the lift. Nevertheless, it is easy to observe that the efficiency of the interceptor is beyond of other trim controllers (e.g. flaps). The proportions of the greater efficiency are so considerable that a closer analysis of the physical model is greatly desirable to suggest new types of interceptors or different proportions and positions.

NOMENCLATURE

ΔG	G elevation (rise in G)
L_{CG}	Distance of centre of mass from transom
i	Interceptor height (perpendicular to the bottom)
β_T	Deadrise angle at transom
$\beta_{0.5}$	Deadrise angle at 50% L_{WL}
$\beta_{0.7}$	Deadrise angle at 70% L_{WL}

i_E	Half angle of entrance.
τ	Dynamic trim
τ_s	Trim at rest
C_P	Prismatic coefficient
C_T	Total-resistance coefficient
Fn	Froude number
Fn_∇	Volumetric Froude number
Rn	Reynolds number
R_T	Total resistance of bare hull
R_{Ti}	Total resistance of hull with interceptor
g	Acceleration due to gravity
ρ	Water density
W	Weight of the craft
∇	Displacement volume
A_T	Wetted transom area
A_X	Area of maximum transverse section

KEYWORDS

Interceptor, Intruder, Trim controller, High speed craft.

EXPERIMENTAL PROCEDURE AND RESULTS

Tests were carried out in towing tank of *Dipartimento di Ingegneria Nanale* of the *Università degli Studi di Napoli “Federico II”* whose dimensions are L = 136.5 m, B = 9.0 m and T = 4.5 m.
The tests have been carried out on a prismatic hull, C 0301, and on a warped model C 954. Figures 1 and 2 show the tested hulls. Next tables show the dimensions and geometric coefficients, respectively of C 0301 and C 954 models. The hydrostatic proprieties of both the models are referred at $L/\nabla^{1/3} = 5.09$.

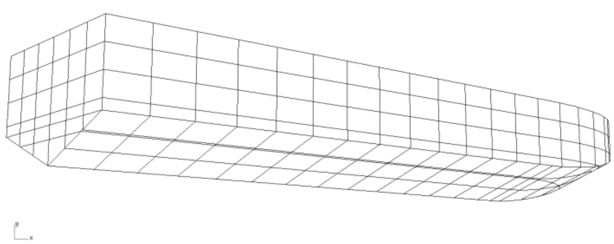

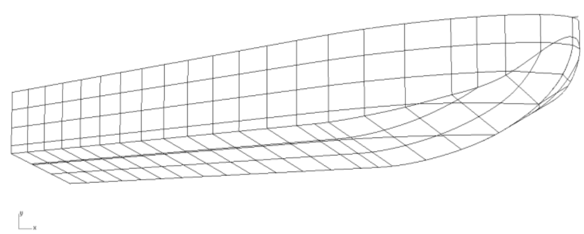

L_{WL}	2.387	m
B_{WL}	0.600	m
L/B	3.978	
Δ	102.8	kg

L_{CG}/L_{WL}	0.45	
A_T/A_X	1.00	
C_P	0.861	
β	20.0	deg

Figure 1: C.0301 model

The Figures 3a and 3b show the performances of both the models, tested as bare hulls (without interceptors). These data have been used as reference for the evaluation of interceptor’s effectiveness and efficiency. C 0301 model has been tested in three different centre of mass positions and at load fraction, $L/\nabla^{1/3} = 5.09$; diversely C.954 model has been tested at $\tau_s = 0$ and five different displacements.

Figures 4a, 4b and 4c show the effectiveness of the interceptors by the R_{Ti}/R_T ratio plotted against Fn_∇.The curves are plotted for constant values of interceptor’s heights i. The figures show that the higher reductions of resistance are experimented just over $Fn_\nabla = 2.0$. For $Fn_\nabla < 2.0$ It is found a direct proportionality between R_{Ti}/R_T and i. For $Fn_\nabla > 2.1$ the higher the speed the lower have to be the interceptors to avoid excessive trim corrections.

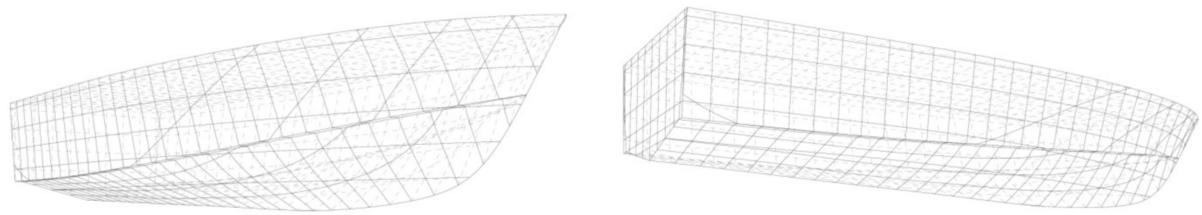

L_{WL}	2.390	m
B_{WL}	0.726	m
Δ	103.5	kg
L_{CG}/L_{WL}	0.40	
A_T/A_X	0.86	

C_P	0.704	
β_T	14.5	deg
$\beta_{0.5}$	21.8	deg
$\beta_{0.7}$	32.9	deg
i_E	27.6	deg

Figure 2: C 954 model

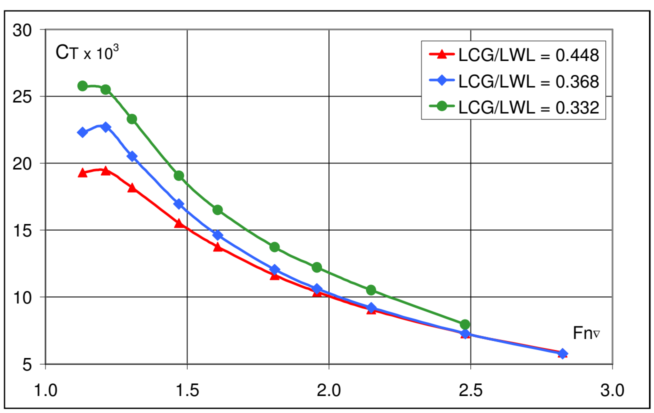

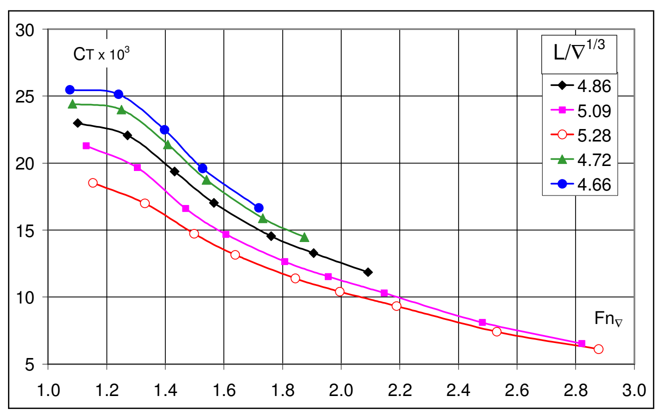

Figure 3a: C 0301

Figure 3b: C 954

Figure 5a, 5b and 5c show the values of dynamic trim related to i/L_{WL} ratio. Observing trim and resistance figures, it is easy to verify that the best performances are characterized by very low dynamic trim. These values are considerably lower than the typical best performance trim of bare hull. In particular – for example – it has been shown that for C 954 model without interceptors, at $L/\nabla^{1/3} = 5.09$ and $Fn_\nabla = 1.88$, the best trim is 4.2 degree; contemporary, in the same dynamic conditions, the absolute best performance has been find with the higher interceptor tested and $\tau = 1.0$ degree.

This observation suggests that the guiding principle commonly associated to the interceptors, cannot be generalized at least for planing and semi-planing crafts, and is essentially incomplete. We are referring to the effectiveness of interceptors strictly by the reduction of the resistance component depending on the trim (for a full planning craft this component is, exactly, W tan τ). The same reasoning explains the limit of the effectiveness observing that for very high speeds, a trim reduction realizes a strong increase of wetted surface and of the related frictional resistance.

To understand the phenomenon, both the models have been tested maintaining constant value of dynamic trim corresponding to the maximum effectiveness interceptor's height, shown in table 1.

As shown in the next figures, highlight that for both the hulls, prismatic and warped, the resistance reductions and raises of G are directly proportional to *i*. This behaviour emphasizes the strong influence of the interceptors on pressure and on the related rising of lift.

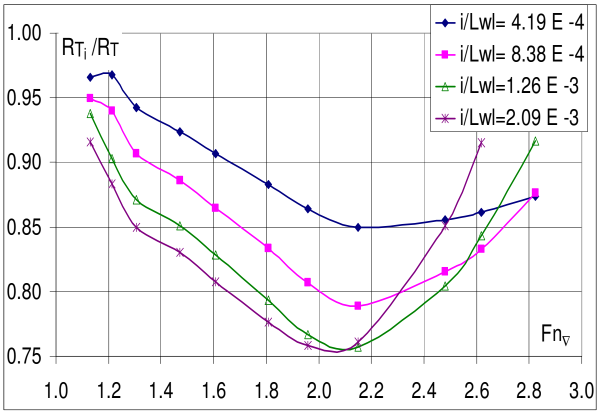

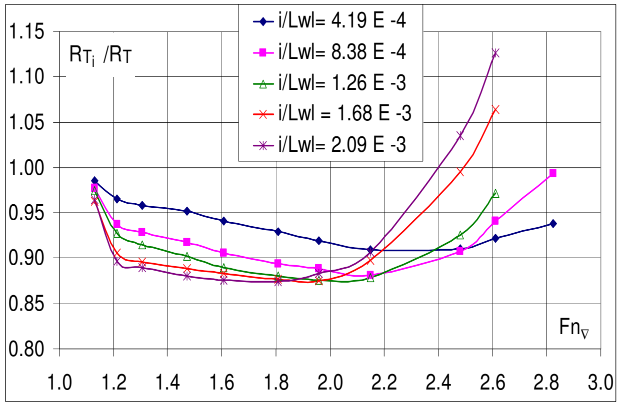

Figure 4a- C 0301 L_{CG}/L_{WL} = 0.332

Figure 4b- C 0301 L_{CG}/L_{WL} = 0.368

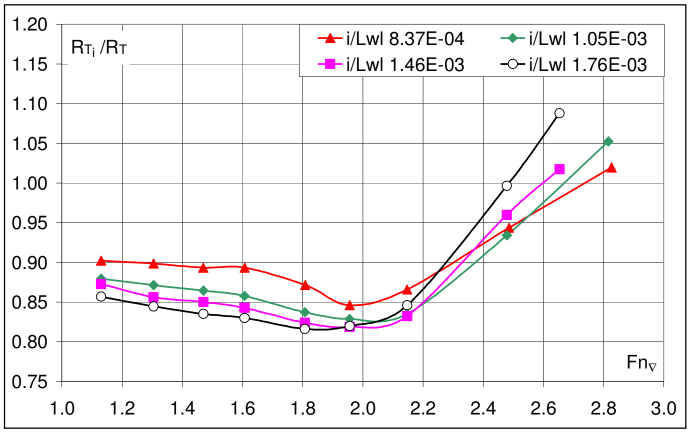

Figure 4c C 954

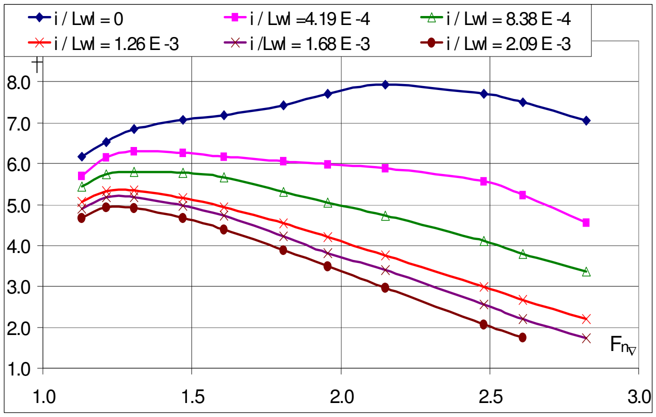

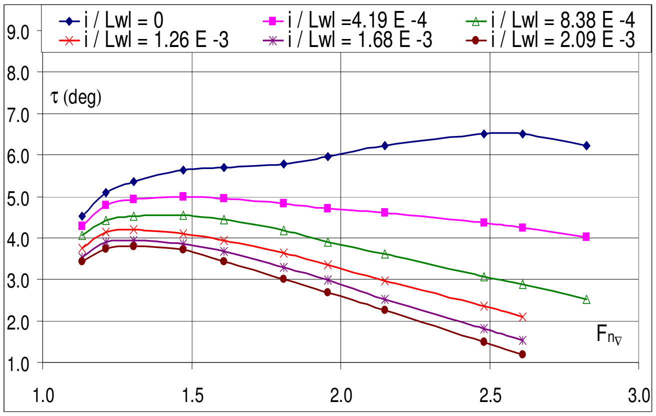

Figure 5a - C 0301 L_{CG}/L_{WL} = 0.332

Figure 5b - C 0301 L_{CG}/L_{WL} = 0.368

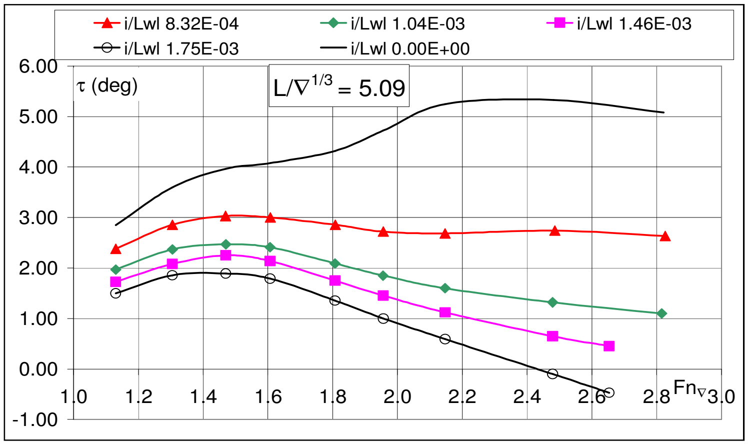

Figure 5c – C 954

Table1: Test Conditions of the model

	i/L_{WL}	L_{CG}/L_{WL}	τ (deg)	Fn_∇	$L/\nabla^{1/3}$
C 0301	1.26E-3	0.368	3.34	1.96	5.09
C 954	1.75E-3	0.400	1.03	1.91	5.09

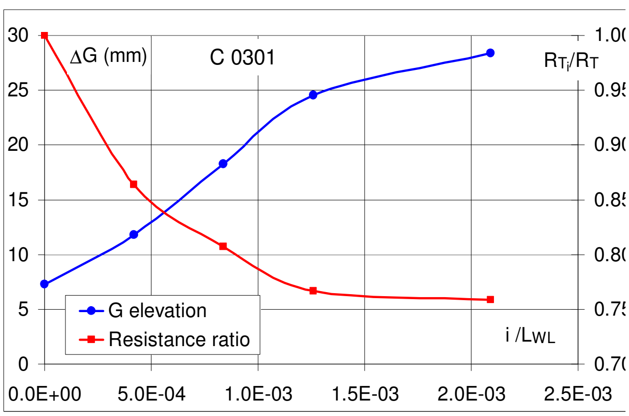

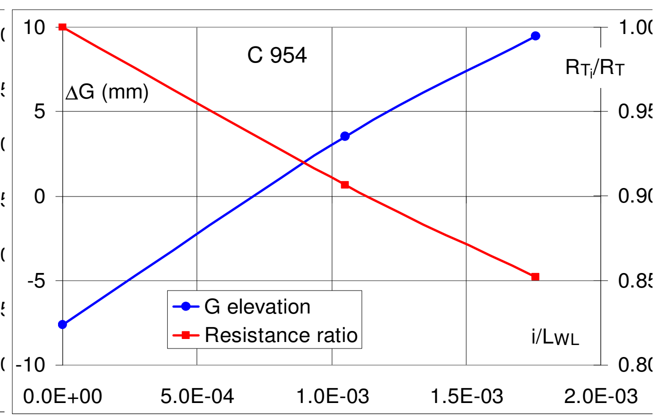

Figure 6a

Figure 6b

Figures show a steeper slope of the resistance curve of C 0301 respect the C 954. Probably, it is not due to warped bottom of C 954 but to the lower value of L_{CG}/L_{WL} of the C 0301. The C 954 model has been tested also to evaluate the influence of displacement on interceptor's effectiveness. Figures 7a and 7b suggest that the phenomenon is relatively insensitive to the hull weight. Note that trim major differences occur at lower speeds where the absolute values of resistance are substantially lower.

NUMERICAL ANALYSIS

To evaluate the effects of the interceptors on ships, the device has been applied at the trailing edge of several flat plates. The flat plates have been trimmed of an angle τ of 2 and 4 degrees with respect to the asymptotic velocity. Interceptors of 0, 3, 4, 5 mm have been considered. Since the performances of flat plate strongly depend on the wet lower surface it is necessary to have the same wet surface to compare correctly the results obtained. To this aim, the model shown in figure 8 has been devised. The inflow surface has been divided in two parts by means of a separator. A boundary condition of velocity inlet of only air has been imposed on the upper surface, while the entry of only water is allowed through the lower surface.

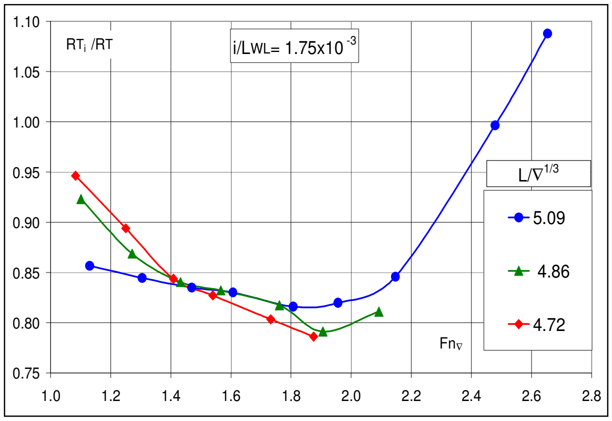

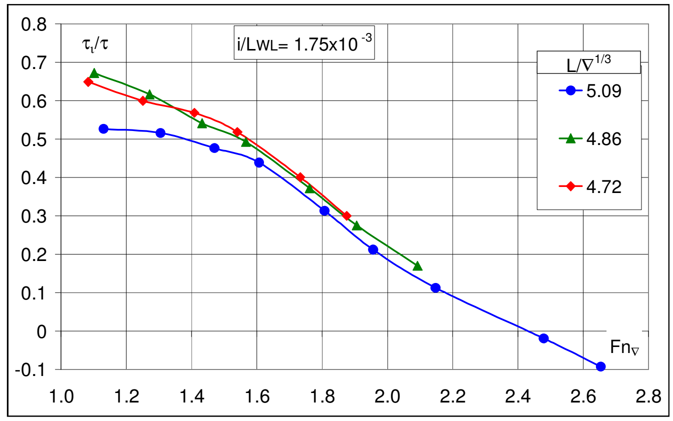

Figure 7a **Figure 7b**

Gravitational effects have been taken into account by means of the hypothesis of open channel flow with the free surface level at the same height of the separator. To reduce the influence of the separator on the flat plate boundary layer, a boundary condition of slip flow has been imposed on it. A pressure outlet and aslip wall boundary conditions have been imposed at the outlet surface and at the top and bottom surfaces of the numerical domain respectively.

To directly compare the numerical results with experimental data, a 2 meter long flat plate and an inlet velocity of 5 m/s have been considered. The resulting Reynolds number is around 10^7, similar to one encountered in towing tank tests. Unsteady RANS simulations have been carried out using the finite-volume commercial software Ansys Fluent V. 6.3. The Volume of Fluid (VOF) multiphase model has been adopted to predict the free-surface flow. The PISO algorithm has been employed for pressure-velocity coupling together with a second order upwind space discretization for the mean flow and turbulence equations. To discretize the convective term in the equation for transport of the volume fraction the High Resolution Interface Capturing (HRIC) scheme has been used, since it assures good accuracy with sustainable computational efforts.

For each case considered, a structured grid of about 60˙000 cells has been made. Turbulence effects have been taken into account by means of the Realizable κ-ε turbulence model. To better understand the behaviour of the intruder on the flat plate performances, a near-wall modelling approach has been applied, recurring to the height of the near-wall cells of 4×10^{-5} m, which led to $y+ \approx 1$. Figure 9 shows a particular of the computational grid in the region of the interceptor for one of the cases considered. To avoid the reflection of the waves, numerical diffusivity has been introduced at the top and bottom walls recurring to a high cell growth rate close to them.

Figure 10 shows velocity vectors close to the interceptor for the flat plate with $\tau = 2$ degree and $i = 3$ mm. The figure shows the vortices generated in air (blue) and in water (red).

Figures 11a and 11b, show the relative pressure coefficients on the plate for 2.0 and 4.0 deg of trim. Numerical results are consistent with experimental data showing a strong increase of C_P. The figures show also that the interceptor affects the pressure on a great amount of the plate. Figures 12a and 12b show the trends of lift and moment coefficients, C_L and C_M, for i varying from 0 to 5 mm. With the strong increase of the C_P distributions, the figures highlight the dramatic effect of interceptors on the lift.

The same figures show the smaller values of the drag coefficient C_D. Values of C_L and C_D so much different reveal the high efficiency of the interceptors and explain why they are better than other trim controllers. The numerical procedures have been performed for 2 and 4 degrees to investigate typical conditions of different Fn. Results show that the effectiveness, in both conditions, reaches remarkable values.

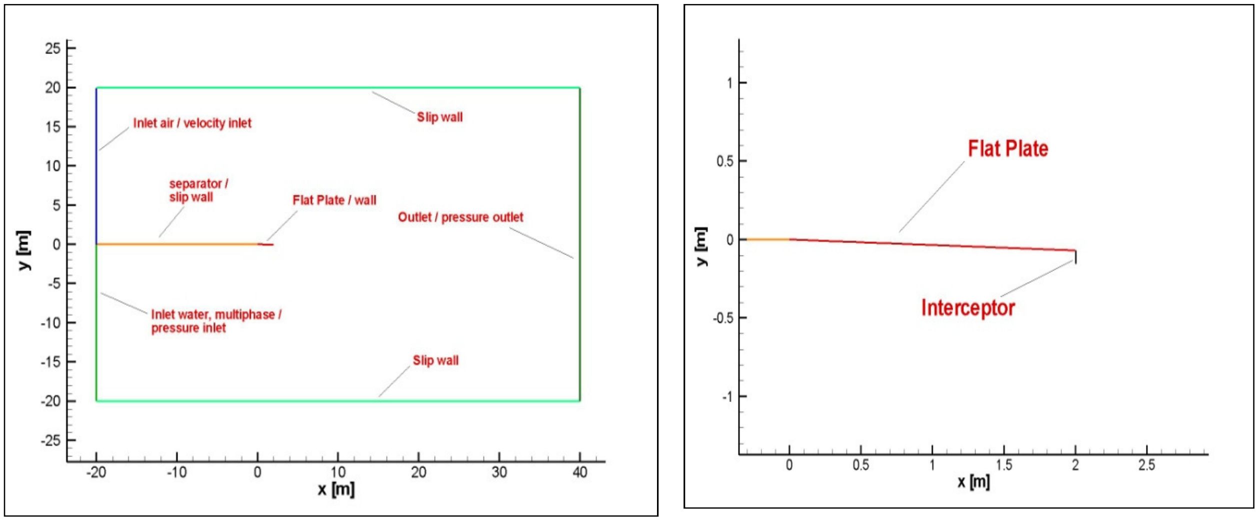

Figure 8

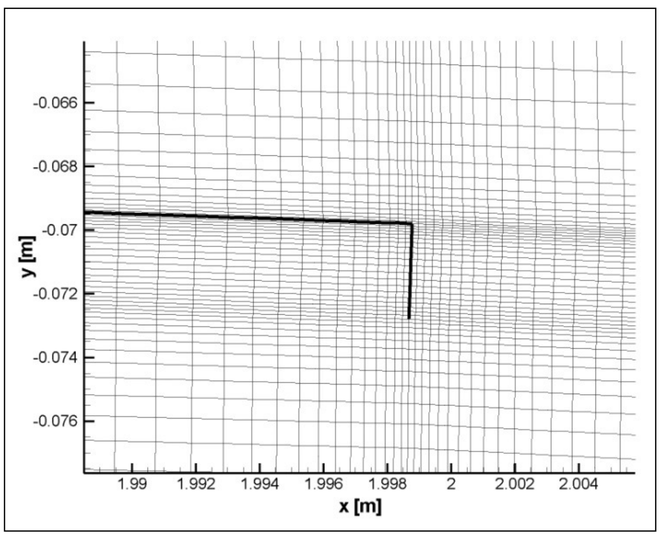

Figure 9

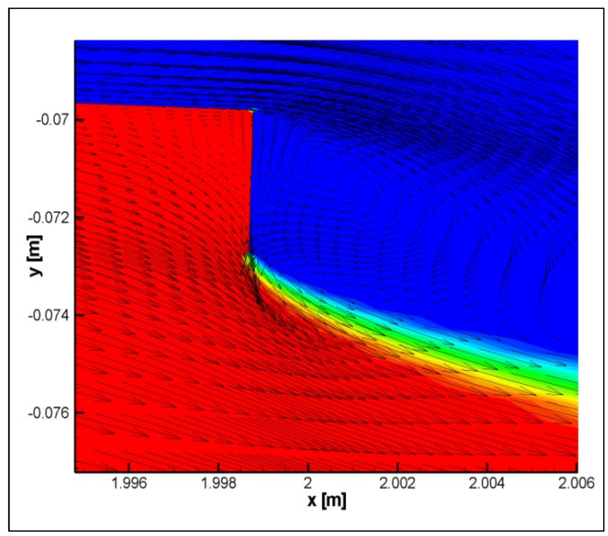

Figure 10

CONCLUSIONS

The experimental and numerical data showed highlight same aspects of the interceptors' physical model that seem useful to optimize the employment of these trim controllers. Particularly we have observed that:

1. the moments to trim caused by the interceptors cannot be the only explanation of the high performances obtainable;
2. both experimental data and numerical simulations have shown the substantial role of the lift coefficient;
3. a strong contribute of the lift increase is due to the great decay length of the overpressure (about 80 % of plate length);

4. numerical results highlight the smallness of the drag coefficients with respect to the moment and the lift due to the interceptors and the consequent high efficiency of these trim controllers;

Obviously, for semi-planing or lower speed, the significance of the lift increase would be less influent. Nevertheless experimental evidence, available in technical literature, has shown the effectiveness of interceptors also in this range of speeds. To understand the physics of this topic, the research will be carried on also analyzing displacement and semi-planing hulls.

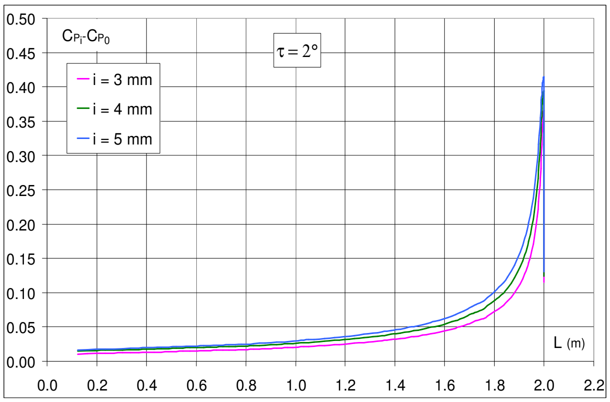

Figure 11a

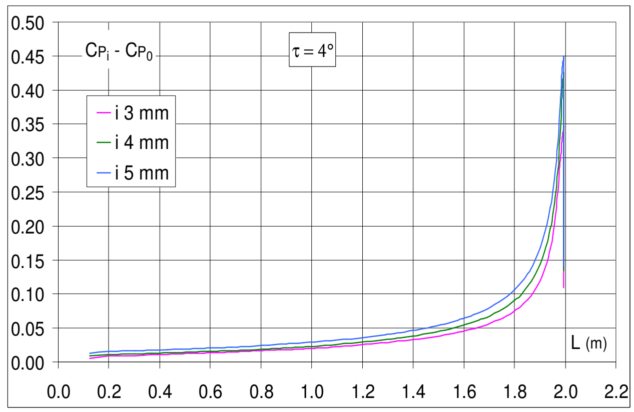

Figure 11b

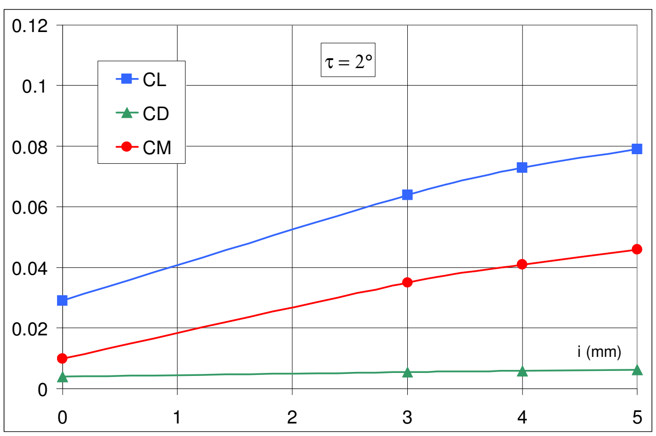

Figure 12a

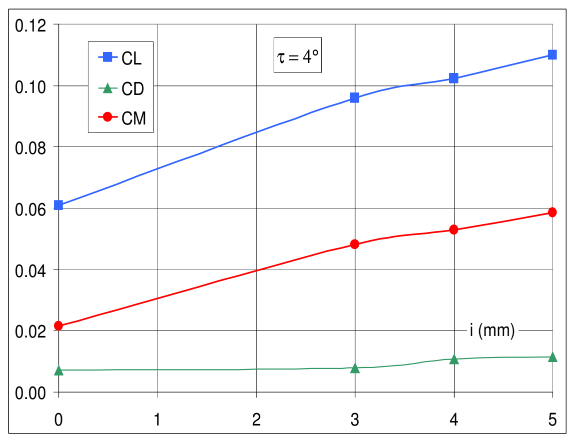

Figure 12b

REFERENCES

Savitsky D., Morabito M. (2010): “Surface Wave Contours Associated with the Forebody Wake of Stepped planning hulls” *SNAME; Marine technology,Vol 47 n° 1, January, pp. 1÷16*

Tsai J.F., Hwang J.L., Chou S .K. (2003): "Study on the compound effects of interceptor with stern flap for two fast monohulls with transom stern", *Proc. FAST 2003*, Ischia, Italy

A. Molini A., Brizzolara S. ((2005): “Hydrodynamic of Interceptors: a Fundamental Study”, *Proc. FAST 2005*, St. Petersburg, Russia

Mancini A., Moriconi A. (2006): "Riscontri sperimentali sul funzionamento e l'utilizzo dell'intruder" *Proc. SEAMED 2006*, Messina Italy

Azcueta R. (2001): " Computation of Turbulent Free-Surface Flows Around Ships and Floating Bodies ", *PhD thesis, Technical University Hamburg*, Harburg, Germany

Pranzitelli A. (2008): "Previsione numerica del campo fluidodinamico e della resistenza al moto di carene." *PhD thesis*, Università degli Studi di Napoli “Federico II”, Naples, Italy

Hirt C.W., Nichols B.D. (1981): “Volume of fluid /VOF/ method for the dynamics of free boundaries” *Journal of Computational Physics*, n° 39, January, pp. 201–225.

Seventh International Conference
On High-Performance Marine Vehicles
Melbourne, Florida, USA
13-15 October 2010

STUDY OF DRAG REDUCTION IN AXISYMMETRIC UNDERWATER VEHICLES USING AIR JETS BY CFD APPROACH

Shereena S G[a], S Vengadesan[b], V.G Idichandy[a] and S.K Bhattacharyya[a]

[a]Department of Ocean Engineering, [b]Department of Applied Mechanics
Indian Institute of Technology Madras
Email ID: skbh@iitm.ac.in

ABSTRACT

This paper presents a computational fluid dynamics approach to study drag reduction of axisymmetric bodies by air jet injection in the boundary layer. MIXTURE model is used to capture the multiphase flow and k-ω SST (shear stress transport) turbulence closure model has been used in computations. Well studied Afterbody1 (Huang et al, 1978) which has a tapered and smooth stern profile is considered. A companion shape of Afterbody1, which has a blunt stern profile, is also studied. The study is carried out with different air jet to body speed ratios and variation in drag reduction is reported. The effect of tapered against blunt aft shape of Afterbody1 has been found to have significant effect on drag reduction performance.

INTRODUCTION

Turbulent flows can occur in the boundary layer near solid surfaces. The energy losses and self-noise due to turbulence friction can be of very high magnitude. It can affect performance of many engineering devices. This necessitates unabated research on strategies for drag reduction. One of the ways to achieve the drag reduction is to delay the onset of turbulent flow, which a drag reducer does by shifting the transition from a laminar to a turbulent flow at a higher flow velocity.

Some of the important drag reduction technologies reported in the literature are introduction of polymers, surfactants, microbubbles in the boundary layer and use of compliant coatings. Gas-based drag reduction technologies include supercavitation, partial cavitation and microbubble ejection. Microbubbles are perhaps the cheapest and the most non-polluting drag reducer where air bubbles are introduced to reduce the frictional resistance. The injected air bubbles modify the energy inside a turbulent boundary layer and thereby lower the skin friction. However, the control of the bubble size and the angle of ejection can impose technical challenges. Introduction of air jets in the boundary layer also gives similar drag reduction effects as that of microbubbles. In the present study, drag reduction is obtained by ejecting air jet in the boundary layer.

The Reynolds-Averaged Navier-Stokes (RANS) equations, commonly used in CFD techniques for studying different practical flows, is used to study the drag reduction of axisymmetric underwater vehicles.

NOMENCLATURE

g	Acceleration due to gravity
$\vec{F}$	Body force
k	Turbulence kinetic energy

n	Number of secondary phases
m	Mixture
$\dot{m}_{qp}$ and $\dot{m}_{pq}$	mass flow rates
p	Secondary phase
q	Primary phase
r	Distance along the radial direction
R	Radius of the body
R_{eh}	Reynolds number
U	Body speed
U_{jet}	Air jet velocities
$\vec{v}_{dr,k}$	Drift velocity for the secondary phase k
$\vec{v}_k$	Mass-averaged velocity of the phase
$\vec{v}_m$	Mass-averaged velocity
$\vec{v}_{qp}$	Relative velocity
α_k	Volume fraction of phase k
ρ_k	Density of phase k
ρ_m	Mixture density
μ_m	Viscosity of the mixture
μ_k	Viscosity of the phase
ω	Specific dissipation rate

ABBREVIATIONS

CFD	Computational Fluid Dynamics
AUV	Autonomous underwater vehicle
RANS	Reynolds-Averaged Navier-Stokes
DR	Drag reduction
SST	Shear stress transport
LDV	Laser doppler velocimeter
PIV	Particle image velocimetry technique
CRSM	Curvature-dependent Reynolds-stress model
MDF	Marker density function
DNS	Direct numerical simulation

KEYWORDS

Underwater vehicle, Axisymmetric body, Computational fluid dynamics, Air jet, Drag reduction

LITERATURE STUDY

A number of drag reduction studies have been done on flat plate as well as on axisymmetric bodies. In a recent review, Truong (2001) has discussed some of the important drag reduction technologies such as introduction of polymers, surfactants, microbubbles and compliant coatings on the wall surface.

Madavan *et al* (1985) used an array of flush-mounted hot films to study the downstream evolution and persistence of the reduction of skin friction in the microbubble-laden turbulent boundary layer over a flat plate. Kim *et al* (1995) considered experimental data to investigate the way in which the reduction in wall shear stress changes with distance from the injection region due to microbubble injection. Kato *et al* (1999) measured velocity and turbulence intensity of a turbulent boundary layer with microbubbles by a laser doppler velocimeter (LDV) system in forward scatter mode for flow over a flat plate. Kodama *et al* (2000) experimentally studied microbubbles using a specially designed circulating water tunnel for experiments. Moriguchi *et al* (2002) examined the effect of microbubbles on drag reduction in a two-dimensional turbulent flow channel, with the aim of clarifying effect of bubble size. Wedin *et al* (2003) conducted an investigation of microbubble flow in experiments performed within a vertical pipe. Hassan *et al* (2005) studied the structure of flow turbulence in a water channel with microbubbles using particle image velocimetry technique (PIV) at a Reynolds number of 5128. Based on effective experimental observation and measuring technology, Wu *et al* (2005) analysed the interaction between liquid turbulent boundary layer and a crowded group of microbubbles. Murai *et al* (2007) experimentally investigated skin friction drag reduction in a horizontal rectangular channel by bubbles that are large relative to the shear layer. Wu *et al* (2008) attempted to find the optimum parametric levels for robust design of the microbubble drag reduction in turbulent channel flow.

Huang *et al* (1978) reported comprehensive experimental results for two axisymmetric body shapes with smooth aft end, designated as 'Afterbody1' and 'Afterbody2' at Reynolds number of 6.6×10^6 and 6.8×10^6 respectively. Deutsch *et al* (1985) studied the injection of gas to form microbubbles in a liquid turbulent boundary layer in water tunnel tests to reduce skin friction drag on an axisymmetric body. Fontaine *et al* (1992) studied the influence of the type of gas on the performance of microbubble skin friction reduction on an axisymmetric body. The gases used were of different density and solubility such as air, helium, carbon dioxide and argon. Helium was found to be more effective than other gases. Sarkar *et al* (1997) numerically studied flow past axisymmetric bodies using four different turbulence models. They found that standard k-ε model with wall function predicted the flow characteristics more accurately than the other models. Wu *et al* (2006) numerically simulated the effect of microbubble flow around an axisymmetric body. They found that around 50% of drag reduction can be obtained by injecting microbubble into the flow domain with most favorable combination of parameters.

Various numerical studies have been done to calculate drag force and drag reduction using microbubbles. Kanai *et al* (2001) developed marker density function (MDF) method to conduct direct numerical simulation (DNS) for bubbly flows. Skudarnov and Lin (2006) found that single phase model with bubbles introduced as species mass source was able to predict drag reduction consistent with the experimental data than that by more complex two-fluid model. Mohanarangam *et al* (2009) studied the phenomenon of drag reduction by the injection of microbubbles into turbulent boundary layer using an Eulerian-Eulerian two-fluid model.

From the literature review, it is observed that drag reduction by using microbubbles is an effective method of drag reduction, hence similar approach can be used to study drag reduction using air jets. From Mohanarangam *et al* (2009) and Wu *et al* (2006), *k-ω SST* model is found to best to capture turbulence in the flow field. Hence this turbulence model is used for the present CFD study.

PROBLEM DESCRIPTION

Two axisymmetric underwater vehicle shapes has chosen for studying drag reduction using air jet by CFD approach. These body shapes are designated Afterbody1 (Fig 1) and Blunt Afterbody1 (Fig 2). The geometry of Afterbody1 is given by Huang *et al* (1978), where an extensive experimental wind tunnel study on this body shape is reported covering detailed measurements of static pressure distribution, mean velocity profiles and distributions of turbulence intensities and Reynolds stress across the stern boundary layers. The geometry of Blunt Afterbody1 is same as that of Afterbody1 in the nose and parallel middle body region as also in total length. In Blunt Afterbody1, the parallel middle body extends the full length and ends there without any streamlined tapering of the stern profile as in Afterbody1. Since base drag is expected to be a significant component of the total drag of the Blunt Afterbody1, its drag reduction characteristics is expected to be significantly different from that of Afterbody1.

The location of the air jet is chosen at the shoulder of the nose shape, where parallel middle body (i.e. r = R) starts. The chosen angle of air jet (with the x-axis) is 30° for all calculations. Both the location and jet angle, through essentially arbitrary, are deemed practical. Since only axisymmetric CFD calculations are made use of rather than 3D CFD calculations, the implied shape of air jet is a circular ring. Air jet inlet size was maintained same for both the body geometries. For various air jet velocities (U_{jet}) to body speed (U) ratios drag reduction calculations are done. ANSYS ICEM software is used to create the mesh. Commercially available CFD software FLUENT has been used for all simulations.

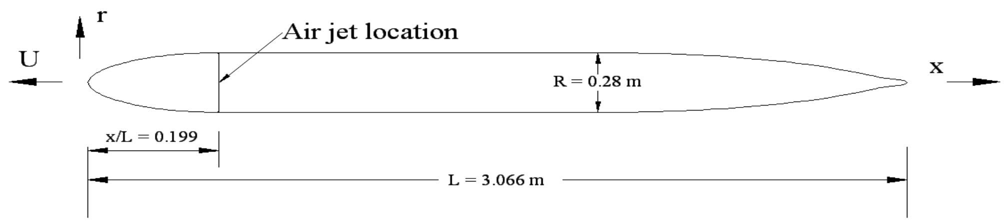

Figure 1: Geometry of Afterbody1 (Huang et al, 1978) showing air jet ring

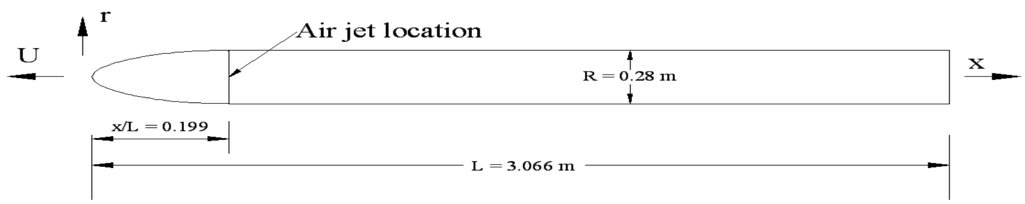

Figure 2: Geometry of Blunt Afterbody1 showing air jet ring

NUMERICAL STRATEGIES

The basic fluid needs only single phase simulation i.e. for water. However, when the air jet is introduced, the flow becomes two phase flow. For simulating two phase flow, the MIXTURE model as implemented in FLUENT is used. This simplified model can be used to model multiphase flows where the phases move at different velocities. The mixture model can model '*n*' phases (fluid or particulate) by solving the momentum and continuity for the mixture, the volume fraction equations for the secondary phases, and algebraic expressions for the relative velocities. The phases are treated as interpenetrating continua.

Governing Equations

The continuity equation for the mixture (*m*) is $\frac{\partial \rho_m}{\partial t} + \rho_m \vec{v}_m = 0$ (1)

where ρ_m is the mixture density and $\vec{v}_m$ is the the mass-averaged velocity given by $\rho_m = \sum_{k=1}^{n} \alpha_k \rho_k$ and $\vec{v}_m = \frac{\sum_{k=1}^{n} \alpha_k \rho_k \vec{v}_k}{\rho_m}$ respectively.

The momentum equation for the mixture is obtained by summing the individual momentum equations for all phases. It can be expressed as

$$\frac{\partial}{\partial t}(\rho_m \vec{v}_m) + \nabla \cdot (\rho_m \vec{v}_m \vec{v}_m) = -\nabla p + \nabla \cdot [\mu_m (\nabla \vec{v}_m + \nabla \vec{v}_m^T \vec{v}_m^T)] + \rho_m \vec{g} + \vec{F} + \nabla \cdot (\sum_{k=1}^{n} \alpha_k \rho_k \vec{v}_{dr,k} \vec{v}_{dr,k}) \quad (2)$$

μ_m is the viscosity of the mixture which is given by $\mu_m = \sum_{k=1}^{n} \alpha_k \mu_k$

$\vec{v}_{dr,k}$ is the drift velocity for secondary phase k , defined as $\vec{v}_{dr,k} = \vec{v}_k - \vec{v}_m$ (3)

The relative velocity (also referred to as the slip velocity) is defined as the velocity of a secondary phase (*p*) relative to the velocity of the primary phase (*q*) $\vec{v}_{pq} = \vec{v}_p - \vec{v}_q$ (4)

The mass fraction for any phase (*k*) is defined as $c_k = \frac{\alpha_k \rho_k}{\rho_m}$ (5)

The drift velocity and the relative velocity $\vec{v}_{qp}$ are connected by $\vec{v}_{dr,p} = \vec{v}_{pq} - \sum_{k=1}^{n} c_k \vec{v}_{qk}$ (6)

Mixture model makes use of an algebraic slip formulation. The basic assumption of the algebraic slip mixture model is that to prescribe an algebraic relation for the relative velocity, a local equilibrium between the phases should be reached over short spatial length scale.

From the continuity equation for the secondary phase *p*, the volume fraction equation for secondary phase *p* is obtained as

$$\frac{\partial}{\partial t}(\alpha_p \rho_p) + \nabla \cdot (\alpha_p \rho_p v_m) = -\nabla \cdot (\alpha_p \rho_p \vec{v}_{dr,p}) + \sum_{q=1}^{n} (\dot{m}_{qp} - \dot{m}_{pq}) \tag{7}$$

For simulating turbulent flow, the *SST* k-ω turbulence model is used in calculations based up on the recommendation of Mohanarangam *et al* (2009) and Wu *et al* (2006), who found that this model is well suited for simulating two phase flows. This model is an effective blend of robust and accurate formulation of the k-ω model in the near wall region and k-ε model in the far field.

COMPUTATIONAL DOMAIN AND BOUNDARY CONDITIONS

Symmetry of the problem is exploited by adopting an axisymmetric domain in a plane as shown in Figure 3. The domain details and boundary conditions are taken from Virag *et al* (2008). The boundary conditions are : (a) segment AB is velocity inlet, i.e. where U is prescribed in x direction; (b) segment CD is the pressure outlet where the gradients of turbulent kinetic energy and dissipation rate are set to zero and the pressure is set to the gauge pressure i.e. p = 0; (c) segment AD is the cylindrical surface where zero shear stress is prescribed; (d) symmetry conditions are prescribed on axis given by the segments BC and (e) no slip condition is prescribed on the body surface (or wall). Standard wall functions are used to calculate the variables at the near-wall cells. At a distance of X_{jet} from the nose of the body, air jet is introduced at an angle of θ (see Figure 4). The boundary condition used is velocity inlet with air speed of U_{jet}.

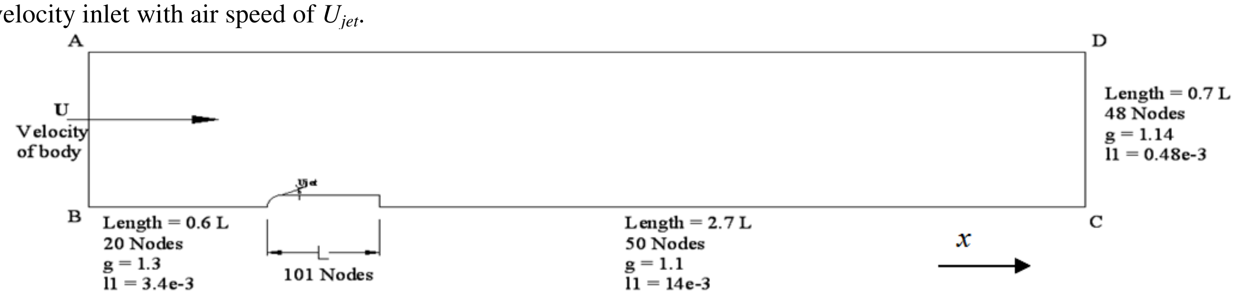

Figure 3: Computational domain

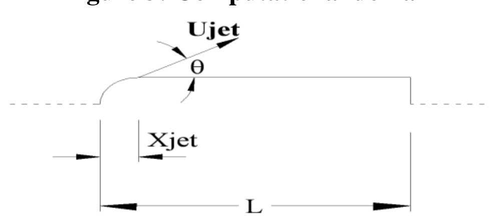

Figure 4: Enlarged view of domain details on the body

At the velocity inlet (segment AB), one needs to specify a representative value of turbulent intensity parameter T_u and length scale l. In all calculations, the values of these parameters have been chosen as T_u = 0.05 (i.e. 5 %) and l = 0.001L, where L is the characteristic length of the body.

Grid and Discritization

Since the body is axisymmetric, a 2D axisymmetric mesh is used for the analysis. The mesh is made finer near the body and coarser away from the body. Along the length of the body uniform mesh is maintained. Since SST k-ω

model is used, the non-dimensional wall distance (y^+) is maintained in the range of 30 to 300 to capture the turbulence near the body wall (Virag *et al*, 2008). A sample 2D axisymmetric mesh is shown in Figure 5.

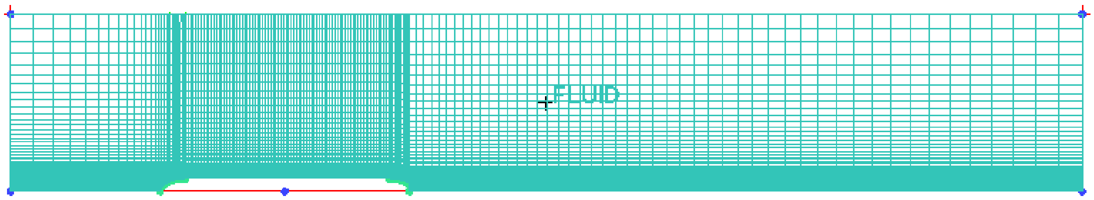

Figure 5: 2D mesh

Second order upwind scheme is used to discrertise the convective terms. All simulations were run using 2D unsteady segregated solver. The convergence criterion of 10^{-4} is set for velocity components and 10^{-3} for continuity, k, ε and ω. The termination of the program is based on the final steady value of drag, when the body attains a steady velocity. The time step used for simulation is 0.0001s.

RESULTS AND DISCUSSION

Validation

Wu *et al* (2006) conducted numerical simulation of microbubble flow around an axisymmetric body where, the flow with microbubbles was treated as mixture flow. They also studied the distribution of microbubbles in the vicinity of the body and the resulting drag reduction under different conditions. They have reported a drag reduction up to 50%. In the present work the same geometry is taken and similar simulations were performed for validation purpose. Velocity of the body was 12 m/s and that of jet was 3.6 m/s, θ =90° (see Fig 4). Since some of the data such as jet diameter, turbulent intensity and length scale were not given in the paper exact results could not be reproduced. However, the results showed similar trend in drag reduction (see Table 1). From this, it was concluded that MIXTURE model and *k- ω SST* turbulence model are the appropriate CFD models which can be used for the present study.

Table 1: Comparison of drag reduction

U (m/s)	U_{jet} (m/s)	F_P (N)		F_V (N)		F_D (N)		Drag Reduction (%)	
		Present	Ref	Present	Ref	Present	Ref	Present	Ref
12	0	10.4	3.89	19.1	17.75	29.5	21.65	-	-
12	3.6	12.77	6.5	3.49	4.19	16.26	10.7	44.8	50

F_P - Pressure drag force, F_V - Viscous drag force, $F_D = F_P + F_V$ (Total drag force)
Ref – Wu *et al* (2006).

Results for Afterbody1 and Blunt Afterbody1

For Afterbody1, drag coefficients without air jet are compared with other published results in Table 2, showing good agreement. For drag reduction study, the body velocity was taken to be 15 m/s and air jet velocity was introduced at an inclination of 30° to the body surface in all calculations for both Afterbody1 and Blunt Afterbody1. The air jet velocities considered for Afterbody 1 were U_{jet} = 0.1, 0.5, 1, 2.5, 5, 7.5, 15 and 30 m/s and those considered for Blunt Afterbody1 were U_{jet} = 1, 5, 15, 30, 50 and 100 m/s. Reductions in drag force for both the bodies are summarized in Table 3, Figure 6 and Figure 7.

Table 2: Comparison of drag coefficient for Afterbody1

Source	C_{PV}	C_{FV}	C_{DV}
Experimental (1978)	-	-	0.0276
Sarkar *et al* (1997)	0.0027	0.0297	0.0324
Present	0.0039	0.0263	0.0302

Table 3: Variation of drag reduction with various air jet velocities

3(a): Afterbody1

U_{jet} (m/s)	U_{jet}/U	Pressure drag F_P (N)	Friction drag F_F (N)	Total drag F_D (N)	Drag reduction (%)
0	0	53	589	643	0
0.1	0.01	51	441	492	23.4
0.5	0.03	56	193	249.9	61.1
1	0.07	**79**	**169**	**249.4**	**61.2**
2.5	0.17	159	147	306	52.4
5	0.33	188	141	329	48.8
7.5	0.50	263	138	401	37.6
15	1.00	457	136	594	7.6
30	2.00	550	133	684	–6.3

U_{jet} (m/s)	U_{jet}/U	Pressure drag F_P (N)	Friction drag F_F (N)	Total drag F_D (N)	Drag reduction (%)
0	0	824	684	1508	0
1	0.07	890	224	1115	26.1
5	0.33	805	164	969	35.7
15	1.00	613	149	762	49.4
30	2.00	539	137	677	55.1
50	3.33	**525**	**128**	**654**	**56.63**
100	6.67	727	122	846	43.8

3(b): Blunt Afterbody1

The comparative drag reduction performance of the two bodies is brought out in Figure 8 as a function of the velocity ratio parameter U_{jet}/U. The total drag force consists of two components, namely pressure and viscous drag. It is found that both pressure and viscous drag has significant role in drag reduction (see Figure 6 for Afterbody1 and Figure 7 for Blunt Afterbody1). The variation of molecular viscosity along the length of the body is shown in Figure 9 and the variation of volume fraction along the length of the body is shown in Figure 10 for both Afterbody1 and Blunt Afterbody1. In Figures 9 and 10, U_{jet} = 1 m/s for Afterbody1 and U_{jet} = 50 m/s for Blunt Afterbody1, the air jet velocities at which drag reductions are maximum. The dynamic pressure distribution along the body wall is shown in Figure 11 for Afterbody1 and in Figure 12 for Blunt Afterbody1.

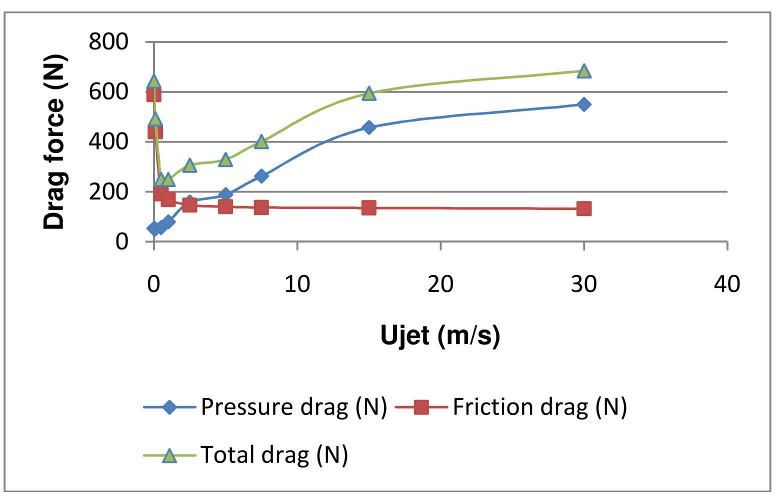

Figure 6: Variation of drag force with velocity of air jet for Afterbody1 (U = 15 m/s)

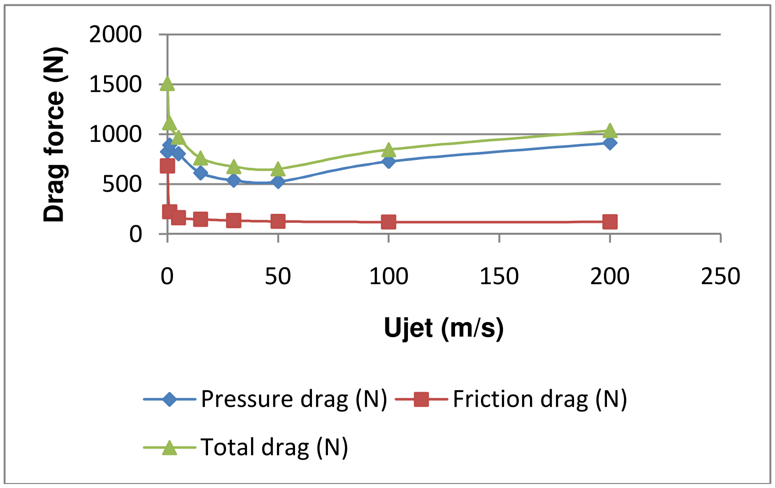

Figure 7: Variation of drag force with velocity of air jet for Blunt Afterbody1 (U = 15 m/s)

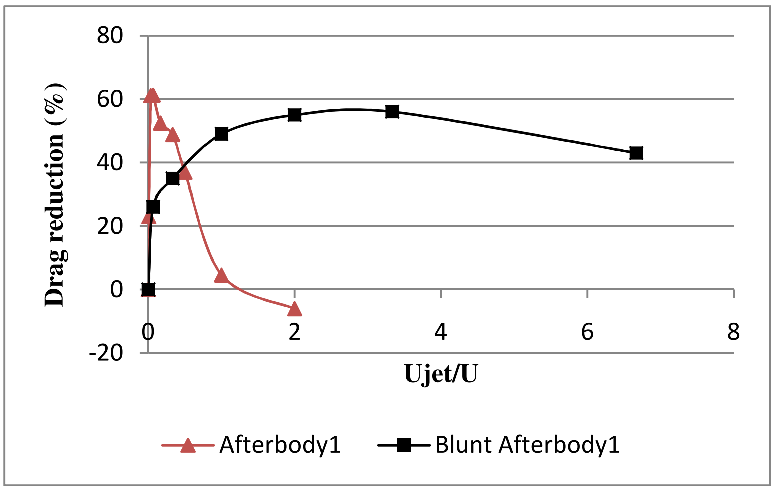

Figure 8: Comparison of drag reduction for Afterbody1 and Blunt Afterbody1

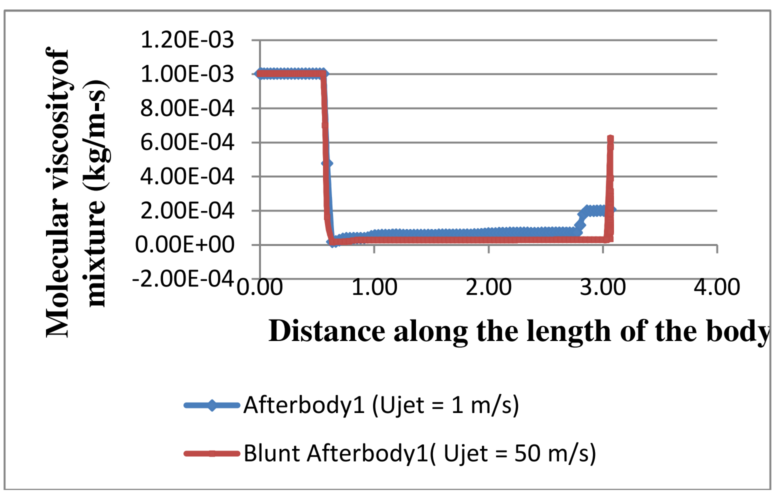

Figure 9: Plot of molecular viscosity of mixture along the length of the body

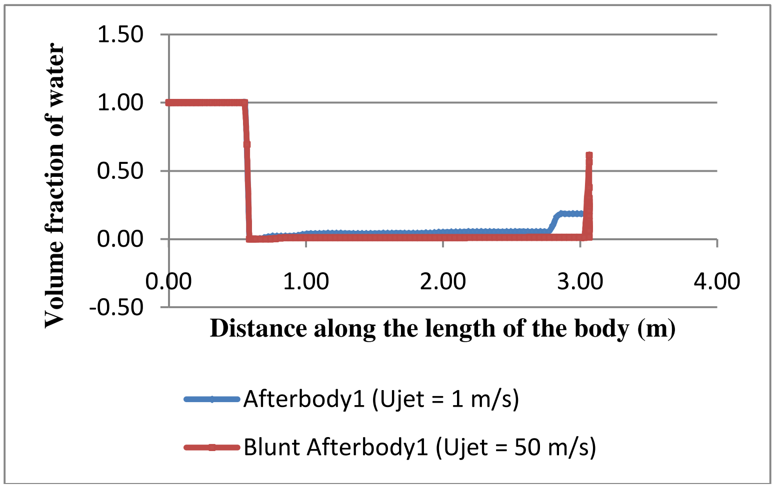

Figure 10: Plot of volume fraction of water along the length of the body

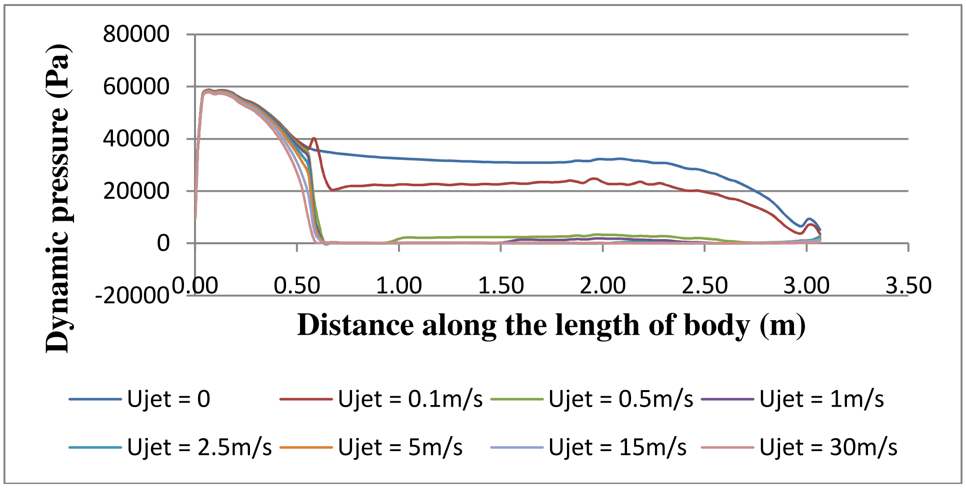

Figure 11: Dynamic pressure distribution along the length of the body for different cases for Afterbody1 (U = 15 m/s)

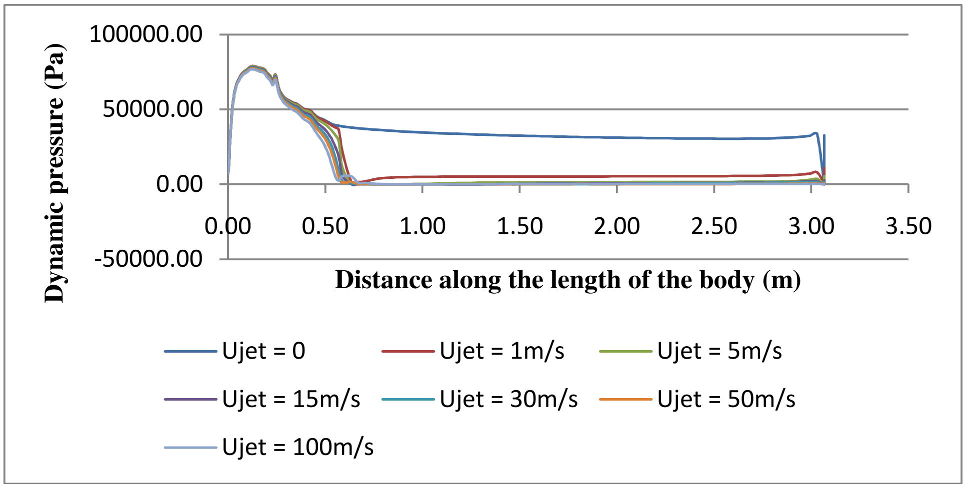

Figure 12: Dynamic pressure distribution along the length of the body for different cases for Blunt Afterbody1 (U = 15 m/s)

Discussion of results

The main observations from Table 3 and Figures 6, 7 and 8 are as follows:

(a) The drag of Blunt Afterbody1 is about 2.3 times that of Afterbody1, indicating strong effect of the streamlined shape of Afterbody1. This is also evident from the fact that the pressure drag component of total drag of Blunt Afterbody1 is about 15.5 times that of Afterbody1.

(b) The drag first decreases with increasing air jet velocity (i.e. with increase of U_{jet}/U), becomes minimum at a particular value of U_{jet}/U and then increases again with increasing air jet velocity. For Afterbody1, minimum drag is attained when U_{jet}/U in the range of about 0.5 to 1 (i.e. U_{jet} in the range of 7.5 to 15 m/s). For Blunt Afterbody1, minimum drag is attained when U_{jet}/U in the range of about 2 to 3.5 (i.e. U_{jet} in the range of 30 to 50 m/s). For Afterbody1, at about U_{jet}/U of 2 (i.e. U_{jet} of about 30 m/s) the drag reduction becomes negative (i.e. drag becomes more than that at $U_{jet} = 0$). However, for Blunt Afterbody1, even at a large $U_{jet}/U = 6.67$ ($U_{jet} = 100$ m/s) the drag reduction remains positive (i.e. drag remains less than that at $U_{jet} = 0$). The nature of the curve in Figure 7 indicates that drag reduction will remain positive for even higher values of U_{jet}.

(c) Maximum drag reductions for both bodies are somewhat similar, 61% for Afterbody1 and 57% for Blunt Afterbody1. However, in the case of Afterbody1, large drag reduction is possible within a smaller range of air jet velocities, whereas in the case of Blunt Afterbody1, large drag reduction is possible over a much larger range of air jet velocities. Also, in the case of Afterbody1, large drag reduction occurs at low air jet velocities, whereas in the case of Blunt Afterbody1, it occurs at much higher air jet velocities.

(d) From the variation of molecular viscosity (viscosity of air is 1.789×10^{-5} and that of water is 1.003×10^{-3}) and volume fraction of water (1 for water and 0 for air) on the body surface along the length of the body as shown in Figures 9 and 10 respectively, it may be seen that the major reason of drag reduction is due to predominant presence of air in the fluid mixture in contact of the body surface that results in reduction of frictional component of drag. The rate of reduction of frictional drag is very less after the initial drop at very low speed when air jet is introduced. In all cases major portion of body surface is covered with a mixture of water and air and the distribution of air content in the mixture along the body do not have much variation.

(e) The dynamic pressure distributions along the body wall for Afterbody1 and Blunt Afterbody1 are shown in Figures 11 and 12 respectively. Pressure drag initially decreases and then increases with increase of the velocity of air jet. Due to this, the variation of the total drag force also follows the same pattern. Pressure drag is formed due to the difference in pressure between the front and rear end pressures of the body for an axisymmetric body. At higher air jet velocity, pressure difference between the rear and front end of the body increases which causes pressure drag to increase. The volume fraction distribution of water on the rear end show that at higher air jet velocity, air is not fully covering the body surface, it goes straight without adequately covering the tail region, which lowers pressure in the rear. In all cases pressure distribution forward to the air jet location remains constant, and as a result pressure and volume fraction in the rear end determines the drag reduction significantly.

CONCLUSION

A computational fluid dynamics approach for estimation of drag reduction using air jets for underwater axisymmetric vehicles has been presented and reasonably validated with other numerical work. The significant role of the stern profile on the drag reduction characteristics has been established. There is a need to study the effect of other parameters such as different body velocities, the angle of air jets, location of air jets, effect of nonzero angles of attack on drag reduction performance etc. More importantly, experimental verification of some of the major features of drag reduction using air jets is required and this task is presently in progress.

REFERENCES

Barraos, E.A., Pascoal, A. and Sa, De. E. (2008): “Investigation of a method for predicting AUV derivatives”, *Ocean Engineering*, Vol. 35, pp. 1627-1636

Deutsch, S. and Castano, J. (1985): “Microbubble skin friction reduction on an axisymmetric body”, N00024-79-C-6043, *Technical memorandum*, The Pennsylvania State University, pp. 1-21

Fontaine, A.A. and Deutsch, S. (1992): “The influence of the type of gas on the reduction of skin friction drag by microbubble injection”, *Experiments in Fluids*, Vol. 13, pp. 128-136

Hassan, A. Y., Claudia, C., Gutierrez,T. and Jose, A.J.B. (2005): “Temporal correlation modification by microbubbles injection in a channel flow”, *International Communication in Heat and Mass Transfer*, Vol. 32, p. 1009-1015

Huang, T.T., Santelli, N. and Belt, G. (1978): “Stern boundary-layer flow on axisymmetric bodies”, *Twelfth symposium on naval hydrodynamics*, Washington, pp. 1-62

Kanai, A. and Miyata, H. (2001): “Direct numerical simulation of wall turbulent flows with microbubbles”, *International Journal for Numerical Methods in Fluid*, Vol. 35, pp. 593-615

Kato, H., Iwashina, T., Miyanaga, M. and Yamaguchi. (1999): “Effect of microbubbles on the structure of turbulence in a turbulent boundary layer”, *Journal of Marine Science and Technology*, Vol. 4, pp. 155-162

Kim, S.Y. and Cleaver, W.J. (1995): “The persistence of drag reduction following the injection of microbubbles into turbulent boundary layer”, *International communications in Heat and Mass Transfer*, Vol. 22, pp. 353-357

Kodama, Y., Kakugawa, A., Takahashi, T. and Kawashima, H. (2000): “Experimental study on microbubbles and their applicability to ships for skin friction reduction”, *International Journal of Heat and Fluid Flow*, Vol. 21, pp. 582-588

Madavan, N.K., Deutsch, S. and Merkle, C.L. (1984): ”Reduction of turbulent skin friction by microbubbles”, *Physics of Fluids*, Vol. 27, No. 2, pp. 356-363

Madavan ,N.K., Deutsch, S. and Merkle, C.L. (1985): “Measurements of local skin friction in a microbubble-modified turbulent boundary layer”, *Journal of Fluid Mechanics*, Vol. 156, pp. 237-256

Mohanarangam, K., Cheung, S.C.P., Tu, J.Y. and Chen, L. (2009): “Numerical simulation of micro-bubble drag reduction using population balance model”, *Ocean Engineering*, Vol. 36, pp. 863-872

Moriguchi, Y. and Kato, H. (2002): “Influence of microbubble diameter and distribution on frictional resistance reduction”, *Journal of Marine Science and Technology*, Vol. 7, pp. 79-85

Murai, Y., Fukuda, H., Oishi, Y., Kodama and Yamamoto, F. (2007): “Skin friction reduction by large air bubbles in a horizontal channel flow”, *International Journal of Multiphase Flow*, Vol. 33, pp. 147-163

Park, S.B., Myung, K.C. and Do, H.C., (19 91): “Reynolds-stress model analysis of turbulent flow over a curved axisymmetric body”, *AIAA Journal*, Vol. 29, No. 4, pp. 591-594

Sarkar, T., Sayer, P.G. and Fraser, S.M. (1997): “Flow simulation past axisymmetric bodies using four different turbulence models”, *Applied Mathematical Modelling*, Vol. 21, pp. 783-792

Skudarnov, P.V. and Lin, C.X . (2006): “Drag reduction by gas injection into turbulent boundary layer: Density ratio effect”, *International Journal of Heat and Fluid Flow*, Vol. 27, pp. 436-444

Truong, V.T. (2001): “Drag Reduction Technologies”, DSTO-GD-0290, *Published by DSTO Aeronautical and Maritime Research Laboratory*, Australia.

Virag, M., Vengadesan, S. and Bhattacharyya, S.K. (2008): “Evaluation of performance of nonlinear k-ε turbulence model for axisymmetric body at an angle of attack”, *10th Annual CFD Symposium*, Bangalore.

Wedin, R., Davoust, L., Cartellier, A. and Byrne, P. (2003): “Experiments and modelling on electrochemically generated bubbly flows”, *Experimental Thermal and Fluid Science*, Vol. 27, pp. 685-696

Wu, C., He, S., Zhu, D. and Gu, M. (2006): “Numerical simulation of microbubble flow around an axisymmetric body”, *Journal of Hydrodynamics*, Vol. 18, No. 3, pp. 217-222

Wu, S., Cheng, H.H. and Tsung, T.L. (2005): “Model test of the surface and submerged vehicles with the micro-bubble drag reduction”, *Ocean Engineering*,. Vol. 34, No. 1, pp. 83-93

Wu, S.J., Kwan, O. and Shiah, S.W. (2008) : “Robust design of microbubble drag reduction in a channel flow using the taguchi method”, *Ocean Engineering*,. Vol. 35, pp. 856-863

Seventh International Conference
On High-Performance Marine Vehicles
Melbourne, Florida, USA
13-15 October 2010

HIGH PERFORMANCE MARINE VEHICLES IN THE SEAWARD EXTENSION OF CITY HIGHWAYS

C Onyemechi and D U Ekwenna
Department of Maritime Management Technology
Federal University of Technology, Owerri, Nigeria

conyemechi@yahoo.com
duekwenna@yahoo.com

ABSTRACT

The work assesses new ways of developing the overall transport system in a sustainable way using methods that extends the road transport system to newly developed marine highways. A model that argues that present transport system is extensible where technology constraints are broken is portrayed. Government policy initiatives that support the sea transport alternative must however be in place to encourage this new developing sustainable transport option. A study was carried out to ascertain ways through which developing countries can benefit from this sustainable transport alternative which reduces road congestion, increases intermodal effectiveness, with comparable cost savings compared to air transport. High performance marine vehicles is viewed in this work as the missing link which developing third world nations must embrace to solve the ever increasing problem of road congestion arising from low transport infrastructure. Methods for assessing modal shares were applied in the work to determine ways for government assessment of modal overload in the distribution of passenger and freight traffic .In this respect, high performance marine vehicles are viewed as just part of the solutions to the existing problem. An analysis of traffic distribution in Nigeria was made to reflect the imbalance in the modal distribution of the entire sector leaning towards the road sector using available freight data.

INTRODUCTION

Modern day road transport development has created new problems in terms of road congestion, air pollution, high freight charges and finally excessive cost of goods in the hand of the final consumer.

The above problem is present in both the developed and the developing nations and alternatives to road transport system is always being sought. However, as a result of the capital intensive nature of the above problem, developed nations more easily find solutions to the problem than developing nations.

Apparent alternatives to the road transport system are evidently the air, the rail and the short sea transport modes. However, in terms of cost, the air and the rail alternatives are far higher that the short sea shipping alternative. The short sea shipping sector thus makes itself the optimum choice for transport switching from the road sector. Marine vehicles available in the short sea shipping sector include short sea roro passenger ships, pure passenger marine vehicles and high performance passenger crafts moving over an air cushion. One other factor in support of the seaward extension of city highways is the fact that it offers a sustainable solution to the problem of road congestion and excessive utilization. Sustainable transport development has been defined to include a transport system that is affordable, operates efficiently, offers choice of transport mode, and supports a vibrant economy Macbeth (2004).

OBJECTIVES

The objectives of this work includes inter alia:

i. To determine ways of switching transport from road to the short sea shipping sector in such a manner as to maintain a sustainable development of the entire transport system.

ii. To ascertain the role of high performance marine vehicles in reducing road congestion in cities adjacent to a nations internal and territorial waters.

iii. To determine the best option for developing third world nations

KEYWORDS

Short Sea Shipping, Motorway, Sustainable transport

LITERATURE REVIEW

The European Union by adoption of its motorways of the sea concept has stated beyond reasonable doubt its belief in the use of rivers and short sea transport as a transport switching alternative to the problem of road congestion. The European white paper transport policy for 2010 under the section "developing motorways of the sea", declared that short sea transport is a real competitive alternative to land transport.

The document sees short sea transport in the same vein with motorways and rail ways. It is viewed as a policy that supports sustainable economic growth, social development and protection of the environment.

Baindur (2008) carried out a study whose problem hedged on methods for reducing the growing dominance of road transport for freight carriage over other modes of transport. Problems resulting from this overload of this sector he opined include congestion, bottlenecks and damage to human health and the environment. According to him, increased use of short sea shipping routes and inland waterways can provide part of the answer to road congestion and inadequate (or inefficient) rail infrastructure. This means that short sea shipping is in competition with the rail sector in servicing hinterland freight flow sector of the overall transport system.

Loon (2009) opined that short sea shipping should be regarded as an integral component of comprehensive intermodal approaches that attract higher cargo volumes, enhance networks and provide genuine door to door services.

The European Transport document sees short sea shipping as a suitable transport option. Out of 25% of Co_2 emissions from the transport sector, marine transport contributes 7%, air12% and road vehicles 75%. Other modes contribute 6%

RESEARCH METHODOLOGY

The work applied the use of regression analysis to assess the contributions of the three different modes of rail, road and short sea shipping (represented by water) to Nigeria's transportation system.

The quantity demanded (total freight available in the sector) was regressed against the independent variables of road freight, rail freight, gross domestic product GDP and short sea shipping freight. The model is extended to emphasize the new role that high performance marine vehicles has to play to ensure the sustainable development of the entire transport system.

DATA PRESENTATION AND ANALYSIS

TABLE 1: NIGERIA'S OUTWARD INTERMODAL DATA COMPARED TO GDP 1989-2002

YEAR.	QDT	GDP	RAIL	ROAD	WATER
1989	881 ,845	224796.7	22,634	499,416	139,128
1990	969,861	260,636.7 .	-	597,319	85,685
1991	3,240,990	324,010.00	5,400	833,640	103,652 .
1992~	1,176,873	549,808.80	10,176	295,411	38,915
1993	2,398,888	697,090.00	-	524,469	99,690
1994	1,579,337	914,940.00	19,099	582,032	99,552
1995	1,674,856	1,977,740	'504	541,032	98,400
1996	1,921,261	2,823,900	16	826,121	160,623
1997	2,498,000	2;939,650	0	656,000	218,000
1998	2,802,000	2,881,310	7000	593,000	218,000
1999	8,204,000	3,325,650	0	3,753,000	101,000
2000	8,763?000	4,980,943	7000	958,000	19,000
2001	10,586,000	5,639,865	0	844,000	45,000
2002	9,654,000	5,901,970	-	993,000	24,000

Source: CBN Annual Statistical Bulletin 2003

REPORT OF FINDINGS

Using the beta coefficients, the trend of dependence of the quantity demanded on the predictor variable can be represented with the equation.

$$QDT = 1621670 + 1.2191 GDP + 17.908\ Rak + 1\ .110\ ROAD - 17.037\ WATER \quad (4.1)$$

Subjected to a t test, the finding from the analysis shows that at 5% level of significance, the predictor variables that still make significant contributions to the shipping demand output are GDP, ROAD and WATER. The rail sector's contribution to shipping output is not significant, according to our result. Again an inverse relationship ie negative sign was observed in the water mode. Explained by our a priori theoretical expectation, it means that the water mode plays a complementary role to the road mode in servicing Nigeria's shipping demand market.

The findings from our research actually reflect the realities of the economy as well as the transport modes to the shipping market. The shipping output demand increases as the gross domestic product GDP increases. The transportation of both import and export goods is dominated by just one mode of transport, the road mode. The inverse relationship with the water mode shows this. This further shows that the water mode must be improved to the extent that it begins to make a positive contribution to Nigeria's shipping market distribution. This offers an evaluation parameter for the assessment of the impact of newly introduced government regulations like the cabotage, introduced to improve water transportation. The view of this work is that to date, the impact of coastal shipping to the overall transport distribution of shipped goods in Nigeria is still negative. The government agent, Nigerian Maritime Administration and Safety Agency (NIMASA) should thus evolve newer ways of boosting activities in coastal water transportation in Nigeria. This offers a sustainable development option for the overall transport sector development. Furthermore, to sustain the road mode efforts should be made to ensure the rail system becomes operational for servicing the maritime sector. To date our research shows a total absence of operational impact on shipping activities in Nigeria.

The sector should be made to work and to impact on shipping output demand. The sector makes no significant contribution to the quantity of goods demanded for both import and export goods. The Nigerian Railway Corporation (NRC) is thus called upon to revise their carrying formula to create services for the maritime mode.

THE SEA MOTORWAY SUSTAINABLE TRANSPORT MODEL

The structure of the model is explained below.

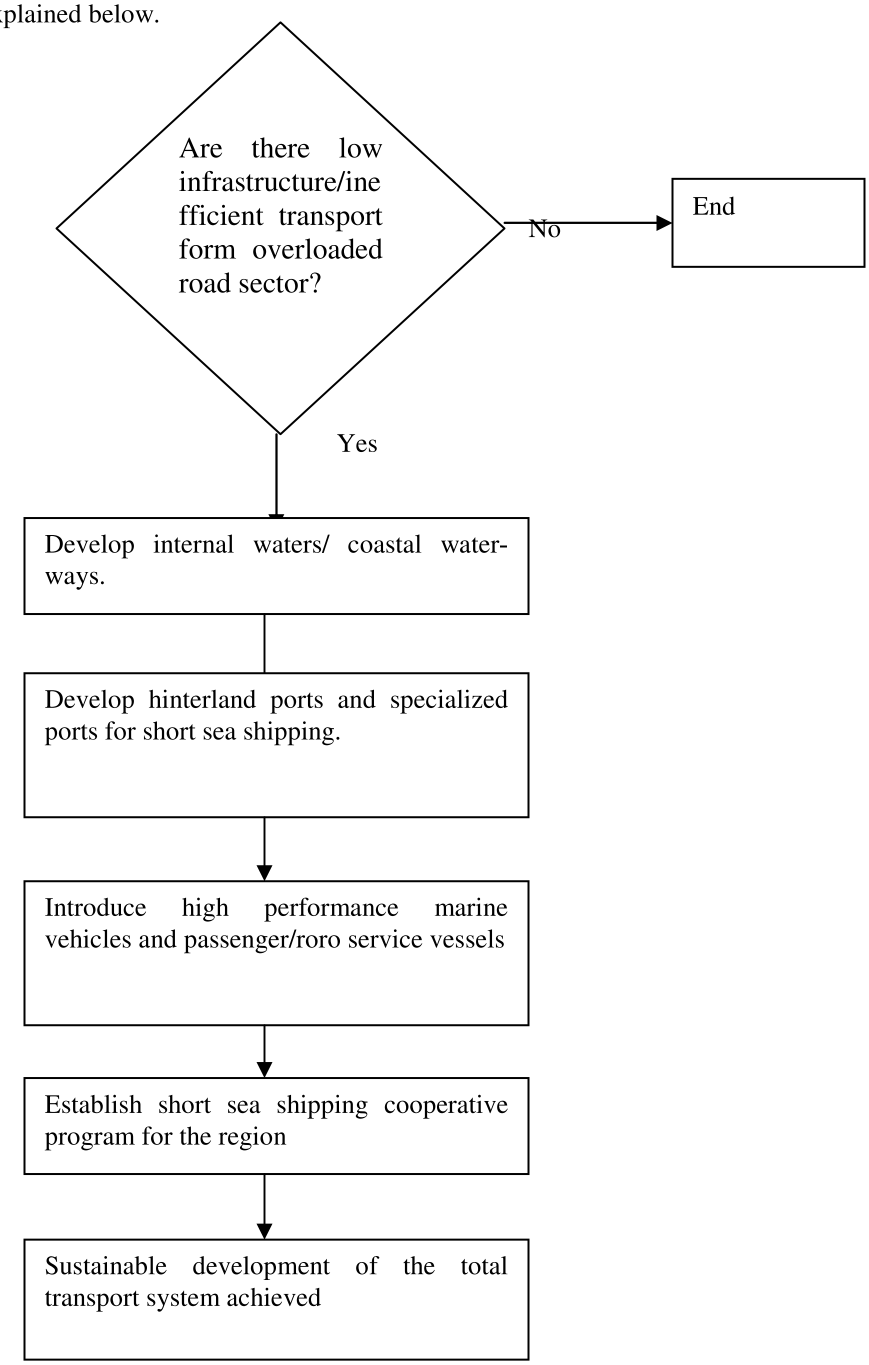

Figure 1: The sea motorway sustainable transport model

THE SEA MOTORWAY SUSTAINABLE TRANSPORT OPTION

The sea motorway sustainable model arises from the existence of poor and inefficient transport system resulting in road congestion, excessive atmospheric emissions, unhealthy environment and other unsustainable conditions. The sea motorway sustainable transport option thus serves in decongesting the overloaded road sector of the total transport system.

For the sea motorway transport option to be active, the river systems and the territorial and coastal transport network of the particular nation must be put in a navigable condition. They should be properly dredged to serve marine vehicles for both passengers and roro freight services. River ports and seaports should also be put in place at appropriate locations to serve the short sea chipping sector. High performance marine vehicles, road and passenger vehicles of all forms should then be introduced into the sector to compete with the road and rail service sectors.

Finally, for the sustainable development of the entire transport system, an agency that will encourage the society to patronize the short sea shipping sector is required. This usually will come through the establishment of the short sea shipping cooperative program. This group will have to advertise the short sea shipping sector to attract both government and commercial society patronage.

CONCLUSION

High performance marine vehicles usually operate under the sphere of short sea shipping where they act in competition to both rail and road services.

The sea motorway sustainable transport model proposed in this work reveals the place of high performance marine vehicles in servicing the short sea shipping sector in particular and the total transport system generally. The work emphasized the sustainable role that the short sea shipping sector plays in the overall transport system.

REFERENCES

1. CBN (2003) Annual Statistical Bulletin Central Bank ,Nigeria.

2. Loon, C.K (2009) short sea Transport and Economic Development in Penang Business Infelligence Jownal-August 2009 Vol .2. No. 2.

3. Macbeth G.A (2004)Sustainable Transportation in New Zealand, IPENZ Presidential Task Committee on Sustainability: IPENZ

4. http//: www.transport –research.info/upload/Documents/200608/20060

5. http//:www.civil.ist.utl.pt/nispt/posters/pdf/0220doutuorameto_deepak_baindur.pdf

6. http://www.internationaltransportforum.org/Europe

Seventh International Conference
On High-Performance Marine Vehicles
Melbourne, Florida, USA
13-15 October 2010

MINIMIZING WAVE WAKE FOR HIGH-SPEED SKI BOATS

Brad A. Carlson
6199 Sequoia Dr., Port Orange, FL 32127
bradallencarlson@hotmail.com

ABSTRACT

The purpose of this paper is to study the minimization of wave wake behind high speed competition ski boats. The wave wake of interest is the first divergent wave from the transom of the vessel. A brief explanation of a water-ski competition is covered, followed by the hull development background of a high-speed ski boat. The high speed craft is explained along with the hull form of interest, a hard chined warped hull. The many features that can be added to a high speed craft to alter the wave wake are covered. The features include: spray rails, radii detail, and transom flaps and how they can be used in combination to obtain desired results. Two generations of high speed ski boat hulls are compared and how their features are different and the effect each feature has on minimizing the wave wake. A qualitative study was done to compare the 2 hulls and with the addition of features to the bottom of the Generation I hull, the wave wake height was decreased on Generation II. Further quantitative studies of the topic would provide the numerical confirmation needed for minimizing wave wake.

INTRODUCTION

Wave wake is the wave generated by the forward motion of a marine vessel, Macfarlane (1999). Wave wake is important in the water skiing industry and in many other industries. However, there is very little data on wave wake and most of it has not been commercially published. Most of the data available is from academic sources and there is still no commercially available empirical methodology for wave prediction, Robbins (2005). For many industries, wave wake has not been a concern in the past, but with growing restrictions on vessels used in sheltered waterways, wave wake is becoming more important, Macfarlane (1999). Wave wake are no longer of secondary importance and occasionally become a prime concern and a contractual requirement, Robbins (2005).

In regards to the water skiing industry, there are competing companies that develop their ski boats to be used in ski competitions and athletes, both professional and amateur, use the vessel that gives them the best opportunity to win an event. Each company wants to have the best boat in the industry because their livelihood depends on it.

The development of hulls that minimize wave wake is new territory for the marine industry. By developing new hull forms that minimize wave wake, characteristics of each hull form can be used to refine future hull designs across the marine industry.

ABBREVIATIONS

Gen. I	Generation I
Gen. II	Generation II
LOA	Length Overall

KEYWORDS

Ski boat; Wave Wake; High-Speed Vessels

EXPLANATION OF WATER-SKI COMPETITION

The vessels dealt with in this investigation are high-speed ski boats used in a competition that involves 3 different water-skiing events. In 2 of the 3 events a smaller wave wake is ideal. The first event of the competition involves a skier with a single ski that is pulled through a slalom course of 6 buoys, 3 on each side of the course placed an equal 11.43m (37.5') off of the centerline. A point is awarded to the skier for getting the ski around each buoy while crossing back and forth across centerline. Once all six points have been gathered for a specific rope length, the rope is shortened and the skier is pulled through the course again to try and obtain points at the shorter rope length. This process is repeated until the skier is no longer able to complete the course at a specific rope length. At the end of the competition the skier with the most points wins that event.

The second event involves a skier with a pair of skis that are meant to go over a fiberglass jump in the water. The object of this event is for the skier to travel the longest distance in the air after leaving the surface of the jump while holding onto a rope and being pulled by the boat. When in route to the jump, the skier will actually slingshot behind the boat from the side of the boat opposite the jump to the side with the jump. This helps the skier create more speed while coming off of the top of the jump, therefore achieving more distance while in the air. The skier that travels the longest distance wins the event at the competition.

The last event involves a skier with a single ski that is twice as wide and two-thirds as long as was the slalom course ski. The purpose of this event is to do as many tricks or stunts as possible in a specified distance. Each trick or stunt has a point value and at the end of 2 runs, the points are totaled and the skier with the most points wins the event. All of the competitors in an event are pulled by the same boat.

With all of the events, the skier crosses the wave wake at least once and sometimes numerous times. The first 2 events are easier with no wake to cross because it disrupts the skier and creates an obstacle. The skier uses the wake in the last event, but the event is done at a much slower speed than the first 2 events. Minimizing the wave wake of high-speed ski boats will help progress the sport of competitive skiing and find applications throughout the marine industry.

HULL DEVELOPMENT BACKGROUND

There are basically 2 ways to reduce vessel wave wake. The first way is hull wave minimization; the second is hull wave cancellation, Robbins (2005). The second method is complex, so the first method is more common to reduce the hull form wave wake. Hull wave minimization is done by changing characteristics such as length/displacement volume ratio, prismatic coefficient, transom area ratio, Froude number, length/beam ratio, trim, beam/draught ratio, and angle of entrance, Robbins (2005). Often the designer is given established design criteria for the vessel, so the number of characteristics that can be changed is diminished.

The designer also has few options due to high costs associated with testing scale models. Scale model testing generally focuses on resistance and propulsion, Robbins (2005), further limiting designers. Due to the design criteria restrictions and limited information from scale testing, recreational boat manufacturers typically use full scale models for testing purposes. The manufacturers do not have the resources to perform the research and development in a cost effective manner, Calkins (1983), and until recently, many manufactures did not use the help and skills of a naval architect. Therefore, recreational boat manufacturers' hull development is mainly a trial-and-error process which can be performed two ways. One way is to modify a proven hull form by adding components to the hull; the other method is by similitude. With similitude a designers takes a proven hull and changes a few primary characteristics such as length, beam, or deadrise, creating a new hull form. The first method typically requires reverse engineering once an improved hull form has been created, while the second method uses the skills of the naval architect to verify the hull form from a digital model.

THEORETICAL FRAMEWORK

Theory behind high speed craft and wave wake will first be explained regarding components used to minimize wave wake. The theoretical concepts that will be explored are high speed craft hull forms, wave patterns, hard chined warped hull, spray rails, transom flap and trim.

HIGH SPEED CRAFT

High speed craft can be grouped into 5 categories based on their hull forms: semi-planing and planing monohulls, multi-hull craft, hydrofoil craft, air cushion-supported hulls, and small waterplane area twin hulls, Cooper (1999). The type of hull form considered in this paper is the planing monohull. Other high speed craft hull forms will not be covered and were not considered for any of the wave wake minimization. A high speed planing hull has some interesting and unexpected characteristics. A high speed planing monohull at low speeds actually has a negative hydrodynamic effect, due to the fact that the water speed over the hull is greater than the hull speed, causing a drop in pressure. The drop in pressure creates a suction and forces the boat to squat in the water and assume a trim, Savitsky (1964). Eventually, when the hull's speed is greater than the speed of the water over the hull, the negative effect is diminished and the boat no longer squats in the water due to the net positive effects.

Another characteristic that sets the planing monohull apart from the other high speed hulls is that the planing monohull depends greatly upon the longitudinal location of the center of gravity of the vessel, Savitsky (2003). The longitudinal center of gravity is the main component that controls the trim angle of the vessel when the negative hydrodynamic pressure becomes positive and the vessel begins to plane. Most planing monohulls are most efficient or have the least resistance at a minimum trim angle of 3 to 4 degrees relative to the water surface. The resistance increases for both higher and lower trim angles, Savitsky (2003). For a vessel that is trying to minimize wave wake, the trim angle may not be as important, but hull efficiency must be considered. A hull begins to plane when hydrodynamic forces become positive and the boat is traveling fast enough that 50 to 90% of the boat's weight can be supported by hydrodynamic forces instead hydrostatic forces, Savitsky (1964). During the transition from hydrostatic to hydrodynamic forces supporting the boat, speed has increased enough that water flow will begin to cleanly separate from the bottom of the transom. The pressure distribution rapidly changes and causes the upward or planing force, Savitsky (1964). Due to this, planing is typically associated with the transom of the stern becoming dry. When a boat is planing, there is the sheet which is the source of spray in a planing surface. The region of its origin was designated by Wagner as the "spray-root" region, Savitsky (1964). This region is now commonly referred to as the high-pressure zone by naval architects. All of the pressure areas and spray areas affect the hydrodynamic drag on a vessel and play a role in the efficiency of the hull. The total hydrodynamic drag of a planing surface is the combined drag created by pressures acting normal to the inclined bottom and the viscous drag acting tangential to the bottom, Savitsky (1964). As a result, the large amount of hydrodynamic drag created with planing hulls requires the largest thrust per pound of displacement of any of the high speed craft hulls, Savitsky (2003).

WAVE PATTERNS

A vessel that is on plane creates a unique wave wake pattern, but there are many factors that affect the wave wake pattern. Factors such as vessel speed, direction, hull form, draft, loading, and trim affect the wave wake, making studies of the pattern complex and difficult, Macfarlane (1999). In 1887, Kelvin found that for any deepwater speed, a vessel will create diverging and transverse waves that form a constant pattern, Macfarlane (1999). The constant pattern has a series of diverging waves that originate at the stem and stern of the vessel and are a constant angle at the cusp of the wake relative to the centerline of the vessel. The transverse waves are for the most part, perpendicular to the centerline and are equal distance apart from each other and also originate at the stem and stern of the vessel. The transverse waves have a velocity that is equal to the boat speed. The wave system that is generated is an irrecoverable expenditure of propulsive energy that is a result of the "wave-making" resistance of the hull, Savitsky (2003). Figure 1 shows the typical wave pattern from vessel generated waves.

HARD CHINE WARPED HULL

A hard chined hull has a sharp edge at the intersection of the hull's sides and the hull bottom, creating what is considered to be the chine. The chine helps create a clean separation of the transverse flow of water from the bottom the hull created at the high pressure zone. The hard chined hull also typically has a sharp trailing edge at the transom to guarantee a clean separation of the longitudinal flow of water, therefore creating a fully ventilated transom. In addition to a hard chined hull, many boats also have a reverse chine that directs the transverse flowing water back down to the water surface, helping create hull lift in the area of the reverse chine. The hull lift is created by positive dynamic bottom pressure at higher speeds and actually causes a reduction in the amount of buoyant hull support, Savitsky (2003). A warped hull does not have constant dead rise. The dead rise is actually greater at the stem of the boat than at the stern, Savitsky (1964). One negative characteristic of a warped hull is the generation of negative pressures along the convex surface of the hull. The convex surface can be detected by convex longitudinal buttock lines or convex curvatures in the transverse plane, Savitsky (2003). The negative pressures can suck the boat down into the water and overcome the positive hydrodynamic pressures from other areas of the boat's hull. An advantage of a warped hull is to decrease the tendency to roll in waves and increase the stability of the boat when sitting static. A warped hull can also increase the lift of the hull slightly, Savitsky (1964). A hard chined warped hull takes advantage of the extra dynamic lift created at higher speeds, but as the vessel lifts from the water, a loss of metacentric stability occurs. The hard chine helps with roll stiffness and stability, but only when the hard chine is immersed in the water, Bailey (1974).

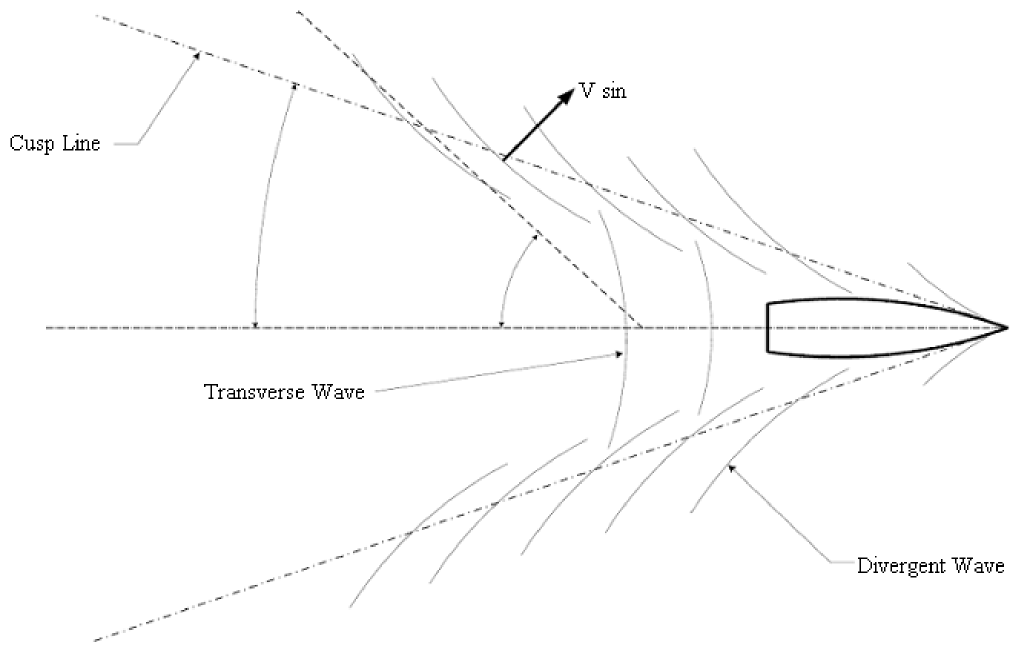

Figure 1: Vessel Generated Waves, Stumbo (1999)

SPRAY RAILS

The main purpose of spray rails on a hull is to control the growth of the thin "bow wave" or the sheet of water that is created by the hull with speed, Bailey (1974). Spray rails can be a variety of shapes and sizes and placed on many different locations on a running surface. The spray rail can either be molded into the hull bottom or fastened to the hull so it deflects water in the desired location of placement. By adding a spray rail to the fore body, water is deflected and decreases the amount of resistance because the deflected changes the trim angle of the running surface. The deflected water will cause the bow to rise because the water is hitting the underside of the rail, therefore creating positive pressure in the deflected water area.

In 1974, Bailey suggested that a spray rail only need to extend over half of the craft and the underside of the rail should be parallel to the water surface at rest. While some of Bailey's theory still applies to modern spray rail development, it should not be used as the standard. Lindgren proposed in 1968 that spray rails have the same influence at all trims, provided they are placed in the optimal locations. This concept also still has some relevance but once again caution must be taken when studying this concept. Lindgren also studied the effect of the size of the spray rail and found that a smaller spray rail tended to reduce efficiency because smaller rails had a harder time keeping the bow from plunging into the water, while larger spray rails prevented the bow from plunging at all speed ranges tested. This idea holds true with current spray rail theory. Nearly all monohull high speed planning craft designed in the 21st century use some kind of spray rail, but the length, location above or below waterline, size, and type of cross section are not always optimally chosen.

TRANSOM FLAP & TRIM

A transom flap has more constraints in size and location than spray rails, but transom flaps still have a large degree of freedom in how they can be used. There are many different names used for transom flaps, but all serve the same purpose, which is to change the trim of the vessel when it is no longer in its static position. Some devices are more easily adjusted than others, but the ease of use does not reduce the effectiveness of the device. The flap is placed on the transom of the boat and like the spray rail, deflects water that passes over it downward, therefore creating lift at the transom. More lift is created the faster the vessel is moving and the greater the angle of deflection, until the lift is maximized.

The transom flap also reduces a hull's ability to porpoise. Porpoising occurs when the center of gravity and the center of buoyancy of a boat are close together but not in equilibrium. There is a dynamic instability in the boat. Porpoising is the rhythmic movement up and down of a boat while moving forward. For any deadrise, there is an angle that porpoising will occur. By decreasing the trim, the tendency to porpoise is decreased and, as expected, by increasing the trim, the tendency to porpoise is increased, Savitsky (1964). The transom flap helps a vessel obtain its best performance by allowing the vessel to run at its optimal trim angle. At the optimal trim angle, resistance is minimized, Bailey (1974). Although the optimal trim angle is desired, Savitsky (1964) pointed out that the optimal trim angle for the lift-to-drag ratio is typically higher than the safe angle to prevent porpoising. Due to this, a vessel is typically run at an unfavorable trim angle. Achieving an optimal trim angle can be solved by modifying the deadrise of the hull.

SKI BOAT HULL FORM EXPLANATION

There are 3 different manufacturers of high-speed ski boats approved to be used in the 3 events of a waterskiing tournament for the 2010 season. All of the boats are similar in size, but have some differences in the principal particulars. The 3 manufacturers produce boats that fall in the LOA of 19'6" to 20'6", with beams of 91" to 95" and displacements of 2600 to 2800 pounds. The boats also all have a running surface length of around 16', but this measurement has the largest variation between each manufacturer. Each manufacturer has its specific name to their hull type, but all are a hard chined warped hull. Each manufacturer uses different variations of spray rails or transom flaps to optimize their hull. Studying each boat manufacturer's hull and each successive generation of hull would be ideal for a thorough investigation, but the lack of availability of the boat manufacturers' high-speed ski boat hulls from conception to present design makes this impossible. One manufacturer will be examined over the last 2 generations of hulls for comparison and analysis. For the sake of identifying each hull, they will be referred to as Generation I and Generation II. Generation II is the newer of the two hulls. The manufacturer and model of the high-speed ski boat will not be mentioned due to proprietary reasons. Gen. I and Gen. II are almost identical, but some characteristics set them apart. Figure 2 shows a plot of the deadrise versus the distance from the trailing edge of the hull for both boats. There is linear warp of the deadrise that occurs on the back halves of the hulls and the best fit linear trendline for the warp is shown. The hull warps about the edge of an intermediate planer surface that is between the keel and the warped surface, is 8.5 inches wide, and spans from the transom to the forward part of the hull where it fairs into the warped surface. The hulls continue to warp moving forward to the stem of the boat, but not in a linear fashion. Both hulls have a step in the keel at the aft end of the stem which creates a V-pad keel and a 3 inch wide flat landing for 3 tracking fins and a thru hull for drainage. Just forward of the propeller shaft thru hull, there is another step in the keel to create an 8 inch flat and a tunnel where the shaft log is cut into. This creates a landing for the strut log and rudder log. The logs are a recess in the keel to decrease the amount of turbulence that is created from water passing over them. Both hulls have a reverse chine that starts at the stem of the hull and ends around midship. The Gen. II hull was developed from a full scale Gen. I hull and reverse engineered to create a symmetrical hull. For this manufacturer this was the first time this had been done with a high-speed ski boat since the hull inception in the 1960's.

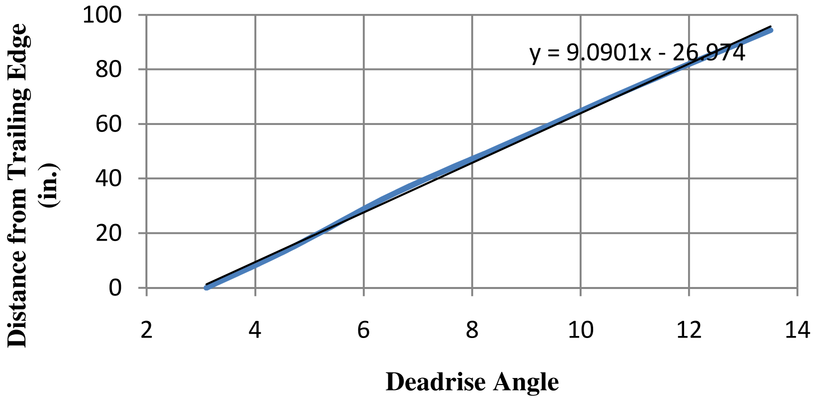

Figure 2: Deadrise Plot of Generation I and Generation II Hull Forms

DIFFERENCES IN HULL CHARACTERISTICS

The objective in developing the Gen. II hull was to have a smaller wave wake than the Gen. I hull. The Gen. II hull was developed from the Gen. I hull so specific differences in the hulls will be discussed and photographs of each hull will be used to show the differences. First, the LOA's differ. The LOA of the Gen. I hull was 19'-6" and the LOA of the Gen. II hull was six inches longer at 20'-0". The six inches added to the Gen. II hull was primarily done above the waterline so there was not a significant impact on the running surface due to the increased length. The beam of the Gen. I hull was 91" and the beam of the Gen. II was 95". As a result of the increased length and beam, the amount of fiberglass material increased, taking the displacement of 2640 pounds for Gen. I to 2800 pounds for Gen. II. Second, the chine beam and also the trailing edge beam differ. The amount of wetted surface area can have a large affect on the hull's performance, so these dimensions were important. The chine beam for the Gen. I hull was 74.5" and the chine beam for Gen. II was 77.75". The trailing edge beam followed the same trend, but the difference was much larger. The Gen. I hull had a trailing edge beam of 50.5", while the Gen. II hull trailing edge beam was 65". Based on the dimensions of the Gen. II hull versus the Gen. I hull and considering the Gen. II hull was derived from the Gen. I hull, the Gen. II hull was basically a larger Gen. I hull with a larger displacement. The first divergent wave wake from the transom of the vessels is the one of interest. The changes to the Gen. I hull that helped Gen. II create a different wave wake will now be discussed.

Figures 3-a and 3-b show the two different hulls side by side; the images clearly show the complexity of the Gen. II hull on the right. The hulls have the same general shape in terms of warp and deadrise at the stem, but the addition of the many features discussed earlier drastically changed the hull. Each of the features will be discussed in more detail.

The first feature to be discussed is the absence of spray rails on the Gen. I hull. At the stem of the hull, there is no intermediate spray rail before the sheet of water comes in contact with the reverse chine. The Gen. II hull has an elaborate system of spray rails referred to as spray diffusers. They are intended to do as their name implies, diffuse the sheet of water that is created from the deadrise of the hull and forward motion through the water. The most forward set of diffusers on the port and starboard sides of the hull run close to parallel to the water surface and refract the water back down to the water surface and under the boat. They provide positive lift in the forward part of the hull while decreasing the amount of spray that is allowed to travel up the hull to the reverse chine. The second set of spray diffusers act more as a guide for the sheet of water and help to position the high pressure water so it is coming in contact with the reverse chine in a desired location. The second set of diffusers also creates some lift in the forward part of the hull. Both sets of spray rails have been molded into the hull and are part of the fiberglass structure. Figures 3-a and 3-b show the spray diffusers and another angle of the spray diffusers on the Gen. II hull are shown in Figure 4 below. Figures 3-b and 4 are taken from the front of the hull looking aft of the port and starboard hull bottoms respectively.

Figure 3-a: Generation I hull bottom

Figure 3-b: Generation II hull bottom

Figure 4: Generation II Spray Diffusers

Another major difference between the Gen. I hull and the Gen. II hull is a feature on the Gen. I hull that was filled in on the Gen. II hull. Just forward of the step in the chine on the Gen. I hull, a pocket started and continued approximately 2 feet that was intended to relieve some of the high pressure spray exiting from the side of the hull. Testing was done by filling in the pockets and the results were conclusive enough to leave the pocket filled due to their ineffectiveness. A feature added to the Gen. II hull to provide "spray relief" was a step in the chine at the location of the directed water from the spray diffusers. Forward of the step a 10 degree reverse chine and at the step over 4 inches, the chine went from minus 10 degrees down to minus 5 degrees. This allowed water to be released from under the hull without being refracted back down at a large angle, therefore causing reflected spray. The high pressure spray was actually laid out over the water surface. Figure 5-a shows the spray relief pocket on the Gen. I hull and Figure 5-b shows the 5 degree step in the chine on the Gen. II hull. Both features were intended to diffuse the spray, but the stepped chine proved more effective.

Along with the spray relief in the chine on the Gen. II, hull there was also a subtle inflection in the surfaces of the reverse chine relative to the adjacent surfaces aft of the location of the step. The fillets in the opposing surfaces of the Gen. I hull were approximately ¾" radii. The fillets in the opposing surfaces of the Gen. II hull aft of the stepped chine were actually 9" radii. By softening the radii in this location, water does not make an abrupt change in direction, therefore decreasing the intensity of the refracted water. Figures 6-a and 6-b show the locations of interest.

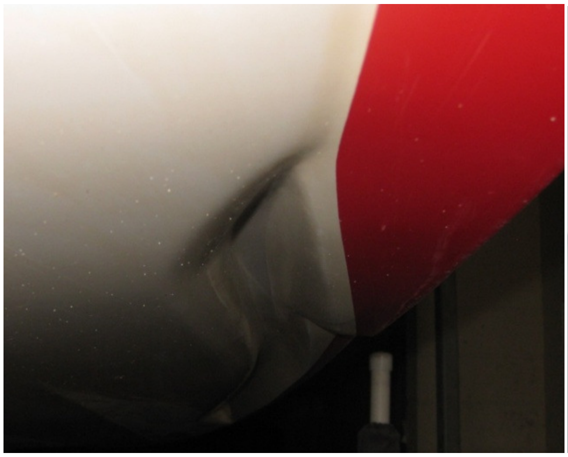

Figure 5-a: Generation I Spray Relief Pocket

Figure 5-b: Generation II Spray Relief Chine

Figure 6-a: Generation I Chine Inflection

Figure 6-b: Generation II Chine Inflection

Although both generations of hulls have a step in their chine where the reverse chine ends, the step in the Gen. II hull is larger than the Gen. I hull. This is mainly due to the increased chine beam of the Gen. II hull. The width of the reverse chine increased in the Gen. II hull, extending itself farther down from the warped surface that was aft of the step. The increase in the width of the reverse chine accounts for all of the increased chine beam width increase. The geometry of the step in the Gen. II hull was also much more defined with sharper corners, but this is more than likely due to old tooling used to create the Gen. I hull, where the Gen. II hull tooling was new. The differences in steps and the location of the chine beam was measured from is shown in Figures 7-a and 7-b.

Figure 7-a: Termination of Reverse Chine

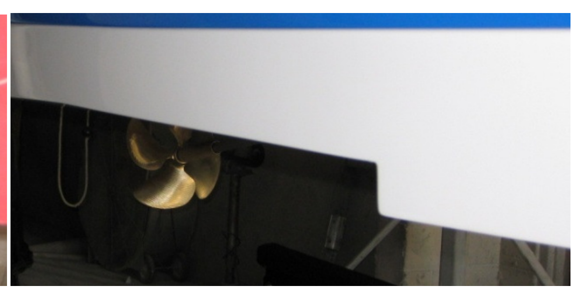

Figure 7-b: Termination of Reverse Chine

The chine beam increased a few inches for the Gen. II hull, but the trailing edge beam is the dimension that increased the most relative to the other increased dimensions. The increased transom width was initially a result of the need for an increase in width for extra storage at the aft end of the boat, but it provided lift in the transom, as well. The wider transom decreased the depth the transom sat in the water because the area of displacement increased. By decreasing the depth the transom sat in the water, the wake closure was not as violent because the hole to fill behind the transom was smaller. The deadrise of both hulls was the same, so there was an increase in the width that started at the step in the chine that increased moving aft for the Gen. II hull. The transition from the step on the Gen. I hull was a slight arc with slowly increasing variable radii to the trailing corner, while the Gen. II hull had a straight transition from the step in the chine to a notch in the chine 12 inches forward of the transom. The notch allowed for the desired separation at the transom. Figures 8-a, 8-b, 9-a and 9-b visually show the differences in the rear corners where the trailing edge beam was measured from.

Figure 8-a: Gen. I transition to trailing edge

Figure 8-b: Gen. II Transition to trailing edge

Figure 9-a: Generation I aft corner

Figure 9-b: Generation II aft corner

Transom flaps differed between the Gen. I and Gen. II hulls to assist with the trim of the vessel. On both hulls, there was a step in the keel where the drive shaft exited the bottom of the hull that created a planer surface parallel to the keel that spanned the constant deadrise surface on each side of the hull. At the intersection of the surfaces, a ridge continued from the start of the step all the way to the transom to create a “tunnel” for water to travel through. In the tunnel was a recess for the strut and a recess for the rudder. At the end of the tunnel at the transom, an adjustable interceptor could be manually raised or lowered to create a transom flap. The only difference between the two boats is that the ridge on the Gen. I hull was a constant height of 0.5” while the ridge on the Gen. II started at 0.5” and grew to 0.75” at the transom. The interceptor on the Gen. I hull could fill the tunnel by travelling 0.5” and the travel was increased on the Gen. II hull to create 0.75” of travel so the tunnel could be filled on the Gen. II hull. The additional tunnel depth with the increased travel created more lift with the Gen. II hull. The amount of interceptor travel is important because the interceptor is moving 90 degrees relative to the water flow. To much travel of the interceptor could cause the interceptor to create little to no lift and all drag. Figures 10-a, 10-b, 11-a and 11-b show the Gen. I hull with the interceptor up and down and the Gen. II hull with the interceptor up and down. The 0.25" of increased interceptor travel on the Gen. II hull can be seen in figure 11-b.

Figure 10-a: Generation I Interceptor Up

Figure 10-b: Generation I Interceptor Down

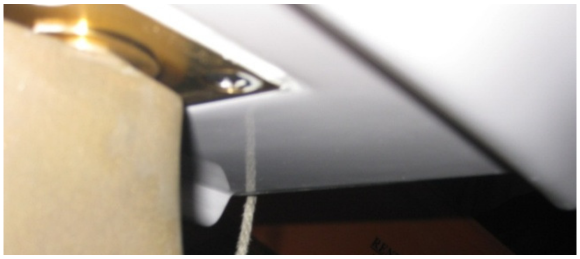

Figure 11-a: Generation II Interceptor Up

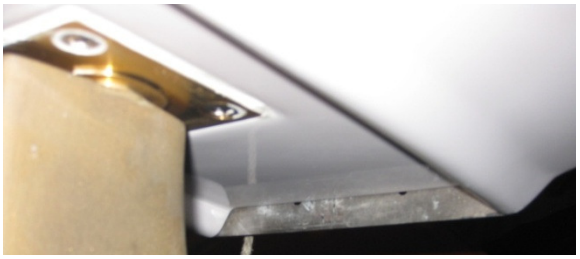

Figure 11-b: Generation II Interceptor Down

The last feature to discuss in regards to differences in the two hulls is the use of transverse and longitudinal lifting strakes on the bottom of the hulls. Figures 3-a and 8-a and figure 12 show the vast majority of the Gen. I hull bottom with no longitudinal strake and no transverse lifting strake. The Gen. II hull has a variety of transverse lifting strakes with a longitudinal strake spanning from one transverse strake to the other. All strakes are located on the warped surface of the hull. The strakes are ½" in height and are 45 degrees relative to the warped surface they intersect. The first transverse strake starts 10" from the change in deadrise from the V-pad keel and is slightly aft of the spray root line and is 14 inches wide until it begins to taper aft at a 45 degree angle to the chine. This lifting strake provides lift at mid-ship. The longitudinal strake starts at the forward transverse stake, runs aft parallel to the keel to 12" forward from the trailing edge, where it makes a 90 degree turn toward the keel and dives into the planer constant deadrise surface of the V-pad keel. The longitudinal strake helps tracking of the boat at high speeds and gives the feeling that the boat is on "rails". These help reduce transverse movement of the hull due to a skier pulling from side to side of the boat. The transverse lifting strake 12" forward from the keel provides lift at the transom, and gives the refracted water distance to settle and have a clean separation from the trailing edge of the boat. The 2 transverse lifting strakes along with the longitudinal strake are shown below in figures 13-a and 13-b.

Figure 12: Generation I Hull Bottom

Although the hull forms are similar, all of the different features about the hulls make them considerably different. All of the changes made to the Gen. I hull to develop the Gen. II hull were done in steps, so their effects could be determined more easily. Finding the right combination of features was a long and iterative process and once the combination was tweaked, engineers began the reverse engineering process of digitizing the hull and creating clean fair surfaces with the use of 3-dimensional modelling software. Figure 14 shows the 3-D model of the Gen. II hull and gives a general location of all the features just discussed.

Figure 13-a: Generation II Lifting Strakes **Figure 13-b: Generation II Lifting Strakes**

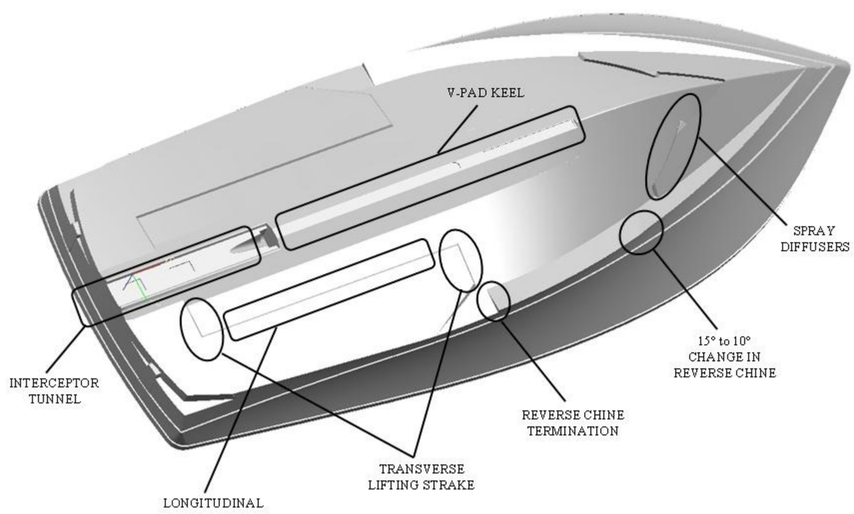

Figure 14: Generation II Hull Bottom

WAVE WAKE COMPARISON

When comparing wave wake, typically the entire wave pattern is of concern, but due to the interest with water skiing events, the only wave wake of concern is the first divergent wave from the transom of the boat. This is the wave the skier encounters when crossing behind the back of the boat. The transverse waves will have some effect on the wave wake the skier has to deal with, but they do not have as large of an adverse affect as the divergent wave if they are large. Most of the comparison of the wave wake was done in a qualitative manner. The wave wake height was analyzed visually as changes were made and a baseline boat was used to gauge improvements. Tools and methods to gather quantitative data have not been refined to point where good data can be gathered. Further studies on gathering quantitative wave wake height would further support visual observations. Also, along with the visual observations there were physical qualitative measurements that were taken. Because the distance a skier is behind the boat based on their rope length the wave wake height was analysed at all the different rope length to cater to all levels of skiers. With every major improvement to the Gen. I hull, the process of visually measuring the wake and physically measuring the wake had to done. Having a quantitative process could greatly reduce the development time needed to improve a hull form. The wave wakes of both the Gen. I hull and the Gen. II hull are shown in figures 15-a and 15-b. The pictures were not taken in a controlled environment, but the conditions in which the pictures were taken were as close to each other as possible. The boat speed in figures 15-17 was approximately 34 miles per hour.

Figure 15-a: Generation I Wave Wake

Figure 15-b: Generation II Wave Wake

From figures 15-a, 15-b, 16, 17-a and 17-b it can be seen the wave wake from the Gen. II hull is an improvement from the Gen. I wave wake. One difference is the width of the wave wake. The Gen. II wave wake appears to be wider at almost all respective distances behind the boat. The increased chine beam and trailing edge beam have some influence on this result. Also, the Gen. II spray and rooster tail appears more controlled and there is less elevation in these components. There does appear to be as much, if not more white wash, but it is all at the water surface. The use of spray rails, the transverse lifting strakes, and larger transom flap can help explain the controlled spray water and controlled rooster tail. Figures 16, 17-a, and 17-b show the Gen. I hull on the left running next to the Gen. II hull. The trim angles of the boats are different and the sprays from the forward parts of the hulls are different, all due to the added features on the Gen. II hull.

CONCLUSIONS

Although numerical data is not available to support the visually and physically differences between the wave wakes of the Gen. I and Gen. II hulls there were large enough differences between the two to demonstrate a decrease in size of the wave wake from the Gen. I vessel to the Gen. II vessel. To further minimize the wave wake would be a difficult task with the constraints placed upon the redesign. By re-exploring some of the theoretical characteristics, there may be an opportunity to improve the design, but one of the major limiting factors would be the amount of drag created with the addition of the extra features. To become a tournament approved and certified boat, the vessel must meet certain acceleration specifications for both the slalom and jump events described earlier. Both the Gen. I and Gen. II hulls passed the their water tests' but the Gen. II hull was pushing the limits much closer than the Gen. I hull. Due to engine size options, the vessels were only able to provide so much horsepower and thrust due to physical limitations of the components involved.

Further development in wave wake measurement would provide numerical support and the conclusion could be more quantitative instead of the qualitative conclusion that was reached. Also, a comparison of the wave wake behind the 3 major manufacturers could provide the athletes with a better understanding of the wake profile so they could adjust their skiing technique to better handle the wake profile. Funding for this type of further research is hard to justify in the recreational market, so it would be beneficial if findings from this study could be used in the commercial market to further minimize wave wake for high-speed vessels.

ACKNOWLEDGMENTS

The author would like to express his thanks to Florida Institute of Technology and to Correct Craft, Inc. for their support, contributions and time throughout the course of this research work.

Figure 16: Generation I (left) versus Generation II

Figure 17-a: Generation I Hull

Figure 17-b: Generation II Hull

REFERENCES

Bailey, D., (1974): "Performance Prediction – Fast Craft." *Small Craft Group*, London, RINA, November 7

Calkins, D. E., (1983): "An Interactive Computer-Aided Design Synthesis Program for Recreational Powerboats." *Society of Naval Architects and Marine Engineers Transactions*, Vol. 91, pp. 49-87

Cooper, M. and Mak, A., (1999): "Revised Requirements for Classification of High-Speed Craft." *American Bureau of Shipping*, Singapore

Doctors, L.J., Day, A.H., "The Generation and Decay of Waves behind High-Speed Vessels." *International Workshop on Water Waves and Floating Bodies*, www.iwwwfb.org/Abstracts/iwwwfb16/iwwwfb16_09.pdf.

Lindgren, H., Williams, A., (1968): "Systematic Tests with Small, Fast Displacement Vessels, Including a Study of the Influence of Spray Strips." Presented to Naval Architects and Marine *Engineers at Diamond Jubilee International Meeting*, New York, N.Y., June 18-21

Macfarlane, G.J. and Renilson, M.R., (1999): "Wave Wake – A Rational Method for Assessment" *International conference for coastal ships and inland waterways*, London, RINA

Robbins, A., Renilson, M.R., (2005): "A Tool for the Prediction of Wave Wake in Deep Water." *International Journal of Maritime Engineering.* RINA

Savitsky, D., (1964): "Hydrodynamic Design of Planing Hulls." *Marine Technology 1*, 1, pp. 71-95

Savitsky, D., (2003): "On the Subject of High-Speed Monohulls." *Presented to the Greek Section Of the Society of Naval Architects and Marine Engineers.* Athens, Greece, October 2

Stumbo, S., Fox, K., Elliot, L., (1999): "Hull Form Considerations in the Design of Low Wake Wash Catamarans." *Proceedings of the Fifth International Conference on Fast Sea Transportation*, FAST '99, Seattle

Seventh International Conference
On High-Performance Marine Vehicles
Melbourne, Florida, USA
13-15 October 2010

DRAG REDUCTION OF NPL ROUND BILGE HULL FORMS IN HYSUCAT CONFIGURATION: AN ANALYTICAL STUDY

Raveendran Manoharan[1] and Prasanta K Sahoo[2]
psahoo@fit.edu

ABSTRACT

Drag reduction of high-speed craft with less consumption of fuel oil has been an area of considerable interest to naval architects for quite some time. Literature study indicates that there is an abundance of innovative approaches to reduce drag for a particular hull form. This paper attempts to concentrate on an analytical study of potential drag reduction of high-speed hydrofoil supported catamarans (HYSUCATS) by use of SHIPFLOW, a CFD package to simulate flow around ship shape bodies.

Although HYSUCAT configuration has been around for a long time, investigation with NPL high-speed round bilge hull forms as demihulls would be a small step in the designing of practical hull forms with hydrofoils. It is expected that significant degree of uncertainty to remain in the prediction of hydrodynamic characteristics of such vessels. The most slender NPL hull form 6a was chosen alongside a symmetrical hydrofoil of profile of NACA 63A010 for the simulations.

In this analytical study a total drag reduction of 58% at a Froude number 1.2 was obtained, primarily due to substantial reduction in wetted surface area and wave resistance. The trends in sinkage forces and trimming moments due to hydrofoil assistance have also been discussed. Furthermore the investigations include longitudinal shift, (vertical) submergence and angle of attack of the hydrofoil. The results have been systematically analysed and discussed.

The effects of symmetrical foil geometry, with respect to span, chord length and aspect ratio have been investigated and results for various foil dimensions discussed and discrepancies explicitly stated. Consequently, the investigations were intended to concentrate on the means of obtaining the least possible drag without compromising the other parameters a great deal. The challenges include the efficient configuration of the hydrofoils, their shape, size and location. The results of numerical simulation do indicate that substantial reduction in drag can be achieved. However, experimental tests need to be performed to validate the analytical solution which could provide for a more robust knowledge base.

INTRODUCTION

The hydrofoil-supported catamaran (HYSUCAT) is a hybrid of a planing catamaran and a hydrofoil system: the catamaran offering high initial stability and large deck areas and the hydrofoils providing reduced resistance and low propulsion power. The development and design of hydrofoil-assisted catamarans can be divided into two fields of research:

[1] Research Student at the University of Tasmania, Newnham Way, Launceston, Tasmania 7250, Australia
[2] Associate Professor (Ocean Engineering), Florida Institute of Technology, 150 W University Boulevard, Melbourne, Florida 32901, USA

- Retrofitting of existing catamarans with hydrofoils to improve their efficiency and speed: requires the development of suitable hydrofoil systems for use on existing hull forms.

- Development of new hydrofoil-assisted catamarans: includes development of new and improved hull forms and hydrofoil systems that complement each other.

All HYSUCATs demonstrated considerable reduction in propulsion power and excellent seakeeping characteristics in rough water, Hoppe (1995).

Hydrofoil assistance on a catamaran model was first attempted more than 30 years ago and an unexpected resistance improvement of 40% instigated the creation of a research project to investigate the effects in detail. The research project is still in force in spite of designs and model tests resulting in the construction of over 200 HYSUCATs. The ongoing investigations are not only focussing on the resistance improvement alone, but also on ensuring that other performance parameters such as the dynamic trim, course-holding, transverse and longitudinal stability at various speeds, broaching, propoising behaviour, seakeeping etc. are not negatively offset by the addition of a foil system. This multipurpose aspect makes the design of a HYSUCAT a formidable and sophisticated task which very few designers are able to tackle without extensive use of model or prototype testing.

The research work on the numerical investigation of the resistance of a hydrofoil-assisted catamaran with semi-displacement or displacement hulls has not been as extensive as that of planing hulls. This is essentially due to the deficiency in numerical methods that are able to quickly and accurately evaluate both the resistance of catamarans and the sinkage forces and trimming moments on a round-bilge hull. However, the HYSUCAT development of planing catamarans has provided an excellent basis for HYSUCAT development of semi-displacement hulls. To date a number of feasibility studies have been conducted, including extensive model tests, on existing hullforms to prove the advantages of hydrofoil assistance for existing semi-displacement hullforms. This has led to a number of retrofits and new designs being completed by the University of Stellenbosch. The experience gained through retrofit projects and the feedback of prototype data of existing vessels provides valuable insight into the hydrodynamics of these vessels. The development of further improved hydrofoil systems for these vessels now becomes practicable.

NOMENCLATURE

A_T	transom area	LCB	longitudinal centre of buoyancy
A_X	maximum section area	LCF	longitudinal centre of floatation
B	breadth (beam) of hull on DWL	LCG	longitudinal centre of gravity
c	chord-length of foil	(M)	length-displacement ratio, $(L / \nabla^{1/3})$
C_B	block coefficient	P_B	total engine brake power
C_L	coefficient of lift	$P.C.$	propulsive coefficient (P_E / P_B)
D_F	foil drag	s	separation of foils
DWL	design waterline	S_P	sinkage pressure force on demihull
e_P	dimensionless power ratio	(S)	wetted surface coefficient $(S / \nabla^{2/3})$
F_C	chord-Froude number, $(U / \sqrt{gc})$	T	draught at DWL
F_n	Froude number, $(V / \sqrt{gL})$	U	uniform flow velocity
Fn_∇	volumetric Froude number, $(V / \sqrt{g\nabla^{1/3}})$	V	speed
Fn_Δ	Froude displacement number	I_W	wave interference factor
G, g	acceleration due to gravity	L	length on DWL
W	weight of the vessel	L_F	foil lift
Z_{PROP}	vertical component of the propulsion force	η_T	transport efficiency
α_i	resistance regression coefficients	λ	wavelength

B	dynamic trim regression coefficient	∇	displacement volume
E	total resistance and weight ratio	T	dynamic trim angle
Δ	displacement mass		

ABBREVIATIONS

CFD	Computational Fluid Dynamics
FAC	Foil-Assisted Catamaran
FEA	Finite Element Analysis
HYSUCAT	Hydrofoil-Supported Catamaran
HYSUWAC	Hydrofoil-Supported Watercraft
NPL	National Physical Laboratory

KEYWORDS

Catamarans, Hydrofoil, Resistance, HYSUCAT

BASIC HYSUCAT PRINCIPLE

The main foil is situated near the LCG position and spans the tunnel gap between the demi-hulls near the keels. The hydrofoils are designed to carry a maximum load at top speed by lifting the demi-hulls partly out of the water. The hulls carry a part load in order to produce sufficient longitudinal, transverse and course stability. At low speeds, the HYSUCAT weight is mainly supported by the buoyant forces of the hull. On the contrary, the foils carry most of the load at high speed as the dynamic planning forces are dominant to the hull buoyancy forces. The magnitude of these physically different lift force components changes considerably with speed and has a substantial influence on the dynamic length stability of the HYSUCAT. Two trim foil struts are employed near the transom a certain distance above the keels, as displayed in Figure 1, in order to have the foils operating at speed near to the water surface. This foil system is self-stabilizing at speed and maintains a favorable trim angle of the planing surfaces.

Properly designed hydrofoils have very low drag-lift ratios and planing hulls have much higher drag-lift ratios. The combination of the hulls with the foils, must therefore, result in a craft with drag-lift ratios in between the hull and the foil, thus a hybrid will be more efficient than the catamaran. The larger the hydrofoil lift, the lighter the hulls will be and the lower their resistance component.

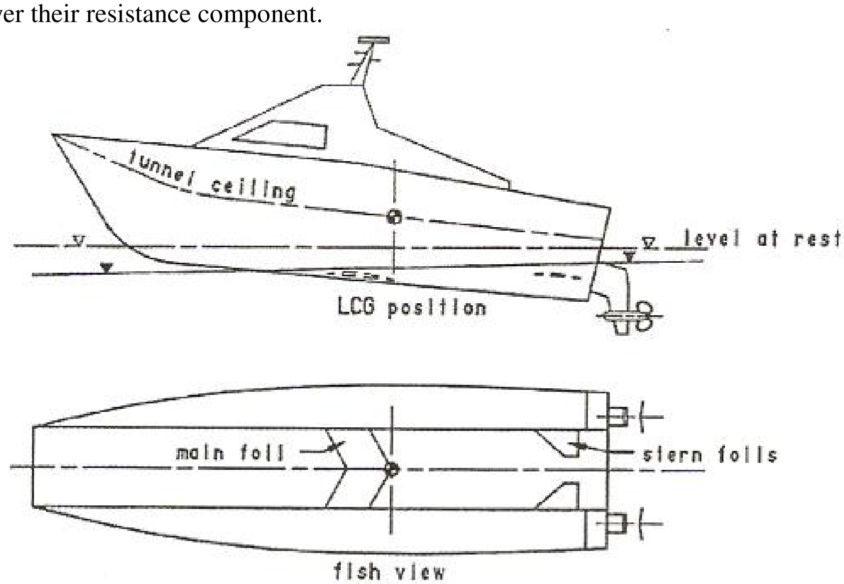

Figure 1: Layout of a Typical HYSUCAT Arrangement (Hoppe, 1995)

The foil lift reduces gradually when the hydrofoil approaches the water surface from beneath at increasing speeds. The foil resistance increases near the surface, hence it should operate at submergence ratios of 0.2 for efficient foil operation. The circulation around the hydrofoil creates pressure forces, which in conjunction with the pressure field of the planing surfaces with the positive effect that the foil and the hulls work more efficiently. The effective aspect ratio of the foil is considerably larger than the geometrical aspect ratio as the effective aspect ratio increases due to this interference effect.

The foil efficiency increases with aspect ratio. The lift creation of the foil is accompanied by a downwash mass flow (induced velocities). The larger the downwash mass flow, the more efficient the foil is. The foil functions more efficiently in the combination with the demihulls compared to free-running. A foil near the surface has reduced lift creation, because the downwash mass flow is reduced. The flow interference between hull and foil is a contributing factor of the high efficiency of the HYSUCAT. The induced velocities of the main foil pass over the trim foils that operate in inclined inflow with a consequential increase in drag. Therefore, the trim foils are less efficient and need to be as small as possible to fulfill the trim stabilizing role. The hydrofoils in the HYSUCAT arrangement produce a damping effect at speed in waves and hence contribute to favorable seakeeping characteristics in rough water. The hydrofoils can be designed to have a slight sweep angle to allow for smooth wave penetration at high speed when the craft leaves and re-enters the water periodically, Hoppe (1995).

LITERATURE REVIEW

The paper by Radojcic et al (1997) examines the mathematical representation of calm water resistance and trim of the systematic NPL series used for high speed pilot boats, work boats, patrol craft, etc. The dependent variables of the established predictive technique, by regression analysis, are the resistance-displacement ratio (R_T / Δ) and dynamic trim (τ). Independent variables are length-displacement ratio (L / $\nabla^{1/3}$), the ratio of length to beam (L / B) and the ratio of beam to draft (B / T). This paper analyses broader range speed range, Fn_∇ = 0.8 – 3.0. The series covers the following range of particulars shown in Table 1.

This paper is directed towards mathematical representation of the resistance and dynamic trim specifically for the NPL series as the previous papers for resistance predictions equations, such as Mercier and Savitsky (1973), are based on the resistance data of the NPL series combined with the data of SSPS and VTT series. It results in a more reliable resistance prediction method as the paper is based on the NPL series only.

Table 1: Range of Parameters covered by NPL Series

Geometric Ratios	Range Covered by the Series
F_{nL}	0.3 – 1.2
$F_{n\nabla}$	0.6 – 3.0
L / B	3.33 – 7.50
L / $\nabla^{1/3}$ (M)	4.5 – 8.3
B / T	1.75 – 10.77
Constant values are taken as follows	
LCB	6.4% L aft of amidships
C_B	0.397
A_T / A_X	0.52

Two general types of regression equations for resistance evaluation are speed-independent models and speed-dependent models. The predicted resistance, using speed-dependent models, often does not vary properly with speed, since the resistance computed at one speed is not directly linked to that at another speed. The accuracy of the speed-independent models is believed to be better since independent equations are developed for each speed. The initial polynomial equation used for the speed-independent least square curve fitting had 27 terms.The final speed-dependent models for resistance and dynamic trim have the following form:

$$(\frac{R_T}{\Delta})_{100000} = \sum_{i=0}^{8} \alpha_i \varphi_{n\nabla i} + (\sum_{i=0}^{8} \alpha_{i+9} \varphi_{n\nabla i})x_1 + ... + (\sum_{i=0}^{8} \alpha_{i+117} \varphi_{n\nabla i})x_{27} \quad (1)$$

$$\tau^0 = \sum_{i=0}^{8} \beta_i \varphi_{n\nabla i} + (\sum_{i=0}^{8} \beta_{i+9} \varphi_{n\nabla i})x_2 + ... + (\sum_{i=0}^{8} \alpha_{i+126} \varphi_{n\nabla i})x_{27} \quad (2)$$

Representation for the lower Froude numbers was always relatively poor, so Fn_∇ = 0.6 was rejected from further consideration. Therefore, speed-independent models are valid for Fn_∇ between 0.8 and 3.0, while speed-dependent models are valid for Fn_∇ = 1.0 – 3.0, due to instability between Fn_∇ = 0.8 – 1.0. From the results, the author concludes that both speed-independent and speed-dependent models presented here are reliable and accurate.

NUMERICAL PERFORMANCE PREDICTION OF HYSUCATS

Several researches into the area of hydrofoil assistance for high speed vessels have shown that large reductions in resistance are possible in addition to improved seakeeping characteristics. Due to the looming possibility of increased resistance as a result of foil systems, it is imperative to be able to predict and optimise the resistance of a design prior to, or without, model testing. It is essential to produce a method that allows the designer to evaluate the trends that are apparent in the variation of the various design parameters such as number of foils and their size, longitudinal and vertical position of foils, loading condition etc.

The primary aim of the authors is to create a calculation method to evaluate the resistance and running condition of a foil-assisted catamaran with semi-displacement demihulls. For design purposes, it is important to be able to get quick feedback on the effect of changing foil configuration. Foil section type and location are likely to be changed more often in the quest for better performance or avoidance of cavitation. Hull shape is a more complex parameter and more likely to stay the same through design spiral, especially relevant to retrofit cases. Thus, the method for calculating hull resistance is permitted to be time consuming, as it only needs to be performed once. This also presents the opportunity to derive hull forces from suitable experimental data, i.e. tests where sinkage forces and trim moments are measured in addition to resistance for a range of values of dynamic trim and draft.

For the purpose of the numerical method and future analysis, the forces acting on a hydrofoil-assisted catamaran are considered to come from two separate entities: the foils and the hulls. The output from the foil (Andrewartha and Doctors, 2001) method is combined in a program that iteratively solves for the equilibrium values of sinkage and trim at any vessel speed. To find equilibrium in the vertical direction, the vertical forces can be summed together:

$$\sum F_Z = -S_P - W + Z_{PROP} + \sum L_{Fi} \quad (3)$$

By considering the forces on the hulls and foils separately, the interactions between the two entities are effectively ignored. The interactions are assumed to be of two types: viscous and wave effects. Wave resistance of the hulls and foils can be calculated. It is, however, difficult to evaluate the interaction of the two wave systems; hence it has not been considered in this paper. Nonetheless, it is encouraging to note that at high speeds, the wave resistance of a foil-assisted catamaran is steadily decreasing due to the increased Froude number and reduction in immersed hull volume. The hydrofoil creates a surface wave between the demihulls and this increases the wetted surface area of the demihulls and hence the frictional drag, consequently, the method has been adapted to include the effect.

The theory showed reasonable agreement with the experimental data, except near the hump region. The theory over-predicted the resistance and under-predicted the sinkage and trim at hump speed. The reason for the discrepancy in the resistance values at hump speed is because the free-surface distortion is neglected. In addition, the authors attribute the discrepancy between the sinkage and trim values to the interference of the demihull wave systems at hump speed. However, the effect of the wave interference on sinkage and trim can be accounted for to some extent by examining the difference between the resistance of a demihull in isolation and of the catamaran. By this, a wave interference factor may be defined as:

$$I_W = \frac{R_{W,CAT}}{2 \times R_{W,DEMI}} \tag{4}$$

Tests on a single hydrofoil using a six component force balance were conducted to measure forces from a bare foil. The test matrix included varying the speed (0.5 to 4 m/s), depth (half the chord to three chords) and angle of attack (-4° to 4°) of the foil. By using lifting-line theory for the corrections in effective aspect ratio and by correcting the drag values to allow for the model scale Reynolds numbers, theoretical predictions display good agreement with the experimental data.

At high speeds, where the frictional resistance dominates, the difference between the hull drag with and without the interaction effect of the foil surface and wave is quite large. However, at the hump speed, the agreement between theory and experiment is improved when the foil-surface wave is taken into account. The results show that the hull has a minimal effect on the foil flow. This goes some way to validating the lack of interaction effects accounted for by the theoretical method. It would be desirable to have a method that was able to account for the dynamic sinkage and trim in a more consistent manner as well as be able to calculate the drag due to spray.

ANALYTICAL RESULTS

Prior to investigating the effects of location of the hydrofoil and its configuration, it is necessary to show that the adding a hydrofoil improves the resistance characteristics of a catamaran consisting of NPL round-bilge demihulls. In the present investigation NPL model 6a has been chosen as it is most slender amongst other models, details of which are shown in Table 2 below while body plan is displayed in Figure 2.

SHIPFLOW runs for Froude numbers of 0.1 to 1.2 (i.e., Fn_∇ between 0.31 and 3.7) were setup for the catamaran without hydrofoil. It is to be noted that the data acquired by a former student was not used since parameters such as grid spacing, number of stations etc. were required to be changed. For HYSUCAT configuration, a NACA foil shown in Figure 3 is used. Arbitrarily chosen longitudinal and vertical locations of the hydrofoil were used with an angle of attack of 3 degrees. Upon ensuring the convergence to the proposed residual target, the following graphs were plotted.

Table 2: Particulars of NPL Model 6a

$L/\nabla^{1/3}$	**9.5**
L / B	**15.1**
B / T	**1.5**
LCB	**6.4 %L aft of amidships**
C_B	**0.397**
C_P	**0.693**
C_M	**0.565**

RESULTS FOR HYSUCAT PERFORMANCE

Non-dimensionalised length	=	1	unit
Longitudinal position	=	0.55	units from the forward perpendicular
Vertical position (submergence)	=	0.07	units below the water surface

It can be seen in Figure 4 that the lift coefficient begins to increase from Froude number of 0.4 onwards. The outcome of increase in lift can be observed from Figure 5 that shows the decrease in wetted surface area for Froude numbers of 0.4 and beyond. Below Froude number of 0.4, the lift coefficient is minimal so that the hull is nor risen out of the water and hydrofoil adds to more wetted surface area. As the speed increases, the lift coefficient increases and hence the hull rises out of the water. The additional wetted surface area of the hydrofoil is overcompensated by its lift on the craft. The wetted surface area of the catamaran without hydrofoil remains virtually a constant.

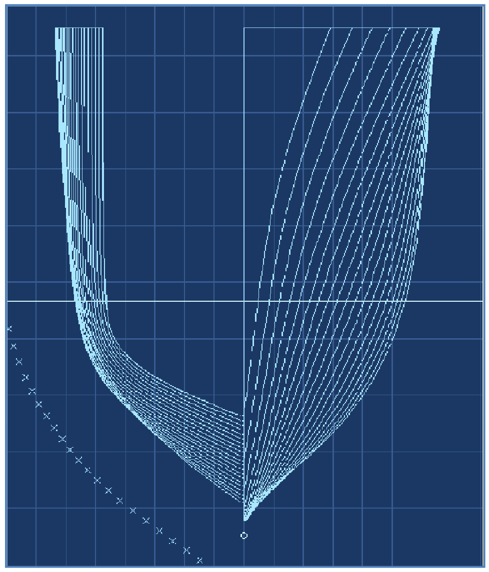

Figure 2: Bodyplan of NPL Model 6a

Figure 3: Cross section of the selected NACA foil (63A010)

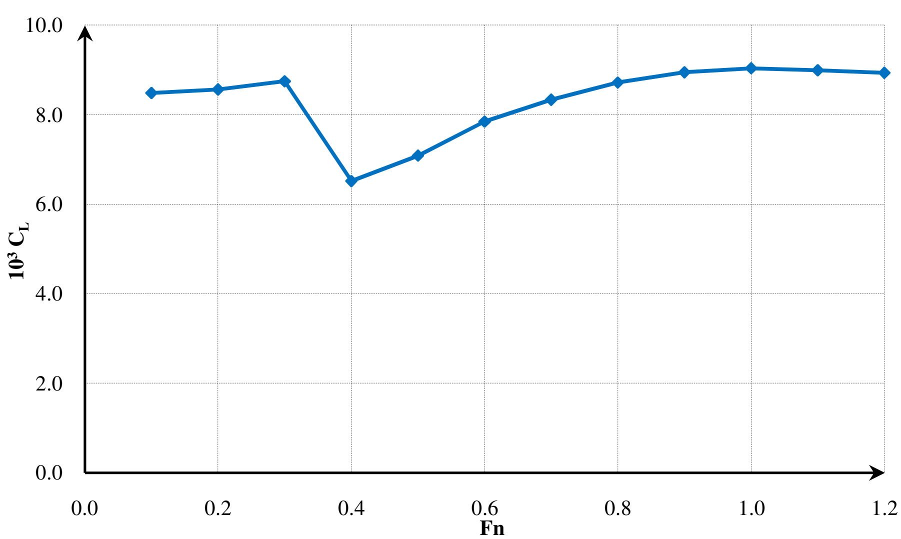

Figure 4: Vertical Lift Coefficient vs. Froude Number

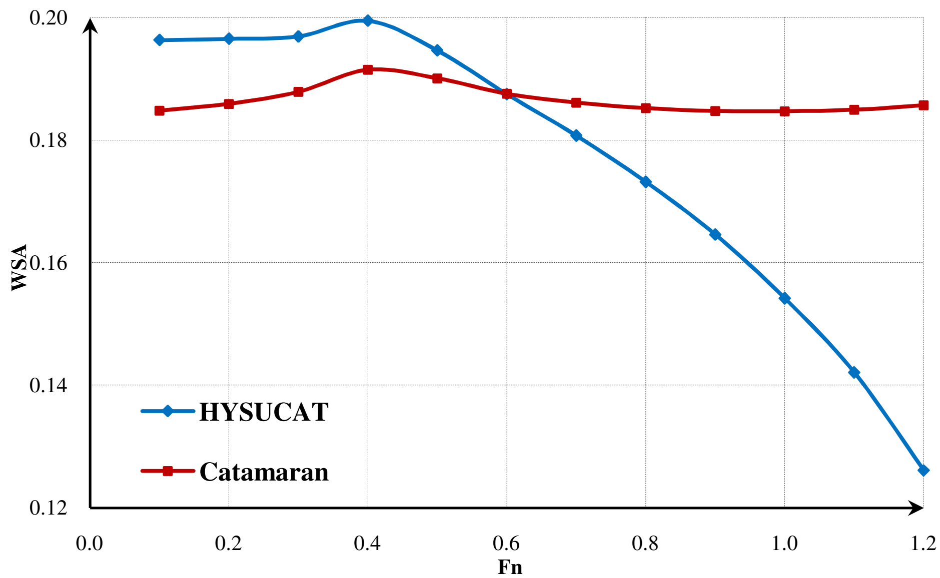

Figure 5: Wetted Surface Area vs. Froude Number

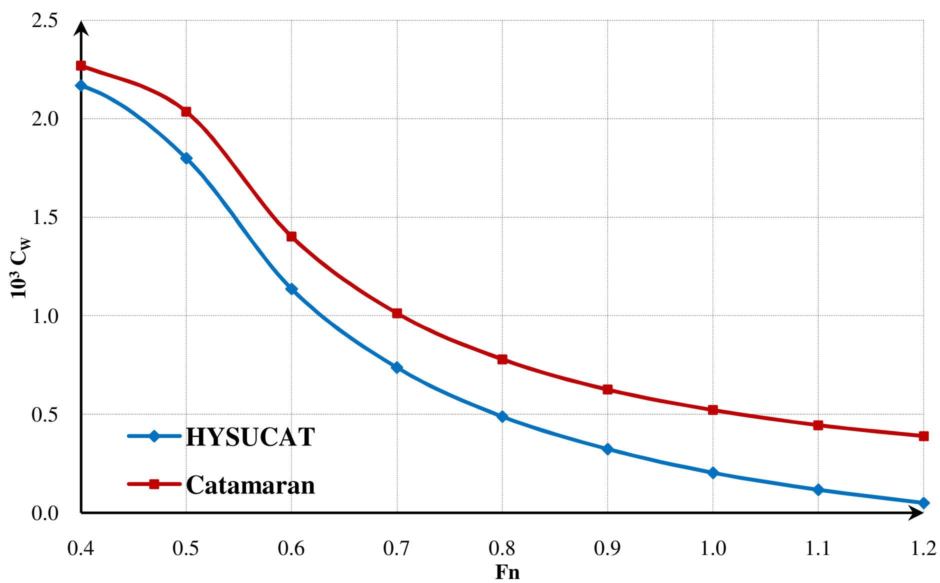

Figure 6: Wave Resistance Coefficients vs. Froude Number

In order to clearly identify the trend in high speeds, the results for runs with Froude numbers less than 0.4 are neglected. It is to be noted that length Froude number of 0.4 corresponds to volumetric Froude number of 1.23 as NPL 6a series has $L/\nabla^{1/3}$ of 9.5. The wave, viscous and total resistance coefficients for HYSUCAT configuration and catamaran without hydrofoil are plotted against Froude number as shown in Figures 6, 7 and 8 respectively.

Both wave and viscous components and hence the total resistance decrease with the increase in speed. Wave resistance in HYSUCAT configuration is considerably lower than that in catamaran without hydrofoil. On the contrary, the viscous drag is considerably higher for HYSUCATs. This can be attributed to the viscous drag of the hydrofoils operating at speed. However, the total resistance from Froude number of 0.8 onwards is lower for

HYSUCATs due to the significant improvement in wave resistance. Table 3 shows the actual differences in percentages with negative values indicating more resistance in HYSUCAT configuration compared to catamaran.

Table 3: Percentage Difference in Various Resistance values

Fn	Wave	Viscous	Total
0.4	5%	-40%	-15%
0.5	12%	-44%	-12%
0.6	19%	-51%	-9%
0.7	27%	-57%	-6%
0.8	37%	-61%	0%
0.9	48%	-64%	6%
1	61%	-63%	16%
1.1	74%	-60%	26%
1.2	87%	-55%	38%

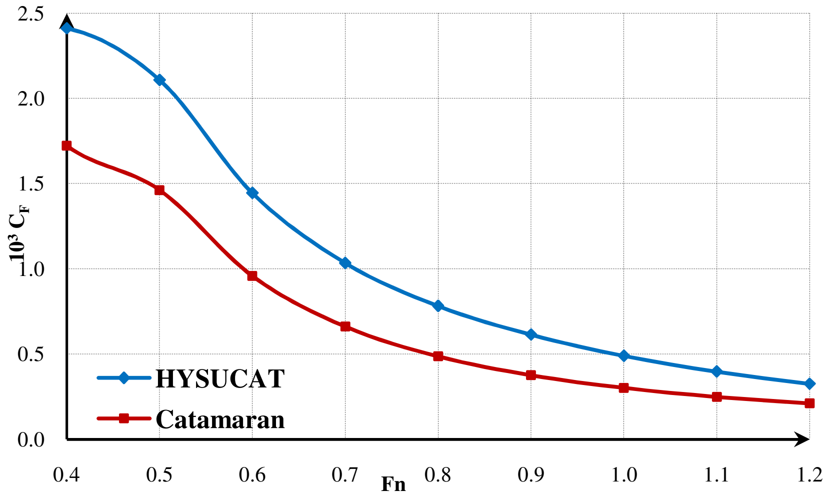

Figure 7: Viscous Drag Coefficients vs. Froude Number

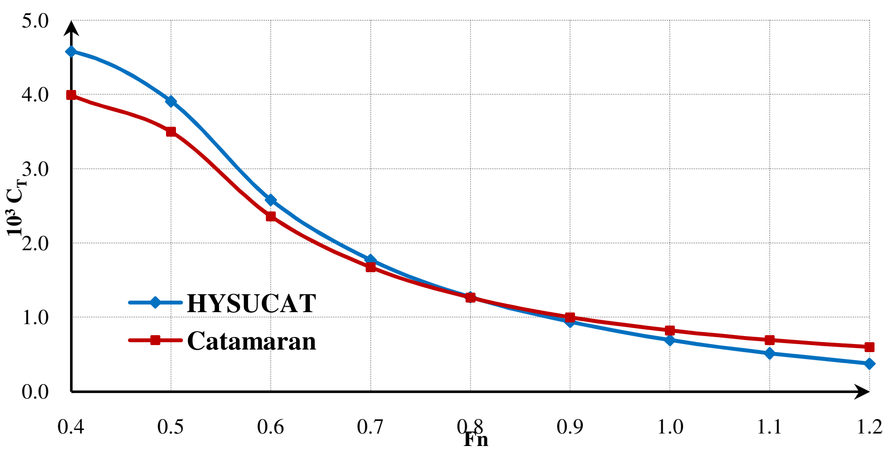

Figure 8: Total Resistance Coefficients vs. Froude Number

EFFECTS OF LONGITUDINAL SHIFT

The second phase of the investigation is to determine the trend with longitudinal shifts of the hydrofoil. The depth of the foil, angle of attack and Froude number were kept as constants to purely concentrate on the effects of the longitudinal shift. The extensive research study recommends Froude number in excess of 1.0 to observe considerable resistance improvement for the selected hull forms.

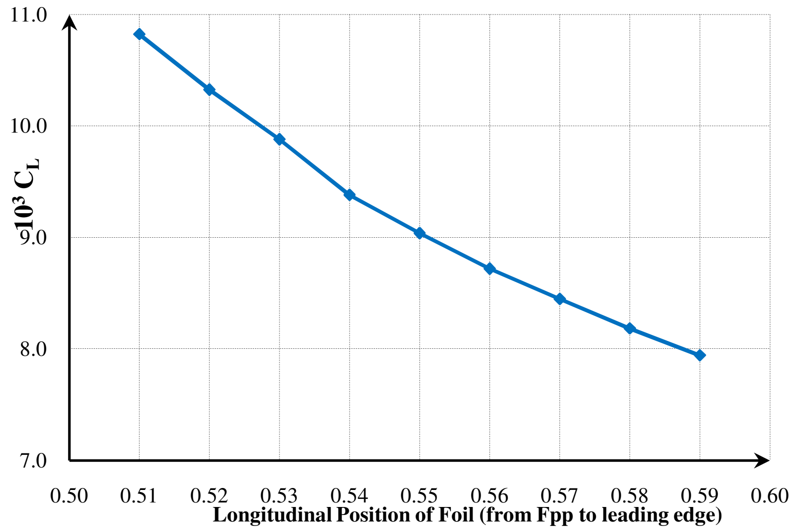

Figure 9: Lift Coefficient vs. Longitudinal shift

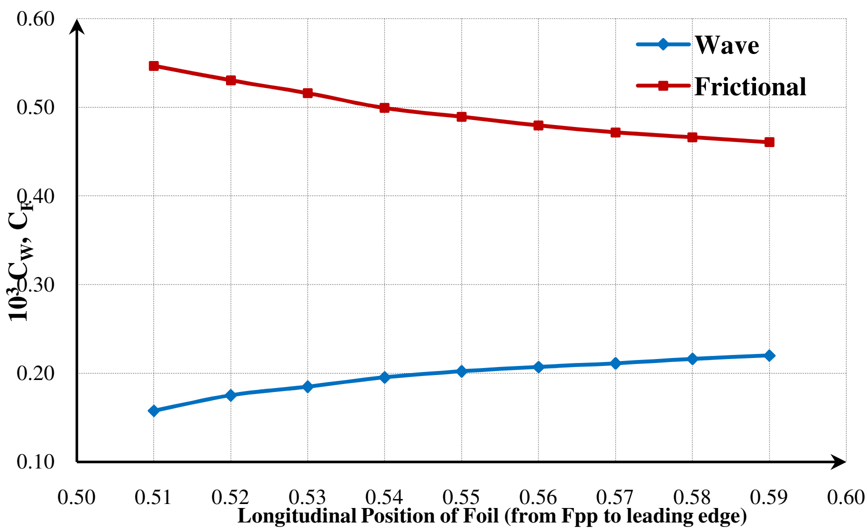

Figure 10: Resistance Characteristics vs. Longitudinal shift

It can be seen from Figure 9 that the lift coefficient decreases as the foil is moved from amidships towards the aft. Consequently, the wetted surface area increases. As the foil is shifted towards the aft, a significant improvement in wave resistance is observed. In contrast, the viscous drag component decreases as the hydrofoil is shifted towards the aft. Since the viscous drag is more dominant in higher speeds, the improvement in viscous drag results in marginally better overall resistance characteristics with foil located further aft. An overall resistance has improved by 4% as the foil was shifted from 0.52 units to 0.59 units from the forward perpendicular of the vessel.

Longitudinal shifts are expected to significantly affect the sinking forces and trimming moments of the HYSUCAT. As the vessel has more volume in the aft section, a decrease in sinkage forces and trimming moments is expected as the foil is shifted towards aft. This can be clearly observed in Figure 11.

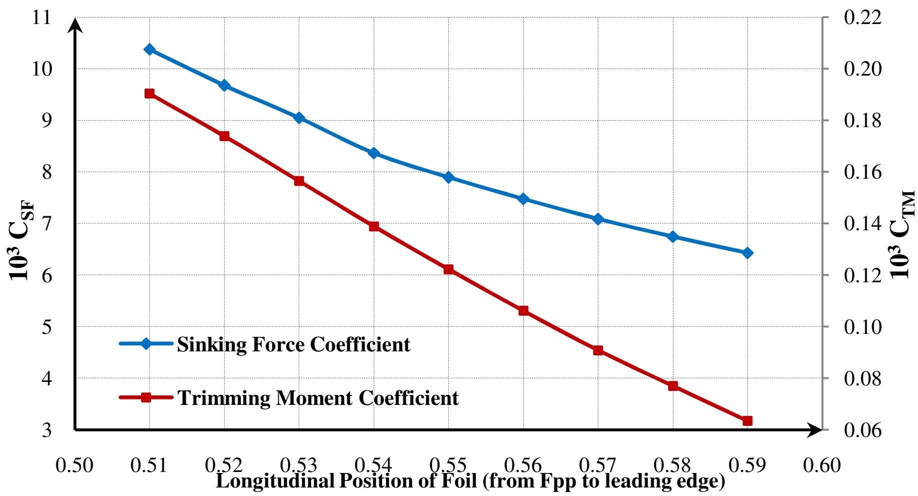

Figure 11: Sinking and Trimming characteristics vs. Longitudinal shift

EFFECTS OF HYDROFOIL SUBMERGENCE

The literature study reveals that when a foil is submerged deep enough to ensure that at high Froude numbers the foil does not rise out of the water or come close to the surface, the effects of depth is minimal. At depth of 4 units or lower, the hydrofoil seems to rise out of the water; therefore depth of 0.05 units onwards was chosen for the investigation purpose. The foil at a depth of 0.11 or higher somehow does not converge to the proposed residual target. The graphs for lift and wetted surface area show a very little trend with increase in depth. A slight decrease in lift and hence a slight increase in wetted surface area is noticeable from Figure 12. Similarly, the relationship between the depth of the foil and the resistance is barely evident as shown in Figure 13.

EFFECTS OF ANGLE OF ATTACK

The final phase of the initial investigations is to figure out the trend with increasing angle of incidence in HYSUCAT configuration. As expected the lift coefficient has displayed immense increase with slight changes in angle of attack and as a result, the wetted surface area reduced quite considerably as shown in Figure 14.

The overall resistance characteristics have improved with increasing angle of attack though the viscous drag increased considerably since the vast improvement in wave resistance as the angle of attack increased. Overall resistance has improved by 16% as the angle of attack was changed from 1 degree to 4 degree. A slight increase in total resistance is observed and shown in Figure 14. This can be attributed to the increasing dominance of the viscous drag over wave resistance at higher angles of incidence.

EFFECTS OF FOIL GEOMETRY

The next step of the investigation is to examine the effects of symmetrical foil geometry in terms of span, chord-length and aspect ratio. In order to thoroughly understand the effects of geometry, it was decided to change the aspect ratio through two methods: (a) chord-length is increased with a fixed span to decrease the aspect ratio; (b) span is decreased with a fixed chord-length to decrease the aspect ratio. The following graphs are plotted from the obtained results.

Increasing span seems to increase the lift coefficient and decreasing chord-length also results in increase in lift coefficient. However, it is to be noted that at an aspect ratio of 3.74, bigger span offered more lift despite the exact ratio and the wetted surface area displays the inverse trend as expected.

The total resistance decreases with the increase in span and increases with decreasing the chord-length. It can be concluded that increasing the span with a fixed chord-length improves resistance characteristics. On the contrary, changing the chord-length with fixed span does not affect the resistance characteristics to a large extent as shown in Figure 16. With high angles of attack, sinkage forces and trimming moments become increasingly significant and it is crucial to identify the trends as shown in Figure 17.

It is evident from the plots that the expected trends from literature survey and hydrodynamics study are substantiated by the SHIPFLOW runs. It is, however, imperative to further validate the hydrodynamic coefficients obtained from SHIPFLOW through the use of an advanced method. ANSYS CFX has been utilised to verify these results.

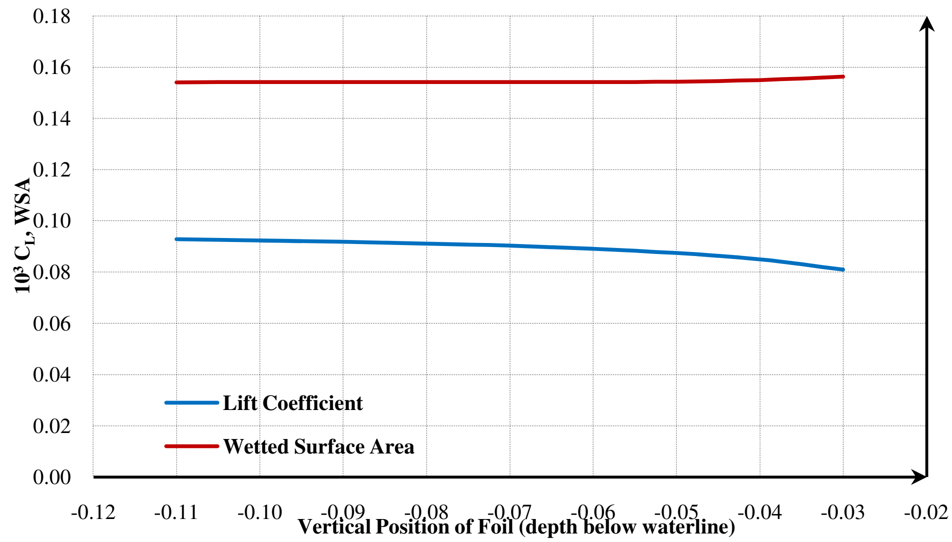

Figure 12: Sinkage and WSA vs. Hydrofoil Depth

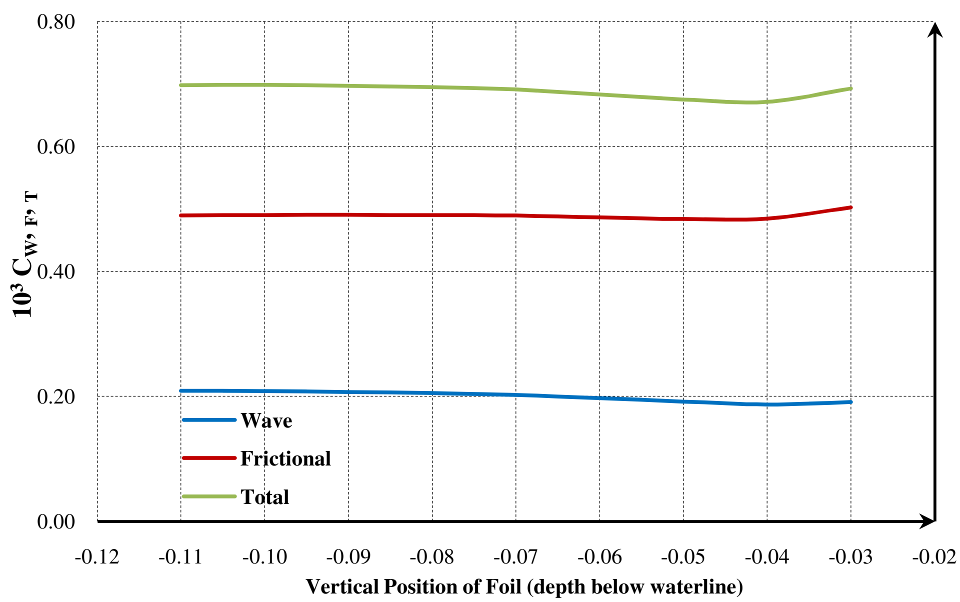

Figure 13: Resistance Characteristics vs. Hydrofoil Depth

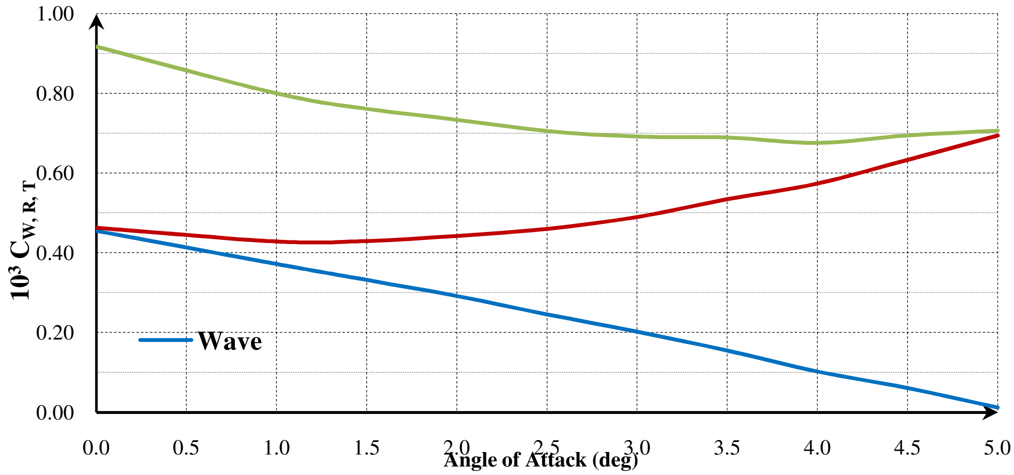

Figure 14: Resistance Characteristics vs. Angle of Attack

CONCLUSIONS AND DISCUSSIONS

Considerable resistance improvement has been achieved with hydrofoil assistance for Froude numbers of 0.8 and above. The improved wave resistance characteristics in low Froude numbers were offset by the added frictional resistance. However, as the rate at which wave resistance improved outbalanced the rate at which frictional resistance increased in higher Froude numbers. This in conjunction with considerably reduced wetted surface area resulted in significant improvement in total resistance characteristics. Total resistance was reduced by almost 60% at *Fn* = 1.2.

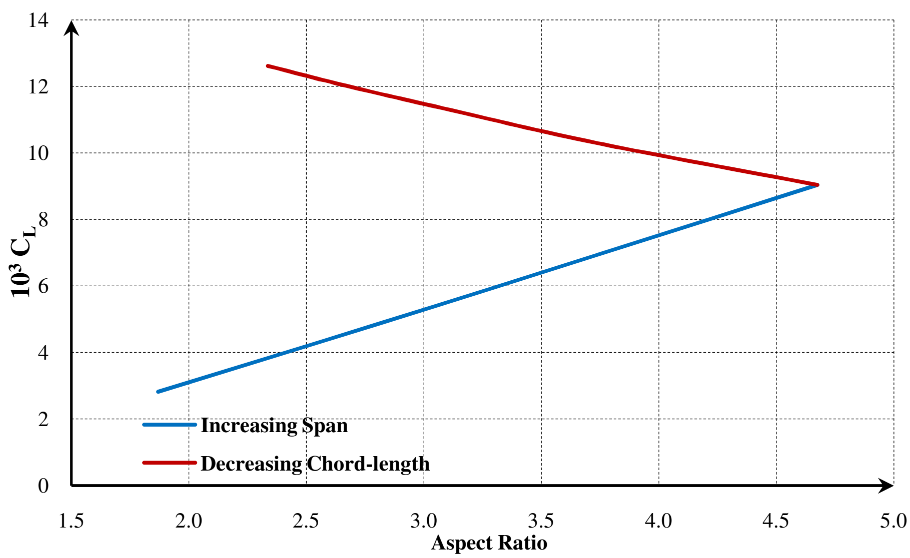

Figure 15: Lift Coefficient vs. Aspect Ratio

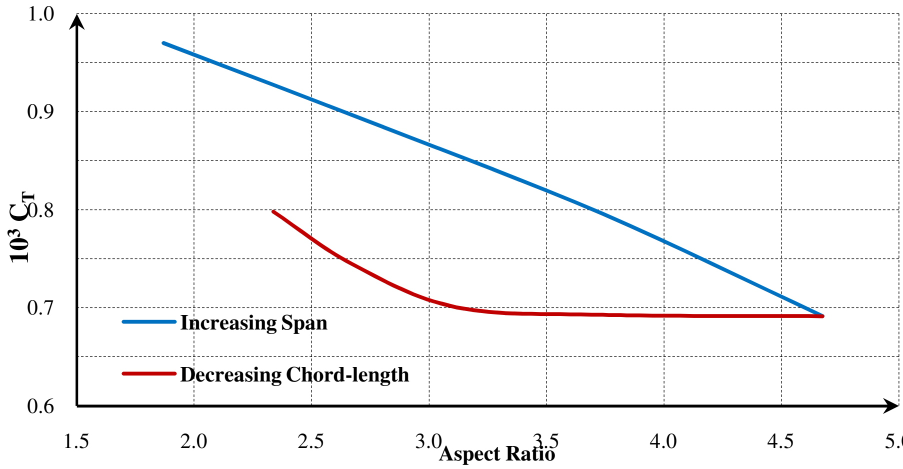

Figure 16: Total Resistance Coefficient vs. Aspect Ratio

In terms of longitudinal shifts, total resistance characteristics deteriorated with the hydrofoil being moved abaft. In other words, the improvement in resistance characteristics with foil moving forward was due to the planing effect caused by the increased stern trim obtained.

The depth of the hydrofoil barely had any effect in the actual resistance characteristics. However, a slight improvement was observed as the depth decreased to an extent. And as expected, the resistance increased as the foil neared the surface due to hull-foil interactions influencing the lift characteristics. Increase in angle of attack significantly improved the total resistance characteristics of the HYSUCAT as the wave resistance and wetted surface area decreased dramatically.

Increase in span resulted in improved resistance characteristics due to two reasons: higher lift obtained through higher span hydrofoil and the reduced interference effects between the demihulls. Changing the chord-length barely affected the resistance characteristics despite a sudden drop in total resistance at low aspect ratios.

From the numerical simulations, it can be concluded that considerable drag reduction is possible with hydrofoil assistance. This encouraging result shall promote this topic to higher levels for more detailed investigations with complete understanding of the behaviour of the HYSUCAT configuration.

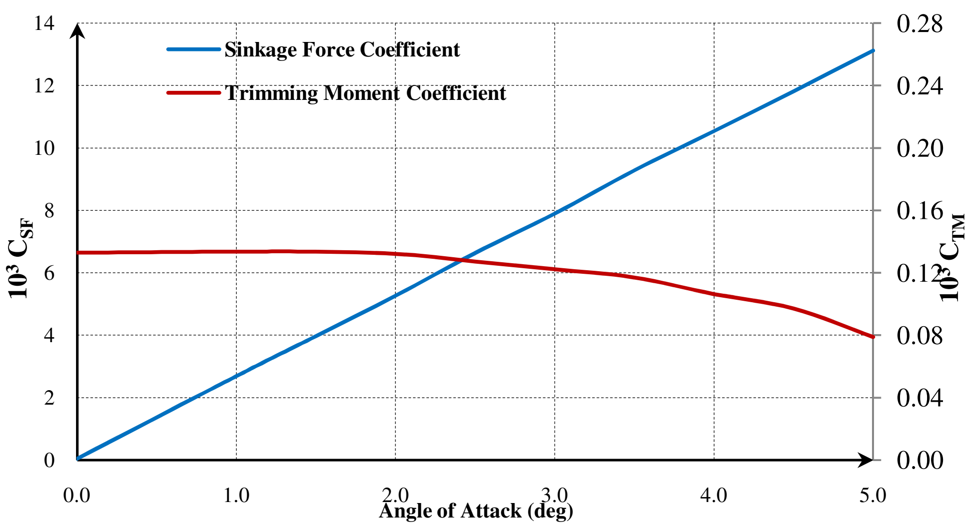

Figure 17: Sinkage Force and Trimming Moment Coefficient vs. Angle of Attack

ACKNOWLEDGMENTS

The authors would like to express their sincere gratitude to Florida Institute of Technology and to The University of Tasmania for their support, encouragement rendered throughout the course of this research work.

REFERENCES

Andrewartha, M. and Doctors, L. (2001): "How Many Foils? A Study of Multiple Hydrofoil Configurations", Proc. Sixth International Conference on Fast Sea Transportation (FAST '01), RINA, Southampton, UK, Vol. III, pp 79-86

Andrewartha, M., Doctors, L., Kantimahanthi, K., and Brandner, P. (2003): "A Numerical Method for Performance Prediction of Hydrofoil Assisted Catamarans", Proc Seventh International Conference on Fast Sea Transportation (FAST '03), Naples, Italy, pp 9-16

Hoppe, K.G. (1995): "Optimisation of Hydrofoil-Supported Planing Catamarans", Proc. Third International Conference on Fast Sea Transportation (FAST '95), Lubeck-Travemunde, Germany, pp 307-318

Hoppe, K.G. (2001): "Recent Applications of Hydrofoil-Supported Catamarans", Proc. of Fast Ferry International, September

Migeotte, G., Hoppe, K.G., and Kornev, N. (2001): "Design and Efficiency of Hydrofoil-Assisted Catamarans", Proc. Sixth International Conference on Fast Sea Transportation (FAST '01), RINA, Southampton, UK, Vol. III, pp 79-86

Radojcic, D., Rodic, T., and Kostic, N. (1997): "Resistance and Trim Predictions for the NPL High Speed Round Bilge Displacement Hull Series", RINA Symposium on Performance and Operation of Small Craft, Southampton.

Srinivasan, V.B., Panigrahi, P.K., Korulla, M., Sha, O.P., and Misra, S.C. (2006): "Experimental Investigation on the Performance of a High Speed Foil Assisted Catamaran", Proc. International Conference in Marine Hydrodynamics, Visakhapatnam, India, pp 547-557

Seventh International Conference
On High-Performance Marine Vehicles
Melbourne, Florida, USA
13-15 October 2010

OPTIMIZATION OF PROPELLER BY COUPLED VLM AND RANS SOLVER METHOD

V.Anantha Subramanian [1] and Senthil Prakash.M.N [2]

[1] Professor, Indian Institute of Technology Madras, India
Email: *subru@iitm.ac.in*
[2] Reader, Cochin University of Science and Technology, Kerala, India
Email: *senthilprakashmn@gmail.com*

ABSTRACT

This paper demonstrates the improvement of a propeller by the coupled Vortex Lattice and RANS solver method. The wake is computed using the RANS solver. The lifting line method performs alignment of blade section to the wake. The VLM enables computation of thrust forces which are used in the fluid domain to recalculate the flow kinematics. An iterative approach is adopted where by the propeller efficiency is improved in stages. The normal velocity component is checked and minimized to decide on the limit of optimization. The method is applied to the case of a 500t deadweight capacity tanker and leads to iterative improvement of the propeller performance for the given speed and inflow conditions. The scheme represents a modern numerical tool towards improved propeller design and performance.

INTRODUCTION

The Vortex Lattice Method (VLM) is a sub-class of the lifting surface method and is useful as a design and analysis tool. It gives the optimum distribution of pitch, camber and mean line offset at various radii by aligning the blade singularities and wake singularities so that normal flow components are reduced to zero and the blade sections perform with the highest efficiency. The RANS solver simulates the flow past the ship hull in towed condition and generates the velocity distribution at the aft of the hull at the propeller inlet zone. This gives the inflow velocity field upstream of the propeller. On the basis of this wake field the Lifting Line Method (LLM) is employed to obtain the circulation at different blade sections. The combination of the two tools leads to a method of improvement of the propeller. The link is achieved by identifying the thrust forces (body forces) from the Vortex Lattice Method and suitably representing them in the fluid domain in the propeller zone. For this purpose a sub-domain is defined in the fluid domain at the location of the propeller disk area. The sub-domain represents the propeller swept volume. It is rotated at the propeller rpm using the rotating reference frame application of the RANS solver, to create the transient effect due to the rotating propeller. This technique effectively simulates the propeller action with consequent modification of the velocity field.

The updated velocity is iteratively used in the LLM to improve the propeller. The updated body forces need to be determined and re-allocated in the fluid domain. This iterative process is continued until there is no change in the circulation. Thus the simulation converges to the working propeller at the prescribed rpm producing the required thrust behind the ship. Thus the propeller - hull interaction is captured. The details of this technique are described here taking the example of the 500t deadweight tanker.

NOMENCLATURE

C_t	Total drag coefficient
k	Turbulent kinetic energy (m^2/s^2)
K_Q	Torque coefficient
K_T	Thrust coefficient
Lpp	Length between perpendiculars
R	Radius of propeller
Va	Inflow velocity (m/s)
ω	Rate of dissipation per unit turbulent kinetic energy (1/s)
w	Wake fraction
η	Open water efficiency

ABBREVIATIONS

CFD	Computational Fluid Dynamics
KCS	KRISO Container Ship
KRISO	Korea Research Institute for Ships and Ocean Engineering
LLM	Lifting Line Method
PBD	Propeller Blade Design
RANS	Reynolds-Averaged Navier-Stokes Equations
SST	Shear Stress Transport
UDF	User Defined Function
VLM	Vortex Lattice Method

KEYWORDS

Hull, Propeller, CFD, Wake fraction

METHODOLOGY

The coupled VLM and RANS Solver method is a new approach towards numerical simulation of the propeller-hull interaction problem. Refer Figure 1, for flow chart of the scheme of optimization of propeller. The method of numerical flow simulation is validated in the case of the KRISO Container Ship (KCS), Hino (2005) without and with propeller, for which published experimental data is available in the public domain. Refer Senthil Prakash *et al.* (2009).

The VLM lifting surface theory based propeller blade design programme Kerwin (1984) PBD 12 is used to find the thrust distribution corresponding to the propeller action. Firstly simulate the motion of towed hull in the RANS solver to obtain the nominal wake distribution. Using the wake distribution find the radial circulation distribution for a given thrust, rpm and geometry of the propeller. The inputs used at this stage are the wake distribution, the advance coefficient, the propeller geometry and the radial circulation distribution. When used in the VLM programme, the result is obtained with co-ordinate – specific thrust distribution as well as induced velocities over the blade mean surface.

Transform the blade coordinates to the main domain coordinate reference system, see Figure 2.

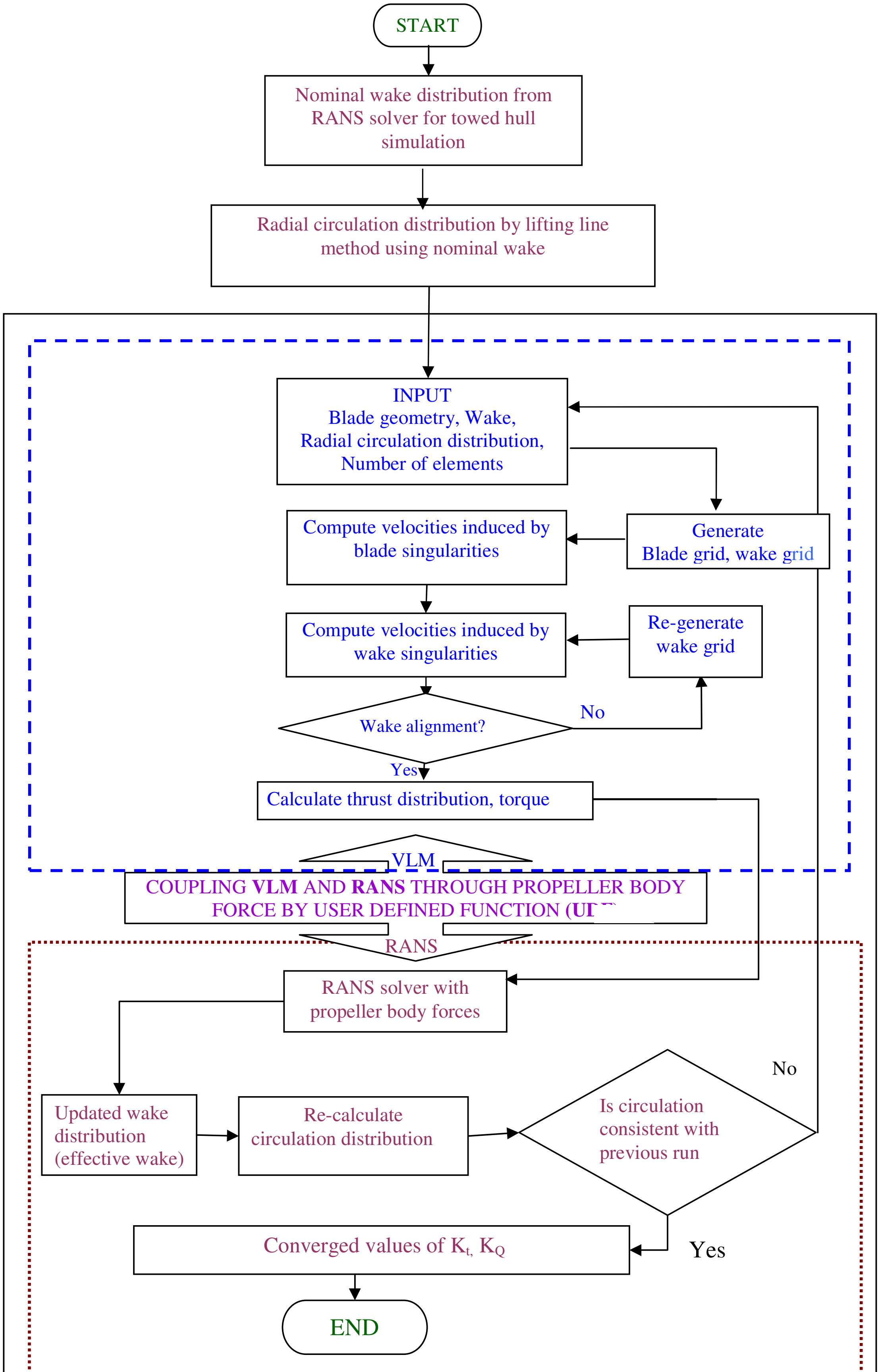

Figure 1: Flow chart for obtaining propeller-hull interaction

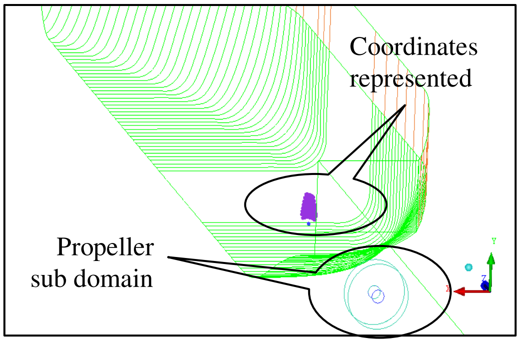

(i) Representation of coordinates of force acting points obtained from VLM

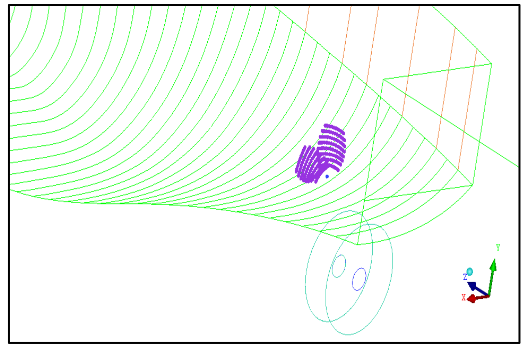

(ii) Co-ordinates copied and rotated through 90 degree for the next blade

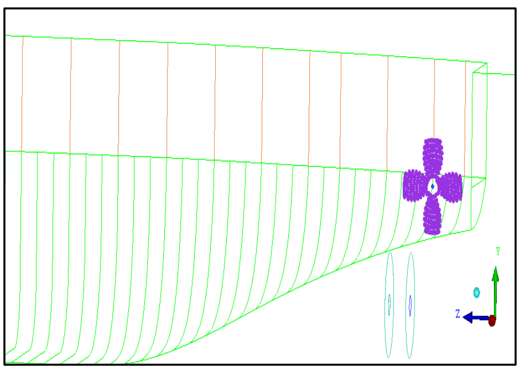

(iii) Co-ordinates copied and rotated subsequently to get the all blades

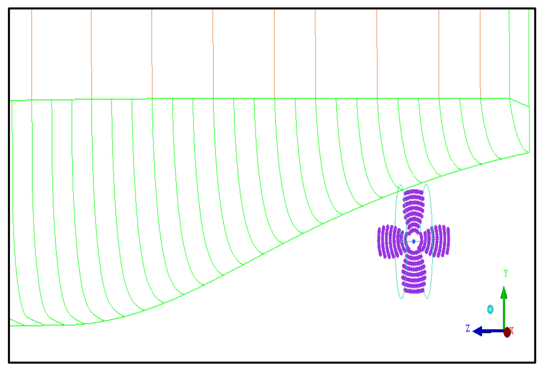

(iv) The blades are shifted to make the centers of the propeller centre and the sub-domain centre to coincide.

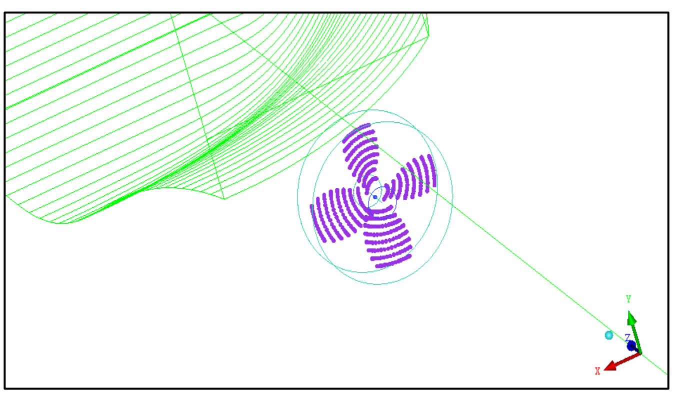

(v) The blades are rotated to make the axis of the propeller to be in the direction of the axis of the hull.

Figure 2: Stepwise sequence of identifying propeller coordinates in the sub domain

Now input the thrust values as modified propeller body forces, into the sub domain representing the propeller swept volume with the help of the user defined function (*udf*). The propeller body forces are mapped onto cell centroids close to the coordinates at which the thrust distribution occur, see Figure 3.

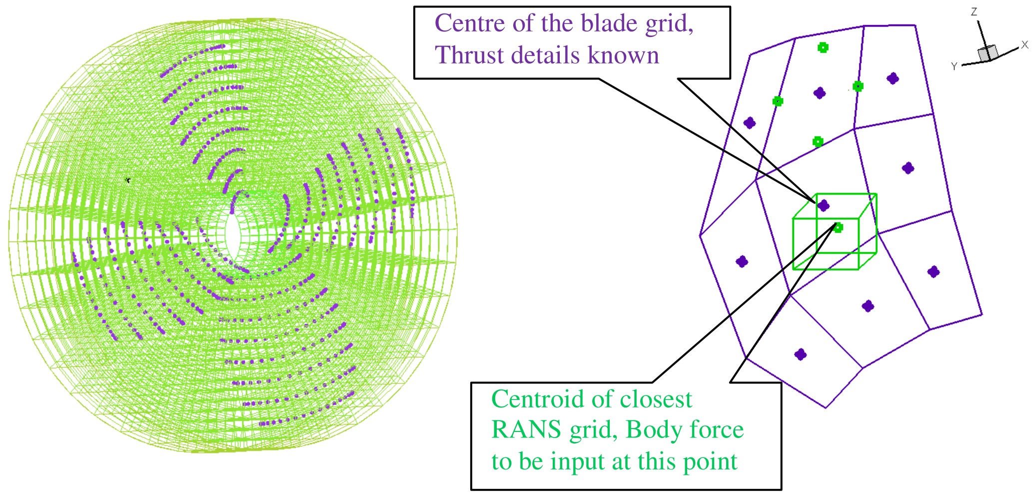

Figure 3: Propeller body forces are calculated at the centre of the panels (Violet dots) of the blade and are to be input at the centre of the nearest cell (green) centre

The *udf* has in-built sub-routines to determine the centroid of the domain cell closest to the transformed blade coordinate, extract the volume of this cell, calculate propeller body force (which is the ratio of the thrust to the volume of the cell), and put this body force back into the corresponding cell centroid. To account for the transient effects created by the rotating propeller, the sub-domain is rotated at the propeller rpm using the rotating reference frame application of the RANS solver, see Figure 4.

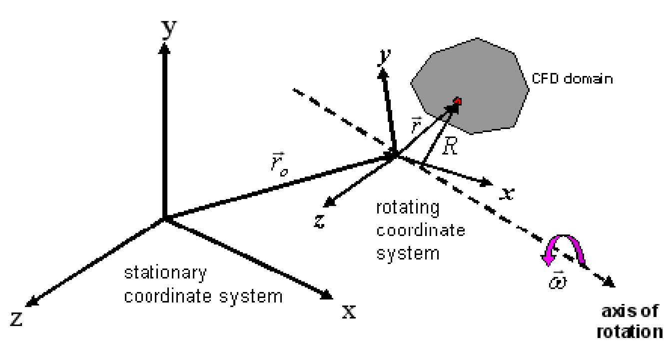

Figure 4: Stationary and rotating reference frames in FLUENT

The RANS solver now gives the modified velocity distribution at the propeller inlet section. This gives the updated wake in the presence of the working propeller (total wake). The effective wake at the propeller inlet for updating the propeller body force is found by subtracting the induced velocity from the total velocity. The updated body force is calculated by the VLM, and the RANS is run iteratively until there is convergence in the circulation distribution. At this stage, the RANS simulation will give the true working condition with realistic propeller rpm and thrust behind the ship, simulating the propeller-hull interaction.

The propeller design process is represented in the upper part of the block diagram in Figure 1. Propeller thrust and torque are obtained in the design process of a wake aligned propeller blade. Based on the wake, the radial circulation distribution is obtained by applying the Lerbs' criteria. By the principles of the lifting surface method, the blade grid and the wake grid are generated and the velocities induced by the blade singularities and wake singularities are computed. Once wake alignment is achieved, the propeller related torque absorption and thrust delivered can be calculated. Coupling the body forces to the fluid domain and running the RANS solver, gives the updated flow velocities under the influence of the propeller. The resulting updated wake distribution now enables to re-calculate the circulation distribution as done in the first step. The propeller is thus iteratively improved for optimum performance. The simulation of the hull-propeller interaction by modeling the actual propeller hull combination tends to be computationally intensive. Refer Dhinesh *et al.* (2009) Hence several runs of simulation which is required for iterative improvement is more practical with the body force modeling of the propeller rather than the propeller itself.

The main domain is created and the propeller sub-domain is separated from it. The first simulation is performed for initial condition towed hull, without introduction of the body forces. The spatial inflow velocity components upstream at the propeller location are obtained. The circulation data enables generation of the body forces.
The VLM code gives the X, Y and Z components of non-dimensionalised forces offered by span wise and chord wise singularities. An empirical correction applied accounts for viscous effects.
Figure 5 and Figure 6 show spatial inflow velocity, wake fraction in the stern region for the towed hull and for the self-propelled condition respectively.

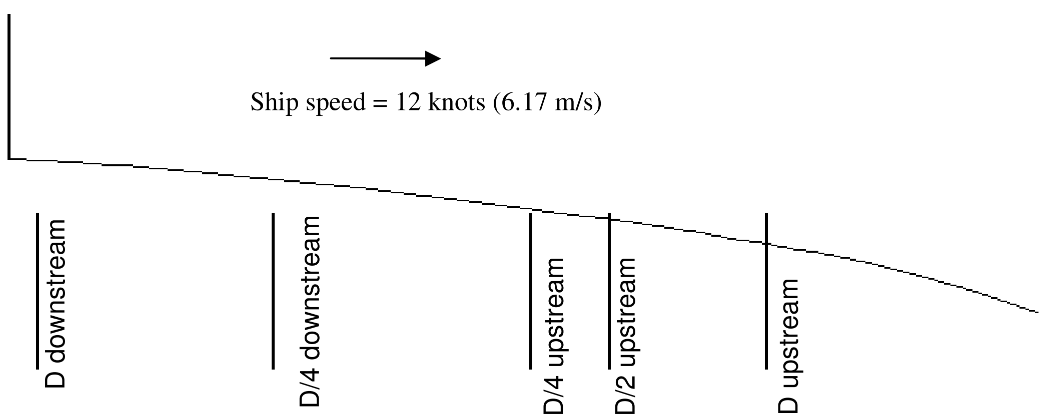

5.23	5.16	5.30	5.20	5.25	5.22	5.39	Inflow velocity, Va (m/s)
0.15	0.16	0.14	0.16	0.15	0.16	0.13	Wake fraction

Figure 5: Spatial inflow velocity, wake fraction in the stern region for the towed hull

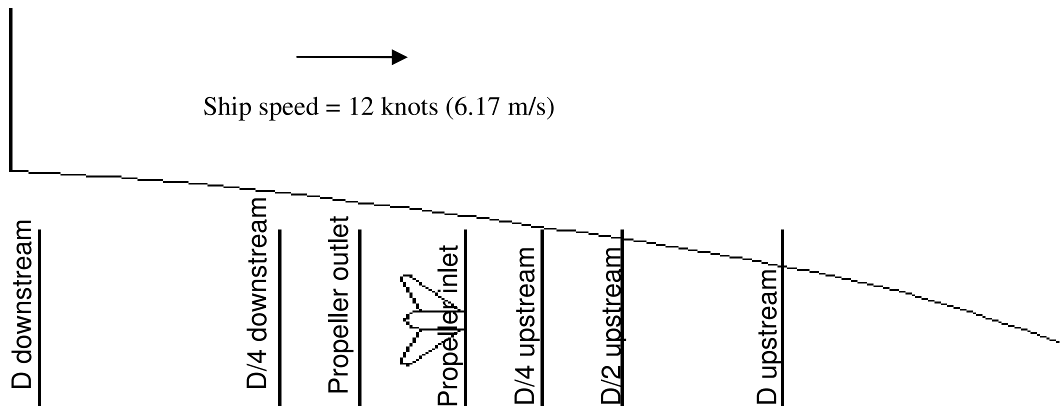

← 6.99	← 7.03	← 7.11	← 6.42	← 6.16	← 5.81	← 5.79	Inflow velocity, Va (m/s)
-0.13	-0.14	-0.15	-0.04	0.002	0.06	0.06	Wake fraction

Figure 6: Spatial inflow velocity, wake fraction at the stern for self propelled condition

COMPUTATIONAL DOMAIN AND GRID SYSTEM

Figure 7 gives the extent of the domain, boundary settings and grids formed for the simulation.

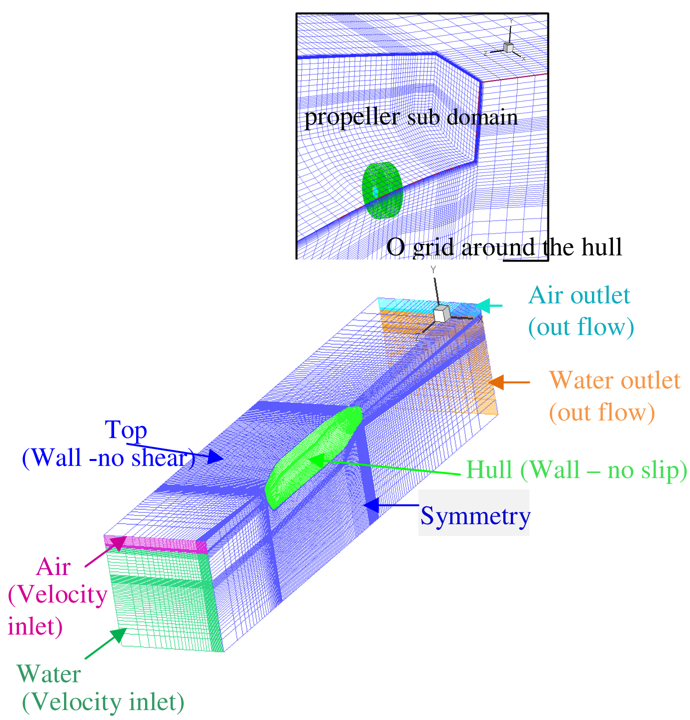

Figure 7: Discretized fluid domain with boundary conditions and propeller sub-domain discretized with O grid.

The computation domain is chosen in such a way that it has just the adequate size so that the computational results are not adversely influenced and without excessive demand on computational time. A domain independency analysis has been conducted by observing the total drag coefficient (C_t) for the minimum domain size and progressively increasing the size in order to obtain independency of solution with any further increase in domain size. Each domain used for calculation is processed using the SST $k-\omega$ model at a free stream velocity of 6.1728 m/s (ship speed of 12 knots) without the propeller body force terms included. Based on the domain independence study the extents of the domain are chosen: Length of the domain upstream the hull is 0.8 Lpp and downstream is 1.2 Lpp. Width and depth of the domain is 0.8 Lpp. Block structured hexahedral grid is used for the domain discretization.

INITIALIZATION

In general all the flow variables may be set to zero values and the simulations are expected to converge towards steady state. The gridded domain is marked and separated in order to demarcate water and air regions as separate entities. The regions are patched and allocated appropriate volume fraction values. In order to initialize, the Z-component velocity at air and water inlet are set to free stream velocity of 6.1728 m/s at the start of computations and all other variables are set to zero. The *udf* is interpreted and the source terms are added.

BOUNDARY CONDITIONS

The boundary conditions are logically selected from past experience: velocity inlet with free stream velocity of 6.1728 m/s at the domain inlet, wall with slip and zero shear (at free surface and at the bottom and side wall) and wall with no slip (over hull surface) conditions are imposed on the solution domain (Figure 7). The velocity normal to the boundary is used to define the flow velocity for both the phase *i.e.,* air and water along with relevant scalar properties of the flow at the inlet.

RESULTS AND CONCLUSIONS

A numerical scheme has been designed and implemented as described in the flow chart in Figure 1. It combines propeller design/analysis and coupling with the fluid domain around the ship hull using propeller body forces and the *udf*. The RANS solver captures the kinematics successfully. The methodology is demonstrated in the case of hull interaction simulation and optimization of the propeller in the case of a 500t oil tanker. Table 1 shows the improvement of the propeller in the iterative scheme employed.

Figure 5 and Figure 6 show the intermediate results of flow kinematics in the propeller inflow zone as well as downstream of the propeller. The nominal and effective spatial wake distributions are brought out from the RANS solver based results.

The evolution of the optimal propeller through the 5 stages is shown in Figure 8. The propeller efficiency has been stepped up from 0.57 starting with the series data based propeller design for initial wake condition to 0.63 (for final stabilized effective wake and matched propeller geometry). There is an overall improvement of nearly 10% in the final wake adapted propeller. In conclusion, the scheme combines two modern numerical tools to design the propeller for significantly improved performance.

Table 1: Iterative improvement of efficiency of propeller for 500t oil tanker

Sl.no.	Stage of iteration	Kt	Kq	η/(1-w)	η
1.	Base propeller chosen from Wageningen B-screw series to give required thrust under zero wake condition (wake not yet known)	0.100	0.0174		0.680
2.	Base propeller at a performance point on the basis of the effective wake obtained at stage 5	0.198			0.580
3.	Modified propeller under nominal wake – stage 2	0.211	0.0363	0.726	0.514
4.	Iteration – stage 3	0.221	0.034	0.808	0.572
5.	Iteration – stage 4	0.207	0.0293	0.882	0.624
6.	Iteration – stage 5	0.207	0.0289	0.891	0.631

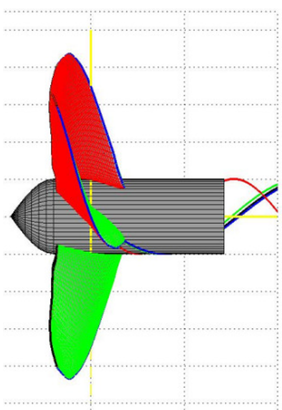

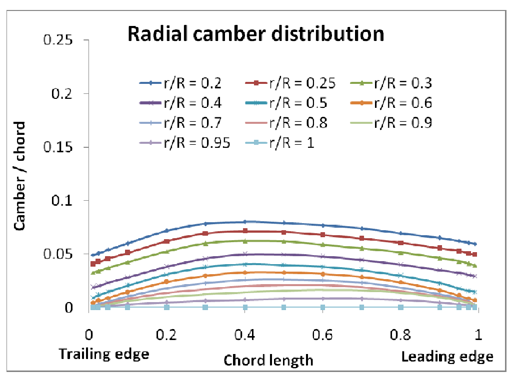

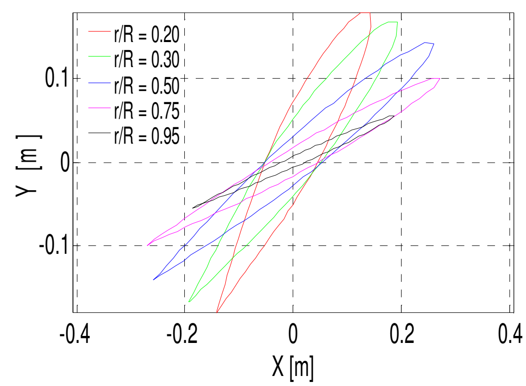

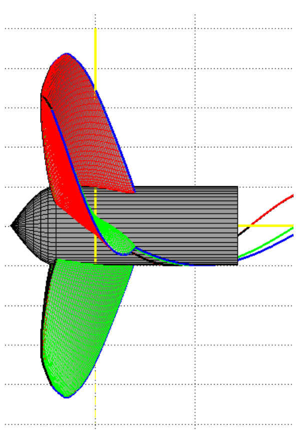

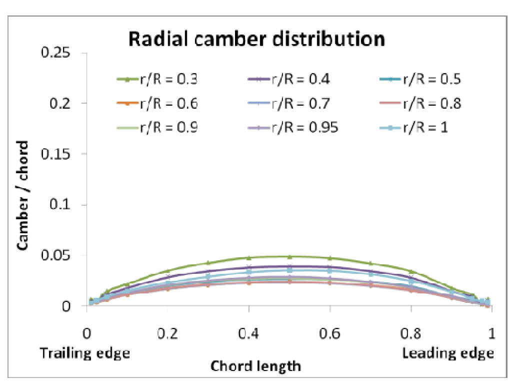

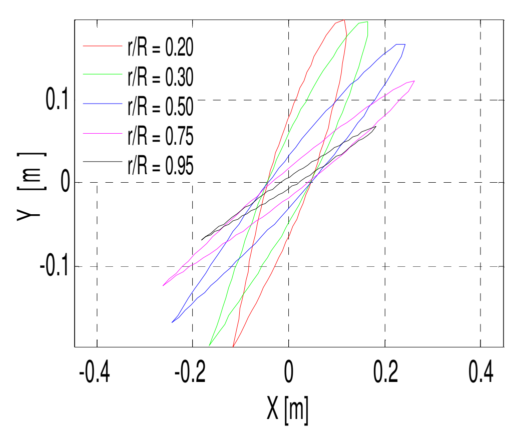

Stage 2

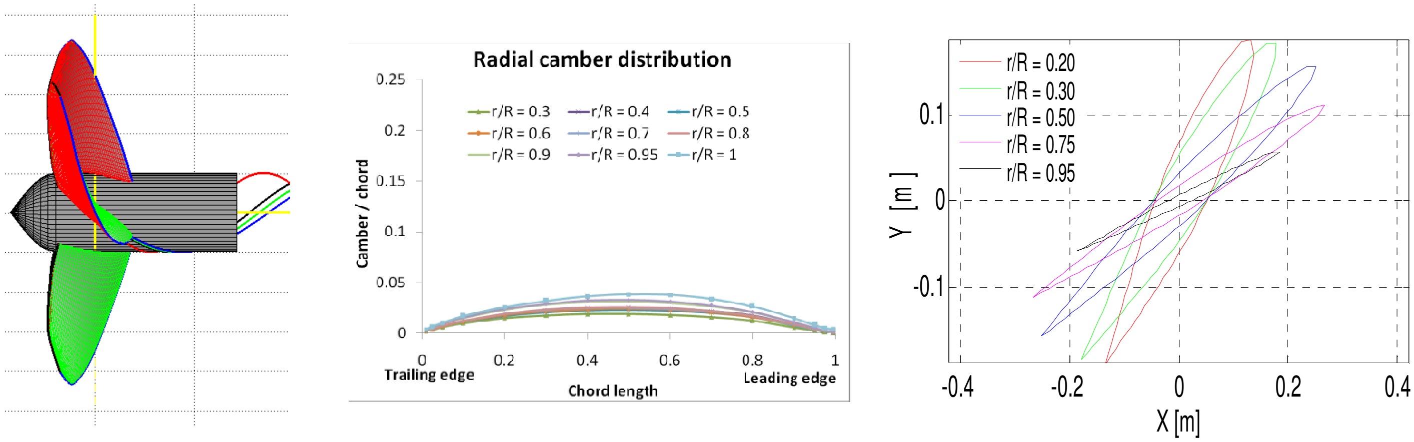

Stage 3

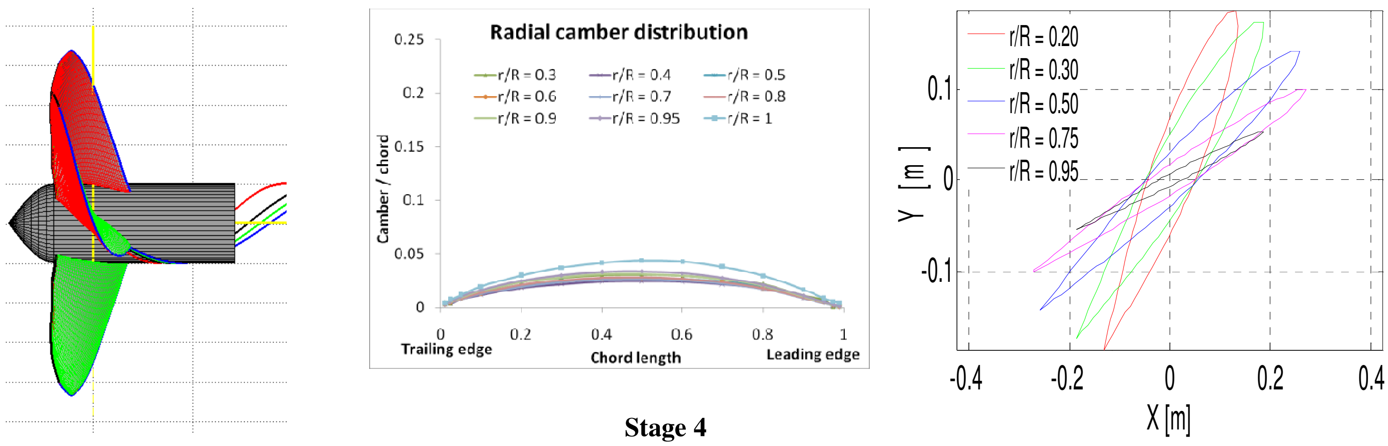

Stage 4

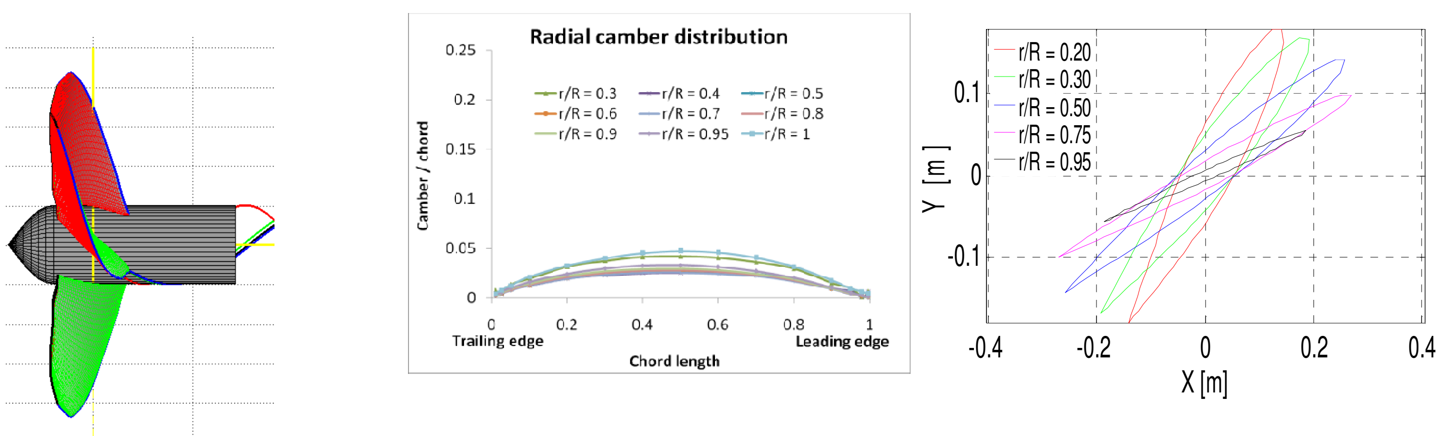

Stage 5

Figure 8: Stage wise improvement of the propeller

REFERENCES

Dhinesh,G.,K,Murali. and V.A.Subramanian. (2009)"Estimation of hull-propeller interaction of a self–propelling model hull using RANS solver", *Ships and offshore structures*, Vol.2, No.2, pp.1-15

Greeley,D.S. and Kerwin.J.E. (1982)"Numerical method for propeller design and analysis in steady flow",*SNAME transactions*,Vol-90, pp.415-453

Hino, T. *Preprints of CFD workshop Tokyo 2005,* National Maritime Research Institute, Tokyo,Japan,2005 .

ITTC Quality Manual, (1999) *Uncertainty Analysis in CFD and Guidelines for RANS codes*,22nd ITTC

Karl, Y., Chao. and Carrica, P.(2005). "Numeric propulsion for the KCS container ship", *Proceedings of CFD workshop* Tokyo (2005), pp 483-489

Kerwin, J. E. (1984). "A vortex lattice method for propeller blade design", *MIT PBD-12 users manual*, Massachusetts institute of technology.

Kerwin, J. E. and Lee,C.S. (1978)."Prediction of steady and unsteady marine propeller performance by numerical lifting surface theory"*SNAME Transactions*,Vol.86,1978, pp.218-253.

Senthil Prakash, M. N. and V. A. Subramanian, (2010), "Simulation of propeller - hull interaction using RANS solver", *International Journal of Ocean and Climate Systems, Vol.1, No.3,4.* pp.189 – 203

Seventh International Conference
On High-Performance Marine Vehicles
Melbourne, Florida, USA
13-15 October 2010

AUTOMATIC PARAMETRIC HULL FORM OPTIMIZATION OF FAST NAVAL VESSELS

I.Biliotti[*], S.Brizzolara[*], M.Galliussi[#], A.Manfredini[#], D.Ruscelli[+], G.Vernengo[*], M.Viviani[*]

[*] Department of Naval Architecture and Marine Engineering, Genoa, Italy
[+] Cetena, SpA, Genoa, Italy
[#] Italian Navy, Studies, Means, Projects and Materials Office, MOD, Rome, Italy

ABSTRACT

The present work shows the outcomes of a research project among the Department of Naval Architecture and Marine Engineering of the University of Genoa and Cetena S.p.A. for the Italian MOD in the frame of National Defence Research Plan. An automatic optimization study of the fore hull forms of a fast frigate is presented; it has been performed with a proper integration of a commercial optimization system, a parametric geometric modelling software and two different ship hydrodynamic analysis tools to predict the steady (wave resistance) and unsteady (seakeeping) performance of each design candidate. The fully automatic optimization algorithm, used to evaluate several thousands of design alternatives, takes into account a constrain set composed both by geometrical tolerances and minimum stability characteristics of the hull defined in a preliminary design study mentioned and briefly recalled in the paper. The parametric definition of the ship hull geometry accurately devised to represent the original hull form solution and to include as many variable shapes and possible, still granting a good fairing of each solution, is described in the paper as well as the technical details of the optimization set up, in terms of high level software architecture; analytical definition of the objective functions; imposition of the design constraints and selection of the optimization strategy.

Interesting conclusions are drawn in the end of the paper from the results of the optimization study which showed a good convergence on the optimum solution The numerical results obtained presented in the paper are going to be validated by a series of model tests in towing tak on the original and optimized hull geometry variants.

KEYWORDS

Hydrodynamic optimization, hull parametric modelling, fast naval vessels, wave resistance, seakeeping.

NOMENCLATURE

B maximum ship breadth;
H_s significant wave height;
L_{BP} length between perpendiculars;
MEI Mission Effectiveness Index;
NP number of points in which the projection of the wave profile on the hull side is calculated from bow up to amidship;
NSS number of Sea States considered for the seakeeping analysis;
NSC number of Sea Conditions considered for each Sea State;
SOE Seakeeping Operability Index relative to the considered Sea Condition;
$R_W(20kn)$ wave resistance at 20 kn;
$R_W(35kn)$ wave resistance at 35 kn;
$R_{W\ 20}$ ratio between the wave resistance at 20 kn and the design displacement;
$R_{W\ 35}$ ratio between the wave resistance at 35 kn and the design displacement;
T ship design draught;
T_p wave peak period;
V_P patrol speed;
V_M maximum speed;
V_{SK} speed for the seakeeping analysis;
Δ ship displacement;
η elevation of the wave profile projected on the hull side;
$\overline{\eta}$ mean value of the wave profile elevation projected on the hull side;
σ^2_{20} variance of the wave profile projected on the hull side from bow up to amidship for the speed of 20 kn;
σ^2_{35} variance of the wave profile projected on the hull side from bow up to amidship for the speed of 35 kn;

INTRODUCTION

The challenge of international market and the search of increasing performances lead the process of ship design to a continuous enhancement both in merchant and naval field, where the dedicated time for a thorough design is ever decreasing. In this context, a key issue is represented by the hull form development which has to ensure a well defined payload and has to maximize the hydrodynamic performances.

Starting from a preliminary design of a 108 m long fast frigate (parent hull) which defined a set of constraints related to geometrical and hydrostatic characteristics of the hull, this study presents an optimization process devoted to two of the most important hydrodynamic aspects for a naval unit: the wave resistance (affecting her maximum speed) and the seakeeping performances (directly related to her operability).

The Mode Frontier optimization environment has been allowed to interface with the Friendship-Framework, which introduces a new parametric approach to the hull geometry, with the hydrodynamic codes WARP and SOAP developed by CETENA S.p.A.; a MOGA genetic algorithm has been adopted for the optimization of the fore hull form of the frigate as well.

The optimization flow, the parametric modelling and the hydrodynamic analysis are thoroughly described and the results of the optimization, in form of comparison with the parent hull, are reported.

In the last part of the research project a set of dedicated tank tests will be performed on the parent hull and on the optimized one in order to validate the results of the optimization.

SYNTHESIS MODEL

The synthesis model adopted for the hydrodynamic optimization is made of the following 4 modules:

- *Hull form design* → Geometric (parametric) hull form modeling;
- *Hull form analysis* → Hydrodynamic analysis (in terms of wave resistance and seakeeping);
- *Hull form merit assessment* → Measure of merit following the adopted objective functions;
- *Hull form variation* → Systematic variation of the geometric parameters automatically performed by the optimization algorithm with respect to the geometric constraints defined by the preliminary design.

In order to get a fully automatic calculation flow, such modules have been integrated with several pre-processors (automatically making the offset compatible with the hydrodynamic codes) and post-processors (re-arranging the output of the hydrodynamic codes and making it simply usable for the optimization code).

The following Figure 1 represents the sketch of the synthesis model adopted for the hydrodynamic optimization which has been developed in the Mode-Frontier ambient.

DESIGN TASK

The parent hull which the optimization process has started from has been defined in the first part of the research project following the technical specifications provided from Italian MOD which identified her operative profile.The twin screw ship was supposed to be mainly employed for patrol missions at speeds between 12 kn and 20 kn, but a maximum speed of 35 kn was requested too. The ship has been supposed to comply with the RINA-MIL Rules so that a preliminary stability assessment has been performed with the aim to verify her compliance with the Rules requirements.

Several seakeeping requirements involving the standard patrol criteria (vertical and lateral velocities and accelerations, pitch and roll angles, propeller emergence, green water and slamming occurrences) have been defined too up to the speed of 25 kn for Sea State 4 (three Sea Conditions → H_s 1.88 m and T_p 4.5 s, 5.5 s, 6.5 s) and Sea State 5 (three Sea Conditions → H_s 3.25 m and T_p 4.5 s, 5.5 s, 6.5 s).

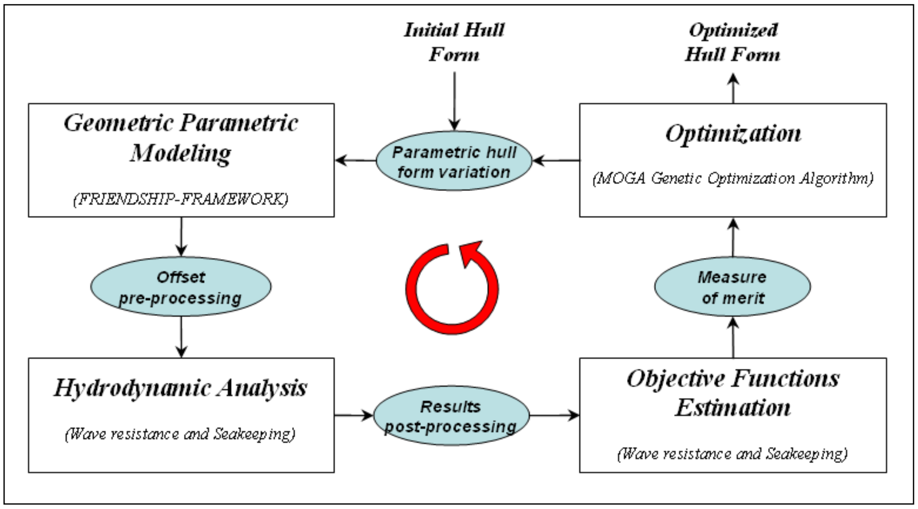

Figure 1:Synthesis model of the optimization

The internal spaces have been arranged on the basis of the specified crew and following the standards of the SMM100 Rules. The technical specifications contained a strict definition of the payload too.

The main characteristics of the parent hull have been resumed in Table 1.

Table 1:Main characteristics of the parent hull

Quantity	*Symbol*	*Value*
Length between perpendiculars	L_{BP}	108 m
Maximum Breadth	B	13.60 m
Design Draft	T	4.2 m
Design Displacement	Δ	~3000 t

PARAMETRIC MODELLING

The approach used to generate the three-dimensional parametric model of the hull surface is built around the FriendShip – Framework software which is based on shape parameters of plane figures and volumes, not only in the classic sense of the naval architecture practice, but also as primary mean for modelling and controlling desired shapes which should be inherently faired (as from Harries and Nowacki, 1999).

The three dimensional, mathematical representation of geometric elements is still based mainly on B-Spline curves and surfaces, in line with the state of the art of the majority of marine industry CAD software. However, the controlling vertices of curves and surfaces do not represent a specific property of the envisioned shape: their location is determined by solving a constrained optimisation problem where one or more formal fairness criteria are applied as objective function. Specific definition parameters, like enclosed area, local tangency or curvature are captured as equality constraints. These entities are a very powerful tool for hull generation and variation (Abt et al, 2003).

The main steps to be followed to build a parametric model for a given hull form can be synthesised in the following points:

- Creation of a suitable set of basic curves;
- Description of a number of cross sections definitions through which the hull surface is split;
- Generation of surfaces, outcome of the combination between basic curves and cross sections.

FAST FRIGATE TYPE 1 PARAMETERIZATION

The parametric model for the fast frigate hull surface has been primarily built around the proper choice of the basic curves set, this depending on key features of hull geometry. Basic curves comprise positional, differential and integral information.

Separated basic curves have been set for the hull and the bulb geometry, these representing separated entities that couldn't be easily merged by means of a continue mathematical description.

Ten curves have been modelled for the hull (Figure 2):

1. Bilge Fullness
2. Curve of sectional slopes at deck
3. Curve of Deadrise
4. Design waterline
5. Deck curve
6. Curve of sectional slopes at the design waterline
7. Flat of Side curve
8. Center Plane Curve
9. Curve of Stem
10. Curve of half angles at the entrance

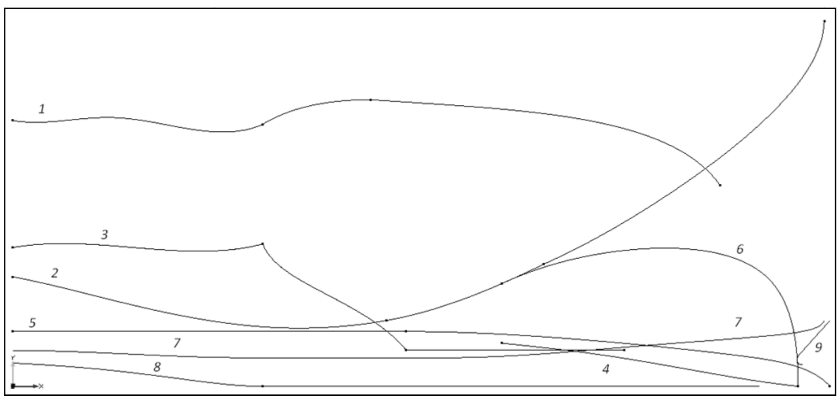

Figure 2: Basic curves defined for the fast frigate type-1 hull form description.

The basic curves are discretized into a certain number of points whose longitudinal positions mainly depend on global form parameters and often match between one curve and the other, so as to make sure that a global parameter variation produces a coherent shifting of all the basic curves that depend on that parameter, providing more feasible resulting hull geometry.

The significant cross sections that describe the hull geometry are four. The cross sections are the outcome of an object-oriented programming which takes place in the so-called *features*: they are programming windows in which points, F-Splines and other types of curves can be inserted and their geometric properties set.

The first cross section starts at the transom stern and ends at the flat of side emergence, while the second starts from the latter and ends close to the enlargement of the sections that anticipates the shapes of the bulb (Figure 3). Then the bulb cross section starts below the design waterline (Figure), while above it has the fourth cross section that ends close to the stem. The latter two cross sections are then vertically divided, that is, there is no unique section definition from the beginning of the bulb onward. The fourth cross section is directly derived from the second, this being only made up by the dry and the flat of side.

The remaining *features* used to complete the surface modelling, including the skeg, are specific fillet surfaces whose task is to join two or more surfaces resultant from other *features* with several options settable.

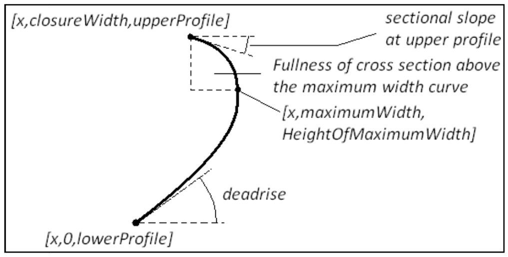

Figure 3: Cross section definition for the foresections below the design waterline and the bulb.

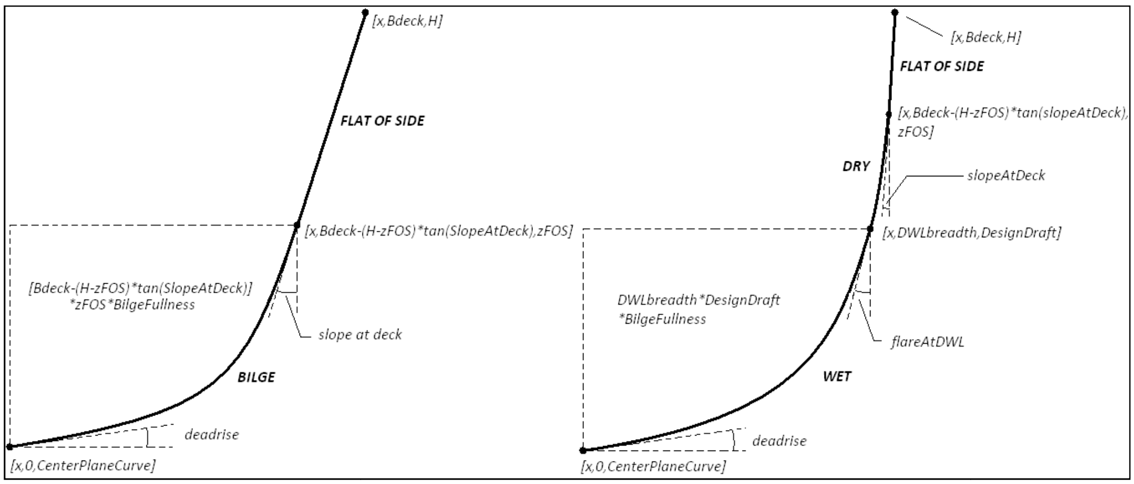

Figure 4: Cross section definition from the transom stern to the FOS emergence(left) and from the FOS emergence to the beginning of bulb(right).

Seven basic curves have been set for bulb modeling:

11. Upper profile
12. Lower profile
13. Maximum width curve
14. Height of maximum width curve
15. Fullness of bulb section above the height of maximum width curve
16. Curve of Deadrise
17. Closure width curve

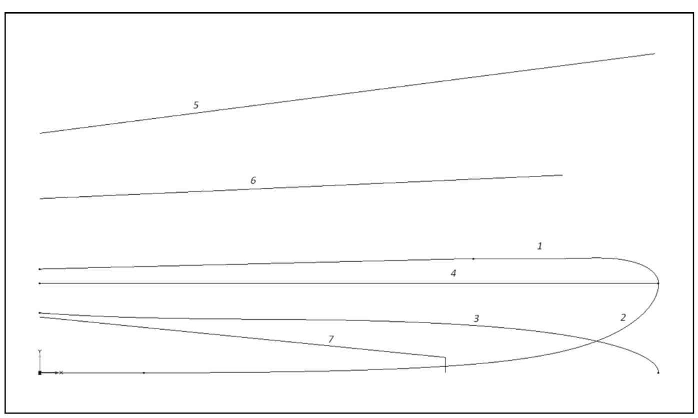

Figure 5: basic curves for the bulb geometry description.

Different hull shapes, obtained by combinations of form parameters values which have a global and local influence on the hull itself, are hereby shown focusing on the forebody, the aftbody and the bulb geometry, to better observe how parametric modelling allows exploring a large amount of highly faired design alternatives for hydrodynamic performance evaluation.

In the modelling flow several parameters have been created, which have a global or local influence on the shape control, and only 14 were selected for systematic variation and optimization. These are parameters which manipulate both global and local shape of the forebody, that is, from the midship section position onward.

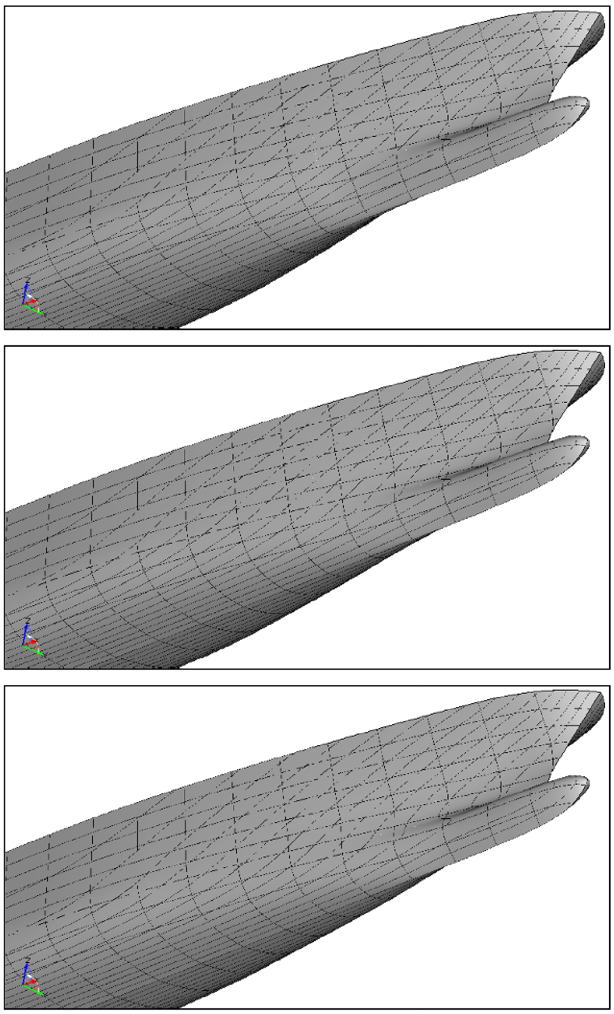

Figure 6: sequence of variation of parameters in the bulb geometry.

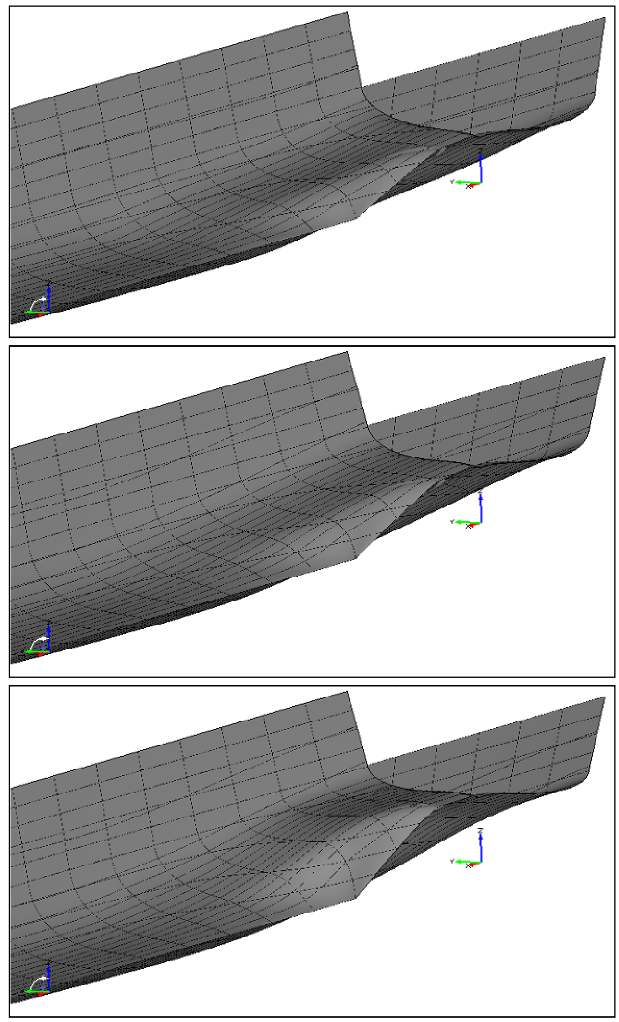

Figure 7: sequence of variation of parameters in the aftbody hull form.

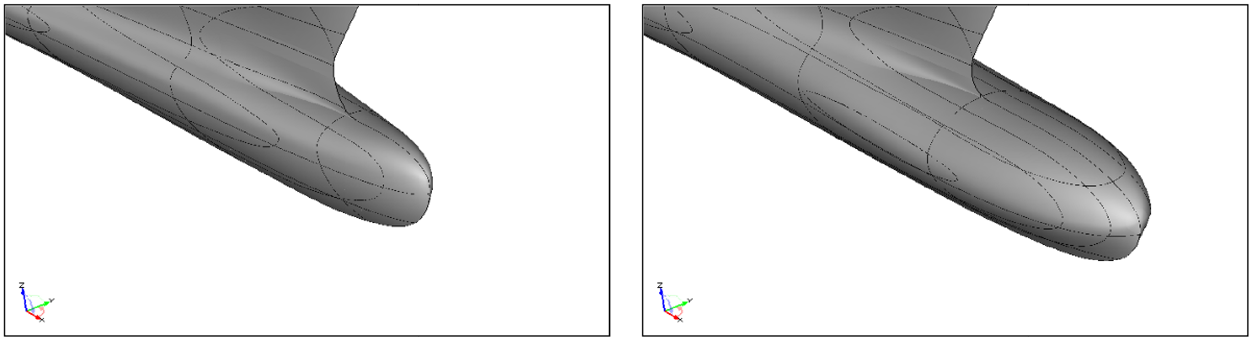

Figure 8: sequence of variation of parameters in the forebody hull form.

HYDRODYNAMIC ANALYSIS

At the preliminary design stage numerical simulations are used for the evaluation of hydrodynamic performance. For a comprehensive investigation both calm-water hydrodynamics and seakeeping need to be taken into account.

Two software tools by CETENA were employed for hydrodynamic analyses within this study:

- *WARP* Wave Resistance Program – A linear potential flow code for calculating a hull's wave resistance in calm water.
- *SOAP* Seakeeping Operability Assessment Program – A state-of-the-art software package for determining seakeeping, operability and comfort on board a ship in a sea-state.

Wave Resistance Analysis

WARP is a panel code developed by CETENA for potential flow calculations around ship hulls, see (Caprino, Sebastiani, Valdenazzi, 1997). It is a linear code which follows a modified Dawson theory for the calculation of potential flows including a free surface.The solution of the boundary value problem is found by distributing Rankine sources over the hull and a portion of the free surface and computing the potential from which then the velocity and pressure distribution can be obtained.

The program has been widely used and systematically tested by CETENA: Similar to other codes based on the same theoretical background, the linear *WARP* is very reliable when comparing different hull forms with each other, i.e., ranking design variants. The prediction of the wave pattern and the wave resistance, however, suffers from the limitations related to the potential theory and the linearization. Often, the wave pattern is under-predicted in the bow region and over-predicted in the stern region and behind the hull, the latter being caused by neglecting viscous effects.

One of the most challenging aspects for the automatization of the computational procedure has been represented by the automatic generation of the hull surface mesh, whose quality directly affects the results of the calculations.

In this way a dedicated fully automatic mesh generator has been implemented and interfaced with the hull form generator. The obtained meshes (an example of which is reported in Figure) have been satisfactory.

Seakeeping Analysis

SOAP is a seakeeping and operability package developed at CETENA. It consists of:

- a seakeeping code for the generation of the seakeeping data in terms of response amplitude operators of the motions at the center of gravity, velocities and accelerations;
- an elaborate post-processor for the evaluation of comfort and operability.

The seakeeping code is based on a standard linear 2D method (strip theory). In the post-processing root-mean-square values of user-selected comfort and operability criteria are determined. The post-processor can incorporate statistical tables for the geographical areas of interest, providing the percentage of occurrence of particular sea-states. A ship's overall operability can be estimated in two ways:

1. the speed reduction necessary to comply with the criteria is evaluated for each heading in each of the selected sea-states, based on a user-selected set of operability criteria and their corresponding limits;
2. the percentage of time operability (PTO) during which the ship fulfils the selected criteria at a fixed speed is evaluated for each heading in a given area.

The code allows fast turn-around time and, in this way, it permits a high number of hull variants to be analyzed during the optimization.

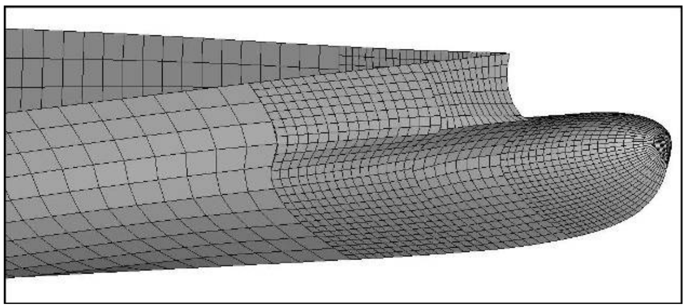

Figure 9: Automatically generated mesh (parent hull form)

OPTIMIZATION

ModeFRONTIER is a software system and environment dedicated to multi-objective optimization. It can be looked at as a platform for the management of all calculations associated with an optimization process. It manipulates the input files used to execute outside software tools in batch-mode, launches these programs in a concerted manner and scans the output files produced during each run for desired data (for instance the current value of an objective function). *ModeFRONTIER* is applicable to optimization problems of very different type and various strategies are readily available:

- *DoE* Design of Experiments – An evaluation of the objective function(s) for pre-selected variations in the free variables, the variations being either specified by the user or generated algorithmically (in the present work a random distribution type *Sobol* has been adopted).
- *MOGA* Multi Objective Genetic Algorithm – A multi-objective optimization on the basis of Darwin's principle of survival of the fittest, using mechanisms such as cross-over, selection, mutation, elitism etc

In the present study a *DoE* has been used for a preliminary investigation of the feasible domain. Then the MOGA algorithm have been utilized to undertake a more specific search, setting out from a favourable starting point found in the *DoE*.

An important aspect of *optimization software environment* is the flexibility in specifying the optimization problem. A graphical user-interface allows accessing all available tools and arranging the work flow so as to suit the individual optimization task. It also offers various graphical options for analysis of the data calculated during an optimization. All data can be presented within so-called *parallel diagrams* which allow playing with the parameter ranges to further assess the optimization problem.

Objective functions

As previously discussed, the hydrodynamic optimization has been devoted to two different aspects:

- Minimization of the wave resistance;
- Improvement of the seakeeping performances of the Unit.

The speed profile of the ship was mainly addressed to the medium low speeds (patrol speeds) but the maximum speed requirement of 35 knot has been considered the most important for the engine dimensioning. In this way both the conditions have been considered in the optimization process. In order to comprehensively deal with the wave resistance, two main quantities for each speed have been calculated: the global wave resistance and the variance of the wave profile projected on the hull side from bow up to amidships.

In relation with the seakeeping, the operability has been identified as the most significant quantity to measure the improvement of the ship performances: in this way a sort of MEI (*Mission Effectiveness Index*) relative to the considered Sea States has been considered. Therefore, since the Mode Frontier optimization ambient allows the multi-objective optimization, the following 5 different objective functions have been accounted for:

$$R_{W20} = \frac{R_W(20kn)}{\Delta} \tag{1}$$

$$R_{W35} = \frac{R_W(35kn)}{\Delta} \tag{2}$$

$$\sigma_{20}^2 = \frac{\sum_{i=1}^{NP} \left(\eta_i(20kn) - \overline{\eta}(20)\right)^2}{NP} \tag{3}$$

$$\sigma_{35}^2 = \frac{\sum_{i=1}^{NP} \left(\eta_i(35kn) - \overline{\eta}(35)\right)^2}{NP} \tag{4}$$

$$MEI = \frac{\sum_{k=1}^{NSS} \sum_{i=1}^{NSC(k)} SOE(i)}{\sum_{k=1}^{NSS} NSC(k)} \tag{5}$$

Constraint Set

As further outcome of the preliminary design, several geometrical constraints have been defined too; they're resumed as follows:

- The length between perpendiculars of the ship has not to be reduced in order to comply with the payload requirements of the technical specifications;
- The waterline in correspondence of the Deck Stiva (top of the double bottom) has not to be reduced in breadth in order to allow the fitting of the engines and of the other main machineries;
- The clearance between the propeller blades tip and the hull stern has not to be reduced;
- The height of the transverse metacenter has not to be reduced in order to keep the compliance with the stability requirements of the RINA-MIL Rules.
- Total displacement variation (with respect to the reference design) not greater than two percent
- Longitudinal center of buoyancy shift (with respect to the reference design) not greater than two percent

The genetic algorithm has been set to consider the influence of the automatically generated design exceeding such constraints; anyway they have not been selected for the succeeding generations of designs.

OPTIMIZATION RESULTS

As discussed above, five objective functions have been chosen; in order to individuate the best design, it has been necessary to establish a sequence of selection based on those functions (that means for example to give a priority to R_{w35} compared with R_{w20}). In general it has been noticed that following different sequence of selection of objective functions different optimum designs are selected; this is probably because the objective functions are all adversarial. Besides, the following three "global" objective functions have been created to have a further tool that drives the decision after the selection of some good designs:

$$FO1 = \frac{\frac{Rw35_{ID}}{Rw35_{C1}} + \frac{Rw20_{ID}}{Rw20_{C1}} + \frac{MEI_{C1}}{MEI_{ID}}}{3} \tag{6}$$

$$FO2 = \frac{\frac{SIG35_{ID}}{SIG35_{C1}} + \frac{SIG20_{ID}}{SIG20_{C1}} + \frac{MEI_{C1}}{MEI_{ID}}}{3} \tag{7}$$

$$FO3 = \frac{\frac{SIG35_{ID}}{SIG35_{C1}} + \frac{SIG20_{ID}}{SIG20_{C1}} + \frac{Rw35_{ID}}{Rw35_{C1}} + \frac{Rw20_{ID}}{Rw20_{C1}} + \frac{MEI_{C1}}{MEI_{ID}}}{5} \tag{8}$$

So the selection of the optimum design has been performed in two times: at the end of the optimization a set of good designs has been chosen, with respect to the five above mentioned objective functions described; then, among the pre-selected designs, the best design has been selected on the base of the three "global" functions. Furthermore, because of the great number of free variable connected with the definition of the shape of the hull, the optimization process has been divided into three steps: first an optimization on global parameter has been carried out, including the length between perpendiculars, the maximum beam at the design water line and the longitudinal position of the main section of the hull. This first step has been a sort of check of main dimensions of the ship and it has led up to the choice of the reference design used in the next step, that has been focussed on the hull shapes from about amidship to the bow; this has been considered the main step of the whole process, especially because the tool used to analyze resistance performances works better for this part of the hull.

Fourteen parameters have been selected and about 3000 designs have been analyzed in this step of the optimization. In Figure 10 two examples of optimization history are shown: they represent the evolution of the objective functions $R_{W\ 35}$ and σ^2_{35} with respect to the progressive number of the designs (abt. 2000) which comply with the above mentioned constrain set (feasible designs). The convergence of the objective functions to values lower than the initial ones can be observed: it is relevant because it indicates a correct choice of the free variables of the problem and of the setup of the optimization chain. A similar trend has been found for the other objective functions relative to the wave resistance at 20 knots ($R_{W\ 20}$ and σ^2_{20}), while the seakeeping performances (MEI), which can be increased with major variations of the hull forms (e.g. main dimensions), have not been significantly influenced.

At the end, for all optimum cases the trend is to increase the length of the forward bulb: this optimize the beneficial interference effect created by the wave pattern generated by the bulb itself with the first wave crest generated by the forward hull shoulder. Besides, it is significant to notice that a shape which would work well for a speed of 35 knots, it would not generally be good for 20 knots speed; so, it has been essential to find the optimum *Pareto* design, that means to find the better compromise in terms of all the objective functions; this has been achieved with the design number 6933.

In Figure 11 the comparison between the wave patterns of the parent and optimized hull for the speeds of 20 and 35 knots is shown. In particular for the lower speed (left) the forward shift of the first peak of the generated wave can be observed, due to the increasing length of the bulb. For the higher speed a significant reduction (abt. 15%) of the fore peak height has been obtained. In terms of residual resistance, reductions of about 2% and 3% have been observed respectively for the speeds of 20 and 35 knots.

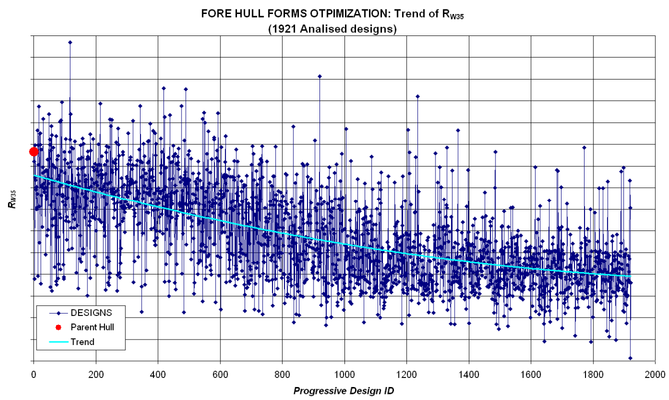

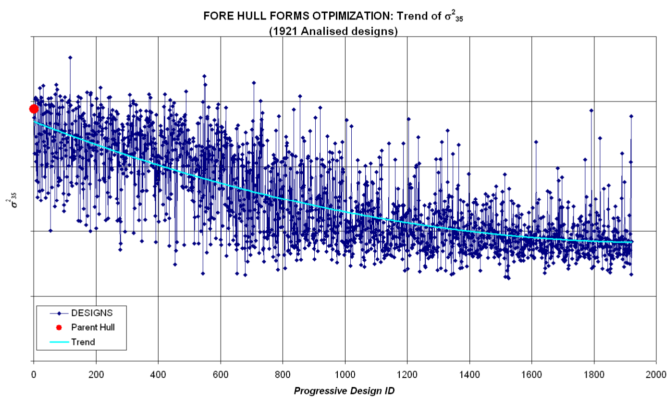

Figure 10: Optimization history of one of the objective functions $R_{W\ 35}$ (up) and σ^2_{35}.(down)

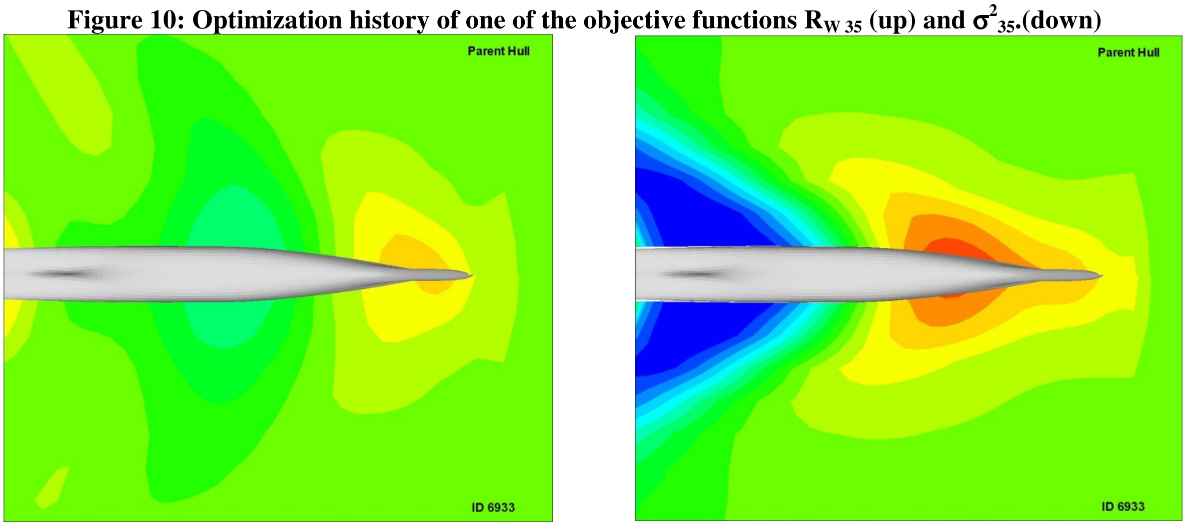

Figure 11: Comparison of wave pattern between parent and optimized hull for 20 knots (left) and 35 knots (right) speed.

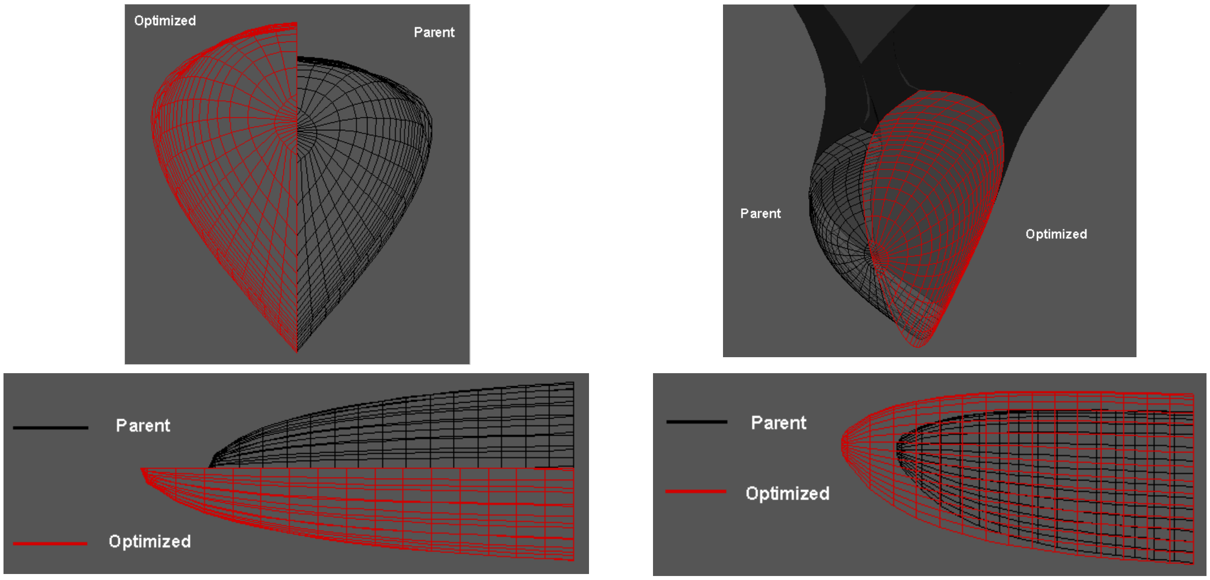

Figure 12: Comparison of forward bulb hull forms of the parent and optimized design variants (in the optimized design also the shape of the rest of the forward part was changed)

Finally an optimization of stern hull shapes has been done. In this case the process has not been able to reach any convergence: this has been caused by the fact that, inside the range of variation of stern parameters, there is not a clear correlation between parameters themselves and objective functions with the result that no significant improvements have been achieved after this step. Probably, with a different tool of analysis which would take into account the effect of viscosity, also this step would lead to different results.

CONCLUSIONS

An automatic optimization computational system has been devised: a fully parametric model of a fast frigate type ship (created with Friendship framework) has been opportunely interfaced with two steady and unsteady hydrodynamic solvers (CETENA proprietary tools for wave resistance and seakeeping performance evaluations) and with a state of the art optimization algorithm (*ModeFrontier*).

A good convergence toward the optimum solution of the in terms of wave resistance performance at two different speed and seakeeping operability has been found, . The process involves four main software: the geometrical modeller *Friendship-Framework*; the WARP software for wave resistance prediction and SOAP tools for seakeeping performance prediction; the optimization environment *ModeFrontier*. Besides, a certain number of software for I/O operations has been created. Although the imposed design objective was very ambitious: optimize the seakeeping, in terms of global operability in two sea states, and wave resistance characteristics of the hull at two very different operating speeds (35 and 20 knots), the optimization model has been able to neatly and efficiently converge to an optimal hull form solution.

The gains in terms of resistance reductions were significant especially at high speed (in excess of 4%), in spite of the evidently good initial hull form designed from shipyard experience and considering also the rather strict constraints imposed on maximum displacement variation and LCB variations (less than 2%).

As expected optimum hull form variations required to optimized the performance at the low speed are in straight contrast with those found for the high speed, so the overall optimum hull form is the one able to find a good compromise between the two very different requirements. Promising is the validation of the numerical results obtained by a set of model tests that are in phase of completion.

ACKNOWLEDGEMENT

The research project has been partly supported by the Italian MOD in the frame of National Plan for Defence Research, managed by SEGREDIFESA.

REFERENCES

Abt, C.; Birk, L.; Harries, S. (2003), "Parametric Hull Design: The FRIENDSHIP-Modeler", *International Conference on Ship and Shipping Research - NAV 2003*, Palermo, June 2003.

Abt, C.; Bade, s.; Birk, L.; Harries, S., (2001) 'Parametric Hull Form Design – A Step Towards One Week Ship Design,' *8th International Symposium on Practical Design of Ships and Other Floating Structures-·PRADS 2001*, Shanghai.

Caprino, G., Sebastiani, L., Valdenazzi, F., 'Metodologie a Pannelli Lineari e Non-Lineari per l'Ottimizzazione Idrodinamica delle Forme di Carena Basate sull'Analisi del Flusso a Potenziale', *CETENA, Report No. 6117*, Genoa, 1997

Harries, S., (1998), 'Parametric Design and Hydrodynamic Optimization of Ship Hull Forms', *Ph.D. Thesis*, Institut für Schiffs-und Meerestechnik, Technische Universität Berlin; Mensch & Buch Verlag, Berlin.

Harries, S.; Abt, C. (1998), "Parametric Curve Design Applying Fairness Criteria", *International Workshop on Creating Fair and Shape-Preserving Curves and Surfaces*, Berlin/Potsdam, Teubner Verlag, 1998.

Harries, S.; Abt, C.(1999), "Formal Hydrodynamic Optimization of a Fast Monohull on the Basis of Parametric Hull Design", *FAST99 - 5th International Conference on Fast Sea Transportation*, Seattle, August 1999.

Harries, S.; Abt, C.; Hochkirch, K., (2001), "Hydrodynamic Modeling of Sailing Yachts", *15th Chesapeake Sailing Yacht Symposium*, Annapolis.

Harries, S.; Nowacki, H. (1999): "Form Parameter Approach to the Design of Fair Hull Shapes", *10th International Conference on Computer Applications in Shipbuilding·- ICCAS '99*, Massachusetts Institute of Technology, Cambridge, MA, USA, June 1999.

Harries, S.; Valdenazzi, F., Abt, C., Viviani, U., (2001), "Investigation on Optimisation Strategies for the Hydrodynamic Design of Fast Ferries", *FAST 2001*.

Koh, L.; Atlar, M.; Mesbahi, E.; Janson, C.-E.; Larsson, L.; Abt, C.(2005): "Novel Design and Hydrodynamic Optimisation of a High-Speed Hull Form", *5th International Conference on High Performance Marine Vessels*, Shanghai, April 2005.

Poloni, C.; Giurgevich, A.; Onesti, L.; Pediroda, V., (1999), "Hybridization of a Multi-objective Genetic Algorithm, a Neural Network and a Classical Optimizer for a Complex Design Problem in Fluid Dynamics", Computer Methods in Applied Mechanics and Engineering, Elsevier Science Ltd., North-Holland.

Spicer, D.; Cook, J.; Poloni, C.; Sen, P., (1998), "EP 20082 FRONTIER: Industrial Multiobjective Design Optimisation", *ECCOMAS 98*, Published by John Wiley & Sons, Ltd.

Vernengo, G., Biliotti, I., Brizzolara, S., Viviani M., Bonvicini A., Ruscelli, D., Galliussi M., Manfredini A, (2009), "Influence of Form Parameters Selection on the Hull Surface Shape Control for Hydrodynamic Design". *International Conference on Ships and Shipping Research NAV 2009*, Messina, Italy.

Seventh International Conference
On High-Performance Marine Vehicles
Melbourne, Florida, USA
13-15 October 2010

ECONOMIC POTENTIALS OF UTILIZATION OF HIGH PERFORMANCE MARINE VEHICLES IN NIGERIA, GULF OF GUINEA AND WEST AFRICA

Dr. D. U. Ekwenna, BSE, MS, PhD, CEng, MSNAME
Federal University of Technology, Owerri. Nigeria. West Africa.
E-mail: duekwenna@yahoo.com

ABSTRACT

In this paper, transport and economics of utilization of fast sea transport in Nigeria, located in the busy sea lane of the Gulf of Guinea, West Africa is discussed. Gulf of Guinea constitutes a large area on the Atlantic coast of West Africa with booming shipping, oil exploration, exportation and marine transportation activities. Nigeria accounts for over 70% of the ocean traffic in the region and it is considered the hub of the international trade in the zone. Nigerian ports with inadequate drafts (10.5 m or 35 ft) and infrastructures to receiving modern vessels, lack of multimodal transport systems (rails and road), numerous creeks and management lapses have been identified to impede efficiency of cargo handling.

In order to compete in today's global economy and to re-engineer Nigeria's seaports, consideration of such factors as short-sea shipping and utilization of high-performance marine vessels (including the novel WIG aircraft) would be crucial in the sustainable development and economic growth of the region.

INTRODUCTION

Gulf of Guinea constitutes a large area on the Atlantic coast of West Africa with booming shipping, oil exploration, exportation and marine transportation activities. Nigeria's shipping market (including crude oil) accounts for about 596 billion tonne-miles, that is, about 3.1 percent of the world total. Over 70% of the ocean traffic in the region is attributable to Nigeria's economy and it is considered the hub of the international trade in the zone.
Nigerian ports with inadequate drafts (10.5m or 35ft) and infrastructures to receiving modern vessels, lack of multimodal transport systems (rails and road), numerous creeks and management lapses have been identified to impede efficiency of cargo handling.

In order to compete in today's global economy and to re-engineer Nigeria's seaports, consideration of such factors as container carriers, short-sea shipping and utilization of high-performance marine vessels (including barges, the novel wing-in-ground-effect craft, WIG aircraft) would be crucial in the sustainable development and economic growth of the region.

ABBREVIATIONS

CFS Container Freight Station
ICD Inland Container Depot
LSCI Liner Shipping Connectivity Index
MT Marine Technology
TEU Twenty-foot Equivalent Unit
UNCTAD United Nations Conference on Trade and Development
WIG Wing-in-Ground

KEYWORDS

Nigeria, Gulf of Guinea, Liner Shipping Connectivity Index, Deep Sea Ports, Short Sea Shipping, Improving Efficiency of freight movement

LITERATURE REVIEW

Buckman (2004) suggests that global shipping services consist primarily of liner and bulk cargo services. The bulk services involving oil tankers and other wet and dry cargo bulk carriers move the world's bulk and primary commodities in international trade; therefore they are certainly very important for the world economies in that regard. However, liner shipping due to its many inherently beneficial characteristics has always generally been considered the real backbone of world trade, and the availability of reliable, stable and regular liner services remains the motive force of international trade and economic well-being for the global community. The significance of liner services for world trade has grown even further in recent times and its impact on the shipping activities in Gulf of Guinea is remarkable. The impetus for it has been the explosive and sustained growth of containerization in the world shipping over the years (Obiozor, 2009).

According to a recent UNCTAD report (2008) containerized seaborne trade is estimated to have increased in the last twenty years, or so, by "a factor of five". That is the equivalent of an average growth rate of 9.8% annually, measured in twenty equivalent units (TEUs). In 2007, the report further states, global container trade was estimated at 143 million TEUs, a 10% increase over the previous year, and, in tonnage terms, the estimated volume is 1.24 billion tons, which is about one quarter of the total dry cargo loaded in the period. Lastly, the report observed that "with globalization, increased trade in intermediate goods, growth in consumption and production levels and expanding 'containerizable' cargo base-(e.g. agricultural cargoes are increasingly transferring to containers given higher freight rates in the bulk sector and economics of scale in the container market)- containerized trade is poised to grow significantly and account for an increasingly larger share of world dry cargo." Indeed, some forecasts imply that the trade would continue to grow by, at least, 10% annually to double the TEU volume by 2016 and more than double it by 2020, at 371 million TEUs (UNCTAD, 2009).

According to Tiwari (2003), it is noteworthy to consider the role of liner shipping services in connecting national economies to world markets and thereby conferring upon them competitive advantages over their less connected competitors in the international market centers for exports and imports.

Since 2004 the UNCTAD has used a **Liner Shipping Connectivity Index (LSCI)** to quantify, and to annually compare, the connectivity of the national economies of the world to international trade, as well as their relative levels of competitiveness in the markets. In the calculations certain service parameters of modern liner shipping were taken into consideration so that as condition in respect of the parameters or variables in each country improve or deteriorate, the country's index would also rise or fall. The specific parameters/variables are the following:

1. The number of containerships deployed on the liner services from/to a country's ports;
2. The container carrying capacity (in TEUs) deployed;
3. The per capita number of ships deployed;
4. The per capita container carrying capacity deployed;
5. The number of liner shipping companies servicing a country's ports;
6. The number of size of vessels deployed;
7. The average size of vessels deployed; and
8. The average number of vessels operated per liner shipping company.

Obviously, if a country has a large number of ships servicing its trade (whether foreign or own flag), and if the ships have large carrying capacity, it would mean that shippers in the country have more opportunities to load their containerized exports (and receive their containerized imports in a more timely manner), and therefore can be said to be well connected to their foreign markets. This would reflect in a higher LSCI for the country. Conversely if, let's say, the country suffers chronically or frequently from port congestions or other logistic problems, liner services to the country would be seriously eroded and its LSCI would fall.

The table below presents a five-year LSCI of some countries, some which are Nigeria's neighbors and/or competitors in the world market. The base year is 2004, the startup year when the maximum value that could be achieved by a country was 100.

Table 1: UNCTAD Liner Shipping Connectivity Index (LSCI) for Selected Countries, 2004-2008; (2004=100)

S/N	RANK	COUNTRY	2004	2005	2006	2007	2008	% CHANGE 2008/04
1	1	China	100.0	108.3	113.1	127.9	137.4	37.4
2	3	Singapore	81.9	83.9	46.1	87.5	94.5	15.4
3	6	USA	83.3	87.6	85.8	83.7	82.5	-1.0
4	9	Malaysia	62.8	65.0	69.2	81.6	77.5	23.5
5	17	Egypt	38.1	39.2	46.7	48.2	48.8	28.2
6	20	India	34.1	36.9	42.9	40.5	42.2	23.5
7	27	Brazil	25.8	31.5	31.6	31.6	30.9	19.5
8	35	South Africa	23.1	25.8	26.3	27.5	28.5	32.2
9	40	Indonesia	25.2	28.8	25.8	26.3	24.8	-4.0
10	51	Nigeria	12.8	12.8	13.0	13.7	18.3	42.6
11	53	Ghana	12.5	12.6	13.8	15.0	18.1	45.3
12	54	Senegal	10.2	10.1	11.2	17.1	17.6	73.7
13	58	Cote D'ivoire	14.4	14.5	13.0	15.0	16.9	17.6
14	71	Togo	10.2	10.6	11.1	10.6	12.6	23.2
15	72	Benin	10.1	10.2	11.0	11.2	12.0	18.7
16	76	Cameroon	10.5	10.6	11.4	11.7	11.0	5.6
17	127	Liberia	5.3	6.0	4.6	4.5	4.3	-19.6

Source: Compiled from UNCTAD Review of Maritime Transport (RMT), 2008

One factor that has contributed to the rapid growth of containerized liner services is, naturally, the demand of shippers and traders for the service. The demand is, in turn, influenced by the lower freight rates which rising economies of scale from the large sized containerships, now common in the trade, make, possible. With declining rates, more users find the services more affordable and new users with containerizable cargo from the dry bulk sector switch to the container sector, as we saw earlier in the case of agricultural commodity exporters who now prefer to containerize in order to benefit from the lower freight rates.

However real this trend is, it is better appreciated with some 'facts and figures' and if we look at the second table here below, the general downward/static trend can be perceived.

Table 2. Average Annual Freight Rate Indices in Major Trading Routes, 2003-2007 (1995=100)

Year	Overall Index	Homebound Index	Outbound Index
2003	101	95	106
2004	98	94	102
2005	104	97	110
2006	100	93	106
2007	93	97	88

Source: Compiled from UNCTAD RMT, 2006 and 2008

Basically, since the base year is 1995, the rates in the other years are being compared to the rates that obtained in 1995, about 15 years ago, so in the five years from 2003-2007, the rates were mostly lower except for the outbound trade. But, even then, the implied annual increments over the intervening period would still be marginal.
Another perceptive on the freight rates can be obtained from consideration of their impact on the market prices of imports and exports. In its 2006 report UNCTAD gave estimates of total freight cost as a percentage of import value

for the world as a whole and for different regions, from 1990-2004. The finding was that for the world, the ratio was more or less constant at 3.6% for the period, and for the developed market economies of Europe, etc. it was also constant but even lower at 2.9%. However, for Africa the figure was approximately 10% and even higher for West Africa per se.

In the 2008 report the effect on market prices was shown from a different angle, namely on the market prices of some specific agricultural commodities exported to Europe from some developing countries. Some of the results are shown in table 3 below.

Table 3: Ratio of Liner Freight rates of selected commodities, 1970-2007 (%, percentages)

COMMODITY	ROUTE	1970	1980	1990	2004	2005	2006	2007
Rubber	Singapore/Malaysia to Europe	10.5	8.9	15.5	7.5	8.0	6.3	6.5
Coca beans	Ghana-Europe	2.4	2.7	6.7	3.7	4.0	3.9	3.5
Coffee	Brazil-Europe	5.2	6.0	10.0	6.5	5.7	5.1	n.a
Coffee	Colombia (Atlantic) to Europe	4.2	3.3	6.8	2.3	3.1	3.0	2.5

Source: Compiled from UNCTAD RMT, 2008

PORT INFRASTRUCTURE AND DEVELOPMENT

Ports are extremely diverse in their size and status, their layout and design-and, not least, in their efficiency. Similarly, the Gulf of Guinea's ports typified by Nigerian ports (Table 4) vary enormously in their physical features: draft, their site, their shape and suitability for today's maritime trade. The increased quantities of cargo are being carried in many different forms aboard larger and more specialized vessels (Bulk Carriers, Container ships, Roll-on/Roll off, Fishing vessels, General Cargo). Ports, therefore, are under increasing pressure on their cargo handling facilities and management to improve the efficiency with which cargo is handled and to speed up the process of seaborne trade.
Re-engineering the Nigerian seaports would entail a holistic approach to re-organising of port operations so as to increase efficiency (Ekwenna, 2009). Specifically, it would examine port performance indicators with the view of ascertaining activities towards achieving reduced costs and improved efficiency at the ports.

The crisis required strategic developments of ports for diffusion. Hence, on the heels of the port congestion of 1975, the Federal Government devoted massive investment and resources to port development over the past national development plan periods. The result was increase in number of ports, port's attractiveness and pricing driven by the volume of Nigeria's international seaborne trade. Furthermore, the committee on Port Decongestion 2001 based on research and findings (Branch, 2003; Onwuegbuchunam and Ekwenna, 2007) recommended the establishment of Inland Container Depots (ICDs), Bonded Warehouse, Container Freight Stations (CFS) and other Off-Dock Terminals.

The new concept of port development engenders reengineering of the port to increase efficiency (UNCTAD/SIDA, 1986). It aims to develop a thorough grasp of different aspects of port activities by providing detailed understanding of the principle and practices of port management within the framework of overall transportation systems. There is a particular emphasis on the management of operations, marketing, and finance and information technology.

Table 4: Physical Characteristics of Nigerian Ports

Nigerian Ports	Maximum Draft, meters
Apapa	9.50
Third Apapa Wharf Extension	10.50
Tin Can Island	9.50
Port Harcourt	8.00
Federal Ocean Terminal, Onne	11.00
Warri	11.50
Calabar	8.00
Bonny Off-shore Oil Terminal	22.86
Escravos/Forcados Oil Terminal	21.95/19.81
Qua-Iboe Oil Terminal	26.56

Source: Nigerian Ports Authority Handbook, Lagos, 1989

RESULTS

The following is the summary of development scenarios and plans to meeting the challenges of the future growth in Nigeria's international seaborne trade and also in the Gulf of Guinea.

1. Identification of Capacity Development Scenarios

Mohammed (2009) forecasts that the demand growth of Nigeria's international trade is estimated to exceed 415 million tonnes by 2020 and beyond; from a mere total cargo throughput of 13.3 million tonnes (import and export) in 1995 to 59 million tonnes in 2009. Furthermore, crude oil lifting at the terminals grew from 81.1 million cubic meters in 1995 to 99.4 million cubic meters in 2008. Total cargo throughput is projected to reach 100.4 million tonnes, crude oil to 116.8 million tonnes and LNG's 164.5 million cubic meters in 2012 and in 2020 cargo throughput is projected to reach 415 million tonnes, crude oil to 141.1 million cubic meters and LNG to 5.2 billion cubic meters.

The increase exerted pressure on the ports facilities and port operations. Both short and long-term port development plan is necessary to meet these challenges. The action plan would consist of expanding the existing port facilities or suggest development alternatives which create a framework for achieving some of the port reform goals, and the involvement of the private sector and simulation of a competitive environment.

2. Development of Deep Sea-Ports and Short-Sea Shipping

The demand growth in the international trade has predicated the utilization of larger ships for lifting cargo. One circumstance that would tend to increase the average ship size is the economy of scale that can be obtained since a larger ship would be more economical. Economy of scale has led to the design and construction of ever-larger crude oil carriers. Port limitations on vessel draft have been the only restraining factor on the maximum size, as evidenced by the eight-meter draft limitation on Nigerian ports. This approach combines economy of scale with better operating economics (a higher performance design) to meet the growth in shipping demand.

However, Suex-max Container ships with dimensions (Draft is 15.5 meters) similar to the latest Maersk vessels cannot enter the ports due to draft limitations. It is suggested to develop deep seaports with draft, quay length and terminal facilities that would accommodate ships in the size ranges. Locations for deep seaports along Nigeria's coastline of about 813 kilometers are suggested to include: Badagry, Lagos, Okitipupa, Escravos, Brass, etc.

3. The Role of Short Sea Shipping and Inland Waterways.

The 3,000 kilometers of waterways of the River Niger, the Benue, the Nun and the coastal creeks constitute one of the main means of transport from North to South and East to West along these rivers and creeks before 1909. Then, waterways were the only practical means of interaction. Recently, in 2009 the Federal government awarded contract on dredging of lower Niger-Benue Basin for inland waterways transportation.

Inland waterways could provide a much cheaper means of transportation and play a significant role in freight haulage with the resolution of the following problems:

1. The geographical and climatic problems of drought, loss of water draft and the seasonality pattern of river regimes that impede regular traffic the year round.

2. The lack of technology and resources for necessary maintenance of waterways for navigation and ease of traffic flow.

3. The development of appropriate facilities such as river ports.

The inland waterways and short sea shipping hold a lot of potentials as an efficient means of supplying raw materials and goods to the industrial concerns, in the hinterland, but enormous resources are needed to develop and sustain the navigability of these waterways. Some technological feats such as locks have been designed along inland waterways in some developed countries such as USA, Netherlands and United Kingdom to overcome the problems and constraints associated utilization of inland waterways. Available data indicate that short sea shipping provides the most efficient and economic mode of transportation when compared with road (1,000 percent) and rail (250 percent). Short sea shipping can also be employed to transship cargo from deep seaports to the ICDs, CFS, and port terminals when necessary. See the figure below:

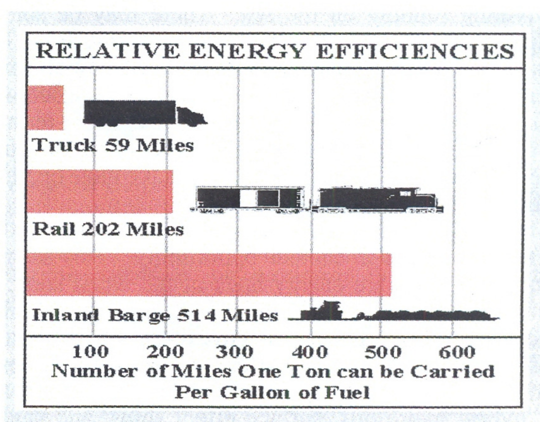

Note: 1 mile = 1.6 kilometer, 1 gallon = 3.8 liters

Figure 1: Relative Energy Efficiencies of the Multimodal Transportation
Source: Technical and Research Panels, Q-36, Maritime Economics - MT

Studies of parameters that will influence the demand for transport capacity in the future would aid to sketching a range of possible solutions designed to meet future transport needs, and the make-up of means of transport, warehouse facilities and terminals for optimal solutions. Olam (2006) posits that such analyses may lead to specific requirements as regard types and sizes of vessel, service speed requirements and handling characteristics. In addition to traditional types of cargo vessel, utilization of high-speed/performance cargo ships especially container carriers, offshore vessels, and new gas-powered ferries is considered. Other vessel types for consideration include: Inland Barge, Catamarans, Pentamarans, Trimarans for transshipment of cargo.

Consideration is also given to the Wing-in-ground-effect craft (WIGs), a type of novel craft. The figure below depicts the typical WIG.

Fig 2: Novel Wing-in-Ground-Effect Craft Source: US Coast Guard Proceedings, Spring 2007

Speed with efficiency makes the WIGs so appealing (Simbulan, 2007). It has the potentials to operate with a higher efficiency than an aircraft and travel at speed faster than a high-speed catamaran. WIG craft (with a cruising speed of 100 to 400 km/hour) fill a niche in the transportation spectrum between marine and air transport. The utilization of WIGs for marine transportation has to be examined in the light of all hazards and risks associated with its operation.

CONCLUSIONS

The study has focused on improving efficiency of freight movement in the Gulf of Guinea with emphasis on Nigeria's transport demand and shipping of its international seaborne trade. The idea is to develop a plan for an integrated freight transport system that can be adapted to the region involving private sector investments.
To implement these goals, a strategic development plan should consist of the following:

1. Cargo flow analysis and forecast on transport demand and shipping
2. Comparative analysis of shipping connectivity and ports' competitiveness
3. Matching of port capacity demand and supply
4. Identification of capacity development scenarios
5. Utilization of high performance marine vehicles to transport/transship cargo to improve the efficiency with which cargo is handled and to speed up the process of seaborne trade.

REFERENCES

Branch, A. (2003), "The Inland Container: A Strategy to Economic Development." London, Pitman Publishers

Buckham, A. (2004), "Global Trade – Past Mistakes, Future Choices." New York, Zed Books, pp.127-129

Ekwenna, D.U. (2009), "Strategic Port Development: A Tool for Meeting the Challenges of the Future Growth in Nigeria's International Trade." *Proceedings of the Annual National Shipping Conference*, Lagos, Nigerian Shippers Council (NSC)

Mohammed, A.M. (2009), *ibid*

Nigerian Ports Authority Handbook, (1989), Lagos

Obiozor, G.C. (2009), "Conformity of International Standard in Delivery of Shipping Services in Nigeria: A Critical Review" *Proceedings of the Annual National Shipping Conference*, Lagos, Nigerian Shippers Council (NSC)

Olam, O. (2004), "The Shipping Sector", Annual Report of Norwegian Marine Technology Research Institute, Trondheim

Onwuegbuchunam, D. and Ekwenna, D. (2007), "Analysis of Determinants of Dry Port Selection in Nigeria" Journal of Research in National Development, Vol. 10 No. 8

Simbulan, M (2007), "Is It a Ship, a Plane, or a WIG?" *US Coast Guard Proceedings,* Washington, D.C.

Technical and Research Panels, Q-36, Maritime Economics (2005), "Relative Energy Efficiencies of Multimodal Transportation Systems" New Jersey, Marine Technology, p.33

Tiwari, P. (2003), "Shippers' Port and Carrier Selection Behaviour in China: A discrete Choice Model," Rotterdam, Maritime Economics and Logistics

UNCTAD (2008), Review of Maritime Transport, World Bank Working Paper.

UNCTAD/SIDA (1986), Improving Port Performance: Management of General Cargo Operations, Geneva, United Nations

Seventh International Conference
On High-Performance Marine Vehicles
Melbourne, Florida, USA
13-15 October 2010

VERIFICATION OF RATIONAL STRUCTURAL DYNAMIC LOADS PREDICTION FOR HIGH-SPEED VESSELS

Manish Gupta, CDI Marine – Band Lavis Div., Glen Burnie, MD, manish.gupta@cdicorp.com
Balji Menon, ABS Americas, Houston, TX, bmenon@eagle.org

ABSTRACT

High-performance vessels, by their characteristics, are very weight-sensitive, and their structural design treads a very fine line between performance and safety. This problem gets compounded even further because high-performance vessels frequently tend to have unconventional and novel hullforms, which have little to no prior design and operational data. Therefore, there is an urgent need for a reliable analytical tool to calculate the structural dynamic loads for new and novel designs, especially during the early design stage. In order to address this critical need, a three-phased program of effort was adopted to develop an integrated methodology to predict the route/mission-dependent rational structural dynamic loads for high-speed vessels. Under Phase I and II efforts, an overall working model of a frequency-domain ship motion and loads prediction was developed incorporating a route-based mission profile module to provide a description of the vessels' overall lifetime loads, followed by an integrated approach using both frequency-domain and deterministic time-domain motions and loads simulation tools to complete the prediction methodology by including the ship slamming and impact loads contributions to the global hull-girder loads. The final Phase III effort was to complete the integrated methodology of rational load prediction by combining the route/mission-based probabilistic approach and the state-of-the-art tool-set into a reliability-based structure design approach. Verification and validation of this integrated prediction model was conducted using available sea trials, experimental data and results using classification society rules for existing ships that included both high-speed monohulls and multihulls. This paper discusses the verification and benchmarking effort of the rational structural dynamic loads prediction against full-scale and model-test data of those high-speed vessels.

INTRODUCTION

Structure designs for conventional hullforms usually rely on past design experience, which today is best represented by Classification Society Rules or U.S. Navy Design Data Sheets. The rules published by the various classification societies are generally derived from limited empirical data that does not adequately recognize variations in a ship's lifetime mission or likely operational scenarios for new hullforms. In particular, it was recently stated by the U.S. Office of Secretary of Defense (OSD) that … "the current state of knowledge for structural design for aluminum hulls and for high-speed advanced hullforms is insufficient to assure acceptable structure failure risk-mitigation over the lifetime of a ship" and continued to say "ABS and other commercial standards have demonstrated deficiencies for open-ocean high-speed ship operation." To this end, several governmental and industry efforts elsewhere have been undertaken to overcome this deficiency.

There is an important distinction between predicting structural loads for large displacement ships and predicting the loads for weight-sensitive vessels such as high-performance and high-speed multihull vessels. This is because often there is very little prior experience to draw upon for operation of such vessels in heavy seas. In addition, past design experience can only apply to ships of similar type, size and speed to those of the past. In the absence of design loads for similar ships, a reliable analytical tool is needed to calculate the dynamic loads for new designs. Alternatively, expensive experimental investigations would be necessary, especially for predicting impact and slamming loads. The key to predicting structural loads is in accurate prediction of the vessel's response to the sea conditions. Various frequency-domain ship response programs can only handle traditional hullforms, except for a very few, such as

VERES and SHIPMO, which also need calibration at high speeds. Time-domain simulation programs and advanced CFD codes are very expensive and time-consuming to run, extremely difficult to validate for novel hullforms and not timely for early-stage design. As commercial and military interest in high-speed vessels continues to grow, the need for reliable structural design and analysis tools is becoming extremely important.

In order to address this critical need, the Center for Commercial Deployment of Transportation Technologies (CCDoTT) awarded a research project to be performed as a three-phased integrated methodology to predict the route/mission-dependent rational structural dynamic loads for high-speed vessels. The objective of this research project was to satisfy both the DoD and commercial sector requirements for fast-sea transport by developing the ability to accurately predict the structural loads that will be experienced by high-speed vessels and which is suitable for use with all of the candidate high-speed hullforms for early-stage design.

Under the Phase I effort, an overall working model of a frequency-domain ship motion and loads model was developed incorporating a route-based mission profile module to provide a description of the vessels' overall lifetime loads. The results of the Phase I effort, *Gupta et al. (2003)*, were very encouraging and were also presented to a wider international audience with excellent acceptance and support. Under the follow-on Phase II effort, an integrated approach was conducted under which both frequency-domain and deterministic time-domain motions and loads simulation tools were identified and evaluated for various monohull and multihull vessels, and then integrated to complete the overall methodology by including the ship slamming and impact loads contributions to the global hull-girder loads.

Upon successful completion of the Phase I and II efforts, the final Phase III effort was conducted to develop a rational load prediction and seamless design procedure, which was the integrated methodology combining the route/mission-based probabilistic approach and the state-of-the-art tool-set into a reliability-based structure design standard. Extensive verification and validation of this integrated prediction model was conducted using available sea trials, experimental data and results using classification society rules for existing ships that included high-speed monohulls, catamarans and trimarans. The verification and benchmarking effort of the rational structural dynamic loads prediction against full-scale and model-test data of those high-speed vessels is discussed in this paper.

NOMENCLATURE

Cb	Block coefficient
Δ	Displacement weight
σ	Root mean square value (RMS)

ABBREVIATIONS

ABS	American Bureau of Shipping
BM	Bending Moment
CCDoTT	Center for Commercial Deployment of Transportation Technologies
CFD	Computational Fluid Dynamics
CY	Calendar Year
LCS	Littoral Combat Ship
NSWCCD	Naval Surface Warfare Center – Carderock
P-M	Pierson-Moskowitz
PSD	Power Spectral Distribution
RANS	Reynolds-Averaged Navier Stokes
RAO	Response Amplitude Operator
RMS	Root Mean Square
ONR	Office of Naval Research
OSD	Office of Secretary of Defense
SS	Sea-State

KEYWORDS

Catamaran, Multihull, Loads Prediction, Structural Loads, Trimaran

PROJECT BACKGROUND

The underlying project whose material is the basis of this paper was the final phase, Phase III, of a three-phase program to develop a prediction methodology and associated tool-set to predict rational structural dynamic loads for high-speed multihull vessels. Phase I was successfully completed in CY 2003 with the development and demonstration of the first part of the prediction methodology, using works of *Band et al. (1976, 1980)*. The first part was to predict the global hull loads that are wave height and frequency dependent and therefore could be predicted using a frequency-domain tool. The first phase also incorporated development of a route or "mission-profile-module" to provide a description of the ships' overall lifetime environment. Thereupon, Phase II was completed in CY 2007 where the methodologies were developed to predict the probabilities of slamming and the loads associated with slamming, which can be predicted using a combination of frequency-domain and time-domain simulation programs using works of *Chuang and Stavovy (1976), Allen and Jones (1978), Giannotti and Fuller (1978), Faltinsen and Zhao (1991), and Sikora et al. (1998, 2005)*. Eventually, evaluation and incorporation of such simulation tools into the overall route/mission procedure was conducted at the end of Phase II. The effort so far provided an integrated methodology to predict rational structural dynamic loads for high-speed multihull vessels and identified the associated tool-sets that can be part of the overall route/mission methodology.

The final phase, Phase III, which was completed in CY 2009, was to conduct extensive verification and adequate validation of the final integrated route/mission-dependent structural loads prediction methodology using available sea-trial and experimental data of various multihull hullforms. In addition, the scope was to also benchmark the structural loads predictions against ABS rules for the applicable hullforms and further collaborate with ABS in developing an approach to incorporate the methodology into their rulemaking process.

The initial task of Phase III was to obtain relevant sea-trial and model-test data of the three (3) hullforms selected. These three hullforms were selected during the previous phases because of the potential availability of both full-scale and model-scale data for these hullforms. Since the majority of high-speed multihull vessel designs are developed by foreign shipyards, obtaining the vessel design and performance data for the current project was difficult. The three selected high-speed hullforms were developed in collaboration with domestic shipyards, and their development was funded, either in whole or in part, by U.S. Government agencies such as the Department of the Navy (DoN) and ONR, which improved the chances of obtaining adequate vessel design and performance data for verification of the methodology.

Of the three hullforms selected, the Catamaran development that was sponsored by ONR provided sufficient data that could be used for the verification effort. However, the other two selected hullforms, Deep-V Monohull and Trimaran, even if developed and funded domestically, have some proprietary aspects to them and are still in a competitive stage for certain government procurement programs. This made it difficult to obtain the relevant data, and therefore limited data of these two hullforms could be obtained for the verification task. Once the verification data were available, the route/mission integrated methodology was executed for the specific operational and environmental conditions under which the data were collected in order to compare the predicted values against the obtained data. In the interest of maintaining the business sensitive and proprietary nature of the verification data, the comparison plots have been normalized and sanitized in this paper.

The prediction methodology used the computer simulations of ship-motions program ShipX with its VERES plug-in. ShipX is a commercially available software program from MARINTEK in Norway. VERES has both frequency-domain and time-domain ship-motion simulation modules. Another ShipX plug-in called Slam-2D was also used to obtain some of the slam load coefficients, as the slam pressure prediction, among various other factors, is highly dependent on appropriate estimation of the coefficients. The use of dynamic load prediction methodology tool-sets, such as VERES and Slam-2D, are discussed extensively in papers and reports published earlier, as listed in the references, and the readers are encouraged to refer to these publications for detailed discussions on these tool-sets.

In essence, the overall objective in terms of specific requirements for this multi-phase program of effort translates to:

1. Support early-stage design quickly,
2. Provide results that are within plus or minus 10%,
3. Be inexpensive to use, update/improve and validate,
4. Provide local and global design loads of the necessary types,
5. Be sensitive to the most significant ship characteristics, and
6. Be a function of the parameters of the commercial route or military mission involved.

DEFINING THE SOLUTION

Before discussing the verification of the structural loads predictions, an outline of the overall process involved is provided in Table 1. In simple terms, the process starts by defining, from environmental records, the probability of the ship encountering seas of varying severity. This is done for the areas in the world in which the ship is expected to operate throughout its entire life. This is followed by determining the frequency of, or joint probability of, when the vessel will be in various conditions of operation such as speed, weight, heading, sea-state, etc. and using all this information to define a number of deterministic load conditions for which to perform ship motions and loads analyses. Then, for each case, a one sigma or RMS value can be determined for each type of load, and a short-term probability distribution of loads about each RMS value can be established. Then, by knowing the probability of occurrence of each load case, these cases can be compounded into a single long-term probability distribution for each type of load.

Table 1: Defining the Solution

1. Define Operational Environment
2. Select Representative Loading Cases
3. Determine Probability of each Case
4. Predict 1- Sigma Load for each Case
5. Define Short-Term Probability Distributions (PDs)
6. Combine Short-Term PDs
7. Produce Long-Term PDs
8. Select Design Loads for Specified Life

By accepting a reasonable level of lifetime failure probability, the design load can then be selected from the long-term probability distribution. Typically, one failure in 20 years among a fleet of, for instance, 20 vessels is considered acceptable. This is essentially what is needed to be accomplished in a nut shell, and as seamlessly as possible, under this integrated route/mission prediction methodology.

Figure 1 illustrates the overall approach starting at the top left. First, a ship is designed at the concept level using a ship design synthesis tool such as ComPASS™. Then, the lifetime environment is defined from the route or mission module, and a frequency-domain tool is used to determine the standard deviation of each load and each of these for a range of representative extreme operating conditions. This includes the wave-induced regular loads on each hull and then, via time-domain simulation, the slamming loads on the hulls and the cross-structure of the ship. Various individual tools are used in the process, as shown in the figure and discussed later.

FREQUENCY AND TIME-DOMAIN MOTION AND SLAMMING SIMULATIONS

Frequency-domain simulation is the source for finding the standard deviation of load for each combination of operating conditions. In simple terms, the simulation allows the calculation, over a range of wave encounter frequencies, of the linear transfer function between the load and the wave height, which is referred to as the Response Amplitude Operator (RAO). The product of the RAO and the wave Power Spectral Distribution (PSD) then provides the load response PSD versus encounter frequency. The standard deviation of the load, which is the sought-after value, is then given by the square root of the area under the response PSD curve.

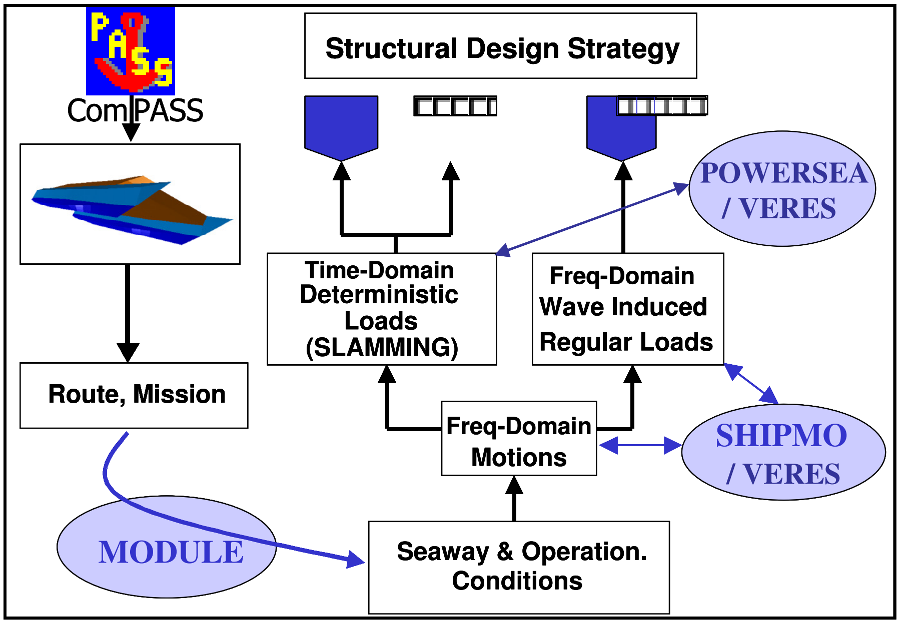

Figure 1: Overall Approach

Frequency-domain simulation factors:

- Any frequency-domain strip theory based code, such SHIPMO or VERES.
- Load Response PSD = RAO x Wave PSD.
- σ = Square-Root (Area under Response PSD).
- Assumes response is linear, but predicts σ (or RMS) values well, but not peak values unless Weibull probability distributions are assumed.
- Remains a flexible/inexpensive valuable tool.

In spite of the fact that the response of most advanced ships is obviously non-linear, it has been found experimentally that agreement between measured and predicted RMS responses is surprisingly good, even for operation in severe sea-states. It should be pointed out, however, that it is only the RMS values that are predicted well. As the responses are non-linear, especially in high sea-states, the distribution of peak responses using the normal Rayleigh probability distribution do not match experimental data, but they do if a Weibull distribution is assumed.

The great advantage of the frequency-domain simulation is that it is simple and flexible, and inexpensive to explore a wide range of operating conditions. As it has now been proven many times to yield useable values of RMS response, it remains a very valuable design tool. The frequency-domain strip-theory codes not only provide all the wave-induced loads, but also the frequency or probability of slamming at various severities. To then actually predict the impact with the water with the resulting time-dependent spatially-distributed pressure pulse and the integrated overall maximum slamming load, a time-domain simulation tool must be used. For this, there are a number of existing codes available, ranging from RANS CFD codes to less complex potential flow panel codes to relatively simple 2-D strip theory codes. Depending on the design time available, RANS codes are a good choice. However, for early-stage design, in which many different configurations are explored in a matter of a few weeks, if not days, strip theory codes are currently the only practical choice.

Time-domain codes:

- CFD Codes (RANS) – Comet, Fluent, CFX, etc.
- 3-D Potential Flow Codes – LAMP, SWAN, Trident, etc.
- 2-D Strip Theory Codes – PowerSea, VERES, etc.
- Strip Theory Codes provide reasonable compromise between the speed of Frequency-Domain Codes and accuracy of CFD/3-D Potential Flow Codes for limited number of runs.

RATIONAL DYNAMIC LOAD PREDICTION CALCULATIONS

As stated earlier, in order to cover a variety of hullforms, three (3) different high-speed hullforms that are of current interest to the Navy and the industry were selected. They are:

(1) Deep-V Monohull (similar to the LCS-1 Monohull)
(2) Catamaran (similar to the X-Craft or Sea Fighter)
(3) Trimaran (similar to the LCS-2 Trimaran)

The hullforms were developed primarily using publicly available data, and efforts were made to emulate the corresponding hullform as closely as possible. The hulls examined are characterized in Table 2.

Table 2: High-Speed Hullforms Selected – Ship's Principal Characteristics

		Deep-V	Catamaran	Trimaran	
Length at Waterline	LWL	100.2	76.0	121.2	m
Length Overall	LOA	115.6	78.4	127.1	m
Beam at Waterline	BWL	13.7	21.1	10.9	m
Beam Overall	BOA	17.5	22.0	30.4	m
Draft - Design	DWL	3.3	3.5	4.5	m
Depth	Depth	10.0	7.8	8.7	m
Displacement	Δ	2,315	950	3,201	MT
Block Coefficient	Cb	0.547	0.735	0.629	

Figure 2 illustrates the Deep-V Monohull and shows the hull lines modeled in VERES. Figure 3 illustrates the Catamaran with its VERES model shown in the upper right-hand box, and Figure 4 illustrates the Trimaran with its input model to VERES in the box at upper left.

All three hull forms were imported into the ShipX workbench. Next, a set of parameters was defined in order to calculate the ship motions. Table 3 shows the input parameters that were defined in the VERES module of ShipX to calculate the motions. In addition to the full range of vessel speeds and sea-states for theoretical predictions, specific vessel speed and sea-state combinations under which the sea-trials or model-test data were collected for the respective hull forms were also defined in VERES. The vessel's headings with respect to the dominant wave direction were also modeled as defined by the collected sea-trials or model-test data. The Roll Radius of Gyration was calculated assuming its value was 40% of the total vessel breadth. All other pertinent ship characteristic values were either calculated or assumed, and defined in VERES in order to emulate the corresponding hul lform as closely as possible.

The sea-states that were evaluated were defined by the Pierson-Moskowitz spectrum formulation with the corresponding wind and sea scales for the respective sea-states. Specific route/mission cases modeled which are speed, sea-state and heading combinations, noted during sea trials or investigated during model tests, are described in the next verification section. The calculations performed were also individually evaluated at the defined motion points of interest on each vessel. For the assessment of the sea-trial or model-test specific cases, the motion points were selected as the hull locations where the sensors were located and the trial or experimental data were collected.

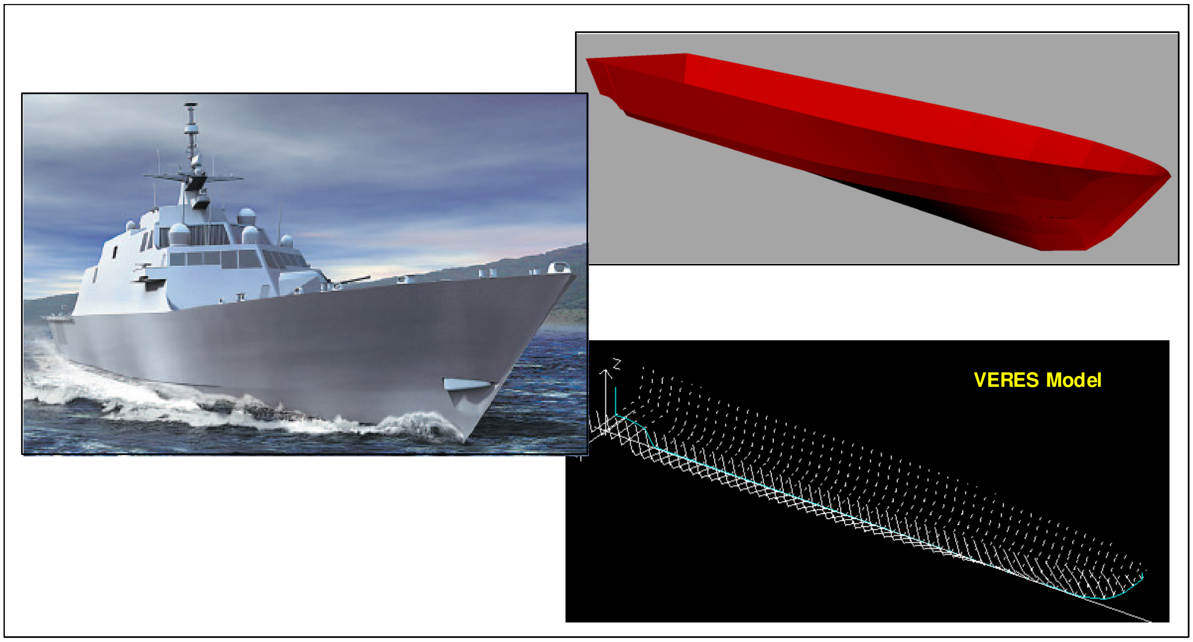

Figure 2: Deep-V Monohull Modeled

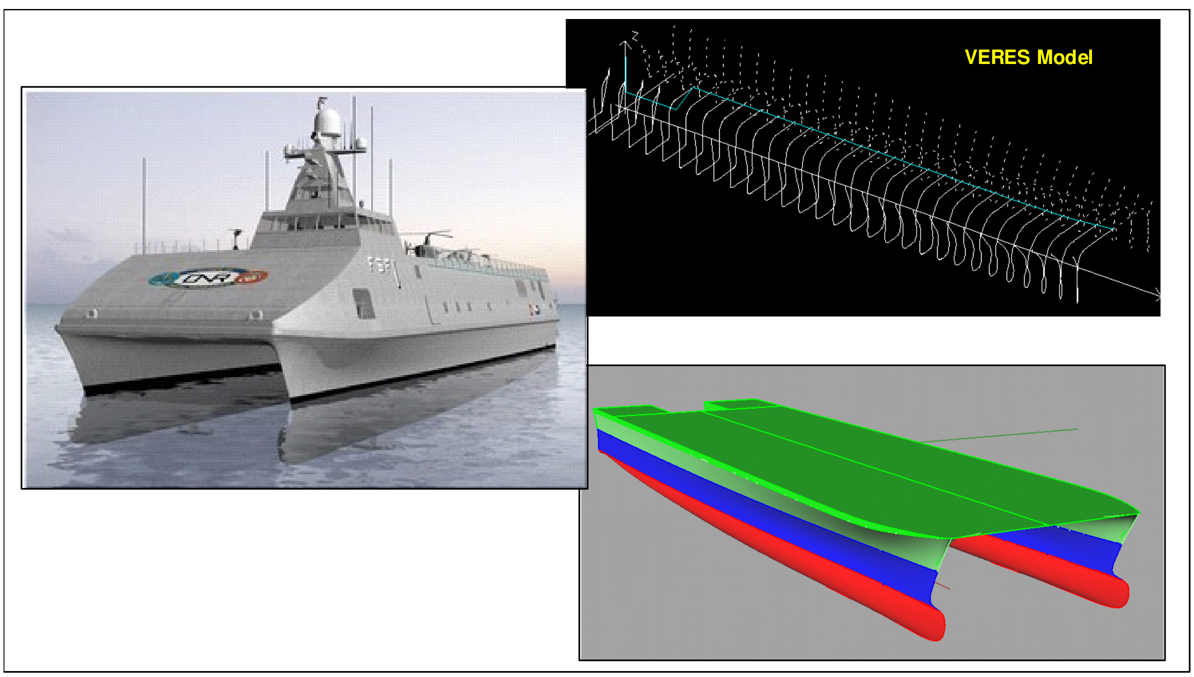

Figure 3: Catamaran Hullform Modeled

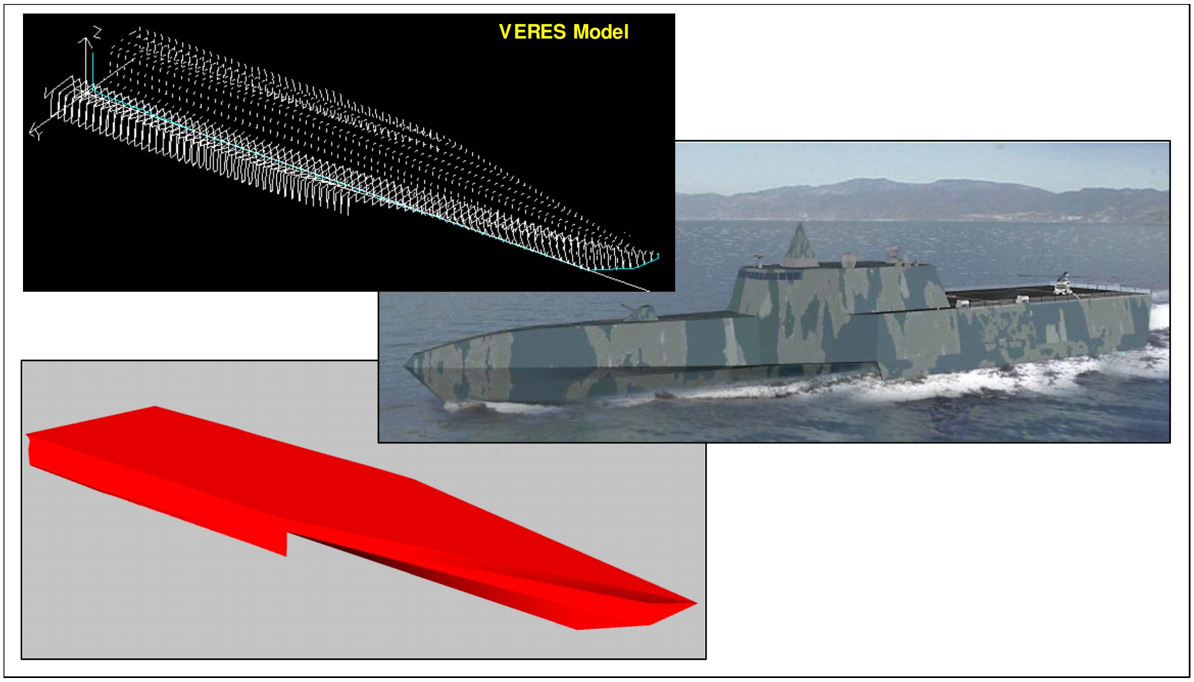

Figure 4: Trimaran Hullform Modeled

Table 3: VERES Input Parameters

Parameter	Input Value
Calculation Type	2D Strip Theory
Spectrum	Pierson-Moskowitz
Wave Type	Long-Crested Seas
Vessel Speeds	As per the Verification Data
Sea-States	As per the Verification Data
Headings	As per the Verification Data
Motion Points	Location of the Sensors

VERIFICATION WITH SEA-TRIAL, MODEL-TEST AND NUMERICAL DATA

The verification and validation of the route/mission-dependent rational dynamic structural load prediction process was performed using model and full-scale test data and other numerical simulation data. The operational and environmental conditions specific to the conditions under which the data was collected were incorporated in the route/mission module of the integrated load prediction methodology. The associated tool-set, such as VERES, ship models were simulated under those conditions, and the predicted motions and loads were analyzed to compare with the verification data.

DEEP-V MONOHULL HULL FORM VERIFICATION

The slam pressure statistics were predicted for several of the operational and sea-state conditions at which the model tests were conducted and for three hull locations where the slam pressure data were recorded. Figure 5 graphically illustrates where the pressure sensors and strain gages were located.

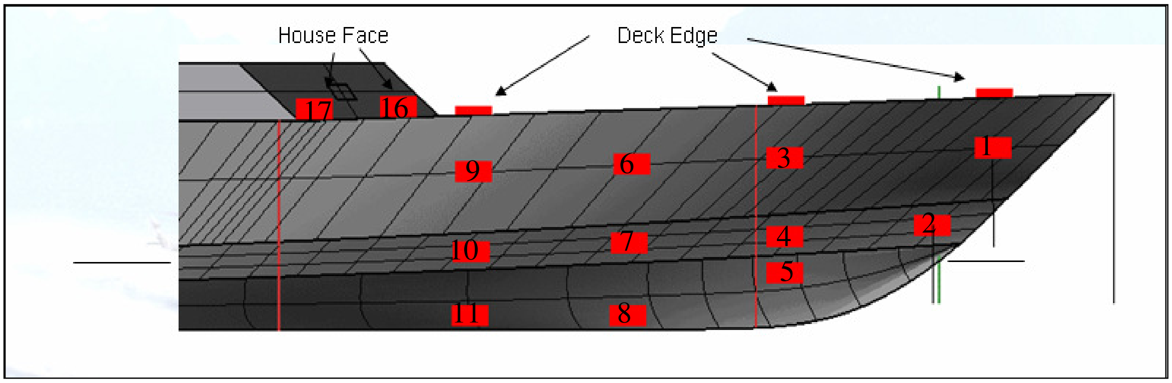

Figure 5: Monohull Model-Test Instrumentation Locations

The data from the hull locations 2, 3 and 4 were selected for comparison due to the fact that they showed the highest slamming values and captured a significant amount of test data, and the results were more completely defined in the available model-test data. Using the data from the Deep-V Monohull model-test Weibull analysis, the slam pressure predictions were compared as shown in Figure 6. The figure shows the comparison for sea-state 5 operation. The model tests were performed using a variety of sea spectra for a given sea-state. However, as stated earlier, the predictions were only done using the Pierson-Moskowitz (P-M) spectrum formulation, using the average of the various significant wave heights and modal periods used for the various sea spectra at the model tests. It should be noted that the selected Deep-V Monohull model-test data is considered proprietary and competition sensitive; therefore, the exact details of the model-test conditions have been sanitized and the corresponding data collected have been normalized for this paper.

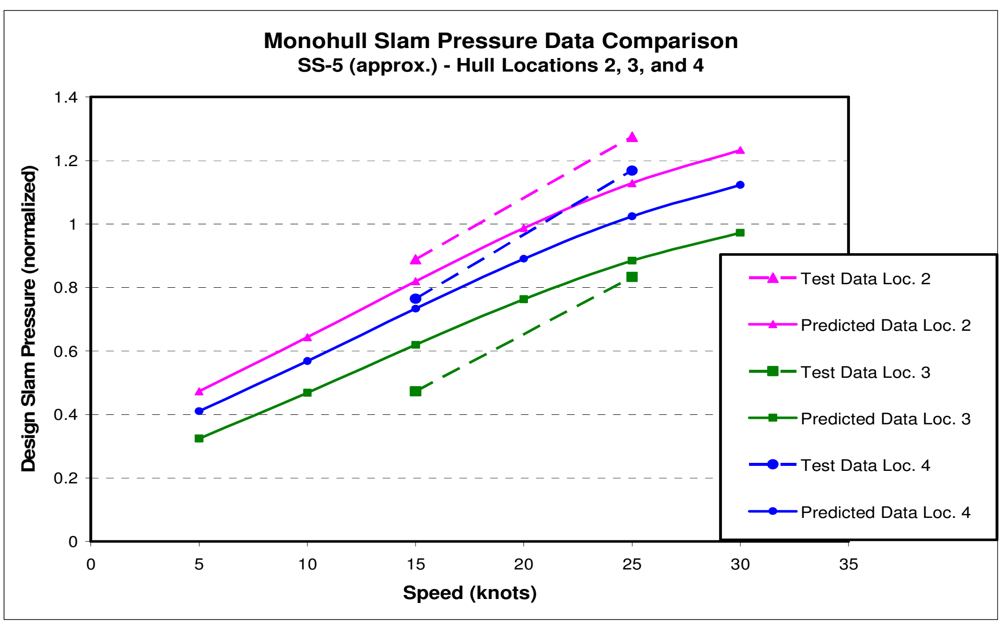

Figure 6: Deep-V Monohull Slam Prediction Verification

The predicted results show a very significant correlation to the trend of measured data for the Monohull. It is important to point out that exact matching of the sea-trial or model-test data to a numerical prediction is not possible for a variety of reasons. For the case of the Deep-V Monohull, the model test was conducted for a variety of sea spectra, whereas the route/mission prediction was only done for the P-M spectra. Also, the model-test data was scaled to the full-scale hullform to be compared to the numerical prediction and, in doing so, slight variations can be introduced. In addition, the slam pressures from the model test were obtained using Weibull analysis of the data collected from the pressure panels and strain gages, and the Weibull analysis was done based on certain determined Weibull parameters, whereas the route/mission predictions were simply the significant short-term statistics of the slamming pressures. In spite of the variations in the process and assumptions between the model-test and route/mission-based rational method, the predicted slam pressures seem to correlate well with the model-test data. It is observed that the rational prediction under-estimated pressures for hull locations 2 and 4, which were below the waterline, and over-estimated for location 3, which was above the waterline.

CATAMARAN HULL FORM VERIFICATION

The slam pressure statistics were predicted for all of the operational and sea-state conditions at which the sea trials were conducted and for the hull locations where the slam pressure data were recorded. Figure 7 graphically illustrates where the pressure sensors and strain gages were located.

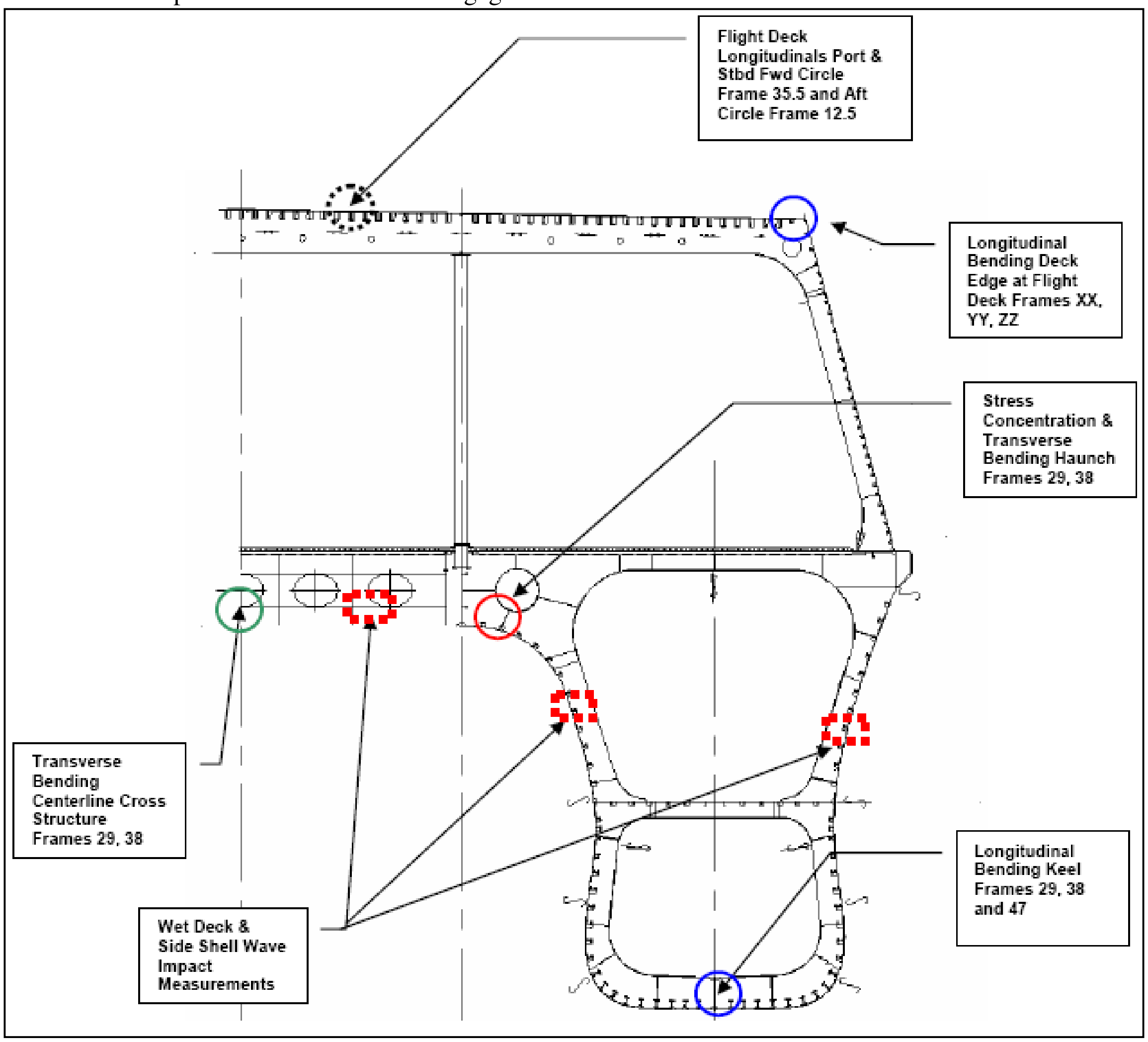

Figure 7: Catamaran Sea-Trial Instrumentation Locations

The data from the hull location Frame 59.5 wet-deck were selected for comparison due to the fact that it captured a significant amount of test data and the results were more completely defined in the available sea-trial report. Using the sea-trials data for the Catamaran, the slam pressure predictions were compared as shown in Figure 8 for a range of high sea-state 4 to low sea-state 5. The sea-trial report stated that due to the complexity of recording slam pressures during at-sea tests, it was not feasible to accurately determine the exact sea-state conditions, i.e., significant wave height and modal period, when the slam event occurred. Thus, the report provided all the various sea-state conditions that occurred during the sea trials and during the time the slam pressures were recorded. The sea-state with 2.65 m significant wave height and modal period of 6.8 seconds was not recorded as being a tested sea condition, but was simulated in VERES only because, from the sea-trial report, one could assume that some of the sea-state conditions were either missed or multiple sea-states, one more dominant than others, could have been present simultaneously. This assumed and simulated sea-state condition corresponds very closely to several data points in the figure. Even without the assumed condition, the predicted results show a very significant correlation to the measured data for the Catamaran hullform.

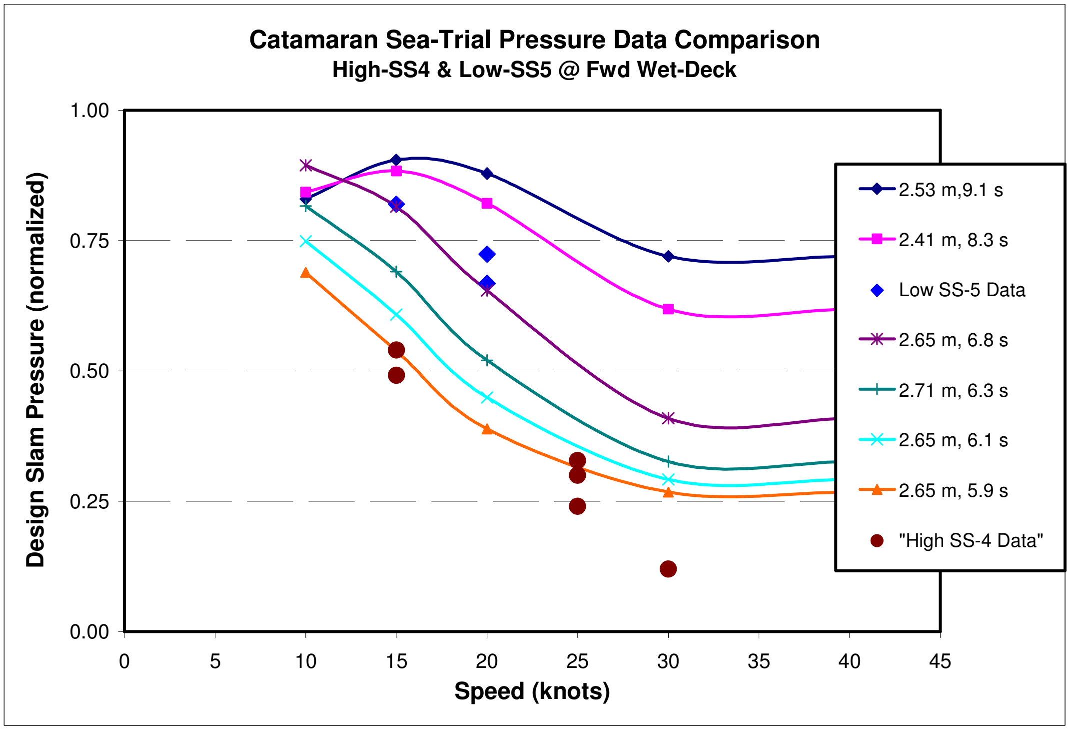

Figure 8: Catamaran Slam Prediction Verification

For the Catamaran hullform, further comparison was also conducted for the longitudinal distribution of vertical bending moment. The vertical bending moment predictions were made for sea-states 3 and 4 as being encompassing of the various sea-states observed during the sea trial. During the Catamaran sea trials, strain data were collected at specific frame locations and later converted to vertical bending moments. The strain data were separately collected for those induced from regular wave-induced bending moments and those induced from whipping moments. Using analytical techniques, phasing information was obtained between the wave-induced and whipping-induced bending moments. Figure 9 compares the vertical bending moments for the wave-induced case only. It should be noted that the exact vessel weight distribution of the Catamaran during sea trials was not known, and weight distribution is a key factor governing the global bending moments. This could be the reason for the difference between the predicted global loads and those obtained from sea trials. Another important factor that can explain the difference is that the predicted bending moments are the significant values, which are the average of the highest 1/3 of all vertical bending moments that can occur in a sea-state in the vessel's lifetime, whereas the sea-trials data is based on a single mission event.

In addition, comparison was also performed for the transverse distribution of vertical bending moment of the Catamaran using the sea-trials data. For the transverse distribution comparison, predictions were made for sea-states 3, 4 and 5. The transverse bending moment data was collected on the Catamaran during a trial run in high sea-state 4 to low sea-state 5 conditions. The comparison is provided in Figure 10. The sea-trials data comparison with the predicted significant vertical bending moment in the transverse direction appears to fare well. It should, again, be noted that even the transverse distribution of global loads is significantly dependent on the vessel's weight distribution.

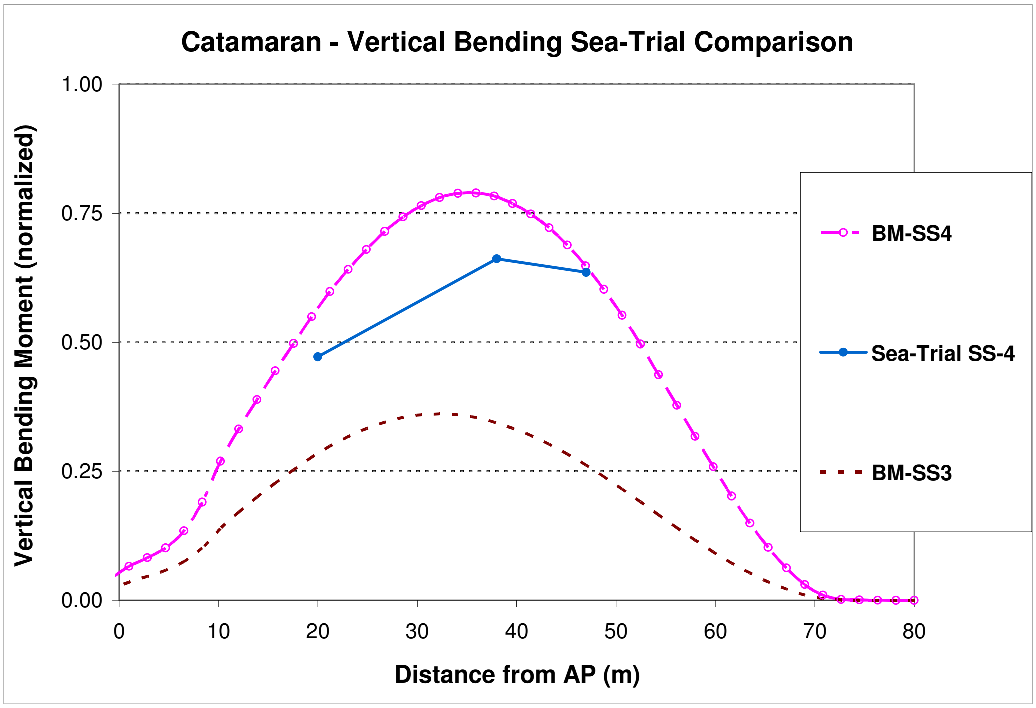

Figure 9: Catamaran Vertical Bending Sea-Trial Comparison

TRIMARAN HULL FORM VERIFICATION

Some limited sea-trial data of the Trimaran vessel was obtained for the verification task. Vessel motion statistics, using the VERES model, were generated for various sea-states and locations that were included in the sea-trial report. Figure 11 compares the predicted vertical accelerations for the bow of the hull at different sea-states with those obtained from the Trimaran sea-trials data. The acceleration values are normalized by the corresponding significant wave height to give the Response Amplitude Operator (RAO) factors for the vertical accelerations. It is important to note that the sea-trials data were not provided in terms of specific sea-states; thus, it is difficult to compare the RAO factors at specific sea-states. However, the sea-trials data, when mapped over the predicted RAO factors at various speeds, do seem to match the trend.

The comparison shows that the predicted motion values, based on the proposed methodology and associated frequency-domain tool, correlate fairly well with the full-scale sea-trials data. It is worth mentioning here that since the exact hullform of the Trimaran was proprietary and not available in the public domain, a close hullform approximation was developed based on design synthesis models and open source literature. The comparison also shows that the sea-trial data follows the same trend in increased vertical acceleration RAO as speed increases with decreasing sea-state.

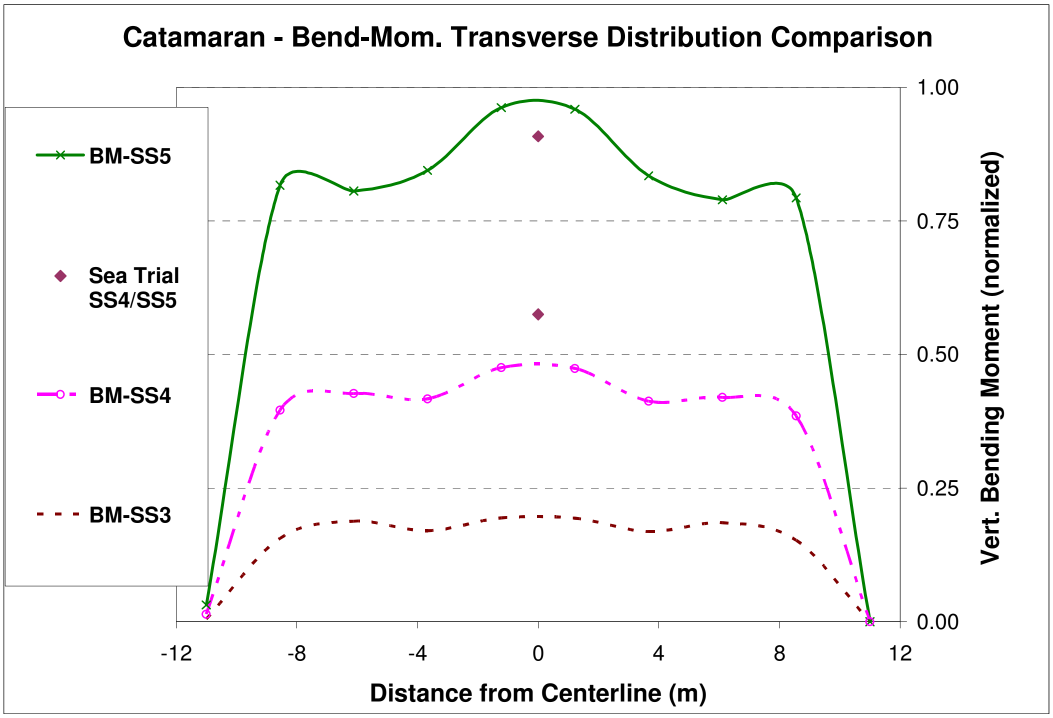

Figure 10: Catamaran Vertical Bending Transverse Distribution Comparison

The vertical bending moment prediction for the Trimaran was conducted for a full-load vessel operating in Pierson-Moskowitz spectrum sea-state 4 conditions. The route/mission prediction model of the Trimaran hullform had loads applied as several discrete masses as a uniformly distributed load along the length of the vessel for the full-load condition. In total, 45% of the weight was distributed evenly along the centerline of the center hull, 7.5% of the weight was distributed along the length of each side hull along their centerlines, respectively, and 20% of the weight was distributed evenly along the length of each wet-deck along their centerlines, respectively.

Figure 12 shows the longitudinal distribution of the predicted maximum vertical bending moments of the vessel at the tested sea-state. The prediction was based on a simulation period of 20 hours in order to be consistent with the sea-trial period of 20 hours. The predicted vertical bending moments were calculated at head seas and all speeds. The longitudinal distribution is along the centerline of the center hull of the vessel. The shape and values from the sea-trial data correlate well with the predicted values. There is a small shift of the maximum vertical bending moment forward for the sea-trial data. This shift could be caused by a difference in the weight distribution and loading condition of the actual tested vessel versus the prediction model, and/or the fact that the prediction model was only a close approximation of the Trimaran hullform.

SUMMARY AND CONCLUSIONS

This paper discusses the efforts conducted and results obtained during the final phase, Phase III, of the overall program of effort to predict rational structural dynamic loads for high-speed multihull vessels. The major part of this final effort was to conduct verification and adequate validation of the final integrated route/mission-dependent structural loads prediction methodology. This was accomplished using available sea-trial and model-test data of various multihull hull forms.

Based on the verification data obtained, the route/mission integrated methodology was executed for the specific operational and environmental conditions under which the data were collected in order to compare the predicted values against the obtained data. The verification of the prediction methodology was accomplished by comparing the predicted motions and loads of the selected hull forms to those data available from full-scale sea trials and model tests.

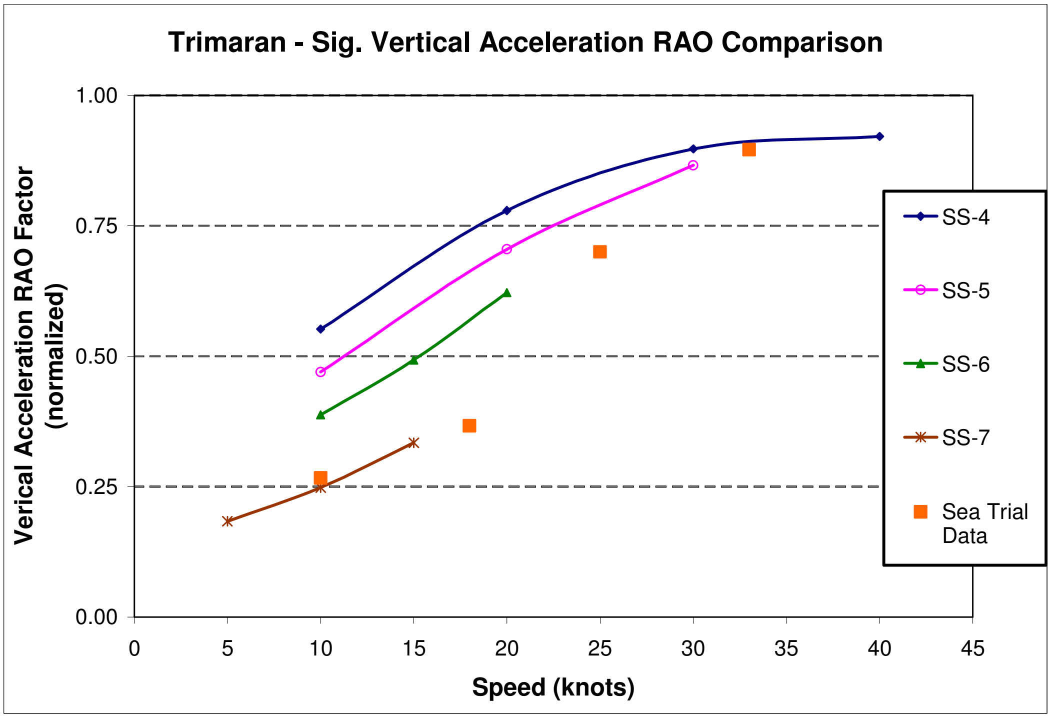

Figure 11: Trimaran Vertical Acceleration RAO Comparison

The comparison of the ship motions statistics to the available verification data provided good correlation, thus ensuring that the simulation models and tool-sets were appropriately analyzing the true hullforms. Excellent correlations were also achieved for the slam pressures measured at the wet-deck of the Catamaran hullform, further providing confidence in the slam prediction methodology. Similar verification was also achieved by comparing the predicted local slam-induced pressure loads on the Deep-V Monohull to the model-test data for the same hull locations and under the same operational and environmental conditions. The predicted results show significant correlation to the trend of measured model-test data for the Deep-V Monohull. In addition, the predicted global hull-girder bending moments were compared to the as-measured values from the sea trials for both the Catamaran and Trimaran, respectively. For both the multihulls, the bending moment comparisons showed excellent correlation and provided further confidence in the prediction methodology and tool-set.

Most often, any differences between the predicted and verification data were attributed to reasons other than the methodology or the tool-set, such as slight differences in the actual hullform being modeled; the differences in the loading conditions, weight distributions and LCG locations; and/or the fact that sea trials only measured the dominant environmental conditions, thereby missing any secondary sea-states or swells. Further, it should be noted that exact matching of the sea-trial or model-test data to a numerical prediction is not possible for a variety of reasons, including variations in the processes and assumptions between the tests and prediction method. However, irrespective of these variations, the predicted loads seem to correlate well with the verification data. As noted earlier, the verification data is considered proprietary and, therefore, when used for comparison, has been sanitized in this paper to maintain its business sensitive nature.

In conclusion, through the course of this CCDoTT program, significant progress has been made in developing a semi-empirical method for quickly predicting lifetime structural global loads, panel loads, and first-order fatigue loads for the design of high-speed vessels, as is desperately needed during early-stage design. It would be fair to state that most of the objectives set out at the beginning of this program of effort were met in due course, and the end product will provide another tool to the ever-challenged engineers and designers of high-performance vessels. The procedure as developed allows recognition of variations in ship mission and can establish loads without the application of excessive factors of safety. This should allow improvements in avoiding "over design" and, thus, save ship weight that can be used for payload and fuel. The procedure can be used for new hullforms, can recognize important ship features, and is highly suitable for early-stage design and, in particular, for parametric comparisons of design options. The process is inexpensive to use, to update and to validate.

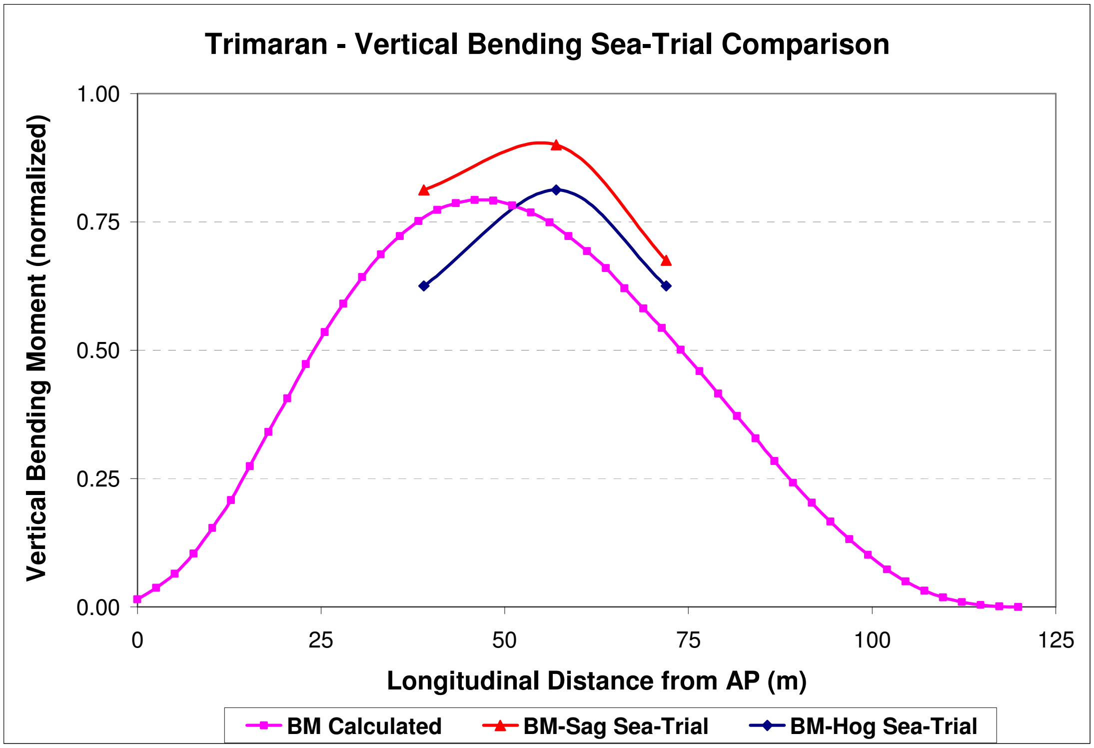

Figure 12: Trimaran Vertical Bending Sea-Trial Comparison

ACKNOWLEDGEMENTS

The authors would like to express their sincere gratitude to the sponsors, CCDoTT and ONR, and specially Stan Wheatley and Steve Hinds (CCDoTT) and Dr. Paul Rispin (ONR) for their continued support and active participation through out the program.

Specific individuals that have made significant contributions to this multi-year program of work, and for which we are very grateful, have included: David Lavis and Greg Morrow (CDIM-BLD); Tom Brady (NSWCCD); Chris Clayson (CDIM-BLD and Digitas); Rebecca Macklem (CDIM-BLD and Vortex Hydro Energy); and Dan Sheridan (DJS Associates).

REFERENCES

Allen, R. G. and Jones R. R. (1978): "A Simplified Method for Determining Structural Design-Limit Pressures on High Performance Marine Vehicles", *Proc. AIAA/SNAME Advanced Marine Vehicle Conference*, San Diego, CA.

American Bureau of Shipping (2007): "Guide for Building and Classing High Speed Naval Craft", ABS, Houston, TX.

Bachman, R. J., Woolaver, D., and Powell, M. (2007): "Sea Fighter (FSF-1) Seakeeping Measurements", *Technical Report NSWCCD-50-TR–2007/010*, Naval Surface Warfare Center, Hydromechanics Dept., Bethesda, MD.

Band, E. G. U. (1980): "Predicting the Unpredictable – Development of Rational Design Loads for High Performance Vessels", *Proc. High-Speed Surface Craft Exhibition & Conference*, Metropole, Brighton, Sussex, UK.

Band, E. G. U., Lavis, D. R. and Giannotti, J. G. (1976): "Prediction of Hydrodynamic Impact Loads Acting on SES and ACV Structures", *Proc. AIAA/SNAME Advanced Marine Vehicles Conference*, Arlington, VA.

Beirne, T.J., Brady, T.F. and Gray, J.A. (2006): "Structural Measurements and Analysis from Sea Fighter (FSF-1) X-Craft Rough Water Trials", *Technical Report NSWCCD-50-TR-2006 Draft-version*, Naval Surface Warfare Center, Hydromechanics Dept., Bethesda, MD.

Brady, T.F., Grassman, J., Rosario, J. and Engle, A. (2005): "Sea Fighter (FSF-1) Structural Instrumentation", *Technical Report NSWCCD-50-TR-2005 Draft-version*, Naval Surface Warfare Center, Hydromechanics Dept., Bethesda, MD.

Chuang, S. and Stavovy, A.B. (1976): "Analytical Determination of Slamming Pressures for High-Speed Vehicles in Waves", *Journal of Ship Research*, Vol. 20, No. 4, pp 190-198.

Faltinsen, O.M. and Zhao, R. (1991): "Numerical Predictions of Ship Motions at High Forward Speed", *Intl. Phil. Transactions of Royal Society of London*, Vol. 334.

Giannotti, J. and Fuller, N. (1978): "Slamming of High Performance Marine Vehicles", *Proc. 11th Annual Symposium, Association of Senior Engineers*, Naval Ship Systems Command, Washington, DC.

Grassman, J. M., Gaies, D. and Lewis, R. (2005): "AUSTAL Hull 260 126-Meter Trimaran Global Structural Response and Seakeeping Trials", *Technical Report NSWCCD-65-TR–2005/11*, Naval Surface Warfare Center, Survivability, Structures, and Material Dept., Bethesda, MD.

Gupta, M., McCain, M. and Eisele, A. (2003): "A Route or Mission-Dependent Approach for the Calculation of Rational Structural Dynamics Loads for High-Speed Multihulls", *Proc. World Maritime Technology Conference*, Society of Naval Architects and Marine Engineers, San Francisco, CA.

MARINTEK Report VERES Version 3.1 – User's Manual (2005): MARINTEK, Trondheim, Norway.

MARINTEK Report SLAM-2D Version 2 – User's Manual (2005): MARINTEK, Trondheim, Norway.

Nigel Gee and Associates (2003): "X-Craft Numerical Sea-keeping Study Preliminary RAO Results", *Technical Report NG427-835-51*, Nigel Gee and Associates Ltd., Southampton, UK.

Ochi, M.K. (1964): "Extreme Behavior of a Ship in Rough Seas – Slamming and Shipping of Green Water", *SNAME Transactions*, Vol. 72.

Sikora, J. (1998): "Cumulative Lifetime Loadings for Naval Ships", *Proc. International Mech. Eng. Congress and Exhibition*, Anaheim, CA.

Sikora, J. and N. Klontz (2005): "Seaway Load Prediction Algorithms for High-Speed Hull Forms", *Proc. Annual Meeting of SNAME*, Houston, TX.

Wang, S., Zhang, L. and Menon, B. (2005): "Seakeeping and Structural Analysis of X-Craft", *Technical Report AA – 05003*, ABS Advanced Analysis Dept., Houston, TX.

Seventh International Conference
On High-Performance Marine Vehicles
Melbourne, Florida, USA
13-15 October 2010

M-SEC: DESIGN AND CONSTRUCTION OF A MODEL MULTIHULL SURFACE EFFECT CRAFT

Brittany Burk, Adam Harris, Michael Melita,
Cameron Roberts, Kaitlin Trump
Florida Institute of Technology
msecfit@gmail.com

ABSTRACT

Undergraduate students within the Department of Marine and Environmental Systems at Florida Institute of Technology have designed and fabricated a model multihull surface effect craft. The focus of the project was to validate a multihull surface effect ship that incorporates a single continuous air cushion. M-SEC hopes to validate a concept which has not been extensively explored before as trimaran hull form concept as surface effect ships are uncommon. Such development of an innovative ship could have innumerable benefits to the military and commercial marine industries.

INTRODUCTION

The intent of this project was to advance the students' working knowledge of hull design and naval architecture, model building, and testing as well as the fundamental theories of hydromechanics. The objective of the project was to build a conceptual model of a trimaran type surface effect ship (SES). The initial hull model was designed using *Maxsurf* and then was further developed in *Rhinoceros*. The M-SEC concept incorporates an SES air cushion to lift the vessel's hull out of the water to improve efficiency and seakeeping characteristics. Testing of the model is currently in progress to ascertain the effectiveness of the surface effect system.

NOMENCLATURE

f	Frequency
V	Vessel Speed
T	Period
λ	Wavelength
M	Vessel Mass
P_c	Cushion Pressure
P_a	Atmospheric Pressure
A_b	Air Cushion Base Area
η_3	Vertical Displacement
P_0	Equilibrium Pressure

ABBREVIATIONS

ACV - Air Cushion Vehicle
ASW - Anti-Submarine Warfare
CNC – Computer Numerically Controlled
CSC – Cannibal Surfboard Company

DMES – Department of Marine & Environmental Systems
ESC – Electronic Speed Control
FIT – Florida Institute of Technology
FRP – Fiberglass Reinforced Plastic
M-SEC – Multi-hull Surface Effect Craft
PVC - Polyvinyl Chloride
SES – Surface Effect Ship

KEYWORDS

Trimaran, Catamaran, Surface Effect Ship, Vacuum Forming, Composite

LITERATURE STUDY

For years, ship builders and naval architects have been exploring innovative designs to build a faster and more efficient vessel. Engineers have created a design that uses air to lift a ship out of the water thus decreasing its wetted surface area. Air cushion technology has been around for decades and researchers are now trying to perfect the inherent advantages that the air cushion has to offer. A surface effect ship is one of the most well known air cushion crafts. Surface effect crafts employ a self-regulating air cushion for lift support; consequently, there is a reduction in wetted surface area and resistance.

A standard SES utilizes a catamaran hull form and two skirts, which are located at the fore and aft of the ship. These skirts are made from a flexible material that forms a seal with the water's surface. The chamber that is created under the ship is called the plenum.

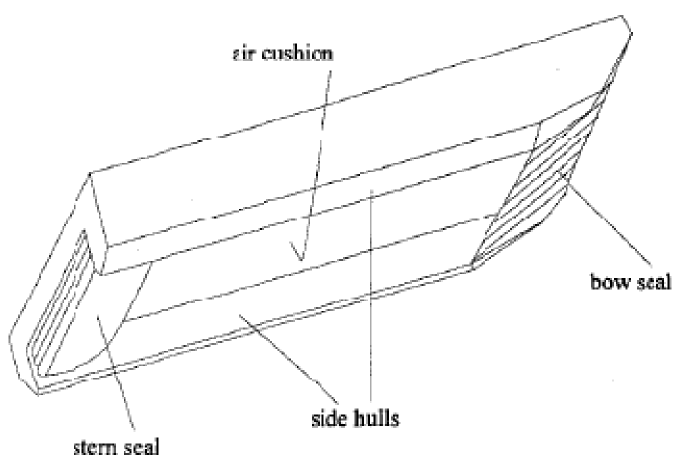

Figure 1: The underside of a surface effect craft (Bertin 1997)

Air cushion vessels that have internal lift, which can be used at rest, are known as "aerostatic" type craft. On these ships, deck mounted air fans force air into the plenum and positive air pressure builds. When there is an excess of pressure in the cushion, air leaks out beneath the edges of the fore and aft skirts, Skolnick (1968). The principle behind this design allows the vessel to "sail along the top of the waves instead of plowing through them" (Mechanical Engineering 2001). While in use, the air cushion is able to support approximately 80% of a vessel's weight, which greatly decreases its draft, Dhanak (2009).

SES hull and cushion designs are constantly evolving. Some designs involve an entirely open and hard plenum chamber, while others include a flexible skirt. There are also cushion designs where the air only exits along the outer edge of the craft. The following picture illustrates only a few of the current lift designs, Skolnick (1968).

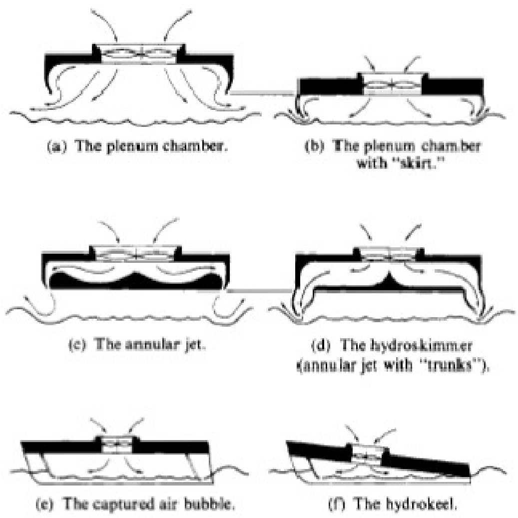

Figure 2: Various lift principles (Skolnick 1968)

As in most machines, the SES comes with its share of drawbacks. One of the designers' main goals is to maintain the stability and ride quality of the SES while decreasing the drag caused by the fore and aft skirts. Air cushion technology is perfect for riding waves with a long wavelength and low frequency. The following formula characterizes a vessel traveling through waves. V is the vessels speed, T is the period, λ is the wavelength:

$$f = \frac{V+c}{\lambda} = \frac{V}{\lambda} + \frac{1}{T} \qquad (1)$$

At low frequencies, the heave and pitch of the vessel are nearly independent of wave height. However, as the wavelength shortens and the frequency increases, the ship's dynamic stability becomes dependent upon wave height, speed, and the design of the air cushion, Dhanak (2009). In order to maintain the highest level of efficiency, the air cushion must react to and contour with the water's surface. Restoring forces produced by the hulls are another large concern that the engineers face. Yet, these restoring forces are much less for a surface effect ship than for a displacement ship. The main reason being the high fineness ratio and the decreased wetted area producing less drag, Skolnick (1968).

There have been many different ideas concerning the skirts method of sealing and air escape rates. The following illustration shows a few main skirt sealing ideas.

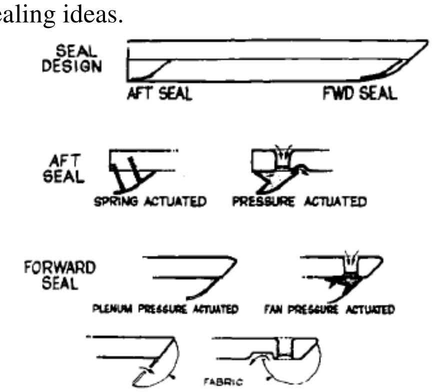

Figure 3: Standard SES seal designs, Skolnick (1968)

The following equation characterizes the vertical displacement forces on a craft:

$$M\frac{d^2\eta_3}{dt^2} = (p_c - p_a)A_b - Mg \qquad (2)$$

When using the above equation, hydrodynamic forces on the vessel's hull may be neglected. In this equation η_3 represents vertical displacement, M is the mass of the vessel, p_c is the cushion pressure, p_a is the atmospheric pressure, and A_b is the cushion's base area, Dhanak (2009). The following equation describes the dynamic pressure within the air cushion:

$$p_c = p_0 + p_a + \mu(t)p_0 \qquad (3)$$

The equilibrium pressure, which supports the mass of the ship, is described by $p_o + p_a$. The final term of the previous equation characterizes the excess pressure created by the lift fans.

$$\rho_c = \rho_a\left(1 + \frac{\mu(t)p_0}{p_0+p_a}\right)^{\frac{1}{\gamma}} \qquad (4)$$

The above equation demonstrates the density within the air cushion when there is no gain or loss of heat. To ensure that the correct data has been calculated we will be comparing our findings to another SES's results, Dhanak (2009).

HULL DESIGN

To construct an accurate model, the first step in M-SEC's design process was to create a digital model in specialized hull design software. *Maxsurf* was chosen as the initial hull design package. The final hull shape was created and imported into *Rhinoceros*. All surfaces were faired and the design was finalized in *Rhinoceros. Mastercam* was utilized to compile machine code to allow the model to be milled on a campus CNC machine.

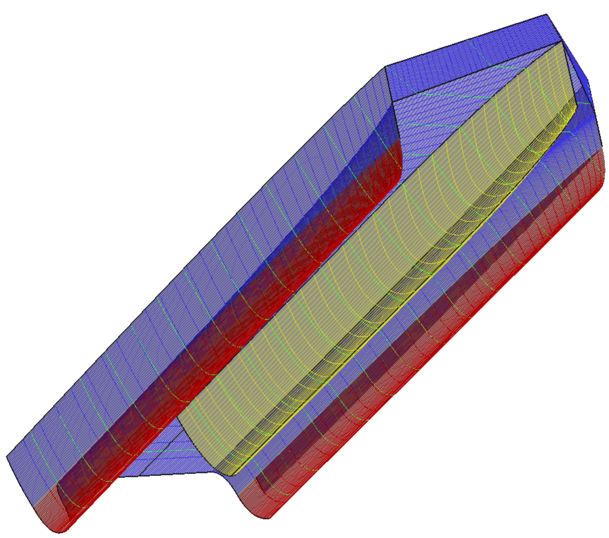

Figure 4: M-SEC wireframe rendering

An important design element was the single continuous air chamber. Dual air chambers in a trimaran surface effect vessel would require separate air systems working together under a computer controlled system to regulate a uniform pressure throughout the craft. It was decided that creating a hull form with a single air chamber would be far more practical in a full size vessel.

A continuous air chamber was attained by shifting forward the central hull by ten inches, or 1/6.6 of the model's length overall as seen in Figure 5. This ultimately creates a U-shaped air chamber where the air cushion can regulate pressure throughout the entire underside of the vessel as shown in Figure 6. Scaling the trimaran model based on a chosen propulsion system gave a required dimension of 66 inches long and 33 inches wide.

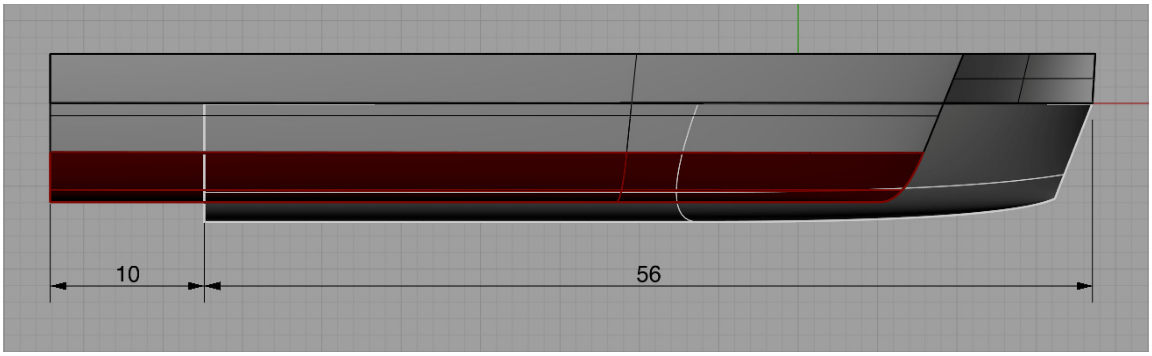

Figure 5: M-SEC Profile View

The main purpose of a surface effect ship is to reduce drag as the vessel moves through the water. The hulls were designed to be narrow, but still wide enough to fit the jet drives and other components. As shown in Figure 5 one may notice the steepness and sharp entry of M-SEC's bows. This not only improves the vessel's ability to slice through rough water, but also allows the skirt systems to be vertically flush with the walls of the hulls ensuring a seal for the air chamber. To improve steering and reduce the possibility of slippage, the central hull was designed to have a slightly deeper draft. This additional draft (evident in Figure 5) acts as a keel.

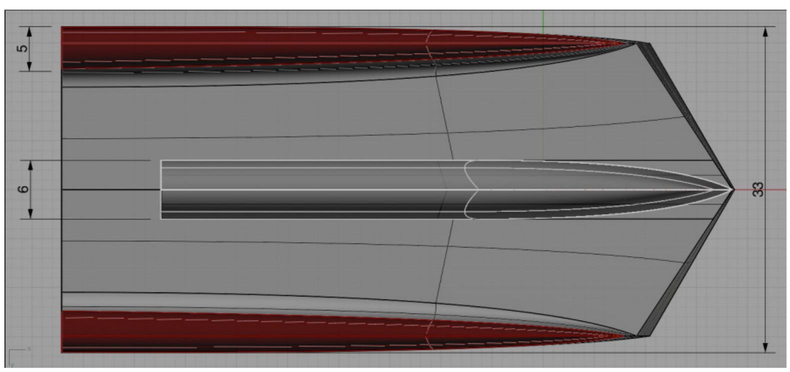

Figure 6: M-SEC Plan View (Rhinoceros)

MODEL SYSTEMS

M-SEC has been fitted with a remote control system to test the trimaran surface effect ship concept. Because of the difficulty of gaining access to a suitable tow tank, the model was set up to be tested locally. Local testing required that the model be capable of producing its own power and lift.

PROPULSION SYSTEM

M-SEC is propelled by dual water jet drives. These drives, produced by Kehrer Modellbau (KMB), provide an economical and durable source of propulsion. Made from machined plastic, these drives are easy to install, easy to maintain, and will not corrode. They are approximately 11.8 centimeters long, 4.4 centimeters wide and 5.0 centimeters high, each weighing 150 grams. Composite propellers spin at approximately 23,000 revolutions per minute within each housing; water is forced from the large intakes on the bottom of the vessel to the outlets. In static testing, each motor produced approximately 30 N of thrust. The drives installed in M-SEC feature forward thrust only, directed by a truncated cone nozzle. Reverse capability is possible with the installation of a different nozzle and an additional control servo. Shown below is a schematic from KMB of the 33-millimeter drive fitted with reversing capability.

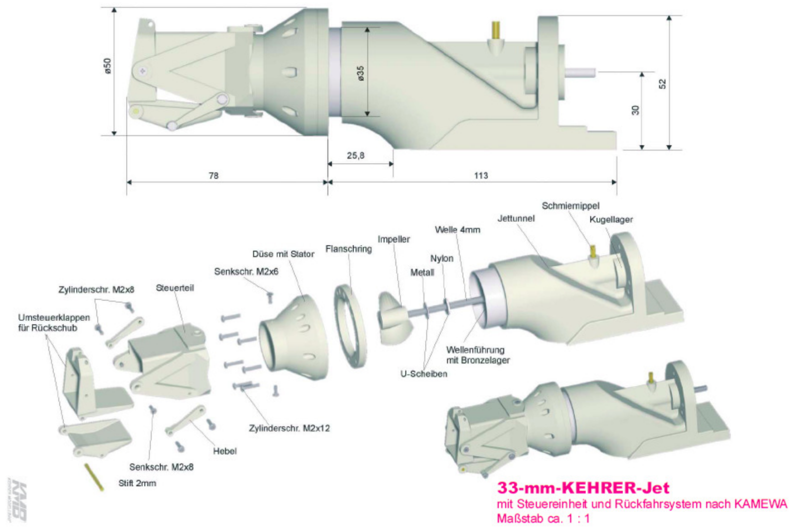

Figure 7: 33mm Kehrer Jet (jet-drive.de)

LIFT SYSTEM

A battery-powered centrifugal blower was selected to provide lift. The blower was reconfigured to fit the requirements of M-SEC with the use of PVC ductwork. The blower was also re-wired for remote operation. Another integral part of the lift system is the skirt structure at the forward and aft ends of the vessel. Spanning the breadth of the aft quarters of the outer hulls is a heavy neoprene “mud flap” skirt. Constructed from numerous layers of two-millimeter neoprene, this skirt allows for low drag and sufficient air retention. Each forward quarter of the vessel is fitted with removable neoprene skirts. These skirts are made removable by mounting them to acrylic plates. These plates are securely screwed to the underside of M-SEC’s deck. When the lift system is activated, air sputters out from underneath the skirts as designed and not from the sides or between individual skirt sections. This design allows for water to pass easily through the skirts while still retaining air pressure within.

CONSTRUCTION METHODS

M-SEC was constructed using an aerospace grade fiberglass and epoxy resin composite. Several different weights and weaves of cloth were used. The specific layers and weights were determined by an industry professional to provide the strongest and lightest final product. Extra cloth layers were added for reinforcement at known high-stress areas such as the ships three bows, along the keels, and surrounding the jet drive intakes.

To produce the initial male mold, sturdy closed-cell insulation foam was assembled in large blocks for CNC milling. Given the size constraints of the campus CNC milling machine, the hull was separated into six sections. Each of these sections was roughly milled to shape and all of them were assembled with the assistance of laser levels. The rough mold was faired and prepared for further use with fairing putty and heavy sanding. A hot wire was used to melt off sections of excess foam not removed in the milling process. This hot wire was also used to roughly shape the topsides of the model. Further hull refinement was performed by a professional surfboard shaper.

The composite construction process was enhanced with a vacuum bagging system to ensure a strong, uniformly saturated matrix of fiberglass and epoxy resin. In this process, all but one of the cloth layers were laid on the underside of mold and the slow-curing epoxy resin was applied to the top layer. The resin was worked through all layers of cloth by hand using aluminum rollers and spreaders. A final lightweight cloth layer was added and a perforated sheet was laid on top to allow excess resin to distribute evenly. The whole assembly was then sealed between two heavy plastic sheets and the air was evacuated using a compressor. The model was held in a 20 psi vacuum for a period of 24 hours to ensure adequate curing time. The plastic seal was then removed from the cured model and the entire vacuum bagging process was repeated for the topsides of the model. Once the entire hull was completed, the surface was sanded and smoothed in preparation for finish work.

FUTURE PLANS

At present the student team is continuing construction on the model to improve aesthetics and functionality. The ultimate purpose of M-SEC is to obtain solid data that validates a trimaran surface effect ship. The students are currently investigating testing methods that could be utilized to obtain such data. Preliminary, non-scientific testing has shown that the surface effect system does provide a significant improvement to vessel mobility. However, irrefutable conclusions cannot be made until reliable test data have been obtained and analyzed.

CONCLUSIONS AND DISCUSSIONS

The intent of this report is to discuss the design and construction process utilized by Florida Tech students to fabricate a model multihull surface effect ship. A trimaran hull form was designed in *Maxsurf* and *Rhinoceros*. A hull model was fabricated using composites and vacuum-bagging methods. Testing of the hullform to ascertain efficiency, seakeeping ability, and lift system effectiveness of a trimaran surface effect craft is currently being conducted.

ACKNOWLEDGMENTS

The students involved with M-SEC would like to thank Dr. Prasanta Sahoo and Dr. Stephen Wood for their guidance throughout this project. The authors would also like to thank the faculty and staff within Florida Tech's Department of Marine and Environmental Systems for their invaluable support. The staff of Florida Tech's Machine Shop and AJ Finan of Cannibal Surfboards was invaluable in the construction of the model hull.

REFERENCES

Bertin, D.; Bittanti, S.; Savaresi, S.M. (1997); "Control of the wave induced vibrations in Air Cushion Catamarans," *Control Applications, Proceedings of the 1997 IEEE International Conference,* pp 749-754.

Dhanak, M. (2009); "Air cushion vehicle response to waves in the surf zone," *OCEANS 2009, MTS/IEEE Biloxi - Marine Technology for Our Future: Global and Local Challenges* , pp 1-8.

Kehrer, Thomas. *Kehrer Modellbau*. Web. 1 May 2010. <http://www.jet-drive.de/>.

"Making full speed: Remanufacturing gives an old vessel a new mission." *Mechanical Engineering-CIME* 123.12 (2001): 62+. *Military and Intelligence Database*. Web. 3 May 2010.

Skolnick, A. (1968); "Transoceanic surface effect ships," *Proceedings of the IEEE* , vol.56, no.4, pp. 700- 712.